



# Acoustic Characteristics of Various Treatment Panel Designs Specific to HSCT Mixer-Ejector Application

*M. Salikuddin, K. Kinzie, D.D. Vu, L.E. Langenbrunner, and G.T. Szczepkowski  
General Electric Aircraft Engines, Cincinnati, Ohio*

## NASA STI Program . . . in Profile

Since its founding, NASA has been dedicated to the advancement of aeronautics and space science. The NASA Scientific and Technical Information (STI) program plays a key part in helping NASA maintain this important role.

The NASA STI Program operates under the auspices of the Agency Chief Information Officer. It collects, organizes, provides for archiving, and disseminates NASA's STI. The NASA STI program provides access to the NASA Aeronautics and Space Database and its public interface, the NASA Technical Reports Server, thus providing one of the largest collections of aeronautical and space science STI in the world. Results are published in both non-NASA channels and by NASA in the NASA STI Report Series, which includes the following report types:

- **TECHNICAL PUBLICATION.** Reports of completed research or a major significant phase of research that present the results of NASA programs and include extensive data or theoretical analysis. Includes compilations of significant scientific and technical data and information deemed to be of continuing reference value. NASA counterpart of peer-reviewed formal professional papers but has less stringent limitations on manuscript length and extent of graphic presentations.
- **TECHNICAL MEMORANDUM.** Scientific and technical findings that are preliminary or of specialized interest, e.g., quick release reports, working papers, and bibliographies that contain minimal annotation. Does not contain extensive analysis.
- **CONTRACTOR REPORT.** Scientific and technical findings by NASA-sponsored contractors and grantees.

- **CONFERENCE PUBLICATION.** Collected papers from scientific and technical conferences, symposia, seminars, or other meetings sponsored or cosponsored by NASA.
- **SPECIAL PUBLICATION.** Scientific, technical, or historical information from NASA programs, projects, and missions, often concerned with subjects having substantial public interest.
- **TECHNICAL TRANSLATION.** English-language translations of foreign scientific and technical material pertinent to NASA's mission.

Specialized services also include creating custom thesauri, building customized databases, organizing and publishing research results.

For more information about the NASA STI program, see the following:

- Access the NASA STI program home page at <http://www.sti.nasa.gov>
- E-mail your question via the Internet to [help@sti.nasa.gov](mailto:help@sti.nasa.gov)
- Fax your question to the NASA STI Help Desk at 301-621-0134
- Telephone the NASA STI Help Desk at 301-621-0390
- Write to:  
NASA STI Help Desk  
NASA Center for AeroSpace Information  
7121 Standard Drive  
Hanover, MD 21076-1320



# Acoustic Characteristics of Various Treatment Panel Designs Specific to HSCT Mixer-Ejector Application

*M. Salikuddin, K. Kinzie, D.D. Vu, L.E. Langenbrunner, and G.T. Szczepkowski*  
*General Electric Aircraft Engines, Cincinnati, Ohio*

Prepared under Contract NAS3-26617  
Prepared under Contract NAS3-27235

National Aeronautics and  
Space Administration

Glenn Research Center  
Cleveland, Ohio 44135

## Acknowledgments

The authors are thankful to D. Cicon and Fred Stern of P&W for their advice and contribution in the selection of liner configurations. The authors recognize the contribution of A. Syed for providing useful guidelines for insitu impedance measurement for bulk absorber panels. The authors are also thankful to F.A. Buck for providing analyses to predict the heat transfer pattern of the panel tray for flow duct test. The authors appreciate the contribution made by H.W. Kwan of BF Goodrich Aerospace (previously Rohr, Inc.) in insertion loss measurement of various treatment panels at Rohr's flow duct facility.

Trade names and trademarks are used in this report for identification only. Their usage does not constitute an official endorsement, either expressed or implied, by the National Aeronautics and Space Administration.

This work was sponsored by the Fundamental Aeronautics Program at the NASA Glenn Research Center.

*Level of Review:* This material has been technically reviewed by NASA technical management.

Available from

NASA Center for Aerospace Information  
7121 Standard Drive  
Hanover, MD 21076-1320

National Technical Information Service  
5285 Port Royal Road  
Springfield, VA 22161

Available electronically at <http://gltrs.grc.nasa.gov>



## **FOREWORD**

This report is prepared by GE Aircraft Engines, Cincinnati, Ohio for NASA-Glenn Research Center (previously known as Lewis Research Center), Cleveland, Ohio under HSR Program, Contract NAS3-26617 & NAS3-27235. Mr. Gene Krejsa was the Project Manager for NASA-Glenn Research Center initially and Dr. James Bridges took over his responsibility at a later date. Mr. Fred Krause was the Project Manager for GEAE. GEAE Program Manager was Dr. R. K. Majjigi.



CONTENTS		
	Topics	Page
	FOREWORD	iii
1.0	INTRODUCTION	1
2.0	TEST FACILITY AND TEST APPROACH	3
2.1	Normal Incident Impedance Measurements	3
2.1.1	Low Frequency Normal Impedance Measurements	3
2.1.2	High Frequency Normal Impedance Measurements	3
2.1.3	Modified High Frequency Impedance Tube to Measure Normal and In-situ Impedance Simultaneously	3
2.1.4	DC Flow Resistance Measurements	3
2.2	Flow Duct Facility with Heated Flow	5
2.2.1	Grazing Flow & Temperature Effects for SDOF Type Liners on <ul style="list-style-type: none"> <li>o In-situ impedance,</li> <li>o DC flow resistance, and</li> <li>o Boundary Layer Profile</li> </ul>	14
2.2.2	Grazing Flow & Temperature Effects for Bulk Absorber (with Facesheets) Type Liners on <ul style="list-style-type: none"> <li>o In-situ impedance,</li> <li>o DC flow resistance, and</li> <li>o Boundary Layer Profile</li> </ul>	15
2.3	Flow Duct Facility for Insertion Loss Evaluation (Rohr)	24
3.0	LINER TEST SAMPLES	29
3.1	Samples for High Frequency Tube Tests	38
3.2	Panels for Flow Duct Tests at ARL	43
3.2.1	Bulk Materials and Facesheets for Bulk Absorber Type Panels	43
3.2.2	Facesheets for SDOF Type Panels	43

	Topics	Page
	3.3 Samples for Insertion Loss Tests at BF Goodrich at Room Temperature	46
4.0	CALIBRATION, TEST PREPARATION, DATA ACQUISITION, AND CHECKOUT	47
	4.1 Calibration of Dynamic Transducers	47
	4.2 Calibration for Cavity Temperature Evaluation	48
	4.3 Test Section Flow and Temperature Profiles	51
	4.4 Preparation of Flow Duct Sample, Flow Duct Test, and Data Acquisition	54
	4.5 Performance Checkout for High Frequency Impedance Tube	59
	4.6 Performance Checkout for Insitu Cavities in the Flow Duct System	59
5.0	HIGH FREQUENCY IMPEDANCE TUBE TESTS	65
	5.1 Normal Impedance for Facesheets Alone	65
	5.1.1 Facesheets for Bulk Absorbers	65
	5.1.2 Facesheets for SDOF Type Liners	76
	5.2 Normal Impedance for Bulk Absorbers	86
	5.2.1 Silicon Carbide Bulk Absorbers	86
	5.2.2 Standard T-Foam Bulk Absorbers	94
	5.2.3 Feltmetal Bulk Absorbers	125
	5.2.4 Different Bulk Absorbers	134
	5.2.5 Bulk Absorbers for Mixer-Ejector Application	134
6.0	FLOW DUCT TESTS AT GEAE	179
	6.1 Data Analysis for Insitu Impedance	179
	6.1.1 Evaluation of Complex Wave Propagation Number in the Bulk Material	179

	Topics	Page
6.1.2	Diagnostic Tests for In-situ Impedance for SDOF & Bulk Absorber Type Liners	185
6.1.3	Rationale for Insitu Impedance Test Procedure & Typical Data	190
6.1.4	Processing & Presentation of Insitu Impedance Data for Ambient Temperature	199
6.1.5	Processing & Presentation of Insitu Impedance Data for Heated Flow Conditions	227
6.1.6	Prelude for Relative Impedance Presentation	240
6.2	Data Processing and Presentation for Boundary Layer Data	245
6.3	Data Processing and Presentation for DC Flow Resistance	245
6.4	Parametric Study of Flow Duct Data	254
6.4.1	Effect of Grazing Flow Mach Number at Ambient Temperature	259
6.4.2	Effect of Grazing Flow Temperature	266
6.4.3	Effect of Facesheet Porosity	282
6.4.4	Effect of Facesheet Thickness	294
6.4.5	Effect of Facesheet Hole Diameter	307
6.4.6	Different Bulk Materials	321
7.0	INSERTION LOSS MEASUREMENT AT BF GOODRICH'S (PREVIOUSLY ROHR) FLOW DUCT FACILITY	327
7.1	Half Inch Deep Panels	327
7.2	Two Inch Deep Panels	341
8.0	ACOUSTIC SUPPRESSION IN THE FARFIELD DUE TO ACOUSTIC TREATMENT OF MIXER-EJECTOR NOZZLES	355
8.1	Internal Noise Extraction Process	359
8.2	Typical Results	372

Topics	Page
9.0 CONCLUSIONS AND RECOMMENDATIONS	397
APPENDIX A	399
REFERENCES	439

## 1.0 INTRODUCTION

HSCT acoustic liner technology development work is a critical element of the HSCT program. This is aimed at designing, developing, and demonstrating promising acoustic liner concepts in scale model aeroacoustic tests and developing an acoustic design methodology for large scale tests. This activity is being coordinated with EPM Program, in terms of providing acoustic design specifications and testing liner material specimens being developed by the EPM Program.

The overall objective of the liner technology program is to develop a design methodology for both bulk absorber (with facesheet) and SDOF (honeycomb with facesheet) type liners to obtain needed acoustic suppression with minimum skin friction loss. Currently, both bulk absorber and SDOF liner designs are being pursued to reduce technical risk (i.e., material, weight, and durability considerations). The liner design methodology contains three basic elements, (1) a correlation of the DC flow resistance and physical properties of a liner at room temperature with its normal impedance at a desired temperature and flow condition, (2) a correlation between the normal impedance and the insertion loss of the liner accounting for liner scaling, and (3) a correlation between liner facesheet properties (i.e., porosity, thickness, hole diameter, and shape of holes for perforated facesheets/or resistivity and type of construction for linear facesheets) and its skin friction loss.

The first correlation determines the required properties of a liner design at room temperature with respect to an established impedance goal for the liner at the actual flow and temperature condition. If for some reason the impedance goal does not yield the desired or maximum acoustic suppression and it needs to be altered, then the corresponding liner characteristics at room temperature can easily be determined without any additional test or analysis. The second correlation determines the acoustic suppression capability of a liner design with known normal impedance, accounting for liner scaling. Finally, the third relationship helps selecting the liner materials, especially the facesheets, which would minimize the friction loss.

The overall approach to arrive at the liner design methodology under CPC program is based on the liner optimization model, which is solely based on the laboratory tests of liner samples, data correlation, and some amount of analytical modeling. Mixer-ejector internal noise, utilized in the correlation process, is extracted as a component source using semi-empirical noise prediction model SMEM (i.e., Stone Mixer Ejector Model) from the measured acoustic farfield data for various mixer-ejector models.

In order to evaluate liner performance for the HSCT program, model ejectors are built and tested in a frequency range up to 80 kHz. Full-scale liners will be tested for frequencies up to about 10 kHz. Temperatures for model scale and full-scale ejectors are of the order of 1000°F or more. To evaluate the liner acoustic properties laboratory tests should be performed in these frequency and temperature conditions. However, laboratory tests are limited to frequencies up to about 20 kHz. The high temperature tests on liner designs are prohibitively costly in the laboratory. However, high temperature DC flow test results for facesheets and bulk materials, evaluated in the laboratory, can be utilized to predict the acoustic characteristics of liner designs at higher temperature conditions. Elevated flow temperatures up to 400°F is achieved in this test program in a flow duct up to a grazing flow Mach number of 0.8 to validate the prediction methods. The intent of the current approach is to extend measurement techniques suitable for applications to the higher frequency and temperature requirements and to utilize the data to develop a liner design methodology.

The development process of liner design methodology is described in several reports. The results of the initial effort (Phase I) of concept development, screening, laboratory testing of various liner concepts, and preliminary correlation (Generic data) are presented in a report “Acoustic Characteristics of Various Treatment Panel Designs for HSCT Ejector Liner Acoustic Technology Development Program”. The second phase of laboratory test results of more practical concepts and their data correlation are presented in this report (Product specific).

A large number of laboratory test results of significant importance are presented in this report. However, limited interpretation of these results could only be done due to the time constraint imposed by HSCT closeout.



## 2.0 TEST FACILITY AND TEST APPROACH

Acoustic laboratory testing at GEAE consists of (1) normal impedance and DC flow resistance measurement at ambient conditions and (2) grazing flow and temperature effects on in-situ impedance, DC flow resistance, and boundary layer profile. Acoustic testing at Rhor (currently BF Goodrich Aerospace) consists of insertion loss measurements in the presence of grazing flow at room temperature.

### 2.1 Normal Incidence Impedance Measurements

**2.1.1 Low Frequency Normal Impedance Measurements:** A low frequency impedance tube with 1.25 inch diameter (described in Ref. 1) is used to measure the normal impedance spectra up to about 6000 Hz at room temperature and pressure conditions. These measurements are conducted at different broadband or discrete frequency noise excitation sound pressure levels to identify the nonlinear behavior of the test samples.

**2.1.2 High Frequency Normal Impedance Measurements:** A high frequency impedance tube of 0.6 inch inner diameter (described in Ref. 1) is used to evaluate the impedance spectra up to about 20 kHz. Either broad band or discrete frequency excitation can be used in this apparatus for impedance evaluation.

**2.1.3 Modified High Frequency Impedance Tube to Measure Normal and In-situ Impedance Simultaneously:** The high frequency impedance tube is modified using additional hardware to measure in-situ impedance of a test sample simultaneously with the normal impedance. This capability provides in-situ data validation, and in-situ impedance measurement technique development, especially for complex test samples like bulk absorbers. Figure 1 shows the modified high frequency impedance tube with the provision of simultaneous in-situ impedance measurement. Provisions are made for test samples with adjustable depth and thickness of the bulk and the facesheet, respectively. The depth of the cavity behind the sample is also adjustable. Two transducers can be mounted in this apparatus, one flush with sample surface and the other at the cavity back wall, allowing the adjustment of sample and cavity depths for in-situ impedance measurement.

**2.1.4 DC Flow Resistance Measurements:** DC flow resistance of bulk samples, facesheets, and their combinations is measured in an apparatus at ambient conditions similar to one described in Ref. 1. Bulk samples of different depths and diameters (1.25" or 2.0") are tested.

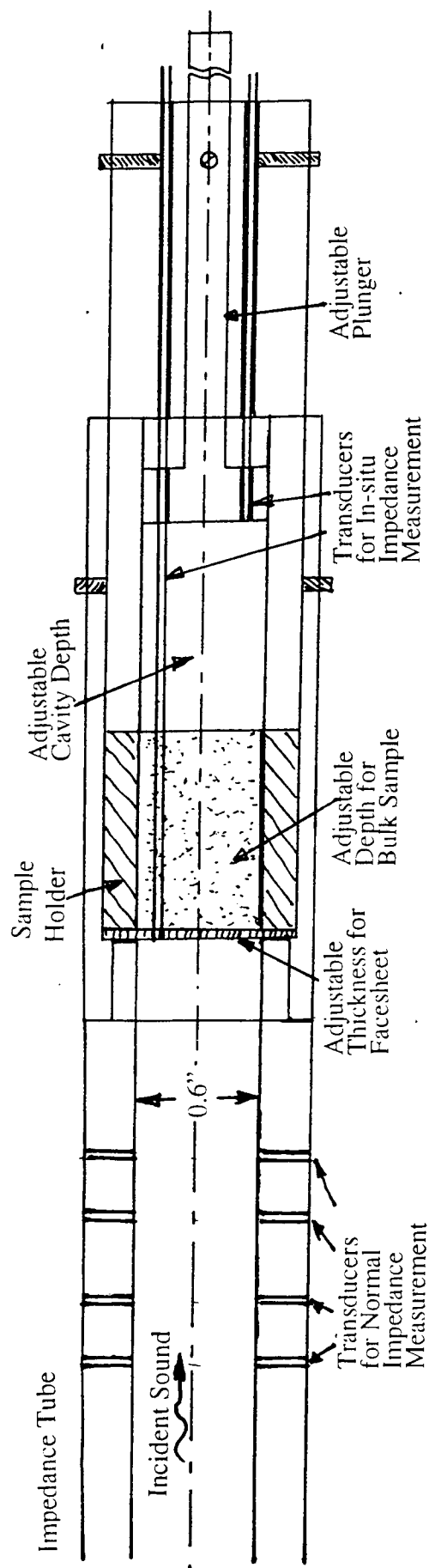


Figure 1. Modified high frequency impedance tube to measure normal incidence impedance and in-situ impedance simultaneously up to a frequency of 20 kHz.

## 2.2 Flow Duct Facility with Heated Flow:

While the grazing flow effects on the in-situ impedance, DC flow resistance, and skin friction loss and other boundary layer parameters (momentum and displacement thicknesses) can be evaluated at the room temperature conditions using the existing GEAE's duct lab flow duct facility, the high temperature effects can not be evaluated. To facilitate this capability a new flow duct is designed and fabricated. This duct is installed in GEAE's Aerodynamic Research Laboratory (ARL) wind tunnel, which has the capability of providing heated flow up to a temperature of about 450°F.

The ARL subsonic wind tunnel facility, shown in Figure 2, is an open jet, continuous flow, ambient wind tunnel with a 2 X 2 feet square section at the throat capable of providing a maximum of approximately 300 ft/sec flow without any blockage effect. The new flow duct is connected to a dual air supply system mounted in the wind tunnel by a sting/strut support (see Figure 3). The centerline of the sting is aligned with the flow duct test section centerline. The cross-section of the sting is 7.0 inches in outside diameter and its length is 93.5 inches. The sting has two flow capabilities with 5.5 lbm/s for each flow stream. Either of the flow passages can be operated from ambient temperature to 860 degrees Rankine; however, only one flow passage can be heated at a time. For the current test program, the flow duct is attached to the 6" diameter outer flow system and the flow through this stream is heated and its rate is increased beyond 5.5 lbs/sec to provide required amount of mass flow.

Figure 4 shows the elevation and top views of the flow duct installed in the 6" diameter flow system of ARL wind tunnel facility. The flow duct has the following four major components:

- #1 Transition Section - From a 6" circular duct to a 4"x5" rectangular duct
- #2 Rectangular duct Of 4"x5" cross section with side glass walled test section
- #3 Sound absorber
- #4 Diffuser

The transition section, transitioning from a 6" circular section to a 4"x5" rectangular section, is 24" long. The circular end is connected to the heated air supply end of ARL wind tunnel facility and the rectangular end is connected to a 4"x5" rectangular duct with three subsections. The first 24" is a straight rectangular duct with four 1" diameter holes, only on the 5" wide top surface, for acoustic driver connection. The next 14" section is the test section. The third subsection is also a 24" long 4"x5" rectangular straight duct connecting the test section in one end and the sound absorber at the other.

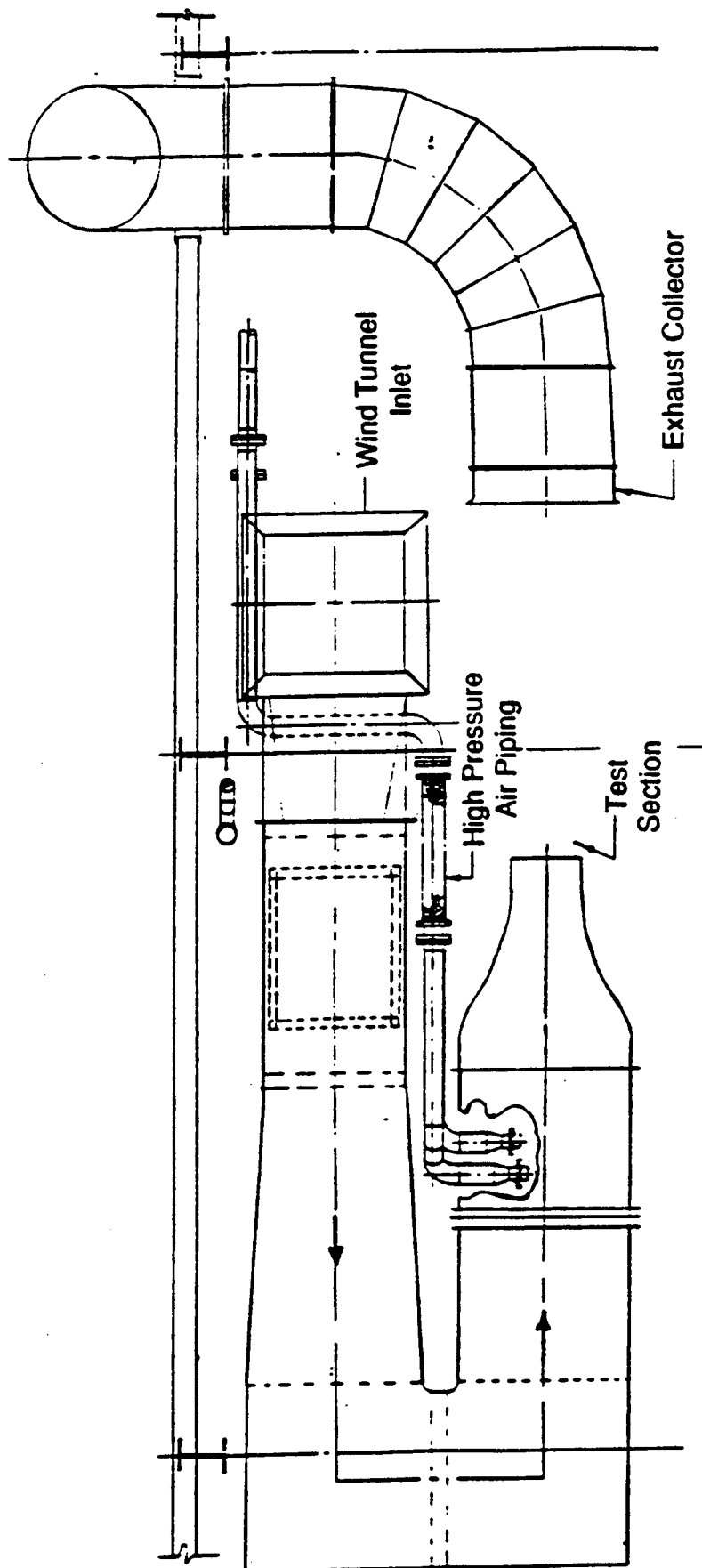


Figure 2. Aerodynamic Research Laboratory (ARL) free-jet wind tunnel.

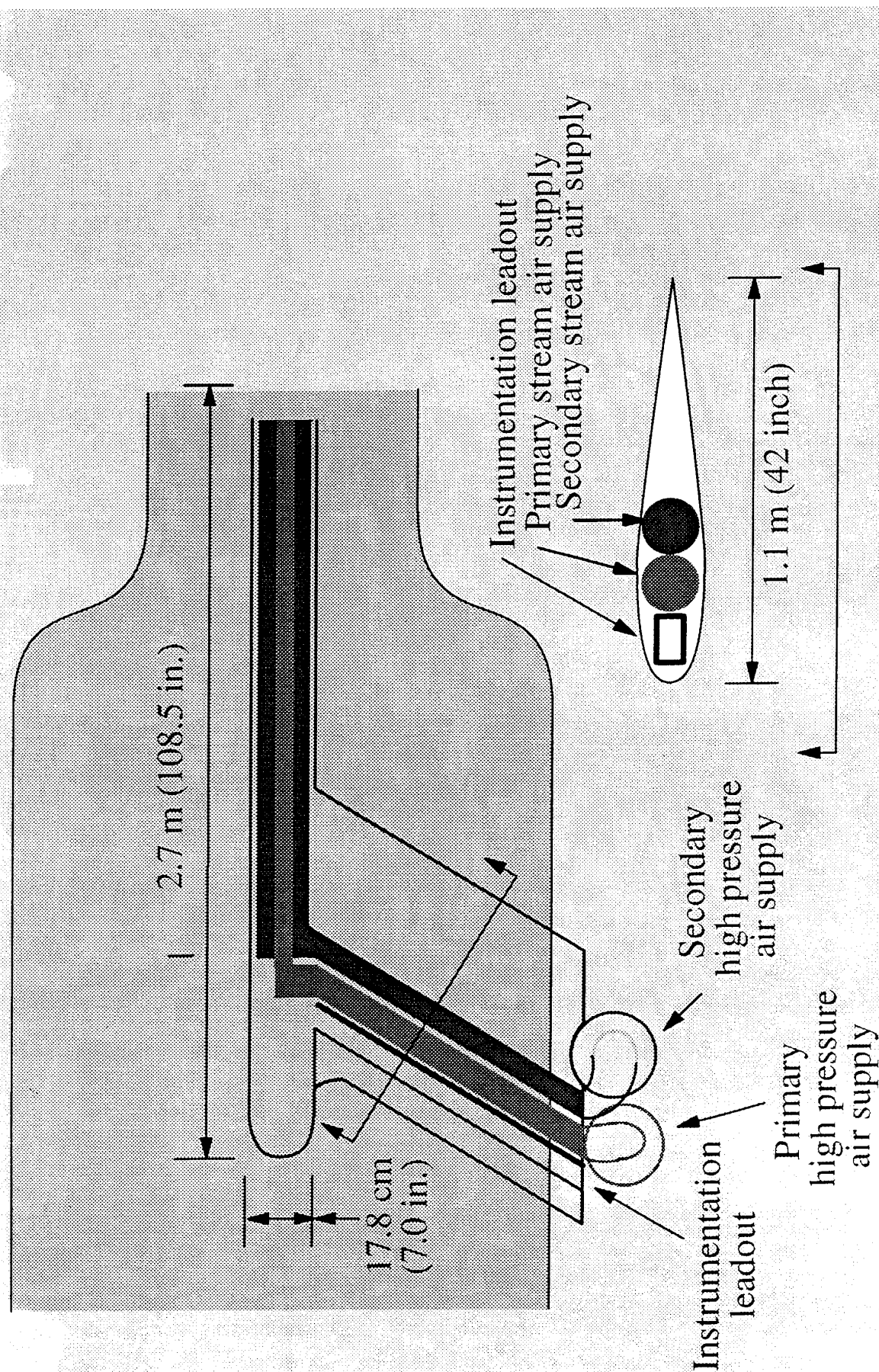


Figure 3. Model support system with dual flow for Aerodynamic Research Laboratory (ARL) free-jet wind tunnel.

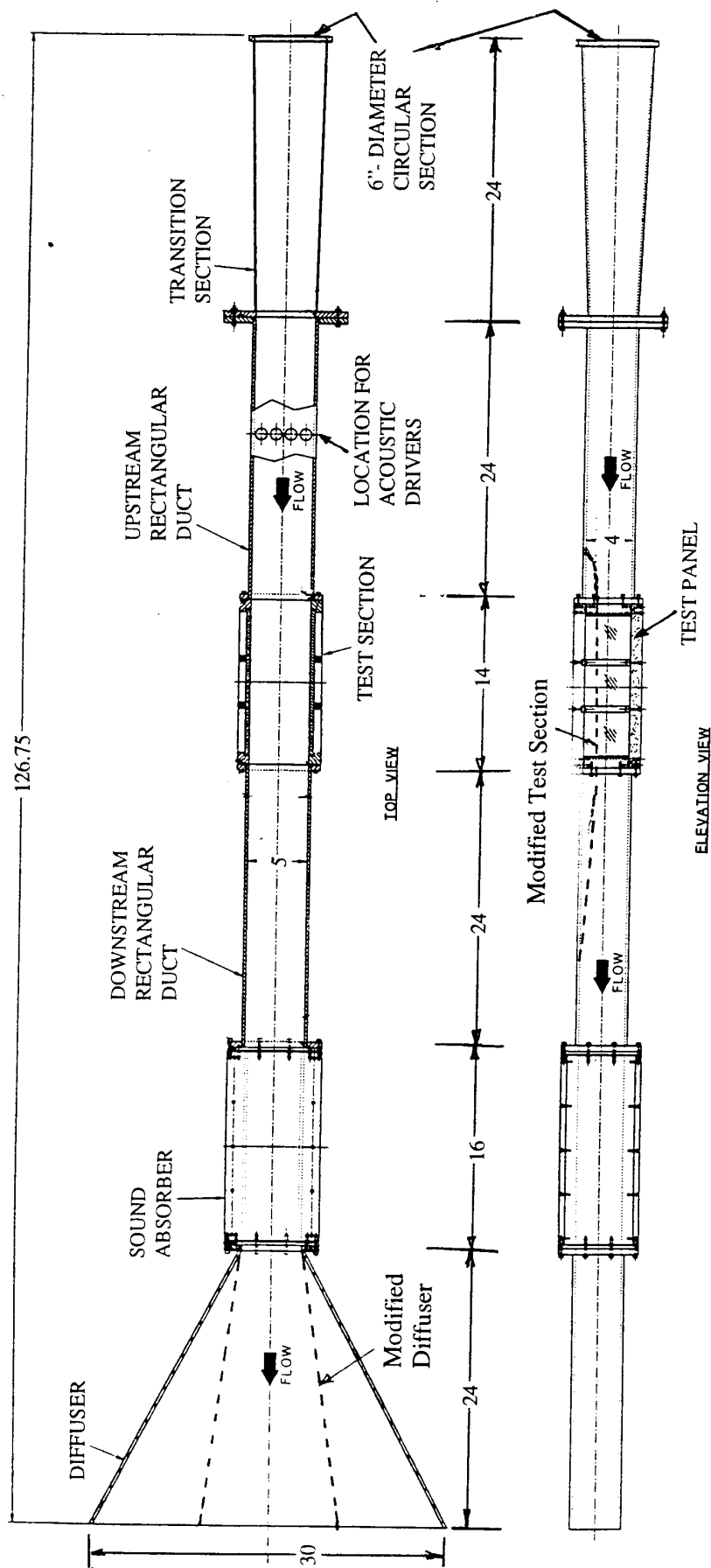


Figure 4. The flow duct apparatus for heated flow and with glass side walls for LDV measurement (all dimensions are in inches).

The 14" long test section portion has two side glass walls, 12"x4" each, for Laser Velocimetry measurements. These glass windows are sealed to prevent leakage. Also, two metallic sidewalls of the same size as the framed glass sidewalls are fabricated. These walls are used for tests not requiring LV measurements. Test samples (14" long) are mounted at the bottom of the test section.

The Sound Absorber is an approximately 16" long 4"x5" (inner dimension) duct with flanges at both ends. Four rigid plated frames to hold 1" deep bulk material sheets (silicon carbide) fabricate this section. The silicon carbide foam is covered with highly porous facesheets. The absorber is connected to the diffuser, the last section of the flow duct. The diffuser is a simple two-dimensional diverging (one direction only) duct with constant 4" (inner) width with standard flange at one end. The sound absorber and the diffuser are essential to absorb and diffuse the flow duct noise generated due to flow and excitation. Thus, the reflected sound field would be minimized, a requirement for acoustic measurements in the test section. In addition, the radiated sound intensity becomes lower for the community. A number of photographic views of the new flow duct system are shown in Figures 6 through 9.

Two problems are encountered during the performance checkout process for the flowduct. The diffuser expansion angle seemed to be much higher than the angle needed for attached expanded flow. Thus, the diffuser is modified by introducing additional plates to reduce the divergence angles to  $7^\circ$  (see Figure 6). The second problem was to achieve uniform temperature in the test section by mixing two flow streams, one heated and the other unheated. Single heated stream was not adequate to produce a Mach number of 0.8 in the test section. Thus, the test section height is reduced to 3" by introducing a properly shaped insert at the upper surface of the duct. The modifications are marked as dashed line in Figure 4 and can be seen in the photographic views, especially in Figures 5 and 9.

Flow duct tests are conducted to evaluate in-situ impedance, DC flow resistance, and boundary layer parameters (i.e., local skin friction coefficient, displacement thickness, momentum thickness, etc.) for bulk absorber and SDOF type liner panels in the presence of grazing flow, up to a Mach number of 0.8, at temperatures up to about 400°F. An adapter (see Figure 5) is made and is connected to the DC Flow cutout of the panel tray. A long copper tube, connected to a flow meter and to a suction pump follows this adapter. Longer copper tube is intended to cool off the hot air before entering the flow meter. Appropriate pressure and temperature measurement probes are installed for DC Flow resistance measurement. A computer controlled traverse system (see Figure 7) is installed on the upper wall of the test section for boundary layer profile measurement using total head pressure and



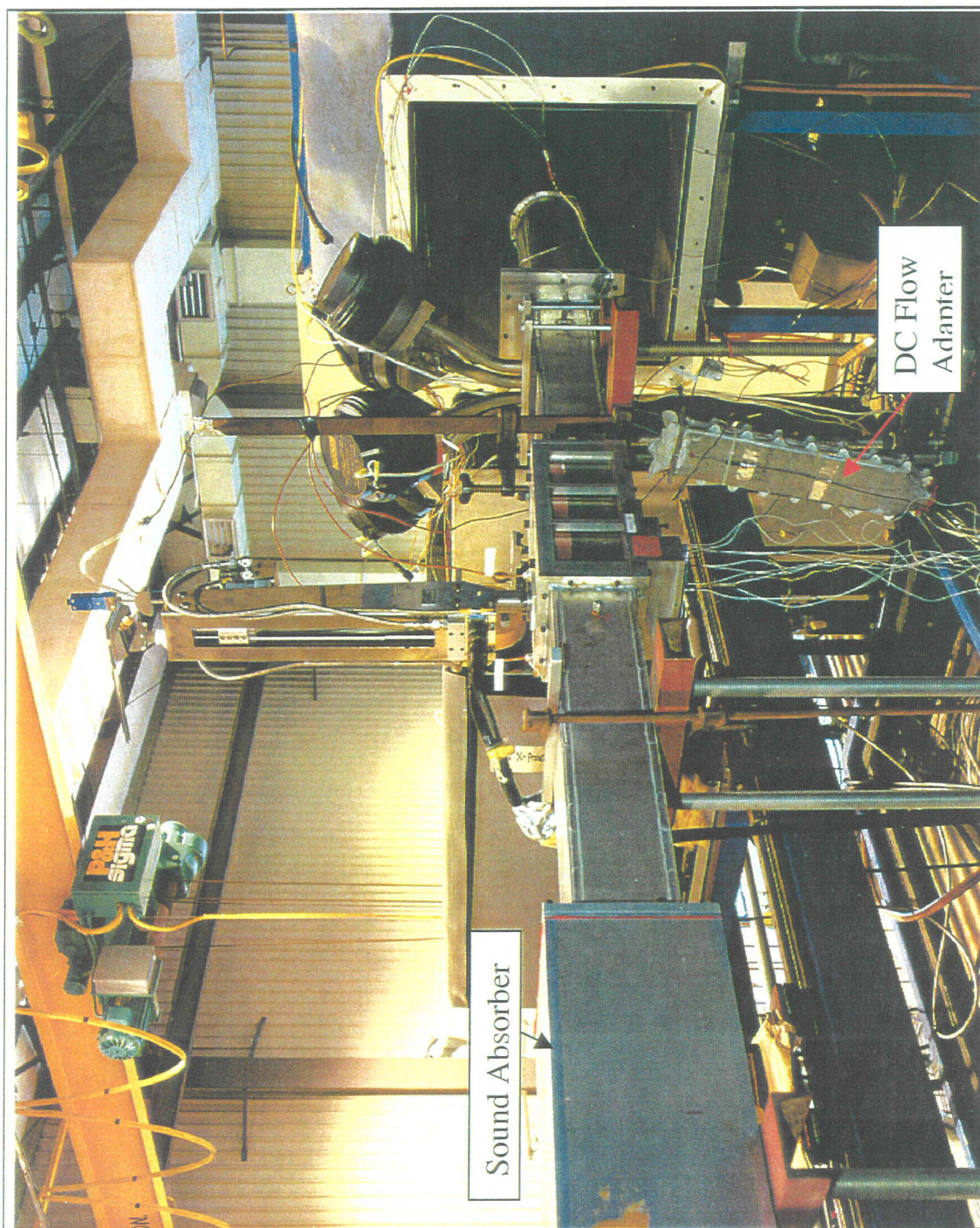


Figure 5. A photographic view of the flow duct with various measurement devices.





Figure 6. Another photographic view of the flow duct.



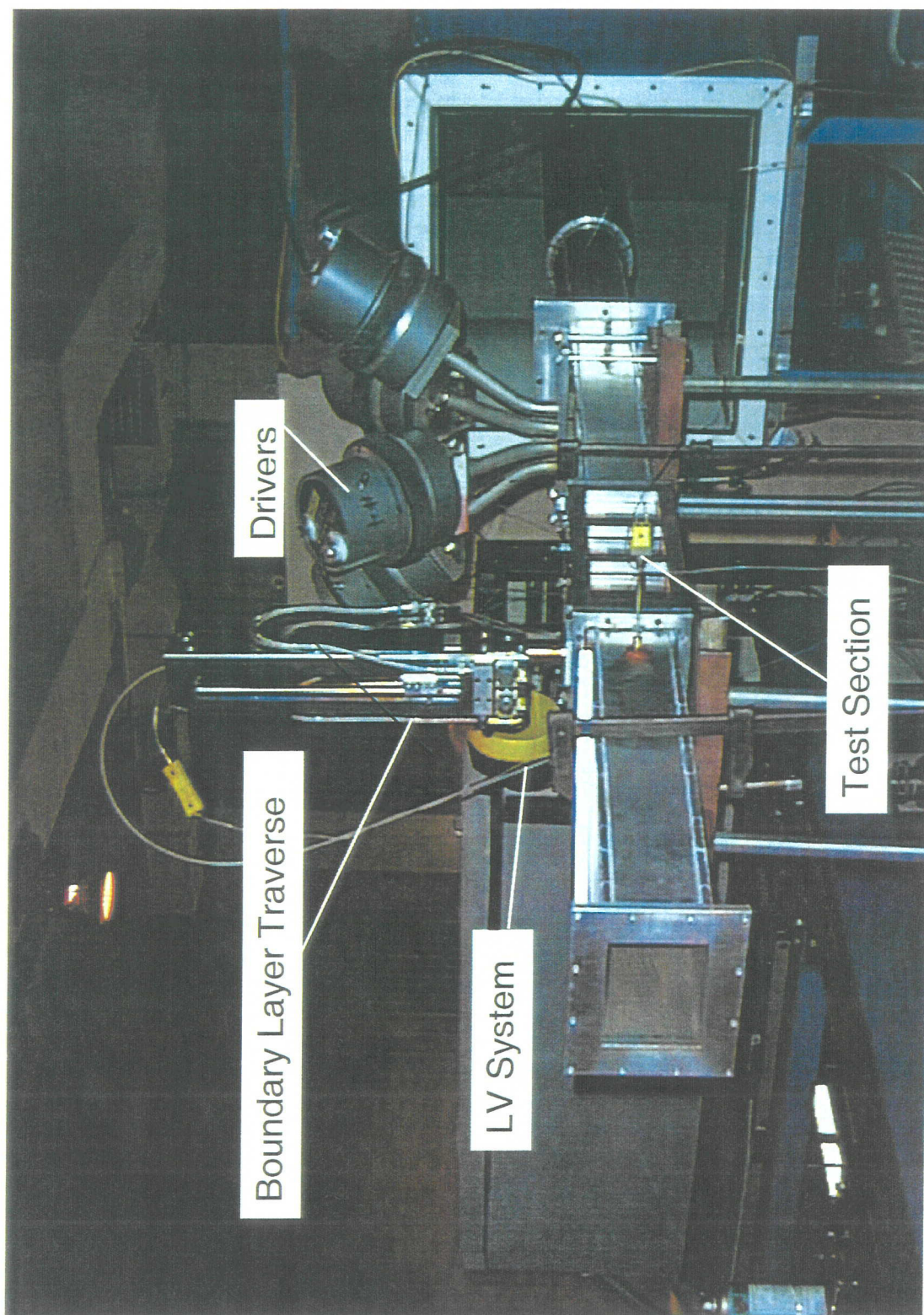


Figure 7. Another photographic view of the flow duct with various measurement devices.



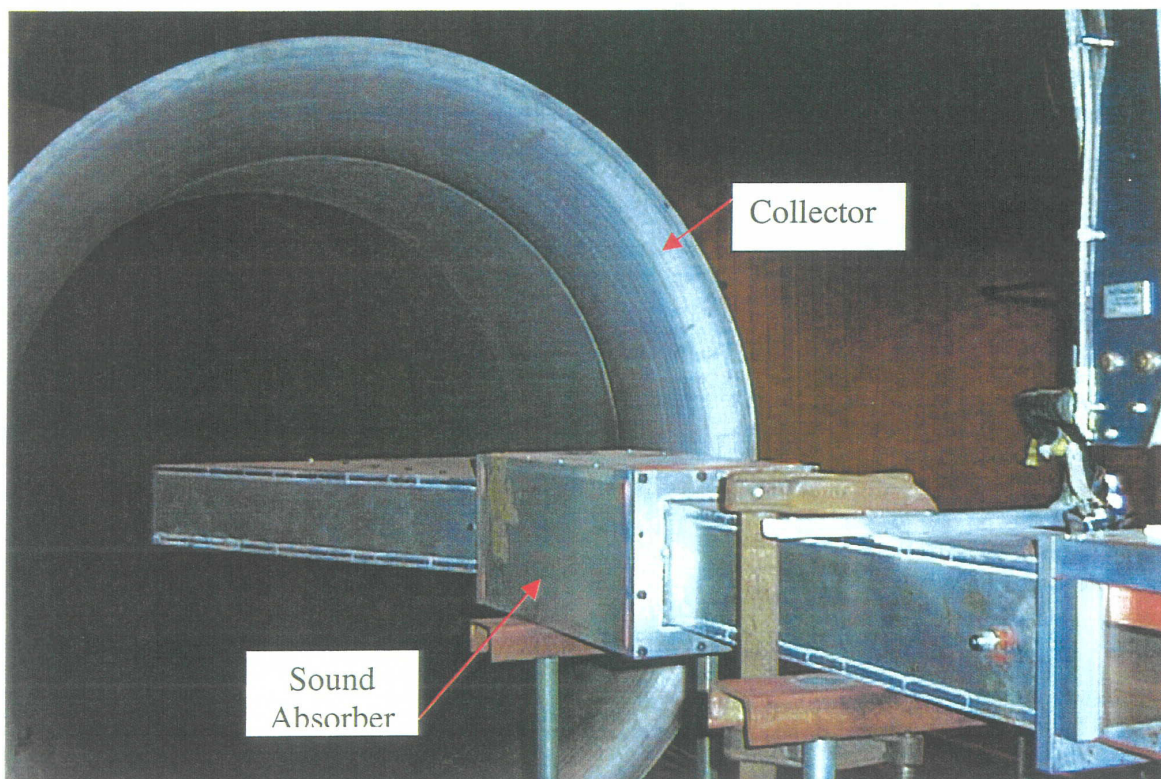
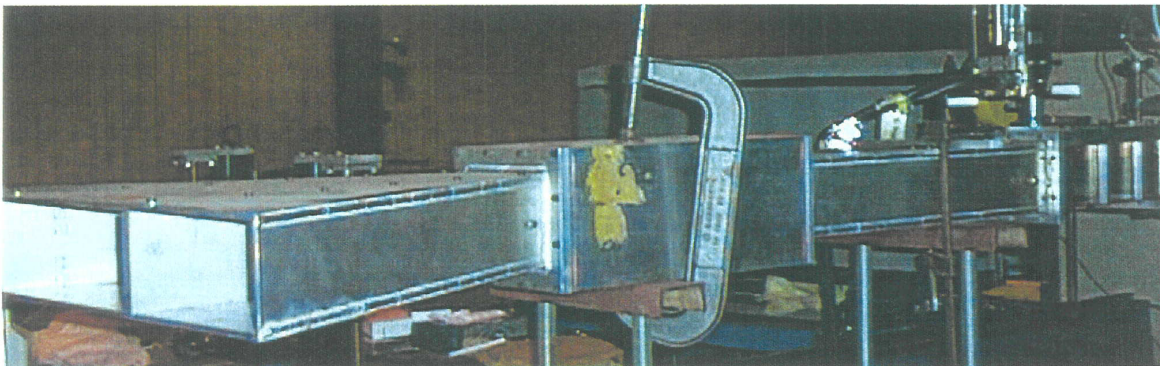
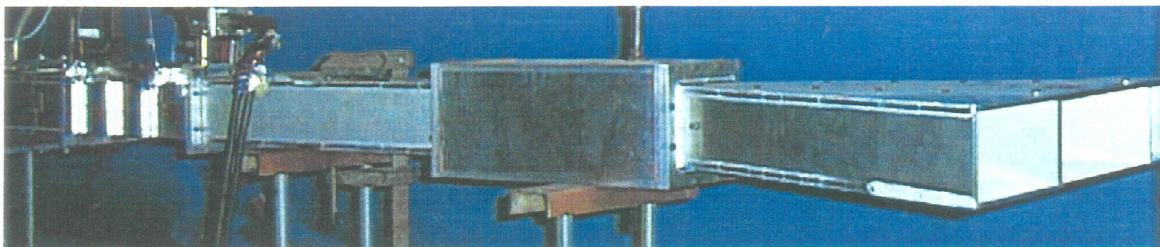


Figure 8. Various photographic views of the flow duct.



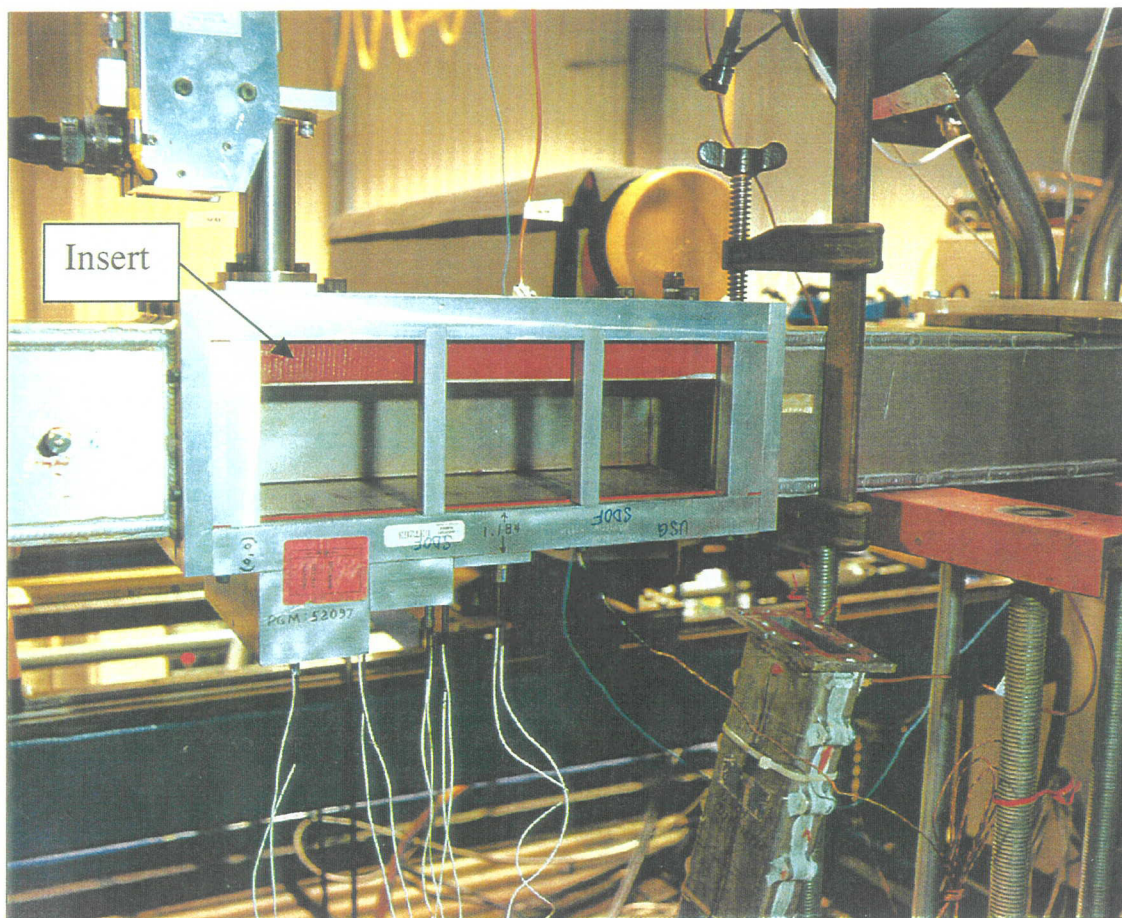


Figure 9. Modified test section of 3.0" height.

temperature probe. Thus, the boundary layer velocity and temperature profiles are measured for each liner panel at a single point. This data is used to evaluate the local skin friction loss and other boundary layer parameters of the panel.

### 2.2.1 Grazing Flow & Temperature Effects for SDOF Type Liners on

- o In-situ impedance,
- o DC flow resistance, and
- o Boundary Layer Profile

Flow duct tests were performed under HSR Phase I program to evaluate grazing flow effects on a limited number of perforated sheets for 1"-deep SDOF type liners (Ref. 1). In-situ impedance results from these tests were acquired up to 12 kHz. The acoustic resistance values were unrealistic at frequencies between 6 and 8 kHz, which was due to the anti-resonance frequency of the cavity. The anti-resonance frequency depends mainly on the cavity depth. At higher frequencies significant randomness was observed for in-situ

impedance, especially for acoustic resistance. Negative resistance values were also observed at some frequencies, especially at no flow condition. For some test panels, the above mentioned anomalies in in-situ results are more severe. Probable causes for such irregularity are the lack of cavity-wall rigidity, possible leakage between the cell and from underneath of the facesheet, and the relatively higher cavity width with respect to higher frequencies, which might have allowed higher order modes to propagate into the cavity.

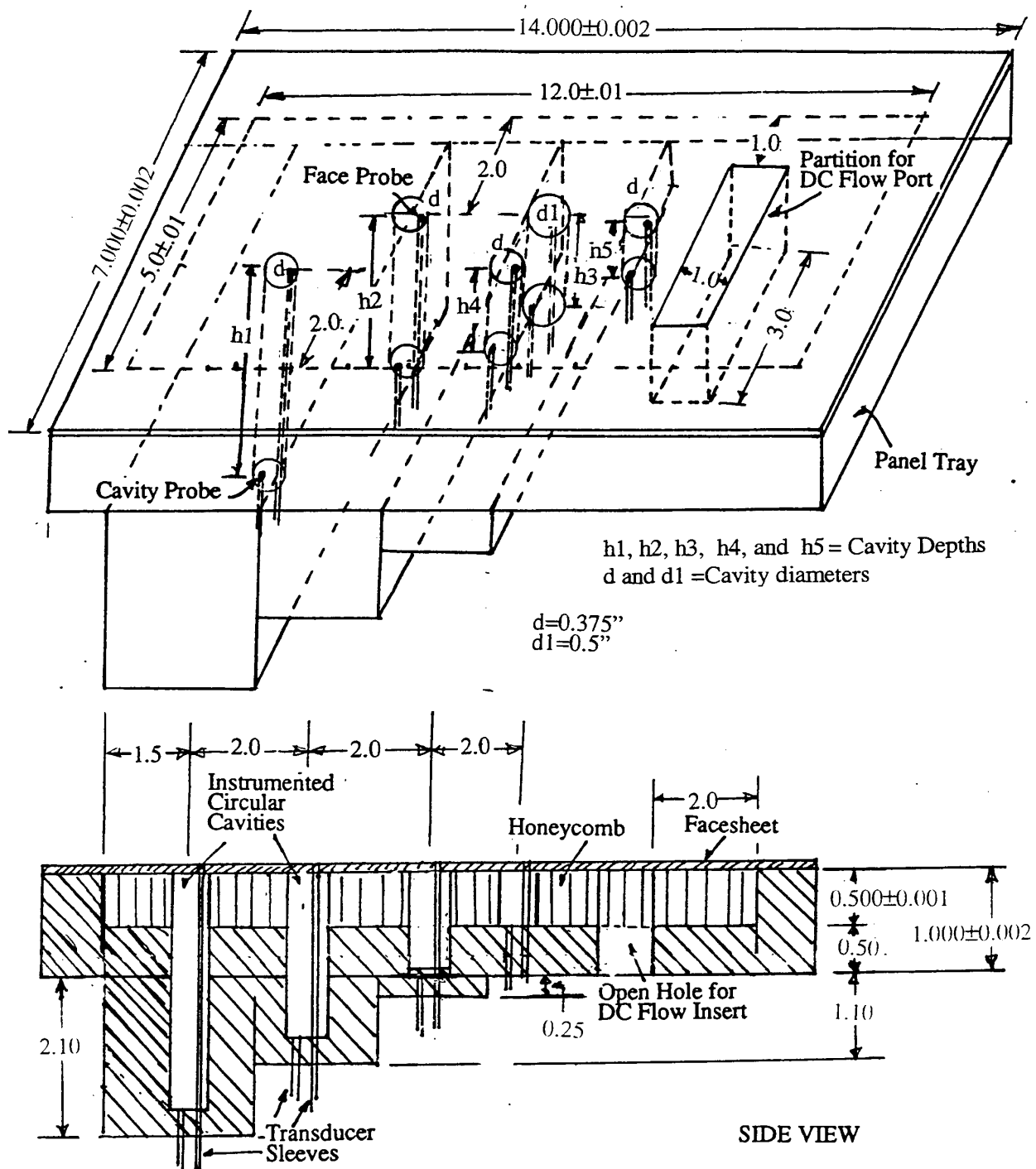
Some of these problems are minimized in the current test program by utilizing more rigid cavity and using cavities with different depth and width. A single panel tray of constant depth of about 0.5", filled with honeycomb, is fabricated (see Figure 10). Five cavities (of circular cross section) with stiffened wall and of different depths and diameters are inserted to the honeycomb filled tray with appropriate transducer sleeves. Partition for DC flow port is also made in this tray as shown in Figure 10. The design is such that different facesheets are easily installed on the panel tray. The facesheet covers the entire tray surface, including the frame area, to accommodate facesheets of different thicknesses. All cavities are instrumented for acoustic measurement. The in-situ results from all the cavities are obtained during a single test. DC flow resistance and skin friction coefficients in the presence of grazing flow are also evaluated. A few of the cavity depths are modified later to change the anti-resonance frequencies. The cavity depths and diameters are listed in Table1.

### **2.2.2 Grazing Flow & Temperature Effects for Bulk Absorber (with Facesheets) Type Liners on:**

- o In-situ impedance,**
- o DC flow resistance, and**
- o Boundary Layer Profile**

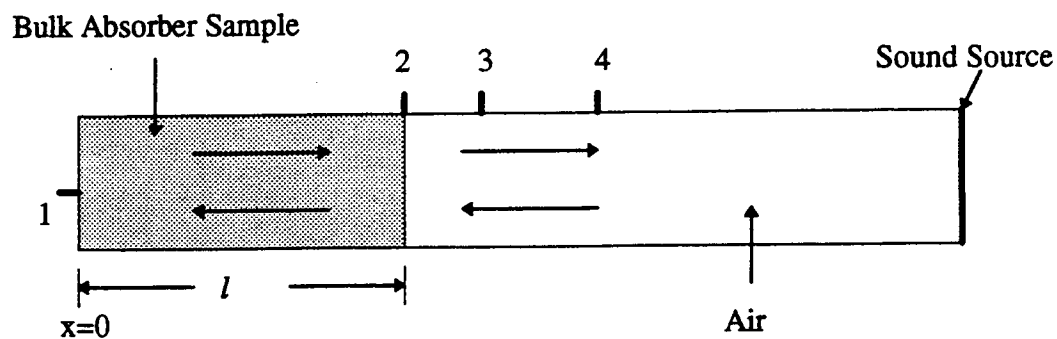
Speed of sound in a bulk absorber is different compared to ambient speed of sound. The acoustic impedance of a bulk is not only a function of its characteristic impedance  $\zeta$ , but also depends on a complex propagation constant  $\kappa$  of the bulk medium. The normal acoustic impedance for plane wave propagation can be evaluated from impedance tube measurements. (see Figure 11(a)). With the assumption of homogeneous medium the acoustic pressure  $p(l,f)$ ,  $f$  being the frequency, in the bulk absorber at  $x=l$  is given by

$$p(l,f) = p(0,f) \cdot \cosh(\kappa l) \text{ or } H_{21}(f) = \{p(l,f)/p(0,f)\} = \cosh(\kappa l) \quad (1)$$

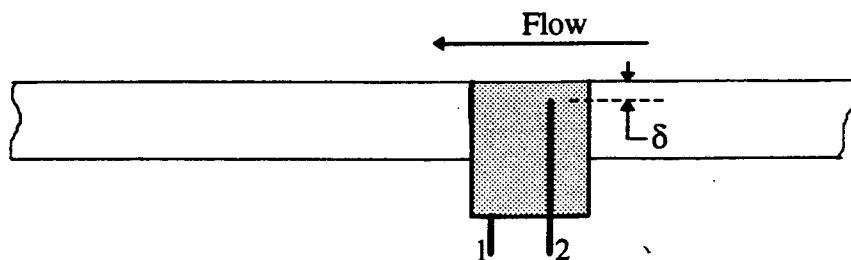


All Dimensions are in Inches.  
A tolerance of  $\pm 0.01$  can be used where not indicated

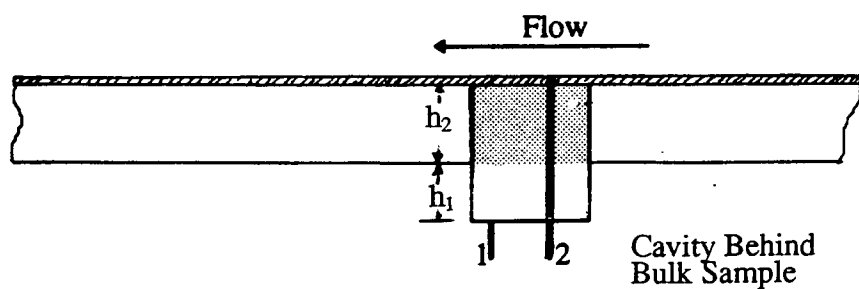
Figure 10. Instrumented SDOF type liner tray with multiple in-situ impedance measurement cavities and open hole for DC flow insert with removable facesheet for flow duct tests.



(a) Normal Impedance Measurement



(b) Propagation Constant Evaluation  
in the Presence of Grazing Flow



(c) In-situ Impedance Measurement for  
Bulk Absorber with and without  
Facesheet in the Presence of Grazing Flow

Figure 11. Various measurement schemes to evaluate acoustic characteristics of bulk absorbers.

Where,  $p(0,f)$  is the acoustic pressure measured in the bulk absorber at  $x=0$  and  $H_{21}(f)$  is the measured transfer function. The acoustic impedance of the bulk absorber is given by

$$Z(f) = \zeta \coth(\kappa l) \quad (2)$$

where,  $\zeta$  is the complex ratio of the characteristic impedance of the bulk absorber material  $\rho_b c_b$  and the characteristic impedance of air  $\rho c$ ,  $\rho_b$  and  $c_b$  being the effective density of the bulk absorber medium and speed of sound in this medium, respectively and  $\rho$  and  $c$  being the density of air and speed of sound in the air medium, respectively. The effective density of the bulk absorber medium is assumed to be the same as air density ( $\rho_b = \rho$ ).  $Z(f)$  can be evaluated using the acoustic pressures measured at locations 3 and 4 in the impedance tube (see Figure 11(a)). Both  $\zeta$  and  $\kappa$  are functions of the frequency  $f$ . In addition, they are functions of the bulk resistivity. In the above expressions, these properties are assumed to be constant throughout the depth of the bulk absorber. Thus,  $\zeta$  and  $\kappa$  can be evaluated by measuring  $H_{21}(f)$  and  $Z(f)$ .

In the presence of grazing flow  $\zeta$  and  $\kappa$ , both are effected. The influence of grazing flow on  $\kappa$  can be determined from a flow duct test as illustrated in Figure 11(b). Two transducers are installed to measure acoustic pressures in the bulk sample, one located at the back wall and the other located at a small distance  $\delta$  from the surface of the sample. The propagation constant  $\kappa$  in the presence of grazing flow can be evaluated from the following expression:

$$H_{21}(f) = \{p(l,f)/p(0,f)\} = \cosh(\kappa(l-\delta)) \quad (3)$$

However, the flow effects on  $\zeta$  can not be measured directly. Thus, the acoustic impedance can be evaluated using the measured  $\kappa$  in the presence of grazing flow and with some assumption of flow effects on  $\zeta$ . An alternate way to account the grazing flow effects is to predict impedance using measured DC flow resistance with grazing flow.

Another important aspect, that needs to be evaluated, is the grazing flow effect on in-situ impedance, DC flow resistance, and skin friction coefficient of bulk absorbers with facesheets. Compared to an SDOF type liner the bulk with facesheets is different with respect to the acoustic propagation and mean flow impacts. The cavity behind the facesheets for SDOF type liners allows the flow and acoustic propagation through the holes in a manner, which is different for facesheets mounted on bulk absorbers. The discharge coefficients of the holes as well as the propagation of sound through the facesheets would be different. In addition, the absence of honeycomb partition behind the facesheets would allow extended



axial propagation of sound. Thus, the in-situ impedance, DC flow resistance, and skin friction coefficients for facesheets mounted on bulk needs to be evaluated.

Figure 11(c) illustrates a procedure to evaluate in-situ impedance of bulk absorber, facesheets mounted on bulk absorber, and the combined values. The bulk sample depth is kept sufficiently small to permit sufficient signal level in the cavity behind the bulk absorber. The in-situ impedance for the facesheets can be evaluated from the measurements made for the bulk sample with and without facesheets. Similar to SDOF type tray several cavities with different depths and widths can be used to evaluate the in-situ impedance for a large frequency range. These results would indicate whether a linear addition of impedances of facesheet and bulk absorber, individually evaluated, is the same as the impedance evaluated by combined structure in the presence of grazing flow. This is an important issue that needs resolution for HSCT liner design.

The insitu impedance  $Z(f)$  for the configuration of Figure 11c can be expressed as follows:

$$Z(f) = - (c_b/c) [p_2(f)/p_1(f)] / \{ \alpha(k h_1) \exp(-ik h_2) - \beta(k h_1) \exp(ik h_2) \} \quad (4)$$

Where;

- $c$  - speed of sound in air at the temperature of interest
- $c_b$  - speed of sound in the bulk absorber medium at the temperature of interest
- $f$  - the frequency (Hz.)
- $h_2$  - the depth of the bulk absorber material
- $h_1$  - the depth of air behind the bulk absorber material
- $k$  - acoustic wave number,  $(\omega/c)$ , in air
- $p_1(f)$  - the acoustic pressure measured at the back wall
- $p_2(f)$  - the acoustic pressure measured at the face sheet (liner surface)
- $\alpha(k h_1) = \cos(k h_1) - i(c_b/c) \sin(k h_1)$
- $\beta(k h_1) = \cos(k h_1) + i(c_b/c) \sin(k h_1)$
- $\kappa$  - complex wave propagation constant (wave number) in the bulk material  $=(\omega/c_b)$

While,  $p_1(f)$  and  $p_2(f)$  are measured during a test, it is also essential that the speed of sound in the bulk absorber medium  $c_b$  be known for the evaluation of  $Z(f)$ . This can be evaluated by measuring the acoustic pressures at the surface and at the back of the bulk absorber without any facesheet and without any air behind it (i.e.,  $h_1=0$ ). In this case the  $c_b$  can be evaluated from the following expression;

$$\cosh(\kappa l) = p_2(f)/p_1(f) \quad (5)$$

Examples of such evaluation are shown later in this report. However, if  $c_b$  is assumed to be the same as the speed of sound in the air the  $Z(f)$  can then be evaluated similar to the SDOF type panels.

Similar to SDOF type panel tray, a single tray to accommodate different bulk materials of varying resistivity with perforated and linear facesheets is designed and fabricated (see Figure 12). Later another tray is also built to expedite the testing. One of the trays is used for silicon carbide and the other is used for T-foam bulk materials. The cavity depths and diameters for these trays are listed in Table 1. The liner trays for SDOF as well as bulk absorber are attached to the flow duct utilizing several holes on the tray frames. The location, size, and the tolerance for these holes are the same for all the trays matching with those on the flow duct test section and are shown in Figure 13. A photographic view of the bulk tray (before mounting the bulk) is shown in Figure 14. Attempt is made to evaluate in-situ impedance of the bulk absorber liner in the presence of grazing flow by evaluating the propagation constant by appropriate acoustic pressure measurements. DC flow resistance and skin friction coefficients in the presence of grazing flow are also evaluated.

Table 1. Cavity depths and diameters for various liner trays.

SDOF Liner Tray

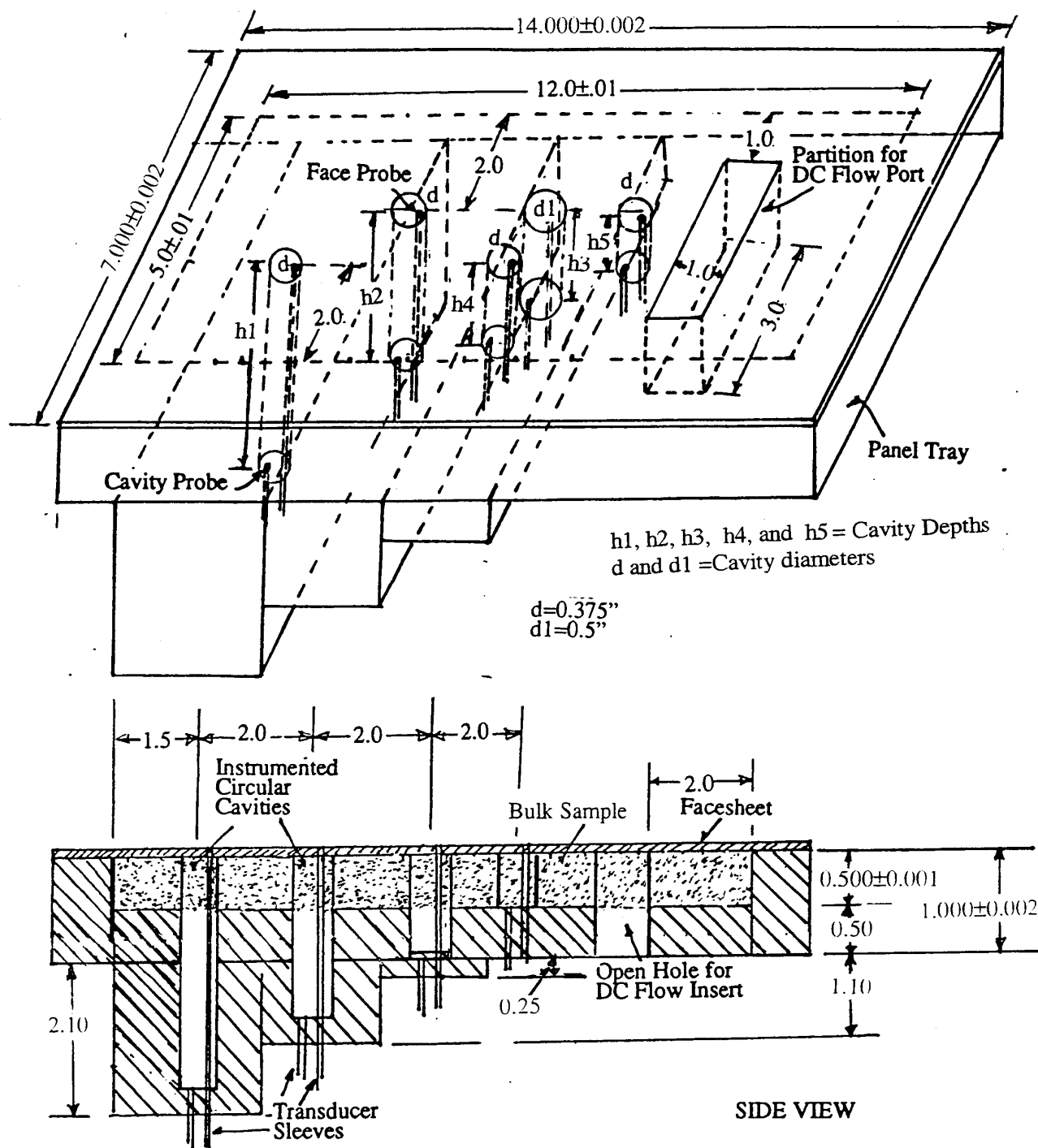
#	Original Depth, in	Modified Depths, in	Cavity Diameter, in
1	2.61	0.7	0.375
2	1.654		0.375
3	1.202		0.5
4	1.184	0.25	0.375
5	0.50		0.375

SiC Liner Tray

#	Original Depth, in	Modified Depths, in	Cavity Diameter, in
1	2.64	0.7	0.375
2	1.656		0.375
3	1.013		0.5
4	1.023		0.375
5	0.504		0.375

T-Foam Liner Tray

#	Depth, in	Diameter, in
1	0.693	0.375
2	1.661	0.375
3	1.018	0.5
4	1.01	0.375
5	0.495	0.375



All Dimensions are in Inches.  
A tolerance of  $\pm 0.01$  can be used where not indicated

Figure 12. Instrumented bulk absorber type liner tray with multiple in-situ impedance measurement cavities and open hole for DC flow insert with removable bulk material and facesheet for flow duct tests.





Figure 14. Instrumented bulk absorber type liner tray with multiple in-situ impedance measurement cavities and open hole for DC flow resistance measurement.

### **2.3 Flow Duct Facility for Insertion Loss Evaluation (Rohr):**

The insertion loss is evaluated utilizing a diffused acoustic field in the flow duct, generated by a reverberant chamber. In this situation, the identity of individual modes is highly diminished and a more uniform sound field propagates through the flow duct. Such a facility exists at BF Goodrich Aerospace, previously known as Rohr Inc. (Ref. 1)). The new panels, tested in this facility, are based on simplified designs of replaceable bulk and facesheet for bulk absorber type and replaceable facesheet for SDOF type liner panels. Two treatment trays, one for bulk absorber type and the other for SDOF type, without the provisions of in-situ impedance and DC flow measurements, are fabricated for insertion loss measurement at room temperature. Two additional rectangular rings of 0.7" and 1.5" deep are fabricated to be attached to the bulk tray, so that the bulks of 1.2" and 2.0" deep are also be tested. Schematics of these trays and rings are shown in Figures 15 through 18.



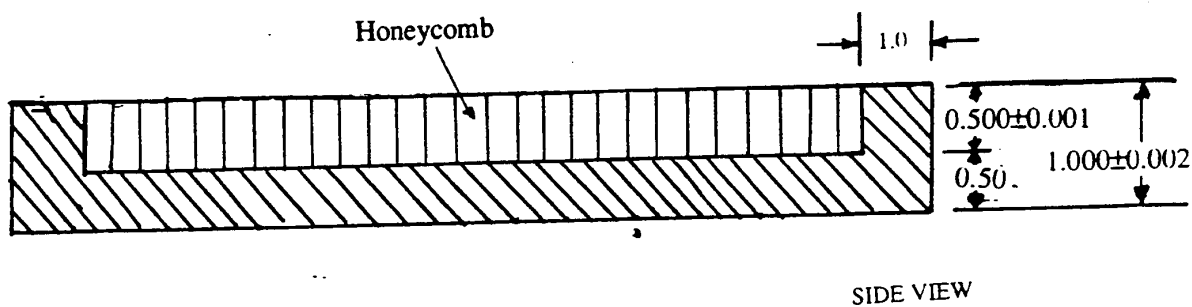
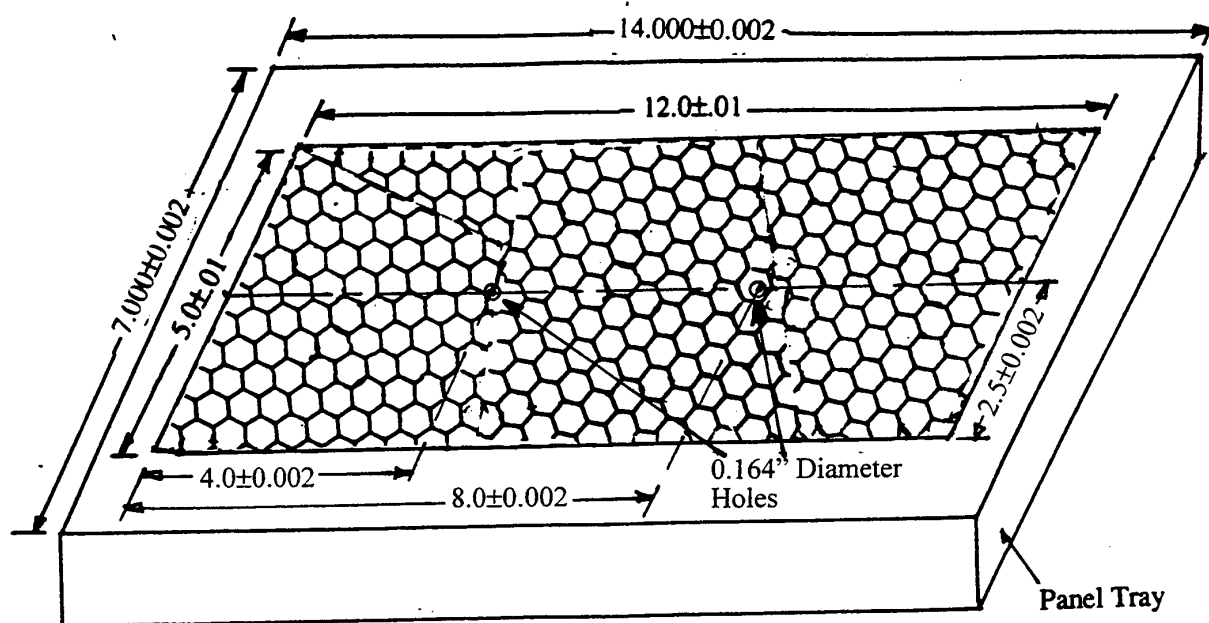
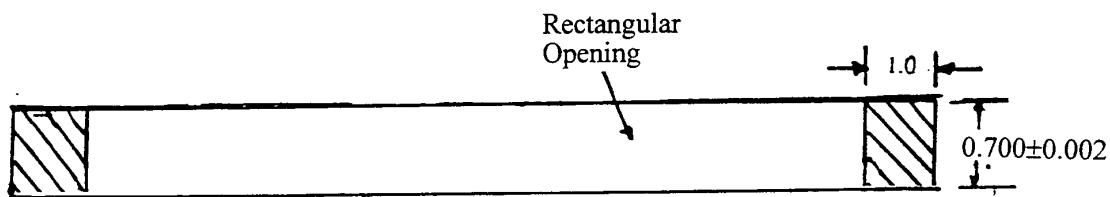
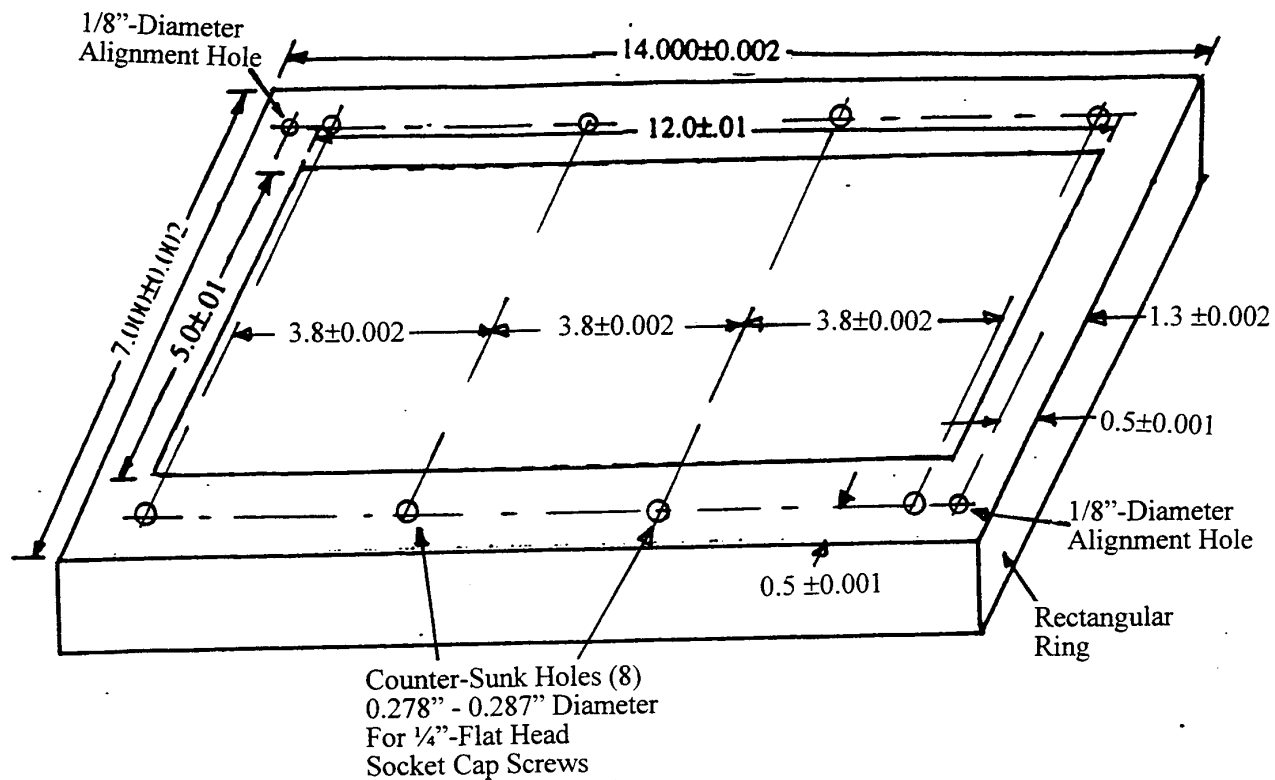


Figure 15. Try with bonded honeycomb for SDOF type treatment panels for insertion loss measurement (all dimensions are in inches).



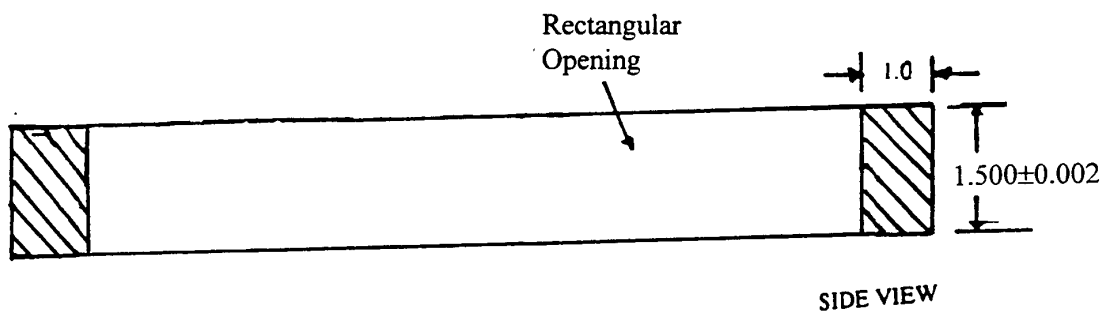
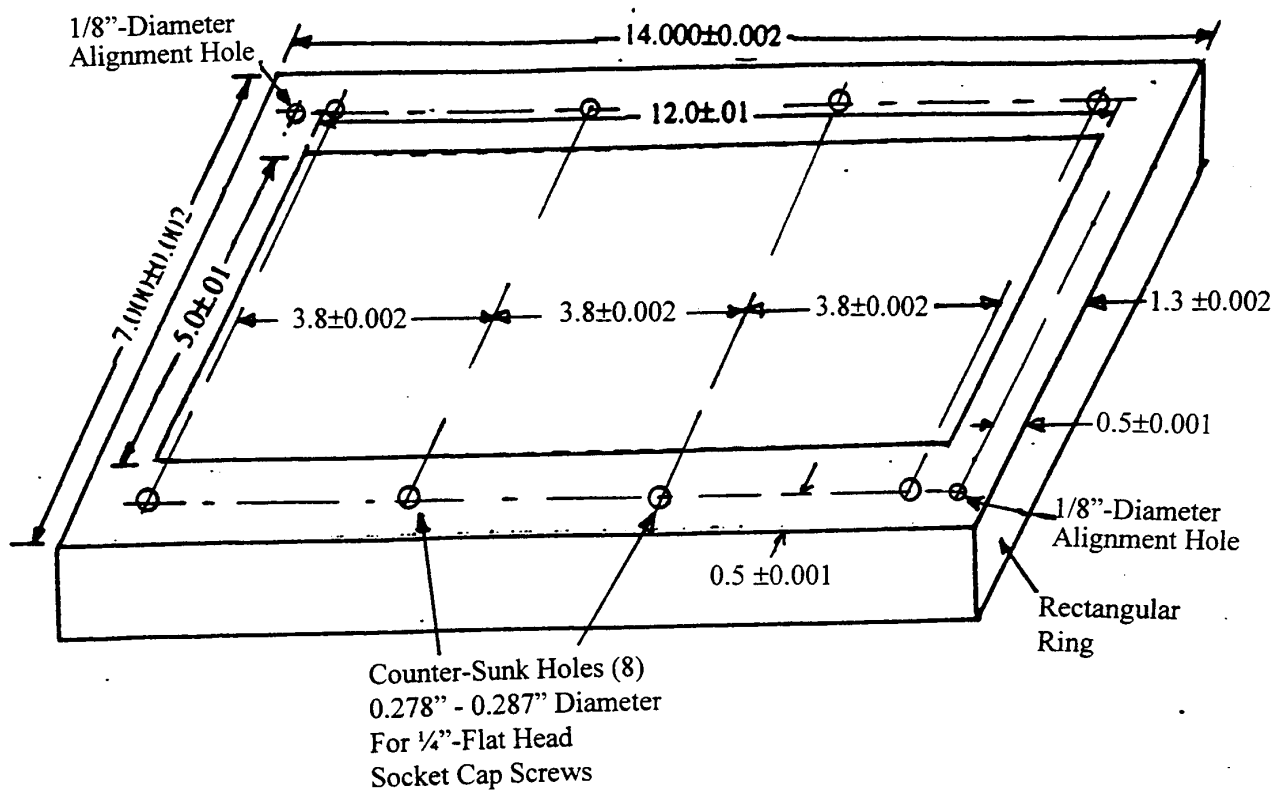




SIDE VIEW

Note: 1.25" long 8 flat head socket cap screws required to attach the ring to the tray of Figure 16 to increase the cavity depth to 1.2".

Figure 17. Rectangular ring of 0.7" deep to match the tray of Figure 16 for insertion loss test of 1.2" deep bulk absorber type panels (all dimensions are in inches).



Note: 2.0" long 8 flat head socket cap screws required to attach the ring to the tray of Figure 16 to increase the cavity depth to 2.0".

Figure 18. Rectangular ring of 1.5" deep to match the tray of Figure 16 for insertion loss test of 2.0" deep bulk absorber type panels (all dimensions are in inches).

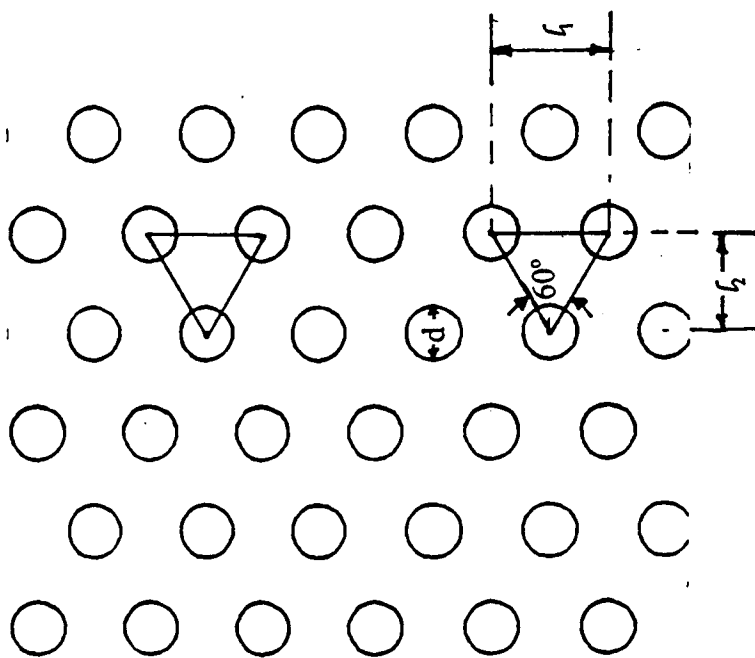
### 3.0 LINER TEST SAMPLES

Tests are conducted to measure normal impedance in the high frequency impedance tube and in-situ impedance, DC flow resistance, and boundary layer profiles in the flow duct at GEAE's ARL in the presence of grazing flow for acoustic panels of bulk absorbers with facesheet and SDOF type. Additional tests to measure insertion loss at room temperature with grazing flow Mach number up to 0.8 for selected liner designs are conducted at BF Goodrich Aerospace flow duct facility. In addition, tests are conducted to measure DC Flow resistance and normal impedance for several samples using static DC Flow rigs and low frequency impedance tube.

In these tests the effect of various physical characteristics of liner components on the measured parameters are evaluated. For bulk absorber with facesheet the bulk and the facesheet properties are varied. For the bulk the type of material and the resistivity are varied, whereas, the facesheet properties varied include perforates with circular, hexagonal, and slotted holes and linear facesheets. Porosity, hole diameter and thickness are varied for perforates with circular holes.

Facesheets of 14"x7" size are used for flow duct test panels, whereas, the facesheets for impedance tube tests are basically circular pieces of 0.94" diameter. Figure 19 shows the hole pattern and the definition of various parameters for perforated sheets with staggered circular holes. Some of the facesheets used for bulk absorber panels with staggered circular hole patterns of different porosity and hole diameters are shown in Figures 20 through 23. While the spacing between circular holes on a facesheet vary along its perimeter, the spacing remains the same for hexagonal holes. This would help in increasing the porosity by maintaining the required mechanical strength of the facesheet. Facesheets of hexagonal hole patterns for bulk absorber panels are shown in Figure 24. The slotted hole patterns for the facesheets are shown in Figure 25.

The parametric variation for bulk and the facesheet are listed in Table 2. Hexagonal facesheet parameters are listed in Table 3. Additional facesheets with staggered circular holes for bulk absorber type panels are procured at a later date to expand the range of various facesheet parametric variations (see Tables 4 and 5). Additional bulk materials of 1.2" and 2" deep are also procured for impedance and DC flow resistance tests (see Table 6). For SDOF type liners the facesheet properties (i.e., porosity, hole diameter, thickness, and hole shape) are varied. Resistivity is varied for linear facesheets. The specific parametric variation of the facesheets is listed in Table 7. Test samples for high frequency impedance tube and flow duct



(a) Staggered Circular Hole Pattern

$d$  = Hole Diameter

$l_1$  = Side of the Triangle

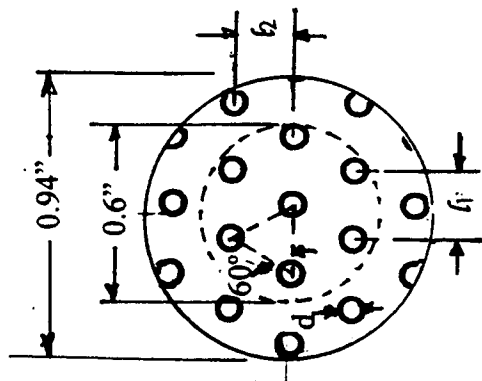
$\Delta$  = Area of the Triangle =  $(l_1^2 \sqrt{3})/4$

$S$  = Porosity = Area of holes within a triangle /  $\Delta$   
 $= (\pi d^2/8) / \{(l_1^2 \sqrt{3})/4\}$

Thus, for a given  $S$  and  $d$  we have the following:

$l_1 = \{(\pi d^2)/(2 S \sqrt{3})\}^{1/2}$

$l_2 = (l_1 \sqrt{3})/2$



(b) 0.94" coupon with small number of holes in the 0.6" diameter area (not to scale)

Figure 19. Hole pattern and the definition of various parameters for perforated sheets with staggered circular holes .

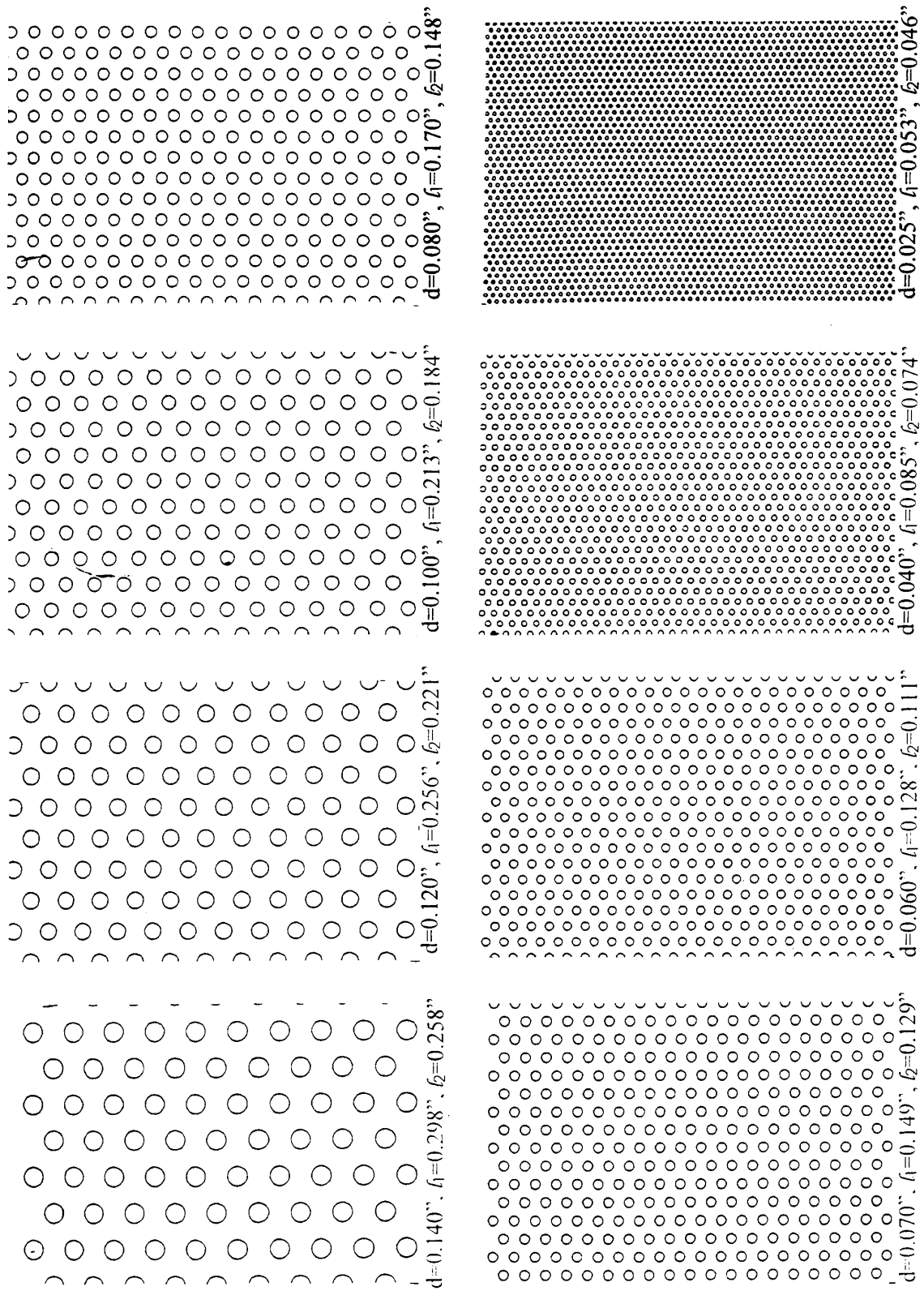


Figure 20. Staggered circular hole patterns for facesheets of porosity  $\sigma = 20\%$  with varying hole diameters.

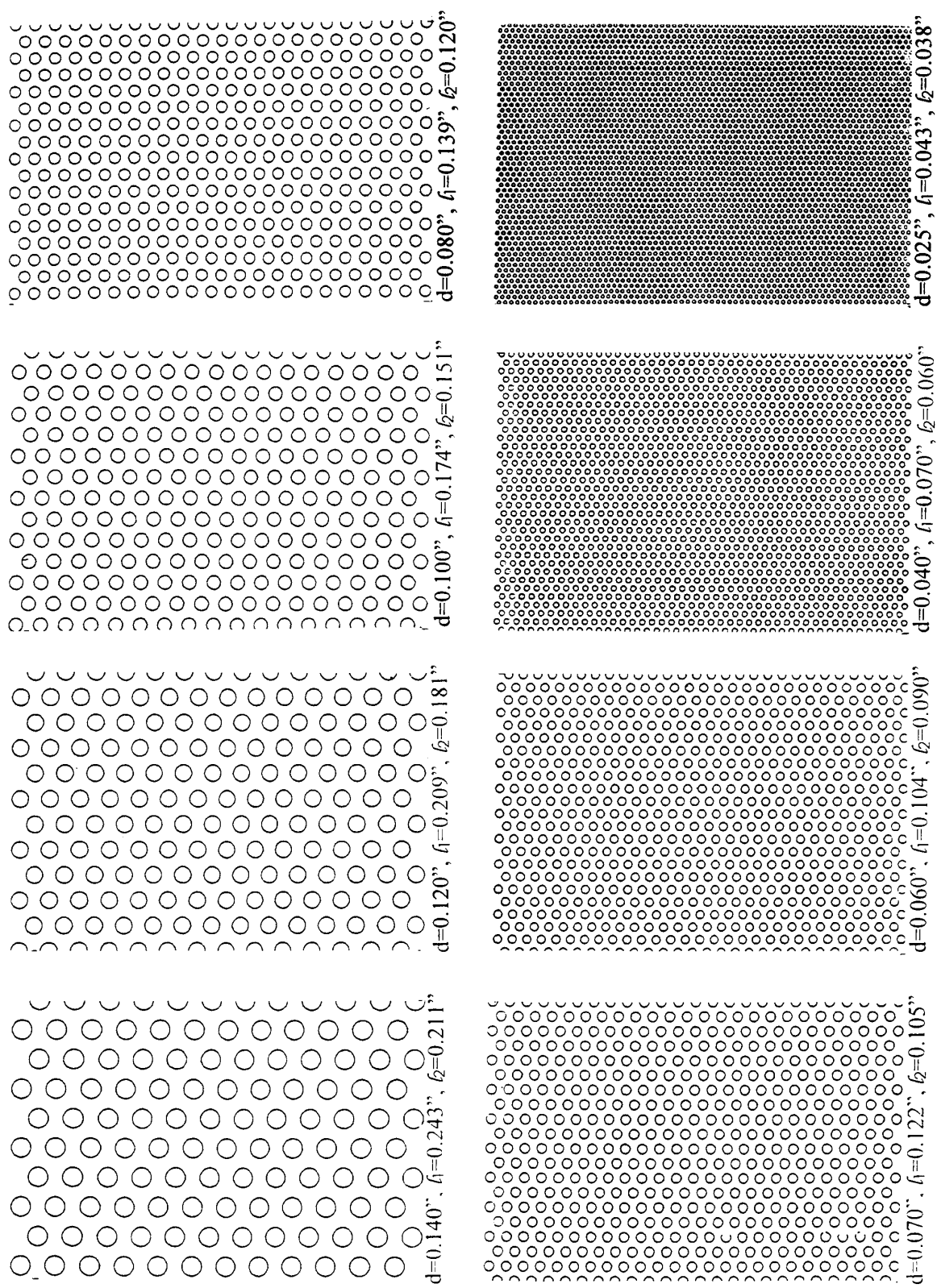


Figure 21. Staggered circular hole patterns for facesheets of porosity  $\sigma = 30\%$  with varying hole diameters.

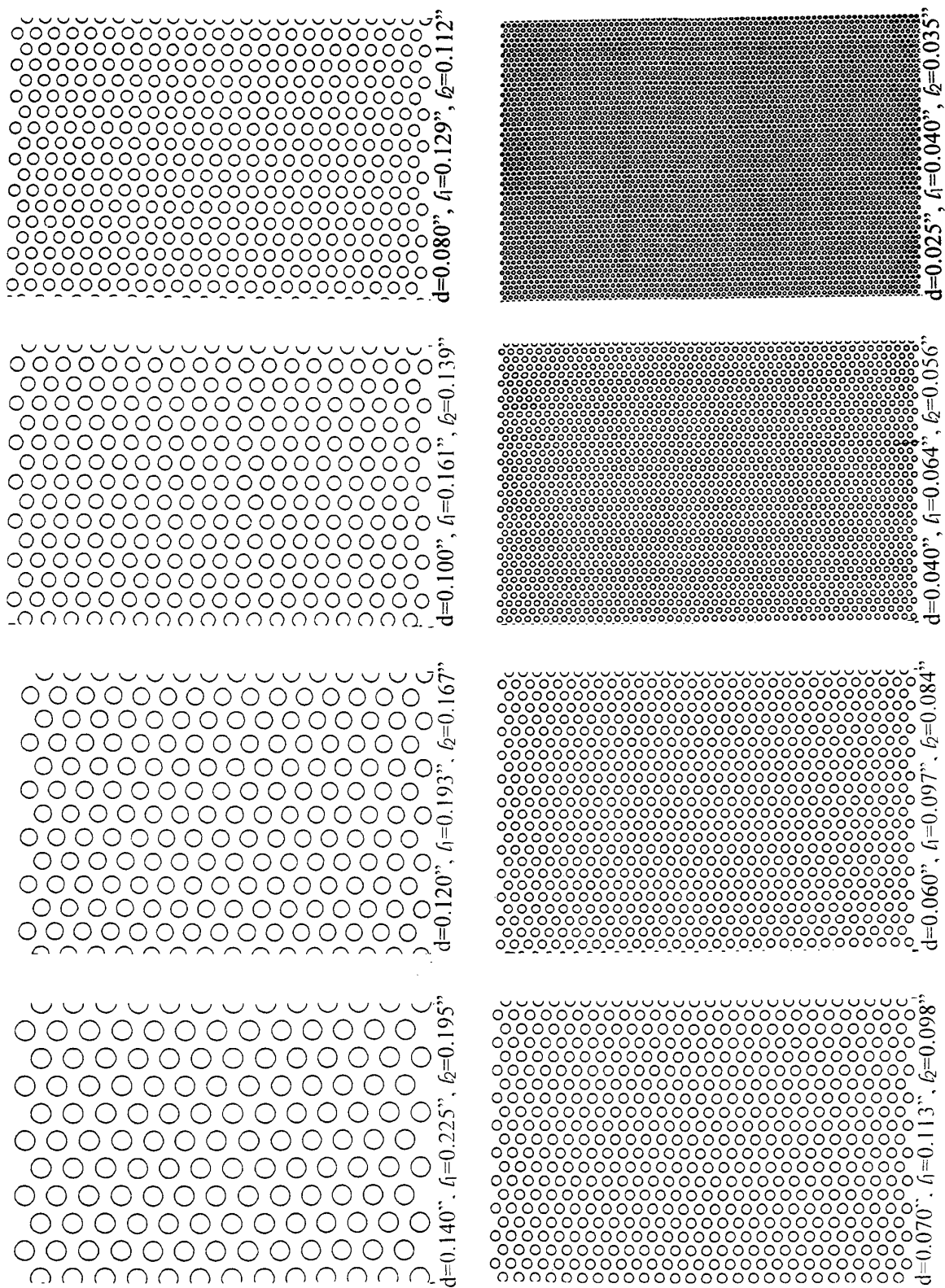


Figure 22. Staggered circular hole patterns for facesheets of porosity  $\sigma = 35\%$  with varying hole diameters.

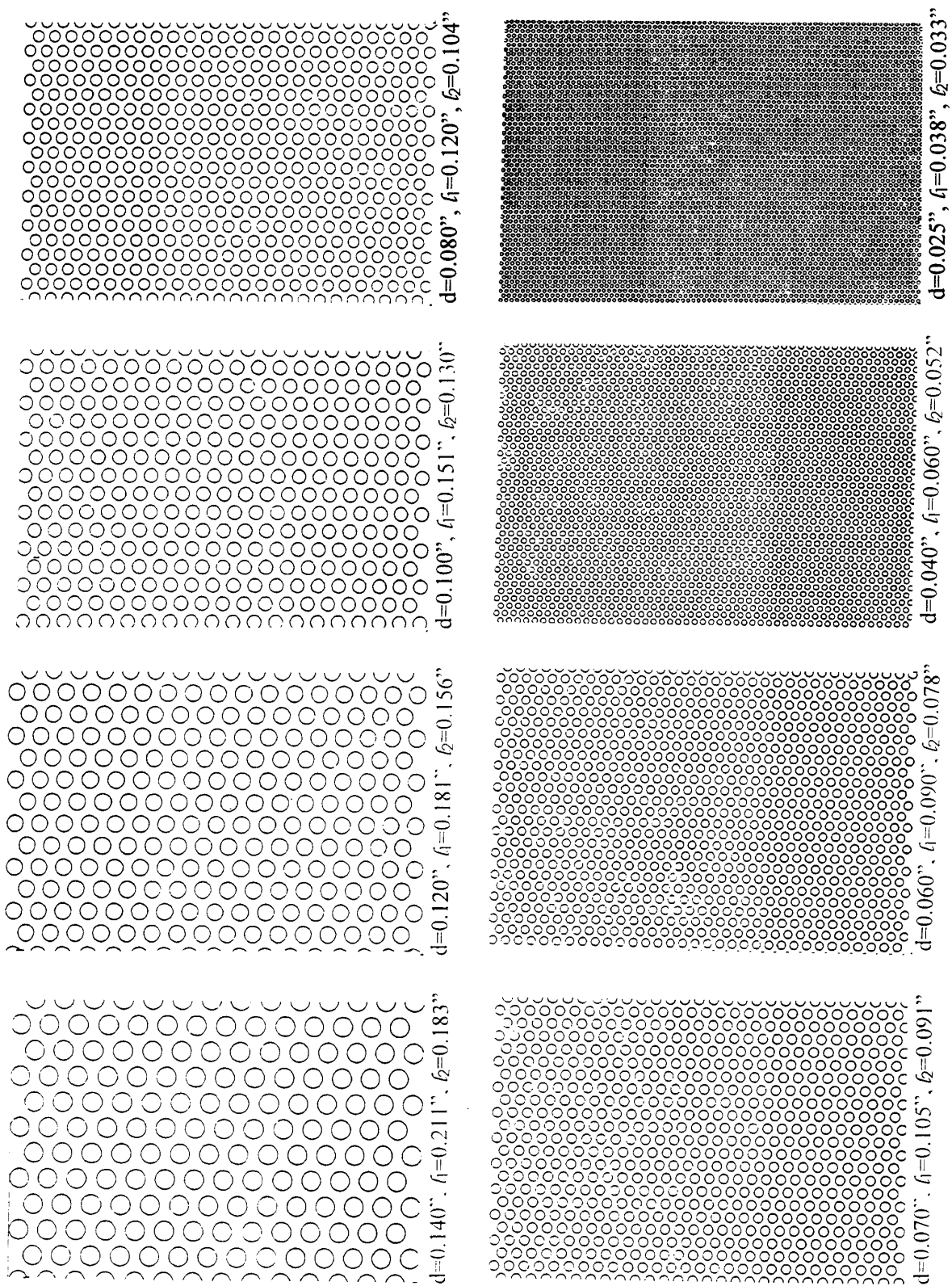


Figure 23. Staggered circular hole patterns for facesheets of porosity  $\sigma=40\%$  with varying hole diameters.



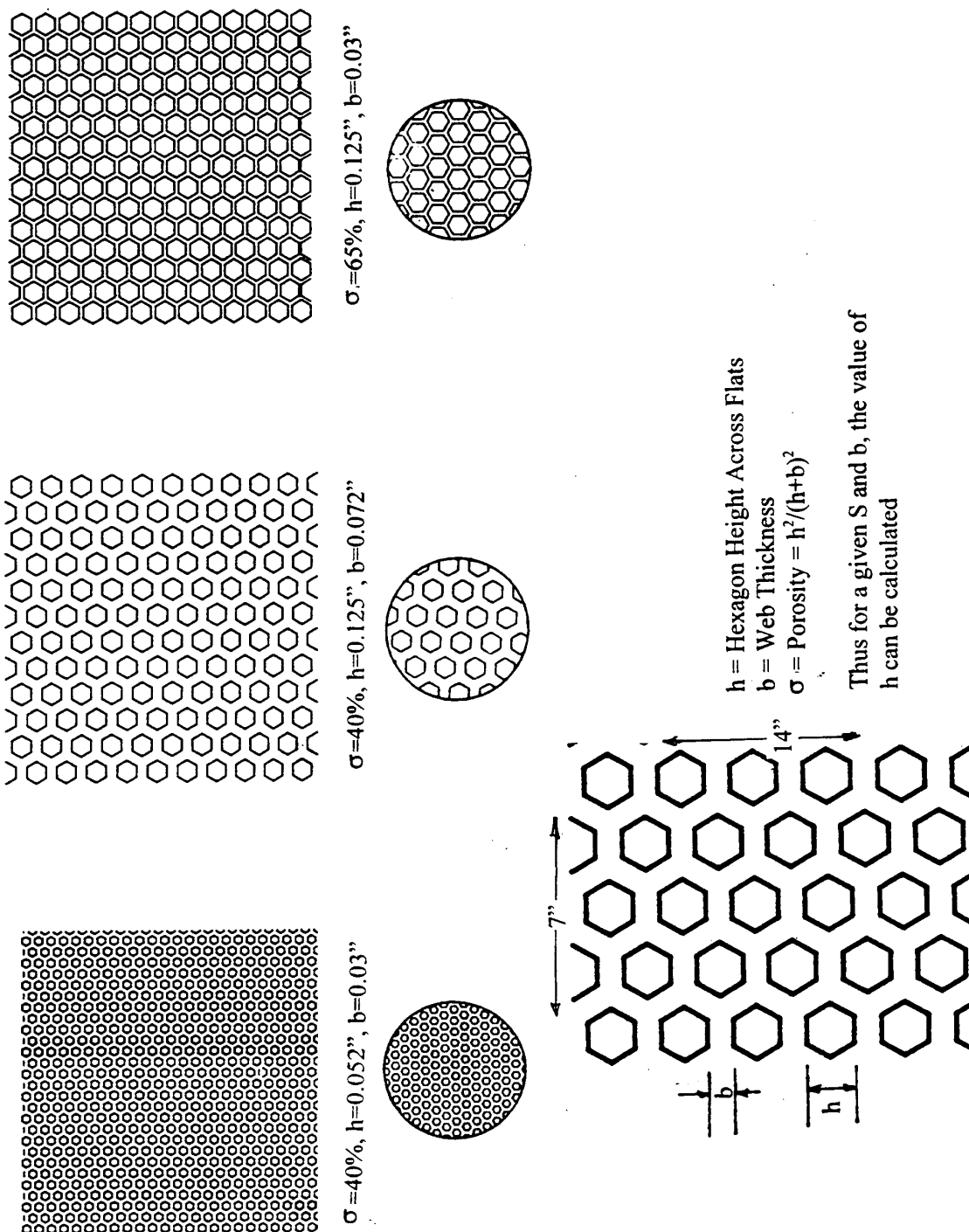


Figure 24. Hexagonal hole patterns for facesheets of different parameters.

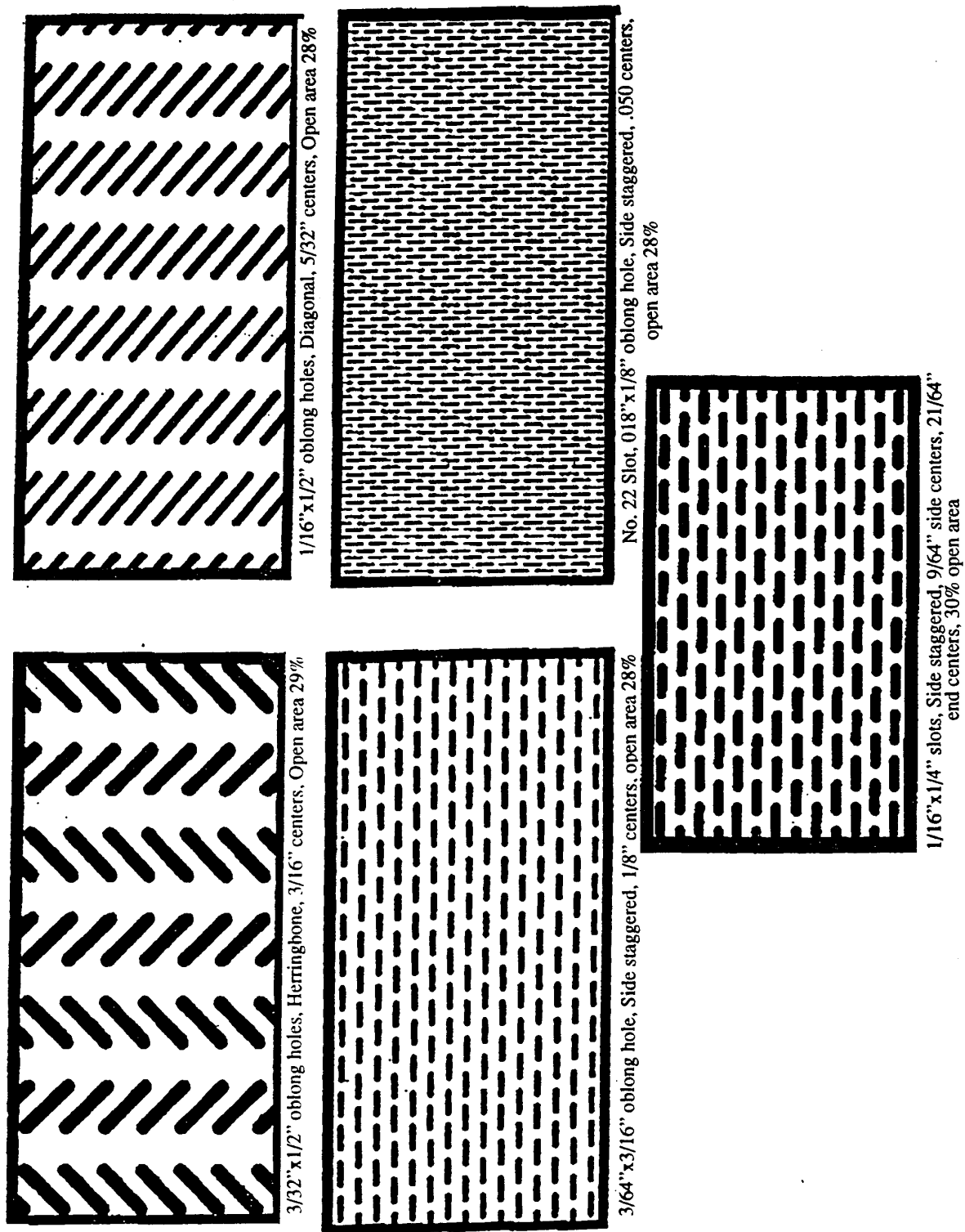


Figure 25. Various slotted sheet designs for bulk absorber type liner panels.

Table 2. Bulk Material and Facesheet Properties for Modified High Frequency Impedance Tube and Flow Duct Tests for Bulk Absorber Type Liners.

## I. Bulk Materials

### Silicon Carbide

Sample	ppi (Resistivity, R100 cgs Rayls/cm)
B-1	100 (7-10)
B-2	200 (30-40)
B-3	400 (80-150)
B-4	600 (300-500)

### T-Foam

Sample	Resistivity Variation (Density, lb/cft)
B-5	Low (8)
B-6	Medium (12)
B-7	High (16)

### Feltmetal Bulk (316 Stainless Steel)

Sample	Resistivity Variation
B-8	5% Dense
B-9	10% Dense
B-10	15% Dense

**Note: For Impedance Tube Tests -**  
0.6"-Diameter Bulk Samples of 0.25", 0.5", 1.0", 1.5", 1.75", & 2" Depths (6 No) are acquired.

**For Flow Duct Tests -**  
All Bulk Samples are 0.5" Deep

## II. Facesheets

### Facesheets with Circular Holes

Config No.	Porosity, $\sigma$ %	Hole Diameter, d inches	Thickness, t inches
------------	----------------------	-------------------------	---------------------

#### Effect of Porosity:

T1-1	20	0.04	0.025
T1-2	30	0.04	0.025
T1-3	40	0.04	0.025

#### Effect of Hole Diameter:

T1-4	40	0.025	0.025
T1-3	40	0.04	0.025
T1-5	40	0.06	0.025
T1-6	40	0.08	0.025

#### Effect of Thickness:

T1-7	40	0.04	0.015
T1-3	40	0.04	0.025
T1-8	40	0.04	0.04
T1-9	40	0.04	0.06

### Linear Facesheets with NLF=1.325

Config No	Resistivity, R100 cgs Rayls	Thickness, t inches
T1-10	5	0.025
T1-11	10	0.03
T1-12	15	0.04

### Facesheets With slotted Holes, Thickness=0.025"

Config No.	Porosity %	Slot Size, inch x inch	Description of slots
T1-13	30	3/32x1/2 Oblong	Herringbone, 3/16" centers
T1-14	30	1/16x1/2 Oblong	Diagonal, 5/32 centers
T1-15	30	3/64x3/16 Oblong	Side staggered, 1/8 centers
T1-16	30	.018x1/8 oblong	Side staggered, .05 centers
T1-17	30	1/16x1/4 slots	Side Staggered, 9/64 side centers, 21/64 end centers

Note: All facesheet samples for Impedance Tube Tests are 0.94" in diameter

Table 3. Hole Patterns for Perforated Facesheets with hexagonal Hole Pattern

No.	Configuration Description	Porosity S, %	Facesheet Thickness, t Inches	Hexagonal Height h, inches	Web Thickness b, inches	No of Holes within 0.6" Dia. Area
T1-18	14"x7" size & 0.94" coupon	40	0.025	0.052	0.03	48.30
T1-19	14"x7" size & 0.94" coupon	40	0.025	0.125	0.072	8.36
T1-20	14"x7" size & 0.94" coupon	65	0.025	0.125	0.03	13.58
T1-21	0.94" coupon only	40	0.10	0.052	0.03	48.30
T1-22	0.94" coupon only	40	0.10	0.125	0.072	8.36
T1-23	0.94" coupon only	65	0.10	0.125	0.03	13.58

tests are constructed from the facesheets and bulk materials of varying physical properties, as listed in Tables 2 through 7.

A set of facesheets with different hole pattern (i.e., circular, triangular, square, and elliptical) with a porosity of 9% are fabricated. The area of each type of holes is maintained the same as the circular hole of diameter 0.04". To minimize the radius of curvature at the corners for triangular and square holes the facesheets are made with 0.01"-thick sheets. Figure 26 shows these hole patterns and their parametric dimensions.

### 3.1 Samples for High Frequency Impedance Tube Tests:

The facesheets for bulk absorber and SDOF type liners for impedance tube tests are basically circular pieces of 0.94" diameter, procured from the facesheet lists of Tables 2 through 4. The bulk samples for high frequency impedance tube tests are cylinders of 0.6" diameter with 6 different depths, namely, 0.25", 0.5", 0.75", 1.0", 1.5", 1.75", and 2.0" (corresponding liner scales are 1/8, 1/4, 3/8, 1/2, 3/4, and full scale) are procured from the list, shown in Table 2, to cover different scale liner applications. The bulk absorber type samples are constructed by using the circular facesheets over the cylindrical bulk pieces without any cavity behind the bulk. The SDOF type samples are constructed by using the circular facesheets over a cavity of desired depth (see Figure 1). For SDOF samples with larger hole diameters the number of holes contained within 0.6" diameter circle become very few. In these cases the coupons are carefully cut to keep the porosity within the 0.6" circle as close to the desired value. Figure 27 shows the examples of such samples.

Table 4. Hole Patterns for Additional Perforated Facesheets with Staggered Circular Holes

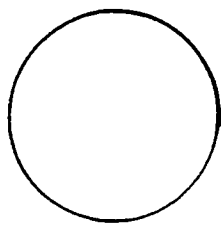
No.	Flow Duct Config	Porosity S, %	Thickness t, inches	Hole Diameter d, inches	Spacing $l_1$ , inches	Spacing $l_2$ , inches	No of Holes within 0.6" dia area
1	401-1	20	0.10	0.07	0.149	0.129	14.694
2	402-1	25	0.10	0.07	0.133	0.115	18.367
3	403-1	30	0.10	0.07	0.122	0.105	22.041
4	404-1	35	0.06	0.025	0.040	0.035	201.6
5	404-2	35	0.10	0.025	0.040	0.035	201.6
6	405-1	35	0.06	0.04	0.064	0.056	78.75
7	405-2	35	0.10	0.04	0.064	0.056	78.75
8	406-1	35	0.06	0.06	0.097	0.084	35.0
9	406-2	35	0.10	0.06	0.097	0.084	35.0
10	407-1	35	0.025	0.07	0.113	0.098	25.714
11	407-2	35	0.04	0.07	0.113	0.098	25.714
12	407-3	35	0.06	0.07	0.113	0.098	25.714
13	407-4	35	0.08	0.07	0.113	0.098	25.714
14	407-5	35	0.10	0.07	0.113	0.098	25.714
15	407-6	35	0.125	0.07	0.113	0.098	25.714
16	408-1	35	0.06	0.08	0.129	0.112	19.688
17	408-2	35	0.10	0.08	0.129	0.112	19.688
18	409-1	35	0.025	0.10	0.161	0.139	12.6
19	409-2	35	0.04	0.10	0.161	0.139	12.6
20	409-3	35	0.06	0.10	0.161	0.139	12.6
21	409-4	35	0.08	0.10	0.161	0.139	12.6
22	409-5	35	0.10	0.10	0.161	0.139	12.6
23	409-6	35	0.125	0.10	0.161	0.139	12.6
24	410-1	35	0.06	0.125	0.201	0.174	8.064
25	410-2	35	0.10	0.125	0.201	0.174	8.064
26	411-1	40	0.04	0.025	0.038	0.033	230.4
27	411-2	40	0.10	0.025	0.038	0.033	230.4
28	412-1	40	0.10	0.04	0.06	0.052	90.0
29	412-2	40	0.125	0.04	0.06	0.052	90.4
30	413-1	40	0.04	0.06	0.09	0.078	40.0
31	413-2	40	0.10	0.06	0.09	0.078	40.0
32	414-1	40	0.025	0.07	0.105	0.091	29.388
33	414-2	40	0.04	0.07	0.105	0.091	29.388
34	414-3	40	0.10	0.07	0.105	0.091	29.388
35	415-1	40	0.10	0.08	0.12	0.104	22.5
36	416-1	40	0.025	0.1	0.151	0.13	14.4
37	416-2	40	0.10	0.1	0.151	0.13	14.4
38	417-1	40	0.025	0.125	0.188	0.163	9.214
39	417-2	40	0.10	0.125	0.188	0.163	9.214

Table 5. Hole Patterns for Additional Perforated Facesheets with Staggered Circular Holes only for Normal Impedance Test.

No.	Porosity S, %	Thickness t, inches	Hole Diameter d, inches	Spacing $\ell_1$ , inches	Spacing $\ell_2$ , inches	No of Holes within 0.6" dia area
40	40	0.025	0.14	0.211	0.183	7.347
41	40	0.10	0.14	0.211	0.183	7.347
42	40	0.14	0.04	0.060	0.052	90.0
43	40	0.025	0.056	0.084	0.073	45.918
44	40	0.025	0.075	0.113	0.098	25.6
45	35	0.06	0.14	0.225	0.195	6.429
46	35	0.10	0.14	0.225	0.195	6.429
47	35	0.14	0.07	0.113	0.098	25.714
48	35	0.14	0.10	0.161	0.139	12.6

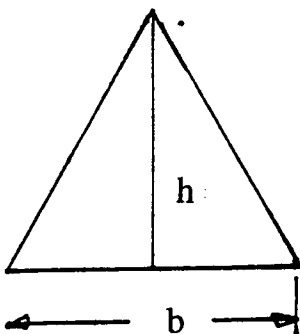
Table 6. Additional bulk absorber samples & their DC Flow Resistance

Nomenclature	Description (Actual Height, Density, & Process)	A, R/cm	R <sub>100</sub> , R/cm
TF19/2"	1.90", 9.7 lbf(7.5+2.2) Standard 7/3, 48 plies (B-19)	8.23	14.49
TF20/2.0"	1.85", 8.6 lbf (7.2+1.4) Standard 7/1 (B-20)	6.24	10.72
TF21/2"	1.94" 11.7 lbf (8.8+2.9) Standard 10/2 (B-21)	10.34	19.21
TF22/2.0"	1.85", 9.7 lbf (8.1+1.6) Standard 9/1, 54 plies (B-22)	4.83	8.90
TF23/1.2	1.15", 11.6 lbf (9+2.6) Standard 10/2 (B-23)	9.31	16.23
TF24/.5"	.45", 11.7 (9.7+2) Standard 10/2 (B-24)	13.81	21.75
TF32/2"	1.95", 1 layer of 50 g/m <sup>2</sup> paper (3 plies thick), 8/1	8.46	12.72
TF33/2"	1.94", 3 layers of 50 g/m <sup>2</sup> paper(3 plies thick), 9.1 lbf (8.1+1)	11.11	16.84
TF34/2"	1.94", ", 9 layers of 50 g/m <sup>2</sup> paper(1 ply thick), 9.1 lbf (8.1+1)	12.64	18.83
TF34c/2"	1.94", ", 9 layers of 50 g/m <sup>2</sup> paper(1 ply thick), 9.1 lbf (8.1+1), coated with mullite		
TF36/2"	1.97", Standard, texturized (floppier), 9 lbf (8+1)	7.43	10.77
TF37/2"	2.0", 24 plies/inch , Standard 8/1		
TF37c/2"	1.8", 24 plies/inch with porous SiC coating, Standard 8/1	2.64	4.86
TF39/2"	1.9", 5 layers of 80 g/m <sup>2</sup> paper (3 plies thick) 8.8 lbf (7.9/0.9)	11.97	17.13
TF39c/2"	1.85", 5 layers of 80 g/m <sup>2</sup> paper (3 plies thick) 8.9 lbf (7.9/1) with porous SiC coating	8.99	13.79
TF40/2"	1.95", 7 layers of 80 g/m <sup>2</sup> paper (3 plies thick) 8.6 lbf (7.6/1)	16.86	22.99
TF40c/2"	1.95", 7 layers of 80 g/m <sup>2</sup> paper (3 plies thick) 8.6 lbf (7.6/1) with porous SiC coating	21.28	29.20
TF41/	3 layers of 50 g/m <sup>2</sup> paper(3 plies thick), 8.2 lbf (7.1/1.1)		
TF42/1.2"	1.1", 3 layers of 80 g/m <sup>2</sup> paper (3 plies thick) 8.7 lbf (7.0/1.7)	22.77	31.10
TF45/1.2"	1.185", 3 layers of 50 g/m <sup>2</sup> paper (3 plies thick) 7.8 lbf 6.8/1.0)	7.67	11.16
TF46/2"	1.96", 3 layers of 80 g/m <sup>2</sup> paper (3 plies thick) 8.6 lbf (7.6/1.0)	7.54	10.76
TF47/2"	1.97", 5 layers of 50 g/m <sup>2</sup> paper (3 plies thick) 8.6 lbf (7.6/1.0)	10.72	14.23
B-25/2"	2.0", 100 ppi Silicon Carbide	6.76	10.72



$d = \text{Diameter of the circle} = 0.04''$

$\text{Area of the circle} = \pi d^2/4 = 0.001256637 \text{ in}^2$

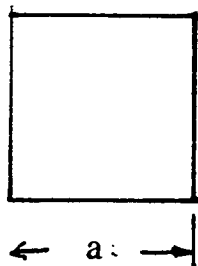


$b = \text{Side of the equilateral triangle}$

$h = \text{Height of the triangle} = \sqrt{3} b/2$

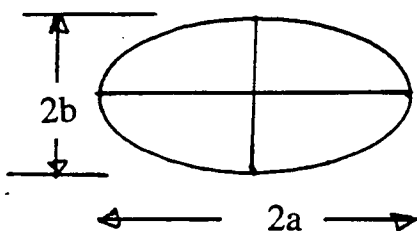
$\text{Area of the triangle} = b h/2 = 0.433 b^2 = \text{Area of circular hole}$

$b = 0.05387''$



$\text{Area of the square} = a^2 = \text{Area of circular hole}$

$a = 0.0354''$



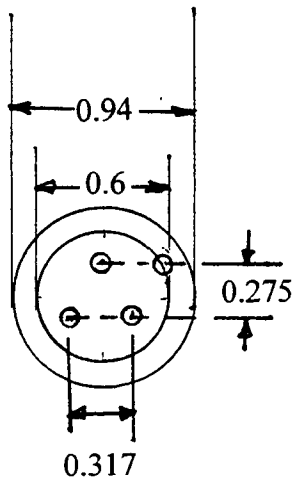
$\text{Area of an ellipse} = \pi a b$

If  $a = 2b$ ; the area  $= 2\pi b^2 = \text{Area of circular hole}$

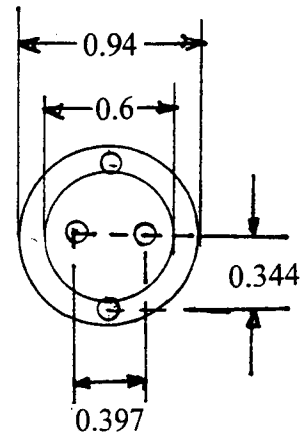
$2b = \text{Minor axis} = 0.02828''$

$2a = \text{Major axis} = 0.05657''$

Figure 26. Various hole patterns and their parameters for SDOF type panels.



Configuration # T2-20  
 Porosity = 9%, Thickness = 0.1"  
 Hole Diameter = 0.1"  
 No of Holes in 0.6" Area = 3.24



Configuration # T2-19  
 Porosity = 9%, Thickness = 0.1"  
 Hole Diameter = 0.125"  
 No of Holes in 0.6" Area = 2.074

Figure 27. 0.94" coupons with small number of holes in the 0.6" diameter area for configurations T2-19 and T2-20, all dimensions are in inches (not to scale).

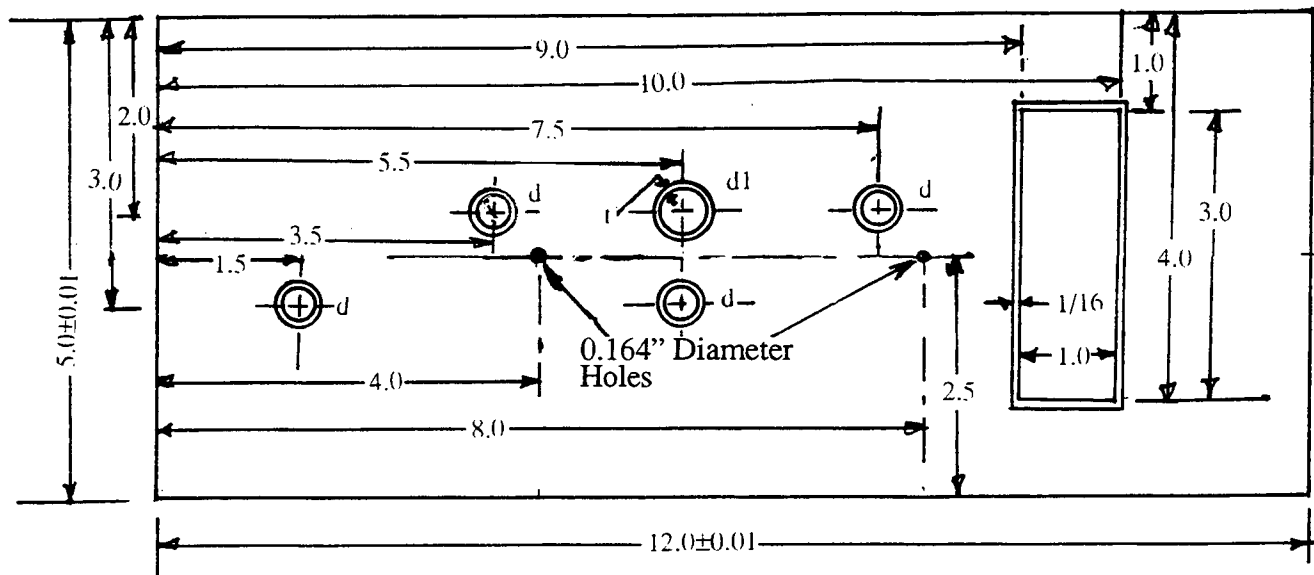


## **3.2 Panels for Flow Duct Tests at ARL:**

**3.2.1 Bulk Materials and Facesheets for Bulk Absorber Type Panels:** A schematic of the tray filled with bulk material and with facesheet is shown in Figure 12. The bulk samples used (see Table 2) are of 12"x5" size with a depth of 0.5". Cutouts are made through the bulk material surface at five in-situ cavity locations and at DC flow partition to match precisely with the outer dimensions of the tubes and the DC flow partition, respectively (see Figure 28). The bulk material removed from these cutouts is sized precisely to the internal dimensions of the in-situ tubes and the DC flow cutout. These pieces are mounted inside these openings during the tests.

Facesheets of different properties (listed in Tables 2 through 5) are used on this tray. Each facesheet is 14"x7" in size to cover the liner tray including the frame surfaces. Thus, the longer edges of the facesheets are properly secured between the tray and the flow duct sidewalls. In addition, by covering the entire tray surface, facesheets of different thickness can be placed without creating any steps along the flow direction. To ensure proper attachment of the facesheet to the bulk surface, two threaded rods (see Figure 29) of 0.164" diameter are welded at the back of the facesheet surface. These rods are put through the bulk depth and the tray back plate and fastened with nuts on the back of the backplate. Thus, the facesheet is pressed tightly against the bulk surface. Two 0.164" diameter holes are drilled through the bulk at locations shown in Figure 28 to allow the facesheet to be properly mounted. In addition, a high temperature sealant is applied between the facesheet and the edges of the in-situ tubes and the DC flow partition wall to prevent leakage.

**3.2.2 Facesheets for SDOF Type Panels:** A schematic of the tray filled with honeycomb and with facesheet is shown in Figure 10. Facesheets of different properties (listed in Table 7) are procured to be used on this tray. Each facesheet is 14"x7" in size to cover the liner tray including the frame surfaces. Thus, the longer edges of the facesheets are properly secured between the tray and the flow duct sidewalls. In addition, by covering the entire tray surface, facesheets of different thickness can be placed without creating any steps along the flow direction. To ensure proper attachment of the facesheet to the honeycomb, two threaded rods (see Figure 29) of 0.164" diameter are welded at the back of the facesheet surface. These rods are put through the tray backplate and fastened with nuts on the back of the backplate. Thus, the facesheet is pressed tightly against the honeycomb. In addition, a high temperature sealant is applied between the facesheet and the edges of the in-situ tubes and the DC flow partition wall to prevent leakage.



- d = Inner diameter of 4 circles, 0.375
- d1 = Inner diameter of one circle, 0.50
- t = Width of the coannular space between  
inner and outer circles for all five cases, 1/16

Figure 28. Bulk material with cutouts for bulk absorber type liner  
(all dimensions are in inches).

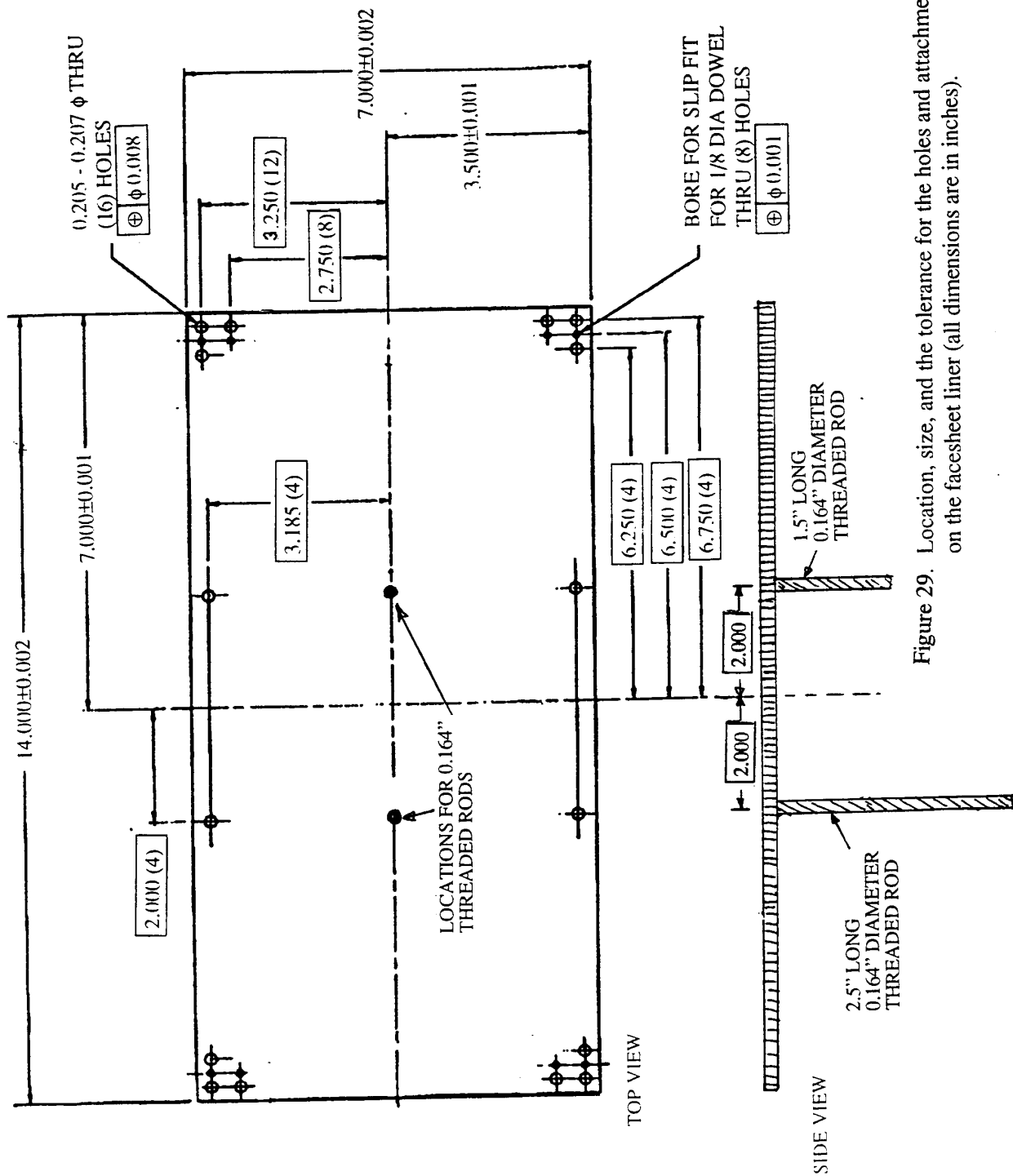


Figure 29. Location, size, and the tolerance for the holes and attachment rods on the facesheet liner (all dimensions are in inches).

Table 7. Facesheet Properties for Impedance Tube and Flow Duct Tests for SDOF Type Liners

## I. With Circular Holes

Config No.	Porosity, %	Hole Diameter, inches	Thickness, inches
------------	-------------	-----------------------	-------------------

### *Effect of Porosity:*

T2-1	7.5	0.04	0.025
T2-2	9.0	0.04	0.025
T2-3	12.5	0.04	0.025
T2-4	15	0.04	0.025
T2-5	20	0.04	0.025

### *Effect of Hole Diameter:*

T2-6*	9.0	0.005	0.025
T2-7*	9.0	0.01	0.025
T2-8*	9.0	0.02	0.025
T2-9	9.0	0.025	0.025
T2-2	9.0	0.04	0.025
T2-10	9.0	0.06	0.025
T2-11	9.0	0.08	0.025

### *Effect of Thickness:*

T2-12	9.0	0.04	0.010
T2-13	9.0	0.04	0.015
T2-2	9.0	0.04	0.025
T2-14	9.0	0.04	0.04
T2-15	9.0	0.04	0.06
T2-16	9.0	0.04	0.08

## *Thicker Sheets & Bigger Hole*

### *Diameters for Full Scale Liner Designs:*

T2-17	9.0	0.04	0.1
T2-18*	9.0	0.04	0.12
T2-19	9.0	0.125	0.1
T2-20	9.0	0.1	0.1

## II. With Non-Circular Holes, Porosity 9.0%

Config No.	Type of Holes	Equivalent Hole Diameter, inches	Thickness, inches
T2-21	Square (Sides=0.0354")	0.04	0.01
T2-22	Elliptic (Major=0.0566" & Minor=0.0283")	0.04	0.01
T2-23	Equilateral Triangular (Sides=0.0539")	0.04	0.01

## III. Linear Facesheets with NLF=1.325

Config No	Resistivity, R100 cgs Rayls	Thickness, inches
T2-24	50	0.035
T2-25	85	0.035
T2-26	130	0.04

Note: Configurations 6, 7, 8, and 18, marked with \* are only for high frequency impedance tube test (not for flow duct test).

### 3.3 Samples for Insertion Loss Tests at BF Goodrich at Room Temperature:

Selected number of bulk absorber panels is tested at BF Goodrich for insertion loss evaluation. The same facesheets, procured for GEAE's facility for in-situ, DC flow, and skin friction measurements, are used in insertion loss measurement trays. However, separate bulk absorber samples of 12"x5"x0.5" without any cutouts are procured for insertion loss measurement. Additional 12"x5" samples of 1.2" and 2.0" deep are also procured for insertion loss test to develop scaling correlation. The selection of treatment designs are based on the measured properties from high frequency impedance tube tests and flow duct tests at ARL. In addition, the NATR test results from NASA LeRC are also considered in this selection. Due to the program closeout SDOF panels are not tested.

## **4.0 CALIBRATION, TEST PREPARATION, DATA ACQUISITION, AND CHECKOUT**

Laboratory tests consist of modified high frequency impedance tube tests, DC Flow resistance tests, the flow duct tests to evaluate grazing flow effects on in-situ impedance, DC Flow resistance, and boundary layer profiles, and insertion loss measurement tests. Modified high frequency impedance tube is used to measure normal impedance up to 20 kHz and to establish a procedure to measure in-situ impedance of a bulk absorber. The flow duct tests are conducted to evaluate in-situ impedance, DC flow resistance, and skin friction coefficient at different flow conditions. In addition, limited Laser Velocimeter tests were planned for the flow duct to study flowfield/acoustic interaction phenomenon and the evaluation of skin friction coefficients from boundary layer profiles. However, these tests are not conducted due to the time constraints. BF Goodrich Aerospace, under a subcontract to GEAE conducts insertion loss measurement tests.

Based on the hardware and the test conditions, the number of possible ARL flow duct tests becomes very large. To accommodate the tests within the budget and the time constraints and also to meet the principal objectives of the program, test configurations are prioritized.

### **4.1 Calibration of Dynamic Transducers**

The existing data acquisition software for high frequency impedance tube and the flow duct is modified for the added data acquisition requirements. The software modification is made to incorporate simultaneously measurement of in-situ and normal impedance in the modified high frequency impedance tube. The flow duct software needed the improvement to acquire data simultaneously from 5 pairs of transducers, installed in each of the five cavities.

Calibration of transducers are performed for higher frequency range (up to 20 kHz) and for higher temperature conditions (up to 450°F). The complex calibration (Transfer function amplitude and phase) between two transducers is obtained by using a 0.37" diameter tube attached to a high frequency (up to 20 kHz) noise generator (acoustic driver) at one end. Two transducers are flush mounted at the other end of the tube. The transducers are connected through the power supply, amplifier, filter, etc, which are used during an actual test. A complex transfer function is derived for a transducer channel with respect to the other (i.e., reference channel) by broadband excitation of the acoustic driver. This provides a calibration for the entire system including the transducers. The absolute level calibration is obtained for the reference transducer by recording the output at a fixed frequency (1000 Hz) for a known

level of excitation (124 dB) at that frequency. This calibration is assumed to be the same for each frequency. The bandwidth for calibration as well as for actual tests is 24.414 Hz.

For high frequency impedance tube tests such calibrations are obtained for each of the seven transducers, 2 through 8, relative to the first transducer (reference). The absolute level calibration is obtained for the first transducer. The set of transfer functions is stored in the computer and is used in the data acquisition code during testing. Figure 30 is a typical example of complex transfer function calibration between the transducers. The data acquisition code provides the complex impedance spectra and sound pressure level spectrum at the surface of the test sample.

For the flow duct transducers, the complex transfer function calibration and absolute level calibration are derived between the two transducers for each of the 5 cavities. For heated conditions the tube attached to the sound source of the calibrator is introduced into a furnace, such that the transducers and the tube would be heated, while the acoustic source would remain at ambient temperature. A thermocouple is introduced into the calibrator tube to measure the temperature. The calibration is obtained by heating the oven to any desired temperature. Figure 31 shows the complex calibration spectra for pair #1 and pair #2 transducers (for cavities # 1 & 2) at different temperatures. The effect of temperature is very small on the transducer response. However, the data analysis code is capable of using the calibration for different temperature. The amplitude spectra become oscillatory at higher frequencies. This is due to the presence of higher order mode, which begins to propagate at a frequency lower than its cutoff value. This is mostly due to the small imperfection in the apparatus. However, the oscillations are insignificant to impact the actual data. Moreover, the spectra are smoothen at very high frequencies to minimize any possible inaccuracy.

#### **4.2 Calibration for Cavity Temperature Evaluation:**

Computation of in-situ impedance would require the cavity temperature. It is unlikely, that the cavities would maintain the same temperature as that of the test section during heated flow conditions. Significant heat transfer would occur, since the metallic tray with the cavities is exposed to ambient temperature outside. It is also difficult to measure temperature of each cavity during actual tests. Thus, tests are conducted to establish the cavity temperatures for heated conditions.

Thermocouples are mounted to measure temperatures in four in-situ cavities (#1, #2, #4, and #5) and DC flow cavity. Another thermocouple is mounted on the outside metal surface of

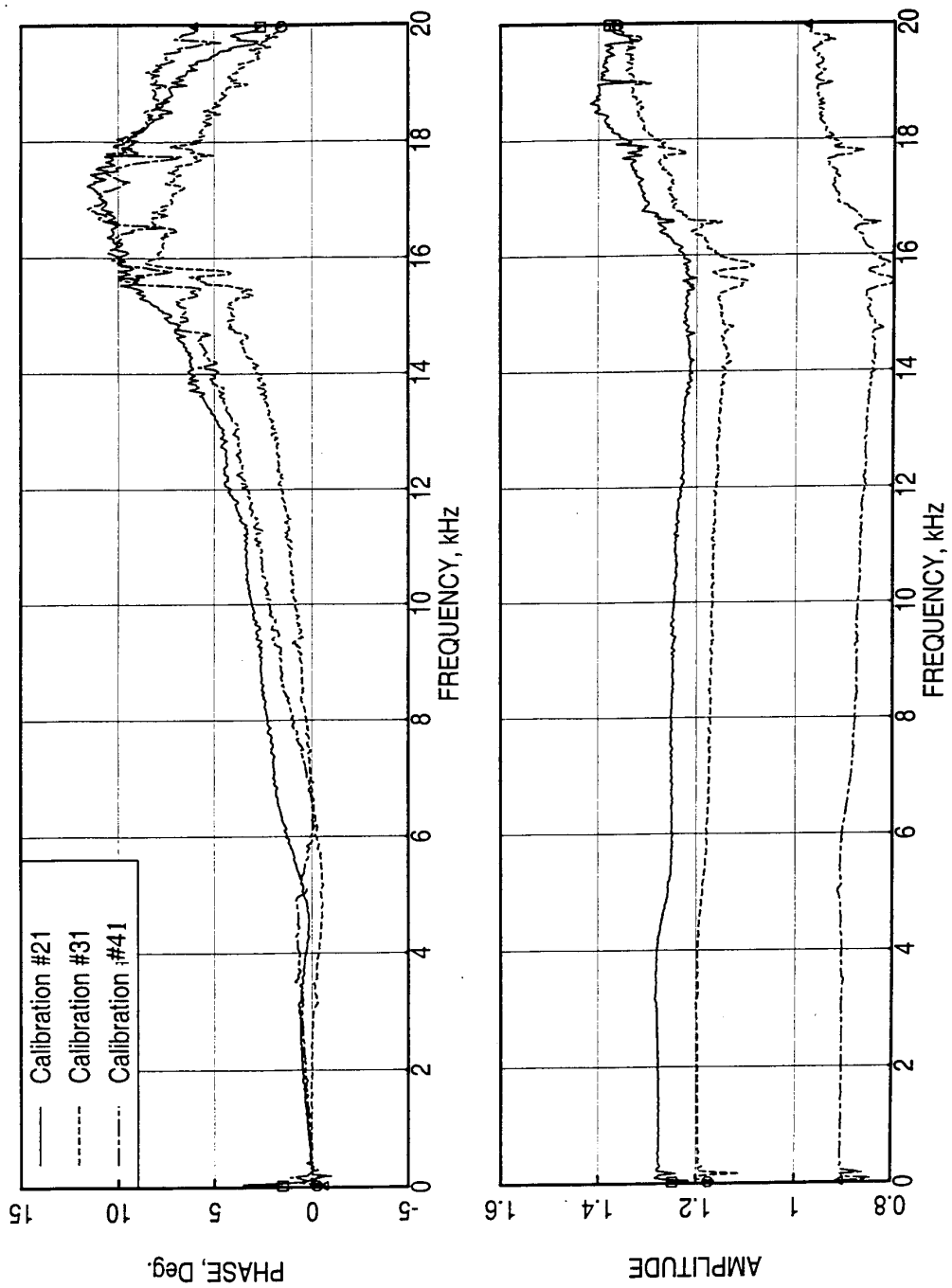


Figure 30. Amplitude and phase calibration spectra for three transducers with respect to the reference for high frequency impedance tube tests.

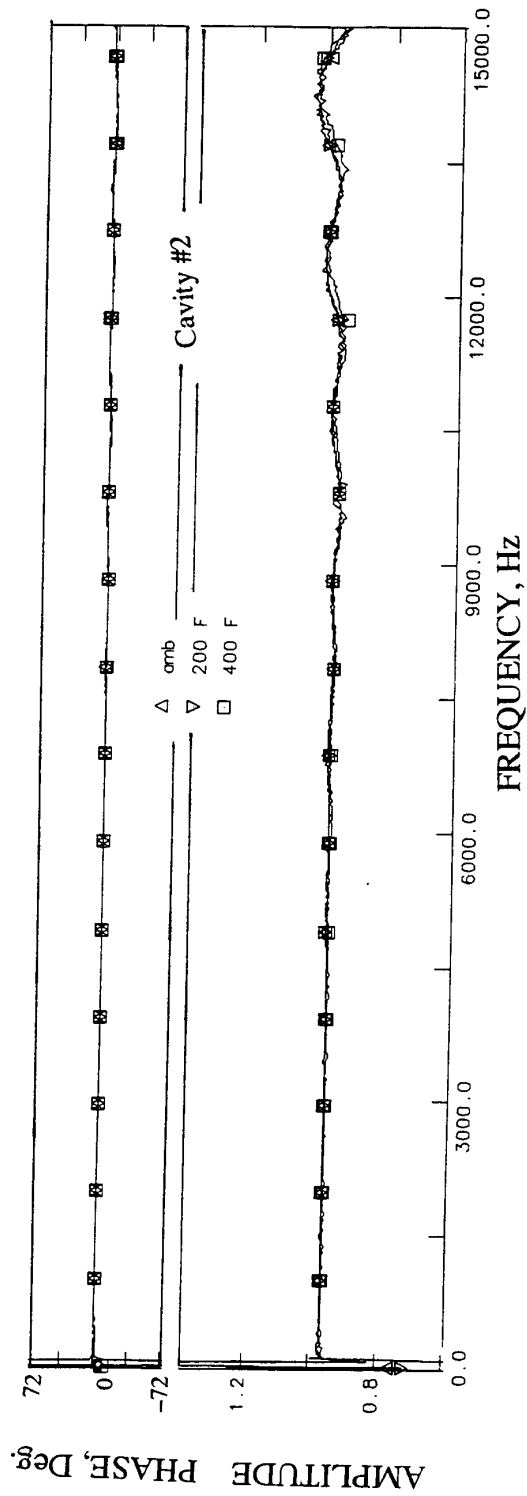
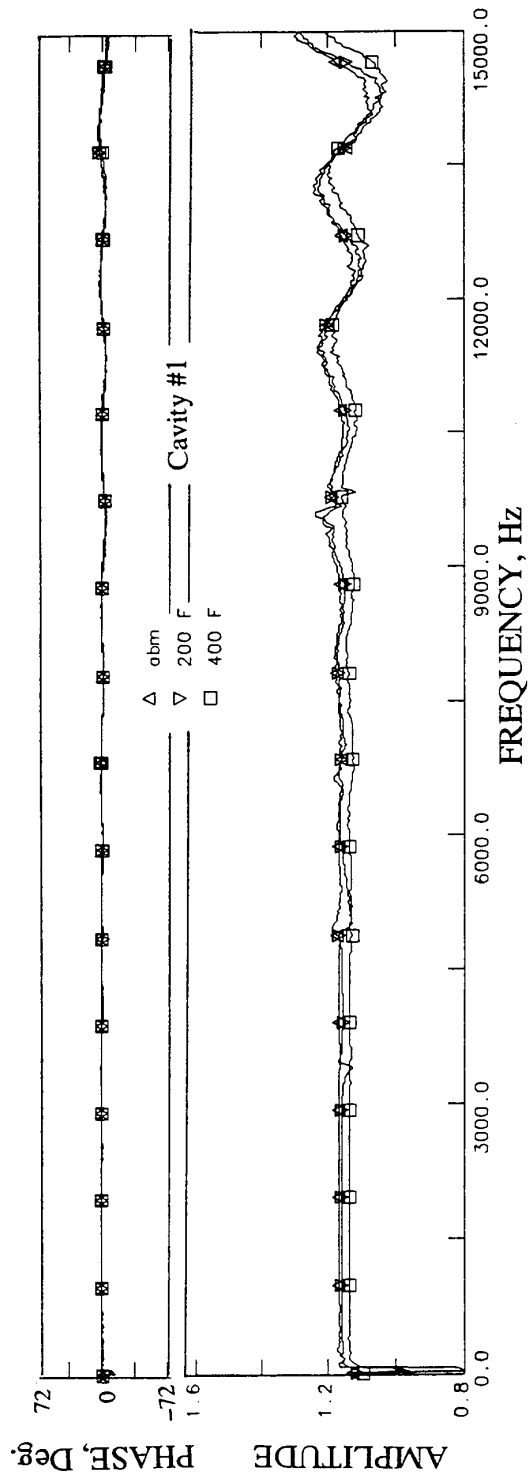


Figure 31. Amplitude and phase calibration spectra for two transducers, each with respect to the corresponding reference, at different temperatures for insitu impedance measurement in the flow duct.



the tray. The tray panel is prepared with a bulk (100 ppi SiC) covered with a facesheet (20% porous,  $t=0.025''$ ,  $d=0.04''$ ) and mounted in the flow duct. Tests are conducted by measuring the temperatures of various cavities and from other thermocouples for different Mach numbers at different test section temperatures. Similar tests are repeated by using only a facesheet without bulk as a test panel. In addition, tests are conducted by insulating the outside surface of the liner tray. Measured data at nominal temperatures of 200°F and 400°F for a SiC bulk absorber with facesheet (20% porous,  $d=0.04''$ ,  $t=0.025''$ ) are shown in Figure 32. In this a normalized temperature difference between the test section and any other location is plotted with respect to mean flow Mach number. The normalized temperature difference is the difference of the temperature ( $\Delta T$ ), between the test section centerline ( $T_{ts}$  °F) and the temperature at various locations, normalized with respect to  $T_{ts}$ . Clearly, the temperatures at various cavities are different from the test section centerline temperature. In addition, the temperature at these cavities does vary with respect to the grazing flow Mach number. However, the variation of temperatures due to different liners and due to insulation of the tray is relatively small. Thus, an average of temperatures measured for different configurations for each cavity is calculated and used in the data analysis. Temperature for cavity #3 is assumed to be the same as that of cavity #4, since the depths and axial locations of these cavities are identical. The temperatures used in in-situ impedance calculation are summarized in the following table;

Mach Number	Actual Cavity Temperature in °F for Flow Temperature of 200°F				
	Cavity #1	Cavity #2	Cavity #3	Cavity #4	Cavity #5
0.30	167	171	173	173	180
0.55	171	178	178	178	189
0.80	154	162	162	162	175
Mach Number	Actual Cavity Temperature in °F for Flow Temperature of 400°F				
	Cavity #1	Cavity #2	Cavity #3	Cavity #4	Cavity #5
0.30	308	320	327	327	351
0.55	332	343	349	349	366
0.80	328	340	346	346	378

### 4.3 Test Section Flow and Temperature Profiles:

A smooth rigid plate is mounted at the bottom of the flow duct test section (in place of liner tray) to checkout the flow duct performance with respect to Mach number, pressure, and temperature profiles. Before reducing the test section height from 4" (i.e., Area at Test Section = 20in<sup>2</sup>) to 3" (reducing the test section area to 15 in<sup>2</sup>) tests are conducted to map the test section Mach number with respect to test section total pressure (Pt). Figure 33 shows the

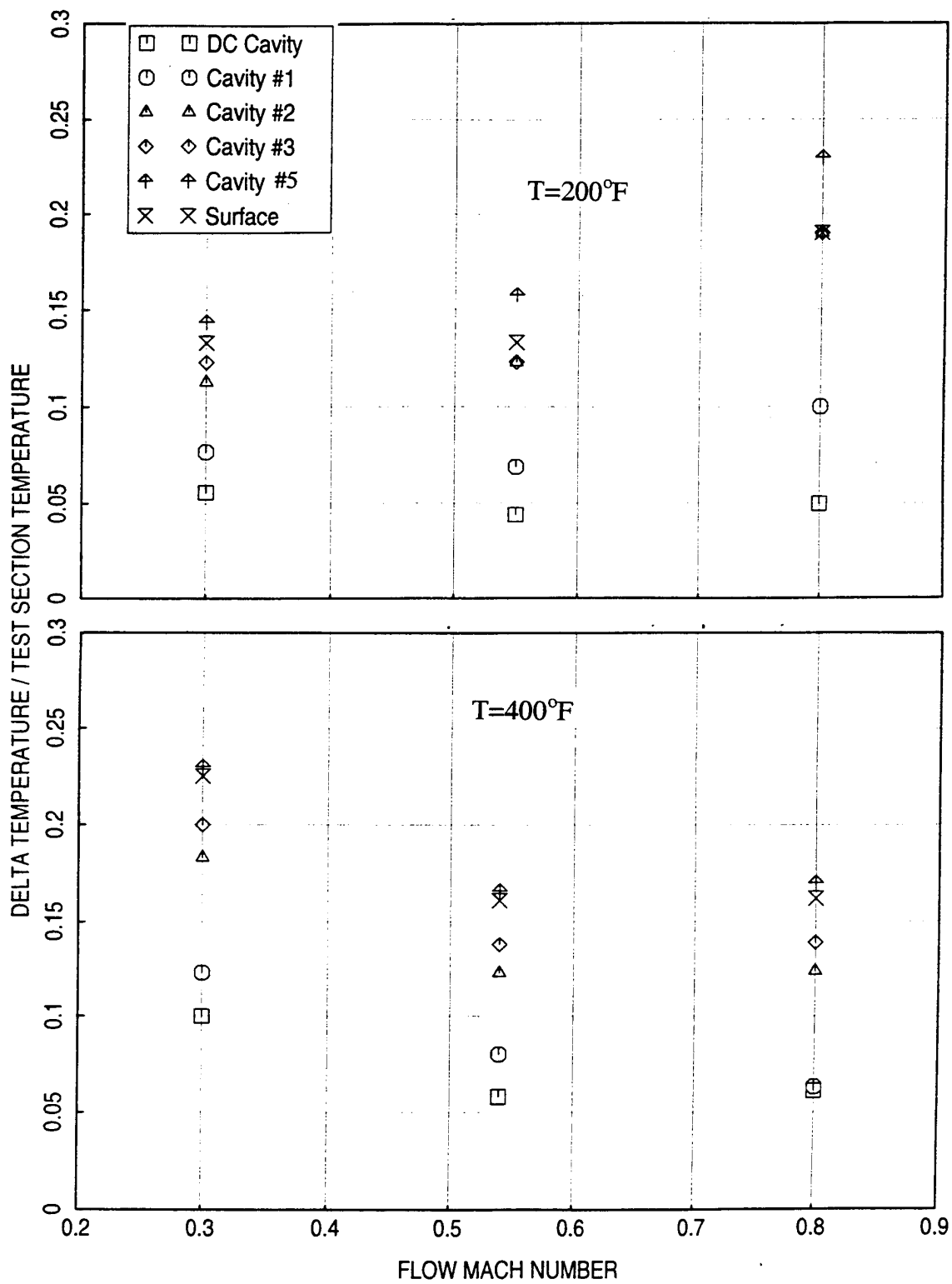


Figure 32. Cavity temperatures with respect to test section flow Mach number for two different flow conditions, duct height=3".

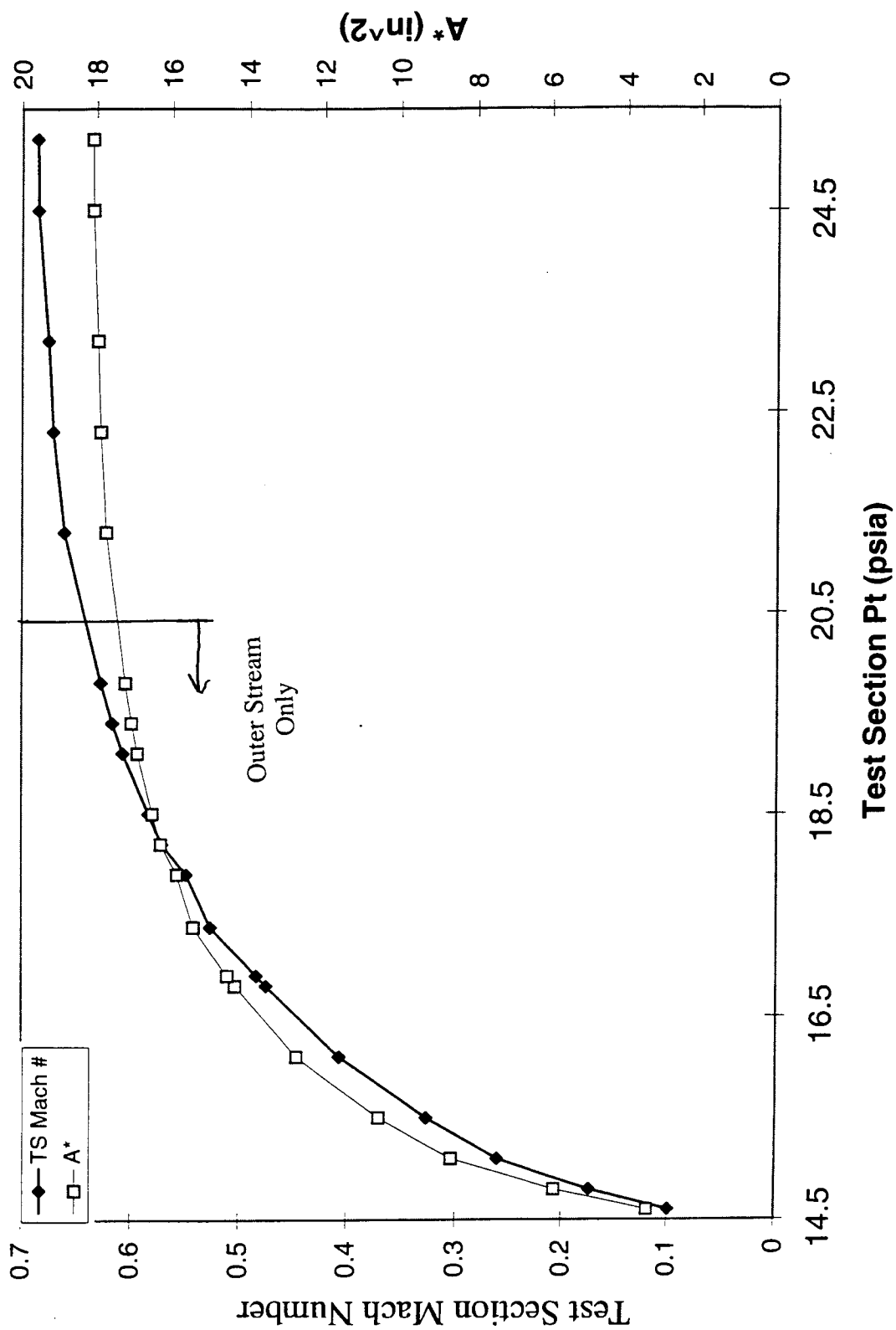


Figure 33. Mach number and choked area ( $A^*$ ) variation with respect to test section total pressure for a 20 in<sup>2</sup> test section cross sectional area at ambient temperature

variation of test section Mach number and corresponding choked area ( $A^*$ ) with respect to test section total pressure  $P_t$ . For only outer stream operational a maximum Mach number of about 0.62 is achievable. With both streams operational the Mach number maximizes at about 0.7. For heated conditions (one stream hot and other stream cold) the mixed temperature profile in the test section is significantly non-uniform. Thus, it is decided to reduce the test section height to 3" by incorporating a properly designed insert on the upper wall of the flow duct.

A PAB3D CFD analysis is performed to the planned modifications. Figure 34 shows the modification and CFD predicted Mach number and static pressure contours. A total pressure of 18.2 psia to a diffuser exhaust pressure of 14.696 psi is required to produce Mach 0.8 flow in the test section. No over acceleration is predicted in the contraction and no separation is predicted in the diffuser. A Mach number of less than 0.35 is predicted at the upstream location of the screen. After the modification of the test section several Mach number, static pressure, and temperature profiles are measured in the test section. Figure 35 shows such variations at ambient condition for different test section centerline Mach numbers. Similar results for a test section centerline temperature of 200°F are shown in Figure 36. The Mach number profiles for all the conditions (all are not shown here) are uniform enough for the current purpose.

#### **4.4 Preparation of Flow Duct Sample, Flow Duct Test, and Data Acquisition:**

**Preparation of Flow Duct Sample:** For bulk panels the 12"x5"x0.5" size bulk sheet is placed on the tray surface allowing the five tubes and DC flow partition to align with the cuts made on the bulk. A hole is drilled through each of the five small bulk cylinders along its 0.5" depth to allow the sleeve for transducer to be placed through. These cylinders then are placed into their respective cavities. Provision is made in the tubes to hold the bulk cylinders at the bottom to make them flush at the surface. The 3"x1" piece of the bulk is placed in the DC flow partition and the edges are sealed. A wire mesh with negligible resistance is installed in the DC flow partition, exactly 0.5" from the surface, to hold the bulk piece in place. Holes are drilled on the facesheet for the bulk absorber aligned with the corresponding transducer sleeve locations. High temperature sealant is applied on the cylindrical surface of the cavities, on the DC flow partition, and on the tray frame. The facesheet is, then, placed over the bulk and the two threaded rods attached to the facesheet are put through the bulk and the base of the tray. Nuts are used from the other side of the tray to secure the facesheet in place. Clamps are used to keep the facesheet attached on the top surfaces of the cavities, DC flow partition, and the tray frame. The tray assembly is allowed to cure for several hours.

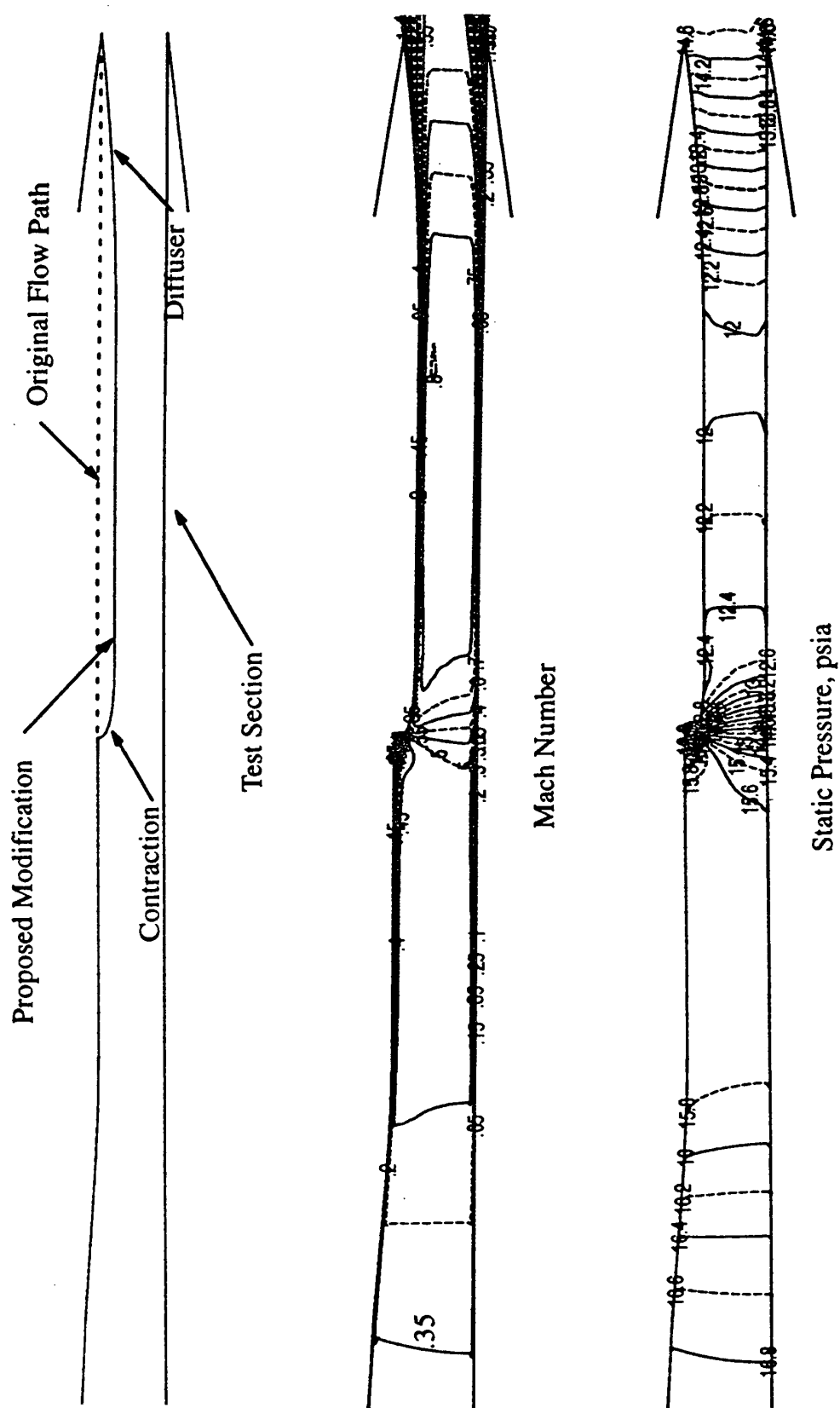


Figure 34. Modifications to the flow duct test section and the CFD predicted Mach number and static pressure contours for a centerline flow Mach number of 0.8 at the test section.

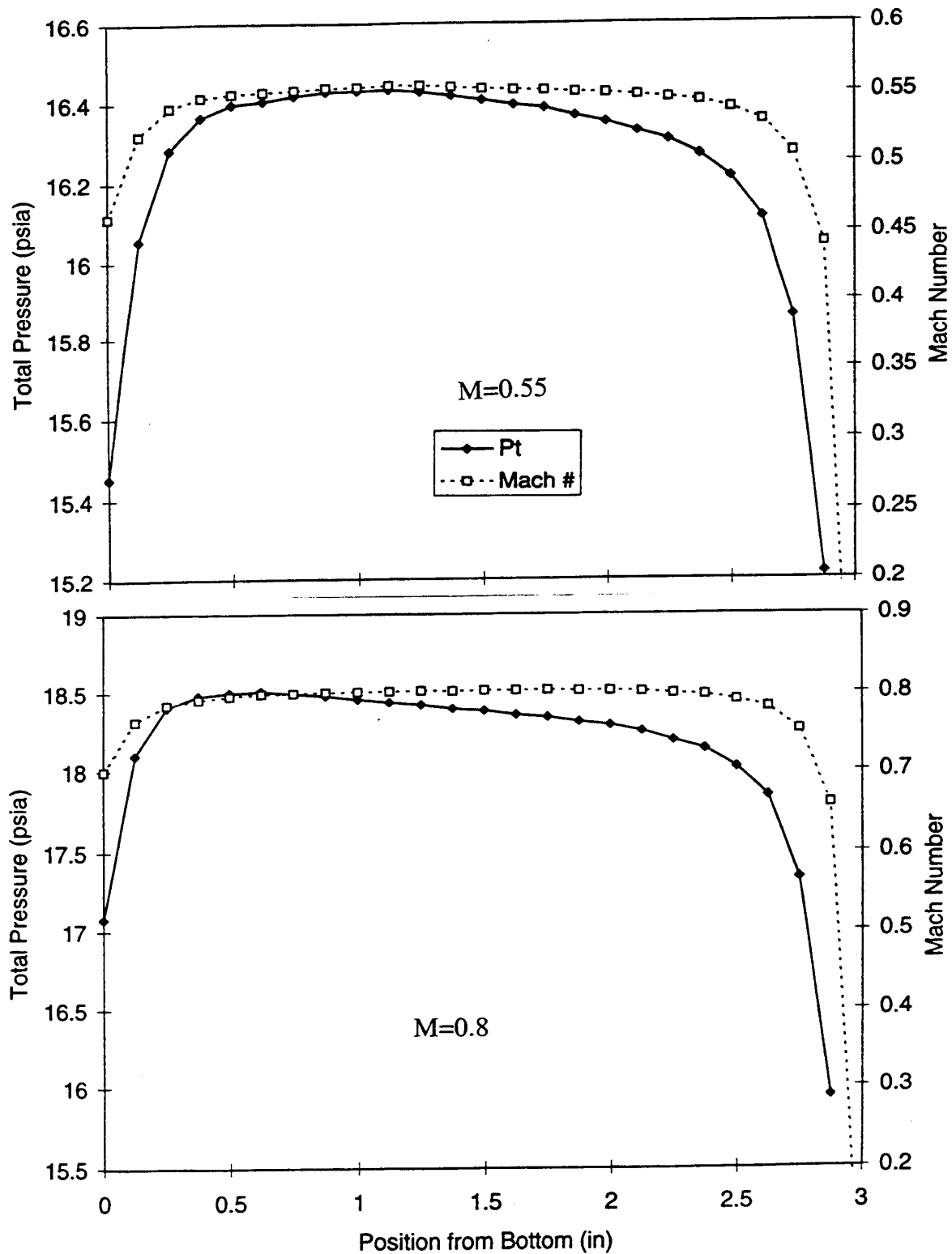


Figure 35. Mach number and total pressure variation in the flow duct test section for different centerline Mach numbers at ambient temperature, centerbody removed and screen installed.

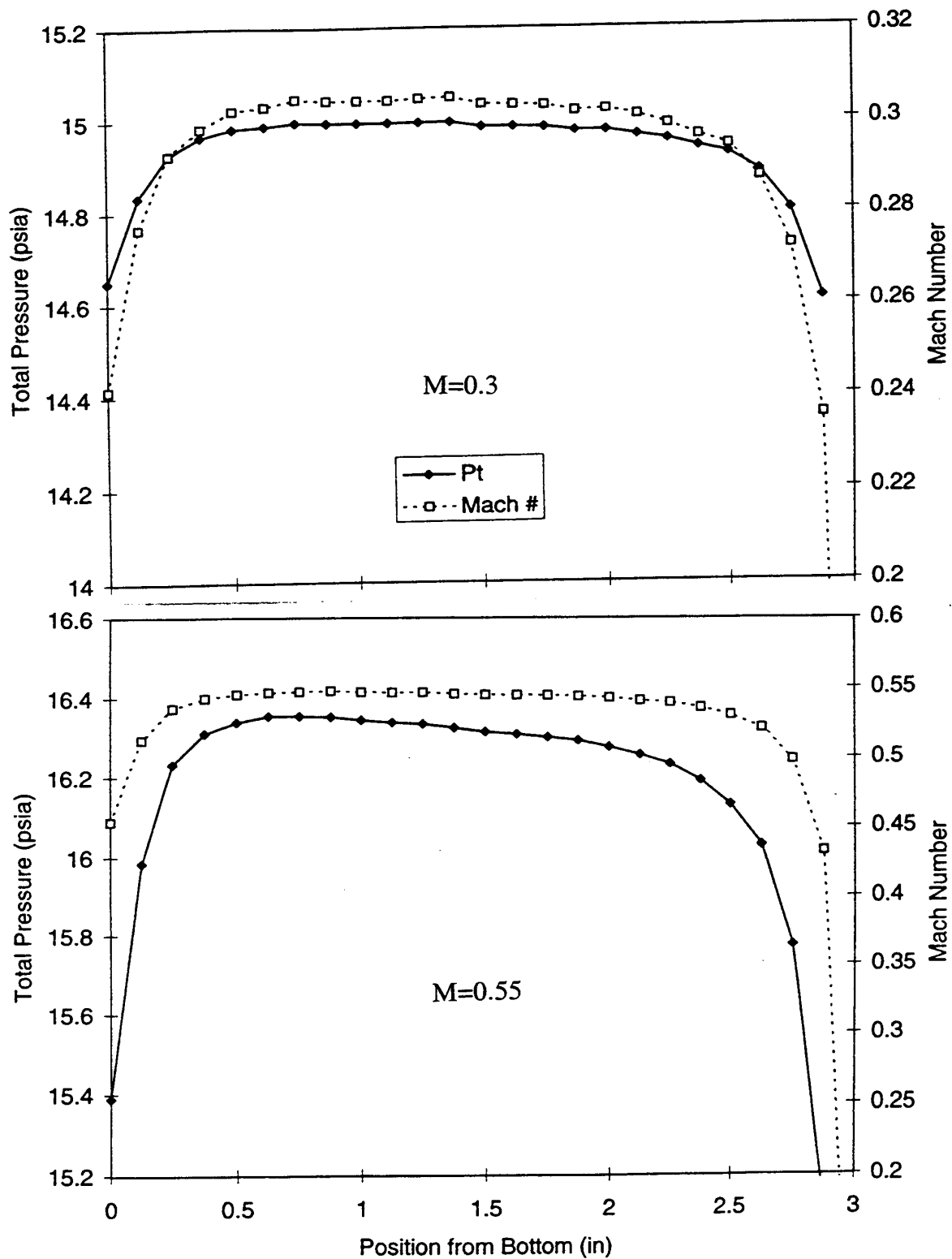


Figure 36 Mach number and total pressure variation in the flow duct test section for different centerline Mach numbers at a test section centerline temperature of 200°F, centerbody removed and screen installed.



While the transducer sleeves flush to the bottom of each five cavities are permanently welded the sleeves for surface transducers are moved up and down to go through the bulk cylinders and the corresponding holes on the facesheet. The top of these sleeves is aligned with the facesheet surface and then is secured using installed setscrews. The calibrated transducers are then introduced through the sleeves in to the respective cavities. The bottom transducers are made flush with the cavity bottom and the surface transducers are flush mounted to the facesheet and then these transducers are secured using setscrews.

For SDOF type liners the procedure to prepare the panel is the same, except the bulk material is not required. Instead, the tray cavity is filled with honeycomb structure. Once the panel is ready, it is mounted securely at the bottom of the flow duct test section. The transducers are connected to the respective cables, which are connected to a VAX computer system thorough power supplies, amplifiers, low pass filters, and A/D converters.

**Flow Duct Test and Data Acquisition:** For insitu impedance and boundary layer measurement tests the DC flow opening is sealed off at the bottom of the tray. Then the acoustic excitation, either broadband or discrete frequency sine waves, is introduced into the duct after achieving the desired flow and temperature conditions in the test section. Broadband excitation is only used for no flow condition, whereas, discrete frequency excitation is used for all cases. Utilizing the data acquisition code the complex pressure field at both transducer locations of each of the five cavities are measured and Fourier Transformed in to respective complex transfer function and sound pressure level spectra. For discrete frequency excitation, the analog data is averaged in time domain triggered by the same electronic signal going to the acoustic drivers. The flow noise is reduced by this process and the signal to noise ratio is enhanced significantly. The averaged data is then digitized and Fourier Transformed. At the completion, the data is stored in a file for further analysis. While this operation continues the computer controlled traverse system is simultaneously utilized to measure the boundary layer velocity and temperature profiles and is stored in files. Once all the tests for a configuration are complete, the DC flow opening at the tray bottom is opened and the DC flow adapter is attached and sealed for leakage. Then the DC flow measurements are made using the suction pump, operated remotely, at different flow and temperature conditions. Acoustic excitation is not required for DC flow tests. Again, the test data is stored in computer files.

#### **4.5 Performance Checkout for High Frequency Impedance Tube:**

Before measuring any normal impedance the apparatus is checked out for its performance. In this effort various cavities are created as test samples and their normal impedance is measured utilizing the transducer calibrations. The reactance data is compared with the analytical results (i.e.,  $\cot(kl)$ ,  $l$  being the cavity depth and  $k$  being the wave number). Some of the results of this checkout process are shown in Figures 37 and 38 for cavity depths of 1.5", 1.0", 0.5", and 0.2". The reactance agreement with the theory is excellent. The resistance of these cavities should be zero, except at and near anti-resonance frequencies. Within the limits of experimental inaccuracies and the non-rigidity of the cavity bottom the resistance levels are acceptable. For very shallow cavity (like 0.2") the resistance at lower frequencies is significantly higher. The reason for such discrepancy is the relatively longer sound wave length compared to the cavity depth.

#### **4.6 Performance Checkout for Insitu Cavities in the Flow Duct System:**

In this study each pair of transducers is installed into the calibrator, one being flush mounted on the bottom surface and the other projected upward by a certain length. Insitu impedance is measured for such arrangement as if the sample surface is the tip of the second transducer. Thus, the projected length becomes the cavity depth. These measurements are made at ambient temperature and at heated conditions by introducing the calibrator inside the furnace (described earlier). The transducer connections are made exactly what would be used during actual tests. The measured reactance is compared with analytical results. Typical results for a pair of transducers (pair #3) at different temperatures are shown in Figure 39. Again, the agreement between data and prediction is excellent for all five pairs of transducers, confirming the accuracy of calibration. Next, the transducers are mounted into the tray cavities, tray being installed in the flow duct test section. Measurement of insitu impedance is made simultaneously for all five cavities (without any test sample). Reactance data for each cavity is compared with prediction and again, the agreement (see Figures 40 and 41) approves the use of this system, including the software, for actual tests.

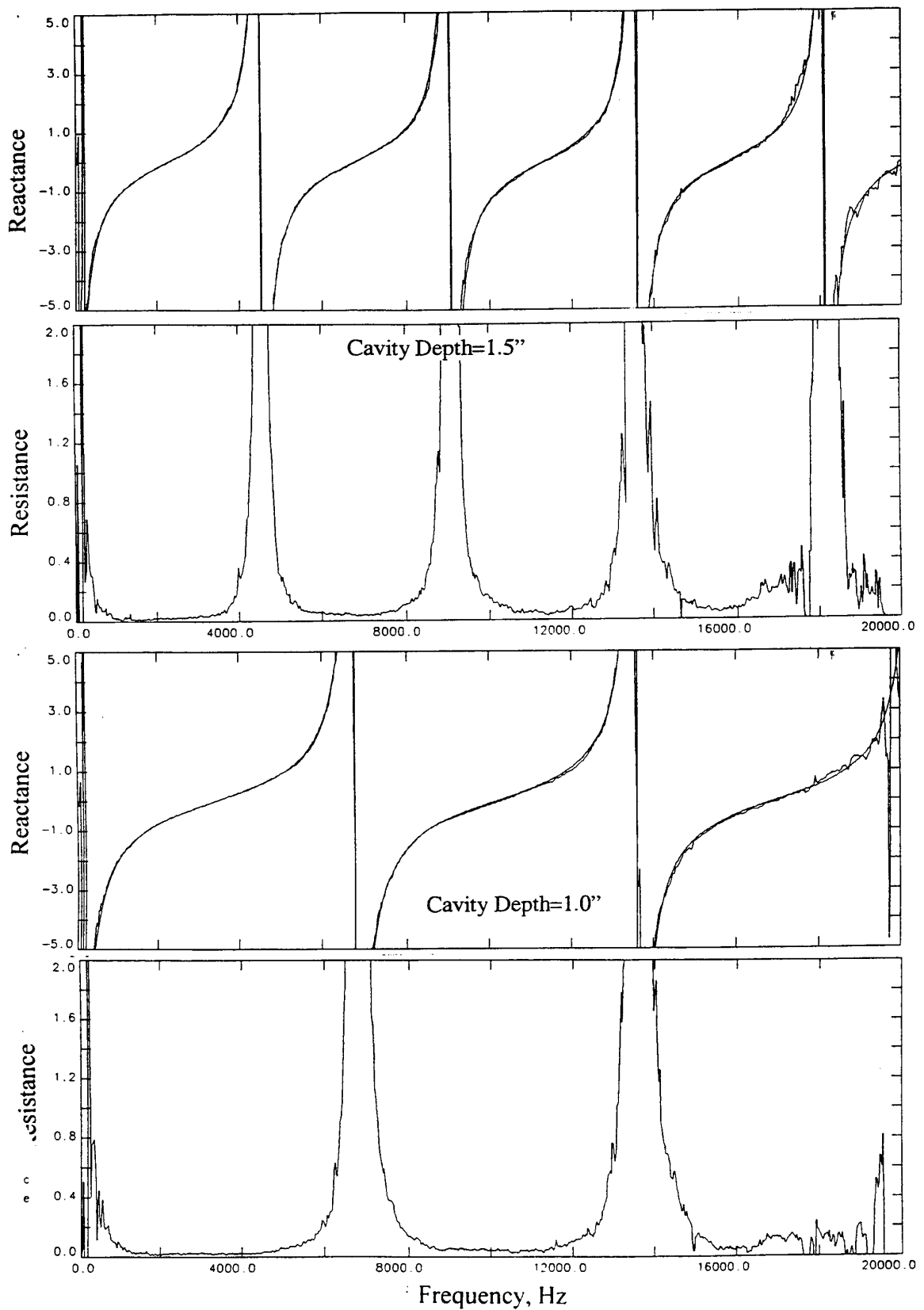


Figure 37. Normal impedance of 1.5" and 1.0" deep cavities measured using High Frequency Impedance Tube and compared with theory.

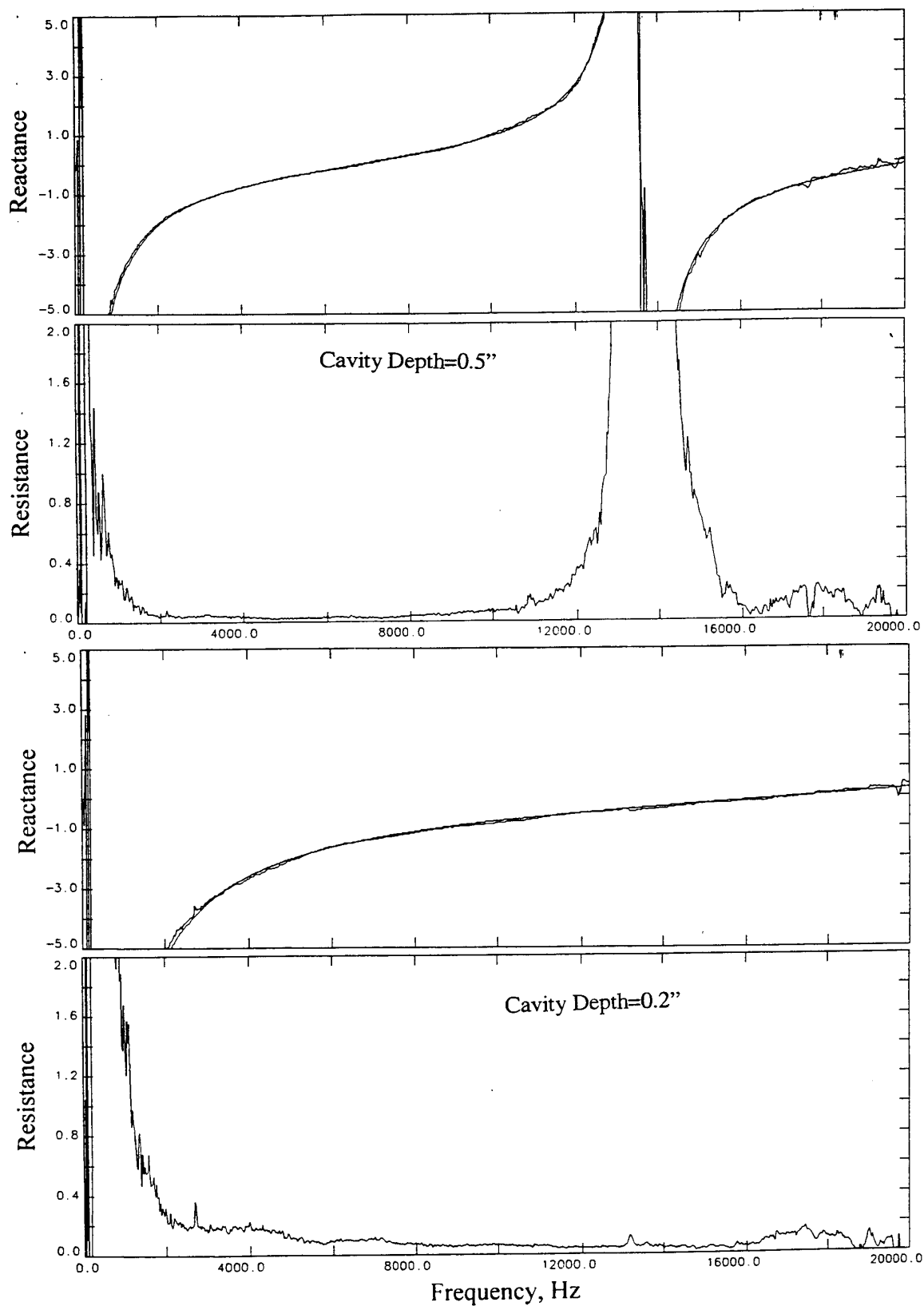


Figure 38. Normal impedance of 0.5" and 0.2" deep cavities measured using High Frequency Impedance Tube and compared with theory.

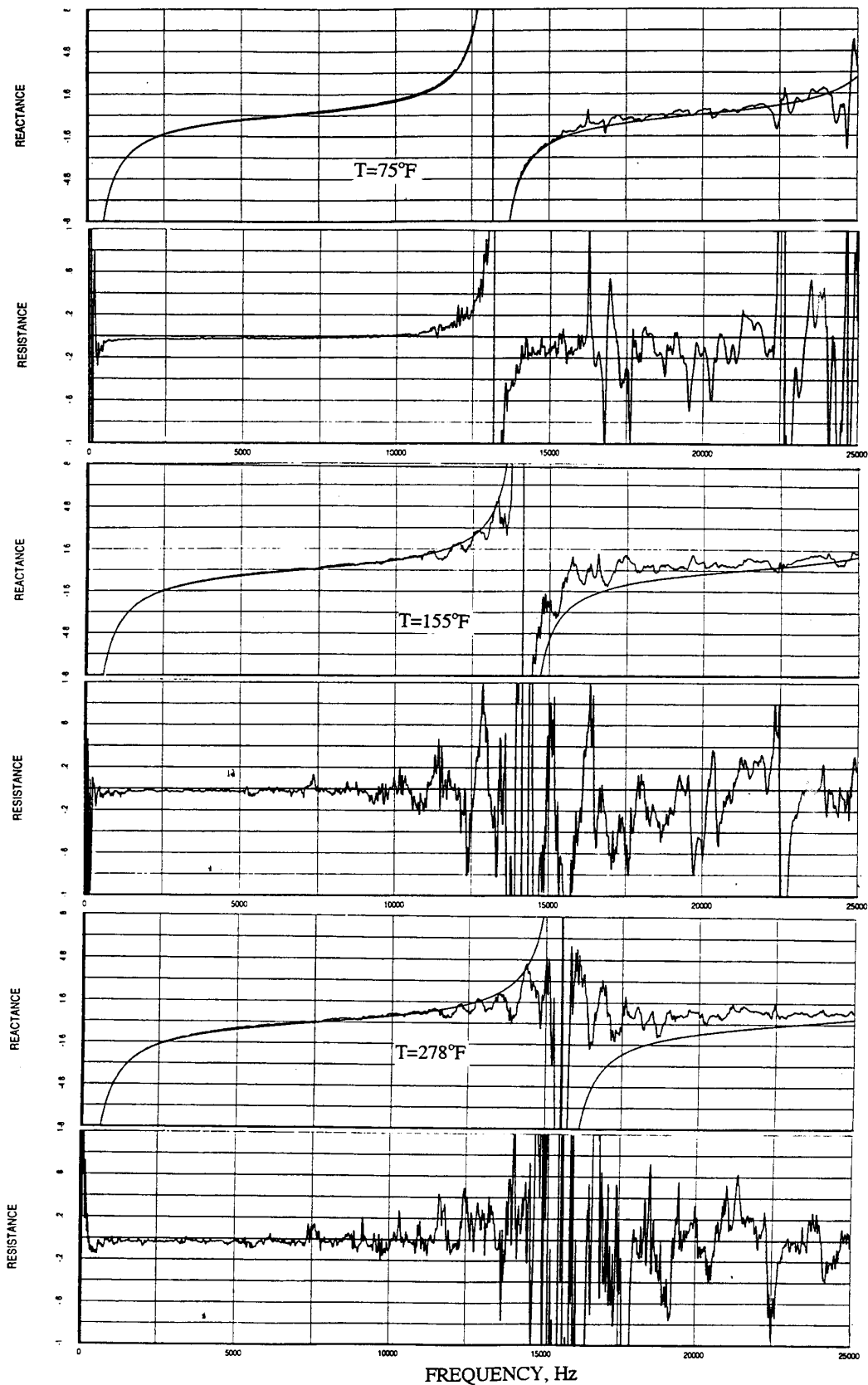


Figure 39. In situ impedance of a 0.52" cavity at different temperatures measured using Pair #2 transducers and compared with theory.

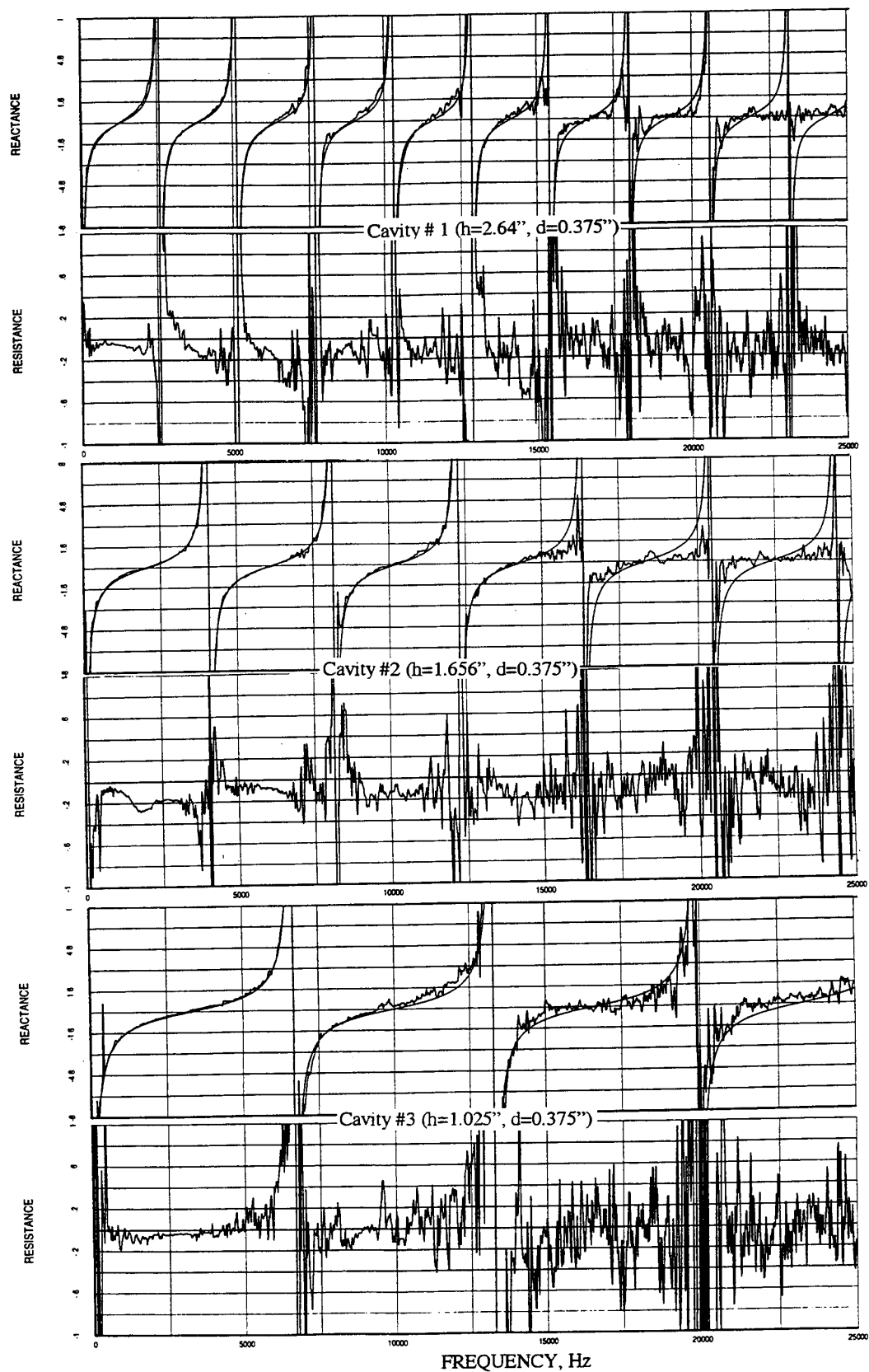


Figure 40. In situ impedance of cavities #1, #2, and #3 measured in the flow duct at ambient temperature and compared with theory.

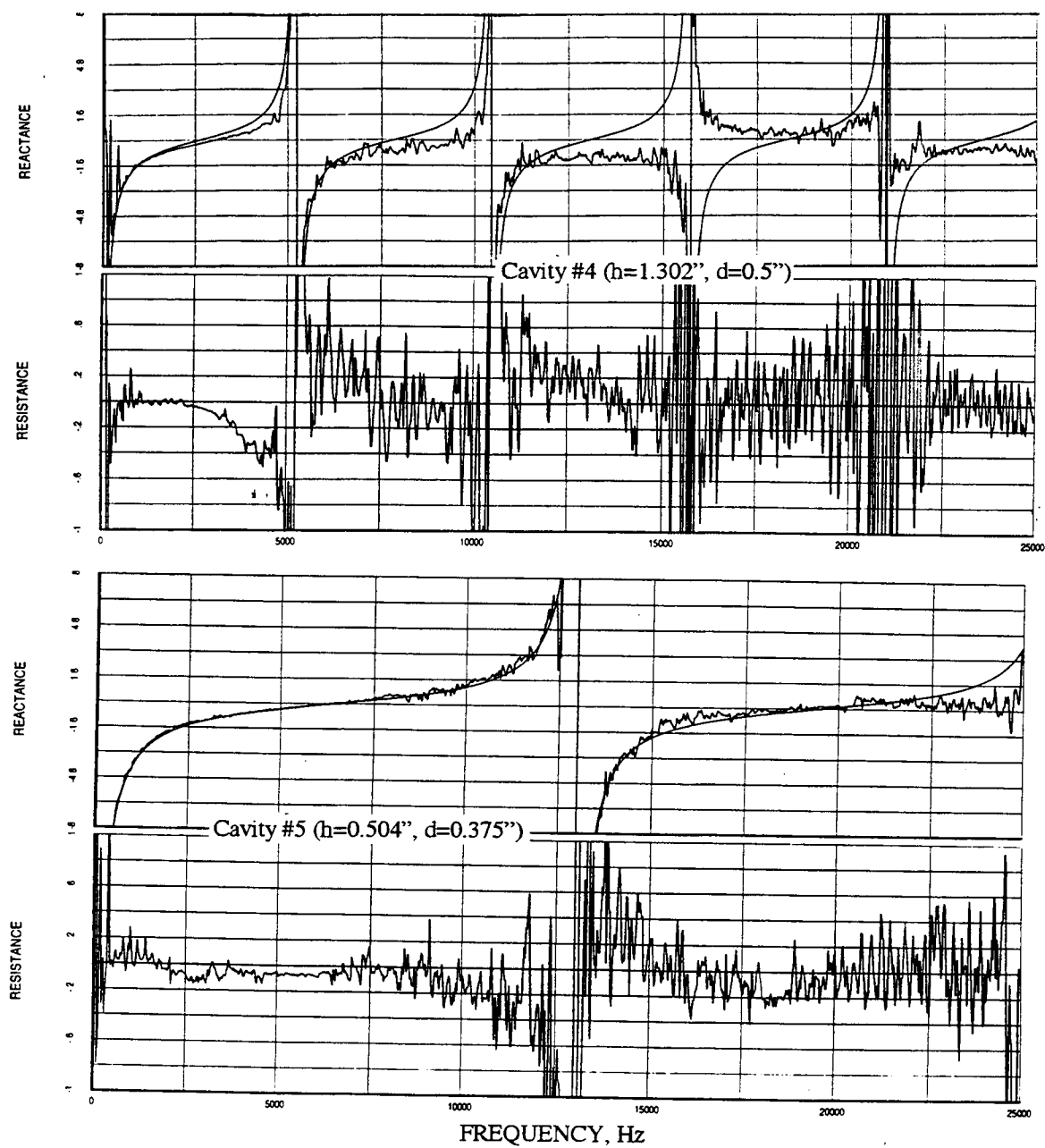


Figure 41. In situ impedance of cavities #4 and #5 measured in the flow duct at ambient temperature and compared with theory.

## 5.0 HIGH FREQUENCY IMPEDANCE TUBE TESTS

Impedance tube tests using broadband sound excitation are conducted for bulk absorber type and SDOF type liner samples. In these tests the excitation level is varied. For SDOF type samples the cavity depth behind the sample is varied to acquire the impedance for the entire frequency range of 20 kHz. For bulk absorber type liner samples there is no cavity behind the bulk samples. The rigid surface of the plunger touches the bulk surface. A large number of bulk/facesheet combinations are tested using the samples listed in Tables 2 through 6. All the samples listed in Table 7 are tested as SDOF panels. In addition, several facesheets, used for bulk absorber panel samples, are also tested as SDOF samples to evaluate their normal impedance compared to the bulk and facesheet together.

For some SDOF type tests several cavities of different depths are used for impedance measurement. Deeper cavity results are more accurate for low frequency regime. Normal impedance of the facesheet alone is evaluated by removing the cavity contribution to the impedance from the data. In addition, the impedance is constructed by using data for different cavities for different frequency ranges. All the data are numerically smoothen to minimize larger oscillation for effective parametric comparison. Figure 42 shows the normal impedance spectra for cavities of various depths. It is clear that the resistance approaching a zero value for lower frequencies can be seen for the deepest cavity. For the cavity of 0.24" (the shallowest cavity tested) the correct resistance appears to begin from a frequency of about 7 to 8 kHz. Similar result for a facesheet over cavities of different depths is shown in Figure 43. In this the corresponding cavity only impedance spectra are subtracted from the measured data. Again, it is clear that the accuracy of impedance for lower frequencies is seen with deeper cavities. In addition, the reactance approaching a zero value at zero frequency is measured with the deepest cavity. Utilizing these results Figure 44 is constructed, which gives the lower and upper limits of the frequencies for a cavity depth for which the impedance results are acceptable.

### 5.1 Normal Impedance for Facesheets Alone:

#### 5.1.1 Facesheets for Bulk Absorbers:

**Data Analysis & Presentation:** Several facesheets from Table 7 are tested using cavities of depths 0.25", 0.5", 1.0", and 1.5". As described above the appropriate portions of the impedance spectra, after removing the corresponding cavity impedance, are combined together and numerically smoothen. These results are plotted in Figures 45(a), 46(a), and



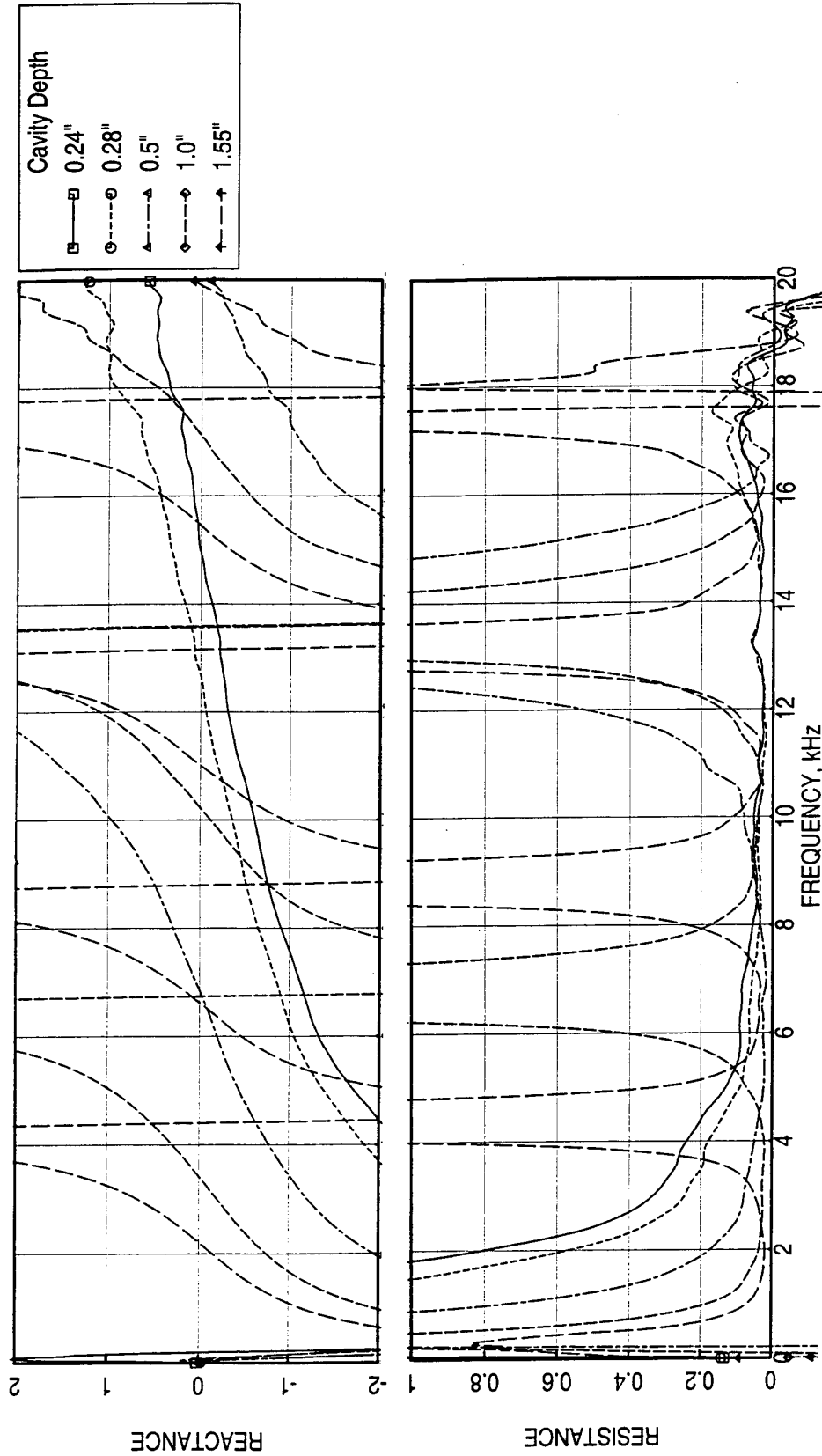


Figure 42. Effect of cavity depth on normal impedance for cavity only configurations, OASPL = 150 dB.

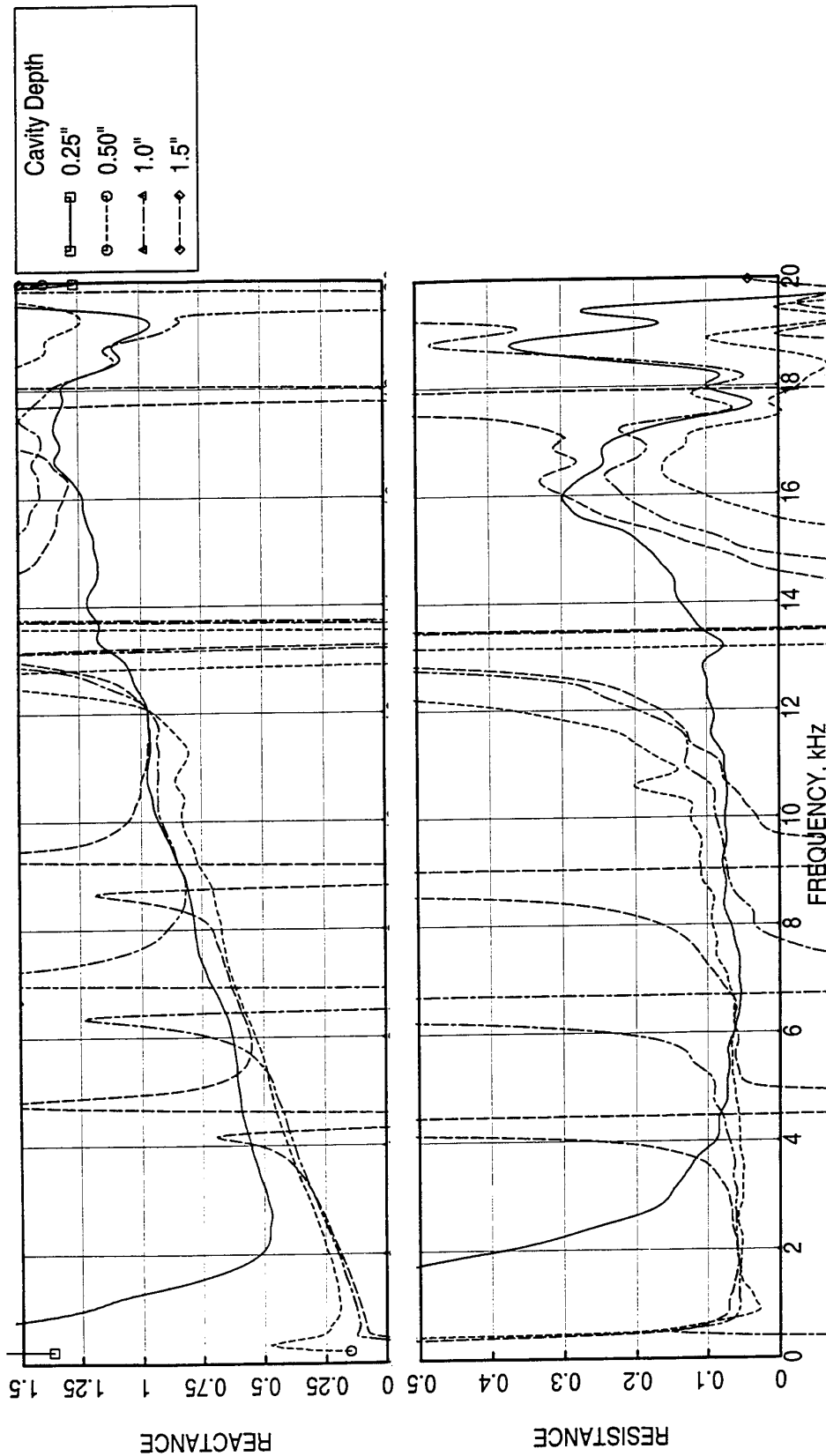


Figure 43. Effect of cavity depth on normal impedance for a facesheet ( $\sigma=40\%$ ,  $t=0.025"$ , and  $d=0.04"$ ), corrected for cavity impedance, OASPL = 150 dB.

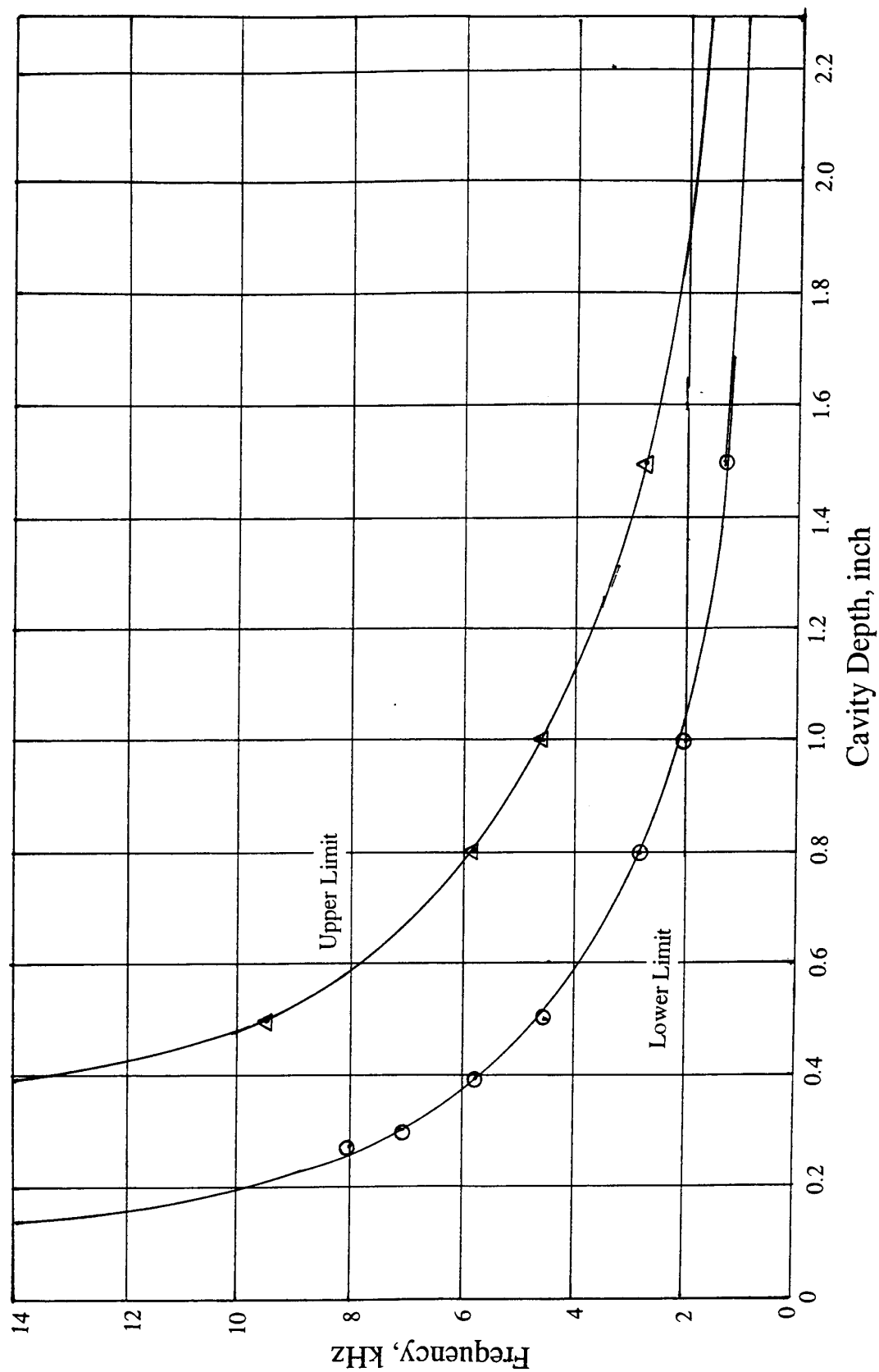


Figure 44. Lower and upper frequency limits of reliable normal impedance for different cavity depths.

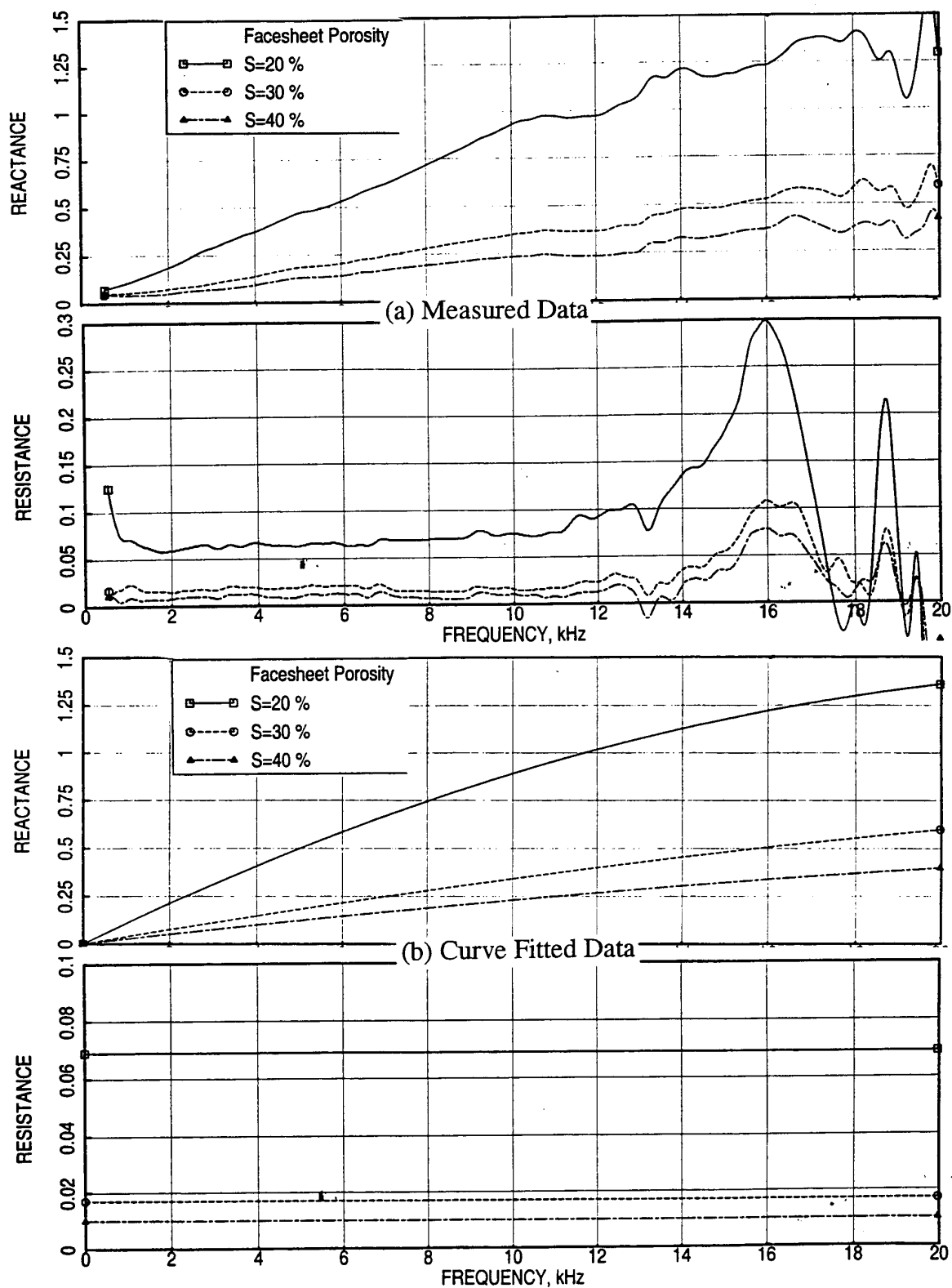


Figure 45. Effect of facesheet porosity on normal impedance, acquired by multi cavity measurements and corrected for cavity effects, for 0.025"-thick facesheets,  $d_c$  0.04", OASPL= 150 dB, (a) measured and (b) curve fitted.

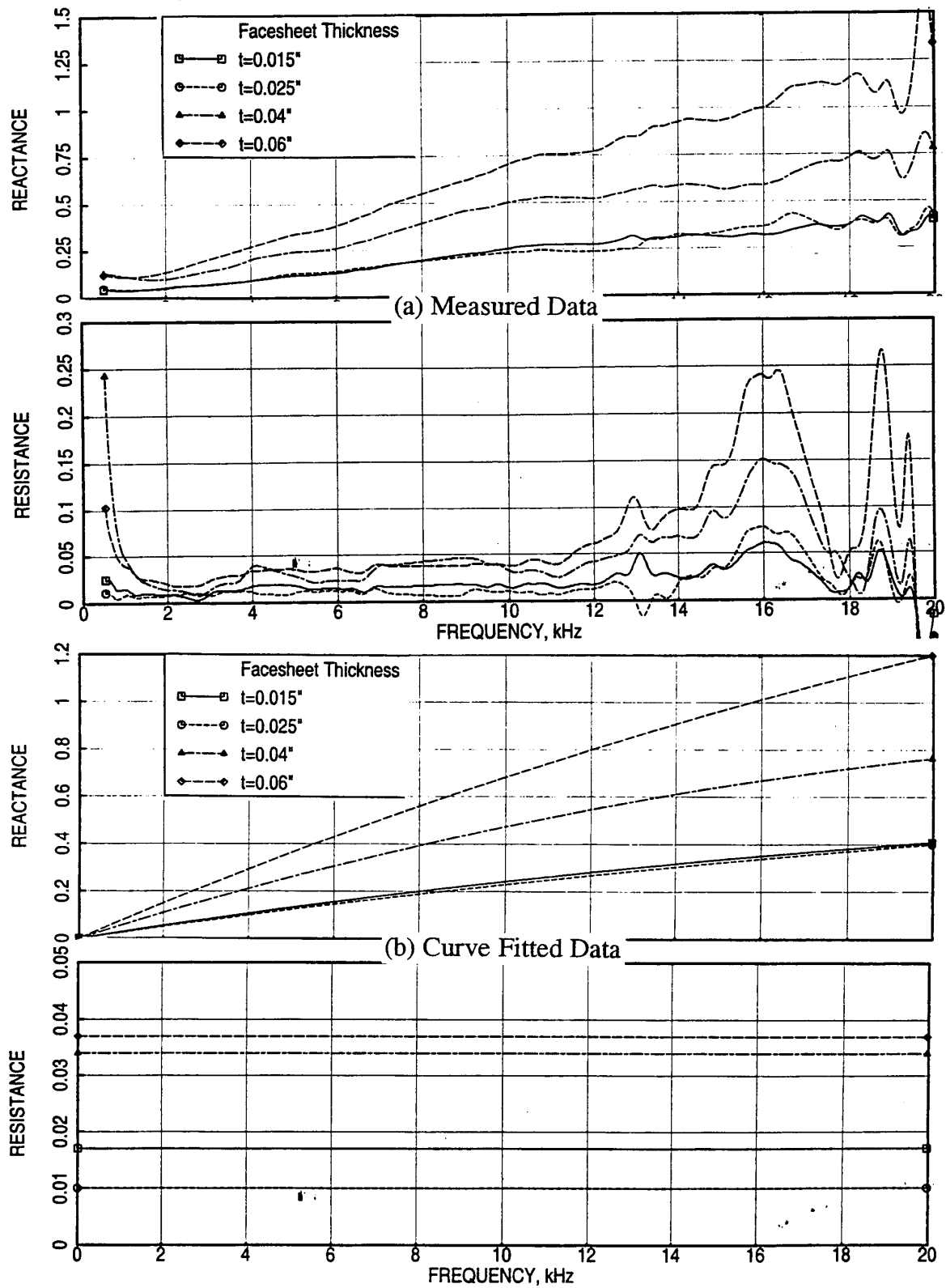


Figure 46. Effect of facesheet thickness on normal impedance, acquired by multi cavity measurements and corrected for cavity effects, for 40 % porous facesheets,  $d=0.04"$ , OASPL= 150 dB, (a) measured and (b) curve fitted.

47(a) indicating parametric variations due to porosity, thickness, and hole diameter, respectively. While the reactance tends to zero at zero frequency and increases with frequency, the resistance remains more or less constant for frequencies up to about 13 or 14 kHz. Above this frequency the resistance increases and peaks at about 16 kHz. and shows a similar peak at about 19 kHz. The possibility of higher order contamination is likely to cause this type of effect above 13 kHz. The effect seems to be prominent since the resistance levels for these highly porous facesheets are relatively small. In addition, with facesheet the cavity anti-resonance frequency decreases by certain amount due to the change in the effective cavity depth. The effective cavity depth depends on the facesheet thickness and porosity. The second resistance peak at about 19 kHz is most likely due to the increase in the cavity depth, which is responsible in shifting the anti-resonance frequency from 20 kHz to 19 kHz.

Based on these arguments the resistance is assumed to be independent of frequency and an average value is calculated using the data up to 13 kHz. For reactance the data is curve fitted using a second order polynomial forcing it to be zero at zero frequency. Thus, the processed data corresponding to Figures 45(a), 46(a), and 47(a) are plotted in Figures 45(b), 46(b), and 47(b), respectively.

Due to the constraint of time a large number of facesheets, mostly from Tables 4 and 5, are tested using a single 0.25"-deep cavity. The typical results after correcting for the cavity reactance are shown in Figures 48 through 50. Figure 48 shows the effect of thickness and hole diameter for 40% porous facesheets. As discussed earlier the low frequency data is not accurate for using a shallow cavity of 0.25" deep. The low frequency limit depends on the effective cavity depth. The effective cavity depth increases with increasing facesheet thickness and thus the lower frequency limit goes down. For the same reason the anti-resonance frequency goes down for thicker facesheets. For example, the effective cavity depth becomes significantly higher for facesheets of thickness 0.125" and 0.14" and the anti-resonance occurs at around 12 kHz compared to 20 kHz for 0.25"-deep cavity. The frequency limitation for reliable data is more severe for facesheets of lower porosities with higher thickness (see Figures 49 and 50). At this situation the tests should have been conducted using different cavity depths to acquire accurate data for the entire frequency range. However, to use the currently acquired single cavity data in a meaning full way the data for the frequency range between lower limit to a frequency before the anti-resonance frequency is utilized to obtain the impedance spectra. The reactance at higher frequency seems to be behaving better compared to the corresponding resistance. Therefore, the upper limit for reactance data, used in data processing, is much higher compared to resistance limit. The

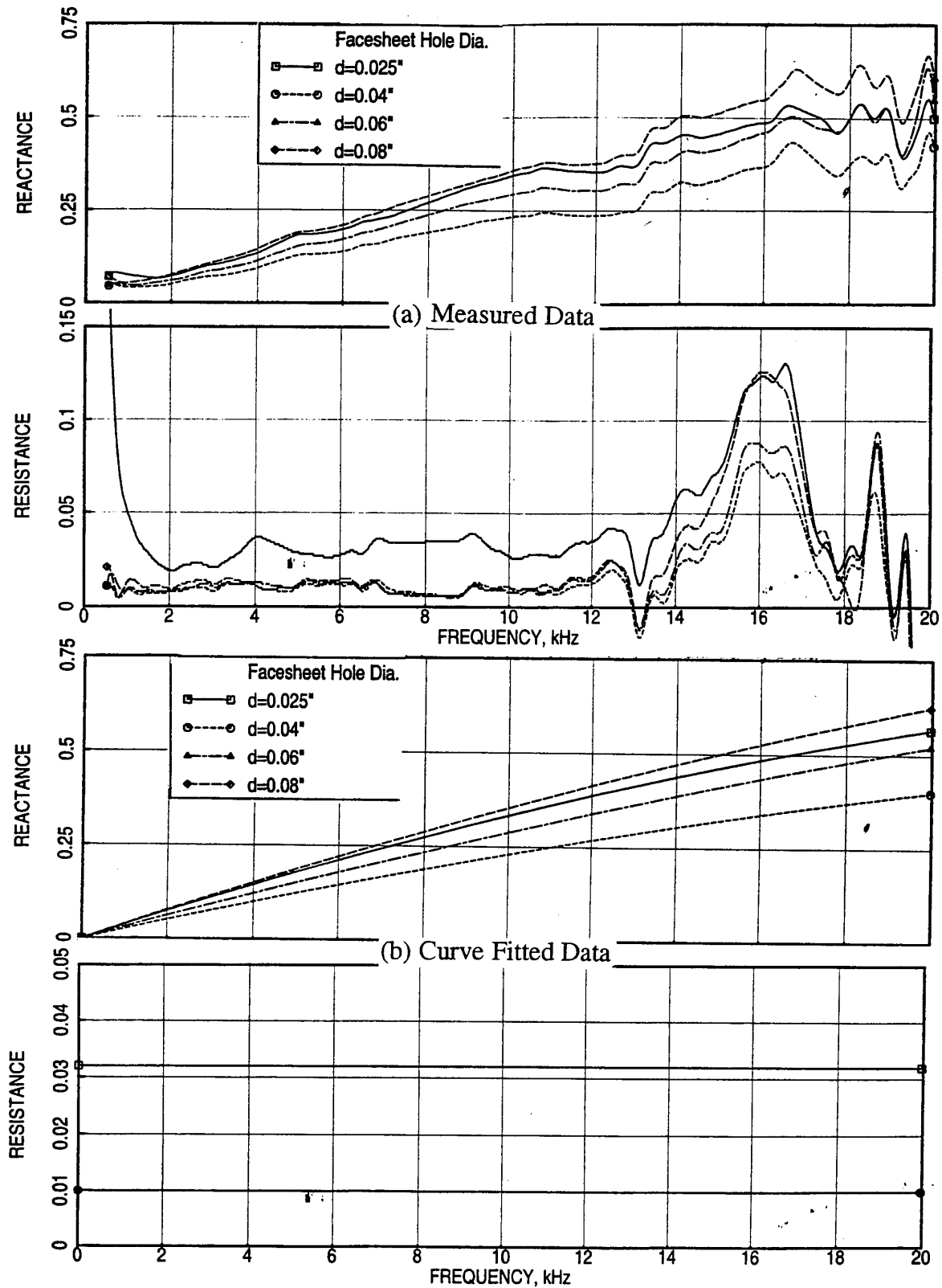


Figure 47. Effect of facesheet hole diameter on normal impedance, acquired by multi cavity measurements and corrected for cavity effects, for 0.025"-thick facesheets,  $\sigma=40\%$ , OASPL= 150 dB, (a) measured and (b) curve fitted.

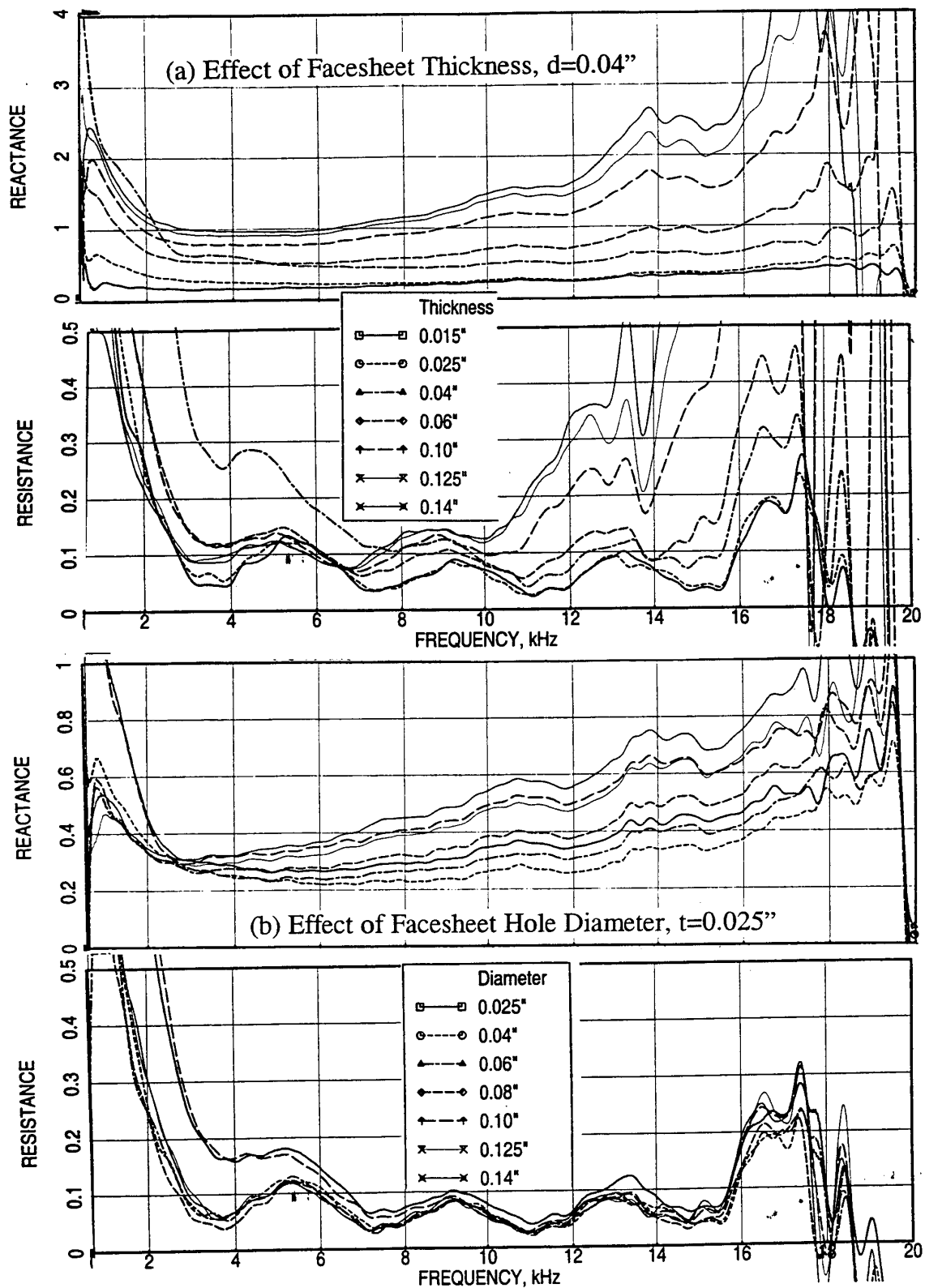


Figure 48. Effect of facesheet thickness and hole diameter on normal impedance, acquired by a single 0.25"-deep back cavity measurement, cavity effect being removed for reactance, for 40 % porous facesheets, OASPL= 150 dB, (a)  $d=0.04''$  and (b)  $t=0.025''$ .



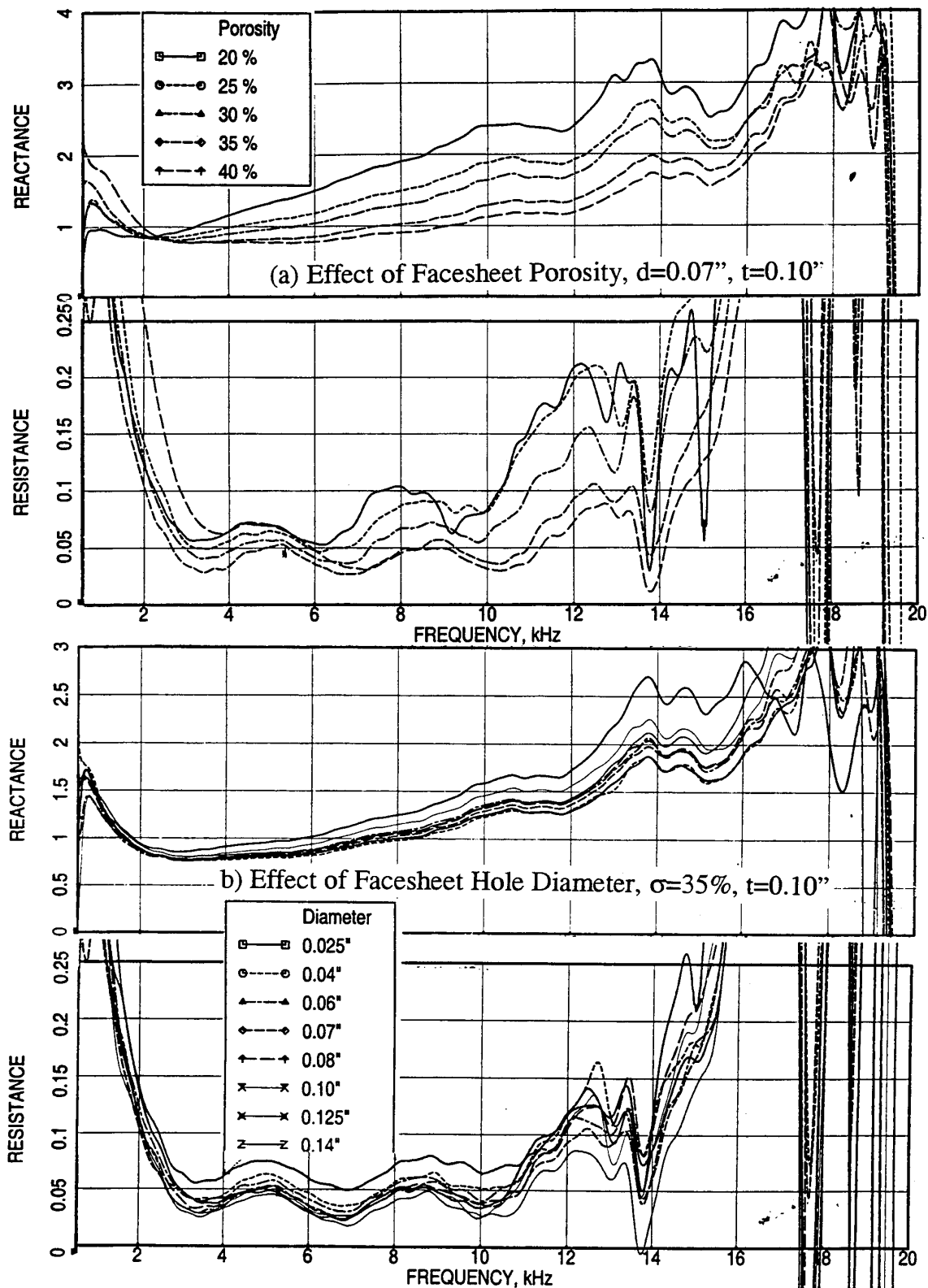


Figure 49. Effect of facesheet porosity and hole diameter on normal impedance, acquired by a single 0.25"-deep back cavity measurement, cavity effect being removed for reactance, OASPL= 150 dB, (a)  $d=0.07''$ ,  $t=0.10''$  and (b)  $\sigma=35\%$ ,  $t=0.10''$ .

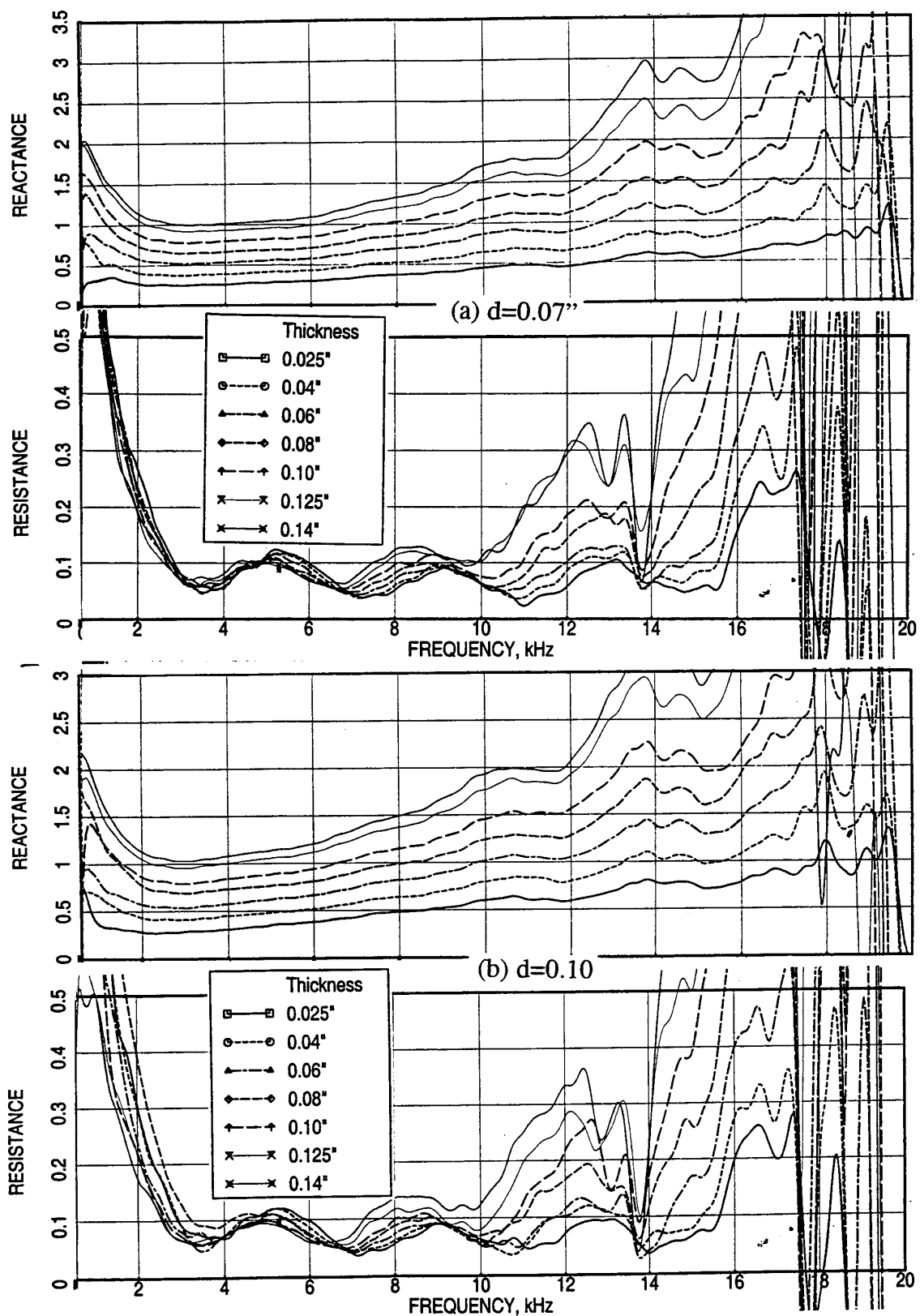


Figure 50. Effect of facesheet thickness on normal impedance, acquired by a single 0.25"-deep back cavity measurement, cavity effect being removed for reactance, for 35 % porous facesheets, OASPL= 150 dB, (a)  $d=0.07''$  and (b)  $d=0.10''$ .

reactance data in this range is curve fitted using a second order polynomial forcing it to zero at zero frequency. For resistance an average value is calculated using the data for this frequency range.

***Parametric Characteristics of Normal Impedance:*** The effect of porosity on normal impedance for perforated facesheets is shown in Figure 51. In general the reactance and resistance increase with decreasing porosity. The levels are higher for thicker facesheets.. The effect of facesheet thickness on normal impedance is shown in Figure 52. The reactance and resistance, both, increase with increasing facesheet thickness. The effect is more dominant for lower porosity samples. The effect of hole diameter with fixed porosity and thickness seems to be small compared to porosity and thickness effects (see Figure 53). For 40% porous facesheets with  $t=0.025''$ , the reactance decreases and then increases with increasing hole diameter. The resistance decreases with increasing hole diameter. For 35% porous facesheets with  $t=0.1''$  the reactance increases with increasing hole diameter and resistance decreases and then increases with increasing hole diameter. Figure 54 shows the effect of resistivity on normal impedance for linear facesheets. The reactance and resistance both increase with increasing facesheet resistivity.

Effect of excitation intensity on normal impedance for highly porous facesheets is relatively small (see Figure 55(a)). In general the reactance decreases and resistance increases with increasing excitation level. For linear facesheets the effect is measurable for resistance and insignificant for reactance (see Figure 55(c)).

**5.1.2 Facesheets for SDOF Type Liners:** For SDOF type liners facesheets of lower porosities are used (see Table 7).

***Data Analysis & Presentation:*** All the facesheets listed in Table 7 are tested using a single 0.25''-deep cavity. The measured data with reactance being corrected for cavity is shown in Figures 56(a), 57(a), 58(a), and 59(a). The impact of cavity is relatively less severe in these cases, since the impedance levels are considerably higher compared to highly porous facesheets for bulk absorbers. However, the characteristics of these results are qualitatively similar to those discussed under section 5.1.1. Therefore, similar procedure is applied to procure and present the data in a meaningful manner.

***Parametric Characteristics of Normal Impedance:*** The effect of porosity on normal impedance for perforated facesheets is shown in Figure 56. In general the reactance and resistance increase with decreasing porosity. The effect of facesheet thickness is shown in

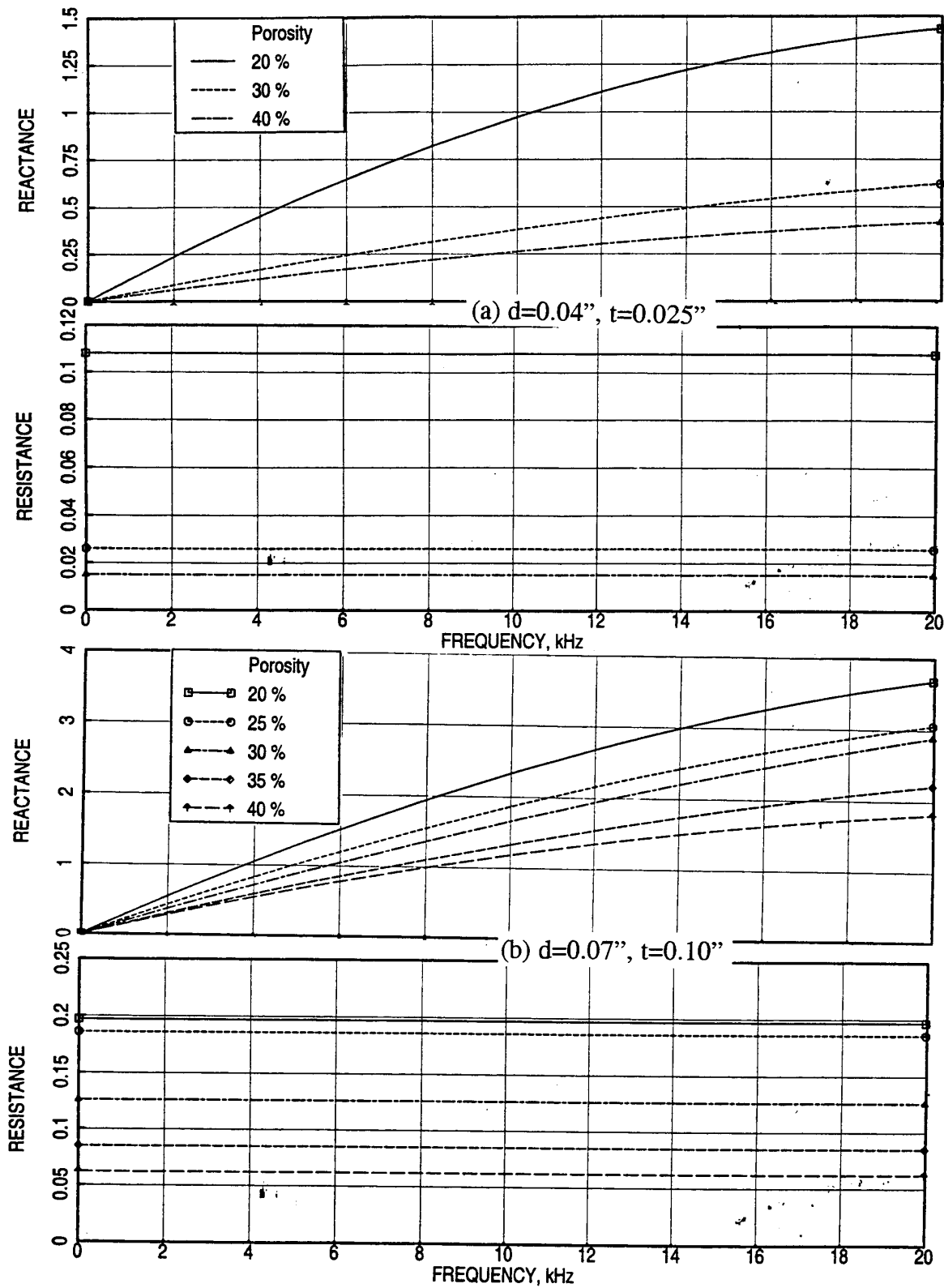


Figure 51. Effect of facesheet porosity on curve fitted normal impedance, acquired by a single 0.25"-deep back cavity measurement, cavity effect being removed for impedance, OASPL= 150 dB, (a)  $d=0.04''$ ,  $t=0.025''$  and (b)  $d=0.07''$ ,  $t=0.10''$ .

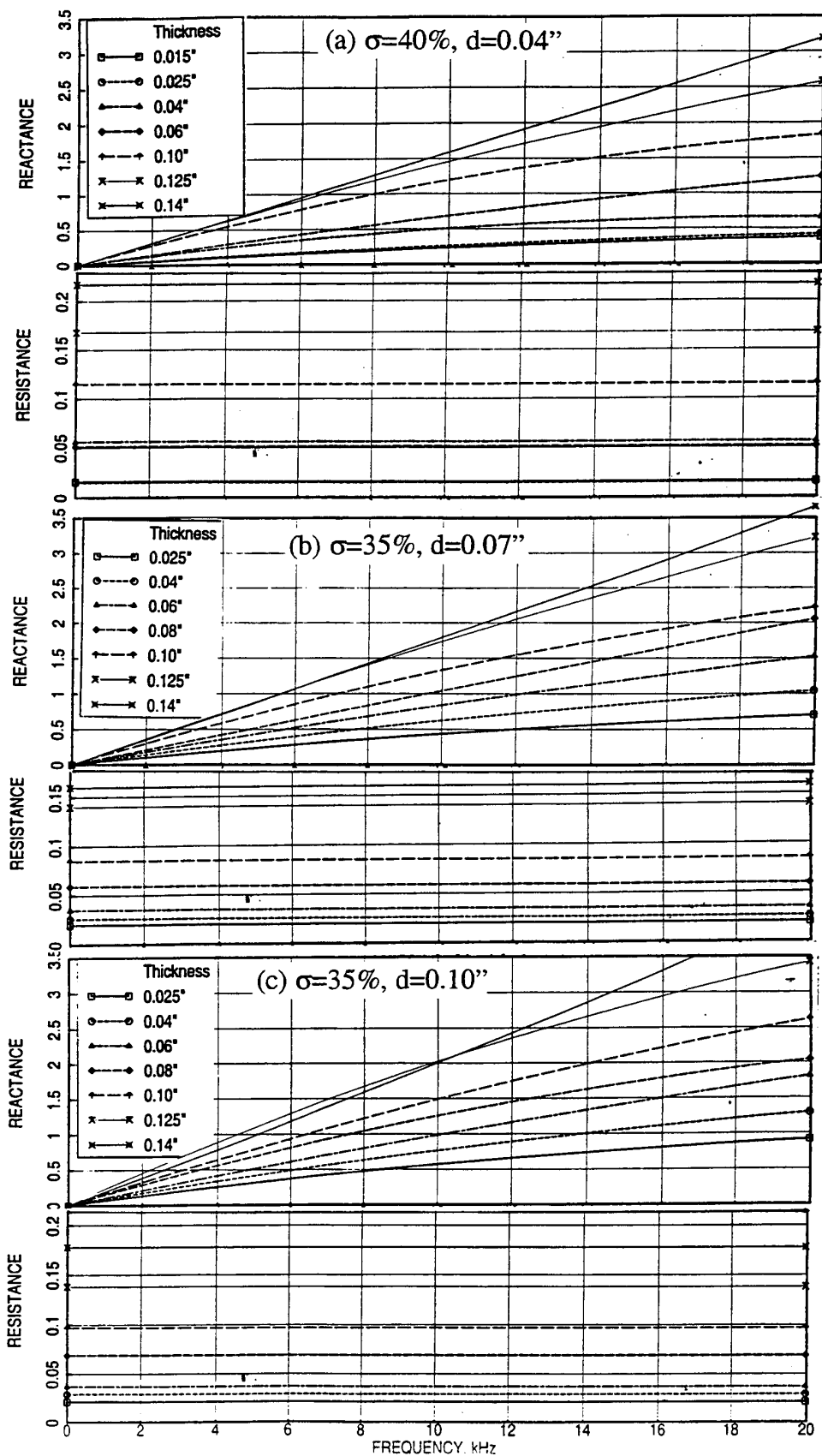


Figure 52. Effect of facesheet thickness on curve fitted normal impedance, acquired by a single 0.25"-deep back cavity measurement, cavity effect being removed for impedance, OASPL= 150 dB, (a)  $\sigma=40\%$ ,  $d=0.04''$ , (b)  $\sigma=35\%$ ,  $d=0.07''$ , and (c)  $\sigma=35\%$ ,  $d=0.10''$ .

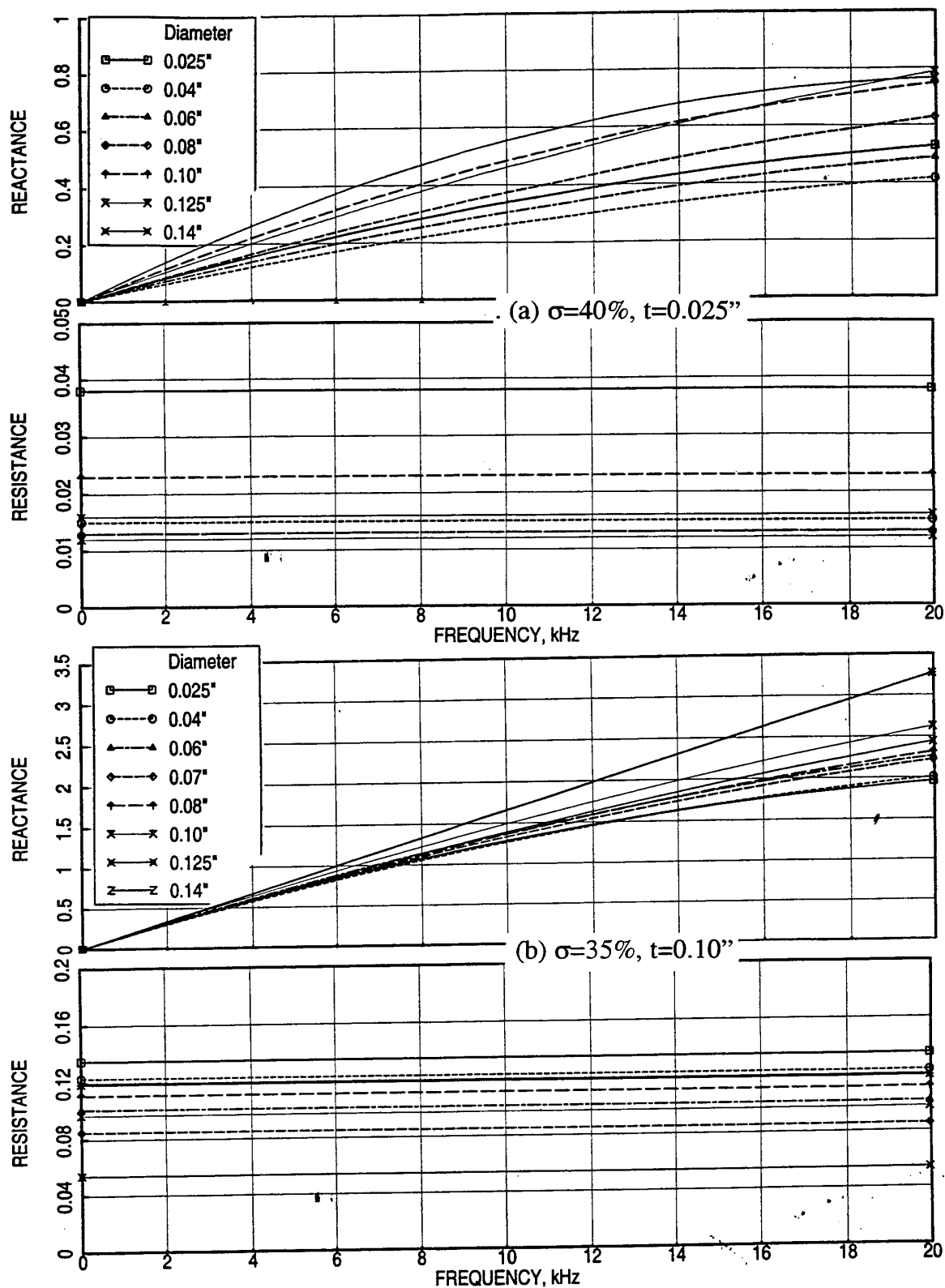


Figure 53. Effect of facesheet hole diameter on curve fitted normal impedance, acquired by a single 0.25"-deep back cavity measurement, cavity effect being removed for impedance, OASPL= 150 dB, (a)  $\sigma=40\%$ ,  $t=0.025''$  and (b)  $\sigma=35\%$ ,  $t=0.10''$ .

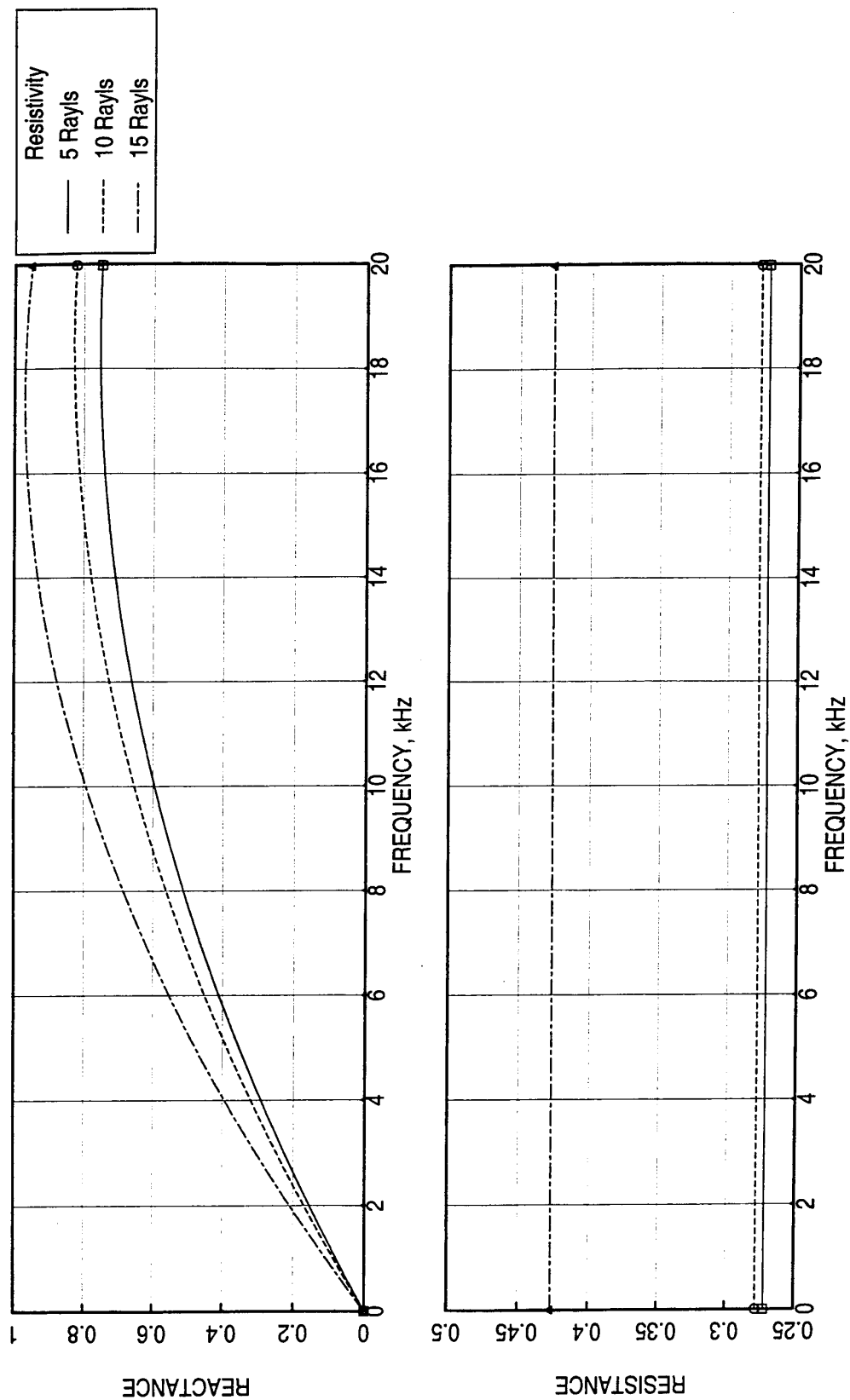


Figure 54. Effect of facesheet resistivity on curve fitted normal impedance, acquired by a single 0.25"-deep back cavity measurement, cavity effect being removed for impedance, for linear facesheets, OASPL= 150 dB.

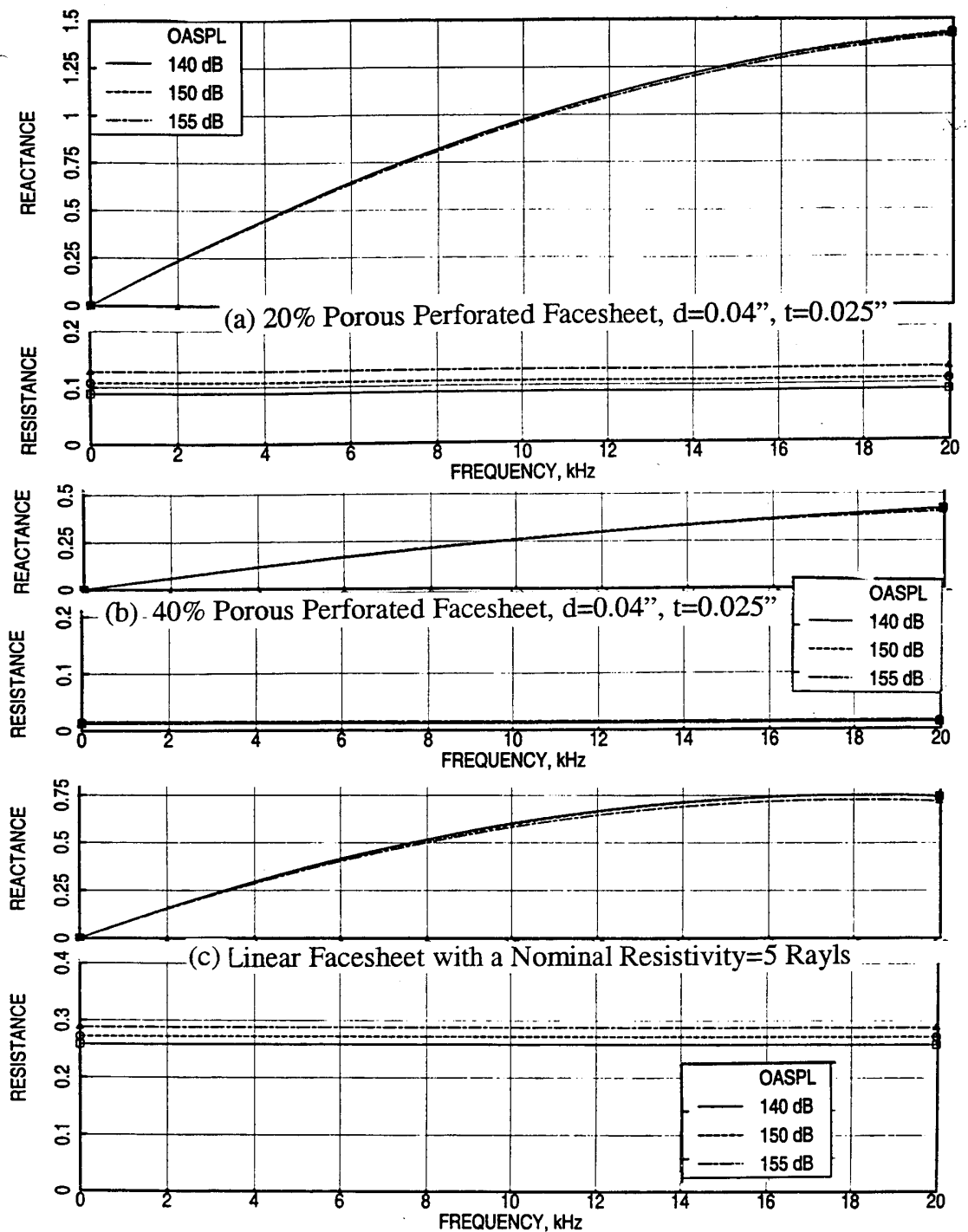


Figure 55. Effect of excitation intensity on curve fitted normal impedance, acquired by a single 0.25"-deep back cavity measurement, cavity effect being removed for impedance.



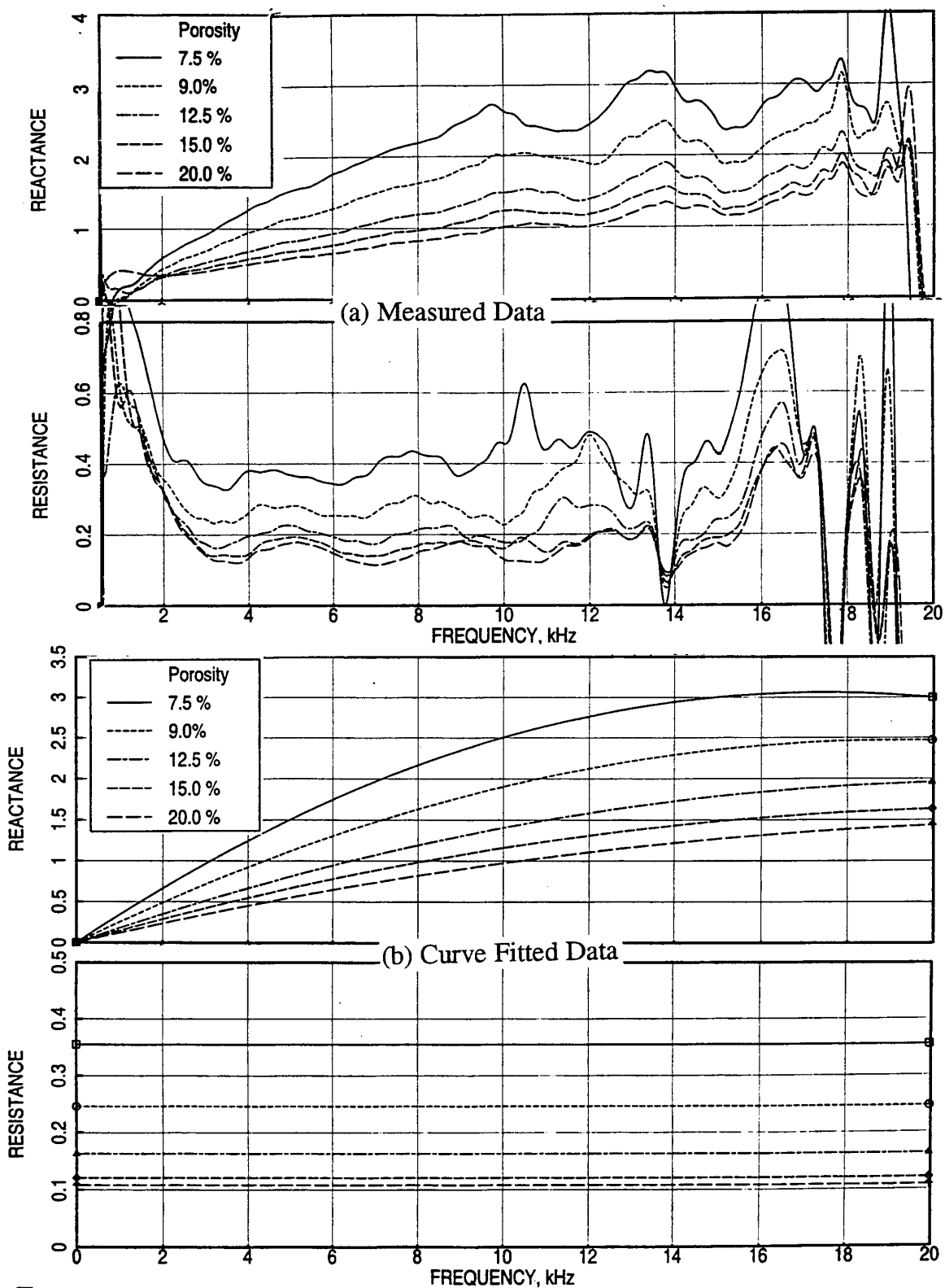


Figure 56. Effect of facesheet porosity on normal impedance, acquired by a single 0.25"-deep back cavity measurement, for 0.025"-thick facesheets,  $d=0.04"$ , OASPL= 150 dB, (a) measured data (cavity effect removed for reactance) and (b) curve fitted data (cavity effect being removed for impedance).

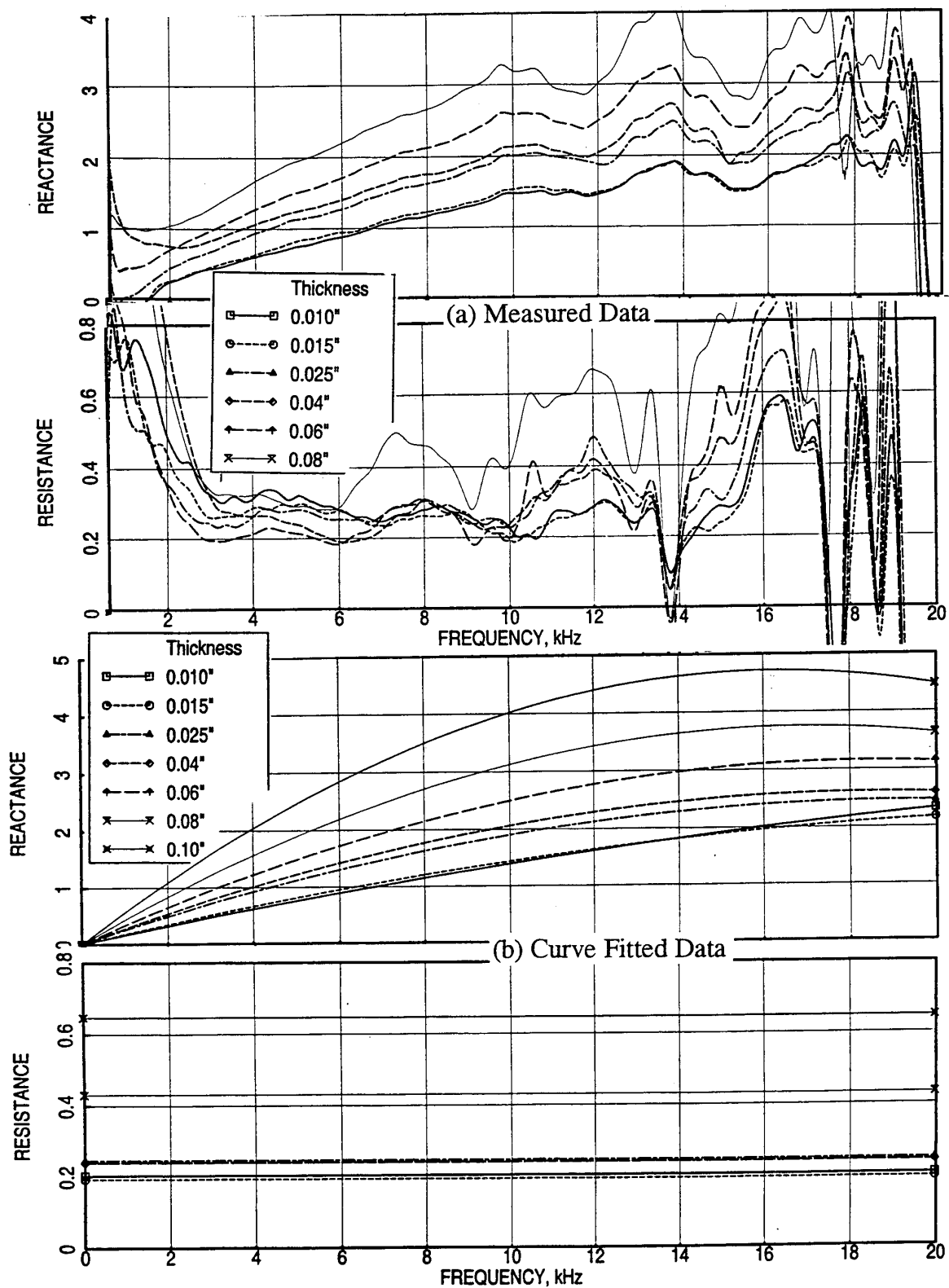


Figure 57. Effect of facesheet thickness on normal impedance, acquired by a single 0.25"-deep back cavity measurement, for 9% porous facesheets,  $d=0.04"$ , OASPL= 150 dB, (a) measured data (cavity effect removed for reactance) and (b) curve fitted data (cavity effect being removed for impedance).

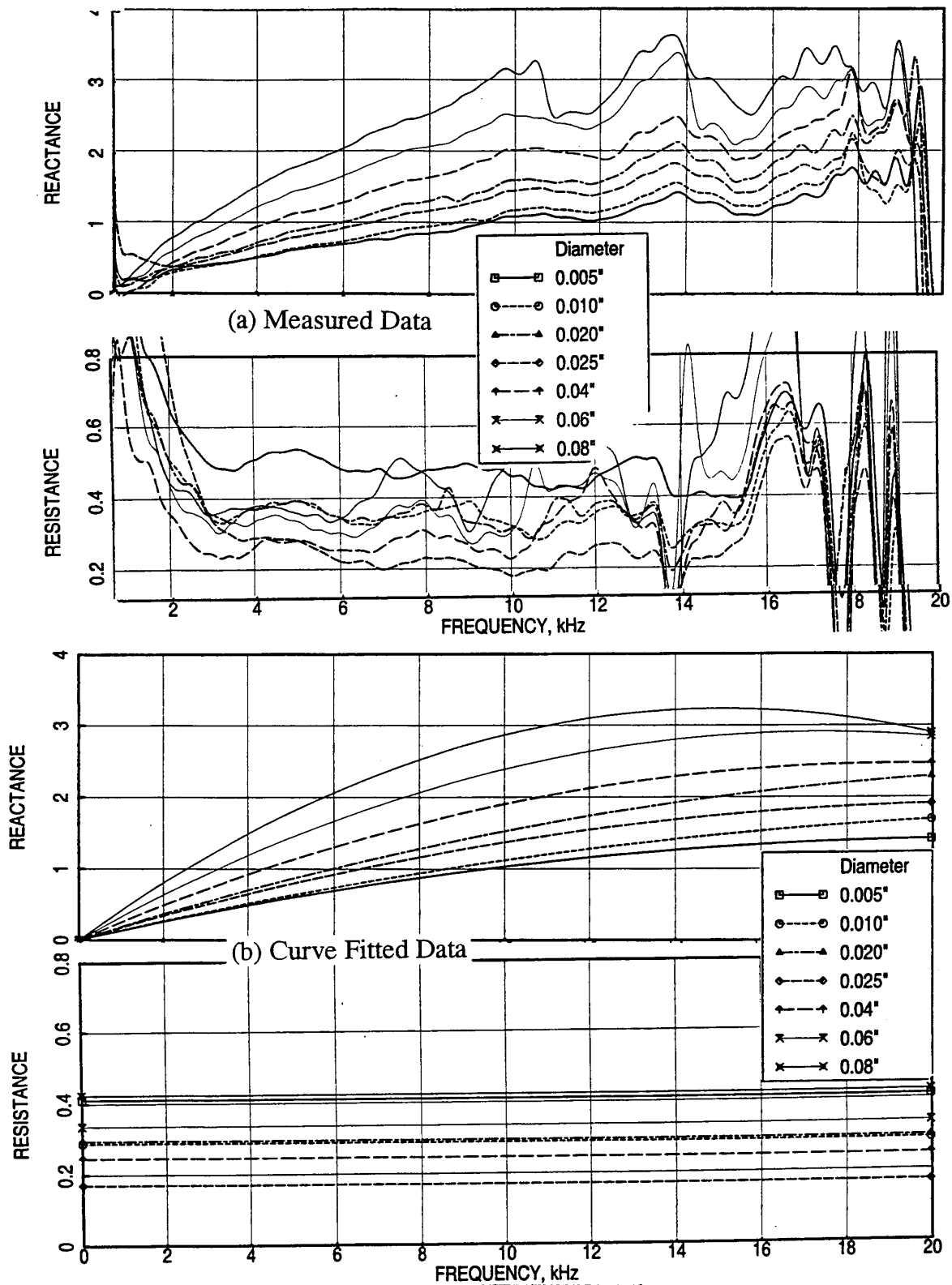


Figure 58. Effect of facesheet hole diameter on normal impedance, acquired by a single 0.25"-deep back cavity measurement, for 9% porous and 0.025"-thick facesheets, OASPL= 150 dB, (a) measured data (cavity effect removed for reactance) and (b) curve fitted data (cavity effect being removed for impedance).

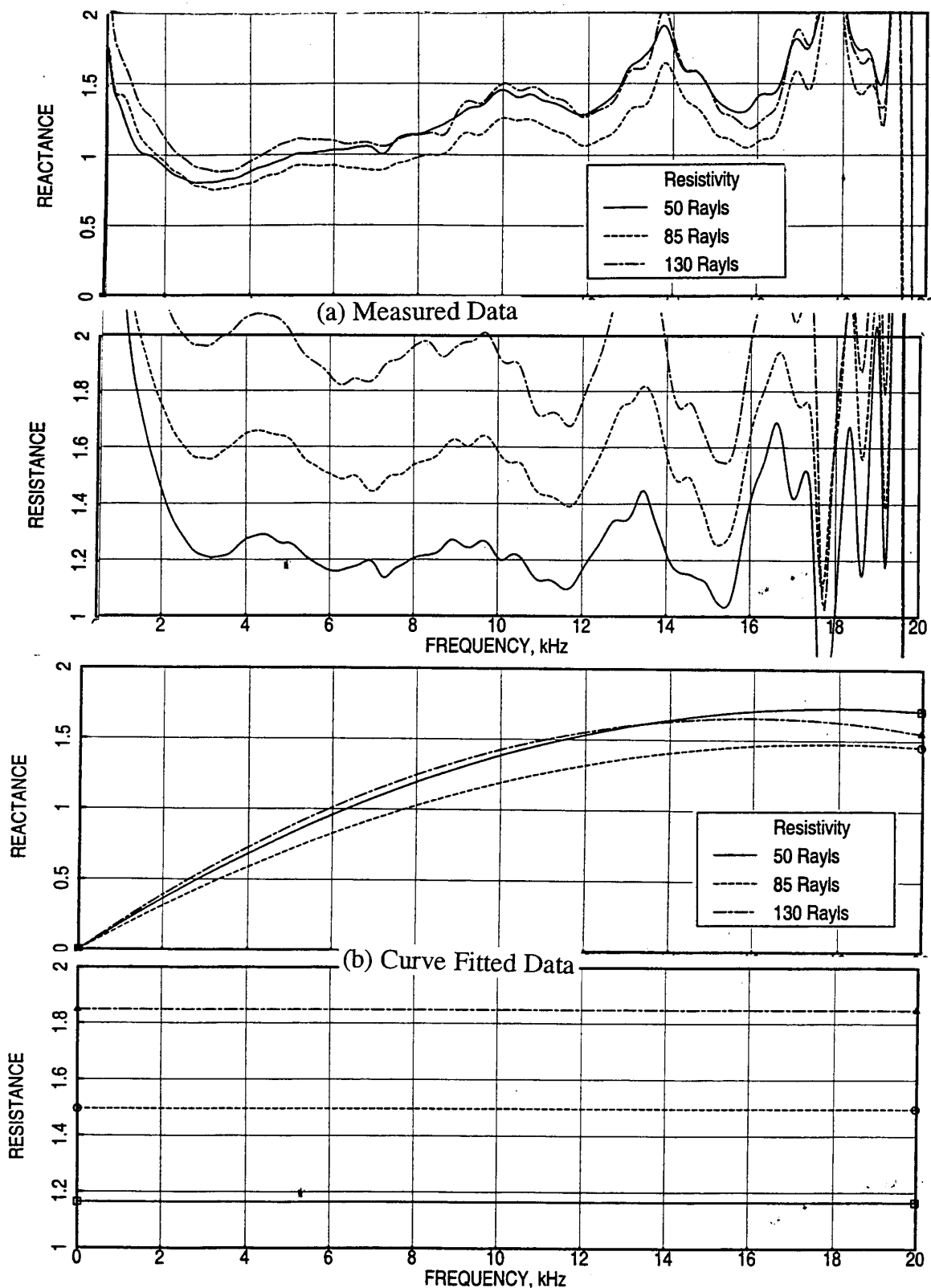


Figure 59. Effect of facesheet resistivity on normal impedance, acquired by a single 0.25"-deep back cavity measurement, OASPL= 150 dB, (a) measured data (cavity effect removed for reactance) and (b) curve fitted data (cavity effect being removed for impedance).

Figure 57. The impedance level increases with increasing facesheet thickness. The effect of hole diameter with fixed porosity and thickness seems to be small compared to porosity and thickness effects (see Figure 58). For 9% porous facesheet with  $t=0.025''$ , the reactance increases with increasing hole diameter. The resistance decreases and then increases with increasing hole diameter. Figure 59 shows the effect of resistivity on normal impedance for linear facesheets. The reactance and resistance both increase with increasing facesheet resistivity.

Effect of excitation intensity is significant on resistance compared to reactance (see Figure 60). In general the reactance decreases and resistance increases with increasing excitation level and the impact diminishes with increasing porosity. For linear facesheets the effect is comparable to the perforated facesheets.

## **5.2 Normal Impedance for Bulk Absorbers:**

**Data Analysis & Presentation:** Bulk absorbers from Table 2 of different depths and from Table 6 are tested without any facesheet and with facesheets of Tables 2 through 5. The data is extrapolated, mostly utilizing polynomial curve fitting at lower frequencies below 500 Hz and at higher frequencies above 17 kHz to remove spurious variations. The presentation of all the test results would require a huge number of figures. Therefore, typical results are presented in this section.

**5.2.1 Silicon Carbide Bulk Absorbers:** Several Silicon Carbide bulk samples of varying pores/inch (i.e., 100, 200, 400, and 600) of different depths are tested. The density of these samples is approximately 12 lbs/ft<sup>3</sup>.

### ***Parametric Characteristics of Normal Impedance due to Facesheet Property Variation:***

The effect of facesheet porosity on normal impedance for 100 ppi Silicon Carbide (SiC) bulk absorbers of different depths is shown in Figures 61 and 62. In general the reactance and resistance increase with decreasing facesheet porosity. The cavity anti-resonance effect is relatively small for deeper bulk samples at higher frequencies. The effect of facesheet thickness on normal impedance is shown in Figures 63 and 64. The reactance and resistance, both, increase with increasing facesheet thickness. The anti-resonance frequency decreases with increasing facesheet depth due to the increase in effective bulk absorber depth. The effect of facesheet hole diameter with fixed porosity and thickness seems to be small compared to porosity and thickness effects (see Figures 65 and 66). For 40% porous facesheet with  $t=0.025''$ , the reactance decreases and then increases with increasing hole

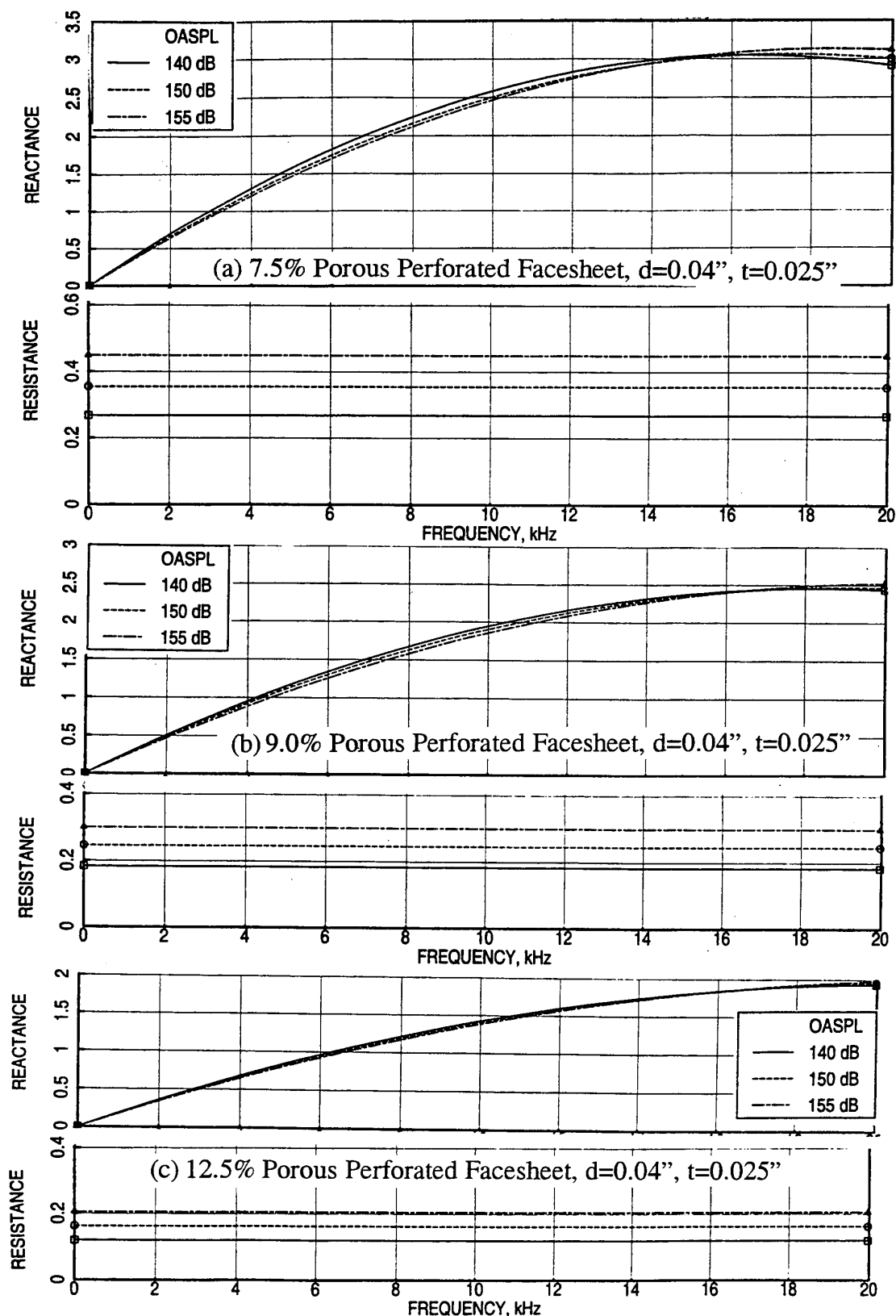


Figure 60. Effect of excitation intensity on curve fitted normal impedance, acquired by a single 0.25"-deep back cavity measurement (cavity effect removed for impedance), for facesheets of different porosities  $\sigma$ ,  $d=0.04''$ ,  $t=0.025''$ , (a)  $\sigma=7.5\%$ , (b)  $\sigma=9\%$ , and (c)  $\sigma=12.5\%$ .

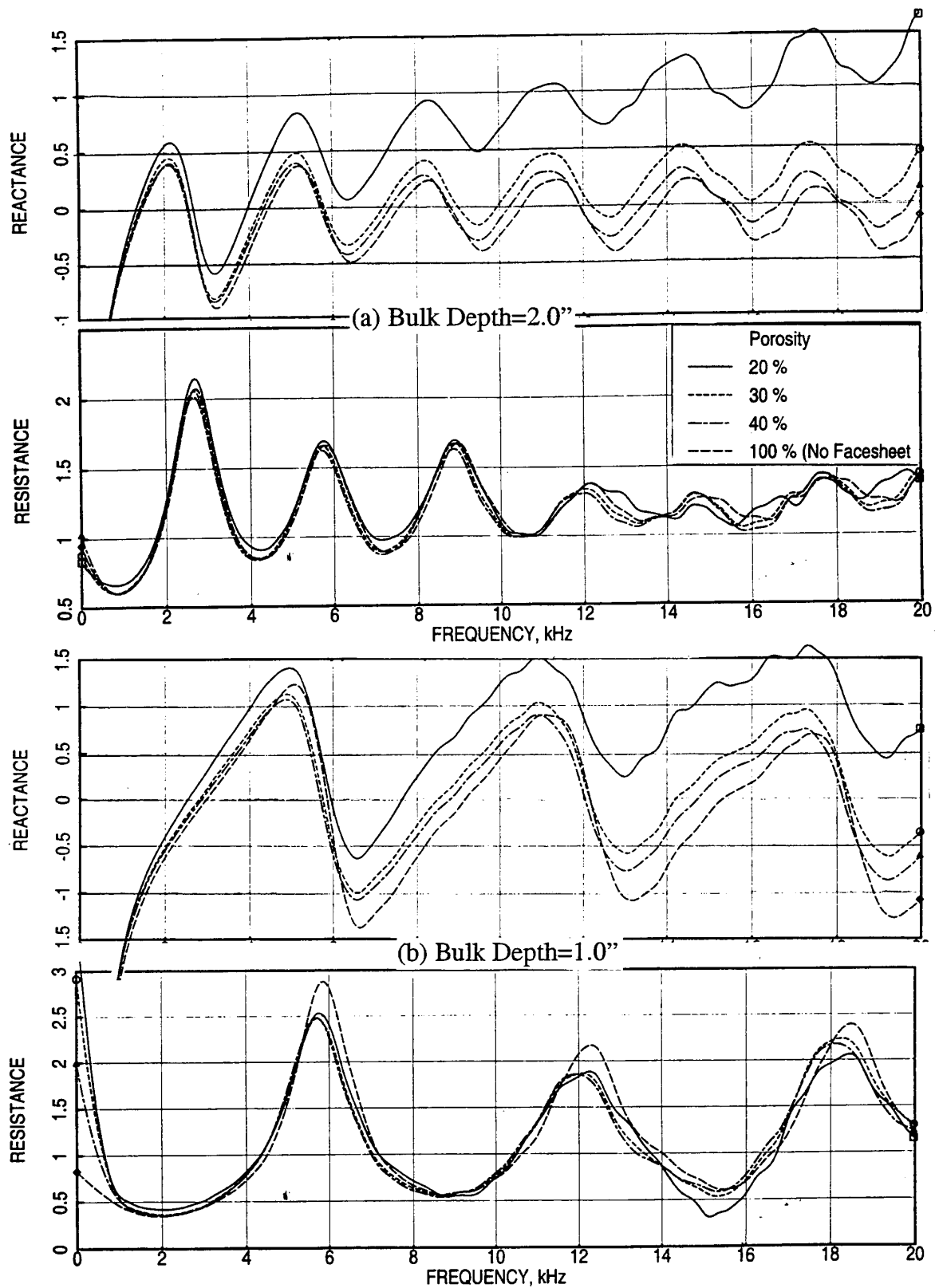


Figure 61. Effect of facesheet porosity on normal impedance for 100 ppi Silicon Carbide bulk absorbers of different depths with 0.025''-thick facesheets,  $d=0.04''$ , OASPL= 150 dB, (a) Bulk Depth=2.0'' and (b) Bulk Depth=1.0''.

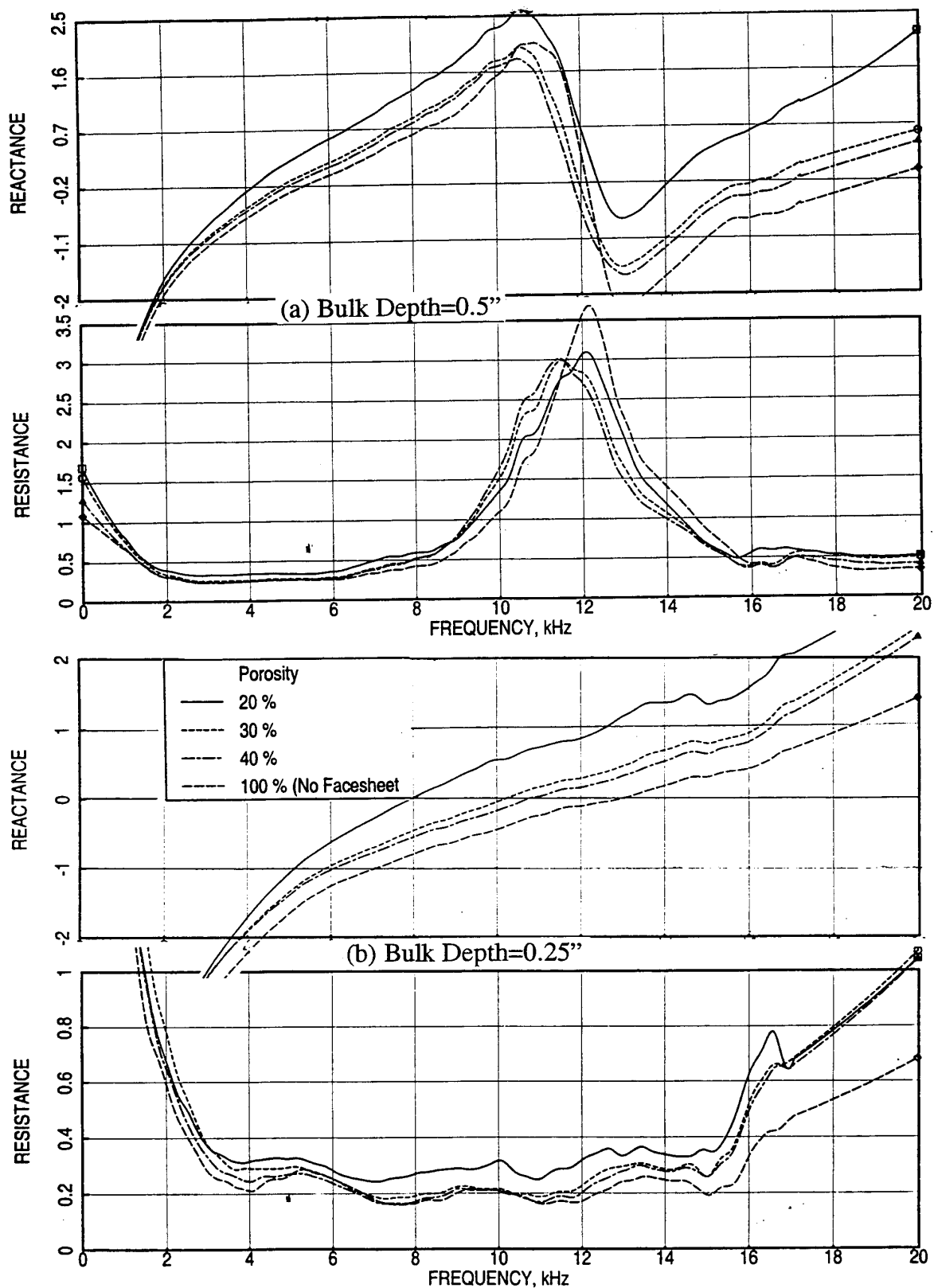


Figure 62. Effect of facesheet porosity on normal impedance for 100 ppi Silicon Carbide bulk absorbers of different depths with 0.025"-thick facesheets,  $d=0.04$ ", OASPL= 150 dB, (a) Bulk Depth=0.5" and (b) Bulk Depth=0.25".



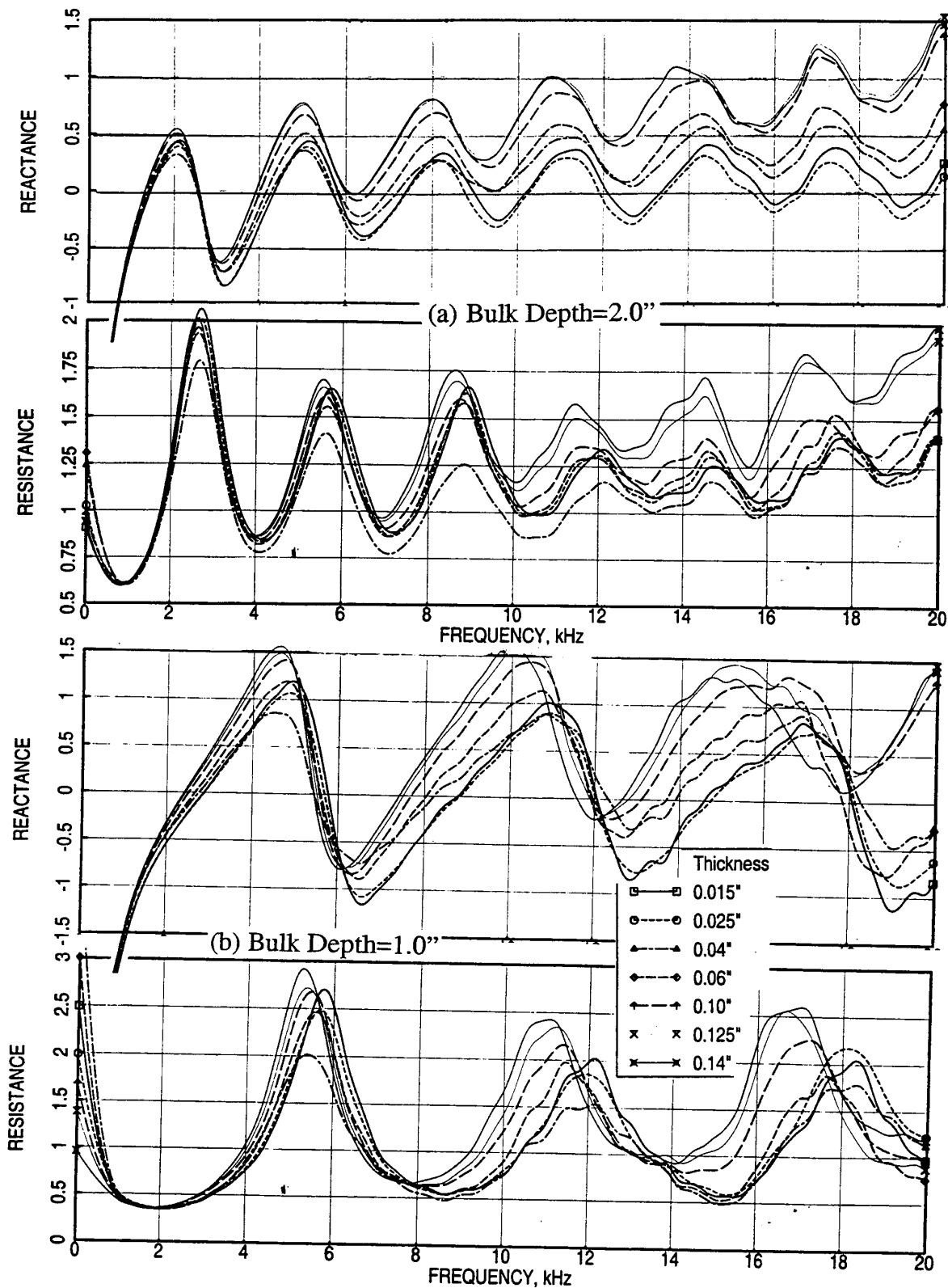


Figure 63. Effect of facesheet thickness on normal impedance for 100 ppi Silicon Carbide bulk absorbers of different depths with 40 % porous facesheets,  $d=0.04''$ , OASPL=150 dB, (a) Bulk Depth=2.0'' and (b) Bulk Depth=1.0''.

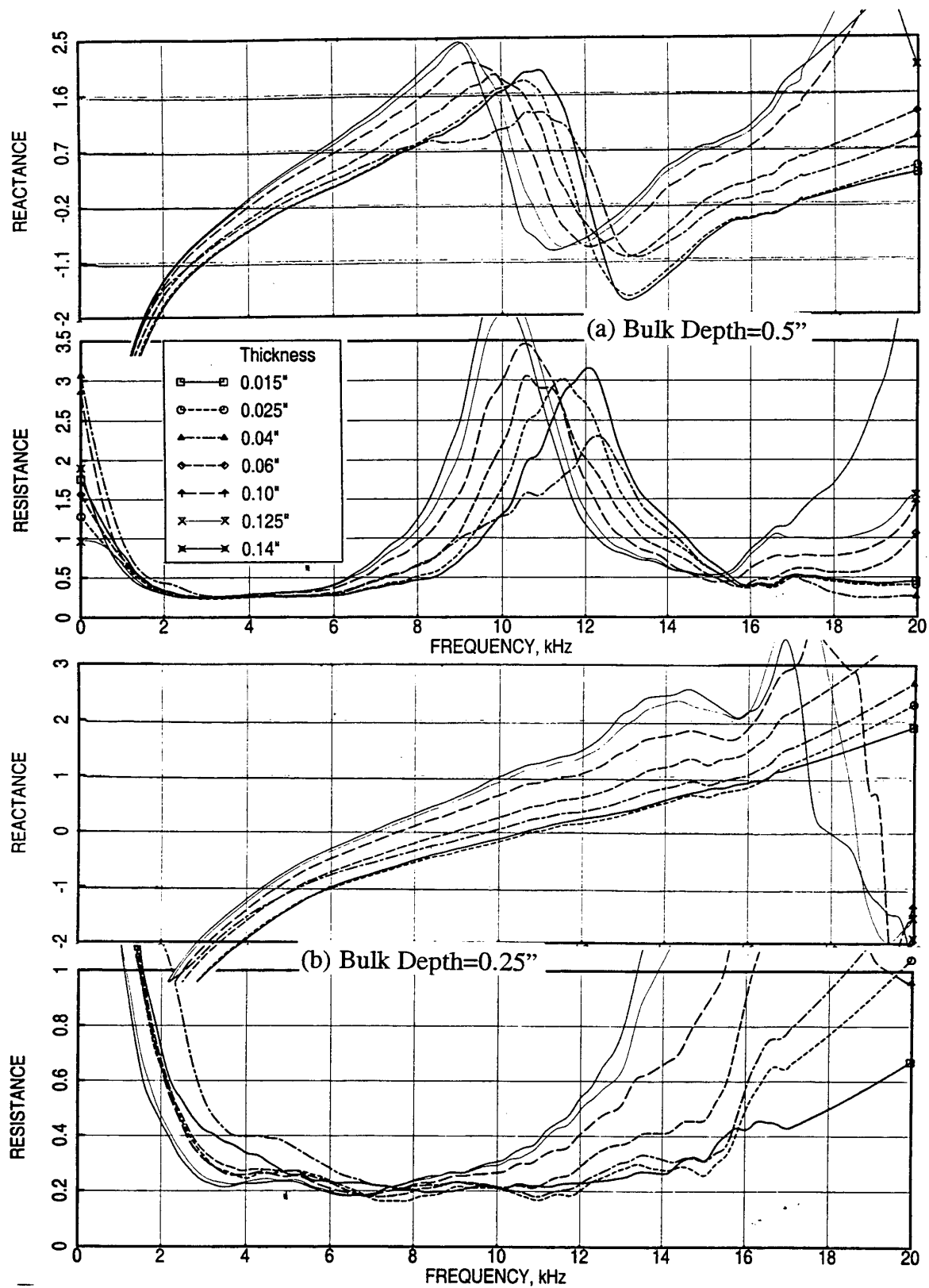


Figure 64. Effect of facesheet thickness on normal impedance for 100 ppi Silicon Carbide bulk absorbers of different depths with 40 % porous facesheets,  $d=0.04''$ , OASPL=150 dB, (a) Bulk Depth=0.5'' and (b) Bulk Depth=0.25''.

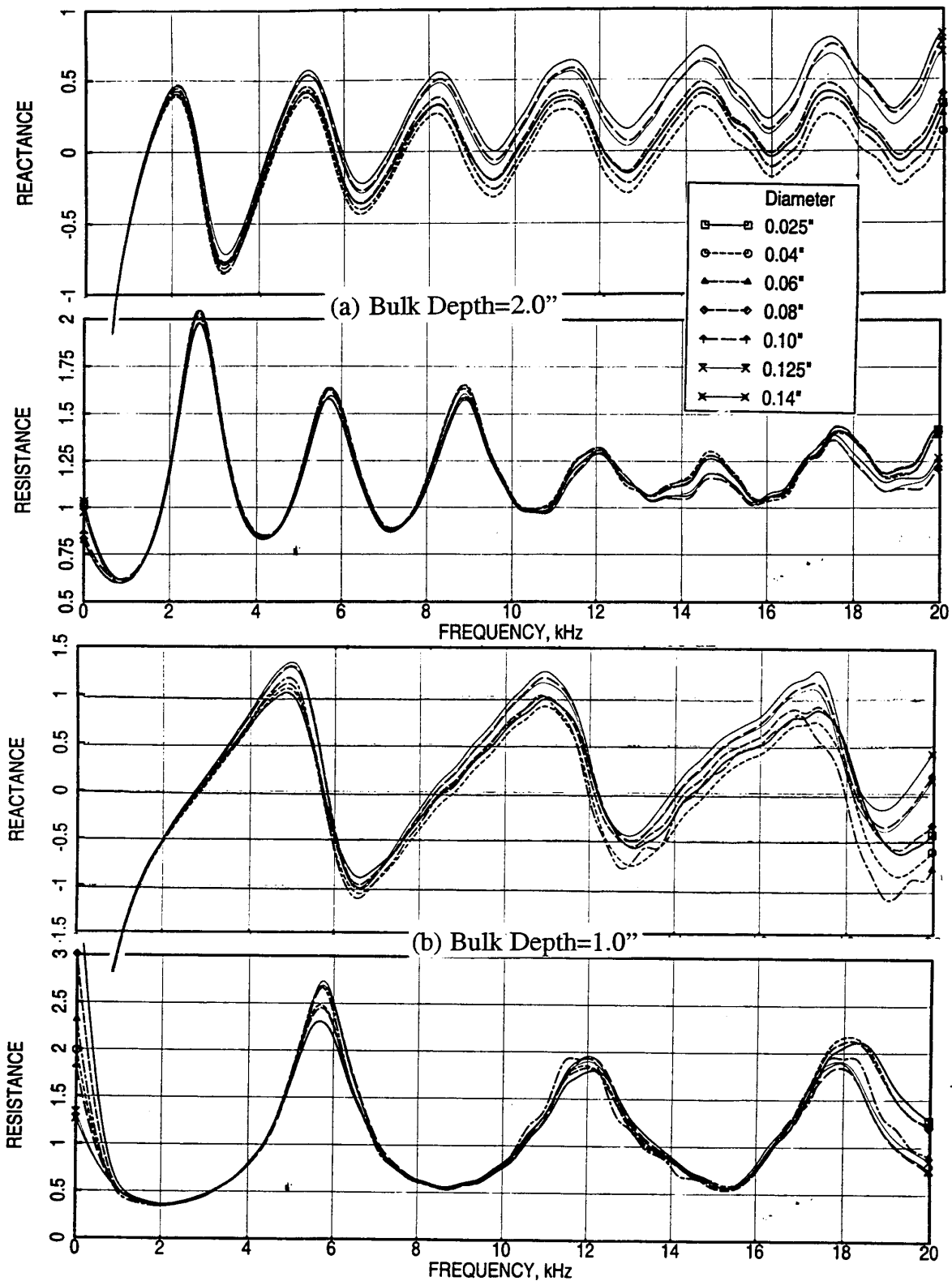


Figure 65. Effect of facesheet hole diameter on normal impedance for 100 ppi Silicon Carbide bulk absorbers of different depths with 40 % porous 0.025" thick facesheets, OASPL= 150 dB, (a) Bulk Depth=2.0" and (b) Bulk Depth=1.0".

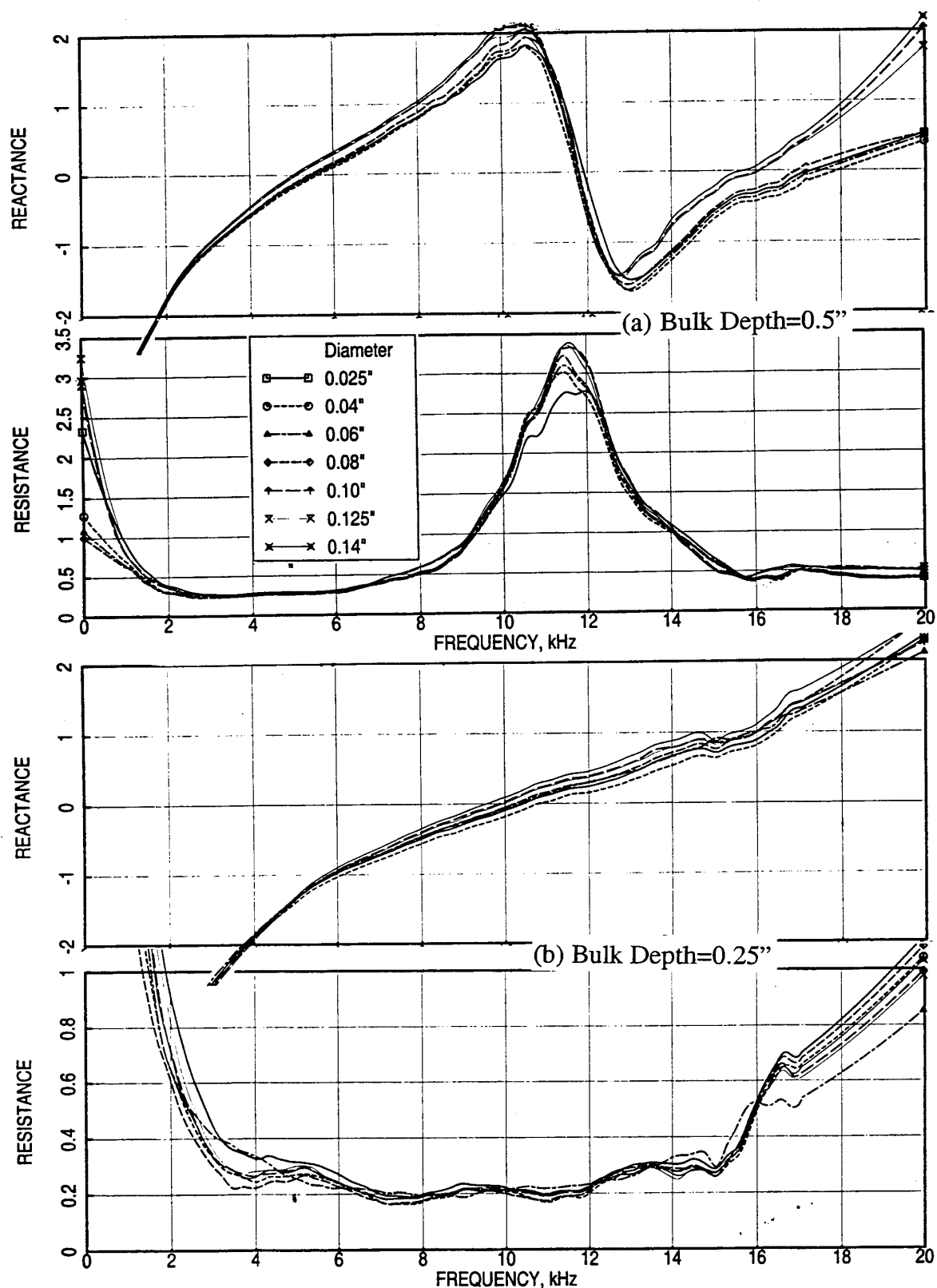


Figure 66. Effect of facesheet hole diameter on normal impedance for 100 ppi Silicon Carbide bulk absorbers of different depths with 40 % porous 0.025" thick facesheets, OASPL= 150 dB, (a) Bulk Depth=0.5" and (b) Bulk Depth=0.25".

diameter. The resistance decreases slightly with increasing hole diameter. Figures 67 and 68 show the effect of resistivity on normal impedance for linear facesheets. The effect seems to be small due to resistivity variation. The general trend is a slight increase of reactance and resistance with increasing facesheet resistivity, especially at lower frequencies. The actual DC flow resistance  $R_{100}$  of these facesheets is about 8.5 and 9.2 as opposed to their nominal values of 5 and 10 Rayls, respectively. Therefore, the difference of impedance due to these two facesheets is almost negligible.

Effect of excitation intensity on normal impedance for 100 ppi SiC, with and without facesheets, is relatively small (see Figures 69 through 71). In general the reactance decreases and resistance increases with increasing excitation level.

Similar results for Silicon Carbide samples with 200, 400, and 600 ppi are generated and examined (not presented here). The characteristics of parametric variations are similar to those observed for 100 ppi SiC bulk absorbers.

***Parametric Characteristics of Normal Impedance due to Pores/Inch (ppi) Variation:*** The effect of pores/inch on normal impedance for Silicon Carbide (SiC) bulk absorbers of different depths, without facesheets, is shown in Figures 72 and 73. In general the reactance and resistance increase with increasing pores/inch. The cavity anti-resonance effect decreases with increasing pores/inch and the anti-resonance frequency decreases with increasing pores/inch, indicating an increase in the effective depth of the bulk. The effect of pores/inch for SiC with facesheets on normal impedance, shown in Figures 74 through 79, is similar to the bulk only configurations. The impact of facesheets, depending on their porosity and thickness, influence the magnitude of impedance variation. For example, the effect of a 20% porous facesheet, shown in Figures 74 and 75, forces the reactance to increase with frequency compared to a constant mean reactance for bulk only configuration. The impact diminishes with increasing porosity as shown in Figures 76 and 77 for a 40% porous facesheet. For thicker facesheets the impact is similar to the 20% porous facesheet case, as shown in Figures 78 and 79 for a 0.06" thick facesheet.

**5.2.2 Standard T-Foam Bulk Absorbers:** Standard T-Foam bulk absorbers are made out of Silicon Carbide type polymer fibers. The process involves 3 dimensional weaving of the polymer fiber and sol-gel (matrix) rigidization to maintain the shape. Laser cutting is applied as required. Several Standard T-Foam samples of varying density (i.e., 8, 12, and 16 lbf) of different depths are tested.

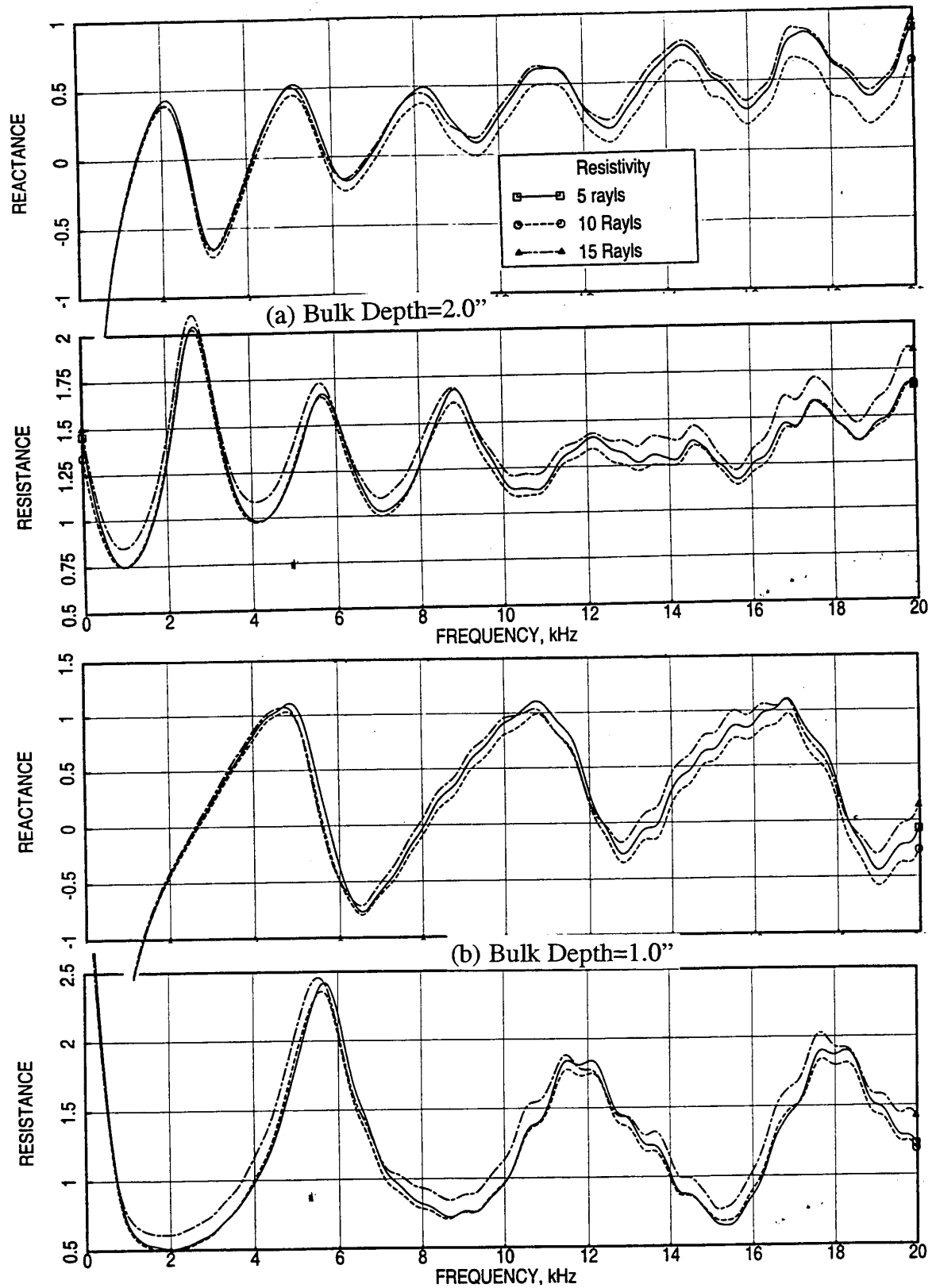


Figure 67. Effect of facesheet resistivity on normal impedance for 100 ppi Silicon Carbide bulk absorbers of different depths with linear facesheets, OASPL= 150 dB, (a) Bulk Depth=2.0" and (b) Bulk Depth=1.0".

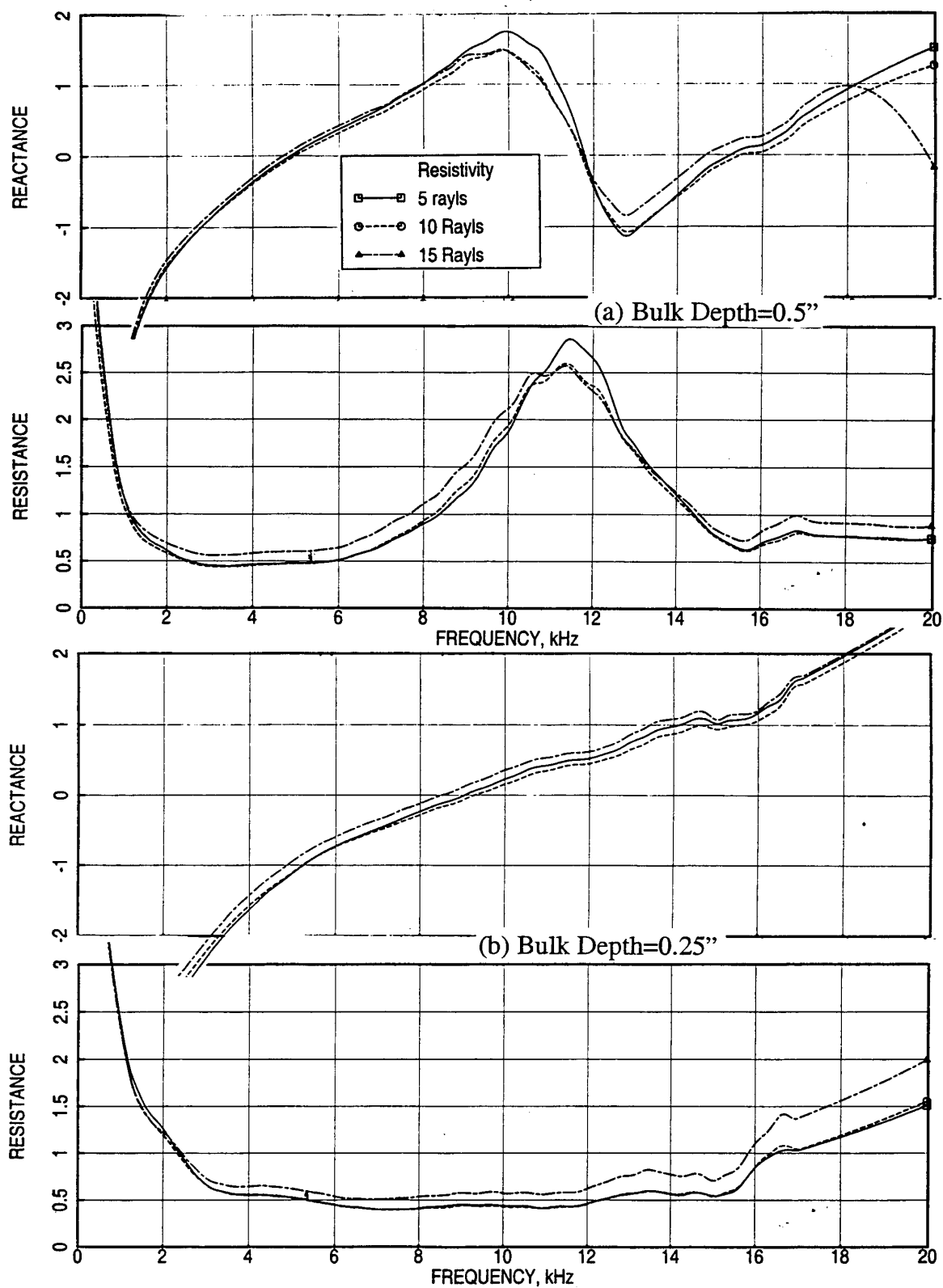


Figure 68. Effect of facesheet resistivity on normal impedance for 100 ppi Silicon Carbide bulk absorbers of different depths with linear facesheets, OASPL= 150 dB, (a) Bulk Depth=0.5" and (b) Bulk Depth=0.25".

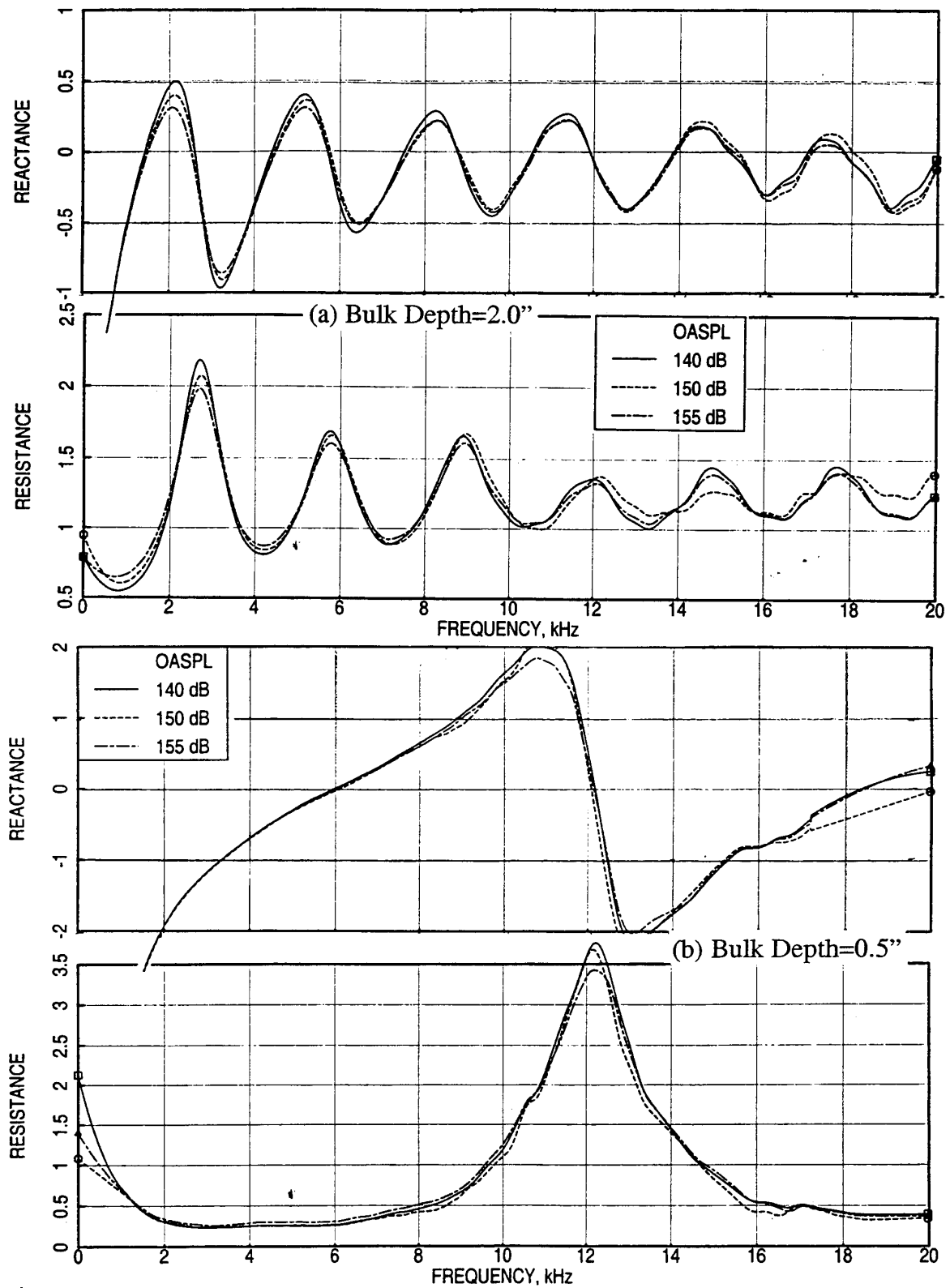


Figure 69. Effect of excitation intensity on normal impedance for 100 ppi Silicon Carbide of different depths, (a) Bulk Depth = 2.0" and (b) Bulk Depth = 0.5".



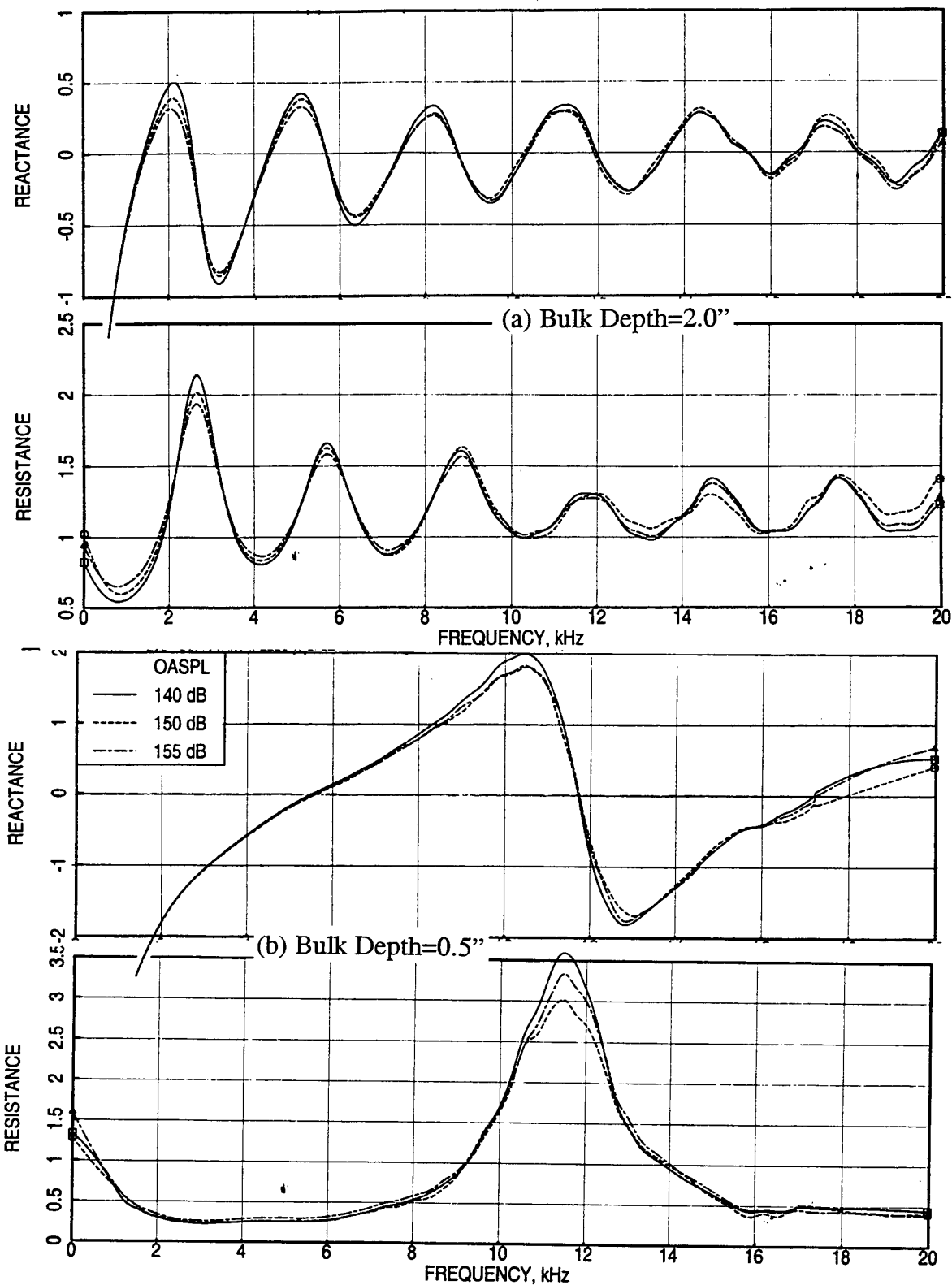


Figure 70. Effect of excitation intensity on normal impedance for 100 ppi Silicon Carbide of different depths with 40 % porous 0.025" thick facesheet,  $d=0.04"$ , (a) Bulk Depth = 2.0" and (b) Bulk Depth = 0.5".

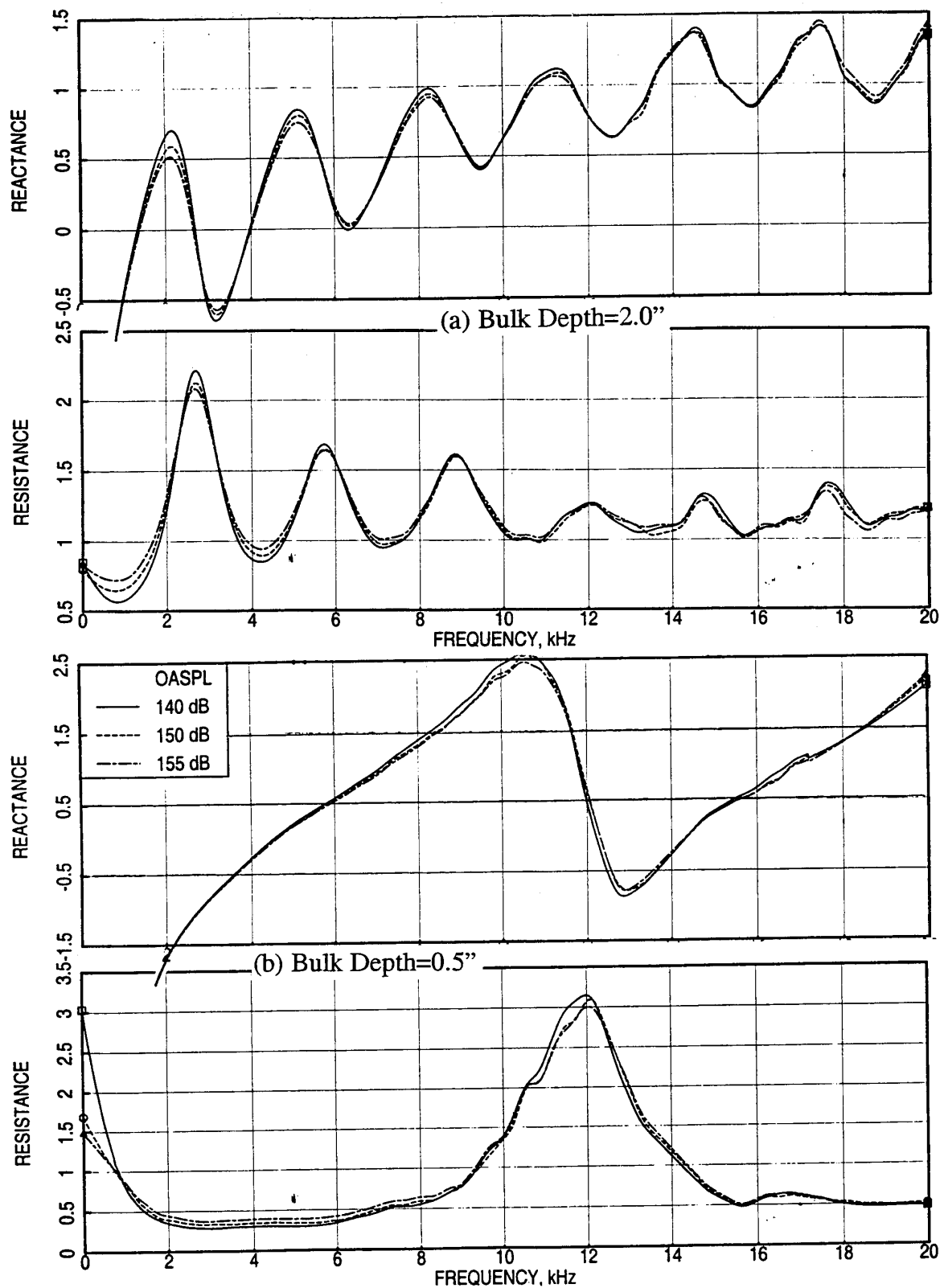


Figure 71. Effect of excitation intensity on normal impedance for 100 ppi Silicon Carbide of different depths with 20 % porous 0.025" thick facesheet,  $d=0.04$ ", (a) Bulk Depth = 2.0" and (b) Bulk Depth = 0.5".

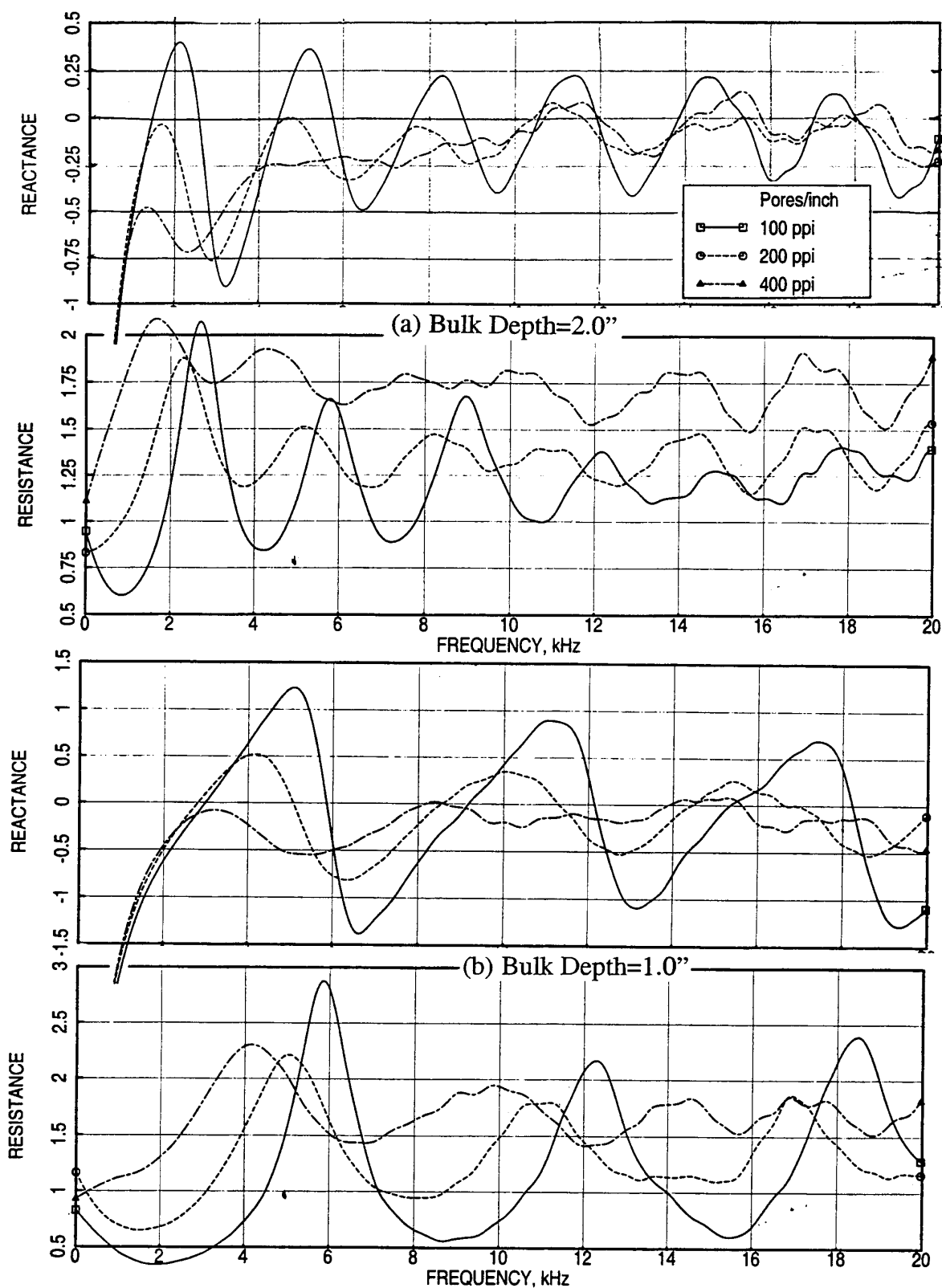


Figure 72. Effect of pores/inch on normal impedance for Silicon Carbide bulk absorbers of different depths, OASPL=150 dB, (a) Bulk Depth=2.0" and (b) Bulk Depth=1.0".

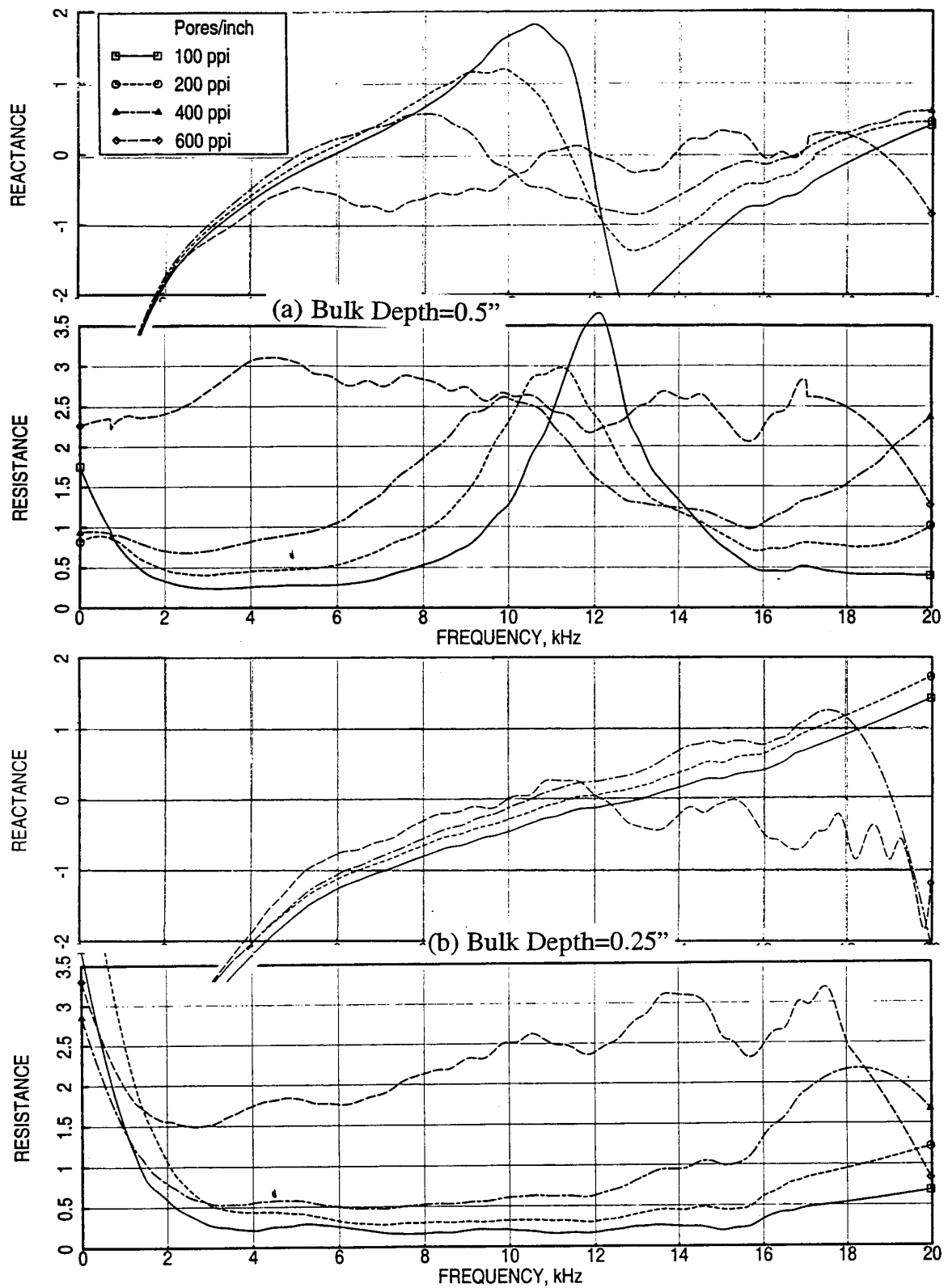


Figure 73. Effect of pores/inch on normal impedance for Silicon Carbide bulk absorbers of different depths, OASPL=150 dB, (a) Bulk Depth=0.5" and (b) Bulk Depth=0.25".

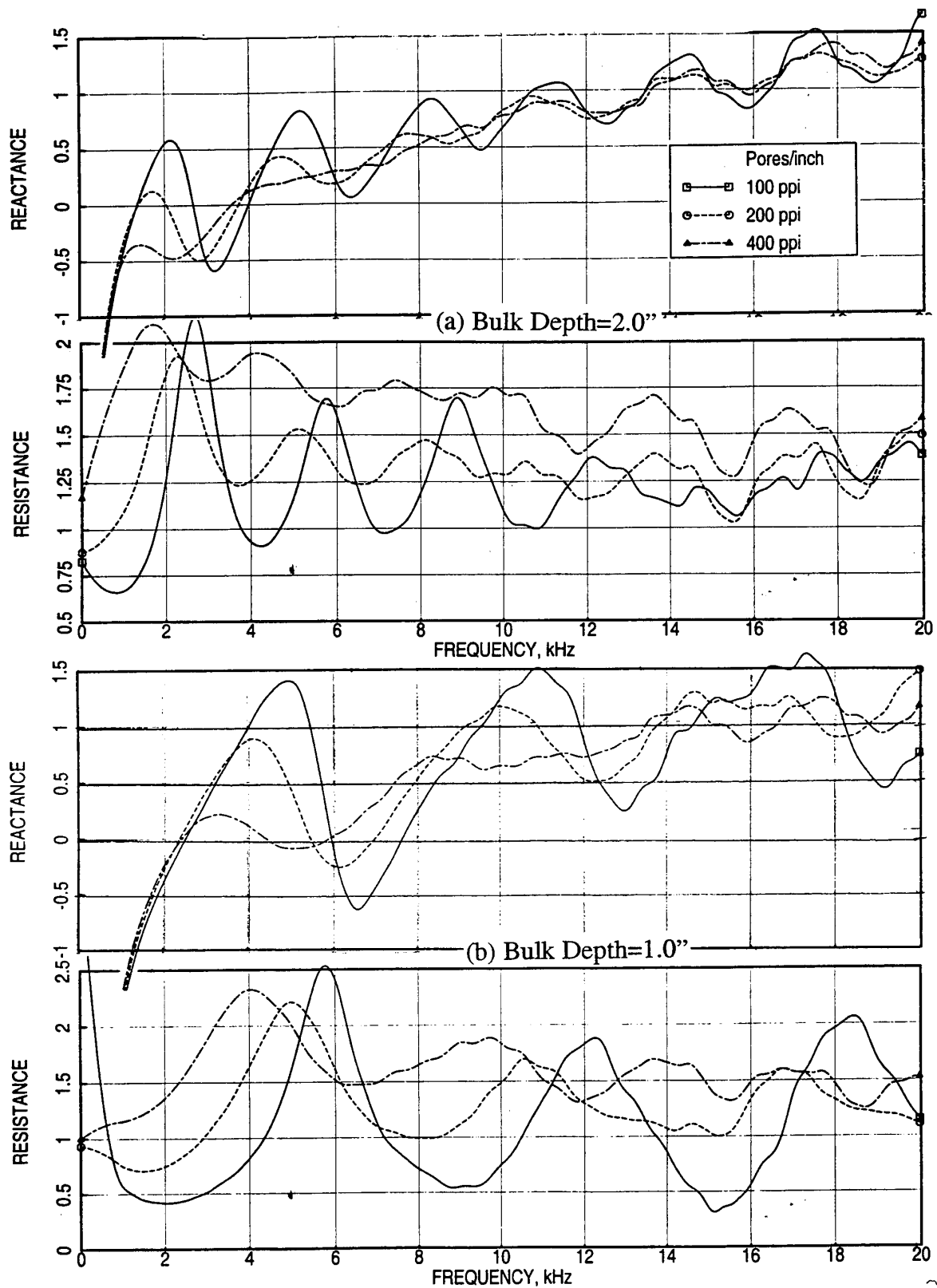


Figure 74. Effect of pores/inch on normal impedance for Silicon Carbide bulk absorbers of different depths with 20 % porous 0.025"-thick facesheet,  $d=0.04$ ", OASPL=150 dB, (a) Bulk Depth=2.0" and (b) Bulk Depth=1.0".

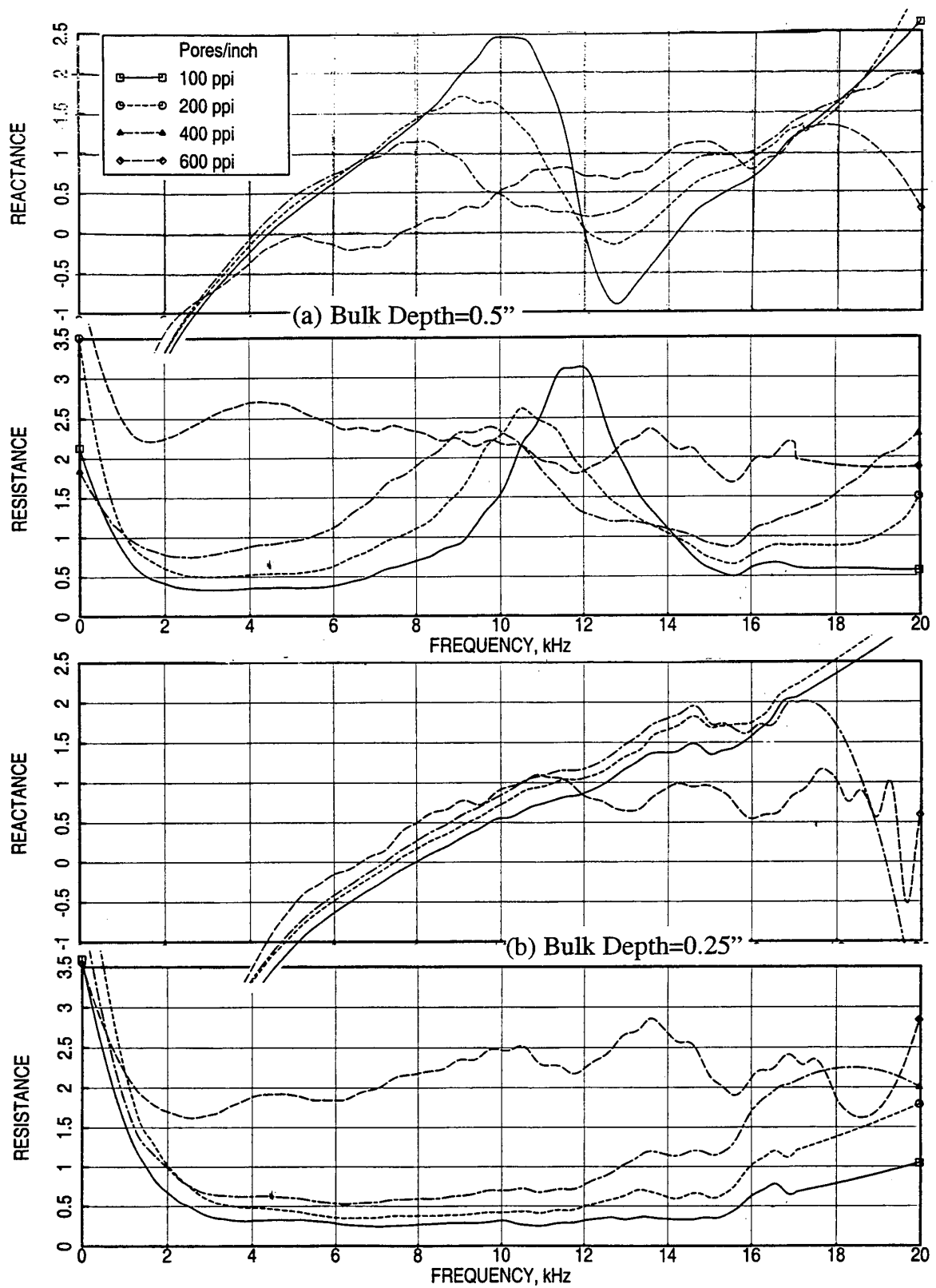


Figure 75. Effect of pores/inch on normal impedance for Silicon Carbide bulk absorbers of different depths with 20 % porous 0.025"-thick facesheet,  $d=0.04$ ", OASPL=150 dB, (a) Bulk Depth=0.5" and (b) Bulk Depth=0.25".

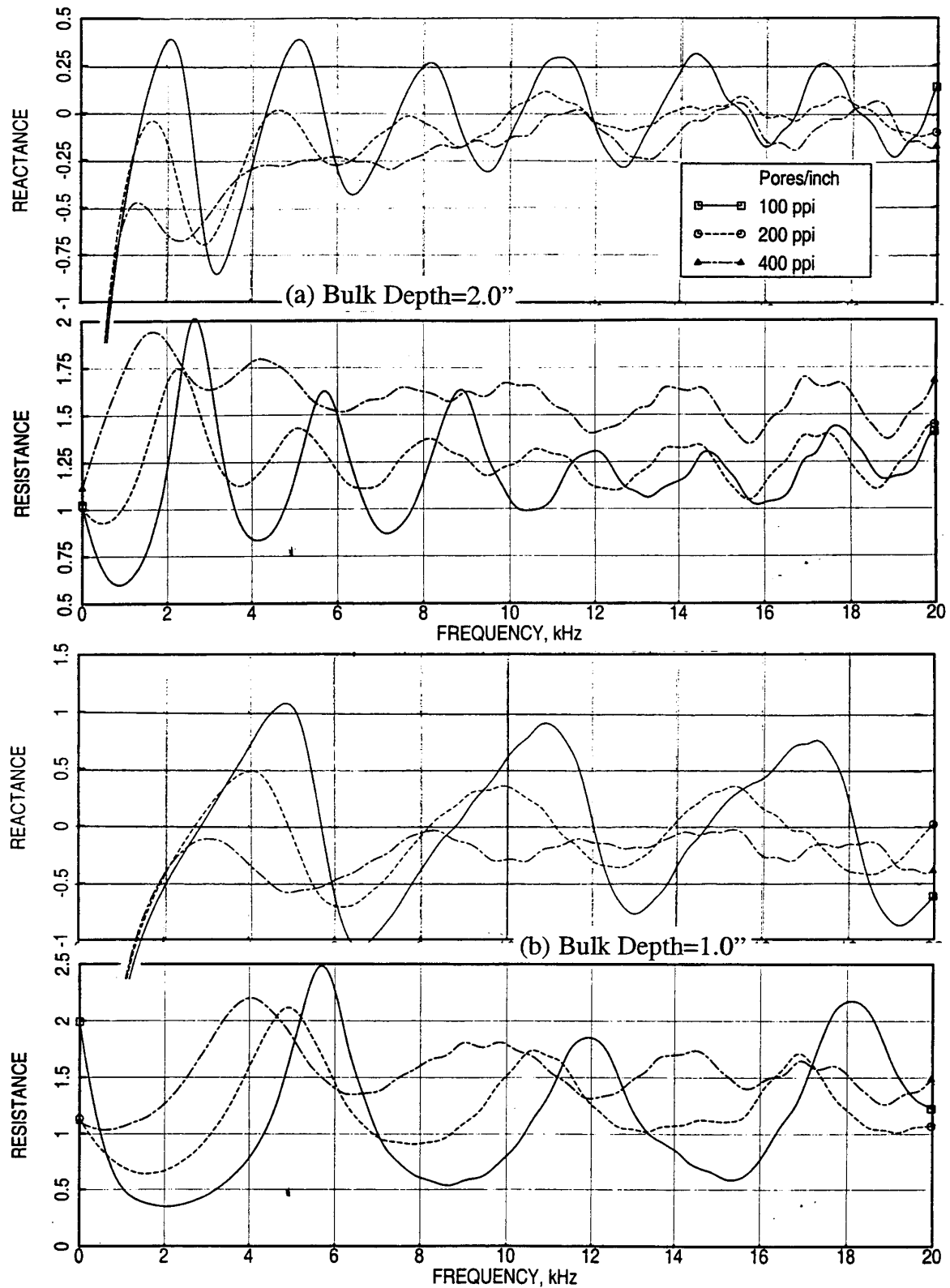


Figure 76. Effect of pores/inch on normal impedance for Silicon Carbide bulk absorbers of different depths with 40 % porous 0.025"-thick facesheet,  $d=0.04''$ , OASPL=150 dB, (a) Bulk Depth=2.0'' and (b) Bulk Depth=1.0''.

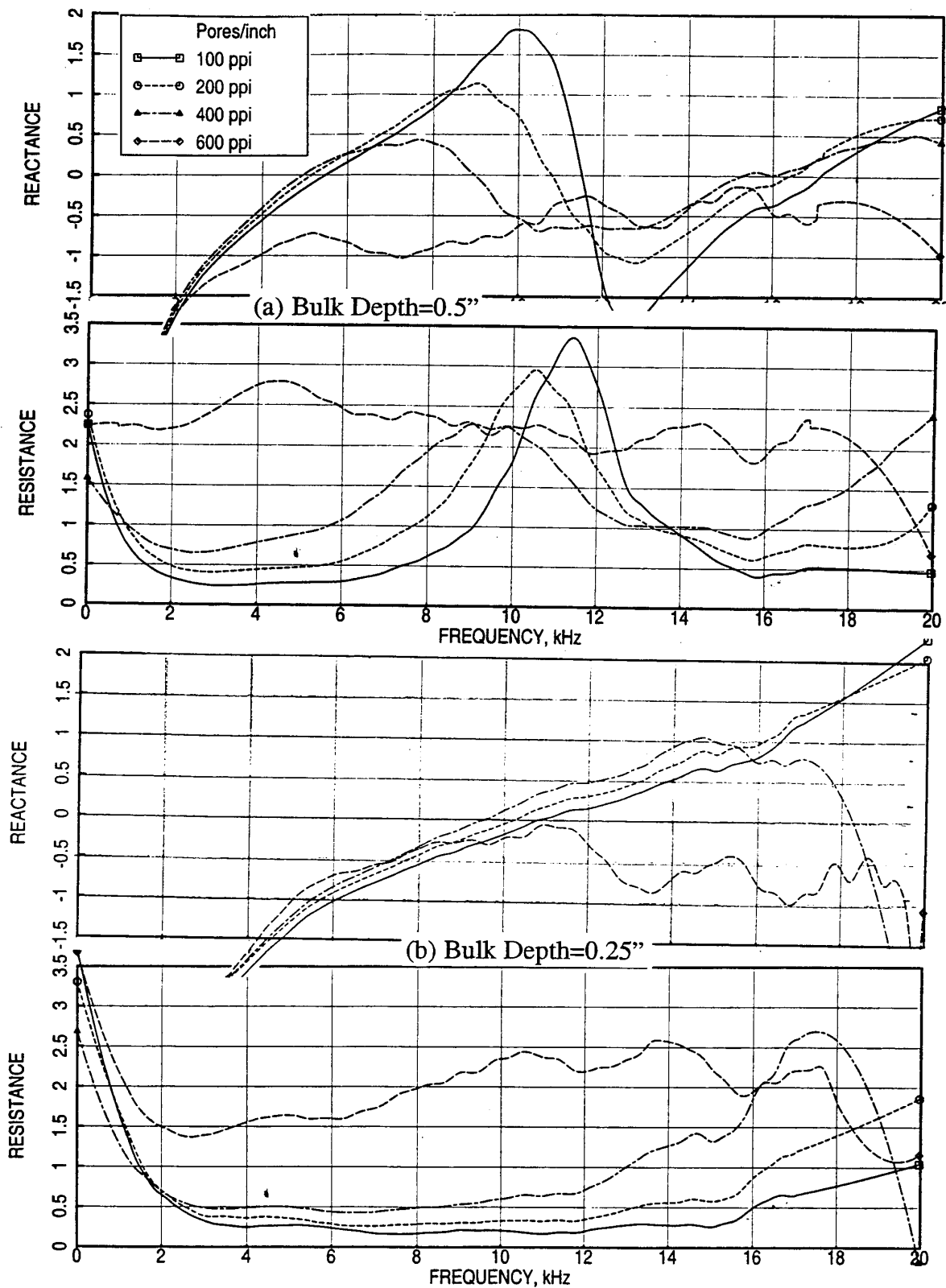


Figure 77. Effect of pores/inch on normal impedance for Silicon Carbide bulk absorbers of different depths with 40 % porous 0.025"-thick facesheet,  $d=0.04$ ", OASPL=150 dB, (a) Bulk Depth=0.5" and (b) Bulk Depth=0.25".



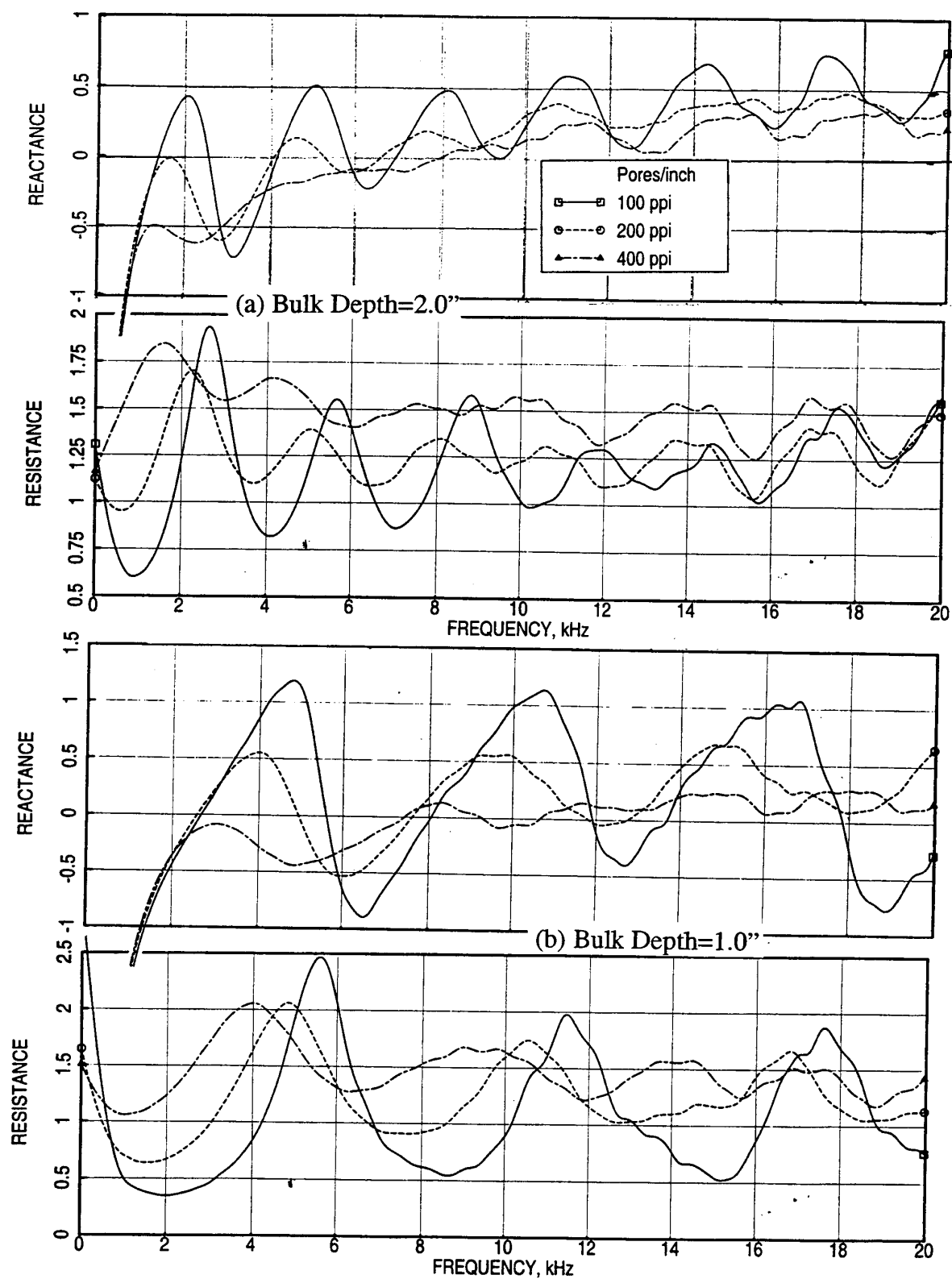


Figure 78. Effect of pores/inch on normal impedance for Silicon Carbide bulk absorbers of different depths with 40 % porous 0.06''-thick facesheet,  $d=0.04''$ , OASPL=150 dB, (a) Bulk Depth=2.0'' and (b) Bulk Depth=1.0''.

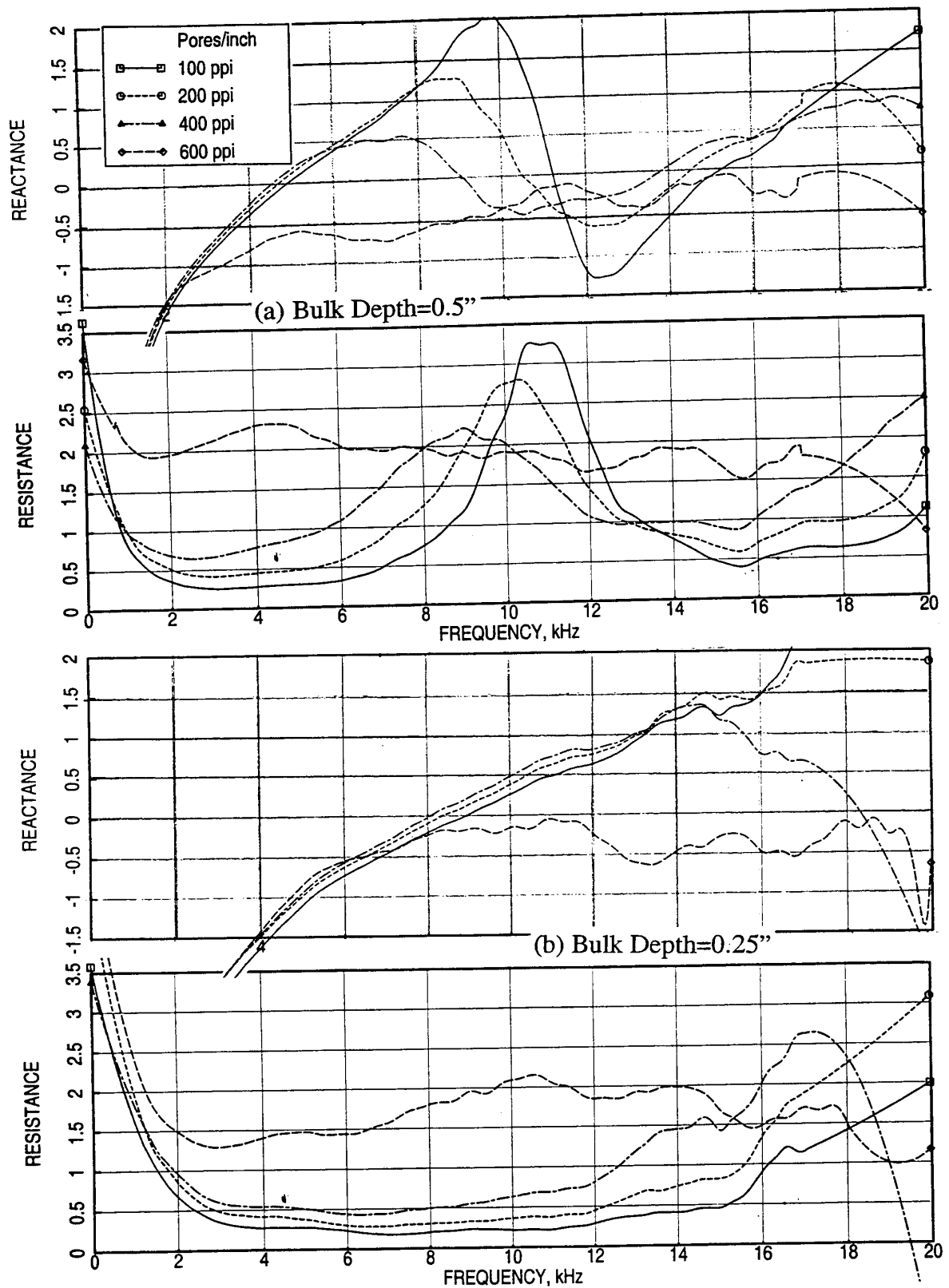


Figure 79. Effect of pores/inch on normal impedance for Silicon Carbide bulk absorbers of different depths with 40 % porous 0.06''-thick facesheet,  $d=0.04''$ , OASPL=150 dB, (a) Bulk Depth=0.5'' and (b) Bulk Depth=0.25''.

***Parametric Characteristics of Normal Impedance due to Facesheet Property Variation:***

The effect of facesheet porosity on normal impedance for 12 lbf standard T-Foam bulk absorbers of different depths is shown in Figures 80 and 81. In general the reactance and resistance increase with decreasing facesheet porosity. The cavity anti-resonance effect is relatively small for deeper bulk sample at higher frequencies. The effect of facesheet thickness on normal impedance is shown in Figures 82 and 83. The reactance and resistance, both, increase with increasing facesheet thickness with an exception for 0.015"-thick facesheet. For this configuration the reactance is higher compared to 0.025"-thick facesheet for 2" and 1" deep samples. The resistance for these samples seems to be lowest for 0.04"-thick facesheet. The anti-resonance frequency decreases with increasing facesheet depth due to the increase in effective bulk absorber depth. The effect of facesheet hole diameter with fixed porosity and thickness seems to be small compared to porosity and thickness effects (see Figures 84 and 85). For 40% porous facesheet with  $t=0.025''$ , the reactance decreases and then increases with increasing hole diameter. The resistance decreases slightly with increasing hole diameter. Figures 86 and 87 show the effect of resistivity on normal impedance for linear facesheets. The effect seems to be small due to resistivity variation. The general trend is a slight increase of reactance and resistance with increasing facesheet resistivity. Effect of excitation intensity on normal impedance for T-Foam, with and without facesheets, is relatively small (not shown here). In general the reactance decreases and resistance increases with increasing excitation level.

Similar results for T-Foam samples of densities 8 and 16 are generated and examined (not presented here). The characteristics of parametric variations are similar to those observed for 12 lbf T-Foam bulk absorbers.

***Parametric Characteristics of Normal Impedance due to Density Variation:*** The effect of density on normal impedance for standard T-Foam bulk absorbers of different depths, without facesheet, is shown in Figures 88 and 89. In general the reactance and resistance increase with increasing density. The cavity anti-resonance effect decreases with increasing density and the anti-resonance frequency decreases with increasing density, indicating an increase in the effective depth of the bulk. The effect of density for standard T-Foam with facesheets on normal impedance, shown in Figures 90 through 95, is similar to the bulk only configurations. The impact of facesheets, depending on their porosity and thickness, influence the magnitude of impedance variation. For example, the effect of a 20% porous facesheet, shown in Figures 90 and 91, forces the reactance to increase with frequency compared to a constant mean reactance for bulk only configuration. The impact diminishes

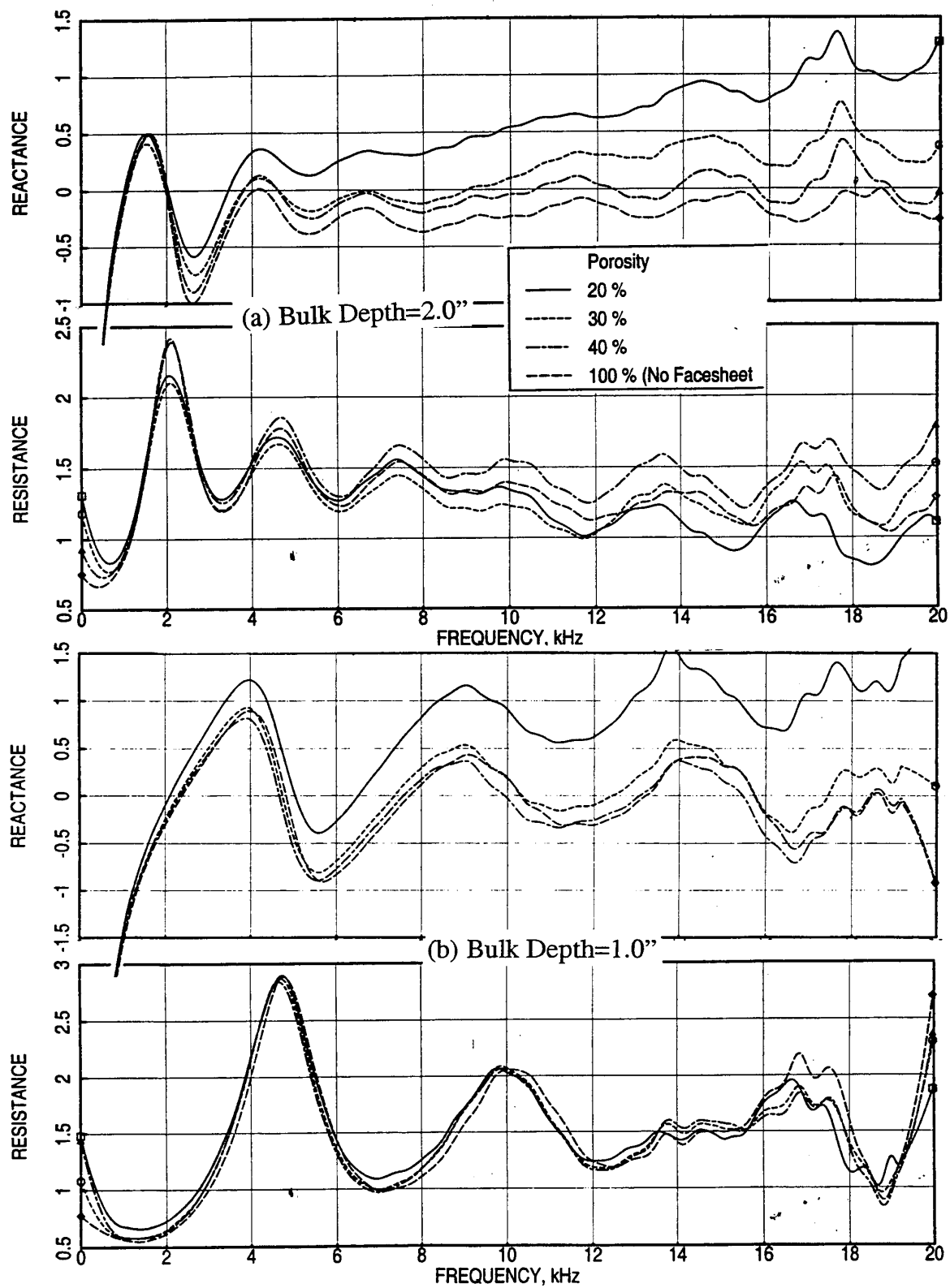


Figure 80. Effect of facesheet porosity on normal impedance for 12 lbf standard T-Foam bulk absorbers of different depths with 0.025"-thick facesheets,  $d=0.04"$ , OASPL= 150 dB, (a) Bulk Depth=2.0" and (b) Bulk Depth=1.0".

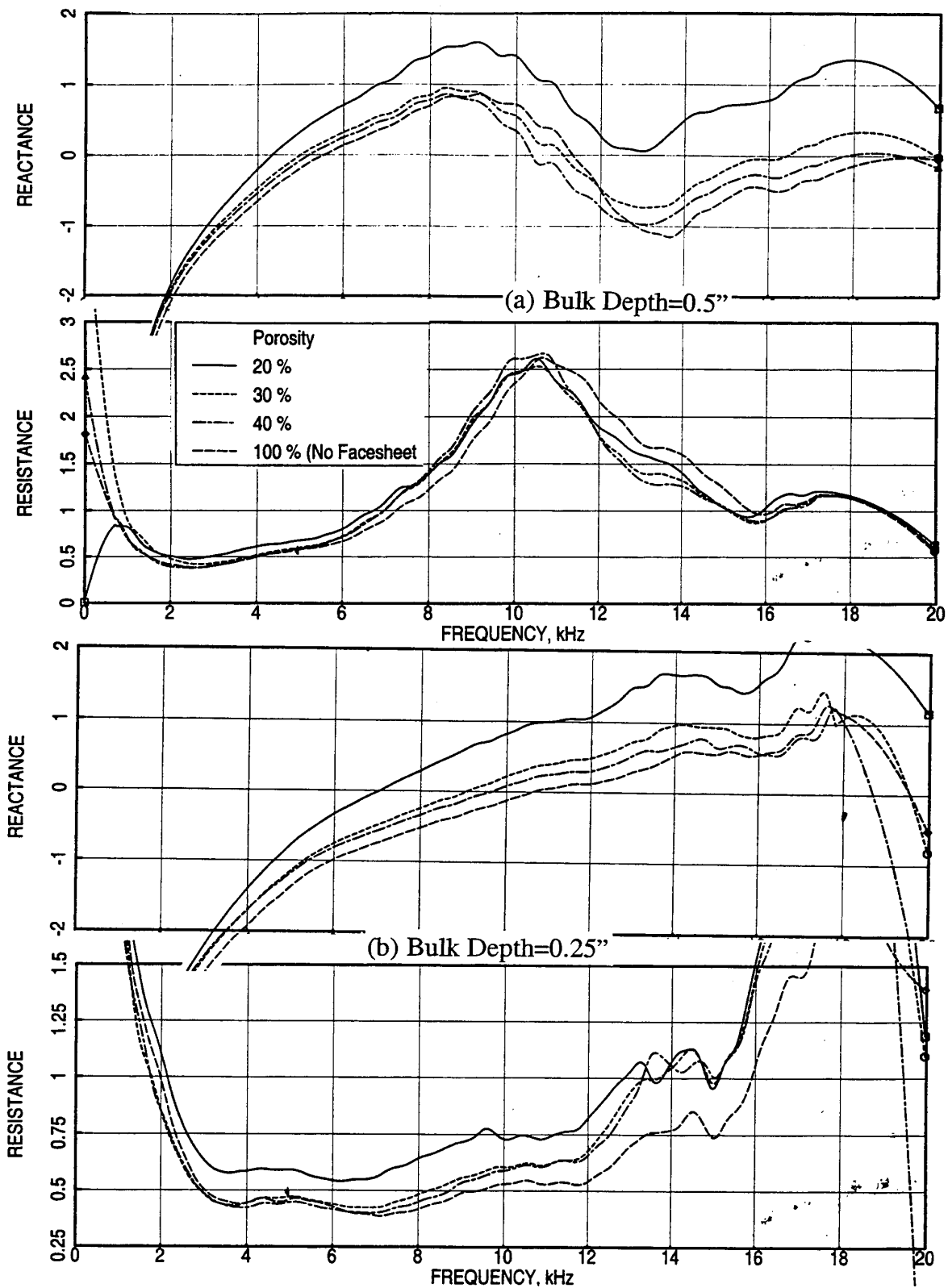


Figure 81. Effect of facesheet porosity on normal impedance for 12 lbf standard T-Foam bulk absorbers of different depths with 0.025"-thick facesheets,  $d=0.04$ ", OASPL= 150 dB, (a) Bulk Depth=0.5" and (b) Bulk Depth=0.25".

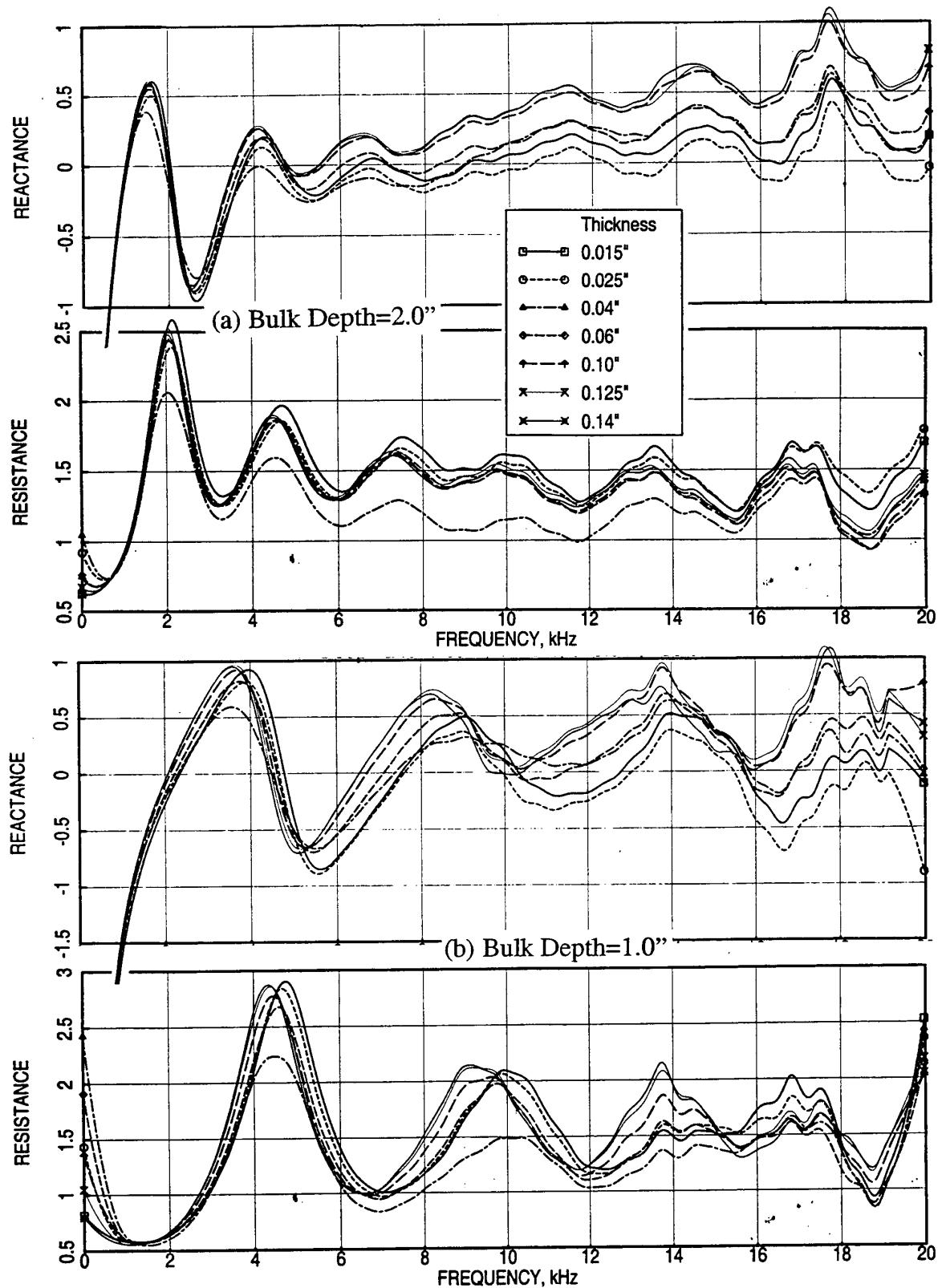


Figure 82. Effect of facesheet thickness on normal impedance for 12 lbf standard T-Foam bulk absorbers of different depths with 40 % porous facesheets,  $d=0.04''$ , OASPL=150 dB, (a) Bulk Depth=2.0'' and (b) Bulk Depth=1.0''.

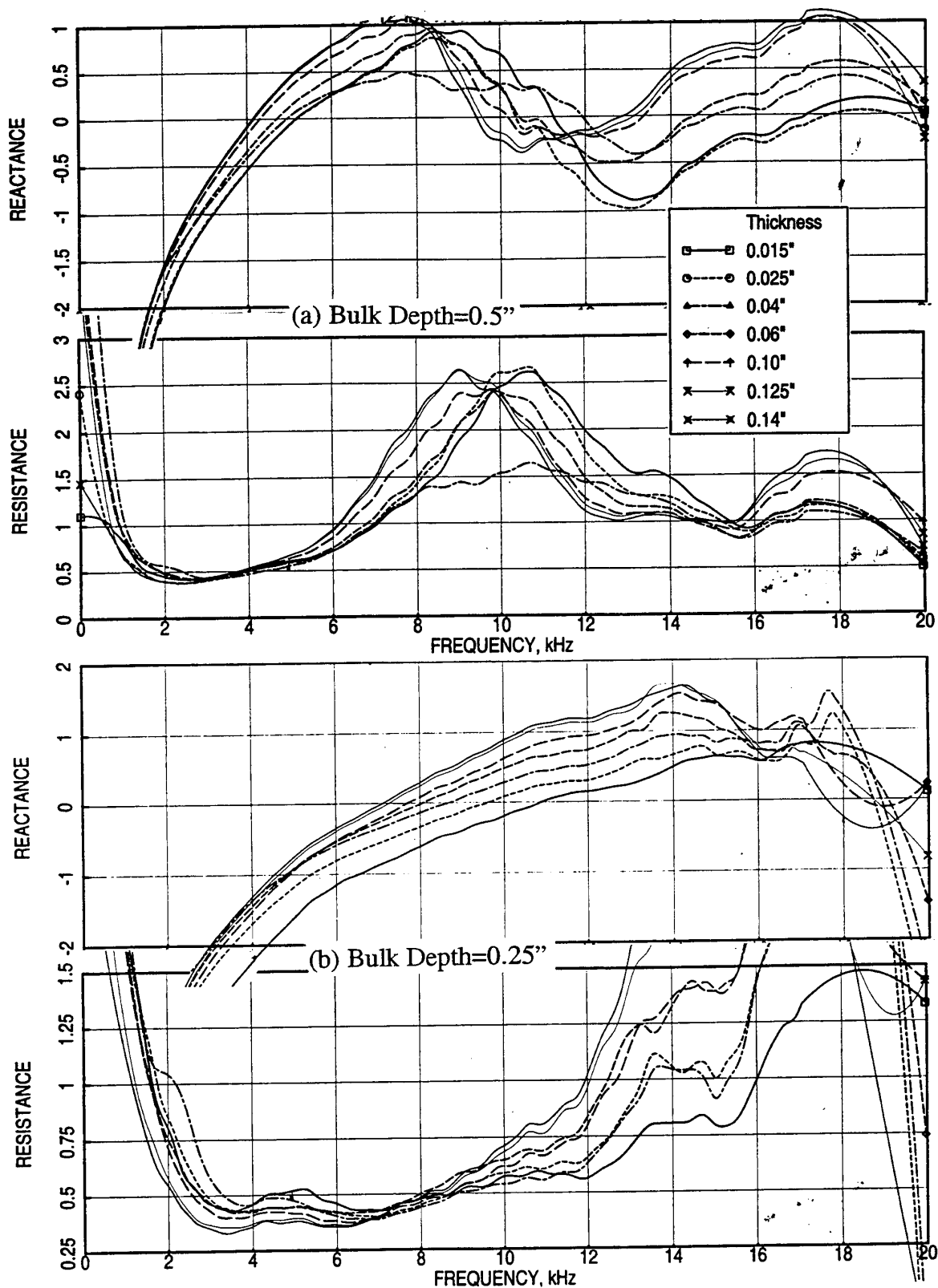


Figure 83. Effect of facesheet thickness on normal impedance for 12 lbf standard T-Foam bulk absorbers of different depths with 40 % porous facesheets,  $d=0.04$ ", OASPL= 150 dB, (a) Bulk Depth=0.5" and (b) Bulk Depth=0.25".

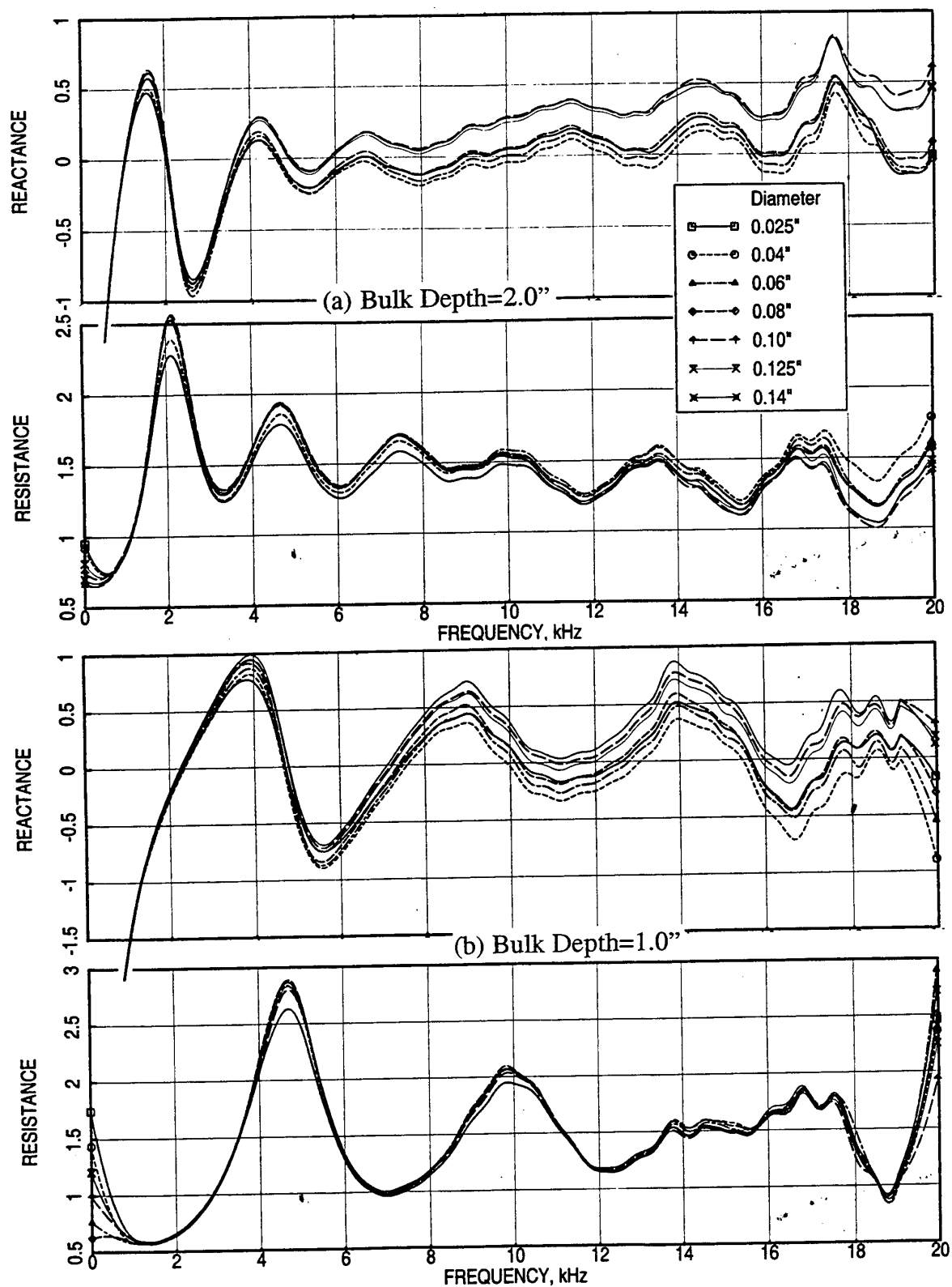


Figure 84. Effect of facesheet hole diameter on normal impedance for 12 lbf standard T-Foam bulk absorbers of different depths with 40 % porous 0.025" thick facesheets, OASPL= 150 dB, (a) Bulk Depth=2.0" and (b) Bulk Depth=1.0".



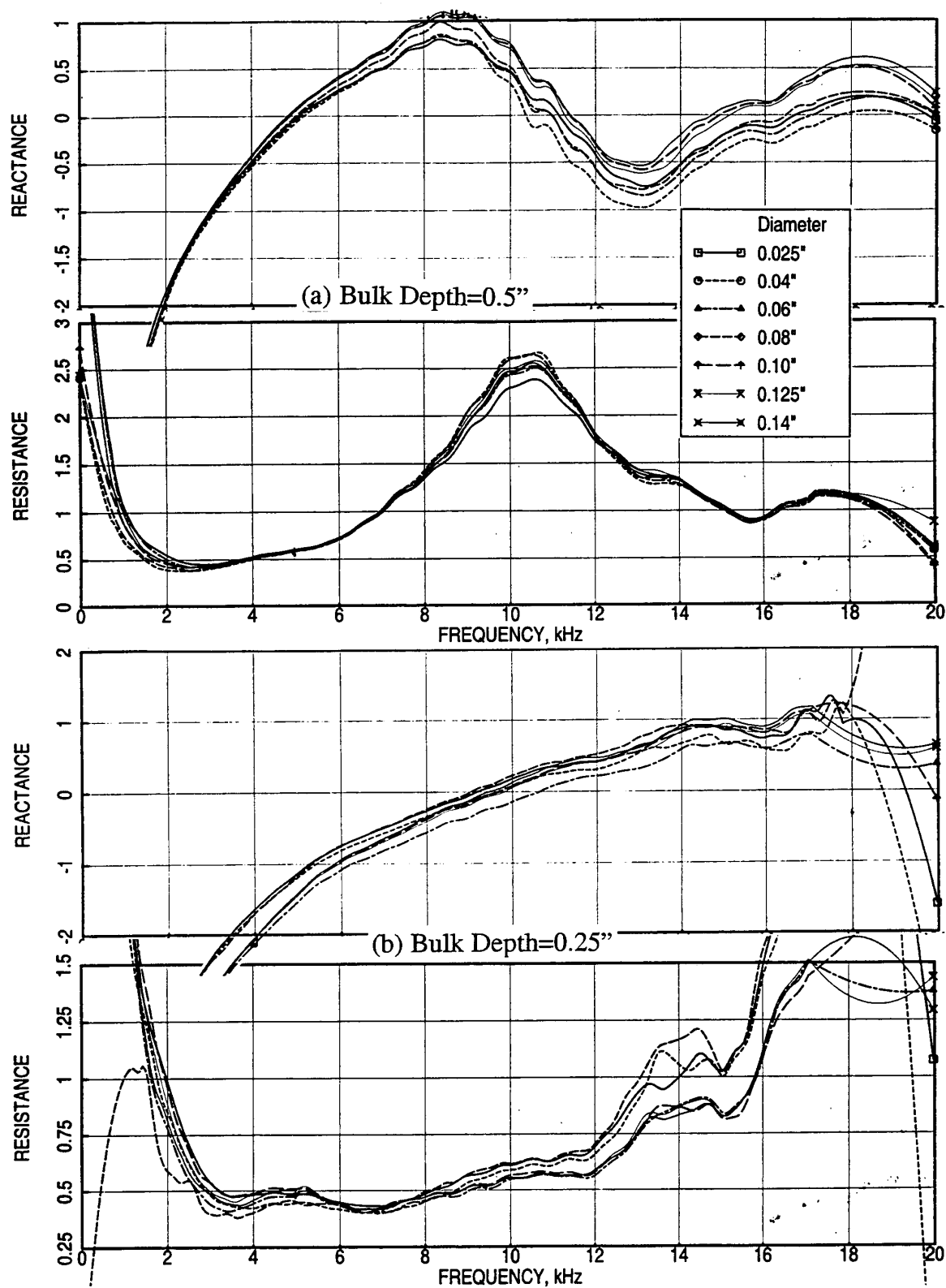


Figure 85. Effect of facesheet hole diameter on normal impedance for 12 lbf standard T-Foam bulk absorbers of different depths with 40 % porous 0.025" thick facesheets, OASPL= 150 dB, (a) Bulk Depth=0.5" and (b) Bulk Depth=0.25".

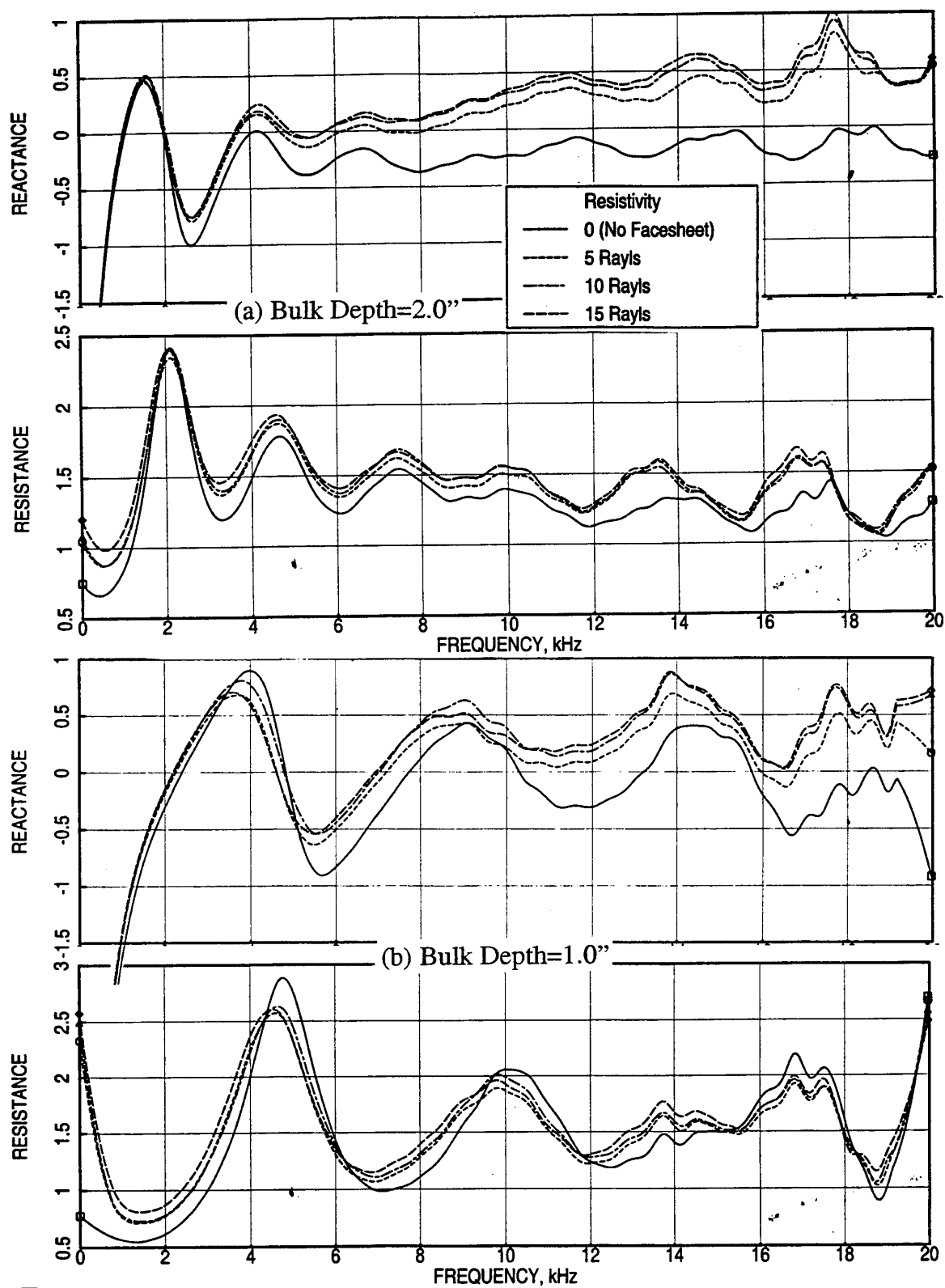


Figure 86. Effect of facesheet resistivity on normal impedance for 12 lbf standard T-Foam bulk absorbers of different depths with linear facesheets, OASPL= 150 dB, (a) Bulk Depth=2.0" and (b) Bulk Depth=1.0".

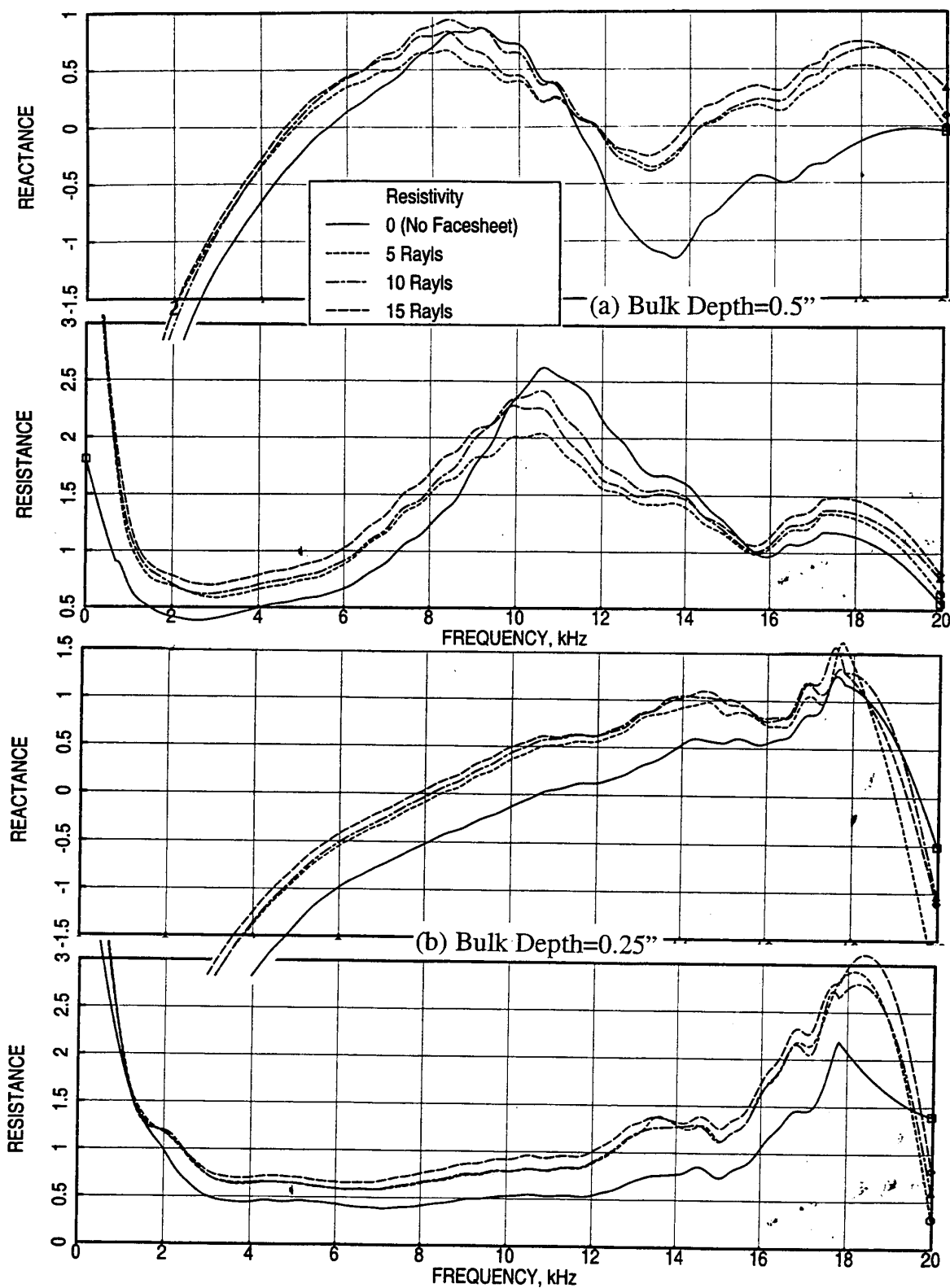


Figure 87. Effect of facesheet resistivity on normal impedance for 12 lbf standard T-Foam bulk absorbers of different depths with linear facesheets, OASPL= 150 dB, (a) Bulk Depth=0.5" and (b) Bulk Depth=0.25".

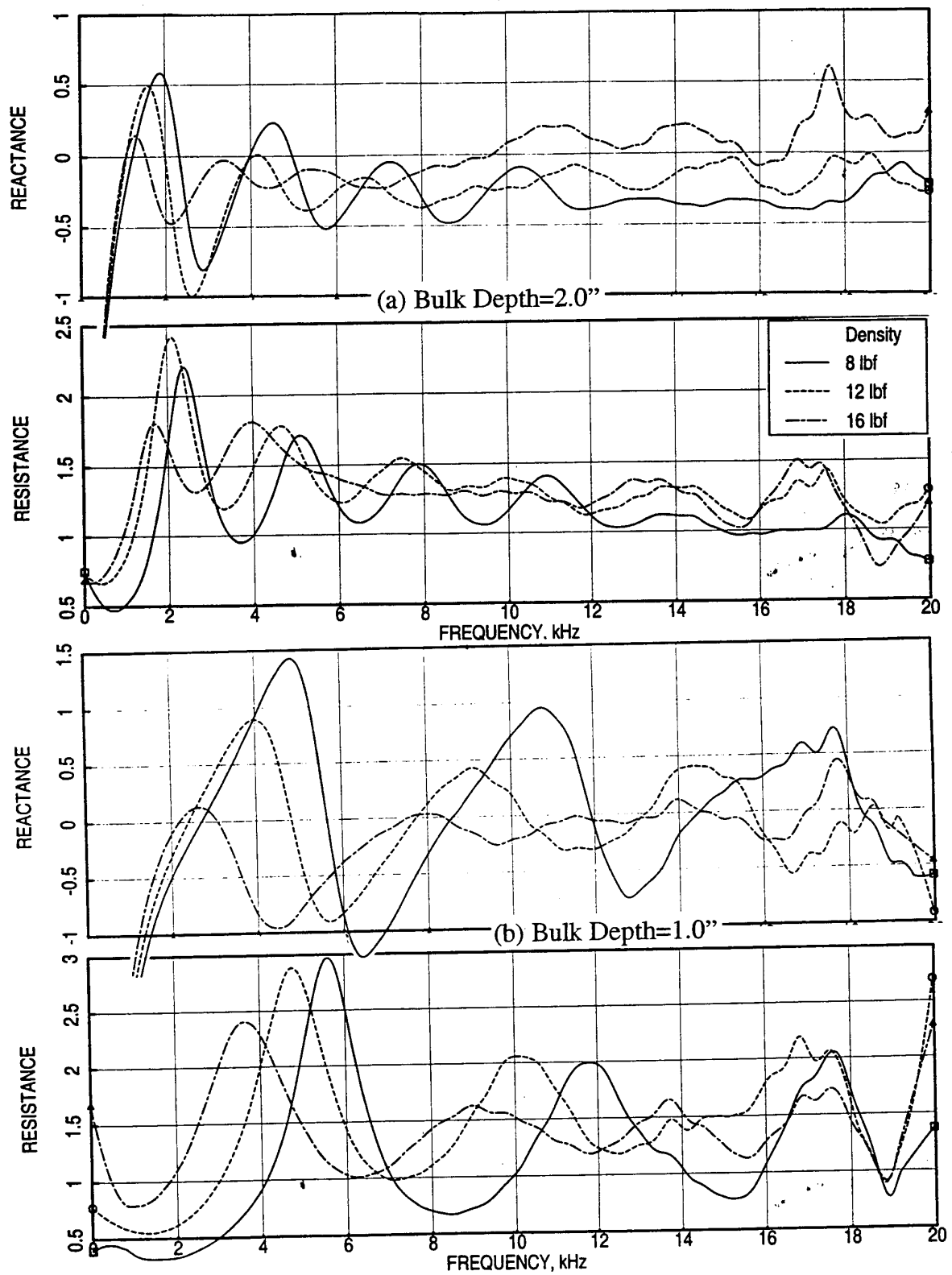


Figure 88. Effect of bulk density on normal impedance for standard T-Foam bulk absorbers of different depths, OASPL=150 dB, (a) Bulk Depth=2.0" and (b) Bulk Depth=1.0".

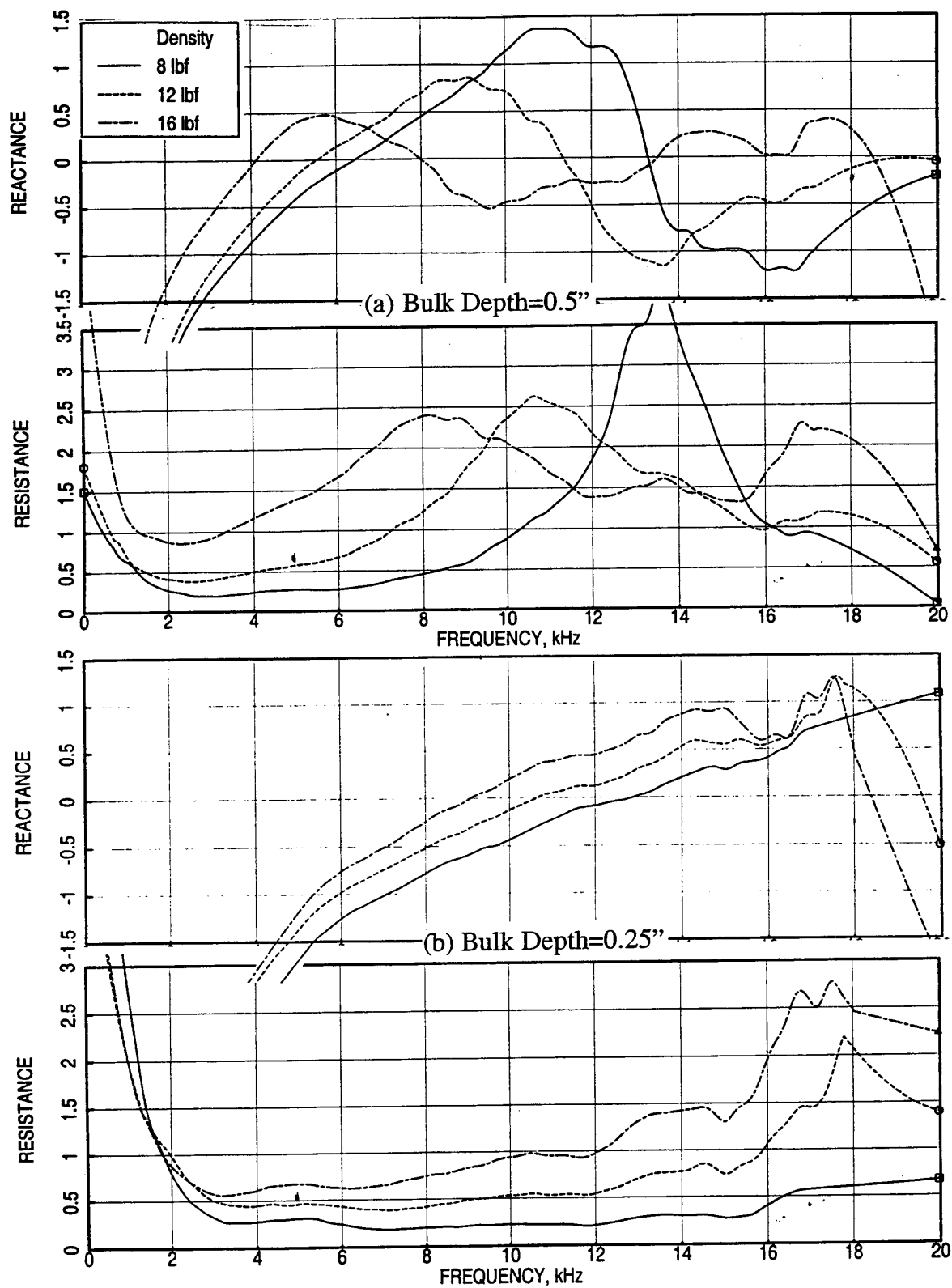


Figure 89. Effect of bulk density on normal impedance for standard T-Foam bulk absorbers of different depths, OASPL=150 dB, (a) Bulk Depth=0.5" and (b) Bulk Depth=0.25".

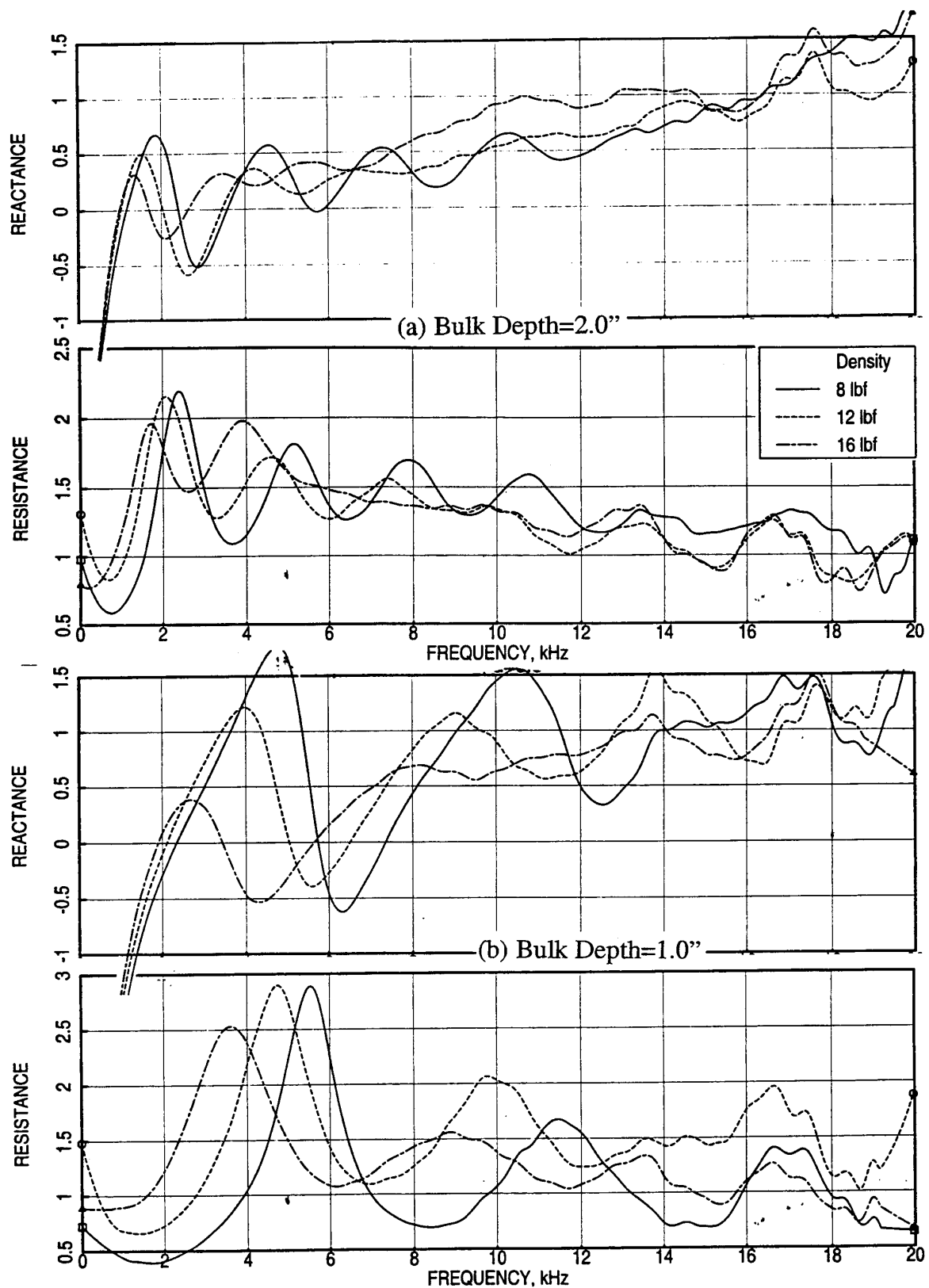


Figure 90. Effect of bulk density on normal impedance for standard T-Foam bulk absorbers of different depths with 20 % porous 0.025"-thick facesheet,  $d=0.04$ ", OASPL=150 dB, (a) Bulk Depth=2.0" and (b) Bulk Depth=1.0".

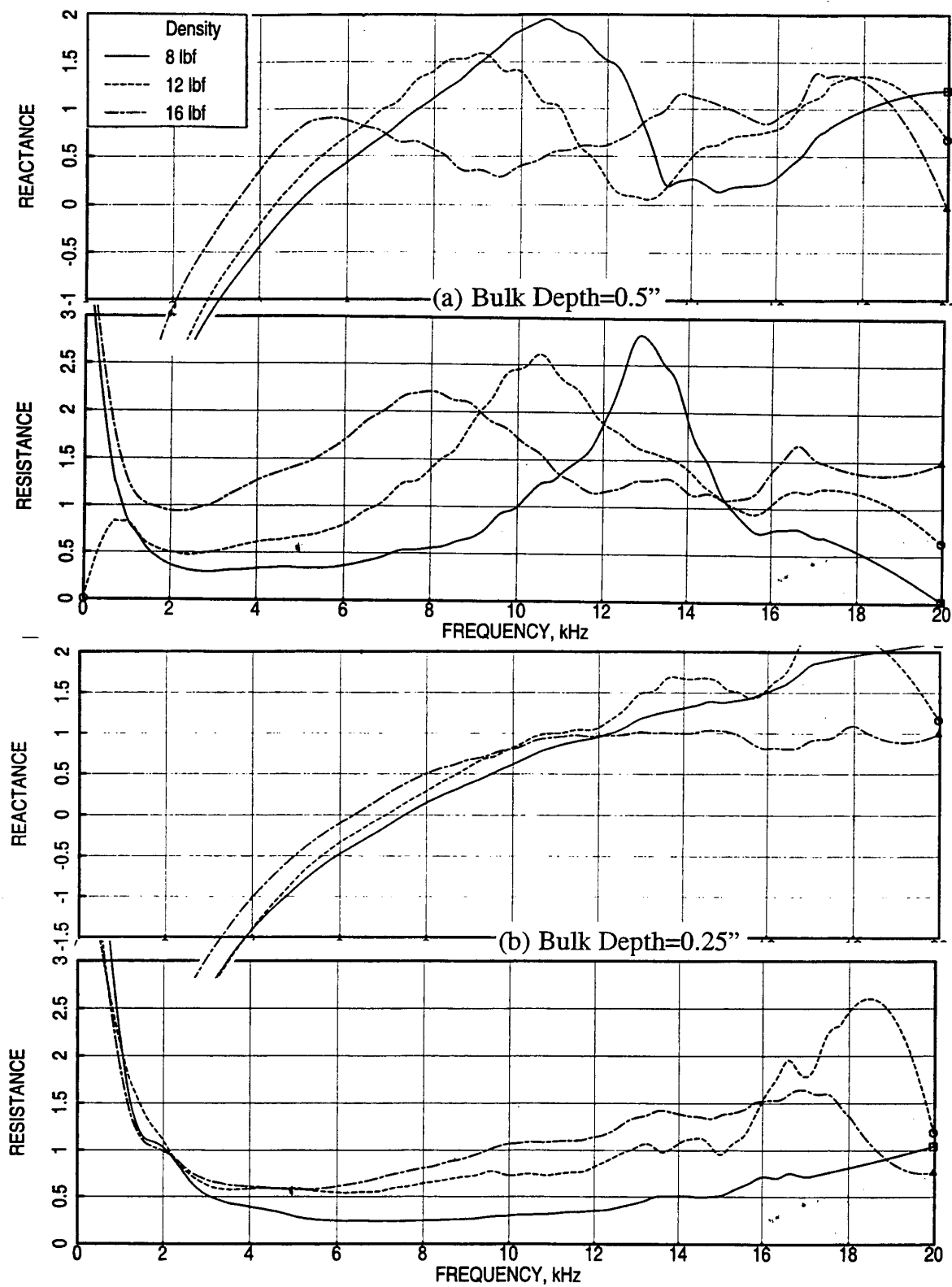


Figure 91. Effect of bulk density on normal impedance for standard T-Foam bulk absorbers of different depths with 20 % porous 0.025"-thick facesheet,  $d=0.04$ ", OASPL=150 dB, (a) Bulk Depth=0.5" and (b) Bulk Depth=0.25".

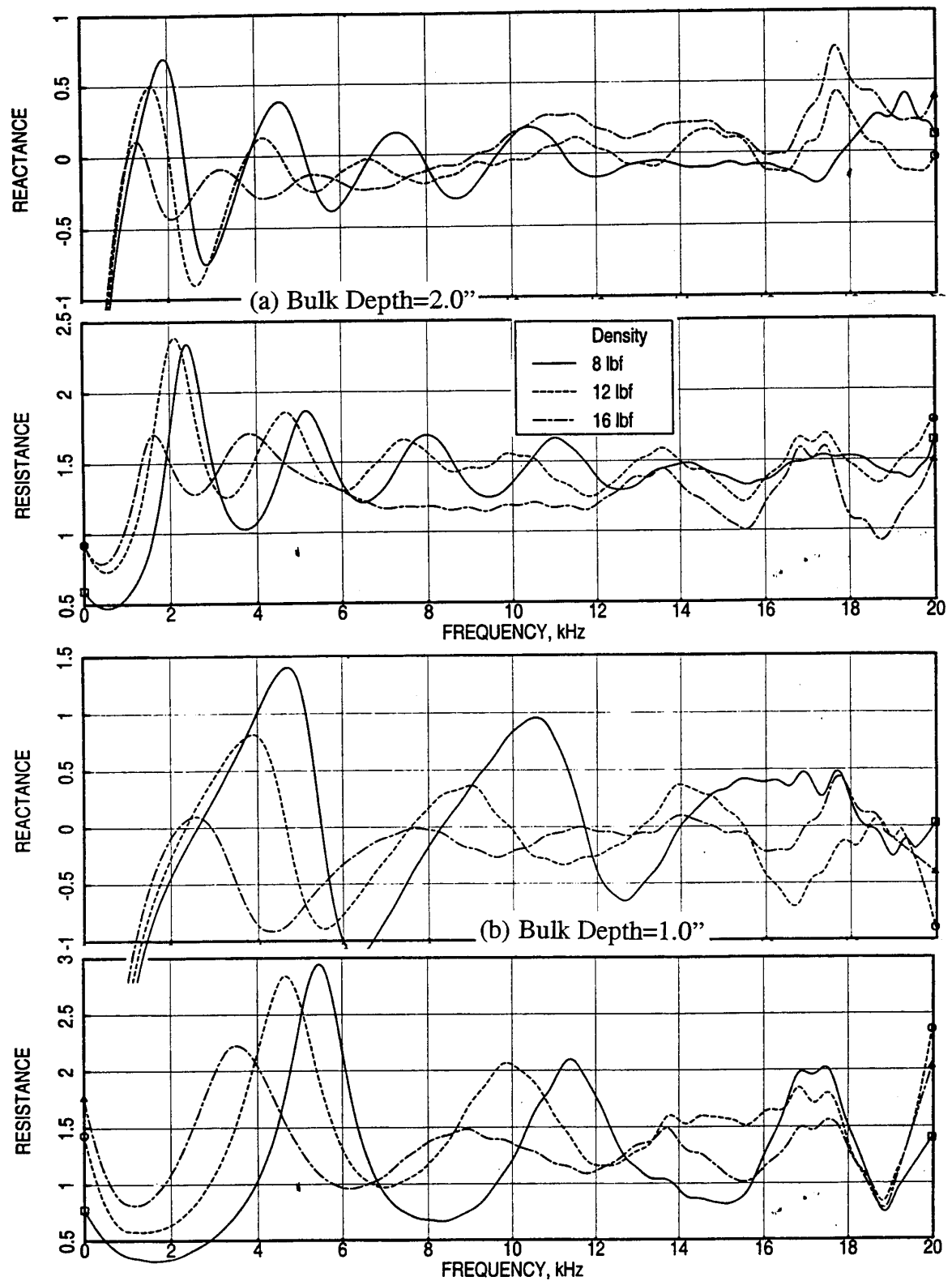


Figure 92. Effect of bulk density on normal impedance for standard T-Foam bulk absorbers of different depths with 40 % porous 0.025"-thick facesheet,  $d=0.04$ ", OASPL=150 dB, (a) Bulk Depth=2.0" and (b) Bulk Depth=1.0".



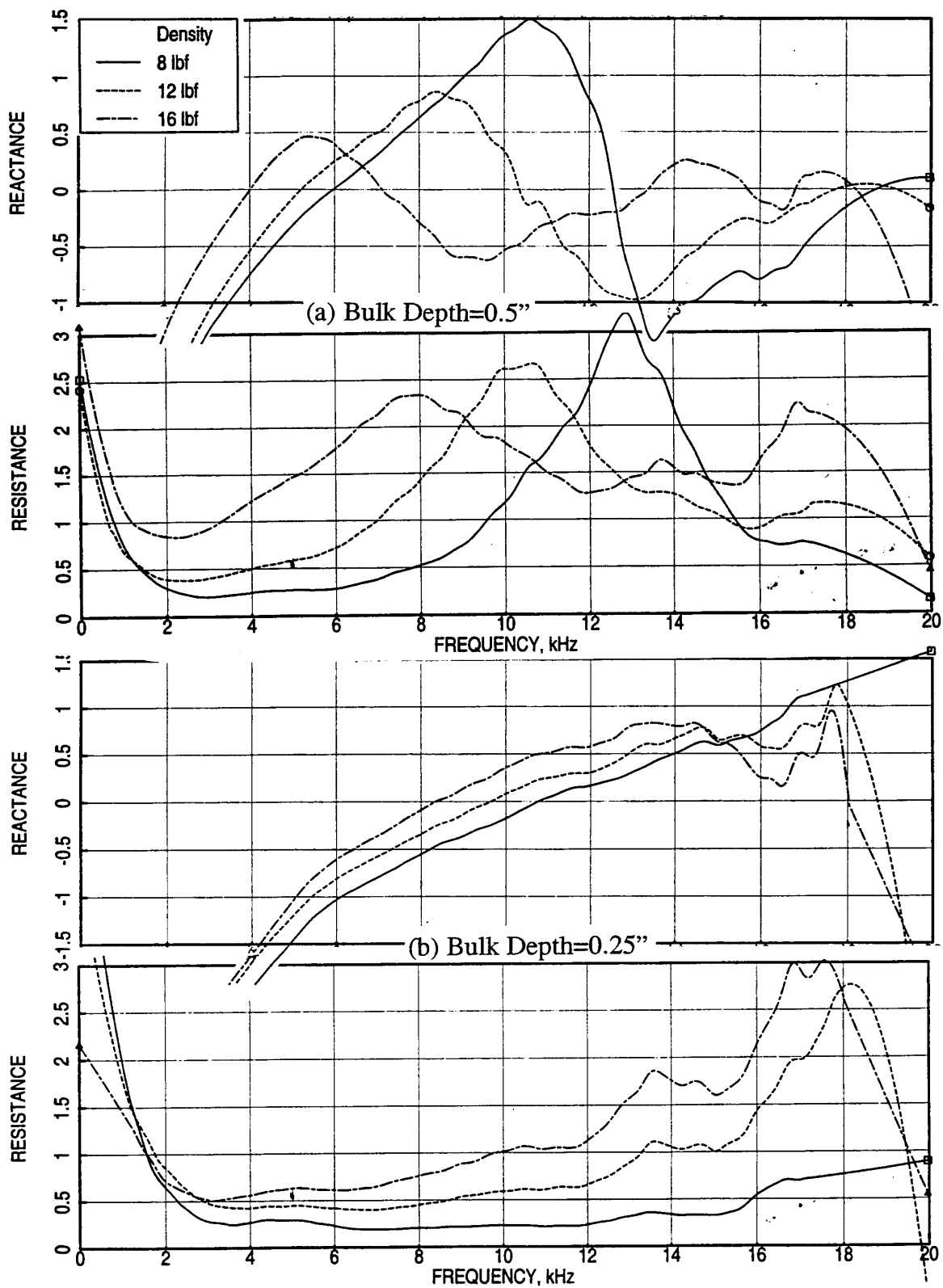


Figure 93. Effect of bulk density on normal impedance for standard T-Foam bulk absorbers of different depths with 40 % porous 0.025"-thick facesheet,  $d=0.04$ ", OASPL=150 dB, (a) Bulk Depth=0.5" and (b) Bulk Depth=0.25".

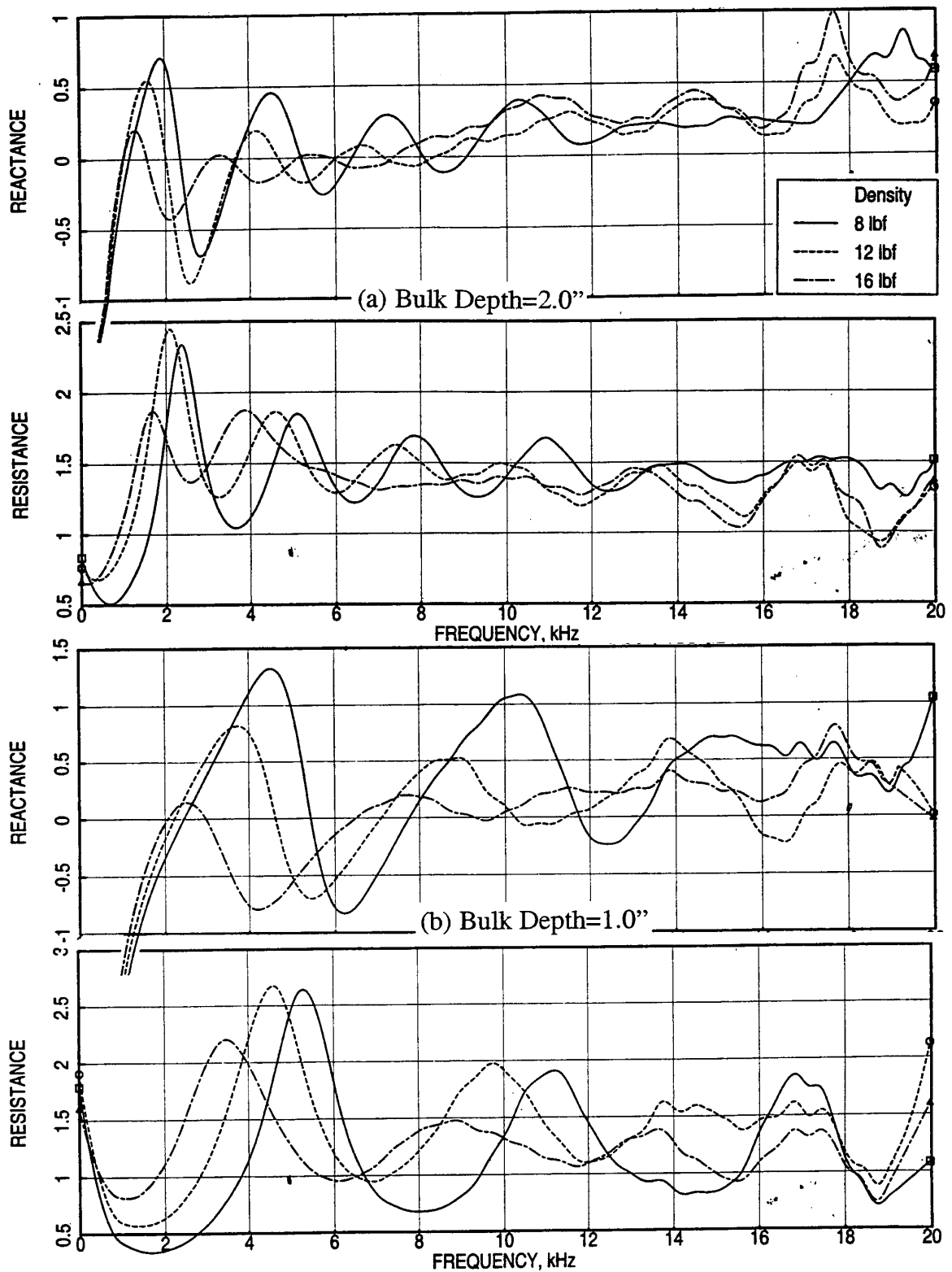


Figure 94. Effect of bulk density on normal impedance for standard T-Foam bulk absorbers of different depths with 40 % porous 0.06"-thick facesheet,  $d=0.04''$ , OASPL=150 dB, (a) Bulk Depth=2.0" and (b) Bulk Depth=1.0".

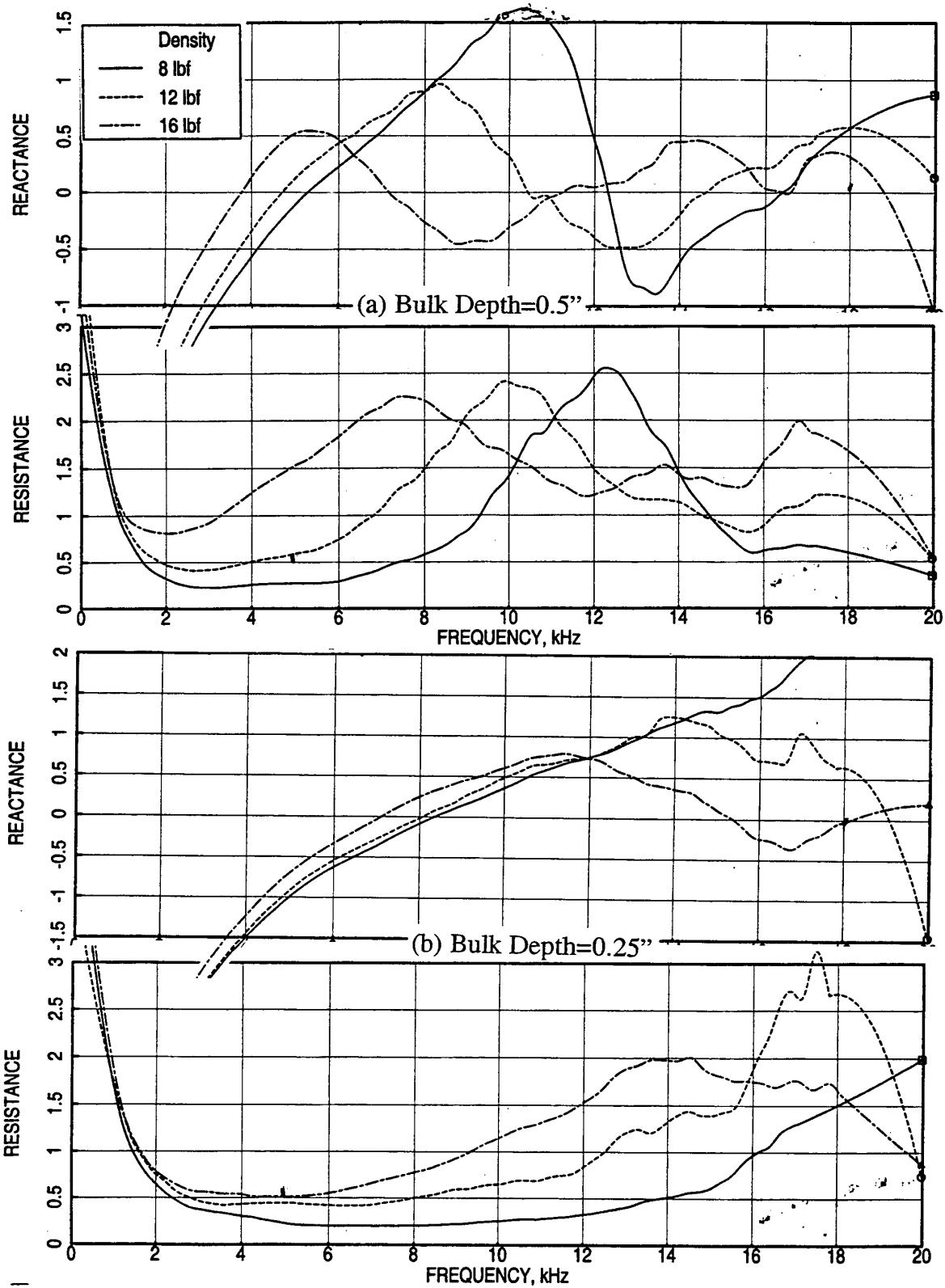


Figure 95. Effect of bulk density on normal impedance for standard T-Foam bulk absorbers of different depths with 40 % porous 0.06"-thick facesheet,  $d=0.04$ ", OASPL=150 dB, (a) Bulk Depth=0.5" and (b) Bulk Depth=0.25".

with increasing porosity as shown in Figures 92 and 93 for a 40% porous facesheet. For thicker facesheets the impact is similar to the 20% porous facesheet case, as shown in Figures 94 and 95 for a 0.06" thick facesheet.

**5.2.3 Feltmetal Bulk Absorbers:** Feltmetal is a trade name for bulk absorbers made out of high temperature steel fibers. The density for these absorbers is relatively higher compared to SiC and T-Foam. The density for Feltmetal is expressed as a percentage of solid steel material. The lowest density that is achieved is 5 %. Feltmetal samples of nominal densities of 5%, 10 %, and 15 % of different depths are tested.

***Parametric Characteristics of Normal Impedance due to Facesheet Property Variation:***

The effect of facesheet porosity on normal impedance for 5 % dense Feltmetal bulk absorbers of different depths is studied and the results are shown in Figures 96 and 97. The reactance and resistance increase with decreasing facesheet porosity. The cavity anti-resonance effect is relatively small for this material and almost insignificant for deeper bulk samples. The effect of facesheet thickness on normal impedance is shown in Figures 98 and 99. The reactance and resistance, both, decrease first and then increase with increasing facesheet thickness. The anti-resonance frequency decreases with increasing facesheet depth, only observed for 0.5"-deep samples, due to the increase of effective bulk absorber depth. The effect of facesheet hole diameter with fixed porosity and thickness seems to be small compared to porosity and thickness effects (see Figures 100 and 101). For 40% porous facesheet with  $t=0.025''$ , the reactance decreases and then increases with increasing hole diameter. The resistance behaves differently for different bulk depths. For deeper absorbers the resistance increases slightly with increasing hole diameter. The trend is reversed for thinner bulk samples. Effect of excitation intensity on normal impedance for Feltmetal, with and without facesheets, is insignificant (not shown here). In general the reactance decreases and resistance increases with increasing excitation level.

Similar results for Feltmetal samples of densities 10 % and 15 % are generated and examined (not presented here). The characteristics of parametric variations are similar to those observed for 5 % dense Feltmetal bulk absorbers.

***Parametric Characteristics of Normal Impedance due to Density Variation:*** The effect of density on normal impedance for Feltmetal bulk absorbers of different depths, without facesheet, is shown in Figures 102 and 103. In general the reactance decreases and resistance increases with increasing density. The trend for reactance is slightly off from the general observation for 2"-deep sample. At higher frequencies the reactance for 10 % dense

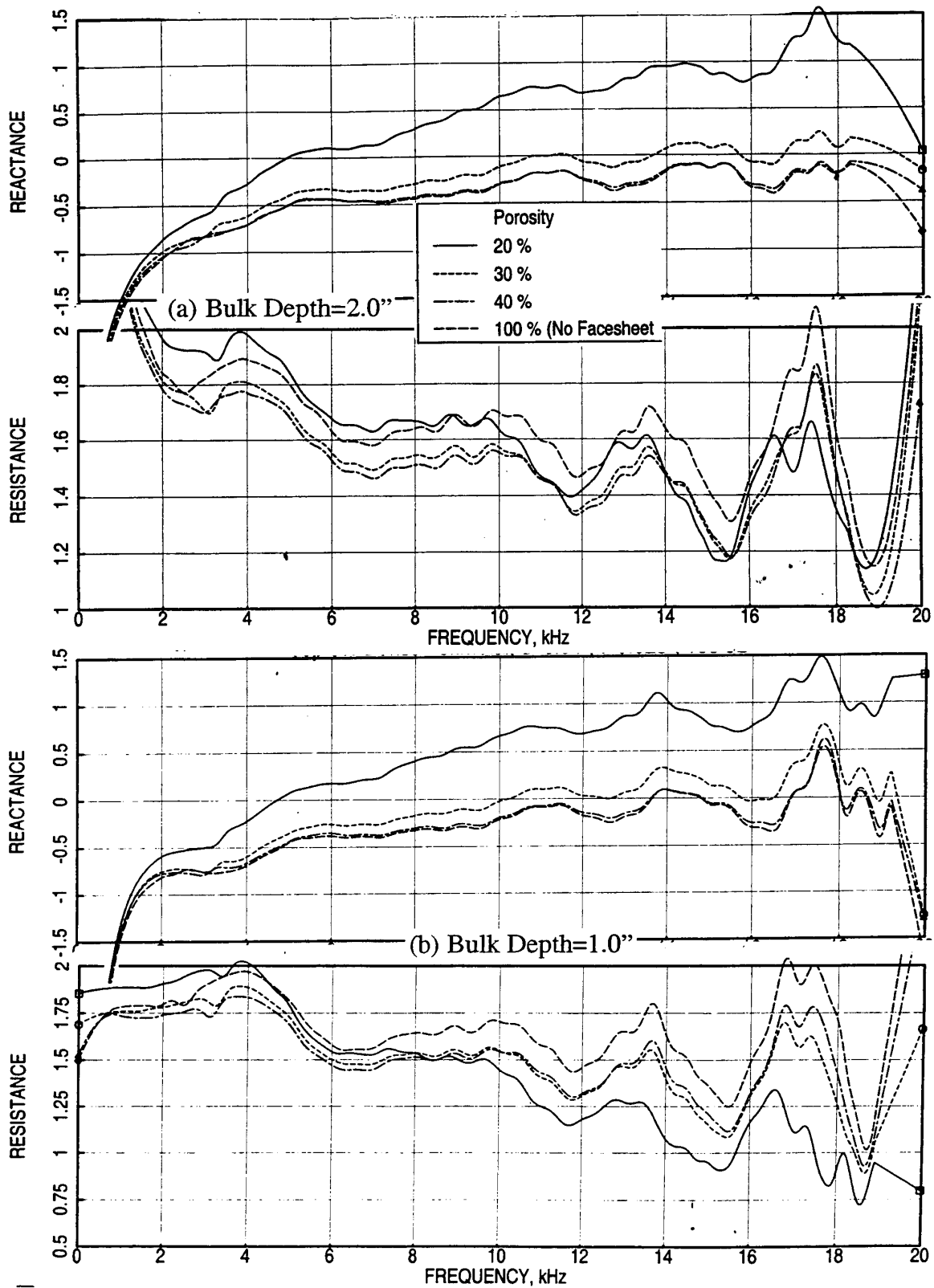


Figure 96. Effect of facesheet porosity on normal impedance for 5 % dense Feltmetal bulk absorbers of different depths with 0.025"-thick facesheets,  $d=0.04$ ", OASPL= 150 dB, (a) Bulk Depth=2.0" and (b) Bulk Depth=1.0".

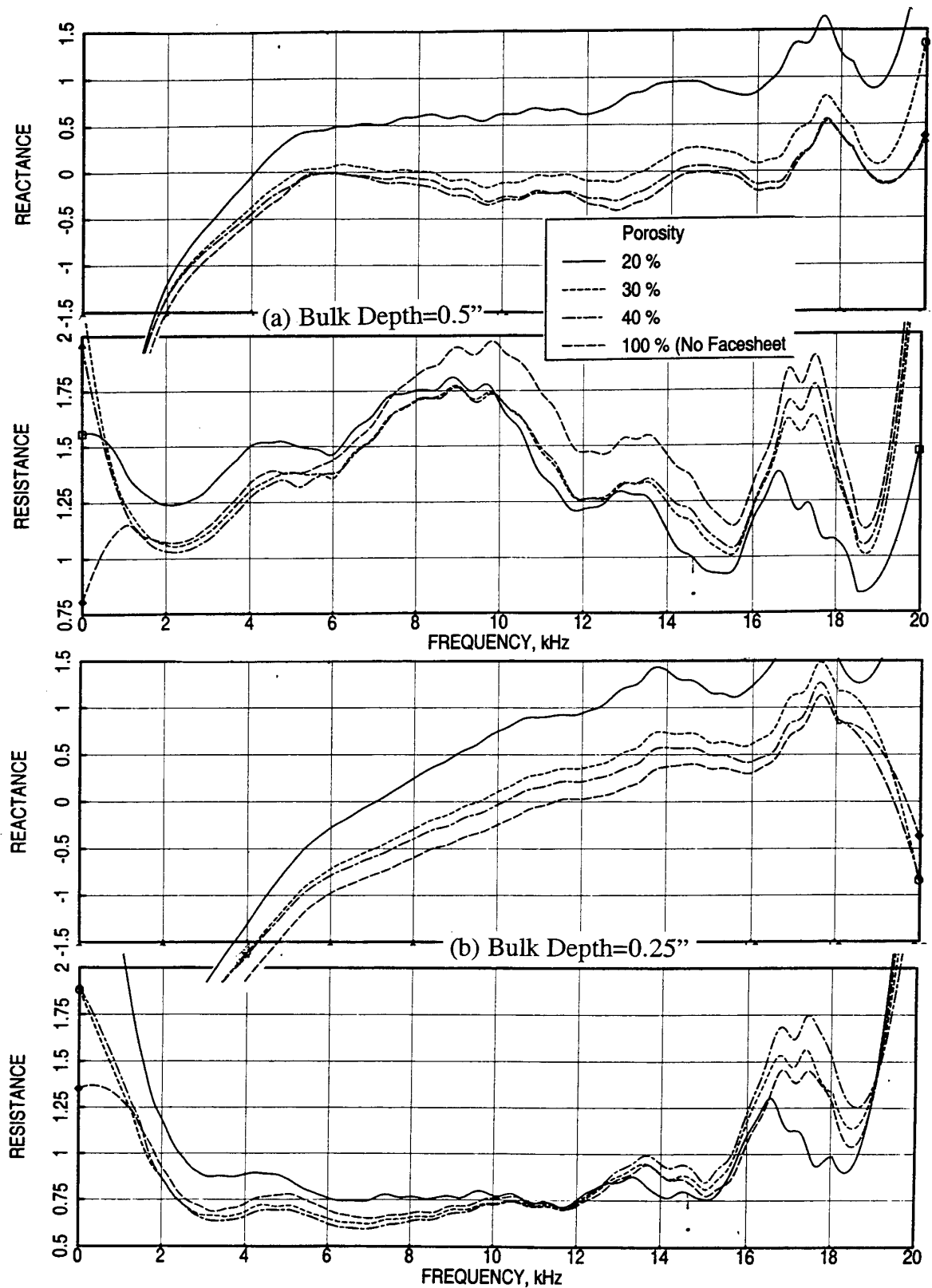


Figure 97. Effect of facesheet porosity on normal impedance for 5 % dense Feltmetal bulk absorbers of different depths with 0.025"-thick facesheets,  $d=0.04$ ", OASPL= 150 dB, (a) Bulk Depth=0.5" and (b) Bulk Depth=0.25".

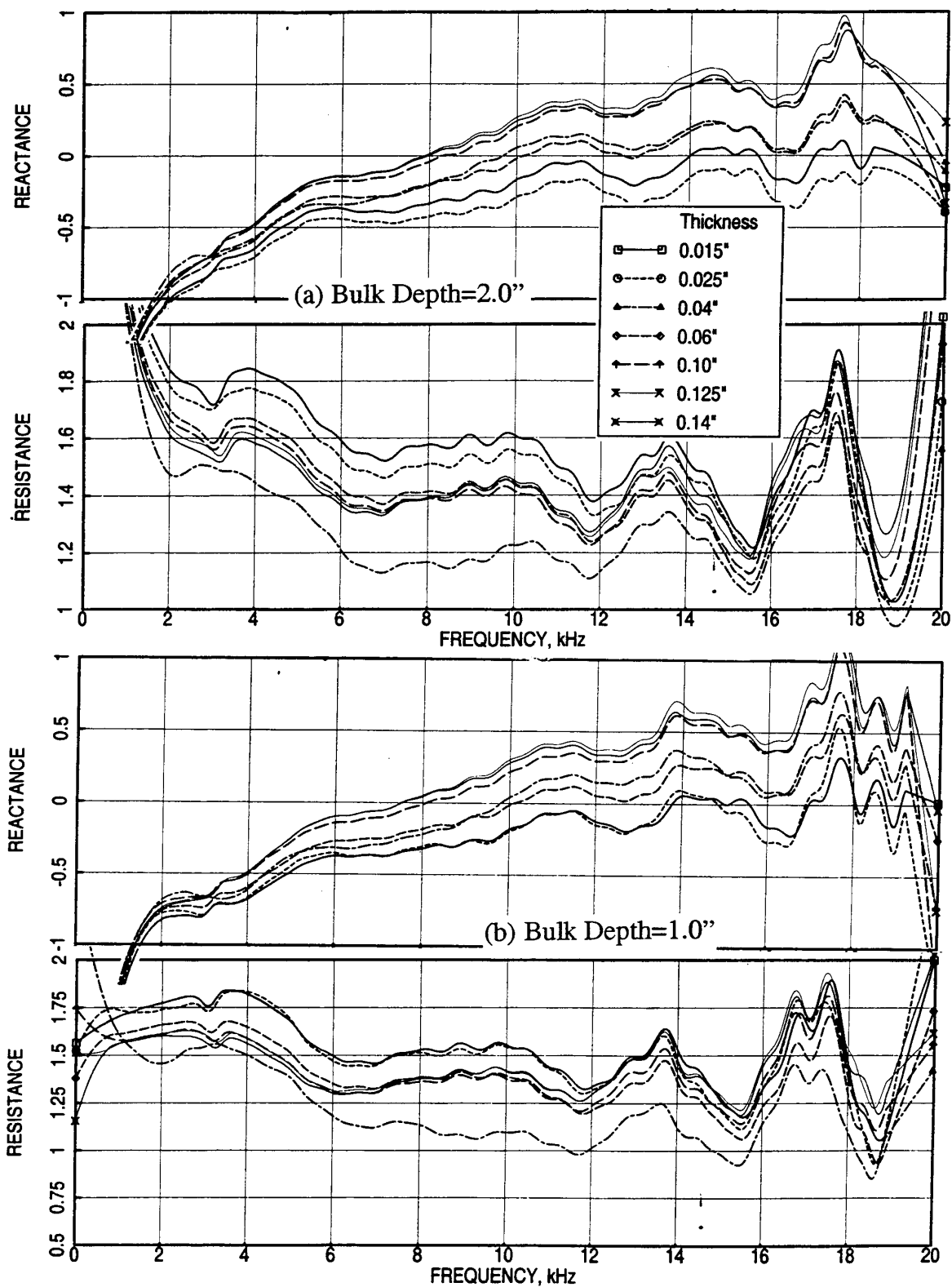


Figure 98. Effect of facesheet thickness on normal impedance for 5 % dense Feltmetal bulk absorbers of different depths with 40 % porous facesheets,  $d=0.04''$ , OASPL= 150 dB, (a) Bulk Depth=2.0" and (b) Bulk Depth=1.0".

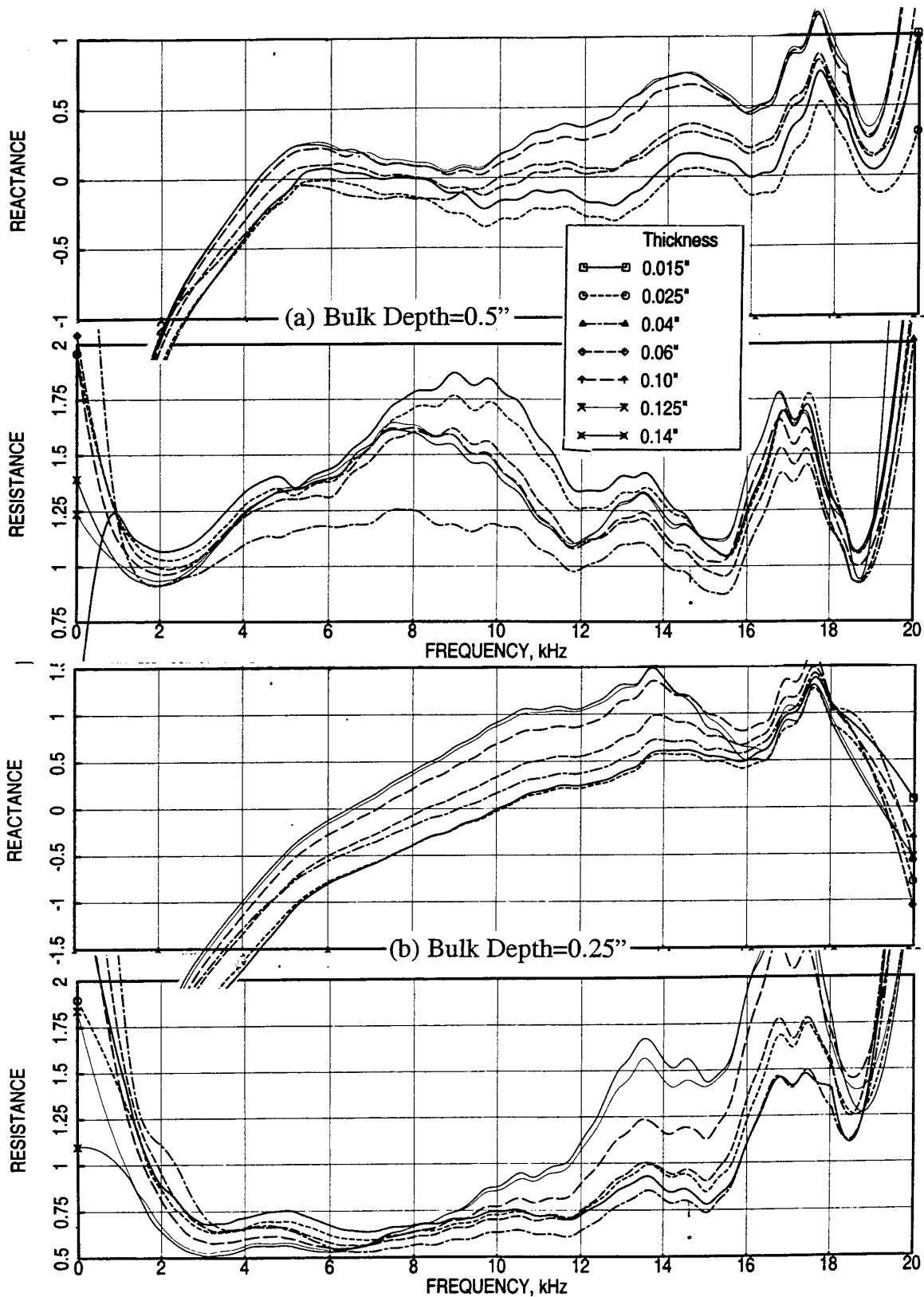


Figure 99. Effect of facesheet thickness on normal impedance for 5 % dense Feltmetal bulk absorbers of different depths with 40 % porous facesheets,  $d=0.04''$ , OASPL= 150 dB, (a) Bulk Depth=0.5" and (b) Bulk Depth=0.25".



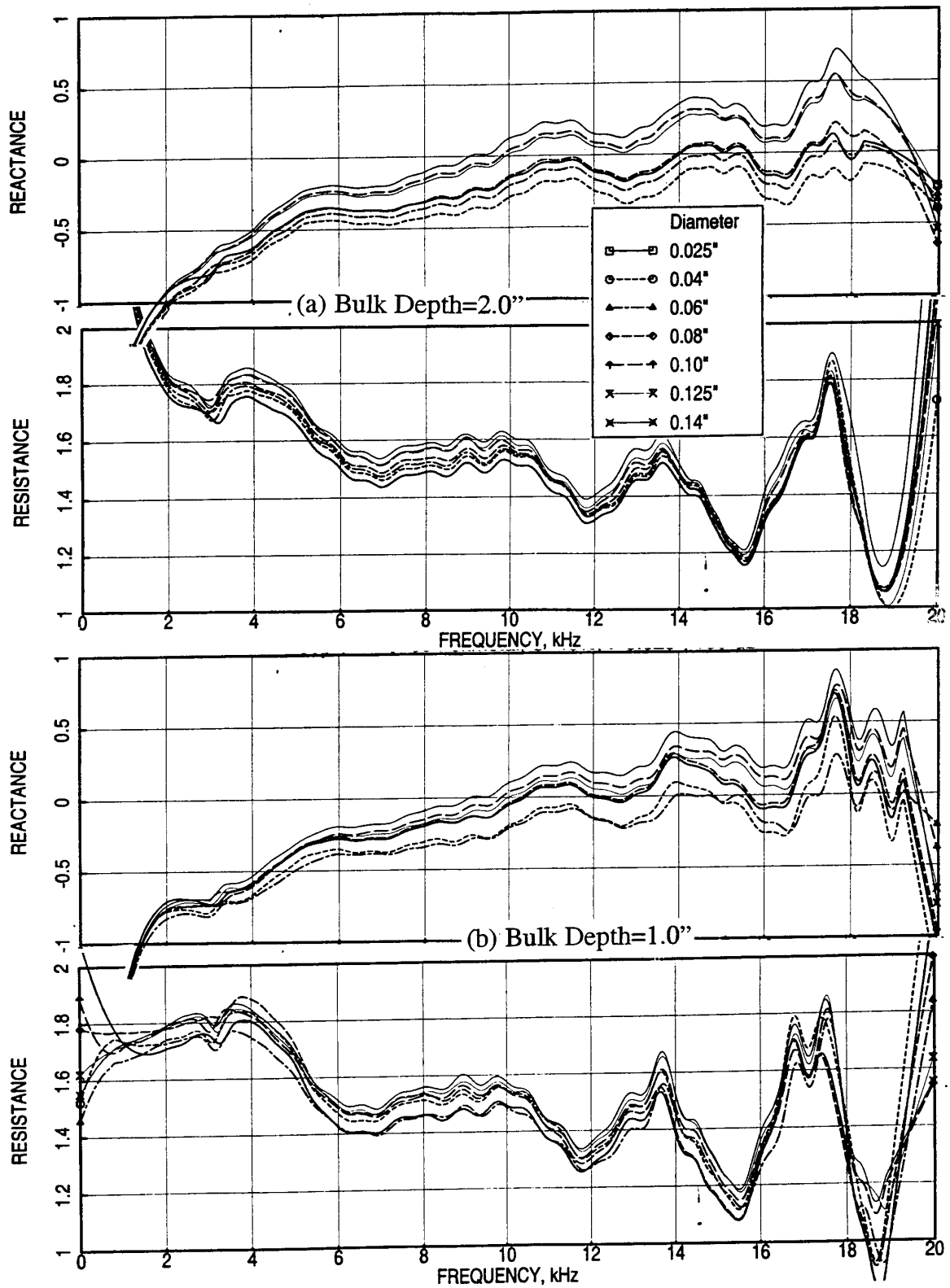


Figure 100. Effect of facesheet hole diameter on normal impedance for 5 % dense Feltmetal bulk absorbers of different depths with 40 % porous 0.025" thick facesheets, OASPL= 150 dB, (a) Bulk Depth=2.0" and (b) Bulk Depth=1.0".

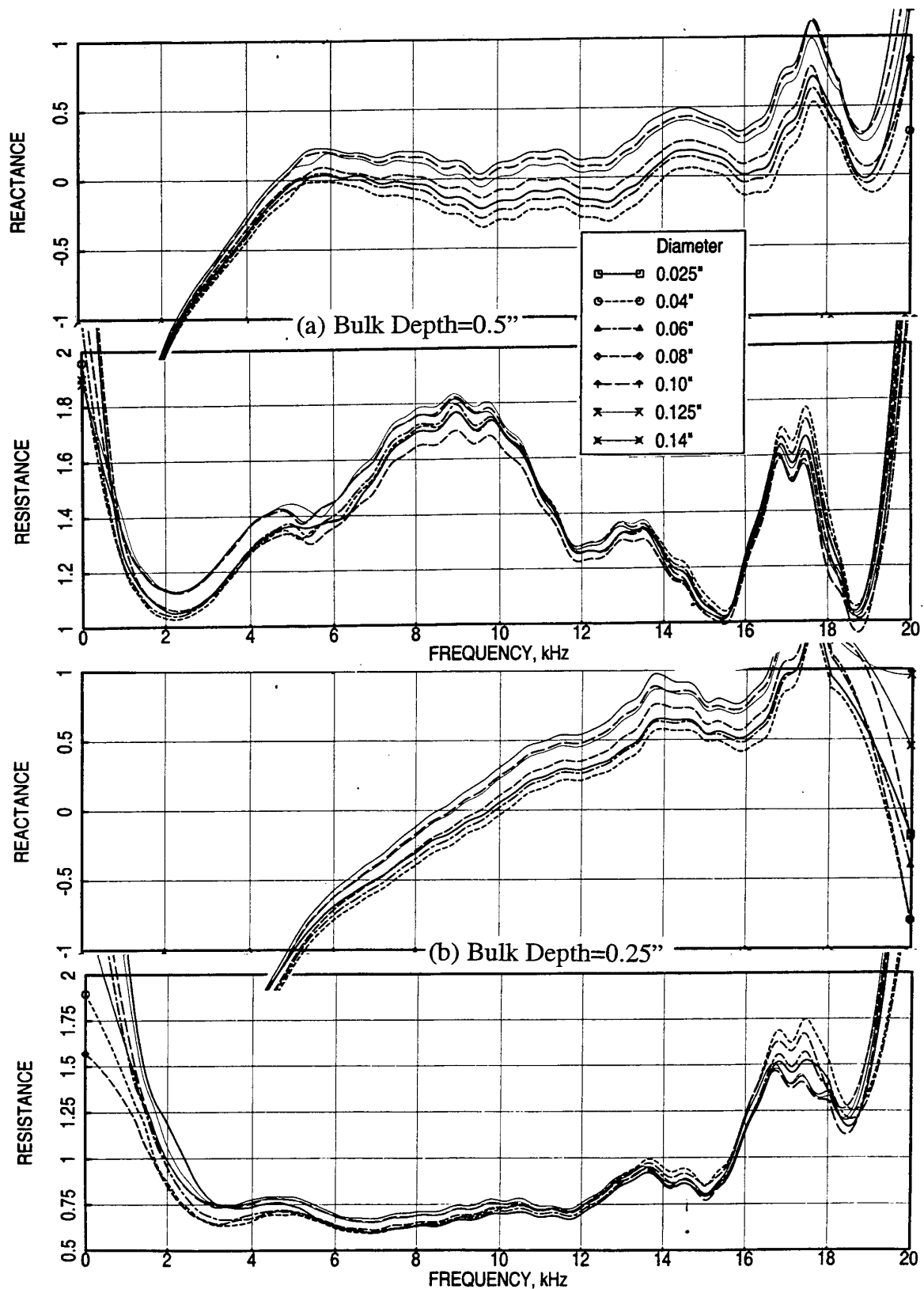


Figure 101. Effect of facesheet hole diameter on normal impedance for 5 % dense Feltmetal bulk absorbers of different depths with 40 % porous 0.025" thick facesheets, OASPL= 150 dB, (a) Bulk Depth=0.5" and (b) Bulk Depth=0.25".

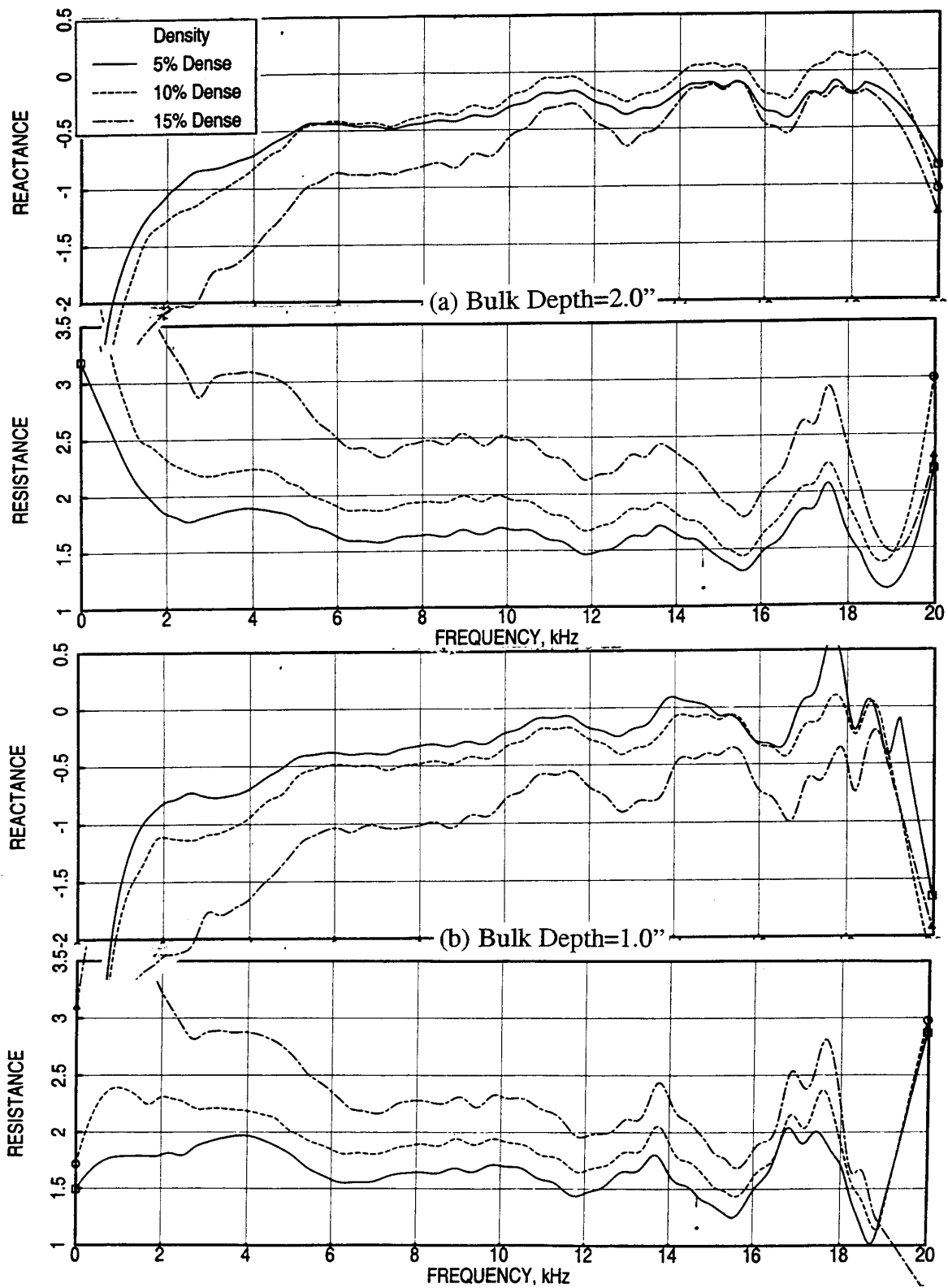


Figure 102. Effect of bulk density on normal impedance for Feltmetal bulk absorbers of different depths, OASPL=150 dB, (a) Bulk Depth=2.0" and (b) Bulk Depth=1.0".

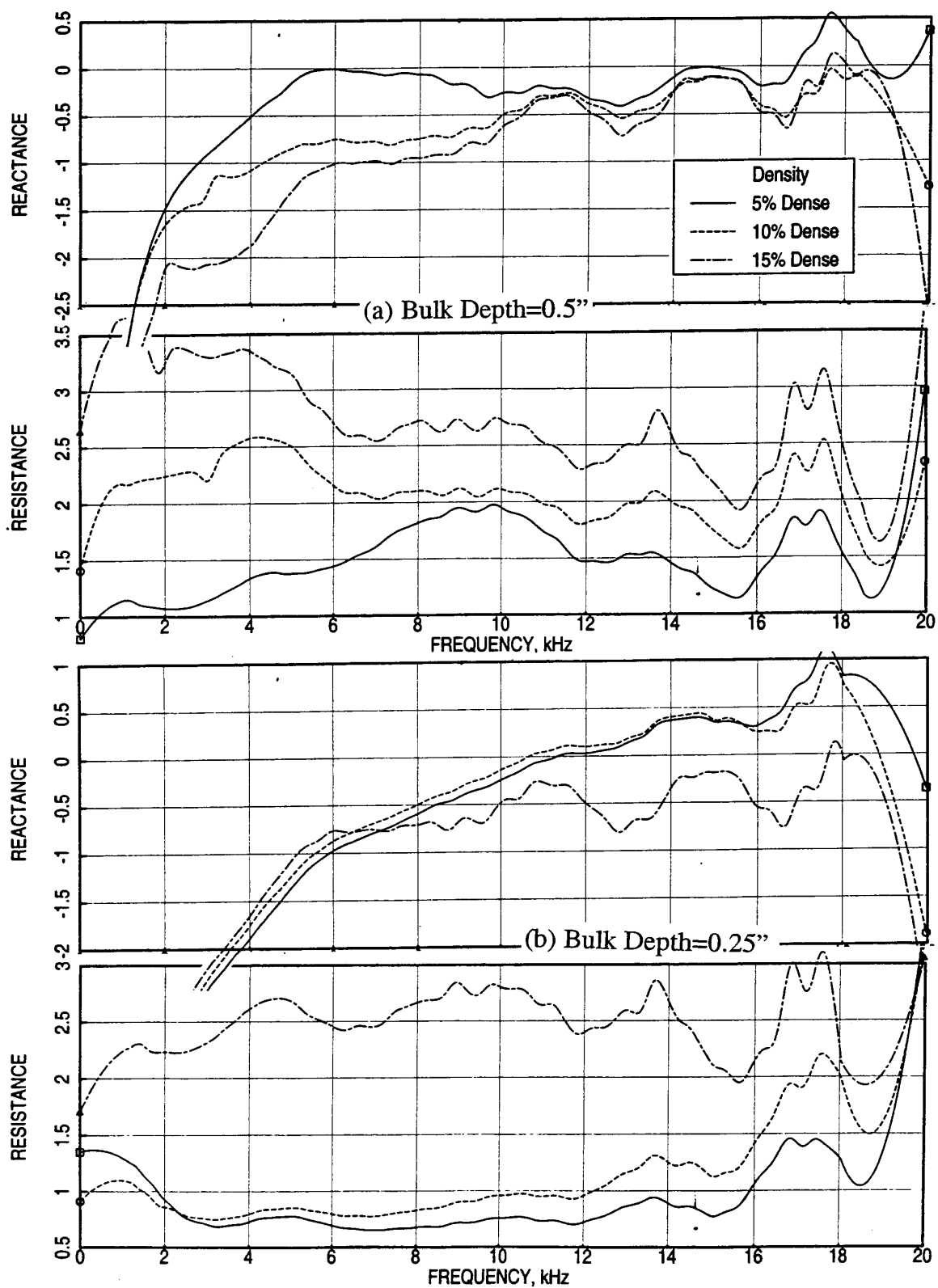


Figure 103. Effect of bulk density on normal impedance for Feltmetal bulk absorbers of different depths, OASPL=150 dB, (a) Bulk Depth=0.5" and (b) Bulk Depth=0.25".

Feltmetal is higher compared to 5 % dense sample. The cavity anti-resonance effect is almost non-existent for denser samples. The effect of density for Feltmetal with facesheets on normal impedance, shown in Figures 104 through 109, is similar to the bulk only configurations, except that the reactance variation with density for 2"-deep samples shows decreasing trend with increasing density for entire frequency range. The impact of facesheets, depending on their porosity and thickness, influence the magnitude of impedance variation. For example, the effect of a 20% porous facesheet, shown in Figures 104 and 105, forces the reactance to increase slightly with frequency compared to reactance for bulk only configuration. The impact diminishes with increasing porosity as shown in Figures 106 and 107 for a 40% porous facesheet. For thicker facesheets the impact is similar to the 20% porous facesheet case, as shown in Figures 108 and 109 for a 0.06" thick facesheet.

**5.2.4 Different Bulk Absorbers:** Normal impedance spectra for individual type of bulk absorbers are examined in the previous sections. The effect on normal impedance due to different bulk types is examined in this section. Any number of combination of bulk types can be put together for this purpose. However, a single combination of 100 ppi Silicon Carbide, 12 lbf T-Foam, and 5% dense Feltmetal samples are included in this study.

The effect of bulk type on normal impedance for bulk absorbers of different depths, without facesheet, is shown in Figures 110 and 111. The reactance is comparable for all three bulk types, except that the 100 ppi SiC and 12 lbf T-Foam show anti-resonance effects more distinctly compared to 5 % dense Feltmetal. The resistance is highest for Feltmetal and lowest for SiC. The anti-resonance frequency of T-Foam is significantly lower compared to SiC, indicating relatively higher effective bulk depth. This also indicates that the sound propagation speed in T-Foam medium is distinctly different compared to SiC. The effect of bulk type for samples with facesheets on normal impedance, shown in Figures 112 through 117, is similar to the bulk only configurations. The impact of facesheets, depending on their porosity and thickness, influence the magnitude of impedance variation. For example, the effect of a 20% porous facesheet, shown in Figures 112 and 113, forces the reactance to increase with frequency compared to reactance for bulk only configuration. The impact diminishes with increasing porosity as shown in Figures 114 and 115 for a 40% porous facesheet. For thicker facesheets the impact is similar to the 20% porous facesheet case, as shown in Figures 116 and 117 for a 0.06" thick facesheet.

**5.2.5 Bulk Absorbers for Mixer-Ejector Application:** Acoustic liner is an essential element for the ejector to suppress internal noise for HSCT application. Thus, suitable bulk materials and facesheets are to be selected to design bulk absorber liners for mixer-ejector

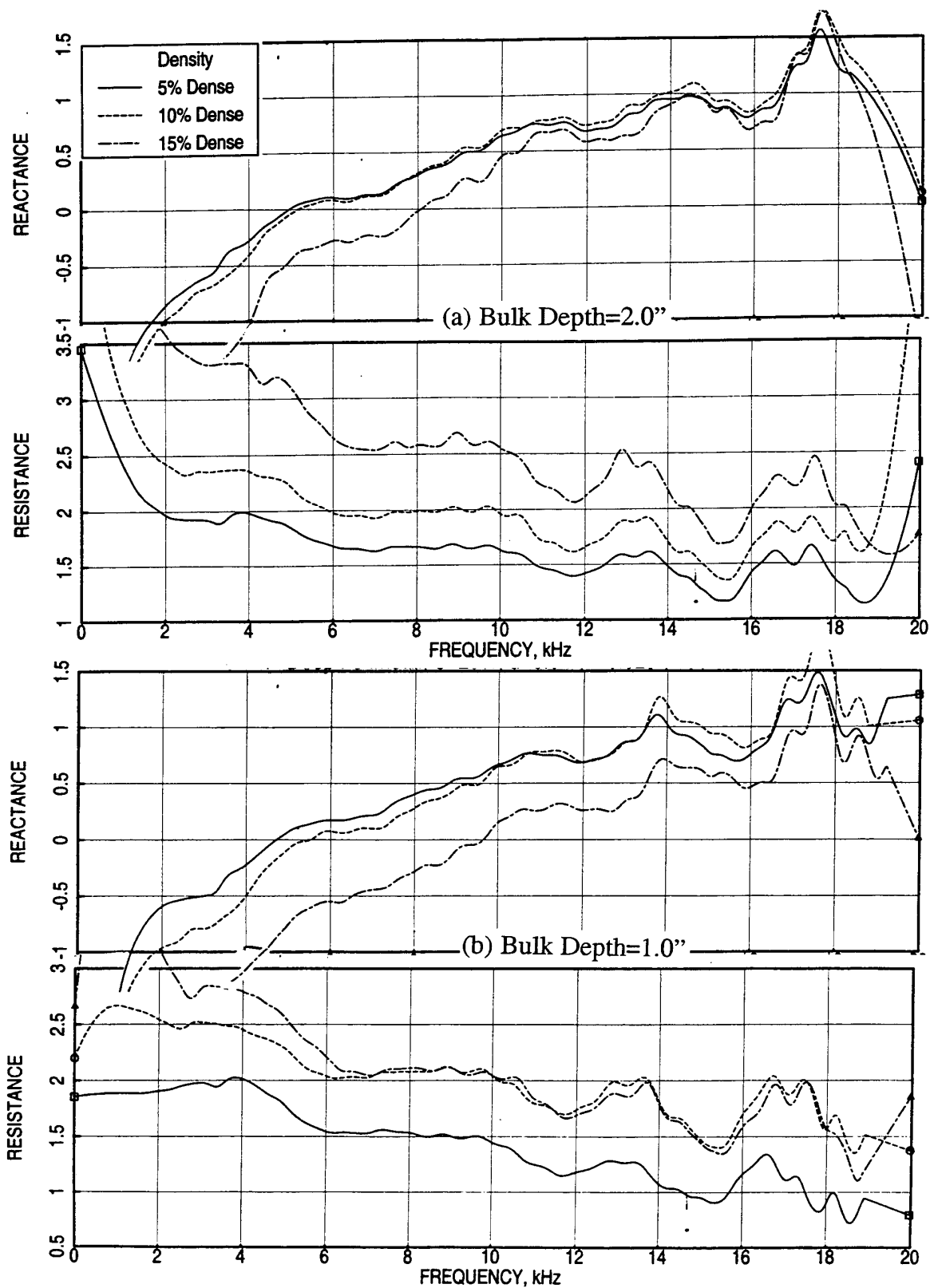


Figure 104. Effect of bulk density on normal impedance for Feltmetal bulk absorbers of different depths with 20 % porous 0.025"-thick facesheet,  $d=0.04$ ", OASPL=150 dB, (a) Bulk Depth=2.0" and (b) Bulk Depth=1.0".

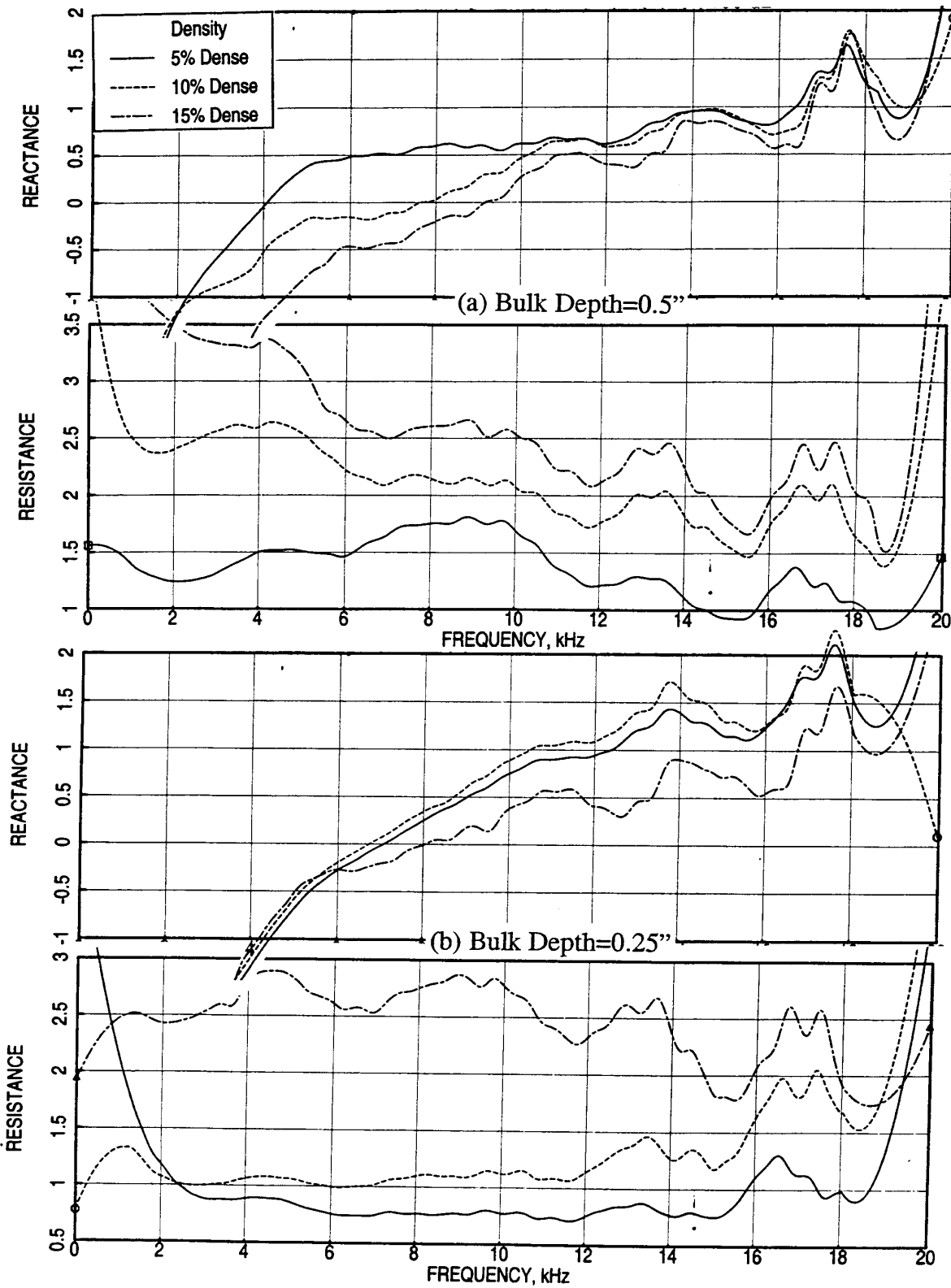


Figure 105. Effect of bulk density on normal impedance for Feltmetal bulk absorbers of different depths with 20 % porous 0.025"-thick facesheet,  $d=0.04$ ", OASPL=150 dB, (a) Bulk Depth=0.5" and (b) Bulk Depth=0.25".

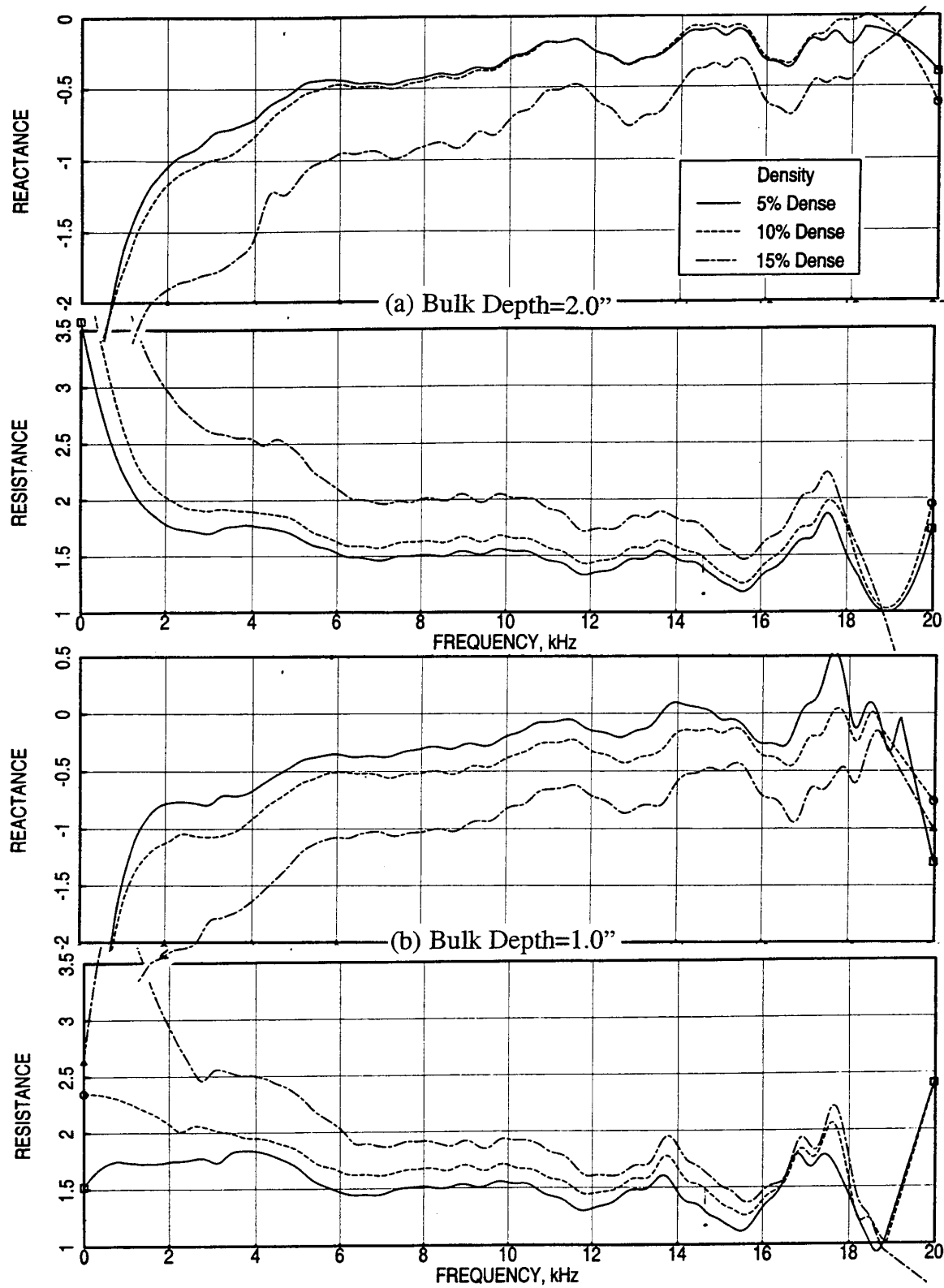


Figure 106. Effect of bulk density on normal impedance for Feltmetal bulk absorbers of different depths with 40 % porous 0.025"-thick facesheet,  $d=0.04$ ", OASPL=150 dB, (a) Bulk Depth=2.0" and (b) Bulk Depth=1.0".



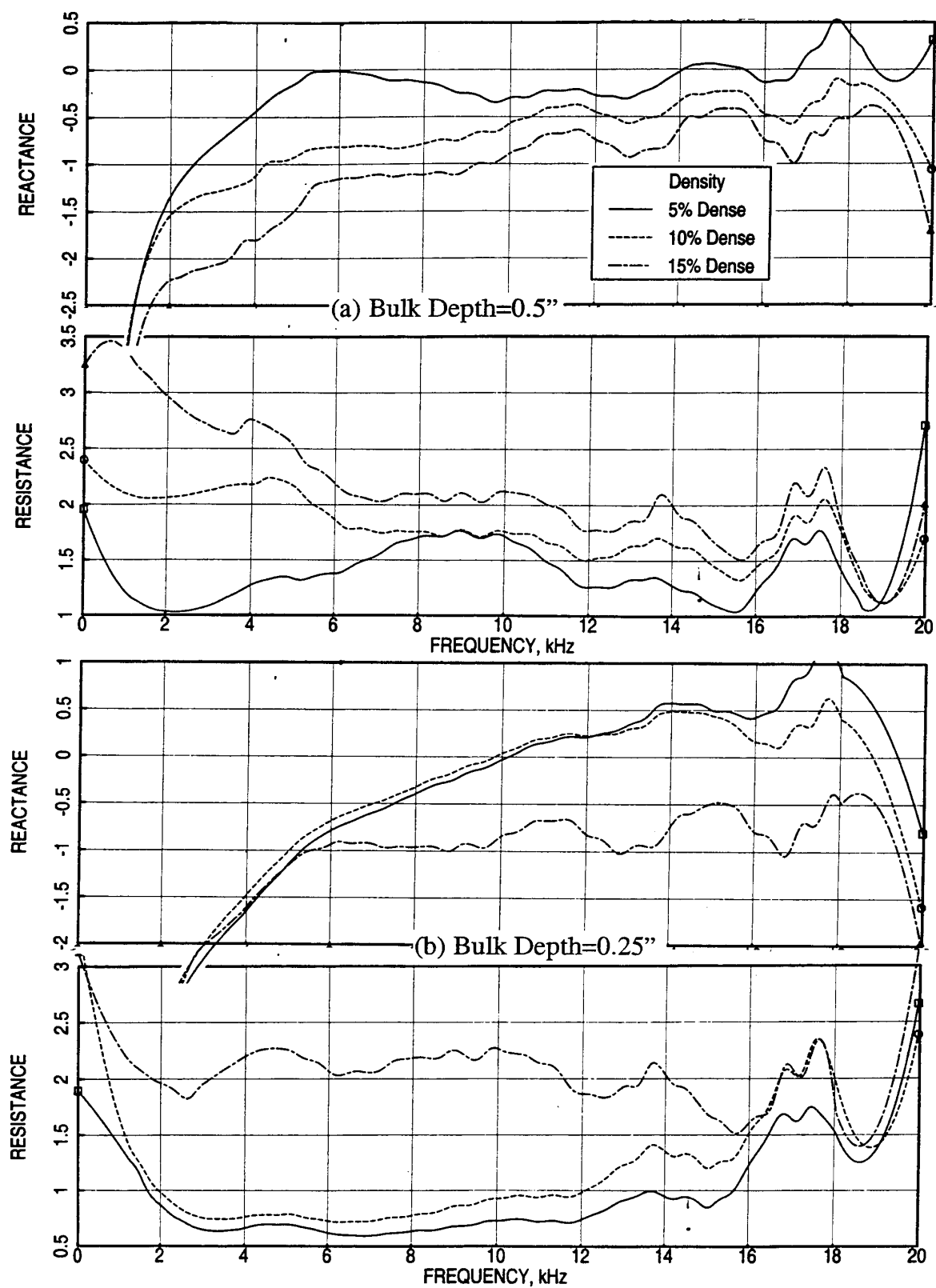


Figure 107. Effect of bulk density on normal impedance for Feltmetal bulk absorbers of different depths with 40 % porous 0.025"-thick facesheet,  $d=0.04$ ", OASPL=150 dB, (a) Bulk Depth=0.5" and (b) Bulk Depth=0.25".

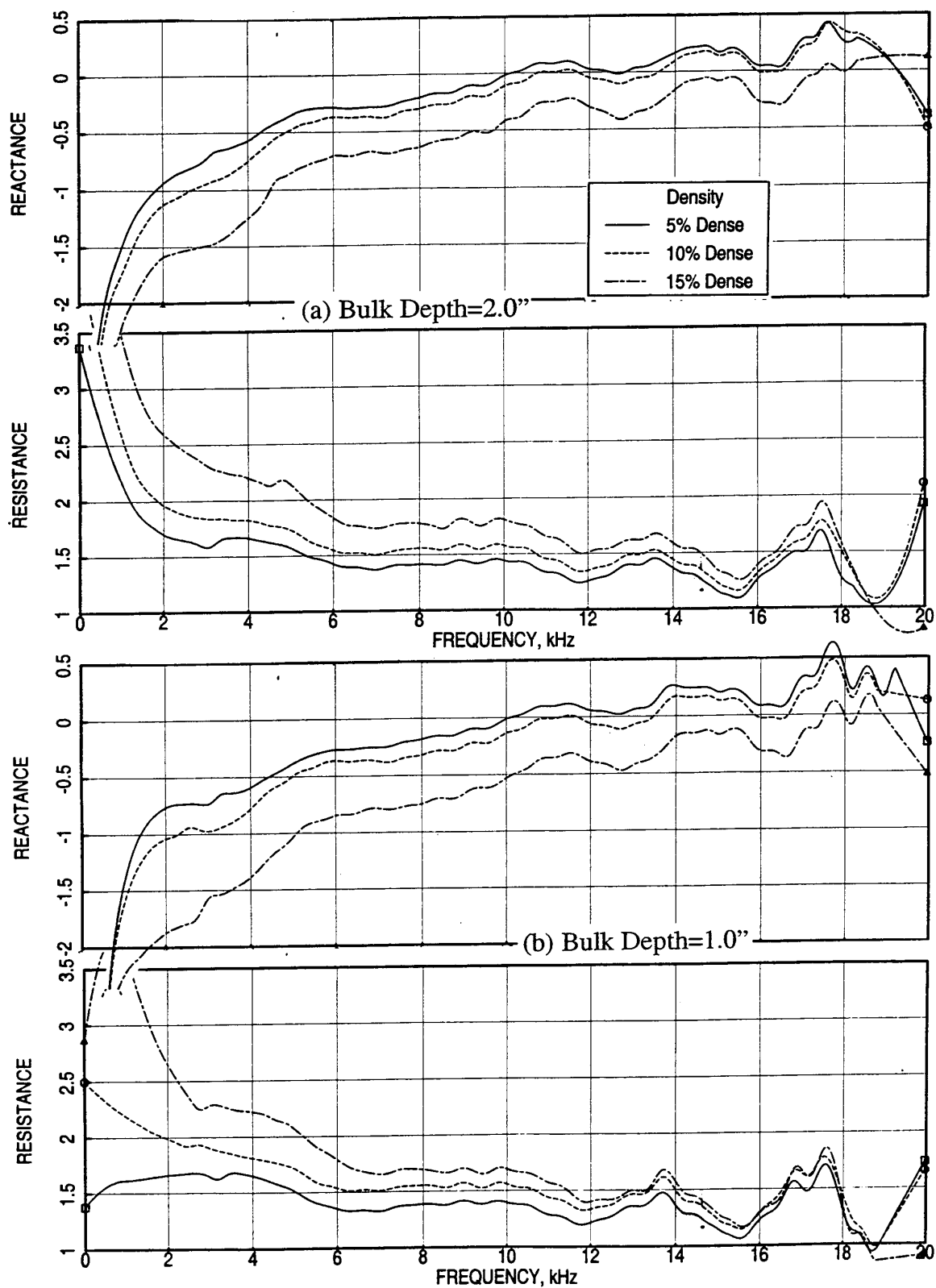


Figure 108. Effect of bulk density on normal impedance for Feltmetal bulk absorbers of different depths with 40 % porous 0.06"-thick facesheet,  $d=0.04$ ", OASPL=150 dB, (a) Bulk Depth=2.0" and (b) Bulk Depth=1.0".

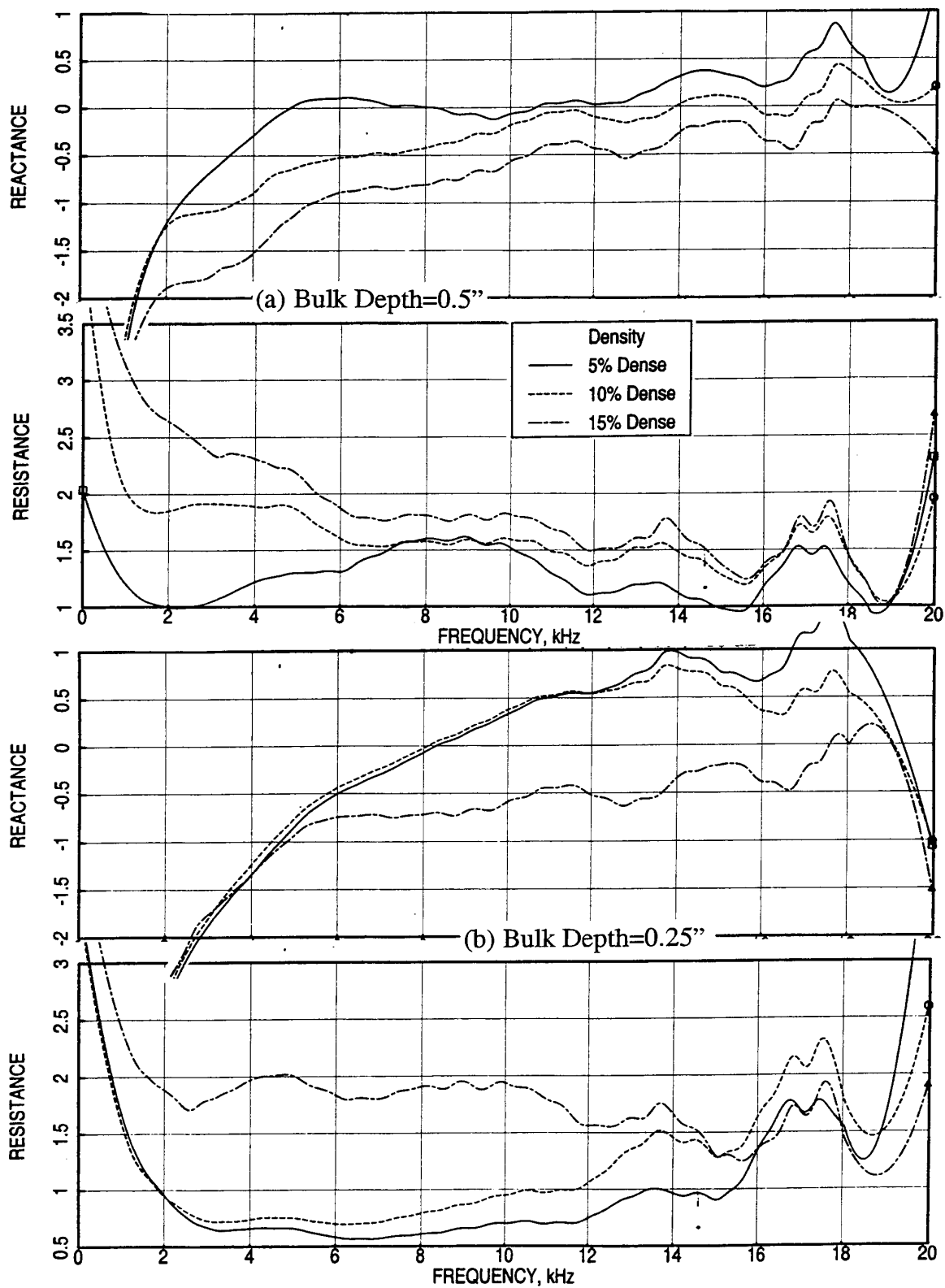


Figure 109. Effect of bulk density on normal impedance for Feltmetal bulk absorbers of different depths with 40 % porous 0.06"-thick facesheet,  $d=0.04$ ", OASPL=150 dB, (a) Bulk Depth=0.5" and (b) Bulk Depth=0.25".

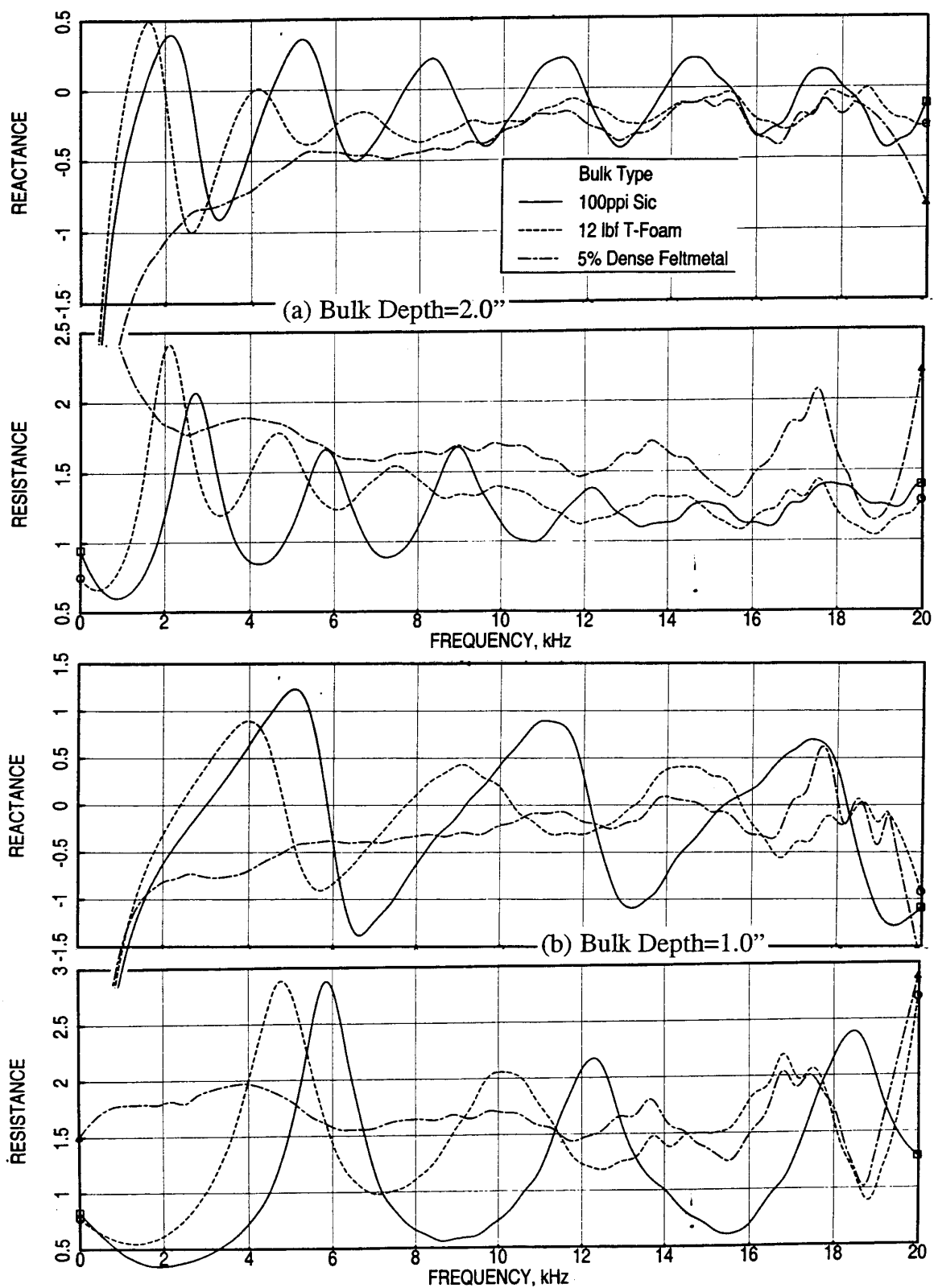


Figure 110. Effect of bulk type on normal impedance for bulk absorbers of different depths, OASPL=150 dB, (a) Bulk Depth=2.0" and (b) Bulk Depth=1.0".

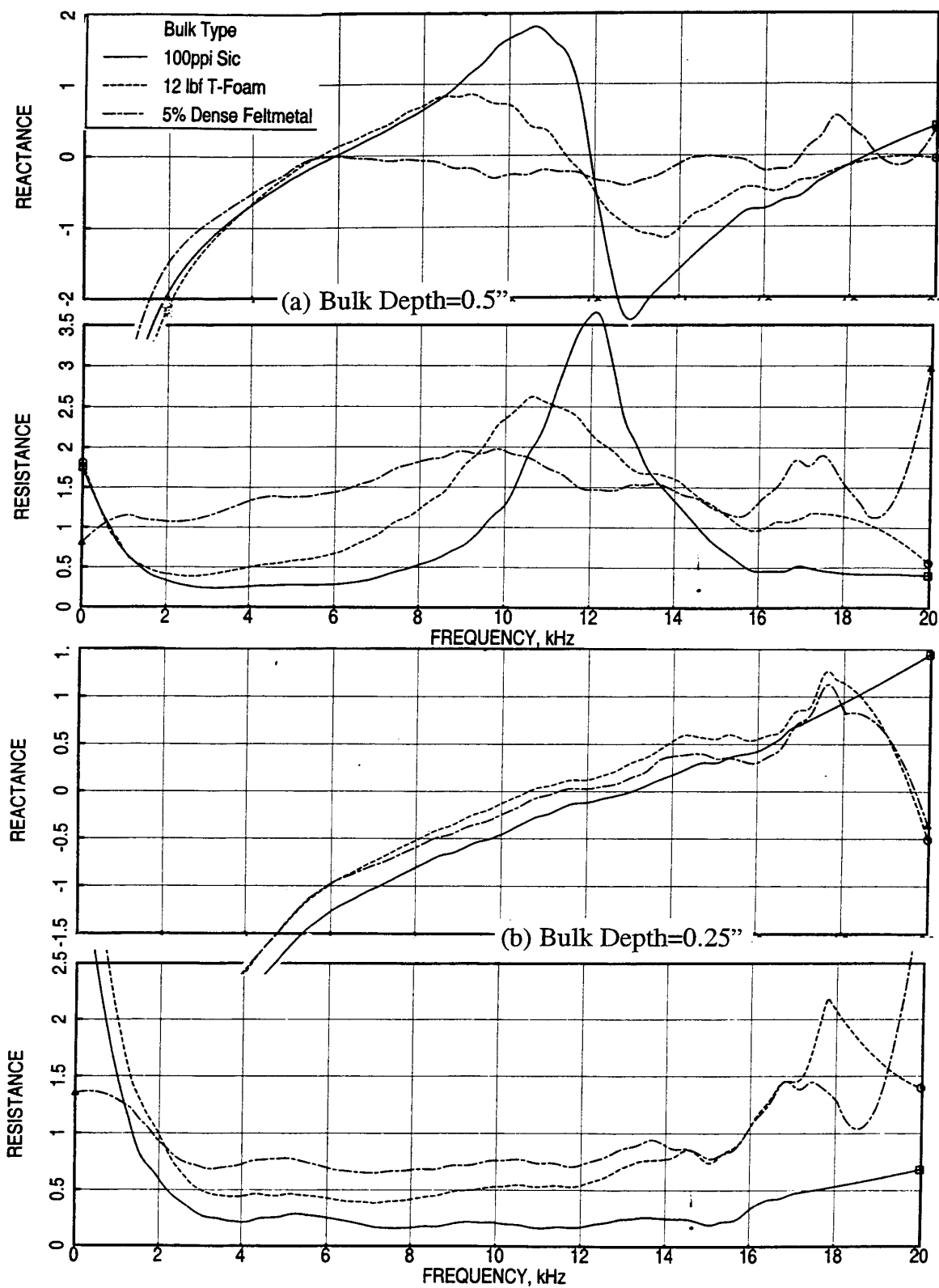


Figure 111. Effect of bulk type on normal impedance for bulk absorbers of different depths, OASPL=150 dB, (a) Bulk Depth=0.5" and (b) Bulk Depth=0.25".

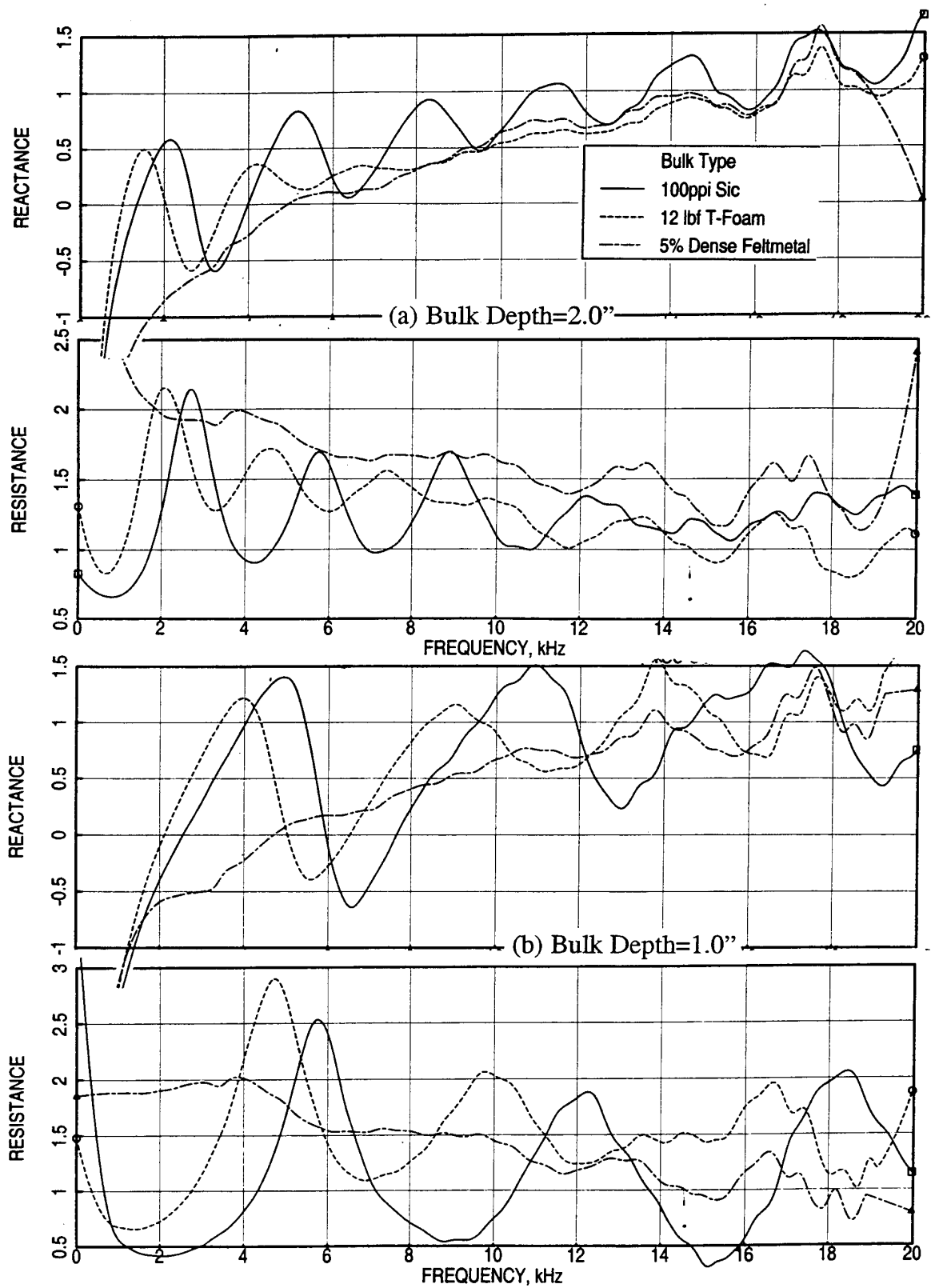


Figure 112. Effect of bulk type on normal impedance for bulk absorbers of different depths with 20 % porous 0.025"-thick facesheet,  $d=0.04$ ", OASPL=150 dB, (a) Bulk Depth=2.0" and (b) Bulk Depth=1.0".

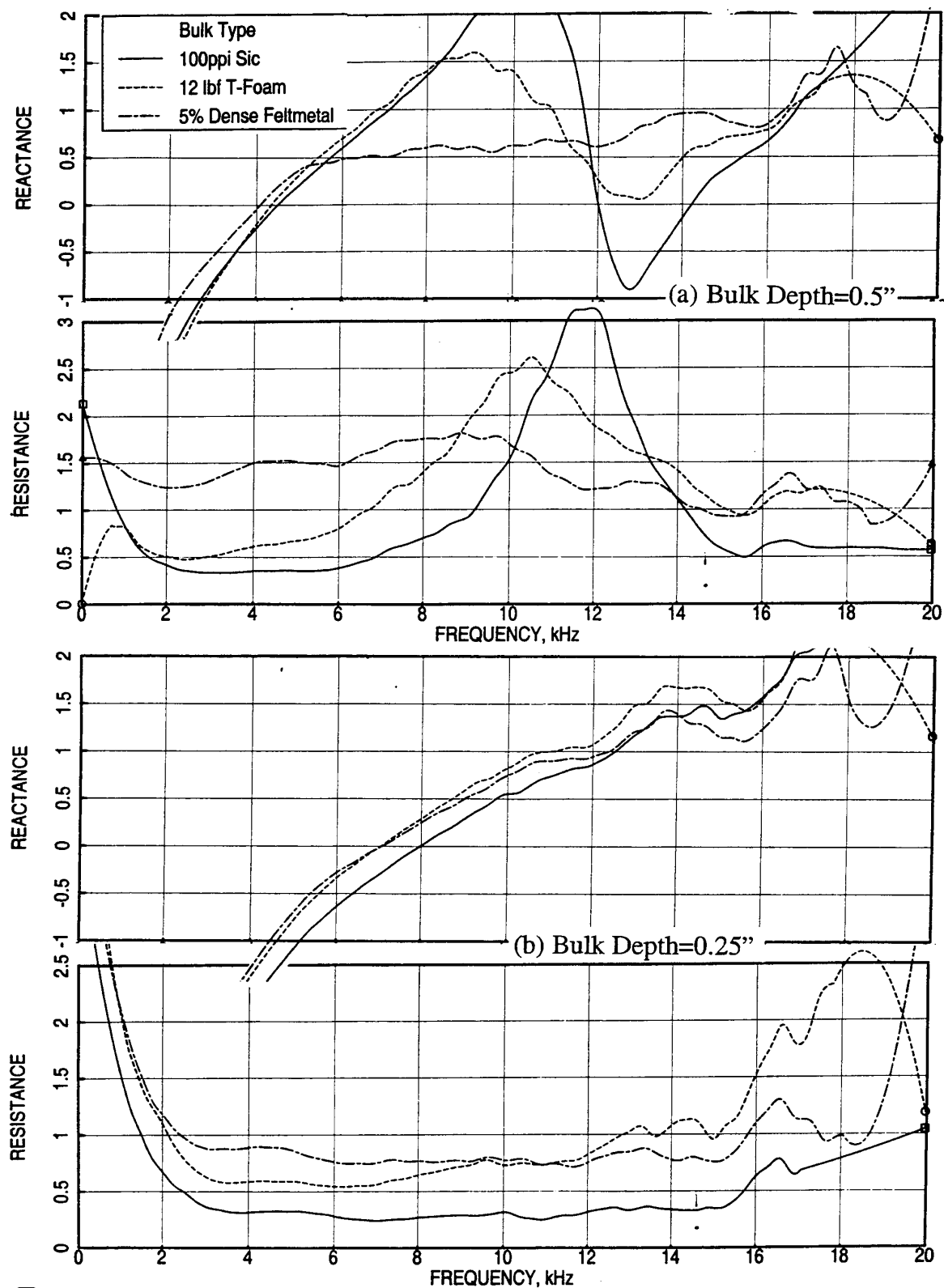


Figure 113. Effect of bulk type on normal impedance for bulk absorbers of different depths with 20 % porous 0.025"-thick facesheet,  $d=0.04$ ", OASPL=150 dB, (a) Bulk Depth=0.5" and (b) Bulk Depth=0.25".

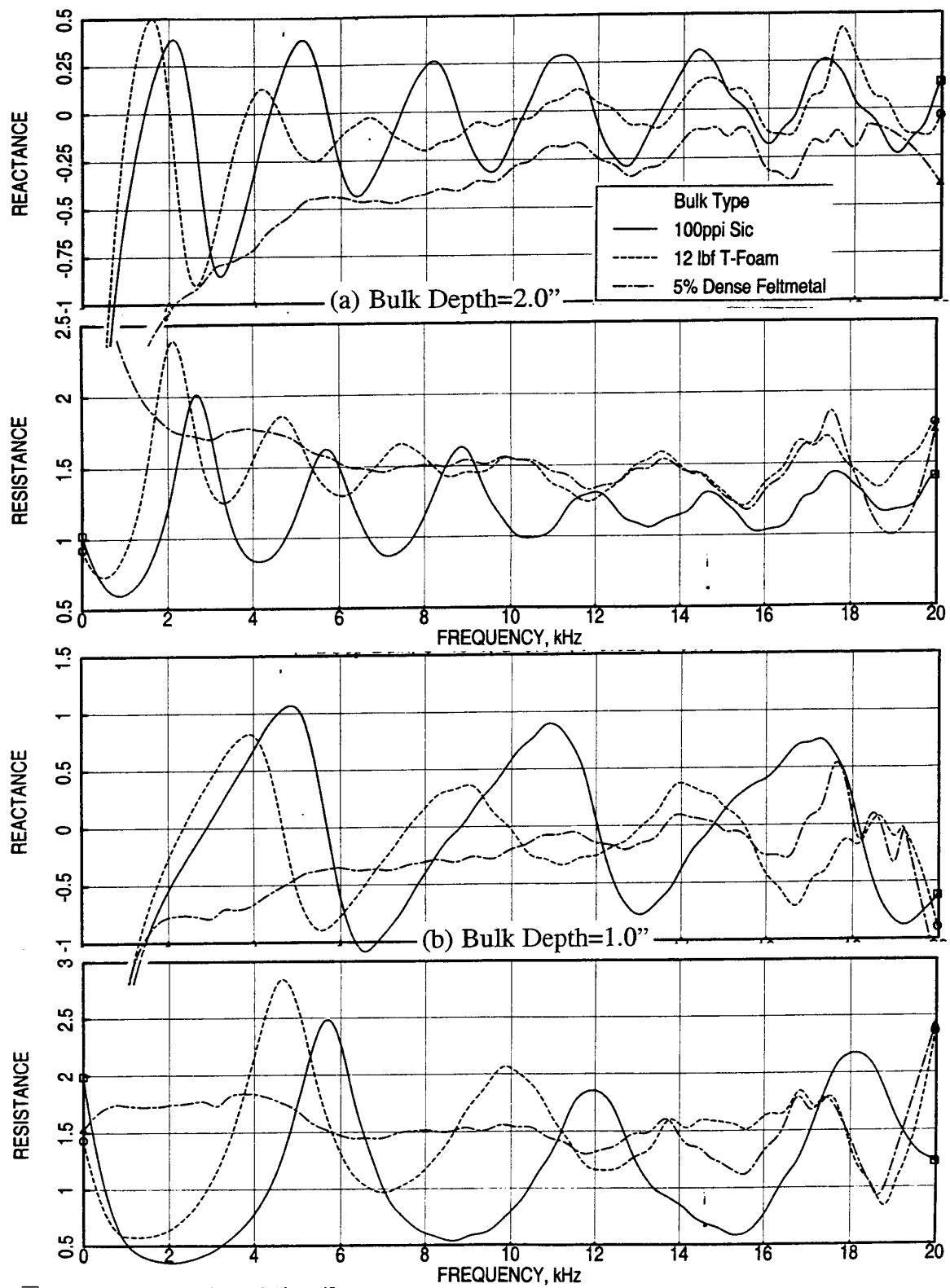


Figure 114. Effect of bulk type on normal impedance for bulk absorbers of different depths with 40 % porous 0.025"-thick facesheet,  $d=0.04$ ", OASPL=150 dB, (a) Bulk Depth=2.0" and (b) Bulk Depth=1.0".



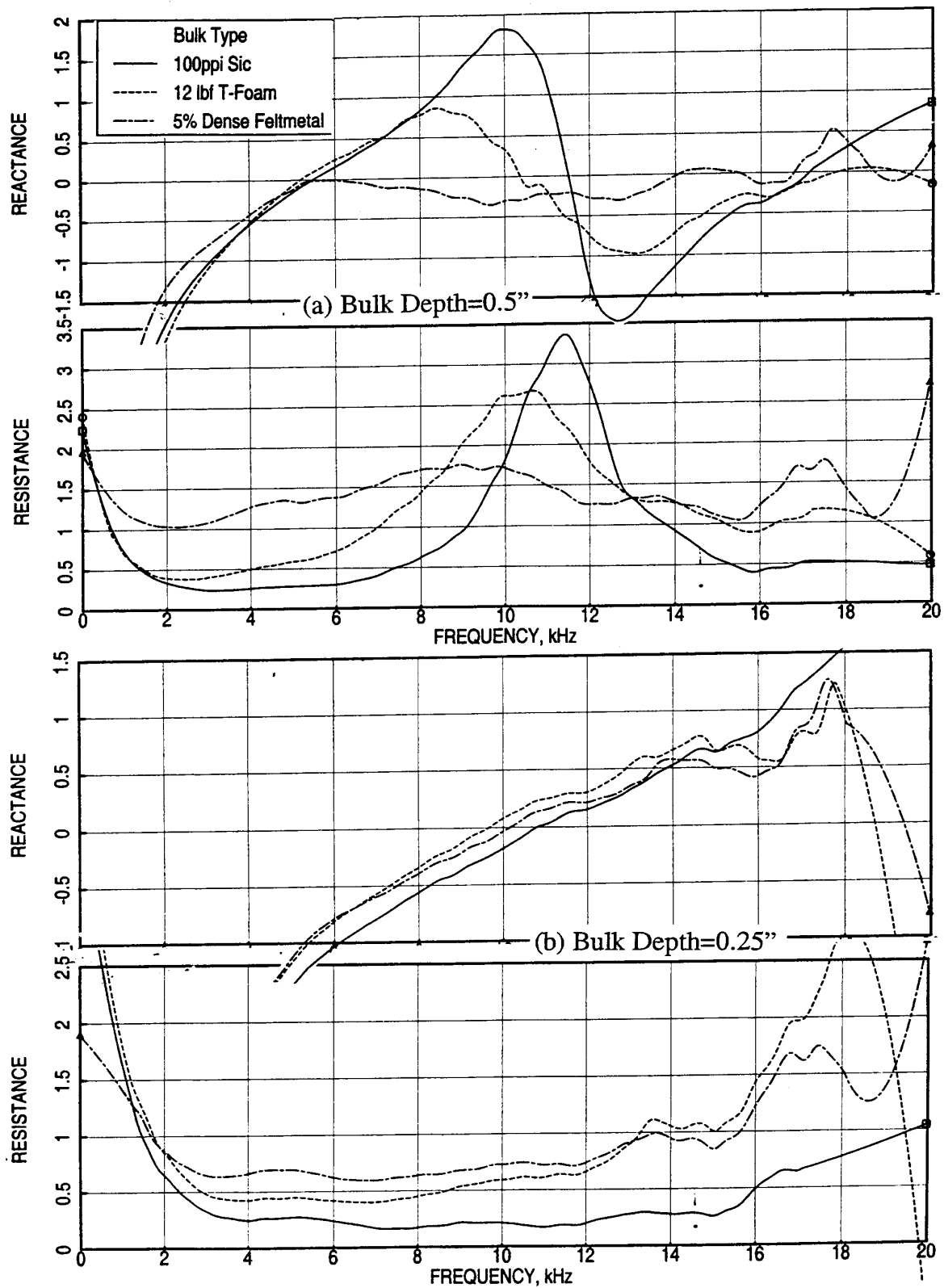


Figure 115. Effect of bulk type on normal impedance for bulk absorbers of different depths with 40 % porous 0.025"-thick facesheet,  $d=0.04$ ", OASPL=150 dB, (a) Bulk Depth=0.5" and (b) Bulk Depth=0.25".

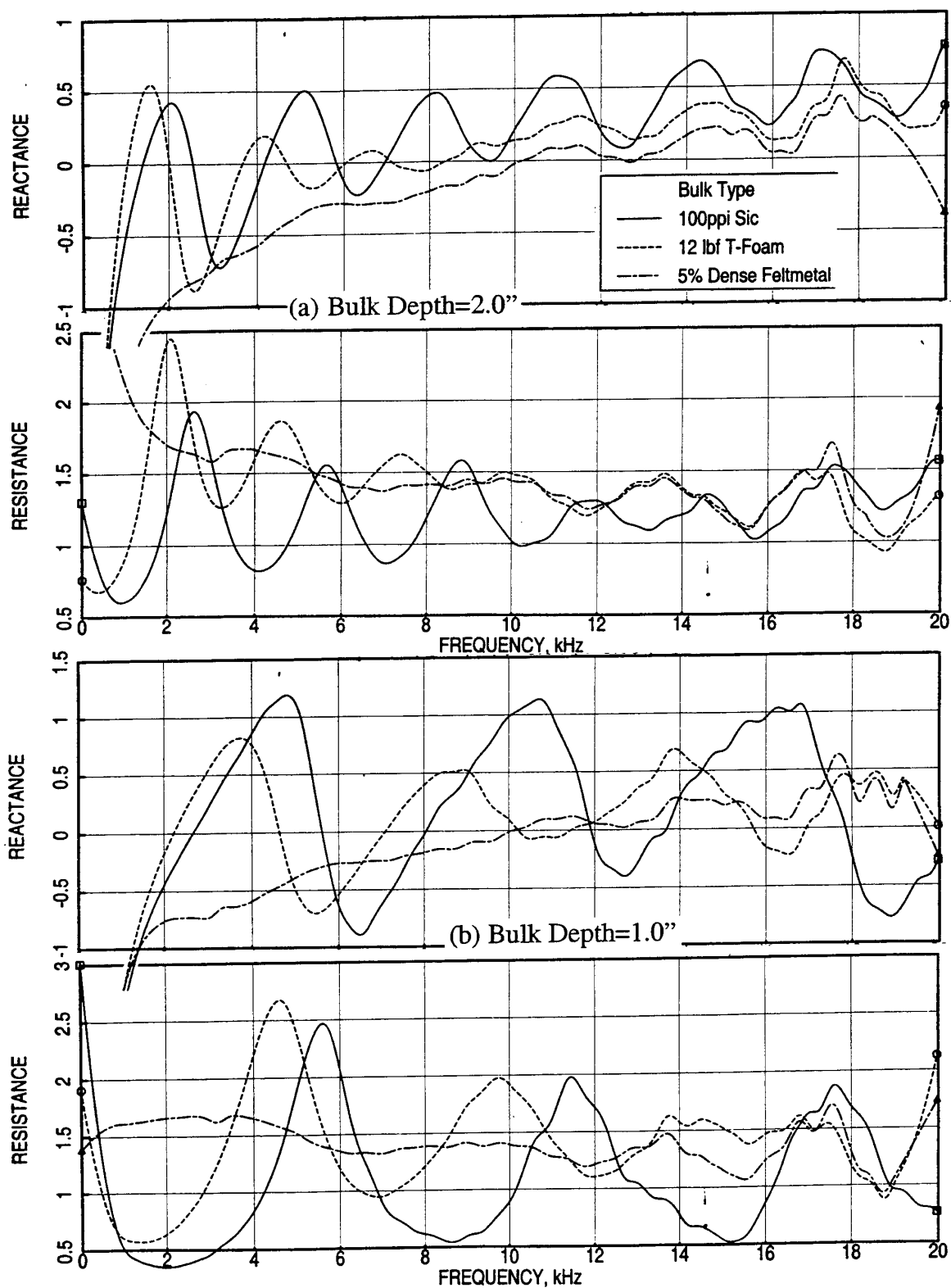


Figure 116. Effect of bulk type on normal impedance for bulk absorbers of different depths with 40 % porous 0.06"-thick facesheet,  $d=0.04$ ", OASPL=150 dB, (a) Bulk Depth=2.0" and (b) Bulk Depth=1.0".

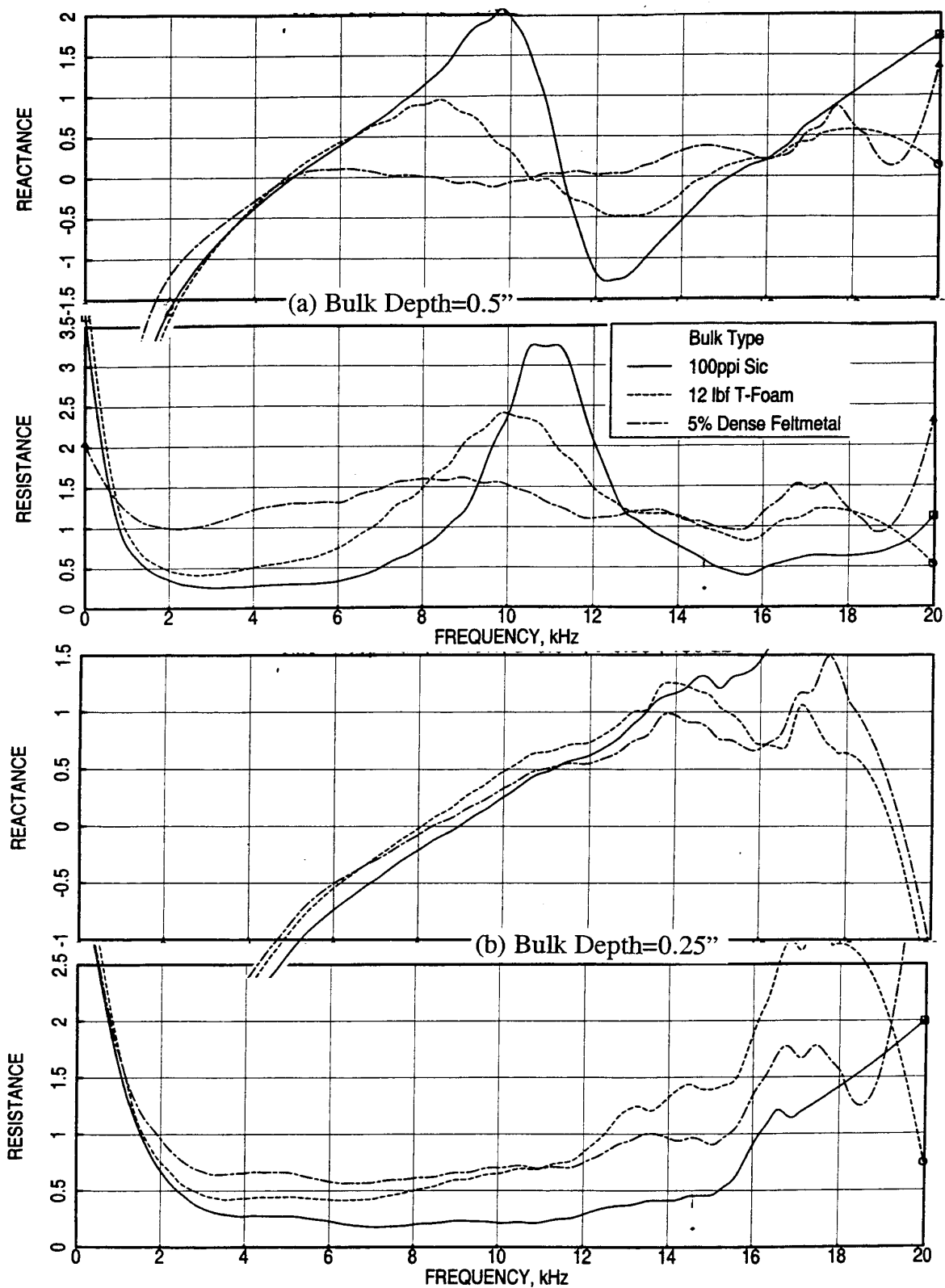


Figure 117. Effect of bulk type on normal impedance for bulk absorbers of different depths with 40 % porous 0.06"-thick facesheet,  $d=0.04"$ , OASPL=150 dB, (a) Bulk Depth=0.5" and (b) Bulk Depth=0.25".

application to achieve maximum acoustic suppression in the ejector. The objective of this design is to achieve the desired optimum impedance at critical frequencies impacting EPNdB for the mixer-ejector. **The optimum specific resistance and reactance ranges between 1.5 to 2 and -0.5 to 0.0, respectively, are chosen for the liner designs for maximum acoustic suppression on the basis of past experience.** Liner design is aimed at three different scale mixer-ejector application, namely, 1/7-scale, LSM scale (60% scale), and full-scale. Depending on the scales the critical frequency range and the liner depths are varied. For 1/7-scale the critical frequency range and liner depth are 7-20 kHz and 0.5", respectively. These parameters are 2 to 6 kHz and 1.2" for LSM scale and 1 to 3 kHz and 2.0" for full scale mixer ejectors. The impedance of liners for different scales are estimated using the measured ambient data corrected for flow, temperature, and acoustic intensity that would prevail in a mixer-ejector environment. In general the resistance would be significantly higher and the reactance would be lower than the measured ambient data.

Based on the EPM requirements two bulk materials, T-foam and Silicon Carbide, are being pursued for HSCT application. For 1/7-scale application, as shown in Figures 77 and 93 for 0.5"-deep SiC and T-Foam, respectively, with 40% porous facesheets ( $t=0.025"$  and  $d=0.04"$ ), the normal impedance would meet the impedance criteria at most of the higher frequency range of 7 to 20 kHz for 200 ppi SiC as well as 12 lbf standard T-Foam. However, the similar results with 2"-deep samples (see Figures 76 and 92) for full scale application exhibit a different pictures. In the frequency range of 1 to 3 kHz. the impedance for 100ppi SiC would come closer to the required levels (note that the peak at about 2 kHz will move to a higher frequency at heated condition). However, the T-Foam exhibits higher resistance and reactance at this frequency range. Similar is the situation for 1"-deep absorbers, which are closer to the LSM scale (i.e., 1.2"). This is further demonstrated in Figures 114 and 115. Thus, tests are conducted for a number of 2.0" and 1.2" deep T-Foam samples with variety of property combinations and construction processes (see Table 6) to establish a suitable T-Foam for HSCT application. Typical results of normal impedance at ambient condition are shown in this section. These results are further used to predict the acoustic suppression for the mixer-ejectors of different scales. Those results are presented in a separate report.

**2"-Deep Samples:** Standard T-Foam processing, as described earlier, includes fiber and matrix (to rigidize the woven fiber). Thus the density of the bulk is contributed by these two elements. Three different T-Foam samples of different total density are tested and the results are shown earlier. A T-Foam with lower density is better compared to more dense materials for full-scale application. However, the normal impedance for all of them are significantly off compared to optimum levels. Thus, a number of 2"-deep samples of varying fiber and

matrix density are manufactured and tested to evaluate if the matrix content has some impact on the normal impedance and DC flow resistance. Measured DC flow resistance of all these samples is listed in Table 6.

Figure 118 shows the DC flow resistance for four such samples. As can be seen that the DC flow resistance is mainly influenced by the fiber density. The corresponding normal impedance without and with facesheet is shown in Figures 119 and 120. Figure 119 is derived using 1.25"-diameter samples, which are tested in a low frequency impedance tube to evaluate low frequency data more accurately. Figure 120 is derived using samples of 0.6" up to 20 kHz frequency range. Again, the impact of matrix is small on normal impedance. The resistance increases with increasing fiber density. The impact of facesheet parameters on each of these samples is measured and shown in Figures 121 through 127. The facesheet parameters include the variation of porosity, thickness, and hole diameter for perforated facesheets and resistivity for linear facesheets. The measured impedance levels for all these samples seem to be significantly off from the desired optimum impedance.

Innovative process developments are pursued to improve the acoustic characteristics of T-Foam to meet the desired impedance goals. One of the processes includes woven papers of the same fiber materials and is placed within the T-Foam depth at various locations. Two different woven papers, 50 gm/m<sup>2</sup> and 80 gm/m<sup>2</sup>, are used in T-Foam construction. The DC flow resistance and the normal impedance of these papers are measured and are shown in Figure 128. The DC flow resistance of both these papers are about 2 Rayls ( $R_{100}$ ). The resistance and reactance levels are relatively small for entire frequency range. Typical T-Foam constructions using these papers are shown in Figure 129. In general, these papers, either single or multiple layers, are placed in between the woven fiber plies.

Figure 130 shows the normal impedance for several 2"-deep T-Foam with woven paper layers. Based on the resistance and reactance of these materials the T-Foam with 3 layers of 50 gm/m<sup>2</sup> 3-ply papers (#33) performs the best in noise suppression. However, the predicted performance of this T-Foam is not the optimum. Thus, further improvement is still required. The normal impedance of some more T-Foams with paper construction is compared with the impedance of #33 in Figure 131. The normal impedance of the T-Foams, other than #37, is very close to #33. However, the acoustic suppression due to these materials is close, but not better, than #33.

Similar results for more T-Foam samples are shown in Figure 132. The corresponding DC flow resistance is shown in Figure 133. The normal impedance of these T-Foam samples with and without a facesheet is shown in Figure 134. Some of the samples are coated with

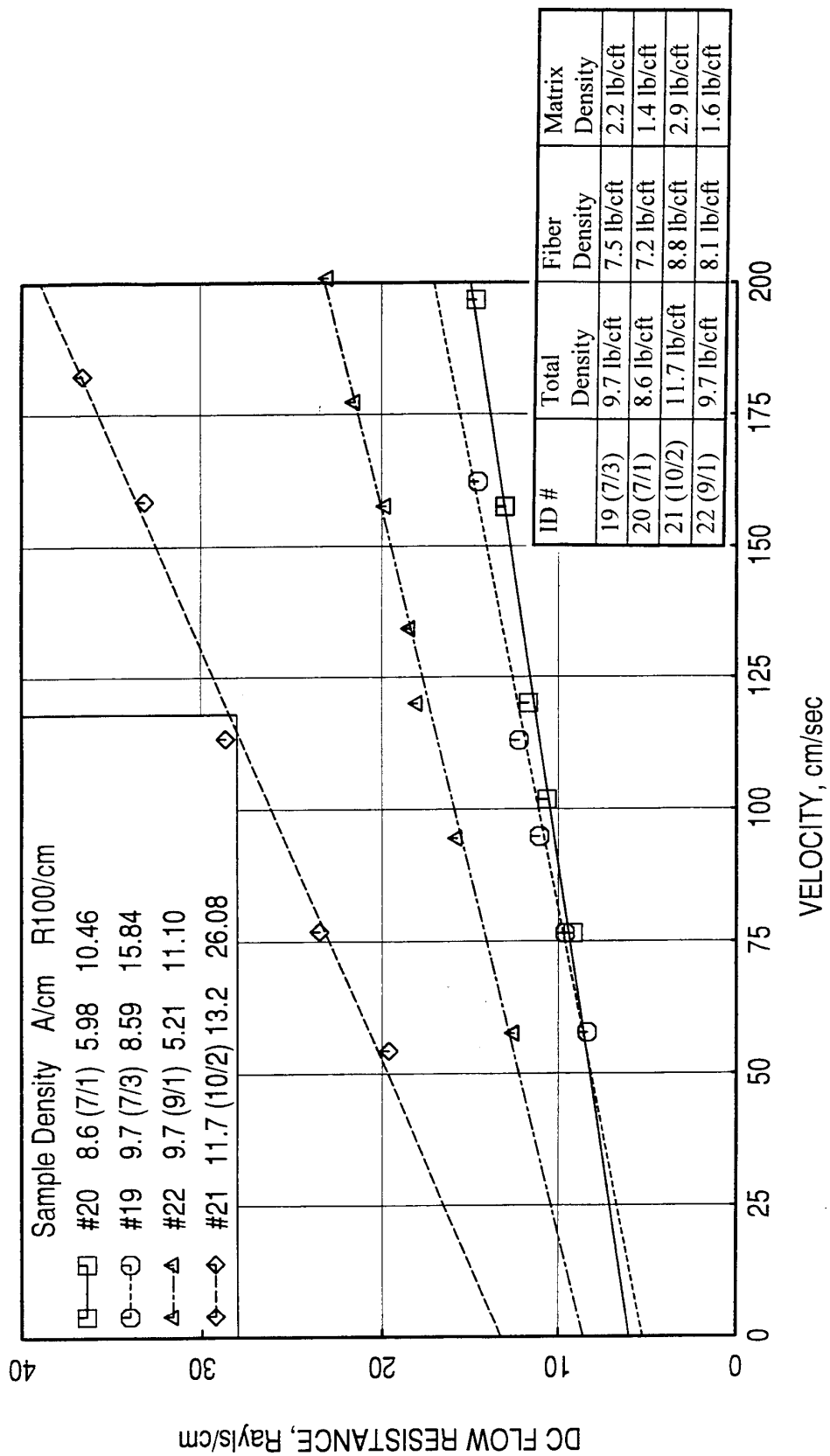


Figure 118. DC Flow resistance for various 2"-deep T-Foam samples with different fiber and matrix density combinations.

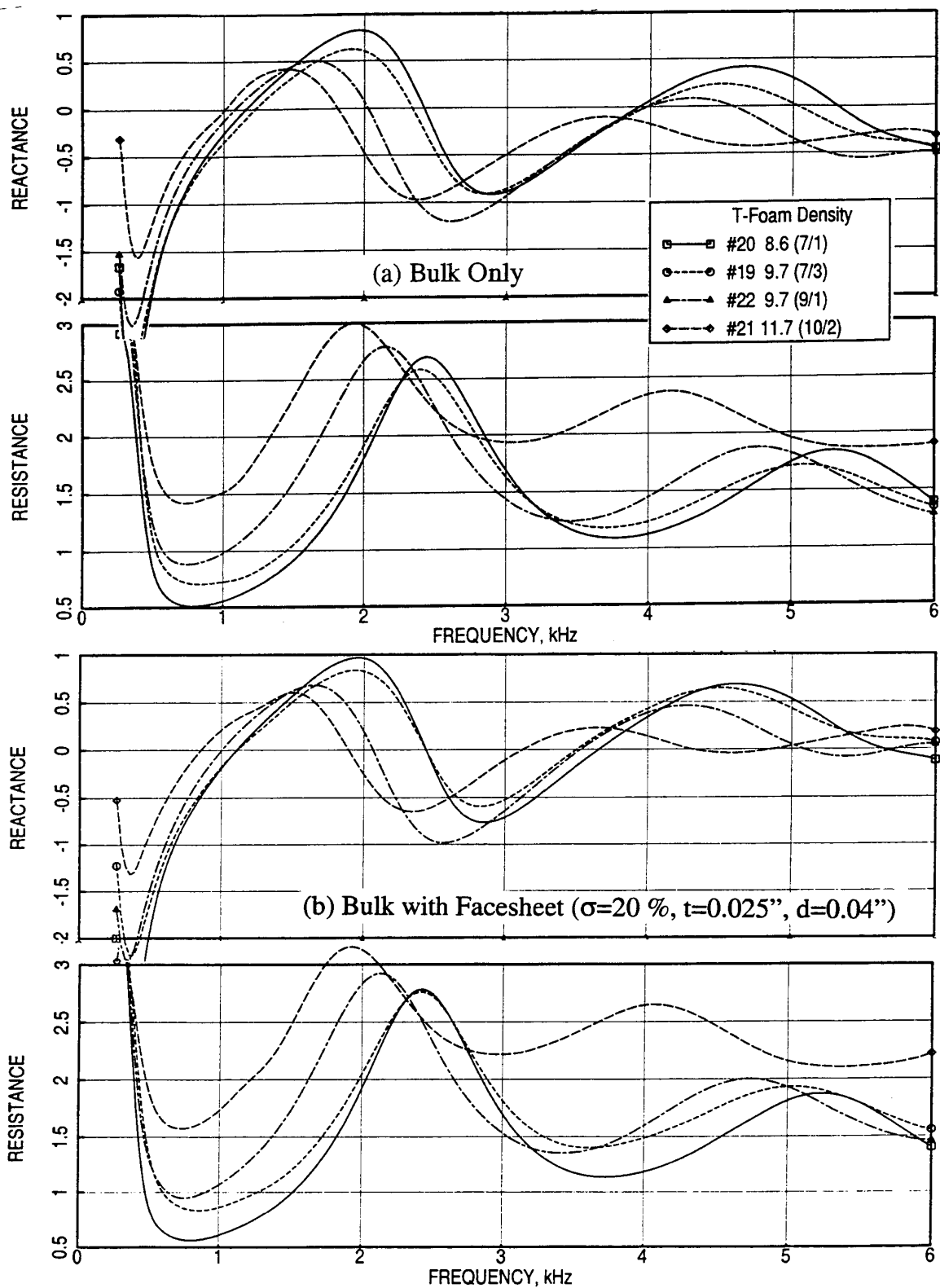


Figure 119. Normal impedance up to 6 kHz, measured by low frequency impedance tube (i.e., sample diameter=1.25") for various 2"-deep T-Foam samples with different fiber and matrix density combinations (a) without facesheet and (b) with facesheet, OASPL=150 dB

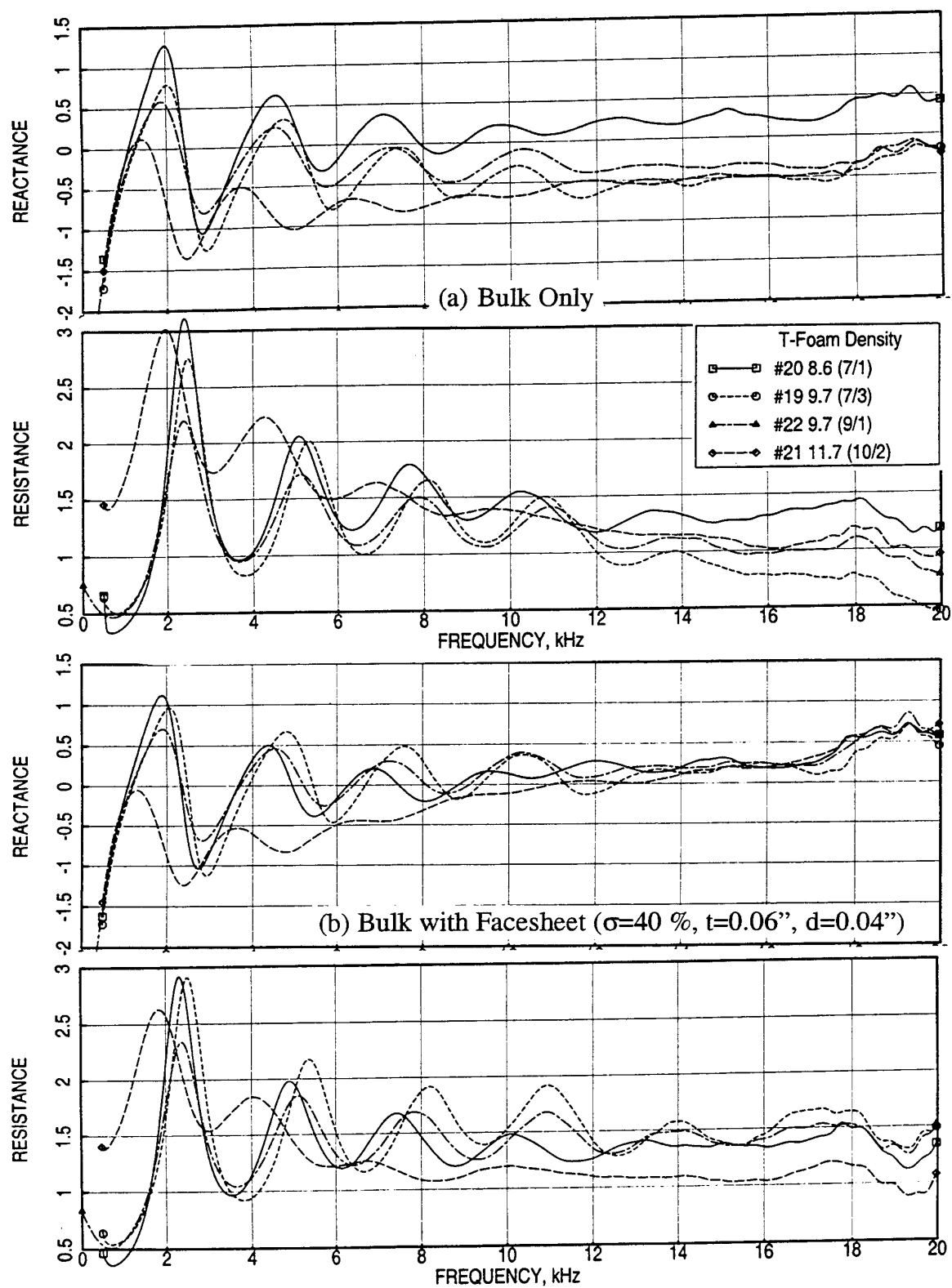


Figure 120. Normal impedance up to 20 kHz, measured by high frequency impedance tube (i.e., sample diameter=0.6") for various 2"-deep T-Foam samples with different fiber and matrix density combinations (a) without facesheet and (b) with facesheet, OASPL=150 dB.



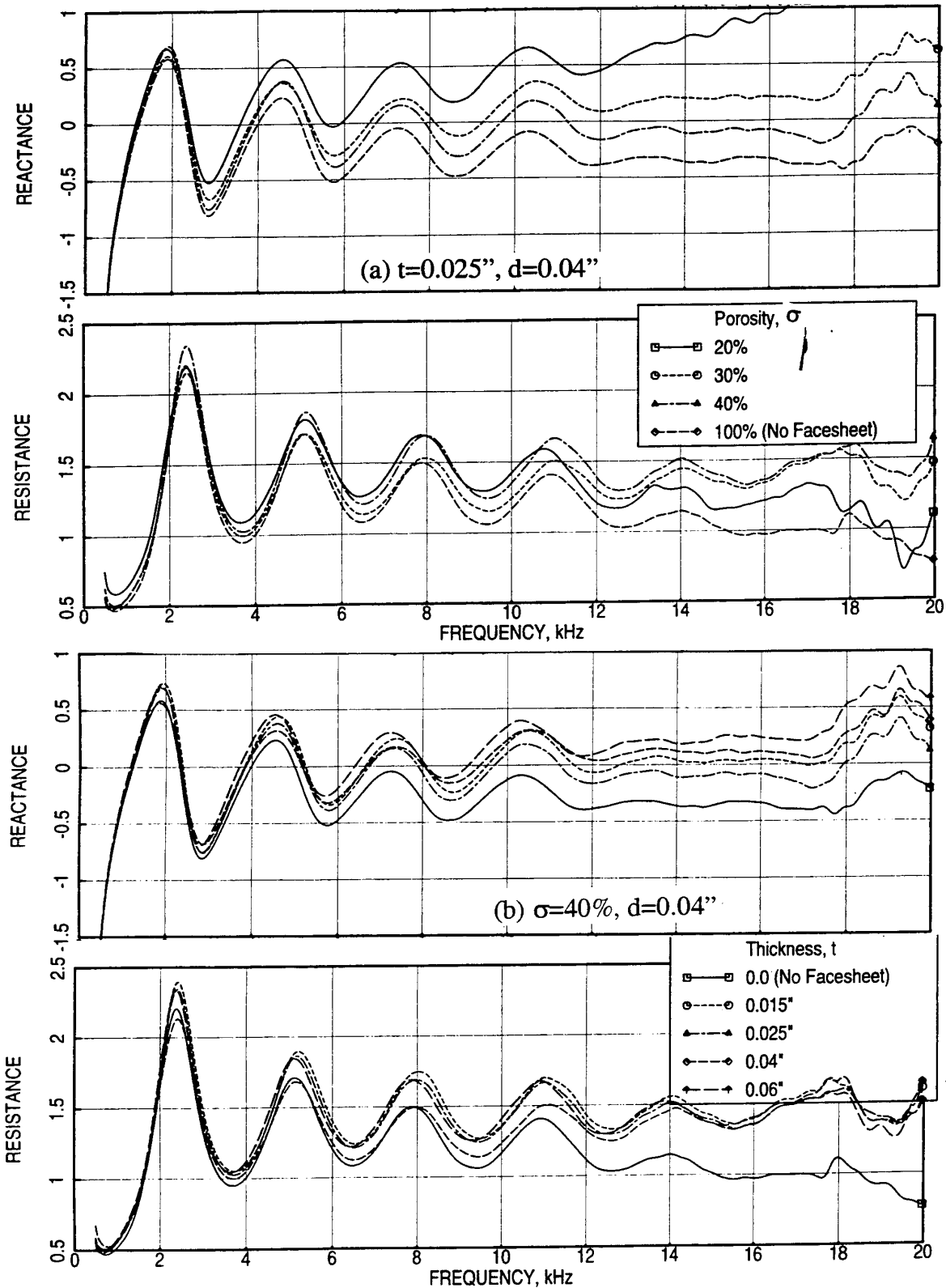


Figure 121. Effect of (a) facesheet porosity ( $t=0.025''$ ,  $d=0.04''$ ) and (b) facesheet thickness ( $\sigma=40\%$ ,  $d=0.04''$ ) on normal impedance for a 2''-deep 8.6 (7/1) lbf T-Foam sample (#20), OASPL=150 dB.

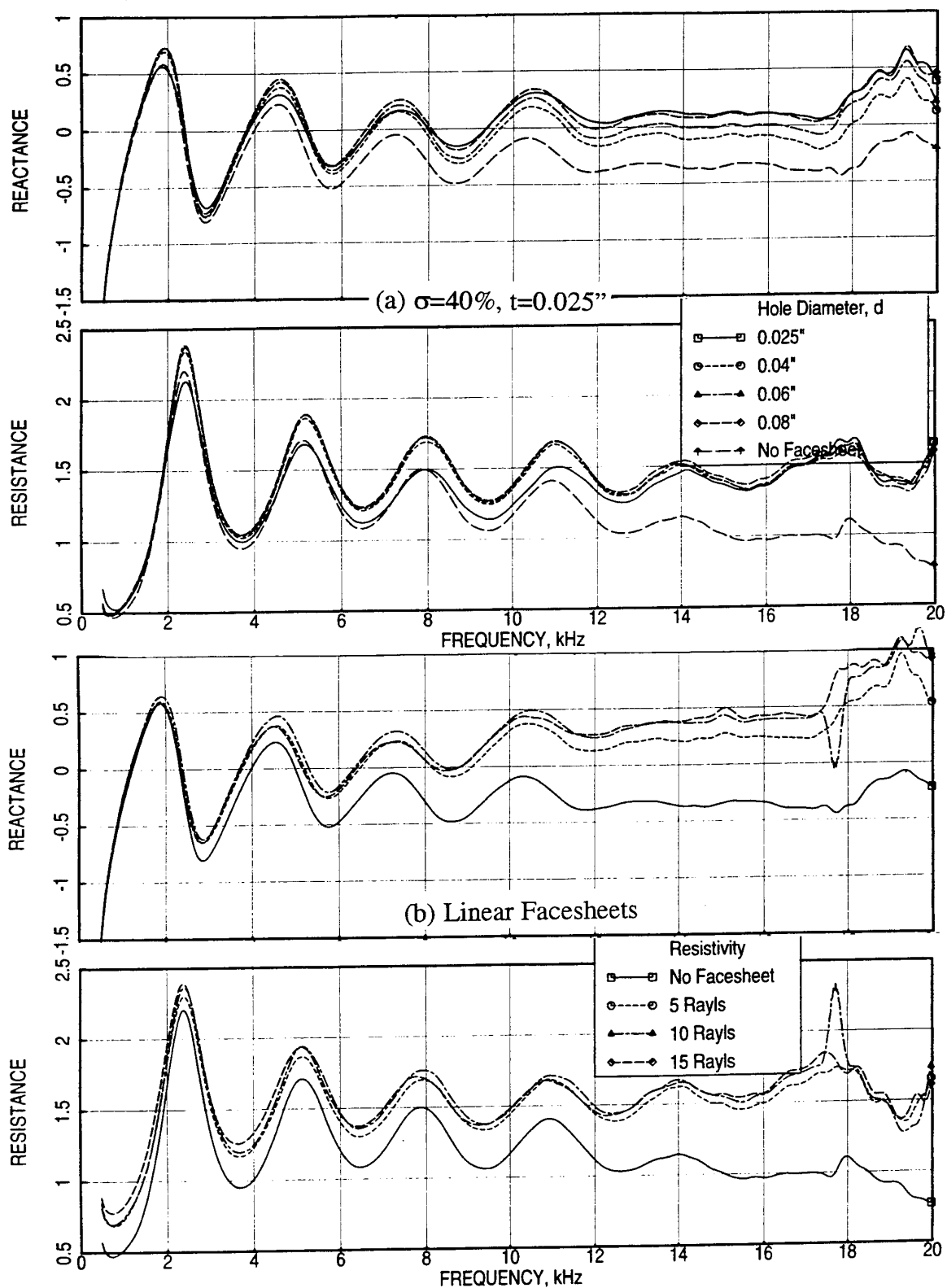


Figure 122. Effect of (a) perforated facesheet hole diameter ( $\sigma=40\%$ ,  $t=0.025''$ ) and (b) linear facesheet resistivity on normal impedance for a 2"-deep 8.6 (7/1) lbf T-Foam sample (#20), OASPL=150 dB.

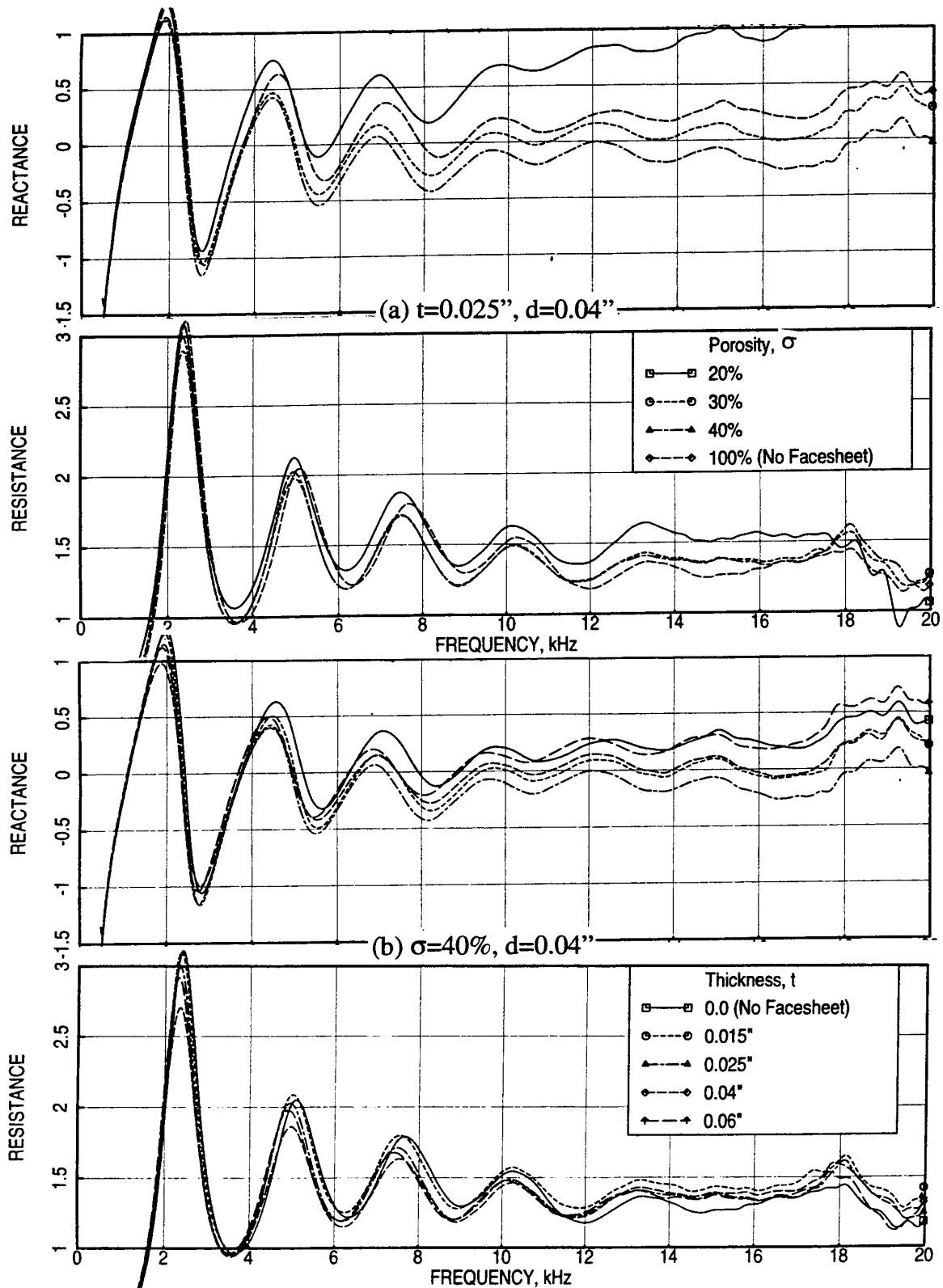


Figure 123. Effect of (a) facesheet porosity ( $t=0.025''$ ,  $d=0.04''$ ) and (b) facesheet thickness ( $\sigma=40\%$ ,  $d=0.04''$ ) on normal impedance for a 2''-deep 9.7 (7/3) lbf T-Foam sample (#19), OASPL=150 dB.

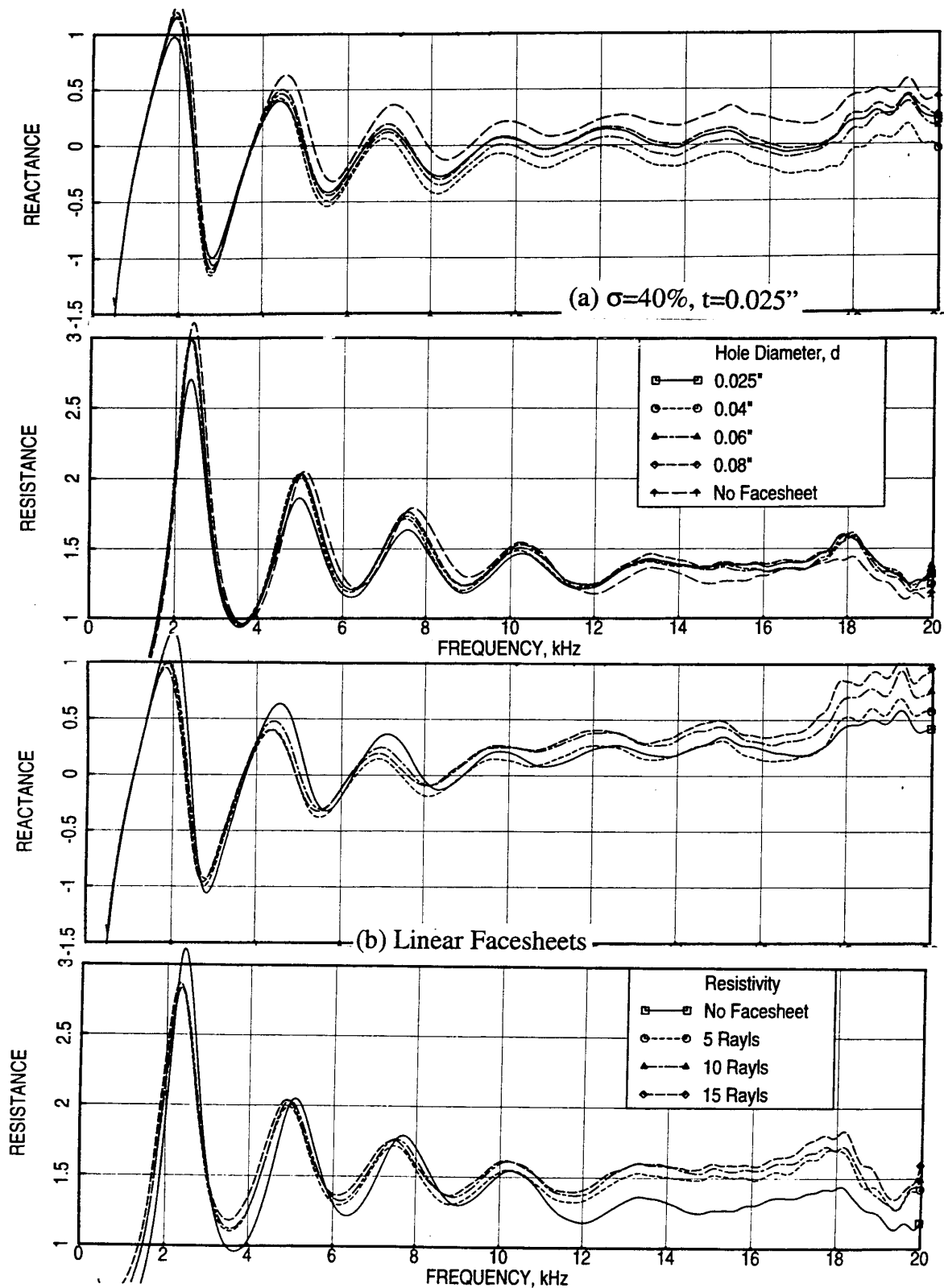


Figure 124. Effect of (a) perforated facesheet hole diameter ( $\sigma=40\%$ ,  $t=0.025''$ ) and (b) linear facesheet resistivity on normal impedance for a 2"-deep 9.7 (7/3) lbf T-Foam sample (#19), OASPL=150 dB.

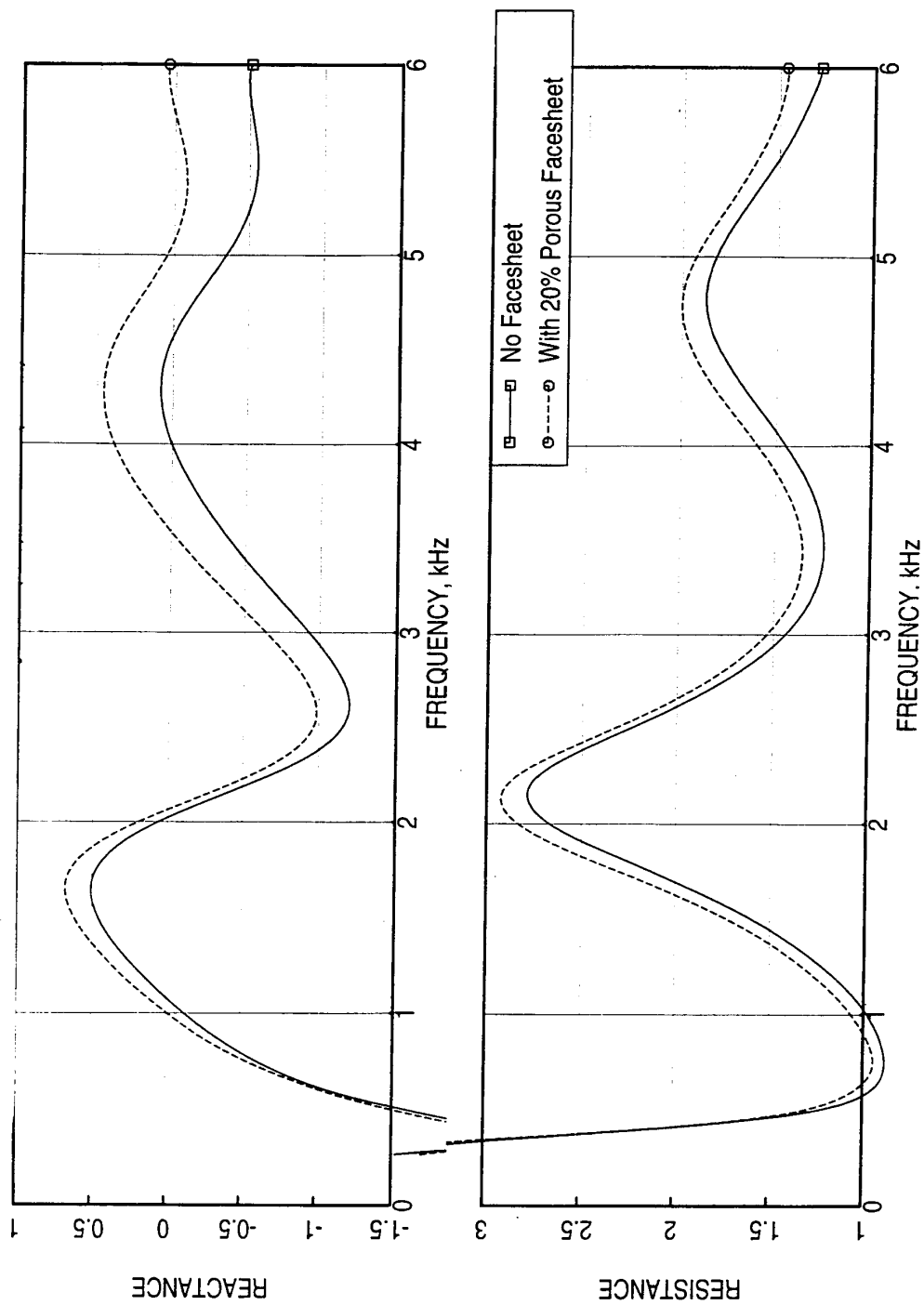


Figure 125. Effect of a perforated facesheet ( $\sigma=20\%$ ,  $t=0.025''$ ,  $d=0.04''$ ) on normal impedance for a 2"-deep 9.7 (9/1) lbf T-Foam sample (#22), OASPL=150 dB.

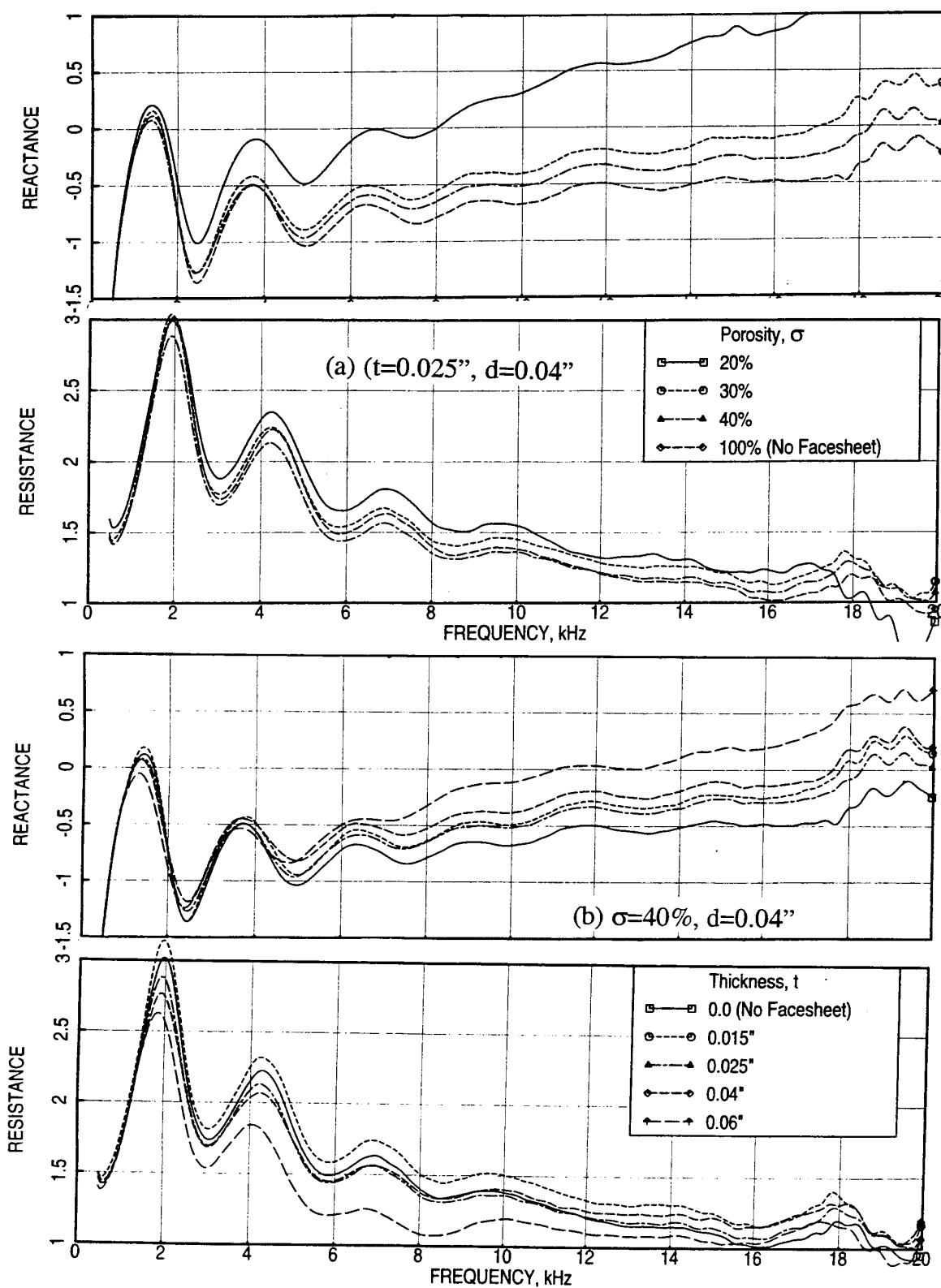


Figure 126. Effect of (a) facesheet porosity ( $t=0.025''$ ,  $d=0.04''$ ) and (b) facesheet thickness ( $\sigma=40\%$ ,  $d=0.04''$ ) on normal impedance for a 2''-deep 11.7 (10/2) lbf T-Foam sample (#21), OASPL=150 dB.

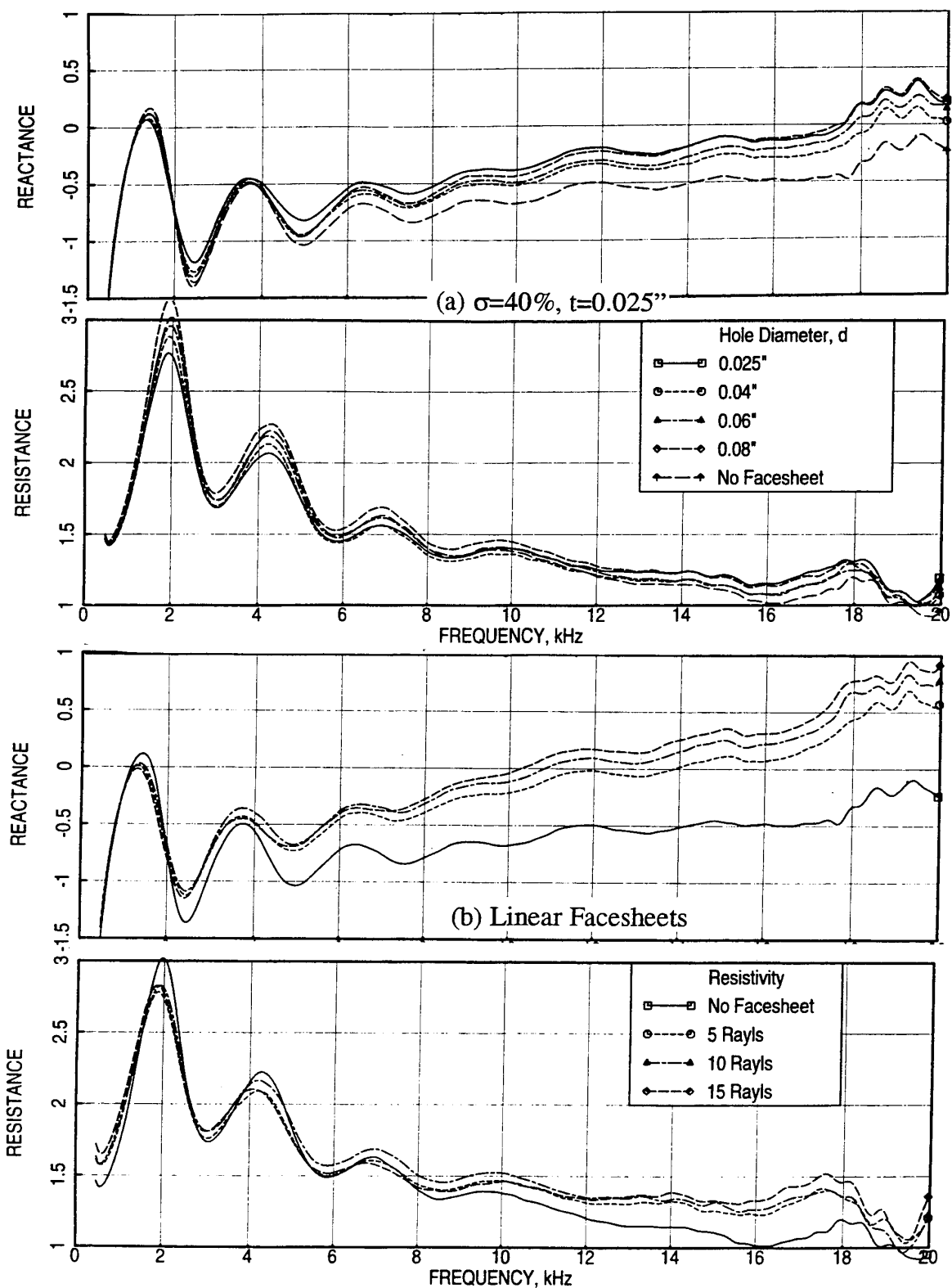


Figure 127. Effect of (a) perforated facesheet hole diameter ( $\sigma=40\%$ ,  $t=0.025''$ ) and (b) linear facesheet resistivity on normal impedance for a 2"-deep 11.7 (10/2) lbf T-Foam sample (#21), OASPL=150 dB.

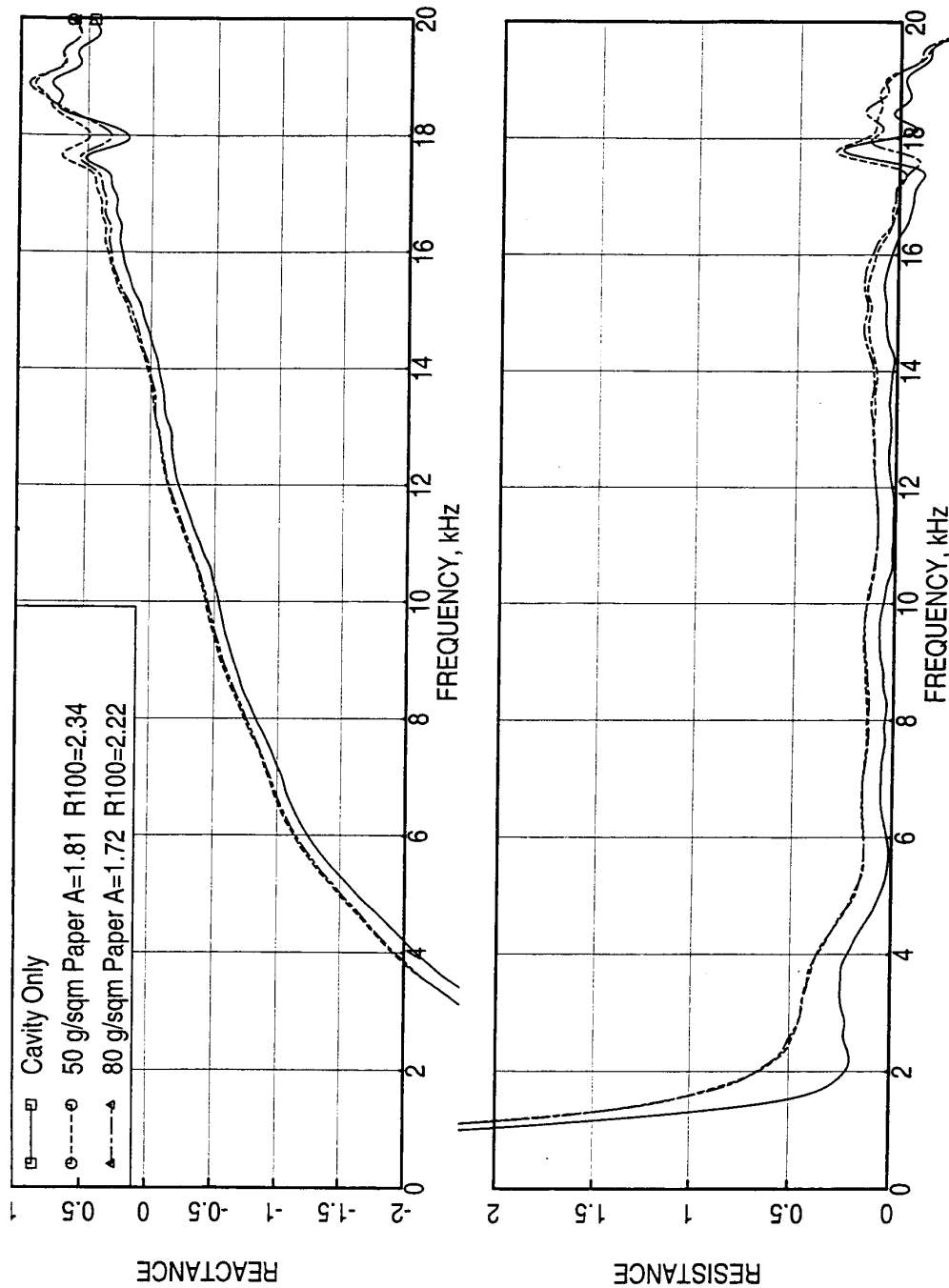


Figure 128. Normal impedance of the woven papers used in T-Foam construction, cavity=0.246", OASPL=150 dB.



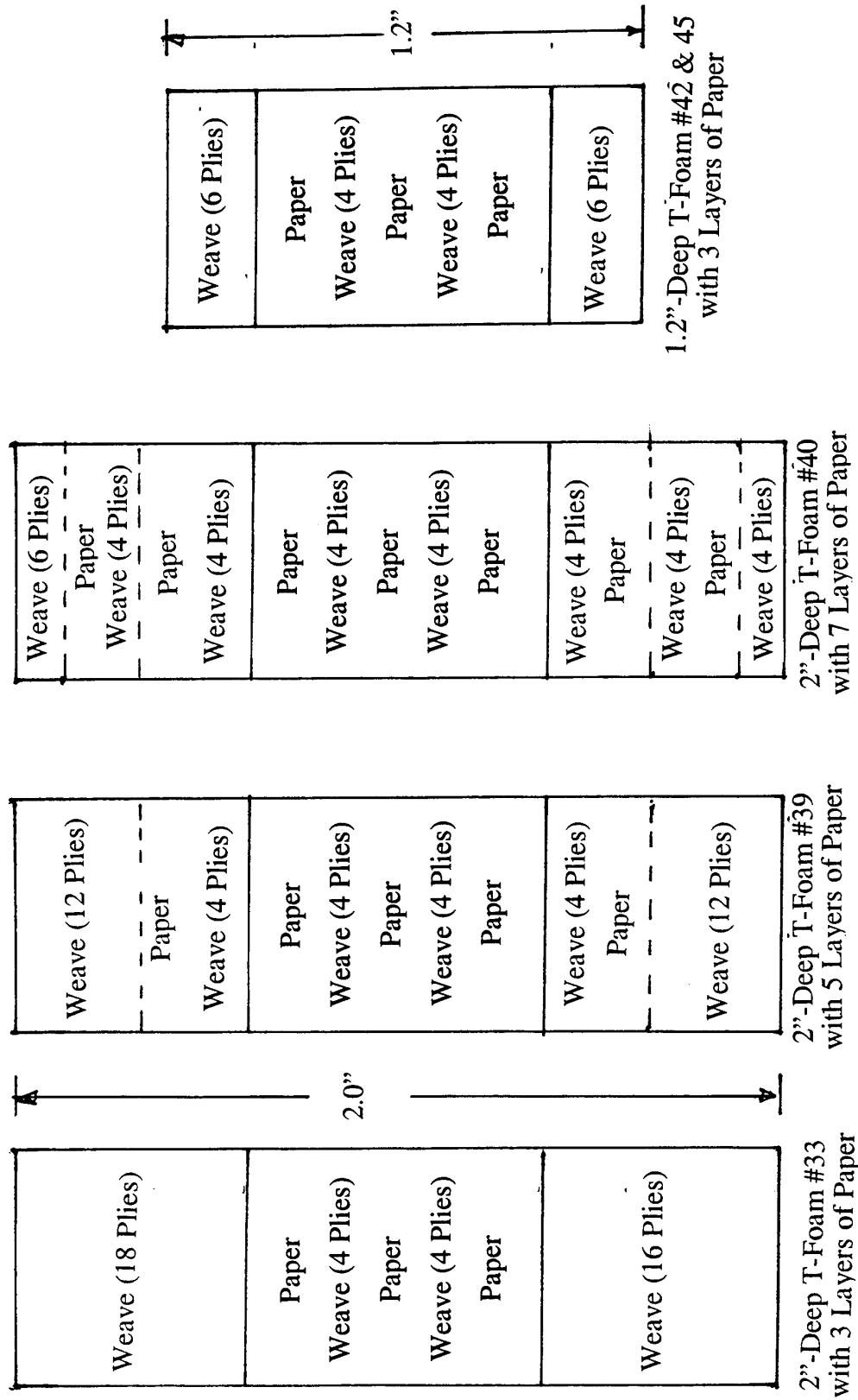


Figure 129. Schematic of a few T-Foam construction with woven paper layers.

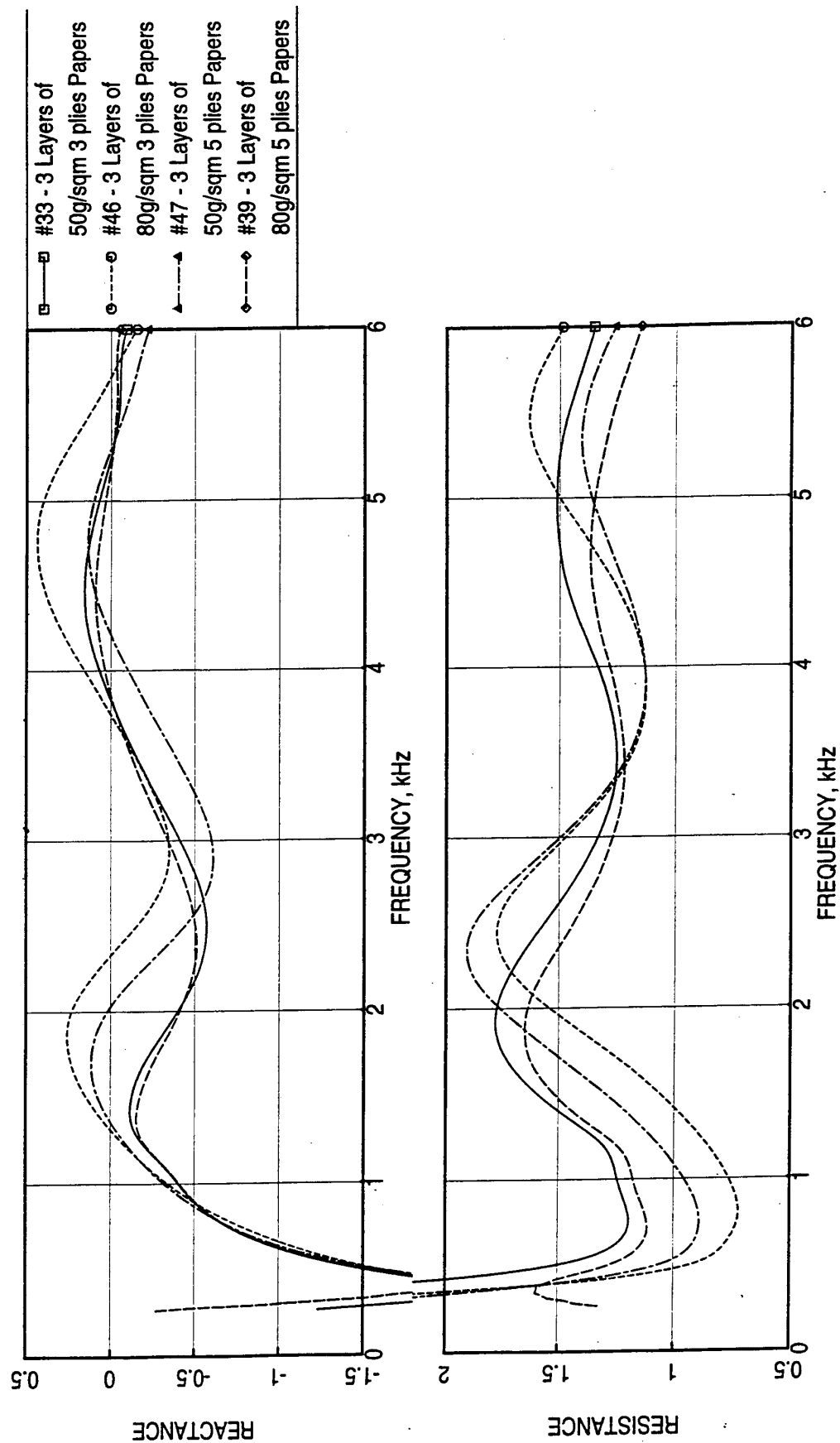


Figure 130. Effect of paper layer construction on normal impedance for various 2"-deep T-Foam samples, OASPL=150 dB.

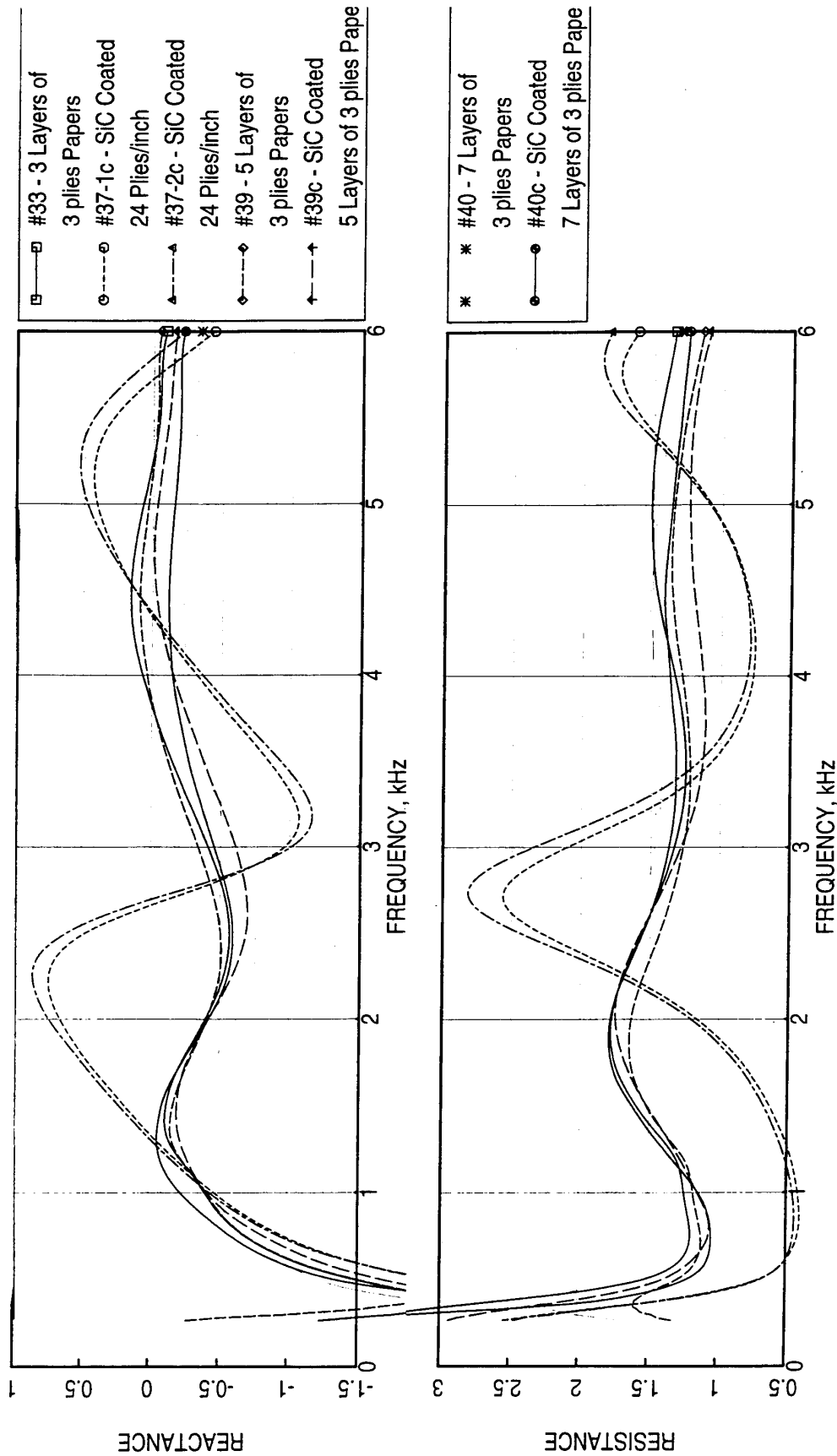


Figure 131. Effect of paper layer construction on normal impedance for various 2"-deep T-Foam samples, OASPL=150 dB.

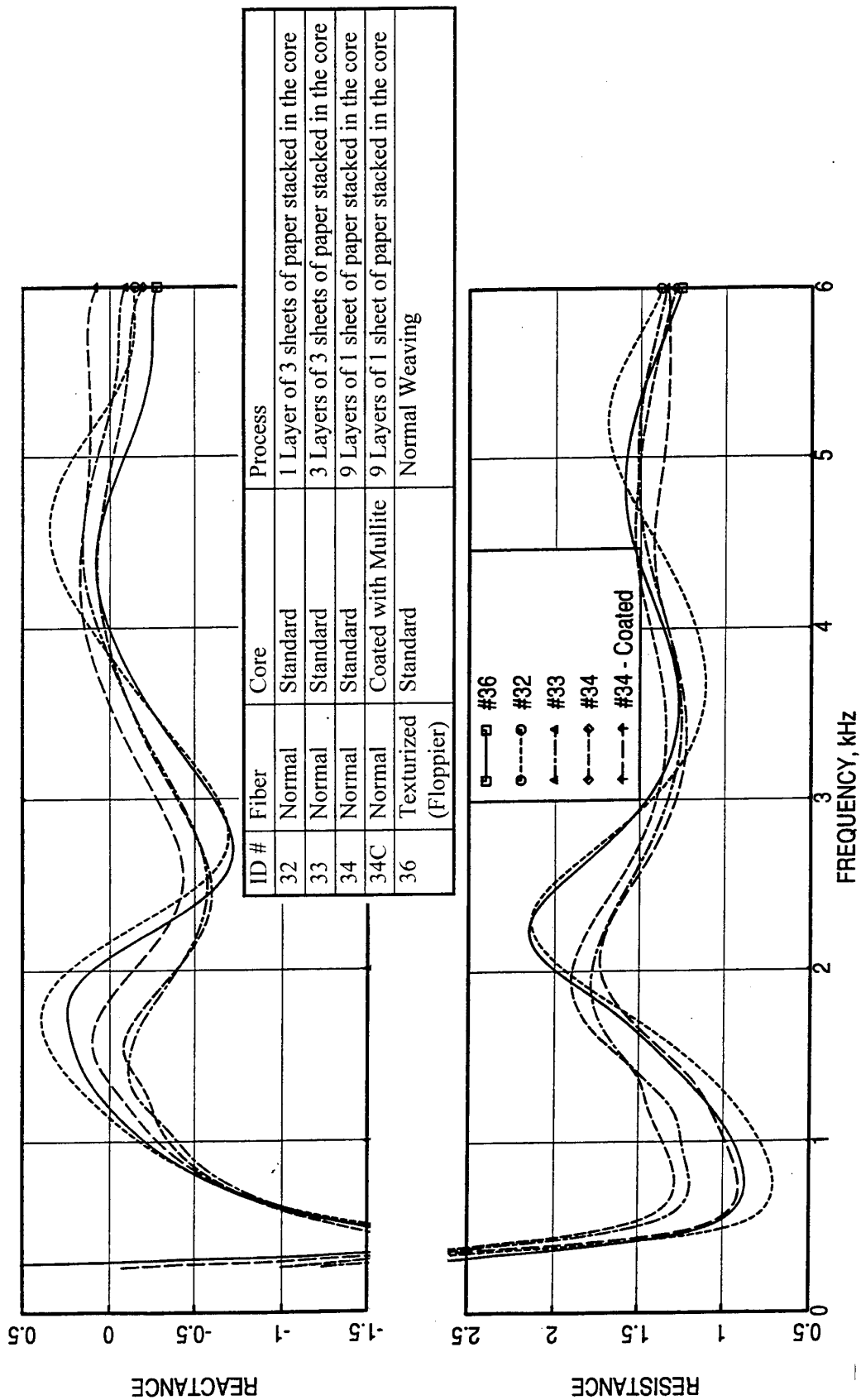


Figure 132. Effect of paper layer construction on normal impedance for various 2"-deep T-Foam samples, OASPL=150 dB.

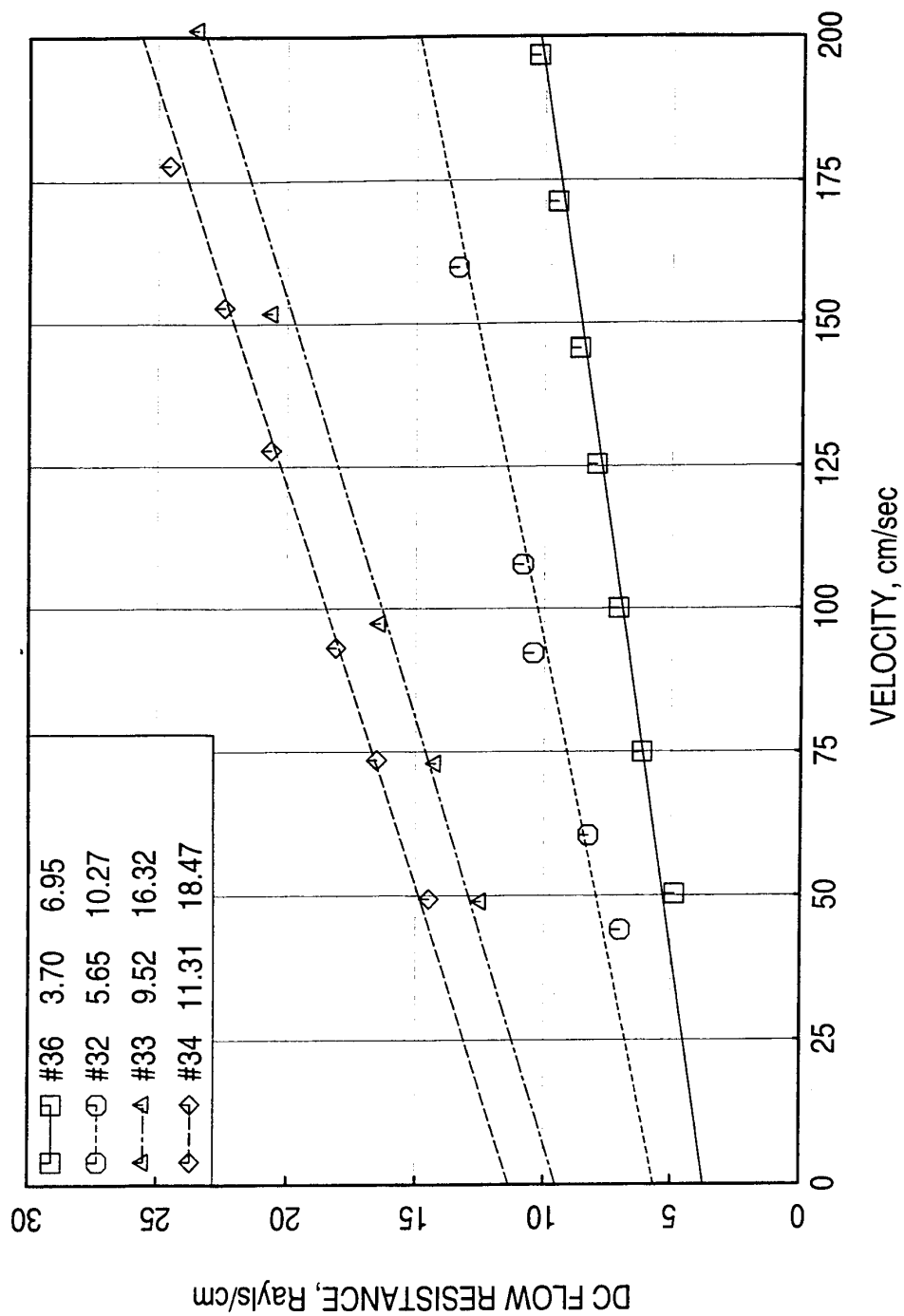


Figure 133. Effect of paper layer construction on DC flow resistance for various 2"-deep T-Foam samples, OASPL=150 dB.

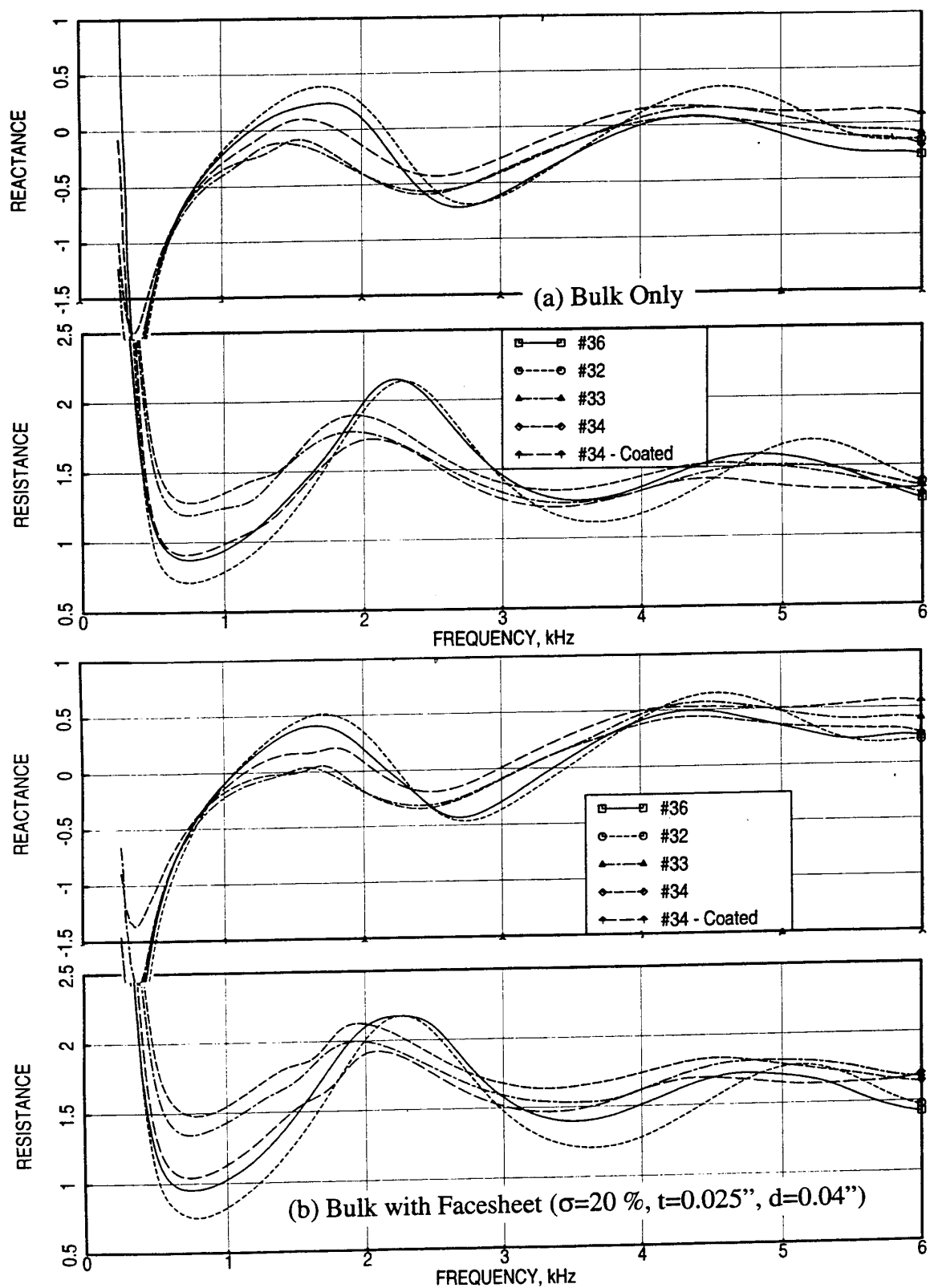


Figure 134. Effect of paper layer construction on normal impedance for various 2''-deep T-Foam samples (a) without and (b) with a facesheet ( $\sigma=20\%$ ,  $t=0.025''$ ,  $d=0.04''$ ), OASPL=150 dB.

Mullite, a process intended to improve the acoustic performance of the T-Foam. The effect of coating on normal impedance is shown in Figure 135. While the coating reduces the resistance the reactance is increased and thereby the acoustic suppression is not improved.

Normal impedance for different 2"-deep bulk materials is compared in Figure 136. The predicted acoustic suppression is maximum due to 100 ppi SiC for full-scale mixer-ejector application. SiC has an inherent problem of corrosion due to the rubbing action of the material against its holder. The erosion can be avoided by padding the top and bottom of the material. Thus, a padded SiC sample, created by using 0.25"-deep T-Foam on both surfaces of a 1.5"-deep SiC sample, is tested. Spectrally the normal impedance of the padded SiC sample is slightly different from the 2"-deep SiC sample without padding. Therefore, the concept of padding the SiC material may be used in HSCT application.

Normal impedance of T-Foam #33 is also plotted in Figure 136. While the impedance levels for this sample are comparable to those for SiC sample the resistance peaks at a frequency (i.e., 2 kHz) more critical for noise suppression compared to the peak for SiC (2.7 kHz). It should be noted that these frequencies would be higher at the temperature of application. Therefore, the peak for SiC will be beyond the 3 kHz limits. However, the peak for T-Foam #33 will still remain within the critical frequency limit of 1 to 3 kHz. Based on these differences the acoustic suppression in terms of EPNdB is lower for T-Foam #33 compared to 100 ppi SiC. Predicted acoustic suppression results are presented in reference 2.

**1.2"-Deep Samples:** Several 1.2"-deep T-Foam samples are fabricated and tested to evaluate the acoustic characteristics for LSM application. The impact of facesheet properties (i.e., porosity  $\sigma$ , thickness  $t$ , and hole diameter  $d$ ) on normal impedance for a standard 12 (10/2) lbf T-Foam is shown in Figures 137 and 138. Examination of these results in the frequency range of 2 to 6 kHz and the predicted acoustic suppression in terms of EPNdB (not shown here) indicates that the bulk material is not suitable for optimum noise suppression. Thus, the improvement process similar to 2"-deep samples by introducing oven papers is tried. Normal impedance spectra for two such constructions are compared with the impedance of a 12 lbf standard sample in Figures 139 and 140. The paper construction has improved the impedance characteristic significantly for optimum noise suppression. The 3-paper layer construction of T-Foam with 80 gm/m<sup>2</sup> (#42) seems to be more effective in noise suppression among all the T-Foam samples studied for LSM application. However, further improvement is necessary to attain the desired level of noise suppression or the amount achieved by SiC materials.

**Samples of Different Depths:** Different liner depths are required for different scale mixer-ejector treatment and their frequency ranges of effectiveness are different. Figure 141 shows

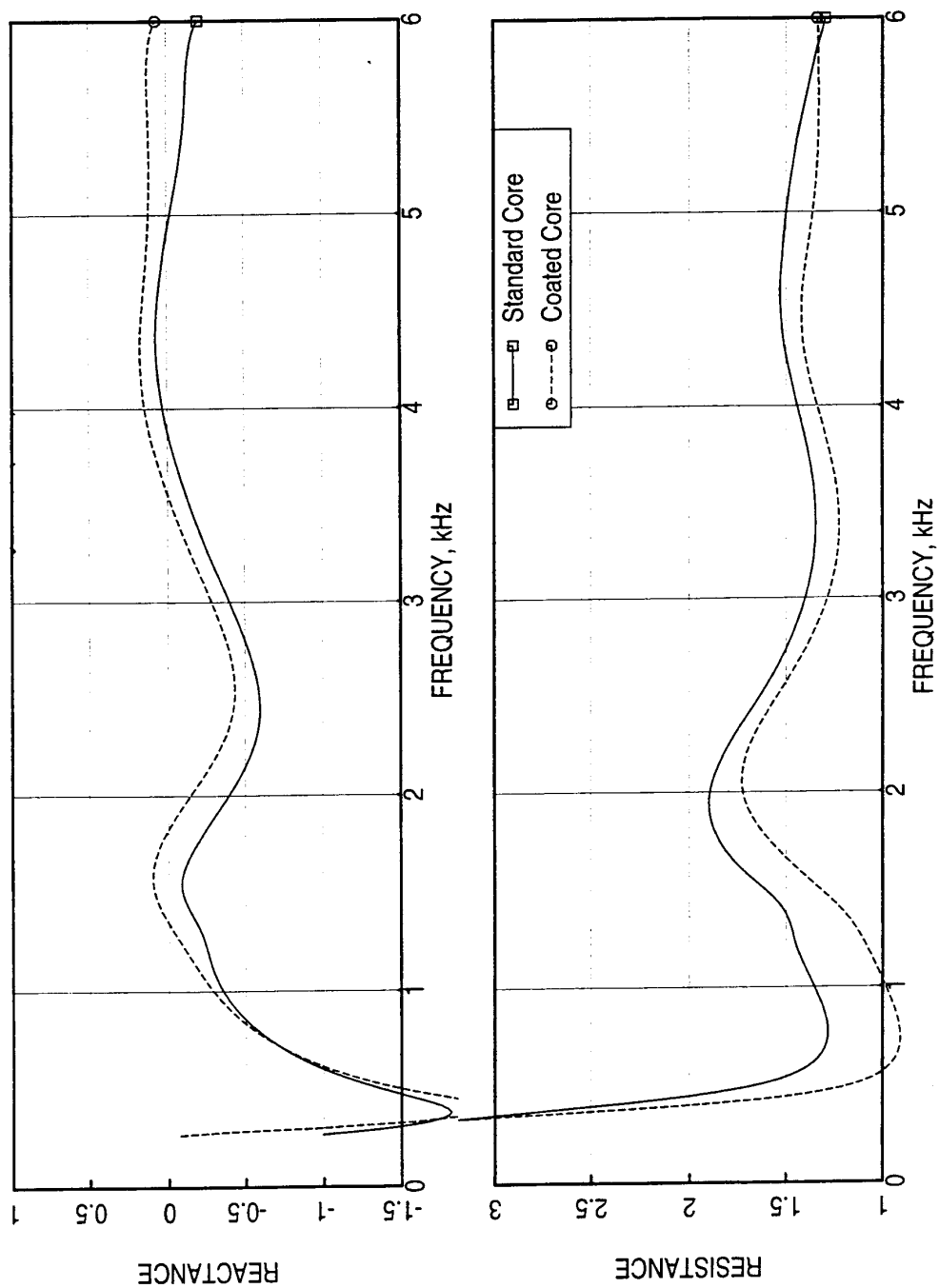


Figure 135. Effect of coated construction on normal impedance for a 2"-deep T-Foam sample (#34), OASPL=150 dB.



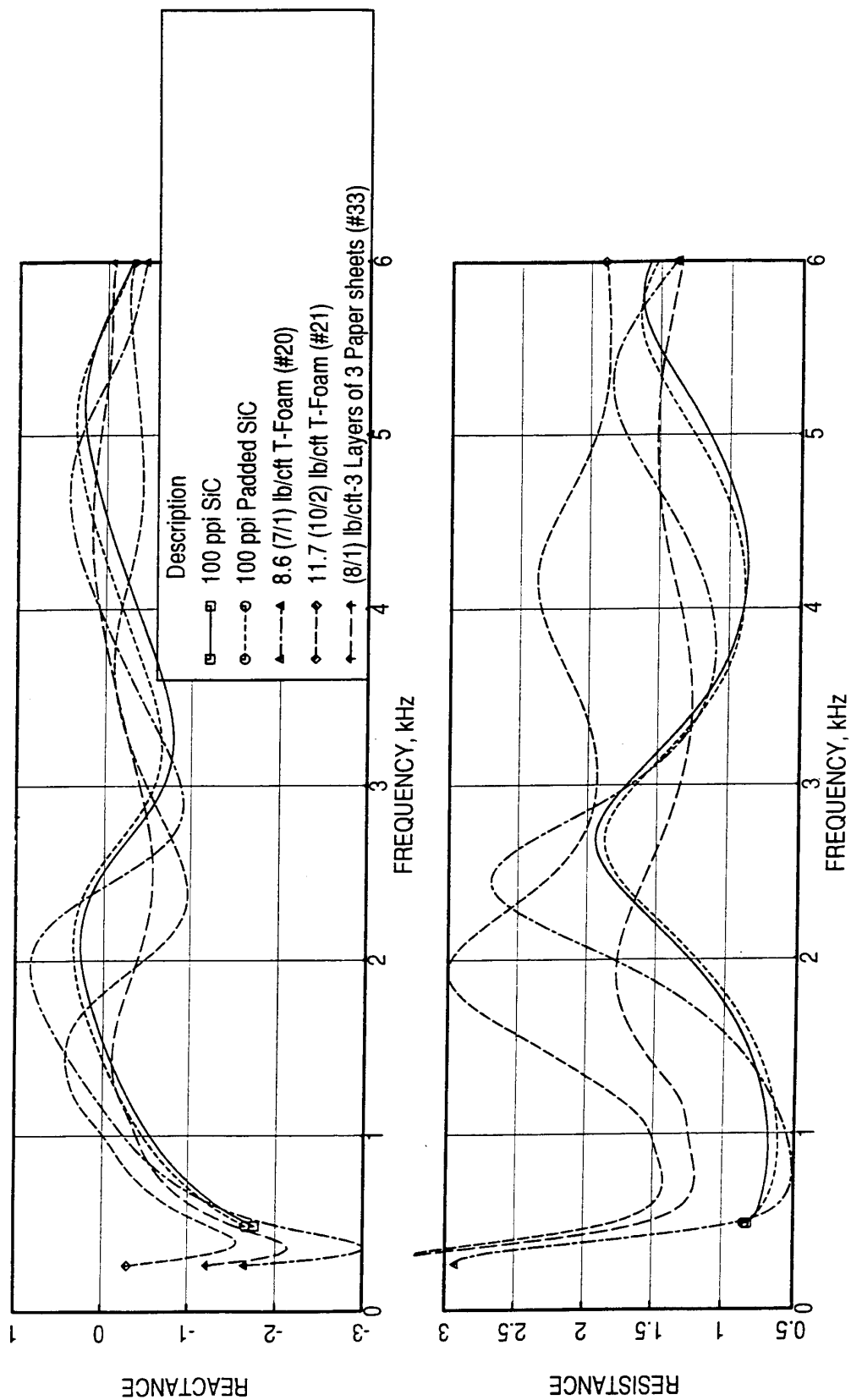


Figure 136. Comparison of normal impedance for various full-scale bulk absorbers (i.e., 2"-deep), OASPL=150 dB.

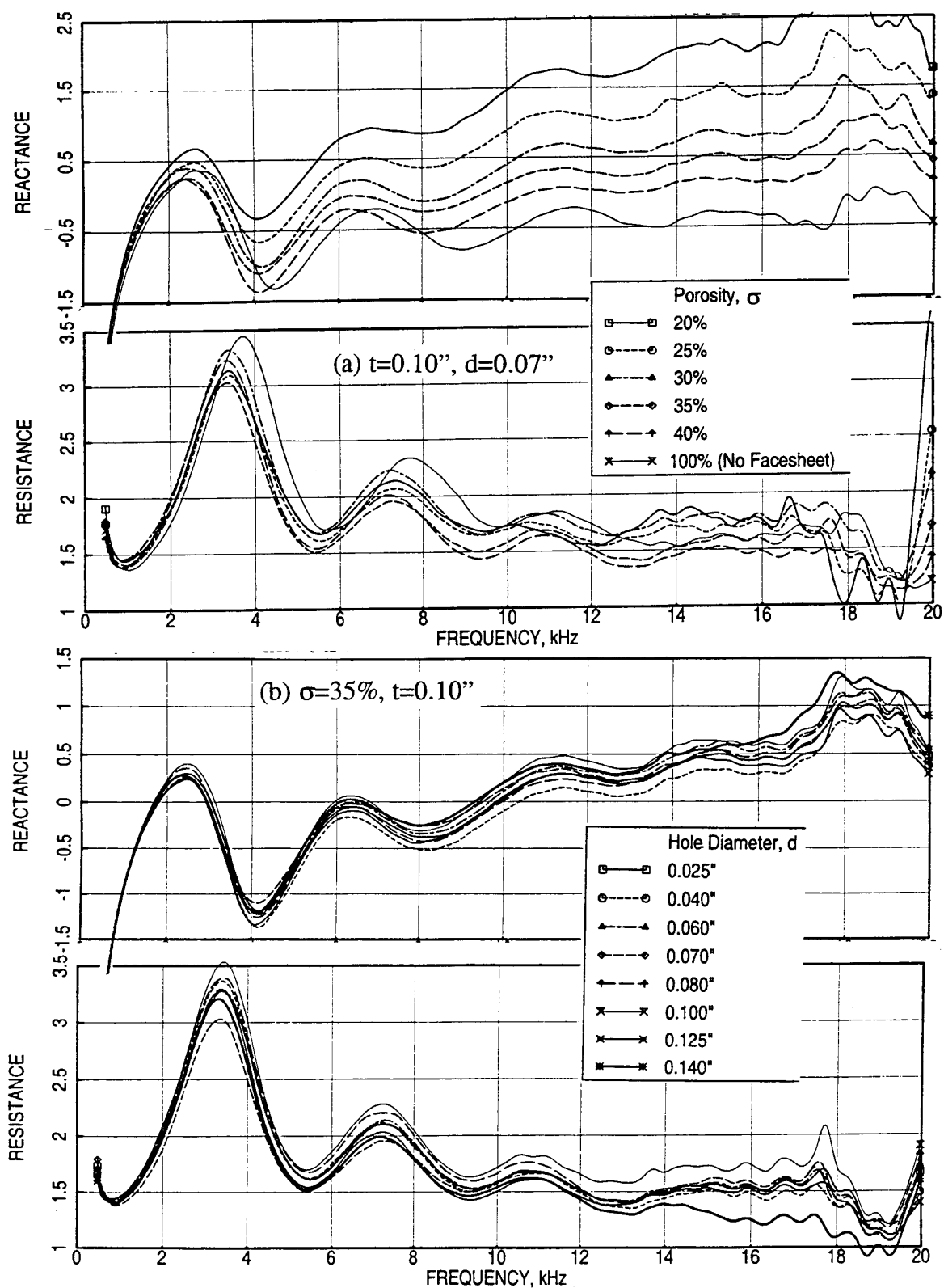


Figure 137. Effect of (a) facesheet porosity ( $t=0.10''$ ,  $d=0.07''$ ) and (b) facesheet hole diameter ( $\sigma=35\%$ ,  $t=0.10''$ ) on normal impedance for a 1.2''-deep standard 12 lbf T-Foam sample, OASPL=150 dB.

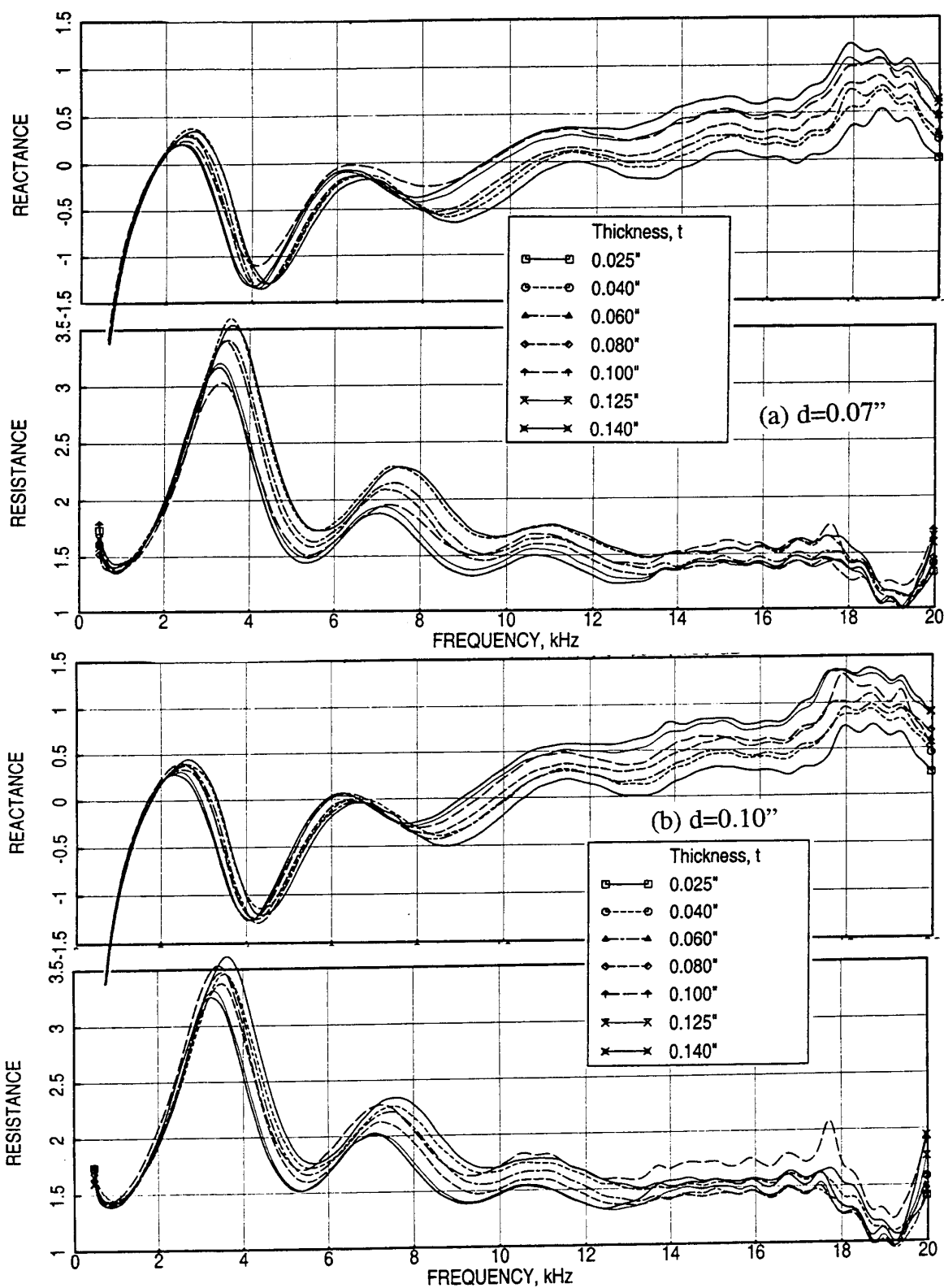


Figure 138. Effect of facesheet thickness ( $\sigma=35\%$ ) on normal impedance for a 1.2''-deep standard 12 lbf T-Foam sample, OASPL=150 dB.

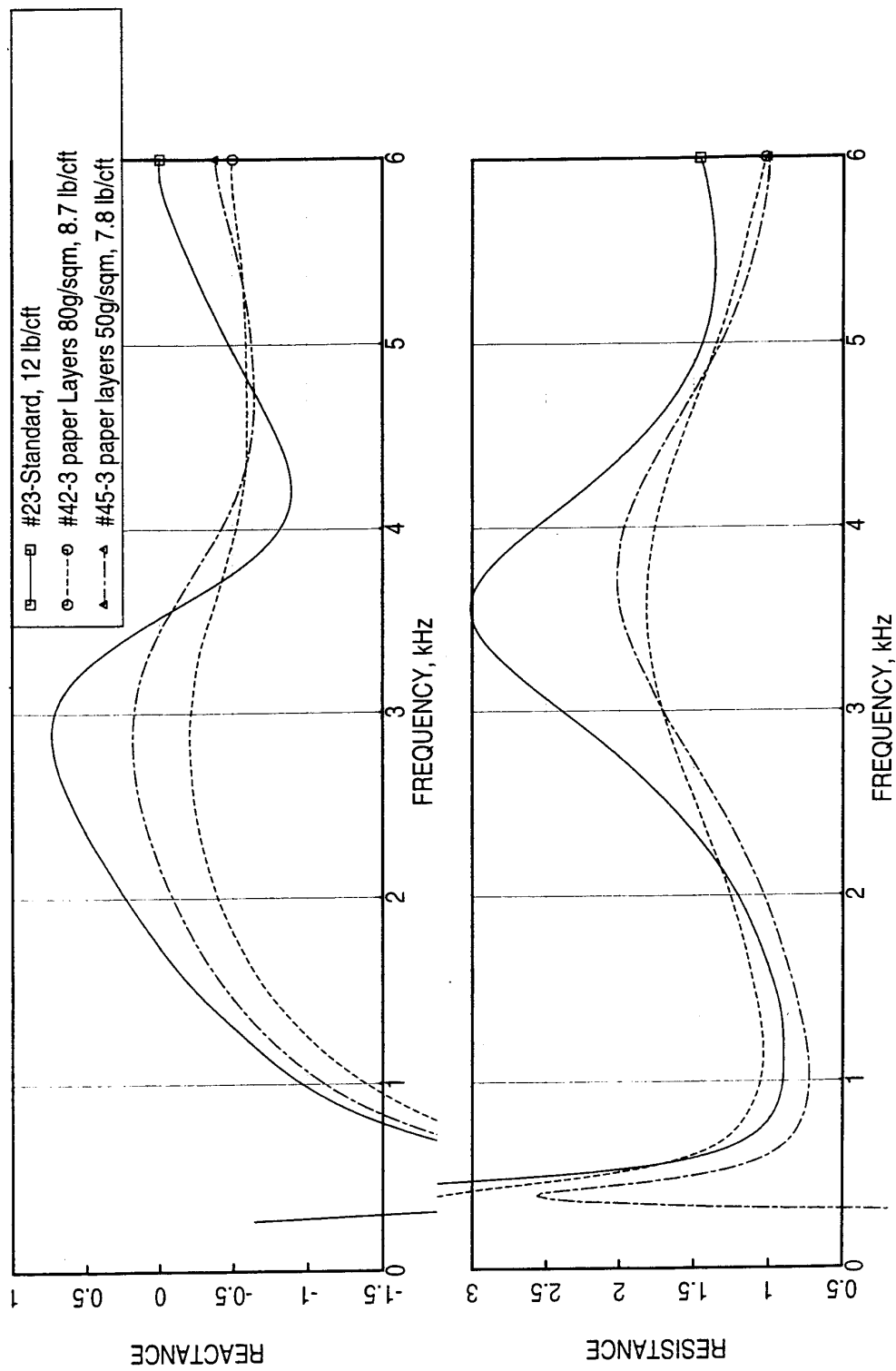


Figure 139. Measured normal impedance spectra up to 6 kHz for various LSM scale T-Foam samples (1.25" diameter) at ambient condition, depth=1.2", OASL = 150 dB.

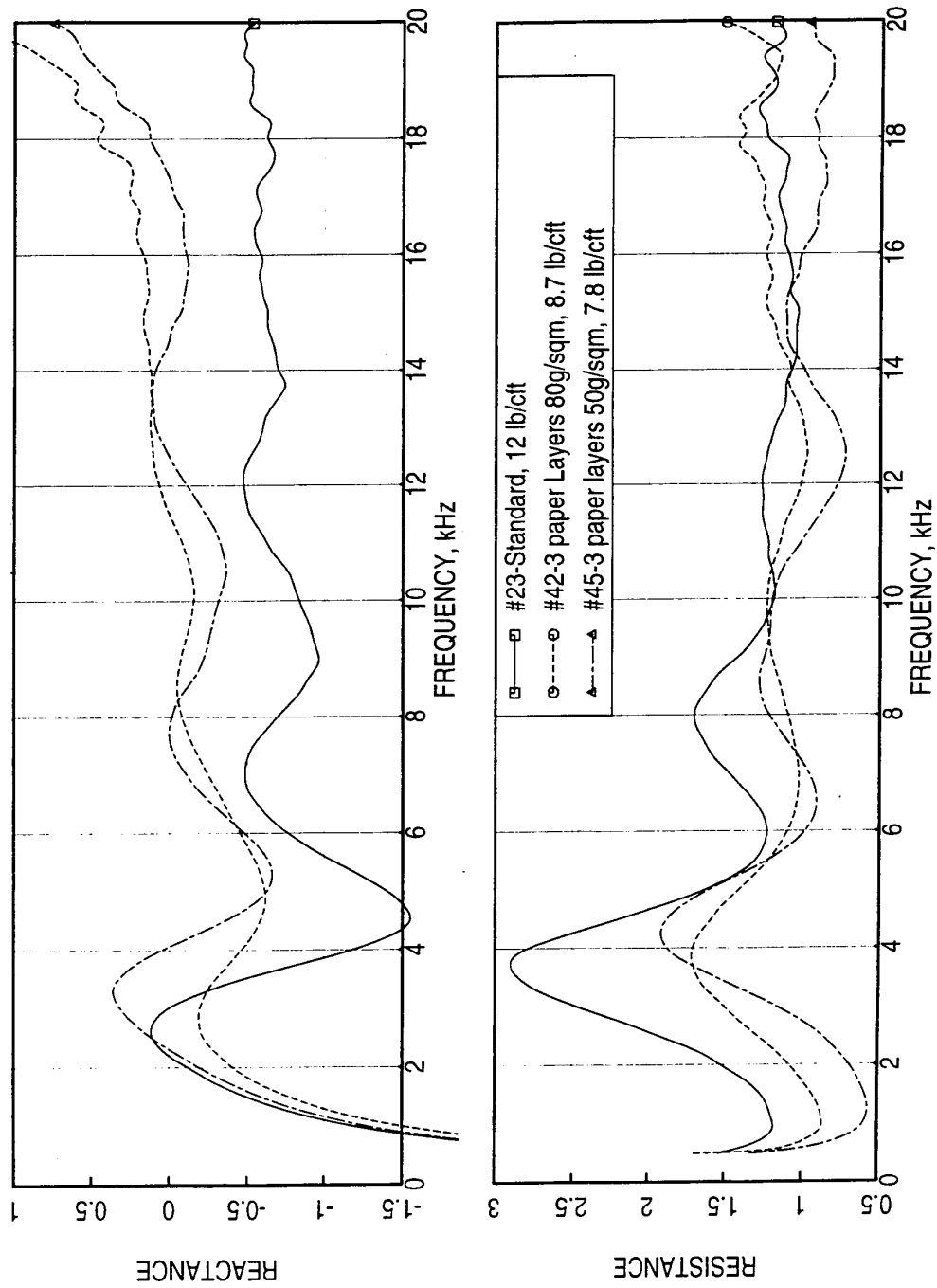


Figure 140. Measured normal impedance spectra up to 20 kHz for various LSM scale T-Foam samples (0.6" diameter) at ambient condition, depth=1.2", OASL = 150 dB.

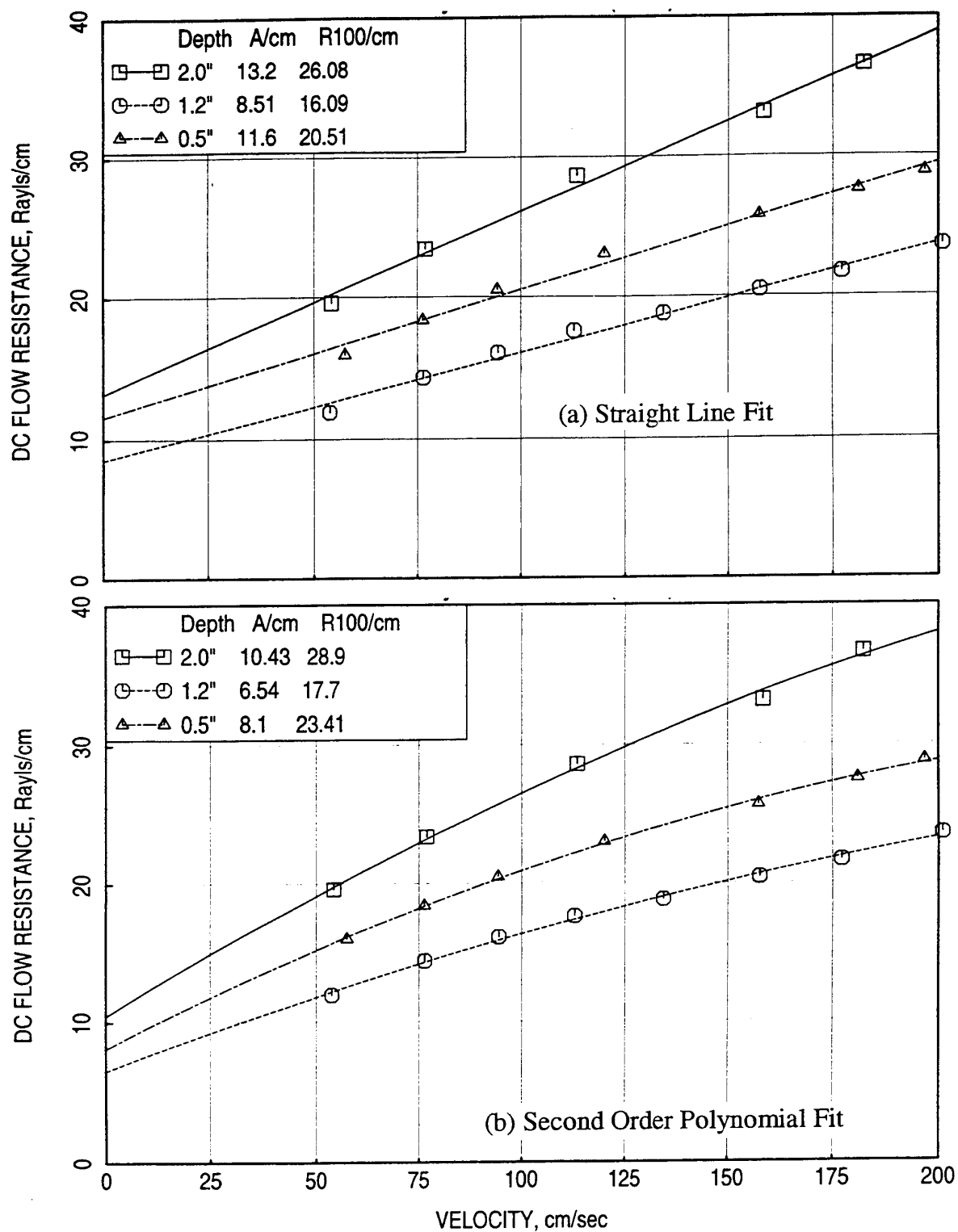


Figure 141. DC flow resistance for standard 11.7 (10/2) lbf T-Foam of different depths.

the measured DC flow resistance of 12 lbf standard T-Foam samples with different depths. The DC flow resistance is expected to be the same for all these samples. However, the manufacturing process of each sample being different, the actual DC flow resistance is different of these samples. The corresponding normal impedance, with and without facesheet, is shown in Figures 142 and 143. For 2" and 1.2" deep samples the level and location with respect to frequency of impedance peaks are unfavorable for acoustic suppression, as discussed earlier.

The results presented under this section (5.2.5) are used to predict acoustic suppression of various mixer-ejectors to establish optimum liner designs. These results are presented in a separate report (Ref. 2).

Some of the normal impedance data files are listed in Tables A1 through A4 in Appendix A (many more data files are not included in these lists).

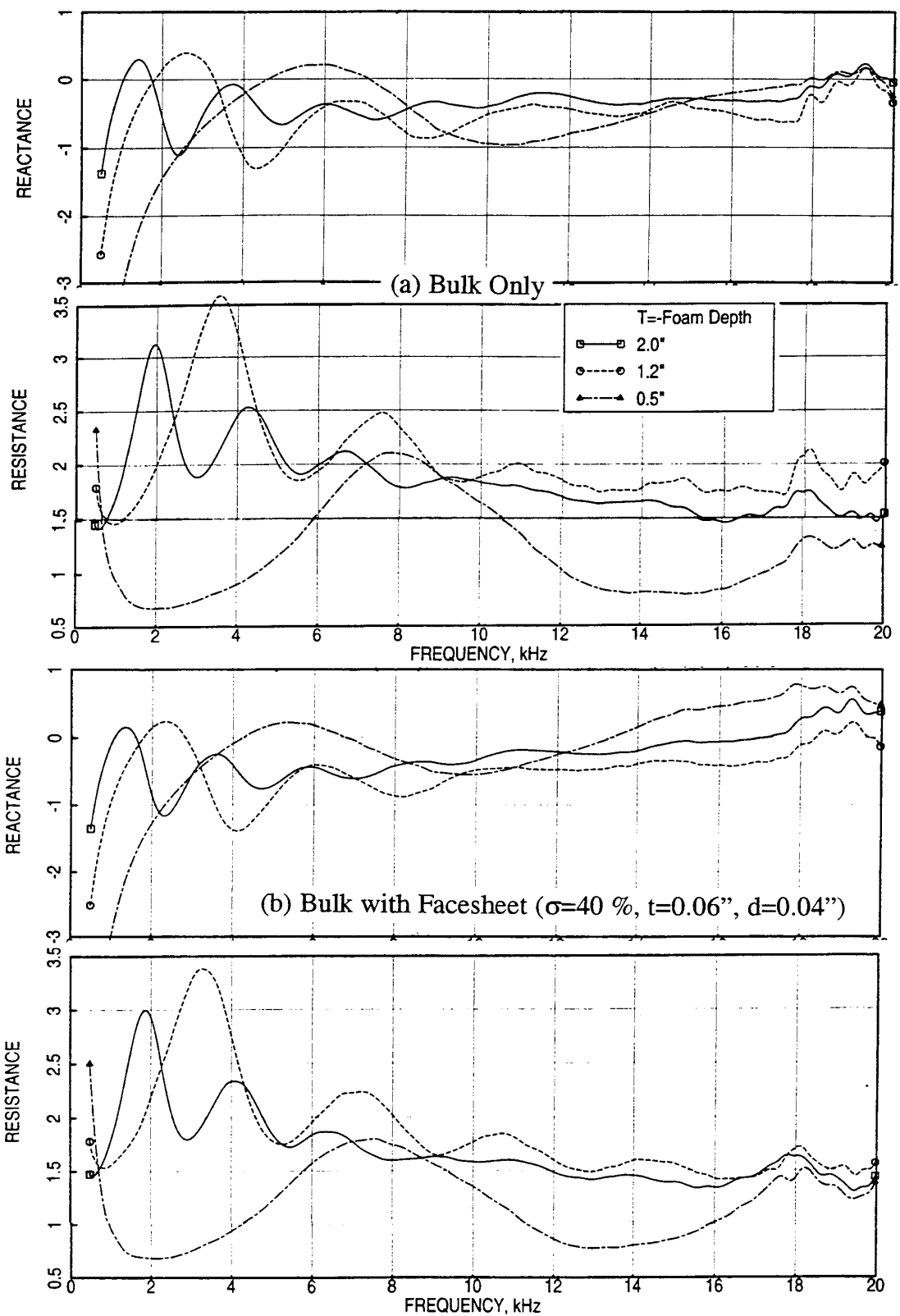


Figure 142. Normal Impedance for standard 11.7 (10/2) lbf T-Foam of different depths (a) without and (b) with a facesheet, OASPL=150 dB



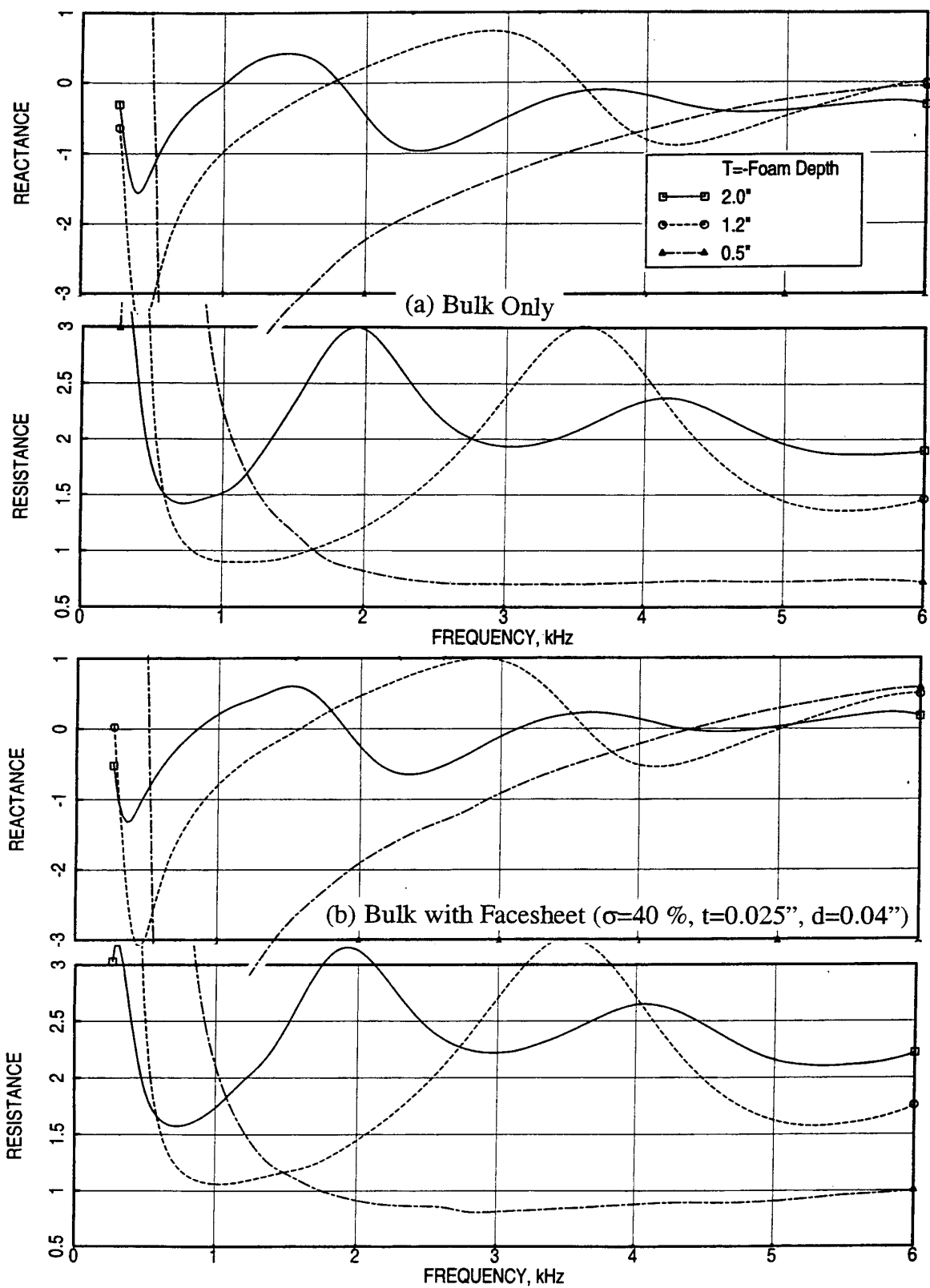


Figure 143. Normal Impedance up to 6 kHz for standard 11.7 (10/2) lbf T-Foam of different depths, (a) without and (b) with a facesheet, OASPL=150 dB

## 6.0 FLOW DUCT TESTS AT GEAE

Flow duct tests are conducted at various flow and temperature conditions for a number of bulk absorber and SDOF type liner panels (see Table 8). In these, three grazing flow Mach numbers (i.e.,  $M=0.3$ ,  $0.55$ , and  $0.8$ ) and three temperature variations ( $T=\text{ambient}$ ,  $200^\circ\text{F}$ , and  $400^\circ\text{F}$ ) are included to study their effects on the measured parameters. Tests are also conducted without any grazing flow ( $M=0$ ) at ambient temperature. During a test the dynamic pressures from the transducers mounted in the five tray cavities are measured to compute In-situ impedance. Discrete frequency excitation at a number of frequencies (about 15) up to about 20 kHz is used for these tests. For no flow condition, a broadband sound excitation is used. The DC flow resistance and the boundary layer profiles at a single location using a total pressure probe are measured at different flow conditions. DC flow resistance measurements are made at grazing flow Mach numbers of  $0.3$ ,  $0.55$ , and  $0.7$  instead of  $0.8$ , since it is difficult to suck air through the samples at  $M=0.8$  for the pump used for the current study.

### 6.1 Data Analysis for Insitu Impedance:

**6.1.1 Evaluation of Complex Wave Propagation Number in the Bulk Material:** For insitu impedance evaluation for bulk absorber panels one of the important aspect is to compute the complex propagation speed of sound in the bulk material. A test is conducted in the flow duct without any grazing flow for a 100 ppi bulk panel without any facesheet. The data measured by the cavity transducers are used to evaluate the complex propagation speed of sound in the 100 ppi SiC by solving the following equation;

$$\cosh(\kappa l) = p_2(f)/p_1(f)$$

Results from 0.5" deep cavity are studied and presented here. Complex pressure transfer function  $p_2(f)/p_1(f)$ , measured in the test, is shown in Figure 144. For 0.5" deep sample the first anti-resonance occurs at about 11.5 kHz. The variation of real and imaginary components of the transfer function, shown in Figure 144, indicates a trend change above the anti-resonance frequency. The complex propagation speed  $c_b$  ( $\kappa=\omega/c_b$ ) obtained from the above equation is plotted in Figure 145 in terms of its real and imaginary components. The components remain almost constant up to the anti-resonance frequency. The real part increases and imaginary part decreases above the anti-resonance frequency. The real and imaginary components of  $\kappa$  are plotted in Figures 146 and 147, respectively. The wave number  $k$  for air is compared with real  $\kappa$  in Figure 146. Both the wave numbers increases

Table 8. Panel configurations for flow duct tests.

Configuration	Facesheet Description		
	Porosity, $\sigma$	Thickness, t inch	Hole Diameter d inch
Bulk Absorber Panels with 100 ppi 0.5" deep Silicon Carbide			
1-4161	40	0.025	0.10
1-8	40	0.04	0.04
1-4121	40	0.10	0.04
1-5	40	0.025	0.06
1-4052	35	0.10	0.04
1-7	40	0.015	0.04
1-4072	35	0.04	0.07
1-4075	35	0.10	0.07
1-4031	30	0.10	0.07
1-12	Linear, 15 Ravls		
1-11	Linear, 10 Ravls		
1-4143	40	0.10	0.07
1-6	40	0.025	0.08
1-9	40	0.06	0.04
1-3	40	0.025	0.04
1-2	30	0.025	0.04
1-1	20	0.025	0.04
Bulk Absorber Panels with Standard 12 lbf 0.5" Deep T-Foam			
6-8	40	0.04	0.04
6-4	40	0.025	0.025
6-11	Linear, 10 Ravls		
6-4143	40	0.10	0.07
6-6	40	0.025	0.08
6-9	40	0.06	0.04
6-3	40	0.025	0.04
6-2	30	0.025	0.04
6-1	20	0.025	0.04
SDOF Type Panels with Facesheets used for Bulk Absorber Panels			
t1-8	40	0.04	0.04
t1-4121	40	0.10	0.04
t1-5	40	0.025	0.06
t1-11	Linear, 10 Ravls		
t1-4143	40	0.10	0.07
t1-6	40	0.025	0.08
t1-9	40	0.06	0.04
t1-3	40	0.025	0.04
t1-2	30	0.025	0.04
t1-1	20	0.025	0.04
SDOF Type Panels with Facesheets of Lower Porosities			
2	9	0.025	0.04
4	15	0.025	0.04
11	9	0.025	0.08
12	9	0.10	0.04
15	9	0.06	0.04
17	9	0.10	0.04
25	Linear, 85 Ravls		

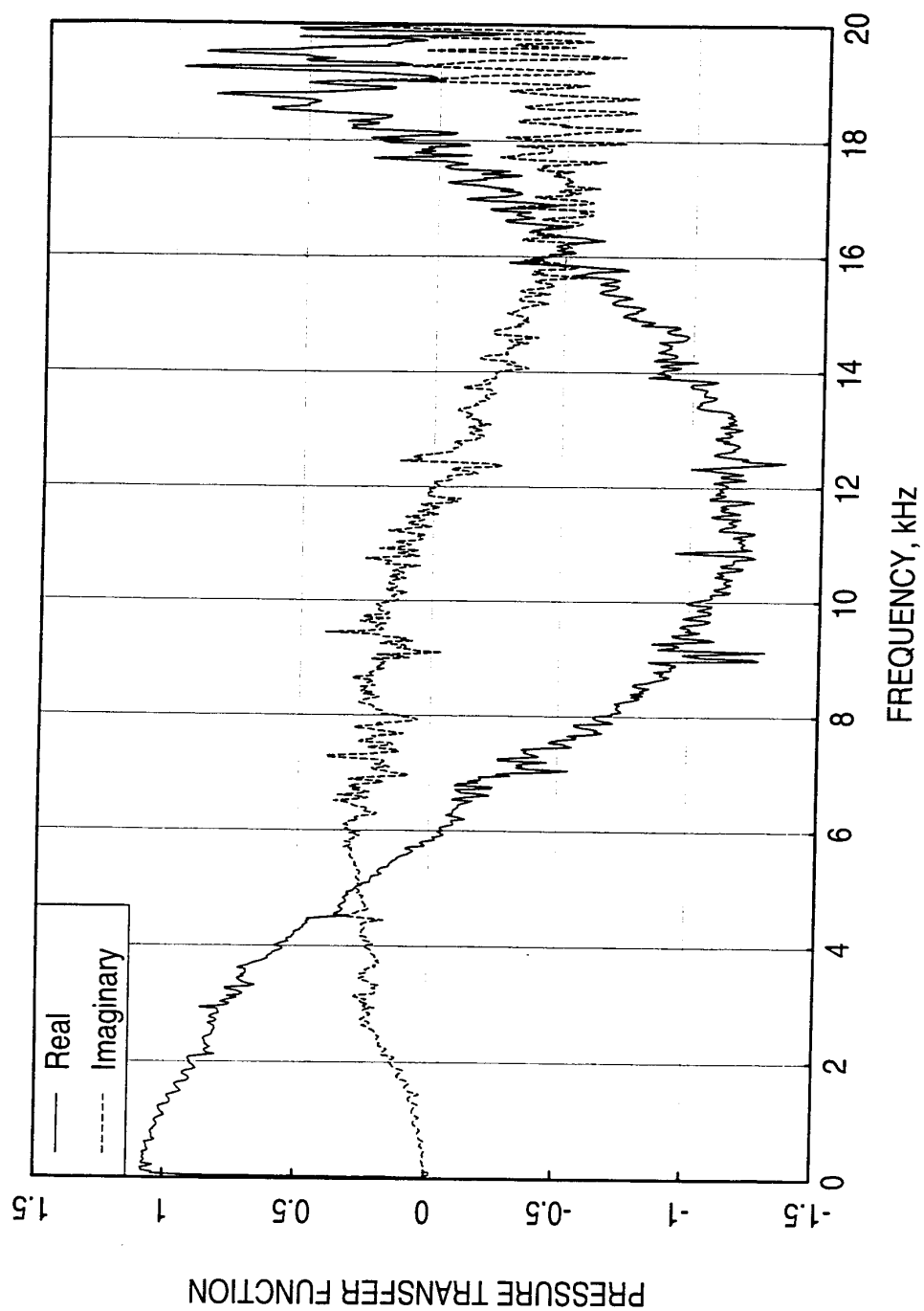


Figure 144. Complex pressure transfer function for 100 ppi 0.5"-deep Silicon carbide sample, mounted in a 0.5"-deep cavity.

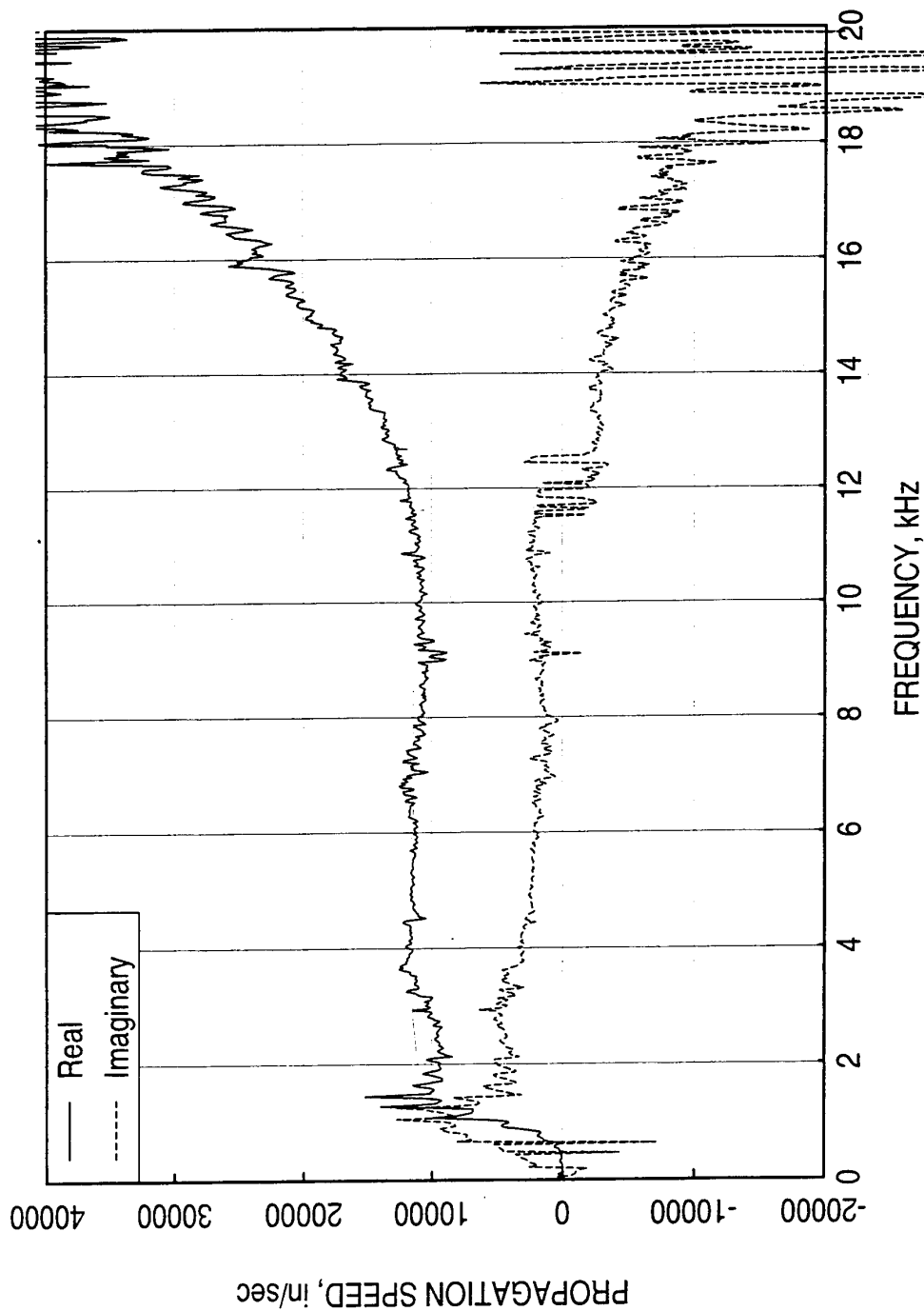


Figure 145. Complex propagation speed of sound ( $c_b$ ) in a 100-ppi 0.5''-deep Silicon carbide sample mounted in a 0.5''-deep cavity.

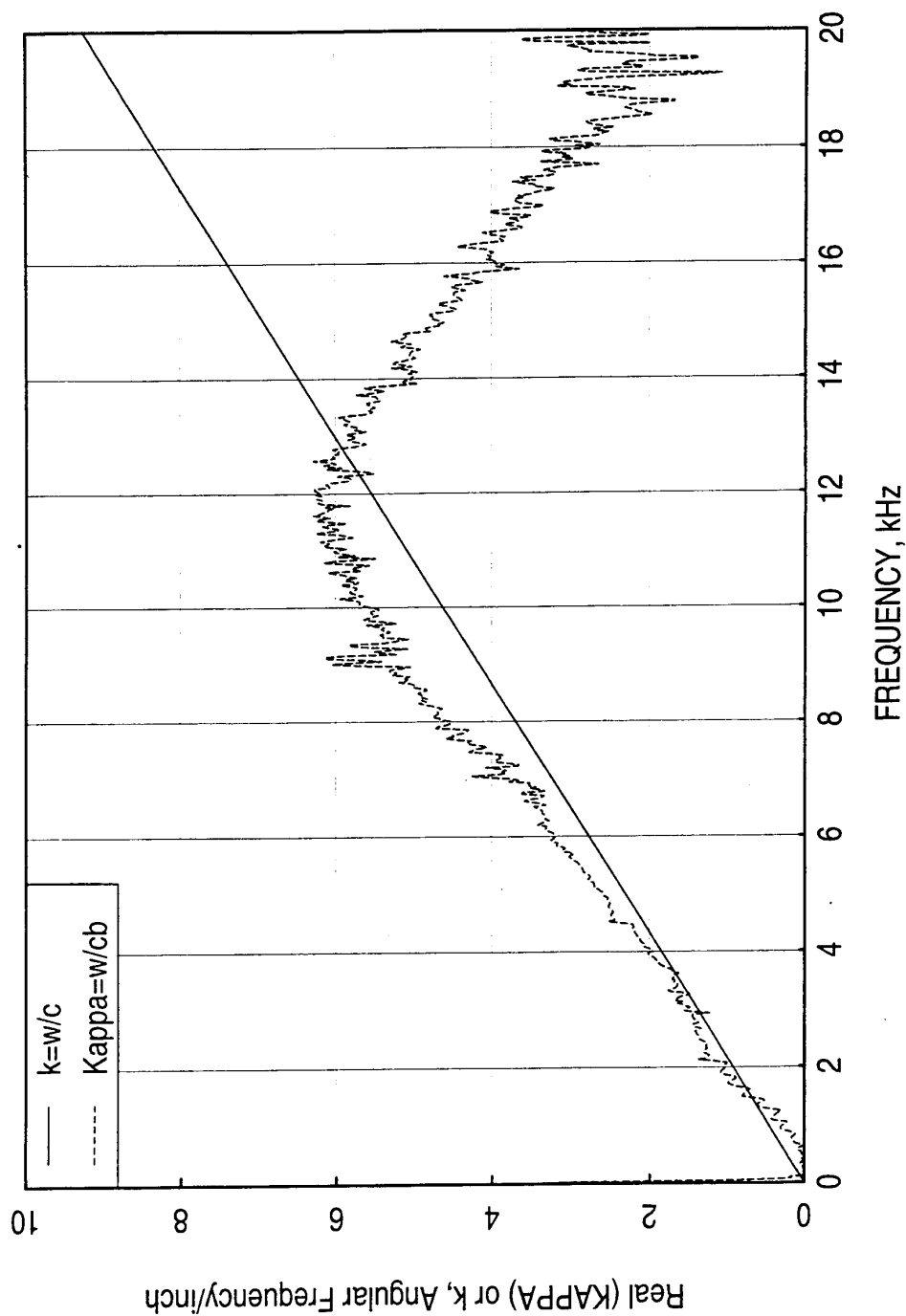


Figure 146. Real part of complex wave number ( $\text{Re}\{\kappa\}$ ) in a 100-ppi 0.5"-deep Silicon carbide sample mounted in a 0.5"-deep cavity compared with  $k=\omega/c$ .

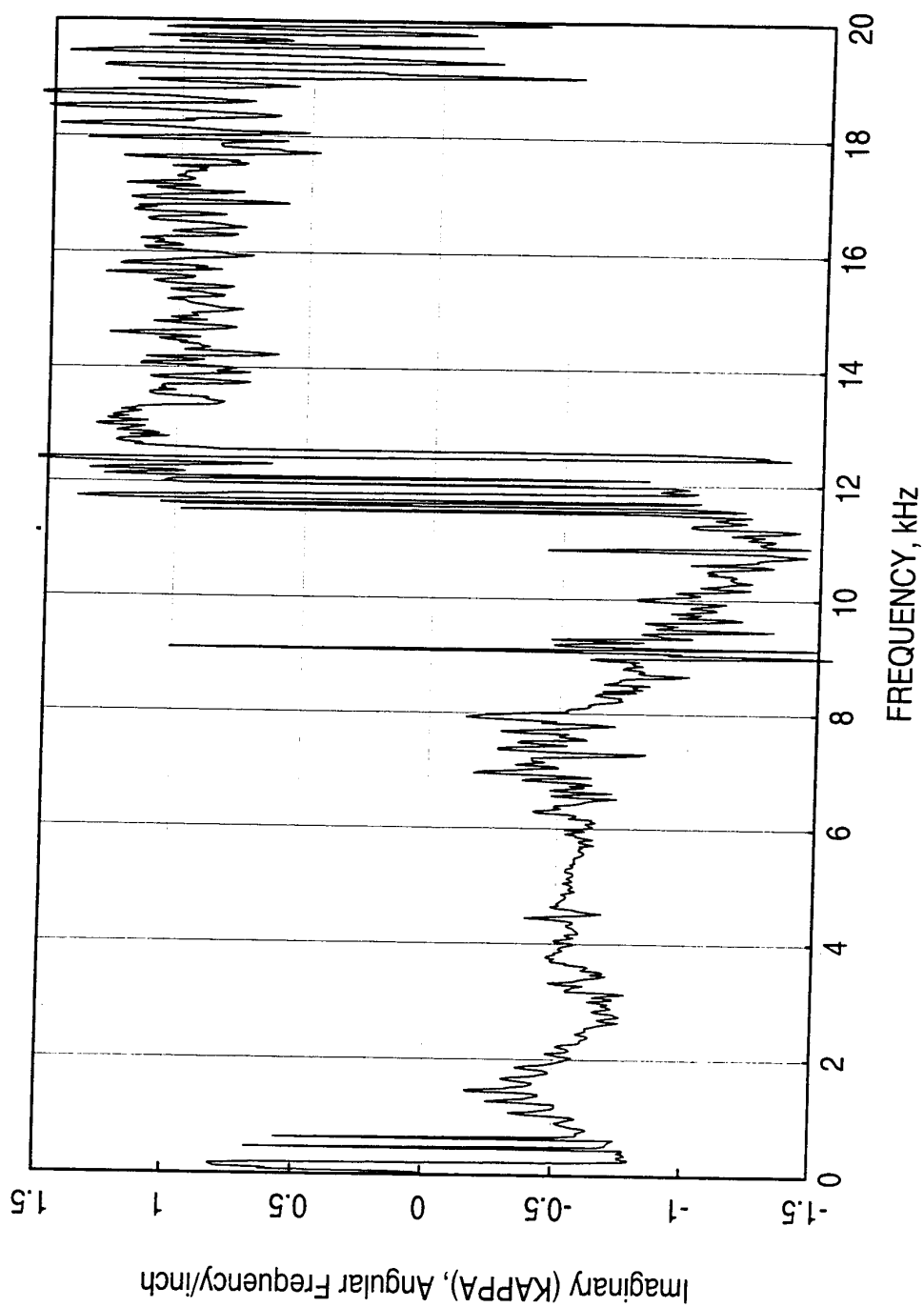


Figure 147. Imaginary part of complex wave number ( $\text{Im}(k)$ ) in a 100-ppi 0.5"-deep Silicon carbide sample mounted in a 0.5"-deep cavity.

with frequency. However, real  $\kappa$  begins to decrease above the anti-resonance frequency, whereas,  $k$  continues increasing. It is important to observe that the real  $\kappa$  values are reasonably close to  $k$  up to the anti-resonance frequency for 100 ppi SiC. Figure 147 clearly indicates a phase shift at anti-resonance frequency.

It is expected that the real  $\kappa$  should behave similar to  $k$ . However, in solving the equation for  $\kappa$  we are unable to resolve the problem above the anti-resonance frequency. Either a discrepancy in the equation (could be a multi value function) or in the numerical solution might be responsible for this behavior. It was planned to acquire an insitu complex pressure transfer data using the modified high frequency impedance tube for a 0.25" deep SiC sample, for which, the anti-resonance frequency would occur beyond 20 kHz. However, the constraint of time due to the HSR closeout program prevented in carrying out this study.

Based on the results for 0.5" SiC sample and the explanations presented it is assumed that the real part of propagation speed in the bulk would remain constant with respect to the frequency. In addition, real and imaginary  $c_b$  can be assumed to be the same as the propagation speed of sound in air and zero, respectively, for bulk materials of lower resistivity, like 100 ppi SiC.

#### **6.1.2 Diagnostic Tests for In-situ Impedance for SDOF & Bulk Absorber Type Liners:**

The first step is to compare the normal impedance with the in-situ impedance to establish the validity of insitu method for SDOF as well as for bulk absorber type liner samples. Figure 148 shows a comparison of normal impedance, measured by impedance tube, with the insitu impedance, measured in the flow duct in the 0.5"-deep cavity for a 20% porous facesheet ( $t=0.025$ " and  $d=0.04$ "). The agreement between the two sets of data is reasonably well, except at and near the antiresonance frequency of the cavity. The insitu reactance is slightly higher compared to normal reactance. This could be due to the temperature difference and the slight difference in the back cavity depth (i.e., insitu cavity depth being 0.504 compared to 0.5" in normal impedance tube setup) between the two facilities.

Similar comparisons are made for 0.5"-deep Silicon Carbide sample with and without facesheets and are shown in Figures 149 and 150. While the agreement between the insitu reactance and normal reactance is very good the agreement for resistance is limited to frequencies away from the antiresonance locations. This could be due to the assumption of same propagation speed of sound in the air and in the bulk. Similar comparisons are made in Figure 151 for a 0.505"-deep SiC sample with different cavities behind it. The normal impedance and insitu impedance are measured simultaneously in the modified high



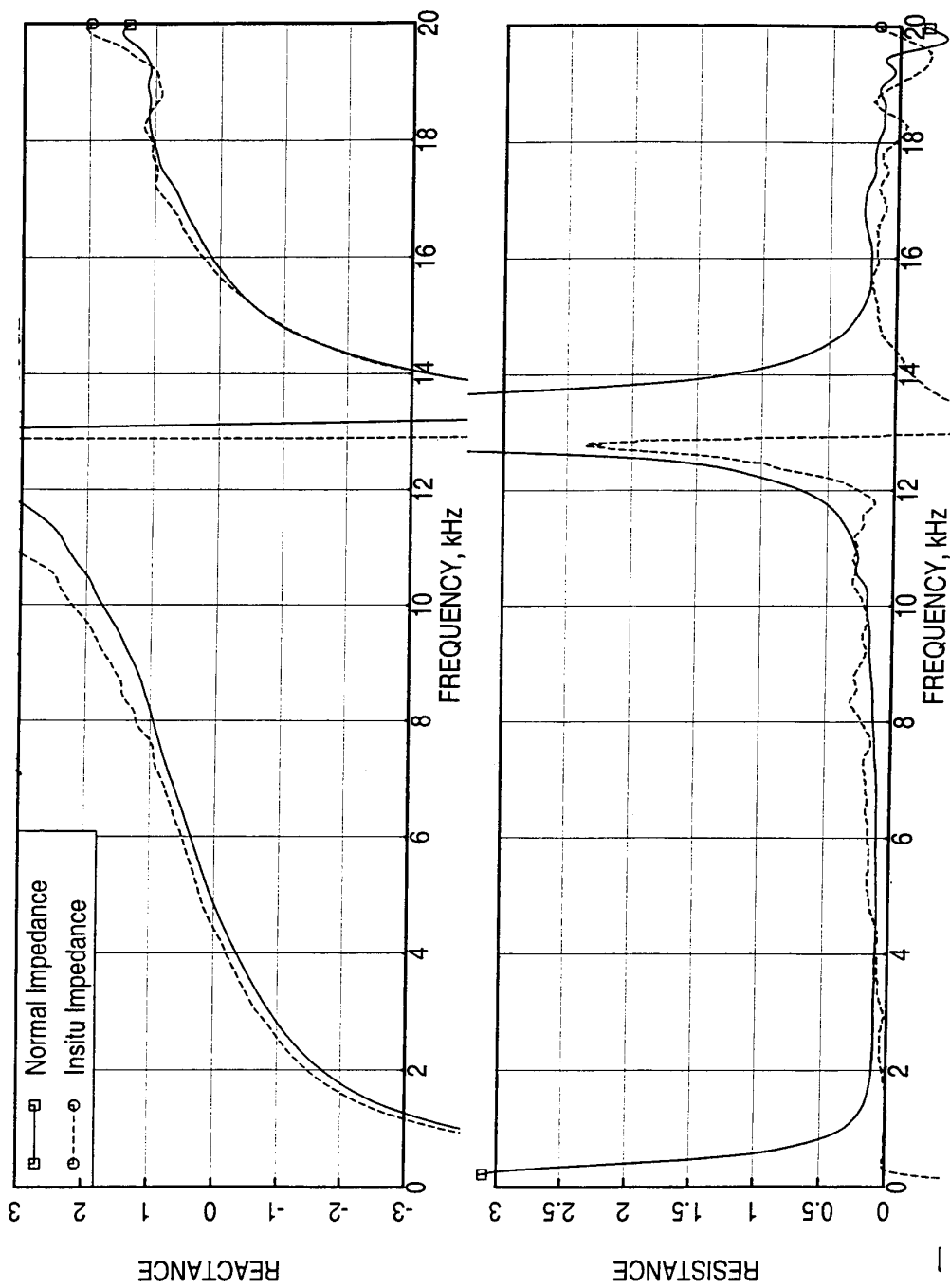


Figure 148. Comparison of insitu impedance with normal impedance for a 20% porous 0.025"-thick facesheet with 0.04" hole diameter with a 0.5" back cavity.

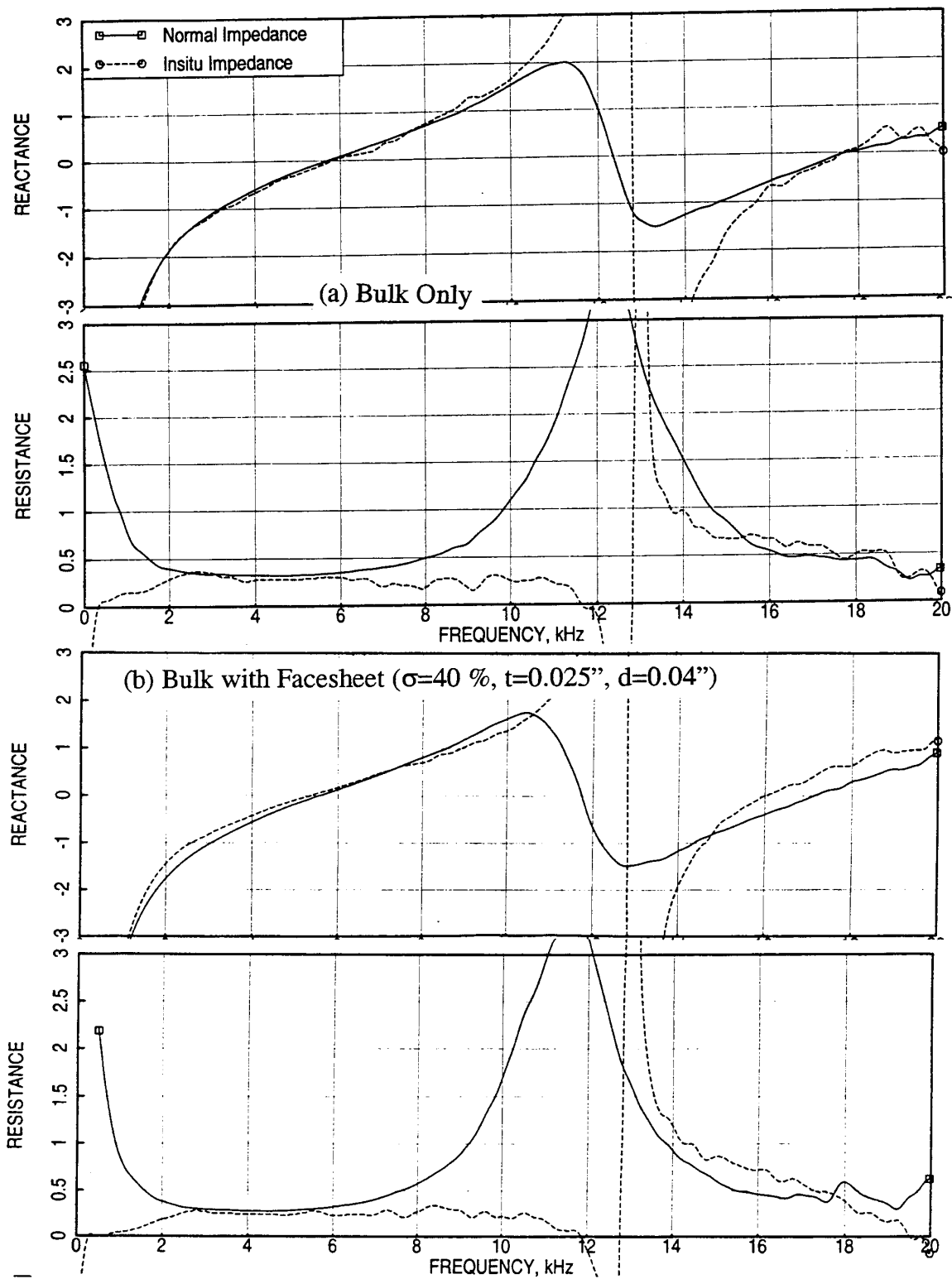


Figure 149. Comparison of insitu impedance with normal impedance for a 0.5"-deep 100 ppi Silicon Carbide bulk (a) without and (b) with a 40% porous 0.025"-thick facesheet with 0.04" hole diameter, no cavity behind the bulk.

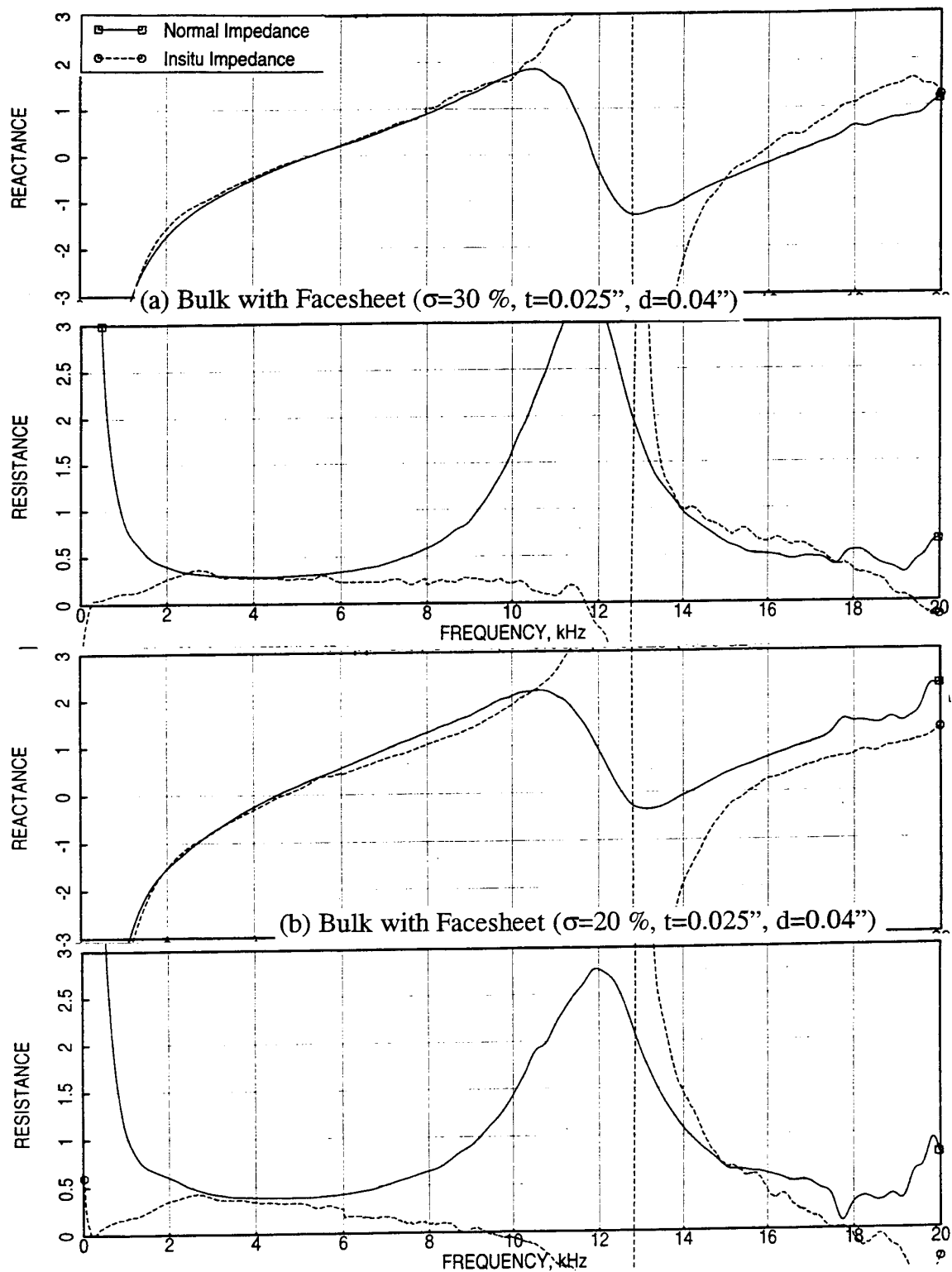


Figure 150. Comparison of insitu impedance with normal impedance for a 0.5''-deep 100 ppi Silicon Carbide bulk with 0.025''-thick facesheet of 0.04'' hole diameter (a)  $\sigma=30\%$  and (b)  $\sigma=20\%$ , no cavity behind the bulk.

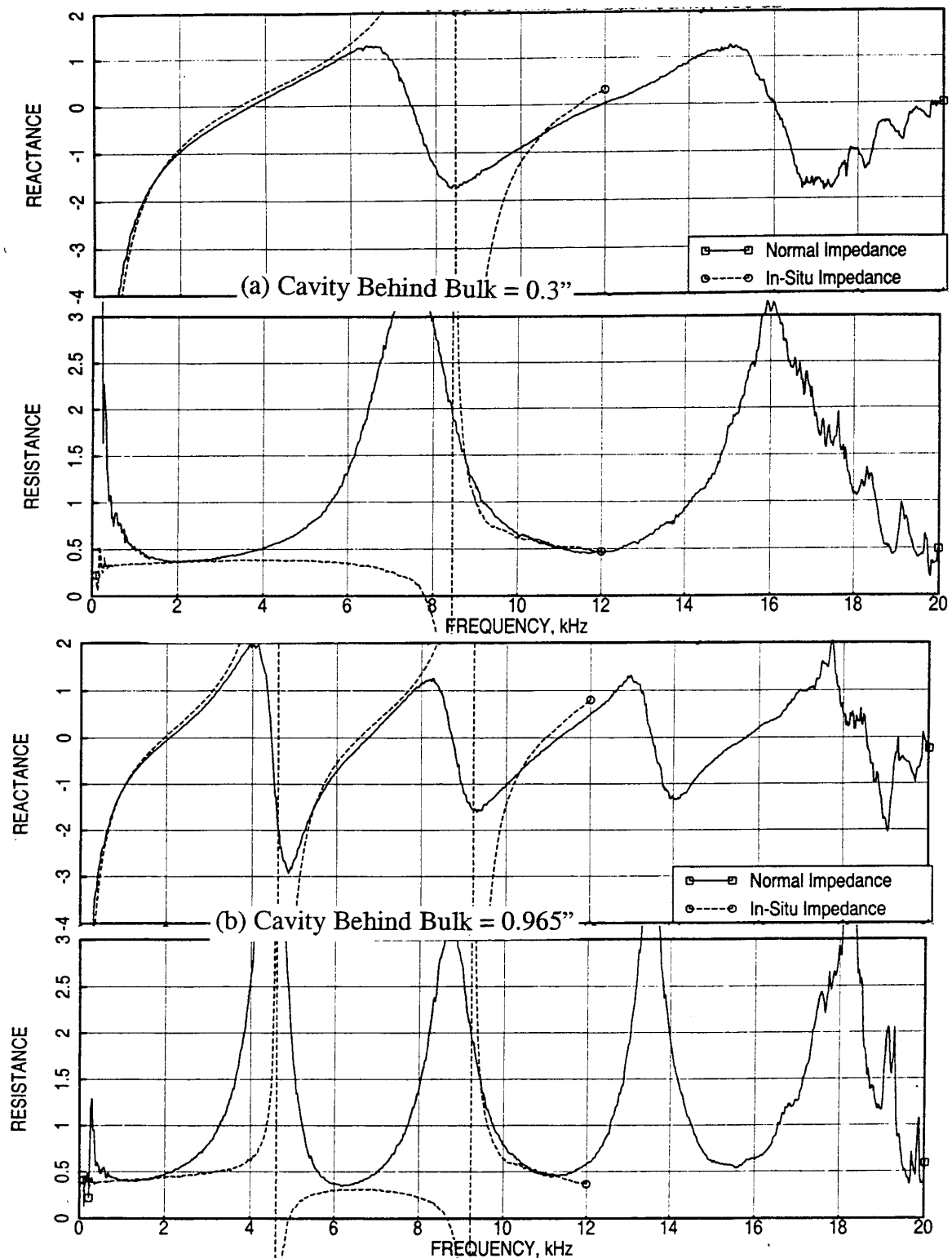


Figure 151. Comparison of insitu impedance with normal impedance for a 0.5''-deep 100 ppi Silicon Carbide bulk, measured simultaneously using modified high frequency impedance tube, OASPL=150 dB, cavity behind the bulk (a) 0.3'' and (b) 0.965''.

frequency impedance tube. The frequency range for insitu measurement was not extended up to 20 kHz in the software used at that time. Again, the reactance comparisons are much better for entire frequency range compared to the corresponding resistances.

The impedance characteristics at and near the antiresonance frequencies seem to be opposite in nature between normal and insitu measurements. To minimize the impact of such differences, one inherent to the type of measurement and the other may be due to propagation speed assumption, relative impedance, rather than absolute level, is derived from insitu measurements. For example, using the measurements for 0.5"-deep SiC sample alone and with a 30% porous facesheet, the relative impedance due to the facesheet is evaluated. In this the impedance of the bulk alone is subtracted from the bulk with facesheet. This is done for both normal and insitu data. The relative normal impedance is compared with relative insitu impedance derived from different cavities in Figures 152 and 153. The relative impedance agreement is significantly better compared to absolute impedance comparisons. Note that the relative impedance is plotted with an enlarged scale compared to absolute impedance.

The relative impedances due to flow and temperature are evaluated with respect to no flow and unheated condition, respectively, from insitu data. These relative levels are added to the measured normal impedance at ambient condition without grazing flow to derive the absolute impedance for a desired flow and temperature condition.

**6.1.3 Rationale for Insitu Impedance Test Procedure & Typical Data:** Tests are conducted to evaluate the insitu impedance of various bulk absorber and SDOF type liners (see Table 8) utilizing five different cavities of the panel tray. The acoustic environment in the duct is created either by broadband or discrete frequency sine wave type excitations. In the presence of flow the discrete frequency signal is enhanced by time domain synchronized averaging. Typical broadband and discrete frequency insitu impedance spectra showing the effect of grazing flow at ambient condition are presented in Figures 154 and 155 for two cavities of different depths. Similar results are obtained for other cavities except the number and locations of antiresonance are different due to the varying cavity depths. Similar results are obtained for heated conditions. Figure 156 shows the insitu impedance spectra at 200°F for a 0.5"-deep cavity. Compared to Figure 154 the anti resonance frequency has been increased due to heated flow. Figures 157 through 159 show the effect of temperature on insitu impedance at different grazing flow Mach numbers for a 0.5"-deep cavity. Again, the anti-resonance frequency increases due to increasing flow temperature.

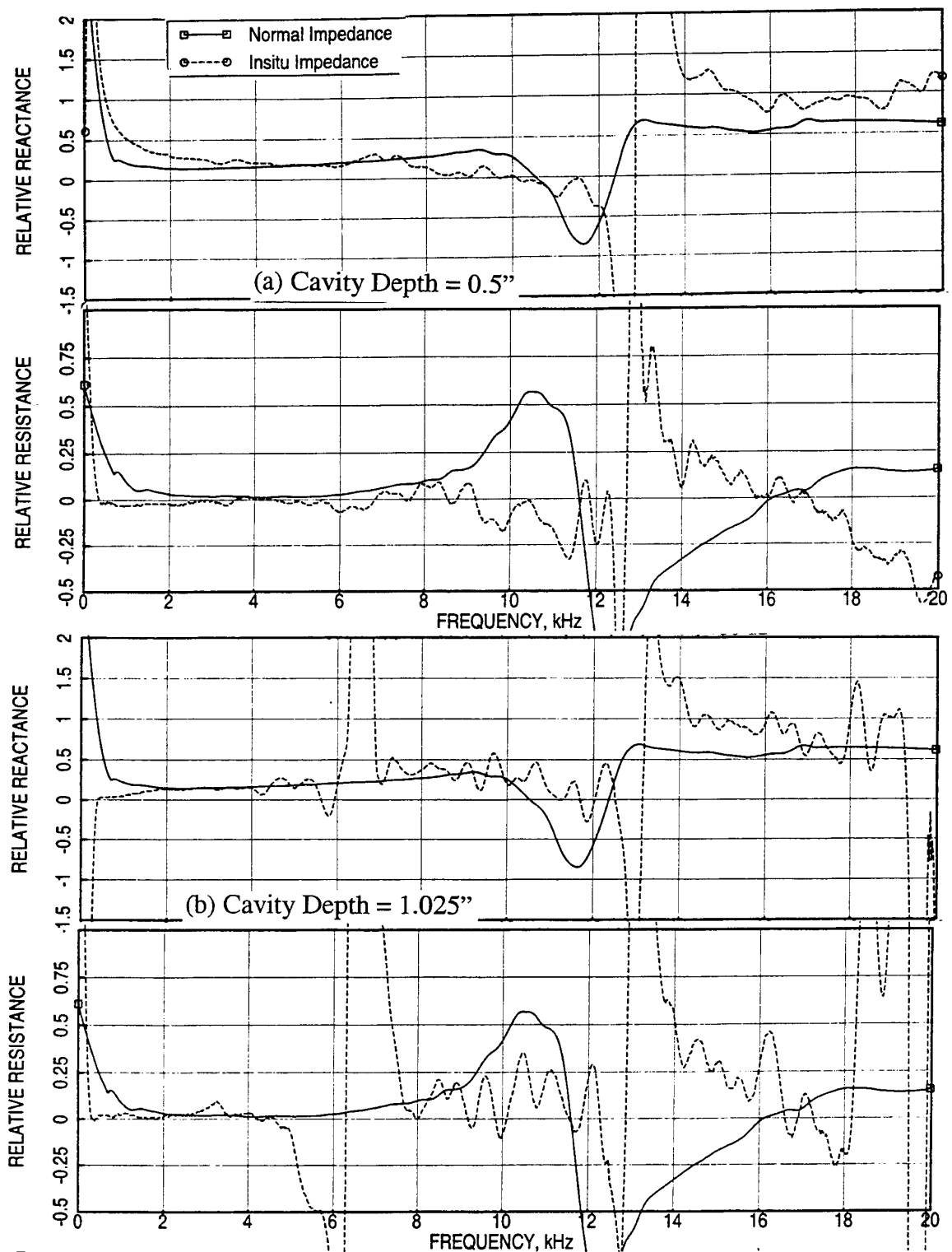


Figure 152. Comparison of relative insitu impedance with relative normal impedance for a 0.5"-deep 100 ppi Silicon Carbide bulk with 30 % porous 0.025"-thick facesheet of 0.04" hole diameter relative to bulk only configuration, insitu cavity depth (a) 0.5" and (b) 1.025".

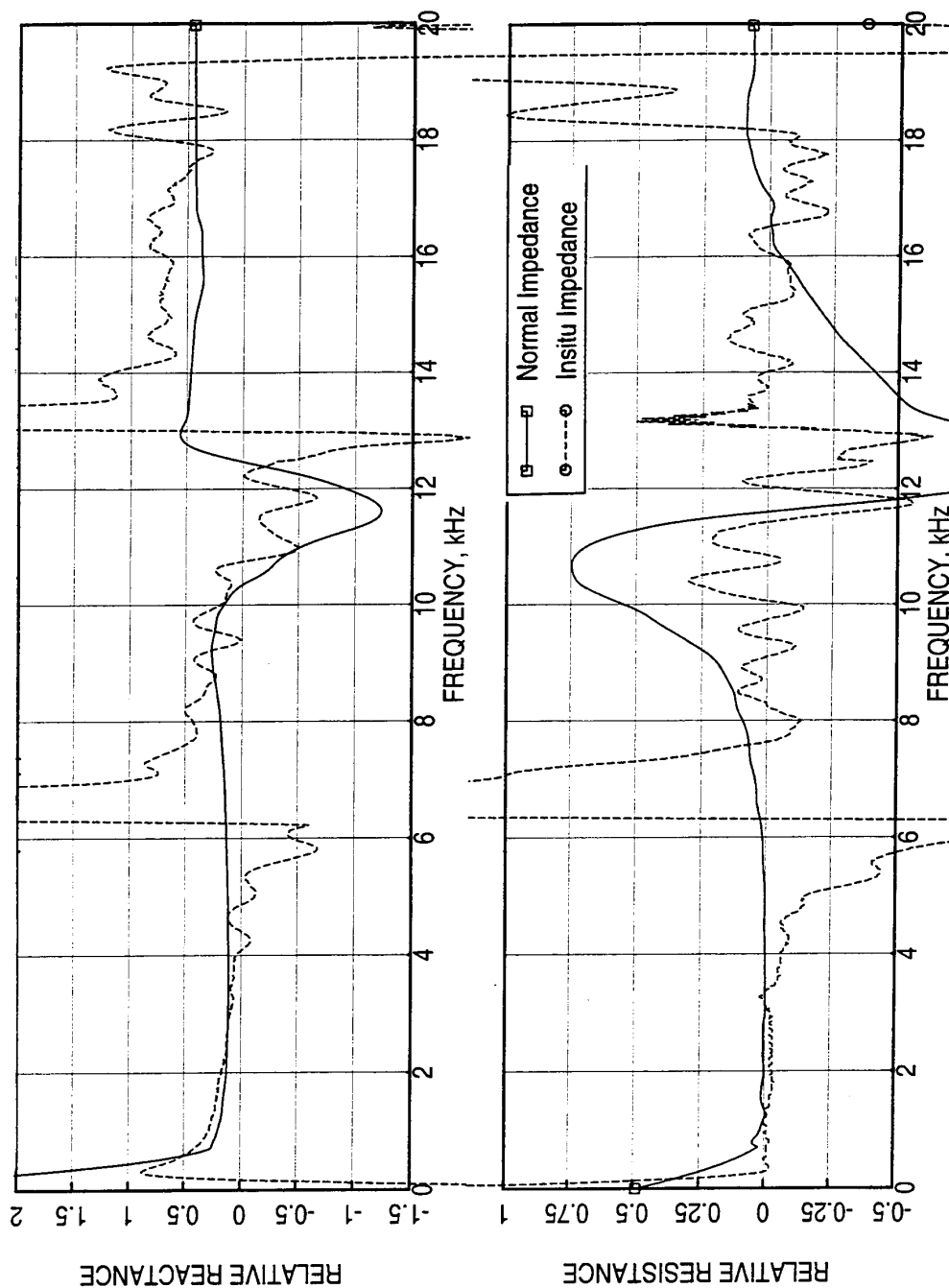


Figure 153. Comparison of relative insitu impedance with relative normal impedance for a 0.5"-deep 100 ppi Silicon Carbide bulk with 40 % porous 0.025"-thick facesheet of 0.04" hole diameter relative to bulk only configuration, insitu cavity depth = 1.025".

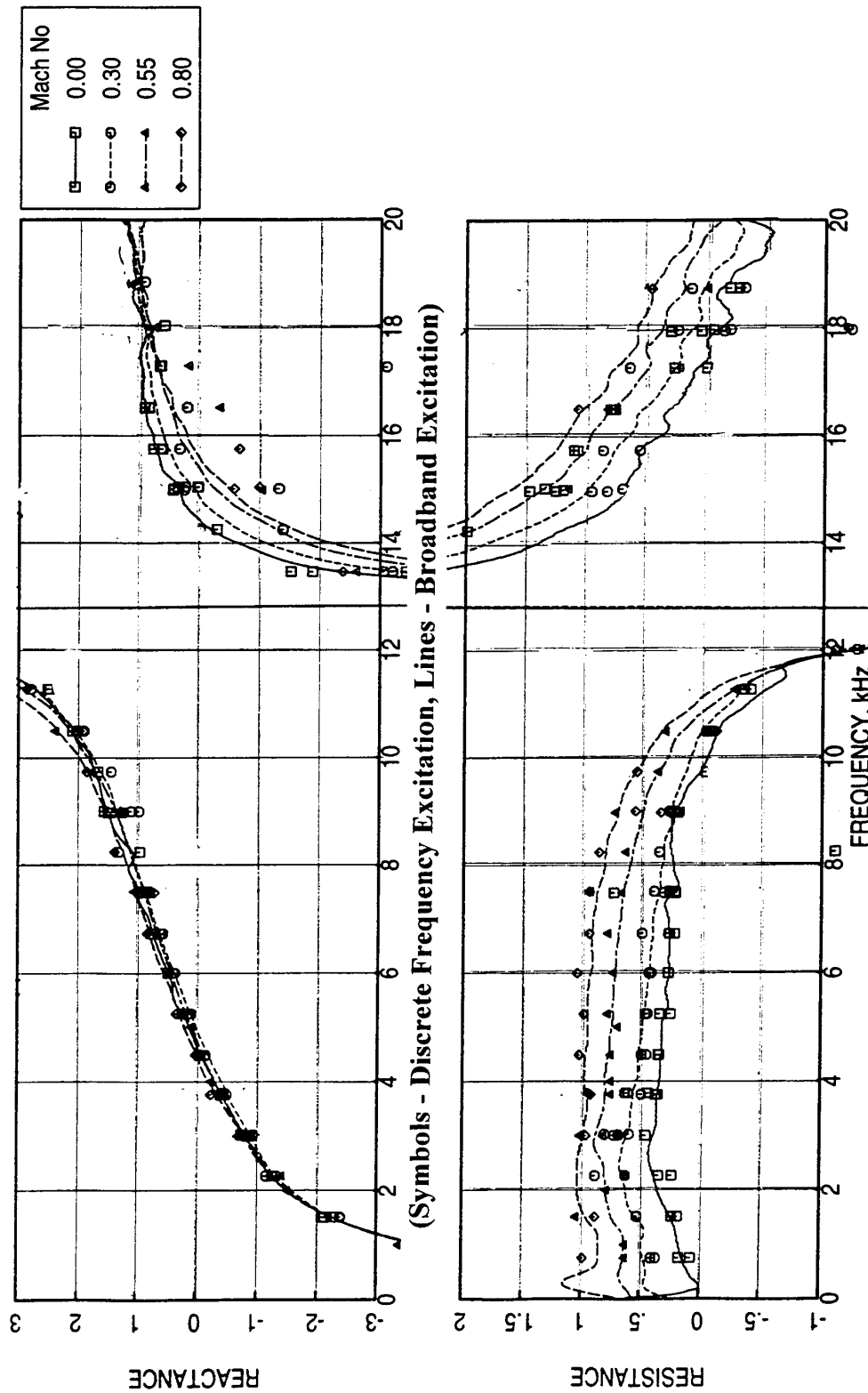


Figure 154. Effect of grazing flow Mach number ( $M$ ) on in situ impedance for a 0.5"-deep 100 ppi Silicon Carbide foam with a 20 % porous facesheet ( $d=0.04"$ ,  $t=0.025"$ ) in a 0.5"-deep cavity,  $T=75^\circ\text{F}$ .



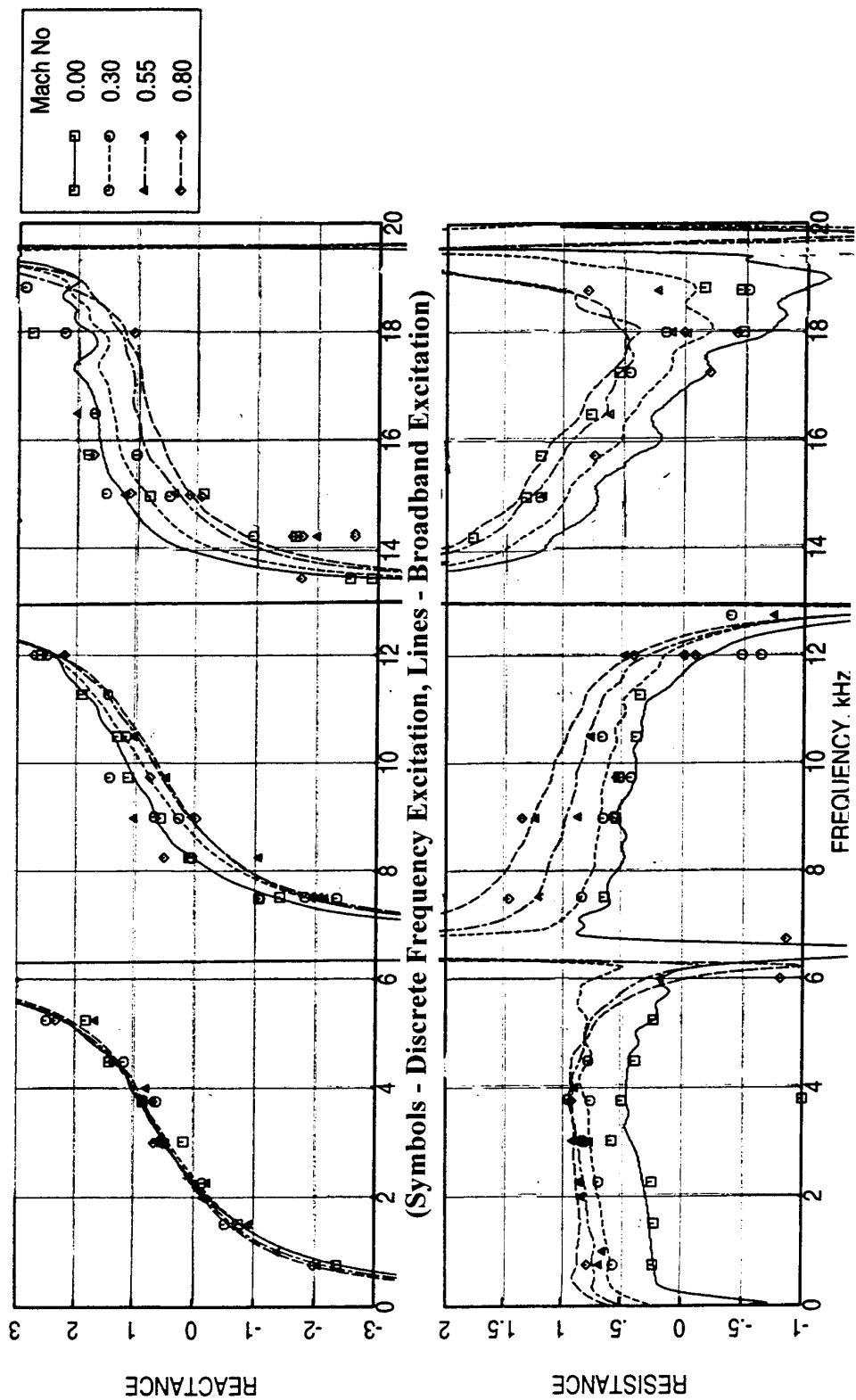


Figure 155. Effect of grazing flow Mach number (M) on in situ impedance for a 0.5"-deep 100 ppi Silicon Carbide foam with a 20 % porous facesheet (d=0.04", t=0.025") in a 1.02"-deep cavity, T=75°F.

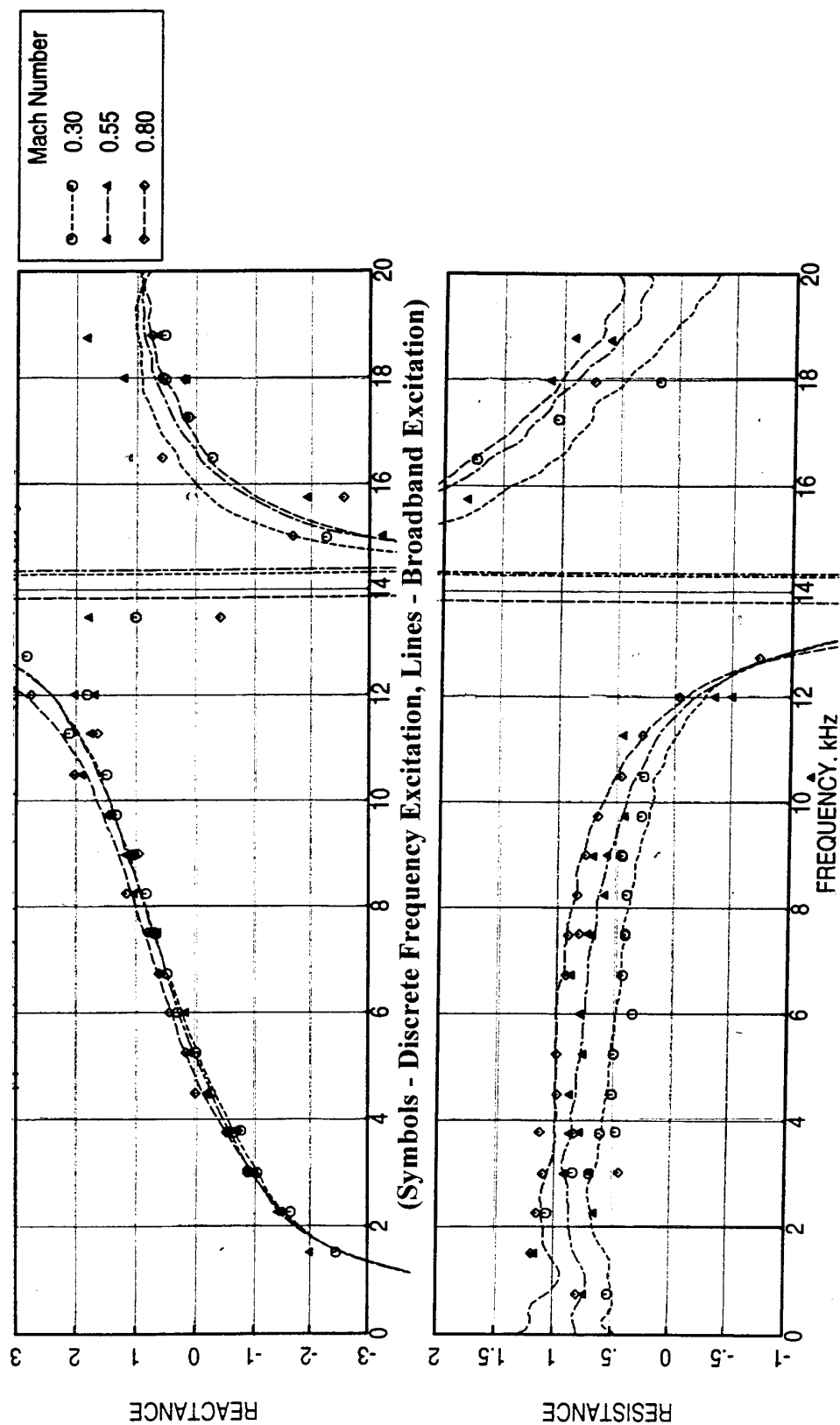


Figure 156. Effect of grazing flow Mach number (M) on in situ impedance for a 0.5"-deep 100 ppi Silicon Carbide foam with a 20 % porous facesheet (d=0.04", t=0.025") in a 0.5"-deep cavity, T=200°F.

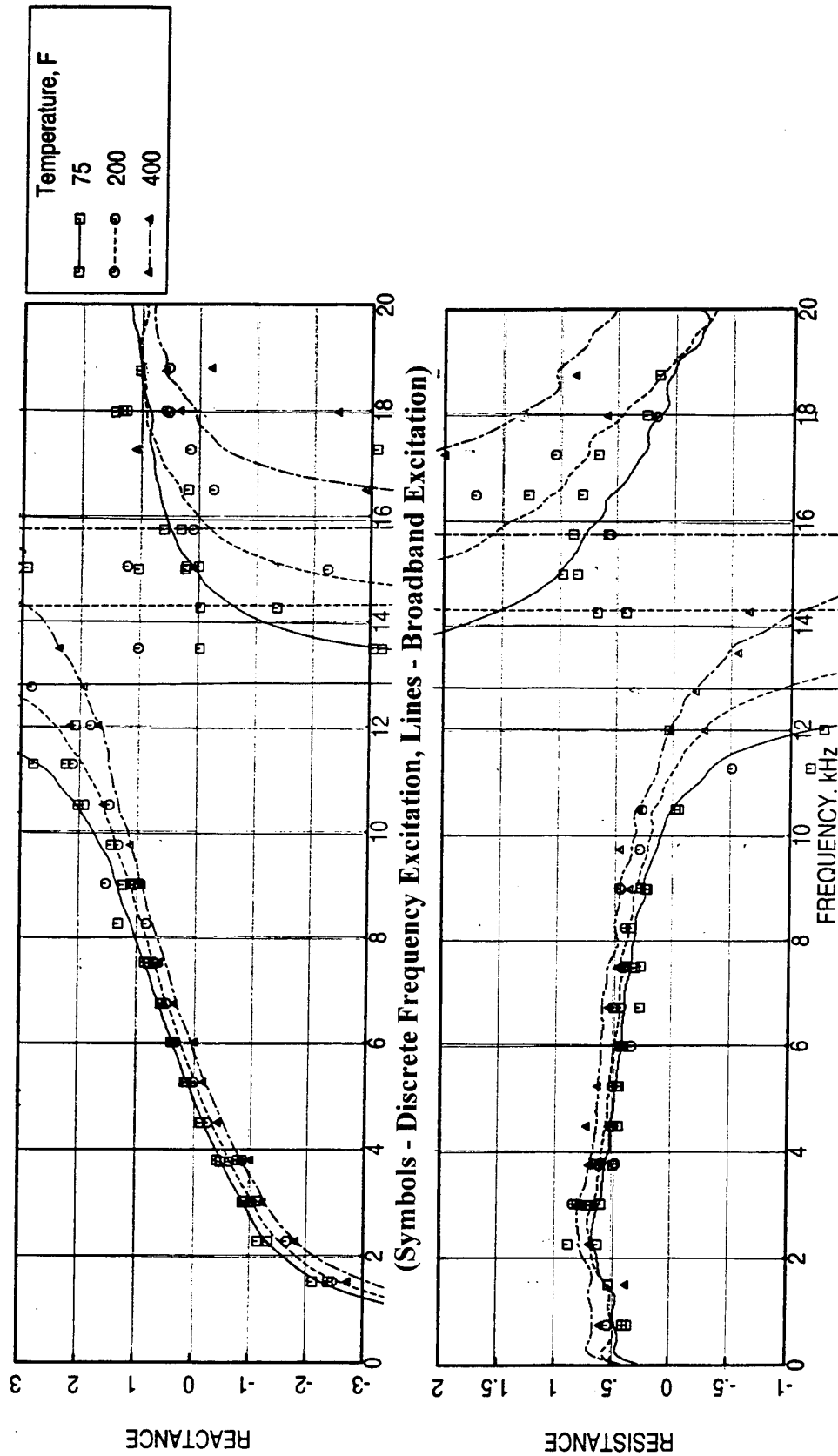


Figure 157. Effect of grazing flow temperature (T) on in situ impedance for a 0.5"-deep 100 ppi Silicon Carbide foam with a 20 % porous facesheet ( $d=0.04"$ ,  $t=0.025"$ ) in a 0.5"-deep cavity,  $M=0.3$ .

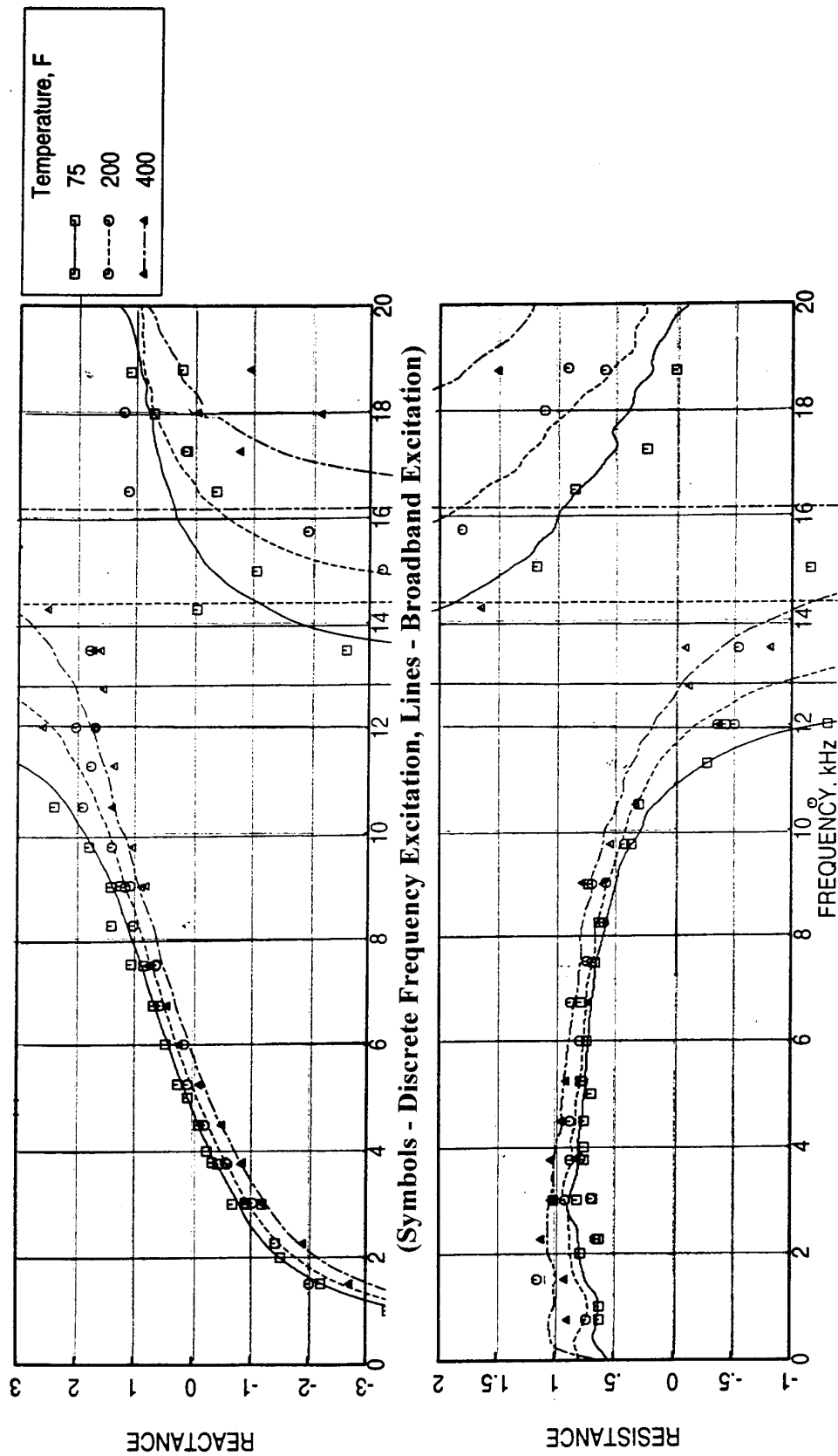


Figure 158. Effect of grazing flow temperature (T) on in situ impedance for a 0.5"-deep 100 ppi Silicon Carbide foam with a 20 % porous facesheet (d=0.04", t=0.025") in a 0.5"-deep cavity, M=0.55.

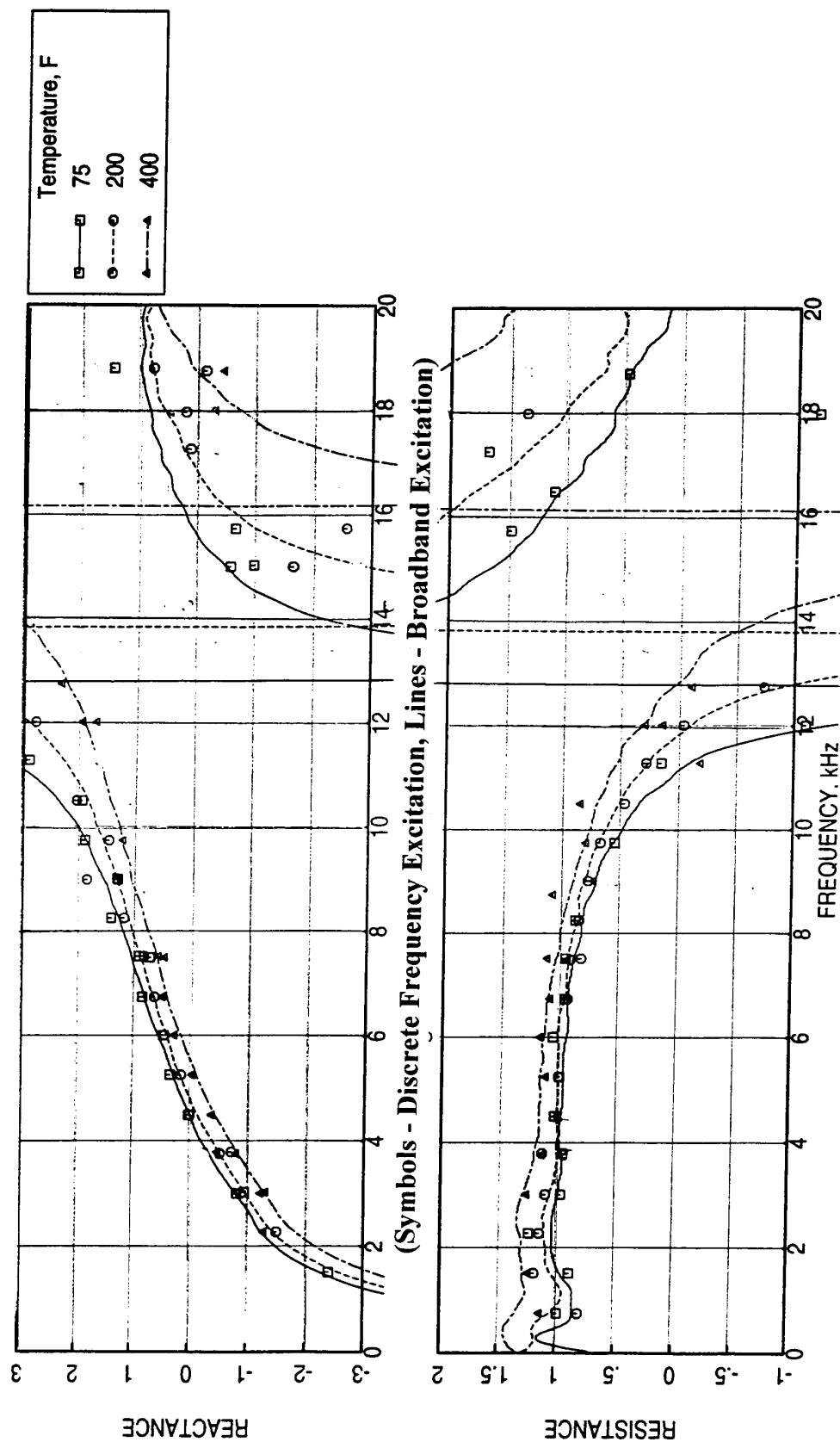


Figure 159. Effect of grazing flow temperature (T) on in situ impedance for a 0.5"-deep 100 ppi Silicon Carbide foam with a 20 % porous facesheet ( $d=0.04"$ ,  $t=0.025"$ ) in a 0.5"-deep cavity,  $M=0.8$ .

Fifteen discrete frequencies are chosen for insitu impedance measurement to cover the entire frequency range of 20 kHz. Data at three harmonics of each frequency are also included in the measurement as long as the harmonics are less than 20 kHz. In this way the steps between two consecutive fundamental frequencies are kept big and thus 15 frequency points could generate data at 35 frequencies. In general, the agreement between broadband and discrete frequency data is good, except for some scattered, mostly for the higher harmonic frequencies. This is further demonstrated in Figures 160 through 162 by plotting broadband and discrete frequency data for one flow condition on each figure. Since, the discrete frequency tests are time consuming and since the broadband data seems to be adequate, it is decided to conduct most of the tests using broadband excitation only.

Another issue involves the broadband excitation in the presence of grazing flow. The grazing flow in the flow duct generates significant amount of broadband noise. The impact of additional broadband excitation is almost negligible as shown in Figures 163 through 166 for different cavities at two grazing flow Mach numbers. Therefore, the broadband excitation is applied only in the absence of grazing flow. The insitu data in the presence of grazing flow is acquired without acoustic excitation.

#### **6.1.4 Processing & Presentation of Insitu Impedance Data for Ambient Temperature:**

**Bulk Absorbers:** Let us consider three configurations of 100 ppi SiC bulk with 0.025"-thick 0.04" hole diameter facesheets of porosities 20%, 30%, and 40% (Config.1-1, Config1-2, and Config1-3) to demonstrate the process to evaluate relative insitu impedance and their use in the evaluation of absolute impedance. Figures 167 through 169 are the insitu impedance at different grazing flow Mach numbers obtained at different cavities for Config1-1. In general, the resistance increases and reactance decreases with increasing Mach number. The results are distorted at and near the anti-resonance frequencies, even though, the relative changes of impedance seem to be reasonable at most frequencies. Thus, the relative impedance for Mach numbers of 0.3, 0.55, and 0.8 are computed relative to the impedance at no flow condition for respective cavities and are shown in Figures 170 through 172. The relative reactance and resistance at frequencies not effected by antiresonances are taken from each cavity for fixed Mach numbers. Unreasonable data points are also excluded from these data sets. A second-degree polynomial is used to least square fit all the reactance and resistance data for fixed Mach numbers. Also, an average of each data set at individual frequencies is calculated and used for least square curve fit. The process and the results for Config1-1 are shown in Figures 173 and 174 for relative reactance and resistance, respectively.

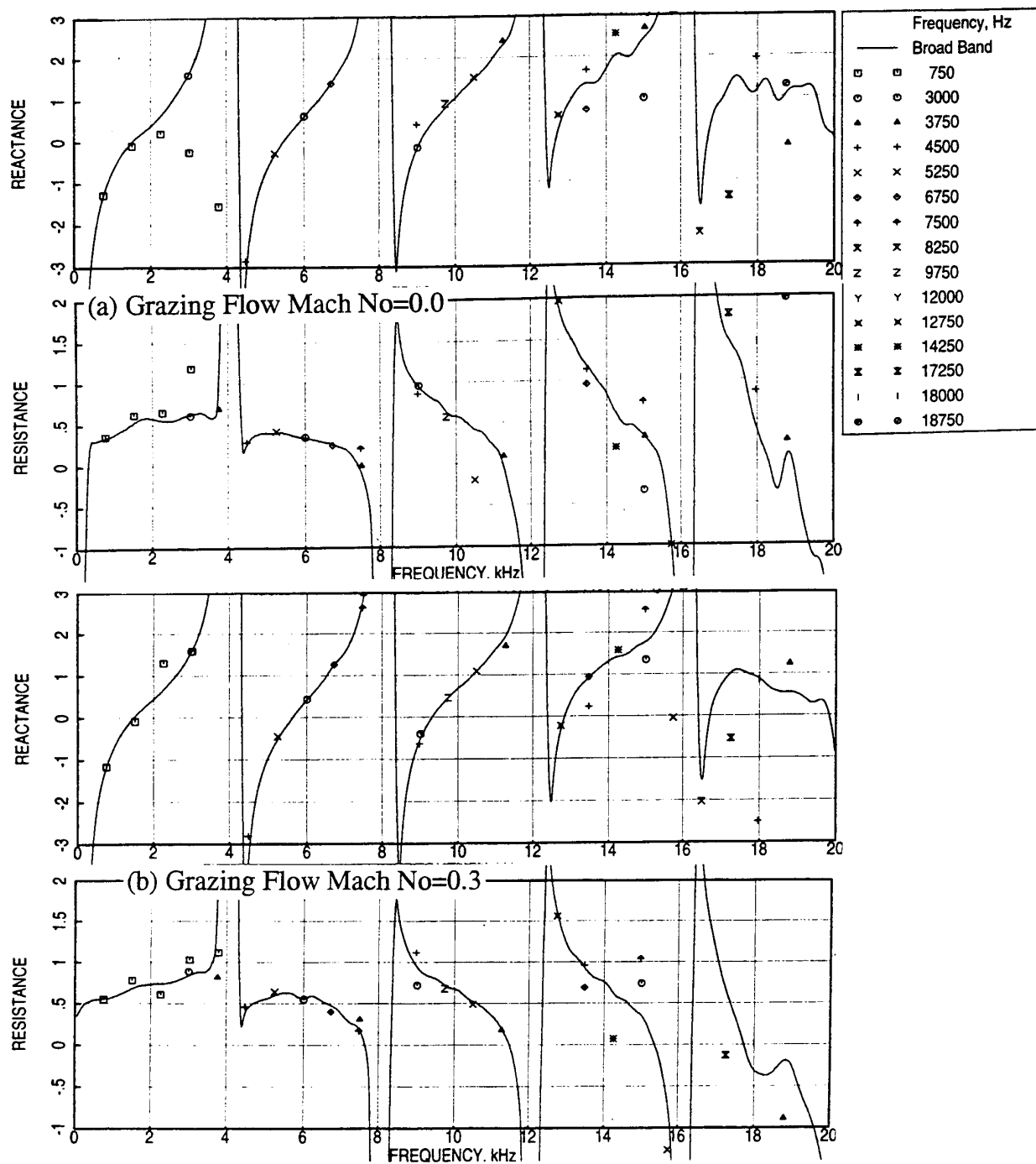


Figure 160. Comparison of insitu impedance due to broadband excitation with those due to discrete frequency excitation for a 0.5''-deep 100 ppi Silicon Carbide foam with a 20 % porous facesheet ( $d=0.04''$ ,  $t=0.025''$ ) in a 1.656''-deep cavity (#2),  $T=75^{\circ}\text{F}$ .

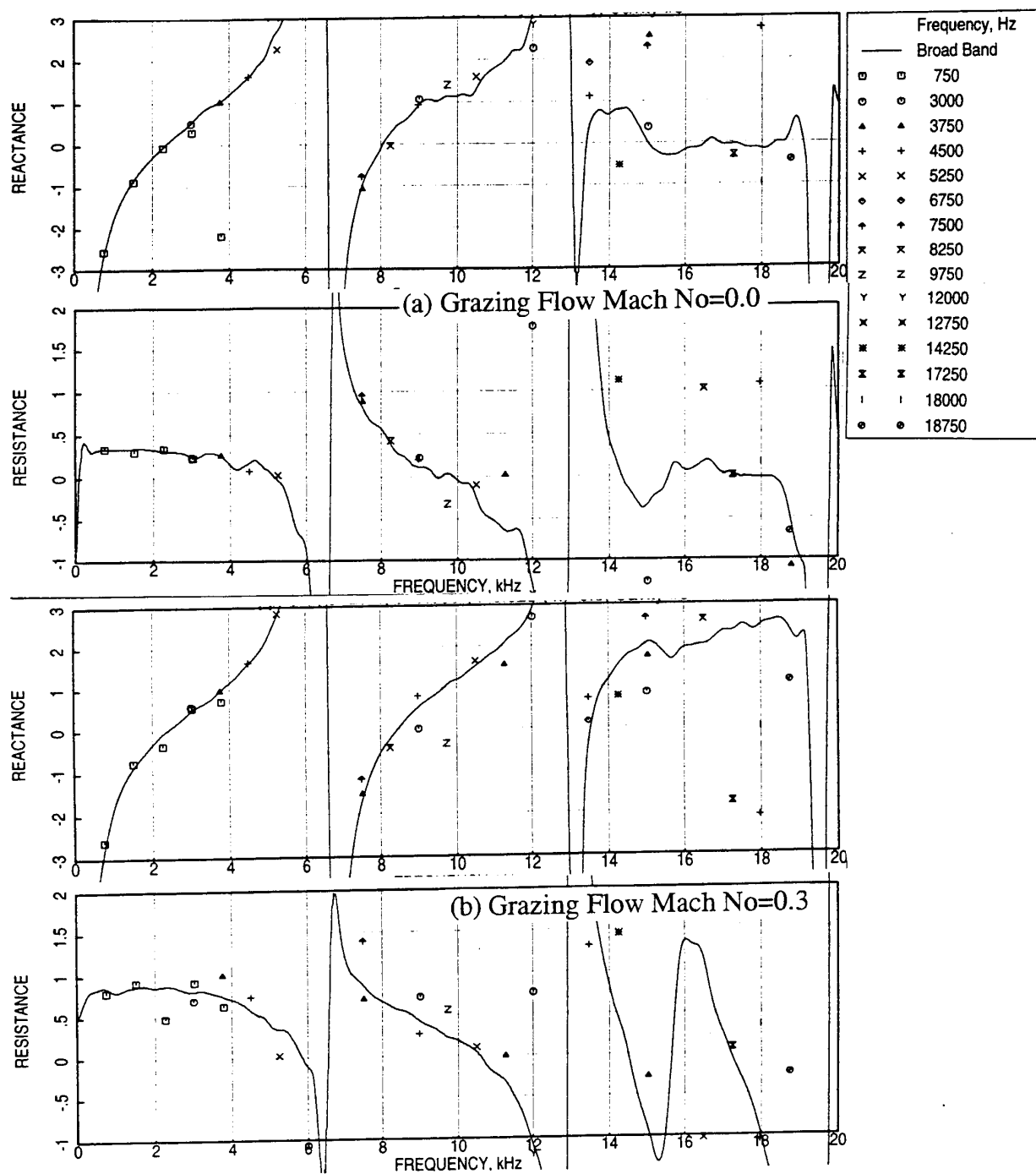


Figure 161. Comparison of in situ impedance due to broadband excitation with those due to discrete frequency excitation for a 0.5''-deep 100 ppi Silicon Carbide foam with a 20 % porous facesheet (d=0.04'', t=0.025'') in a 1.025''-deep cavity (#3), T=75°F.



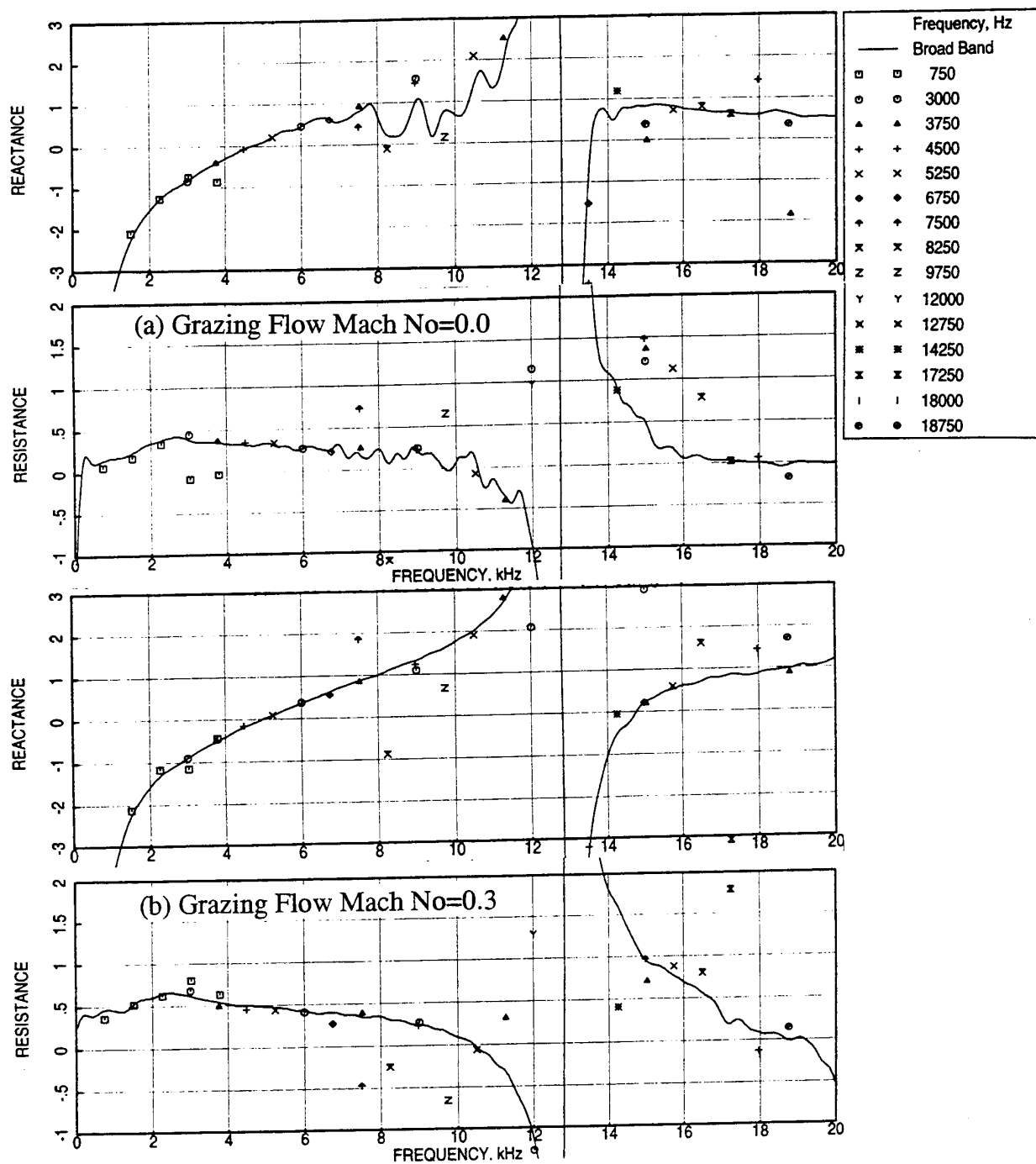


Figure 162. Comparison of in situ impedance due to broadband excitation with those due to discrete frequency excitation for a 0.5"-deep 100 ppi Silicon Carbide foam with a 20 % porous facesheet (d=0.04", t=0.025") in a 0.504"-deep cavity (#5), T=75°F.

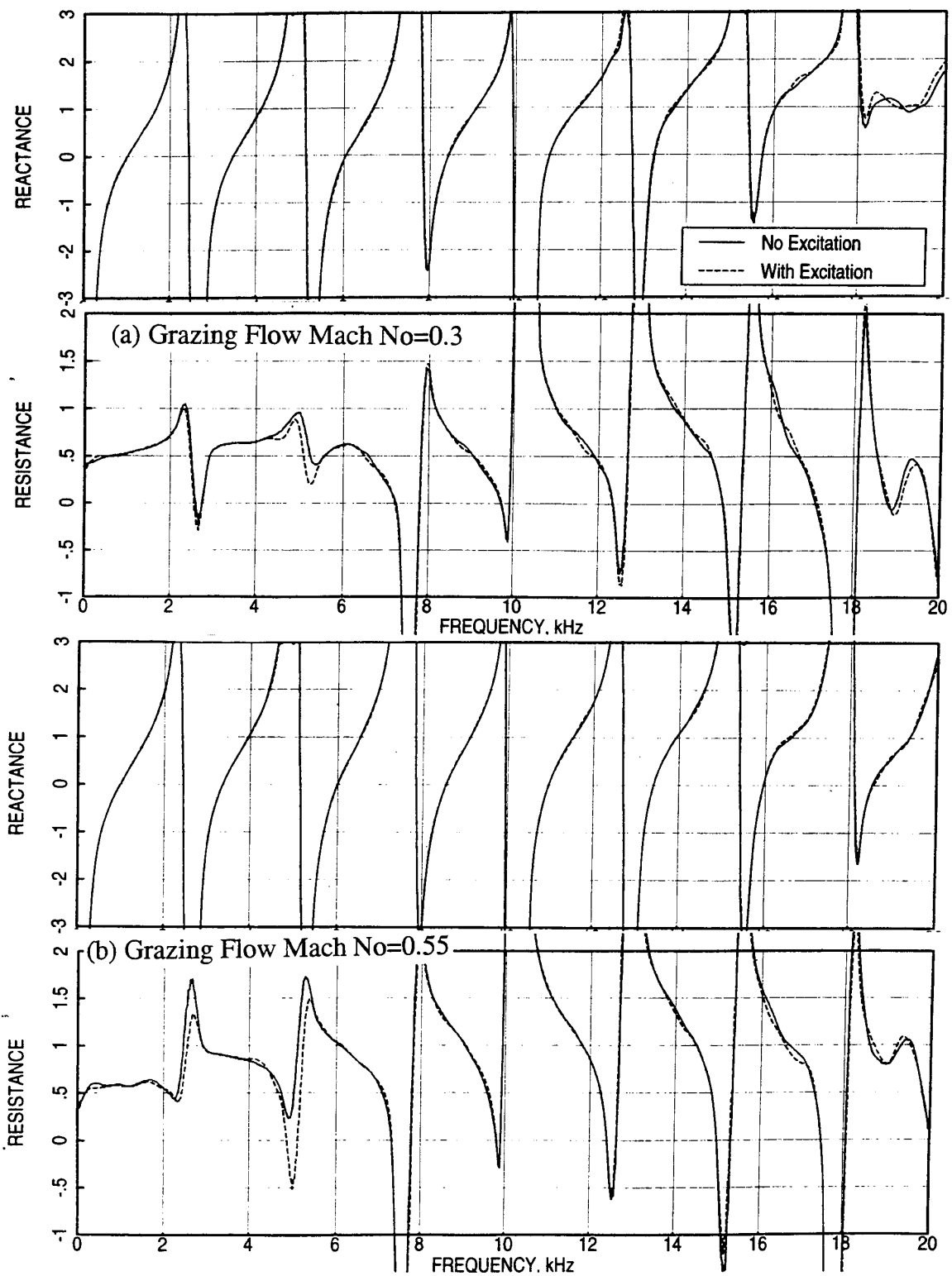


Figure 163. Comparison of in situ impedance between with and without broadband excitation for a 0.5''-deep 100 ppi Silicon Carbide foam with a 20 % porous facesheet (d=0.04'', t=0.025'') in a 2.64''-deep cavity (#1), T=75°F.

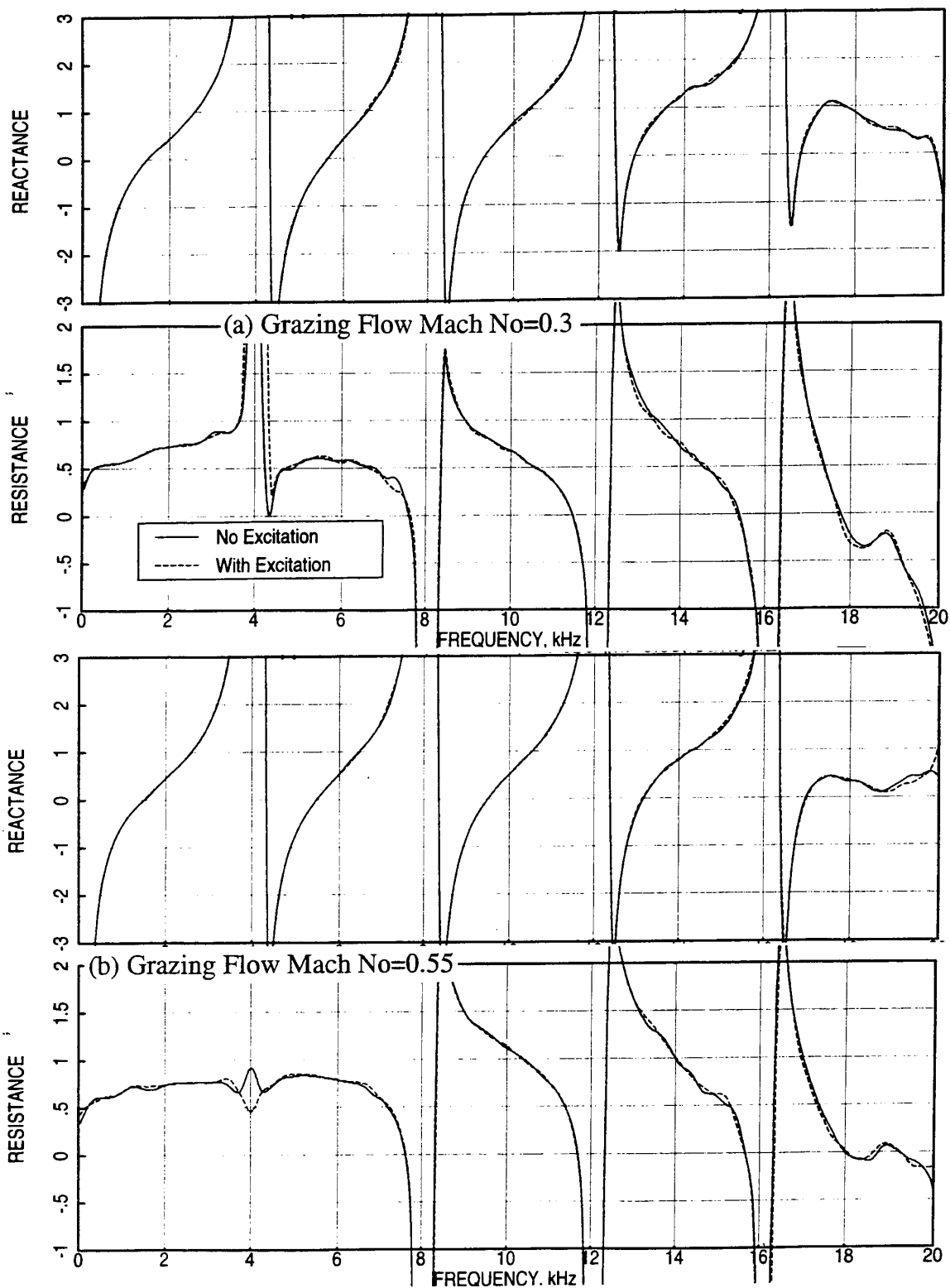


Figure 164. Comparison of in situ impedance between with and without broadband excitation for a 0.5"-deep 100 ppi Silicon Carbide foam with a 20 % porous facesheet ( $d=0.04''$ ,  $t=0.025''$ ) in a 1.656"-deep cavity (#2),  $T=75^{\circ}\text{F}$ .

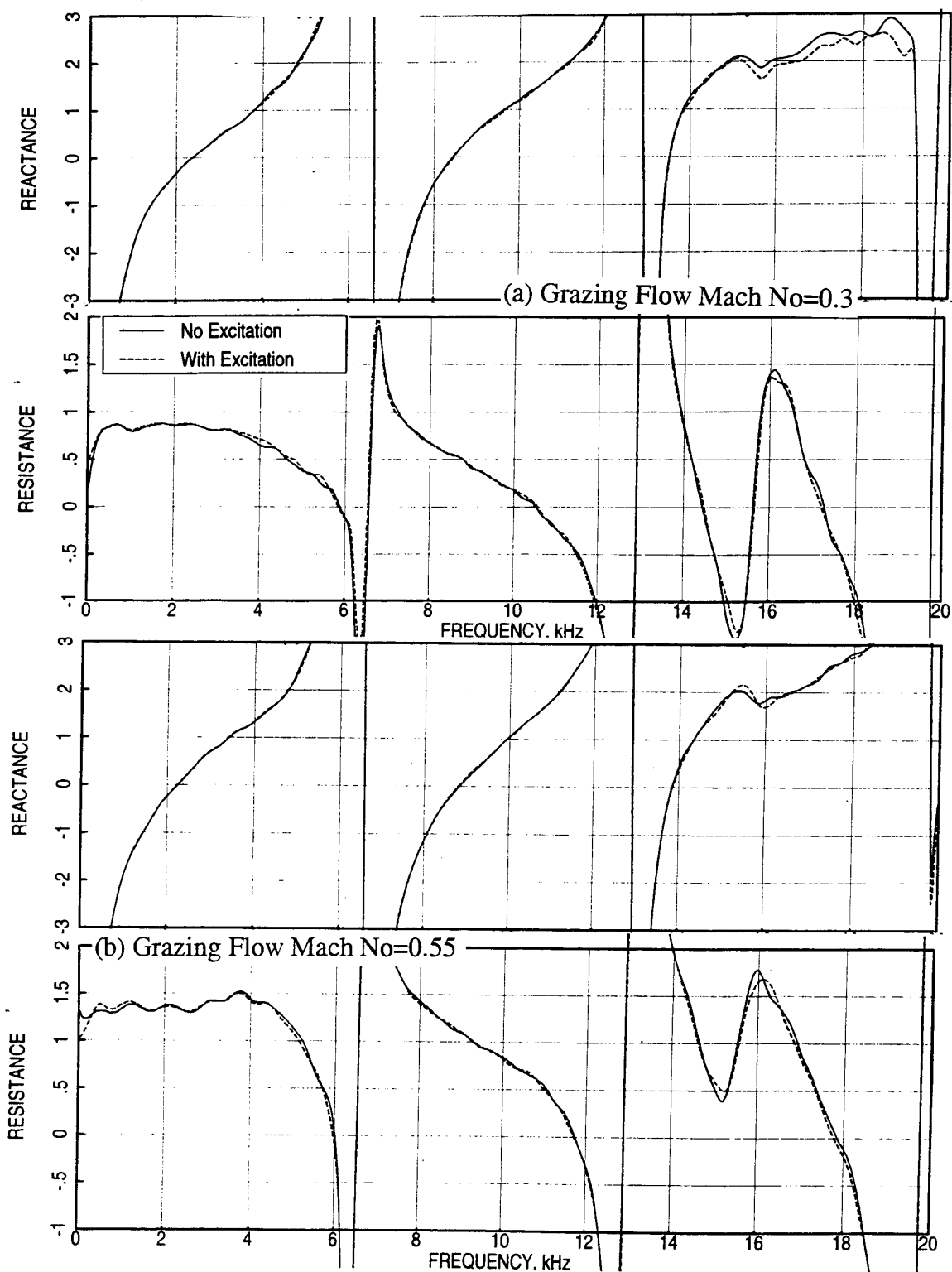


Figure 165. Comparison of in situ impedance between with and without broadband excitation for a 0.5''-deep 100 ppi Silicon Carbide foam with a 20 % porous facesheet ( $d=0.04''$ ,  $t=0.025''$ ) in a 1.025''-deep cavity (#3),  $T=75^{\circ}\text{F}$ .

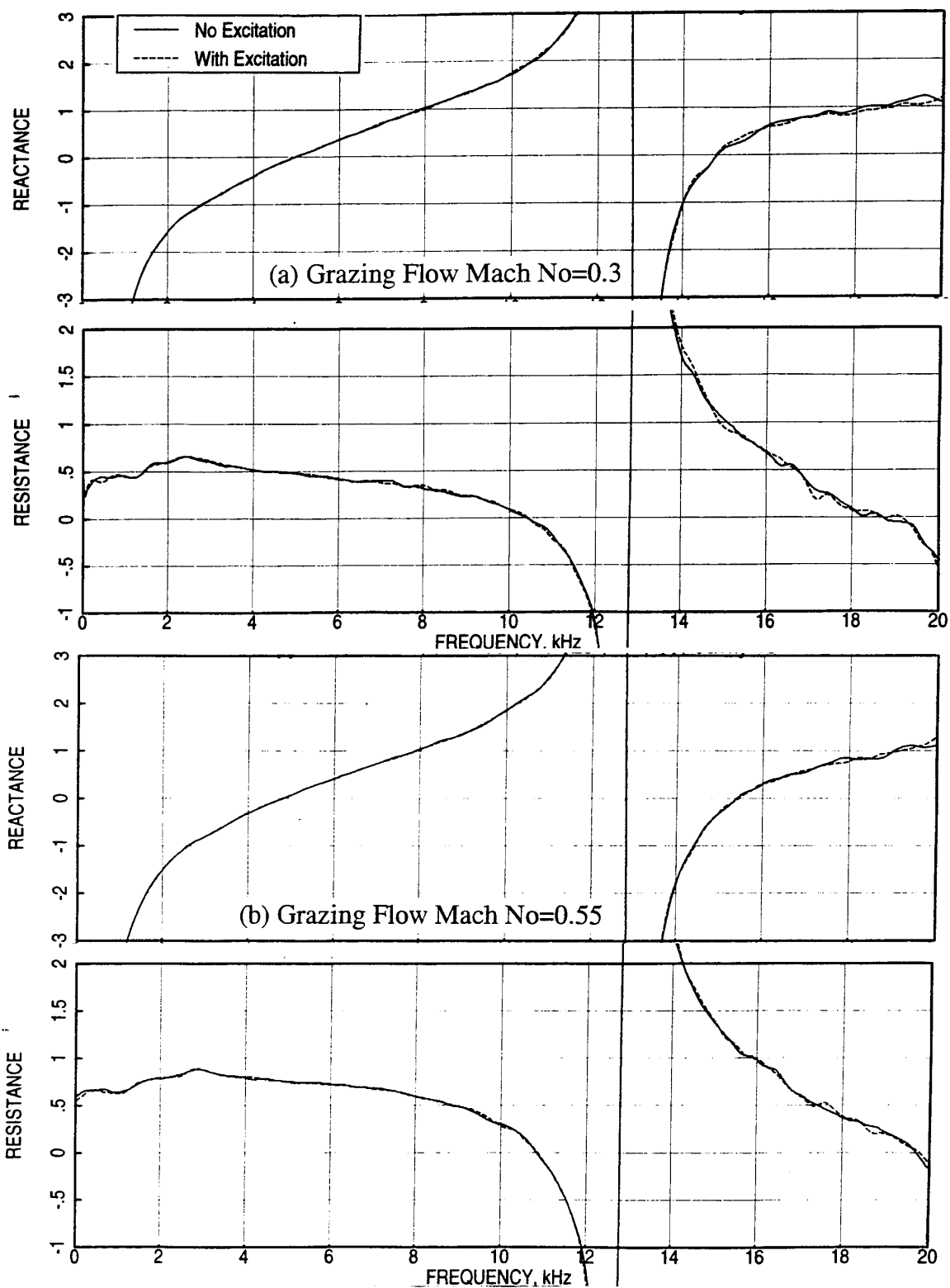


Figure 166. Comparison of insitu impedance between with and without broadband excitation for a 0.5''-deep 100 ppi Silicon Carbide foam with a 20 % porous facesheet (d=0.04'', t=0.025'') in a 0.504''-deep cavity (#5), T=75°F.

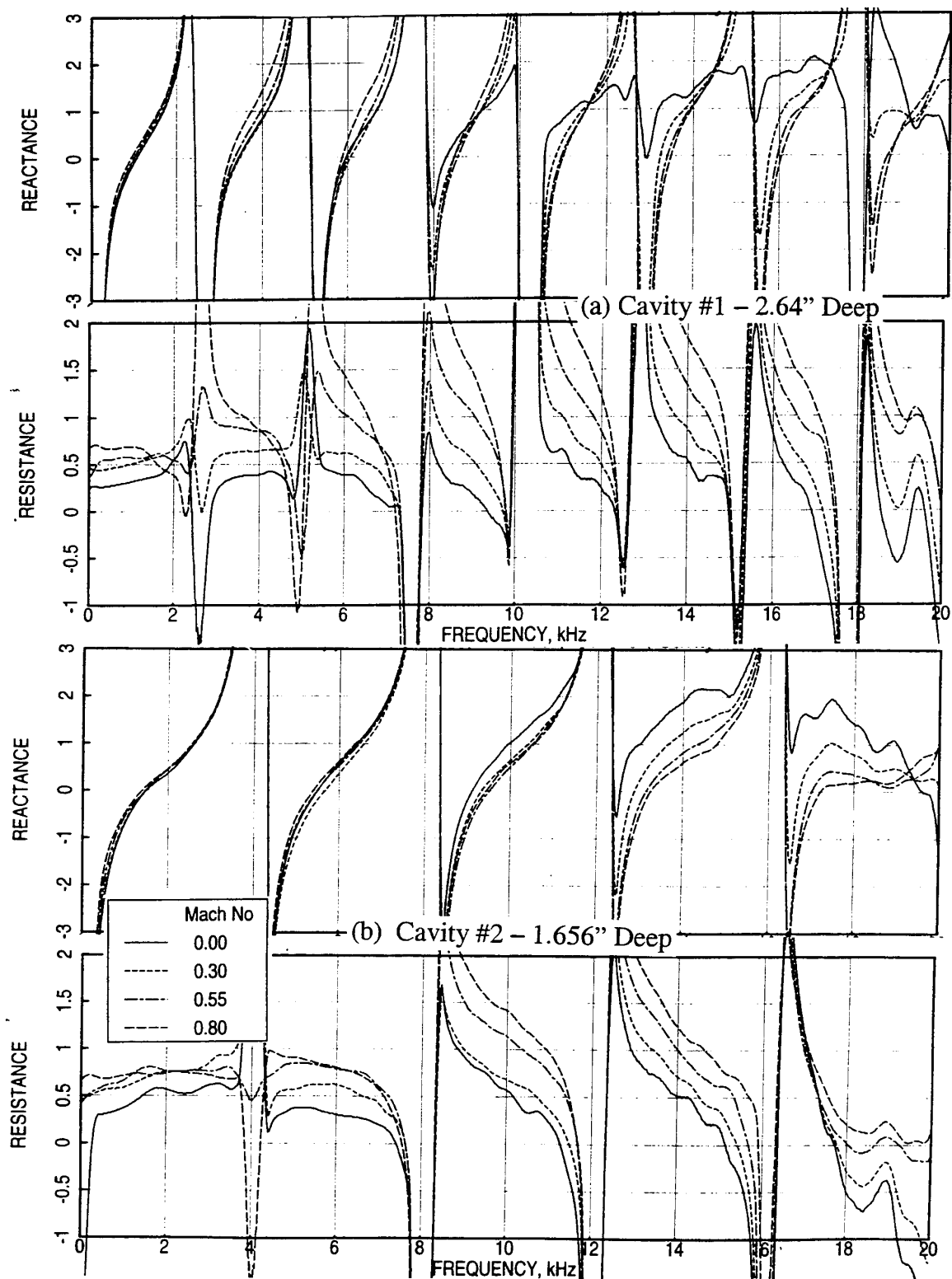


Figure 167. Effect of grazing flow Mach number ( $M$ ) on insitu impedance for a 0.5"-deep 100 ppi Silicon Carbide foam with a 20 % porous facesheet ( $d=0.04''$ ,  $t=0.025''$ ) in cavities #1 and #2 of different depths,  $T=75^{\circ}\text{F}$ .

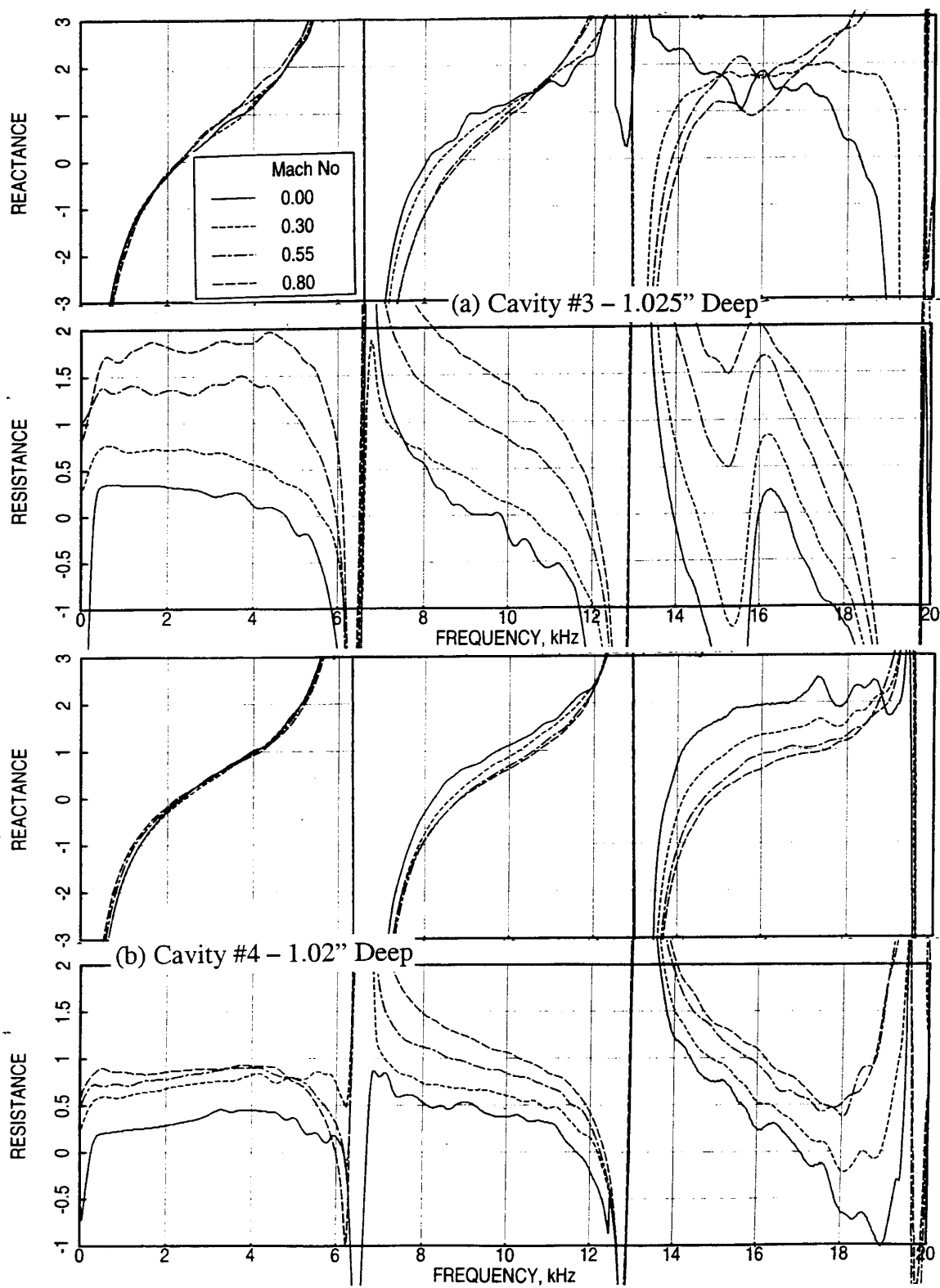


Figure 168. Effect of grazing flow Mach number ( $M$ ) on insitu impedance for a 0.5''-deep 100 ppi Silicon Carbide foam with a 20 % porous facesheet ( $d=0.04''$ ,  $t=0.025''$ ) in cavities #3 and #4 of different depths,  $T=75^{\circ}\text{F}$ .

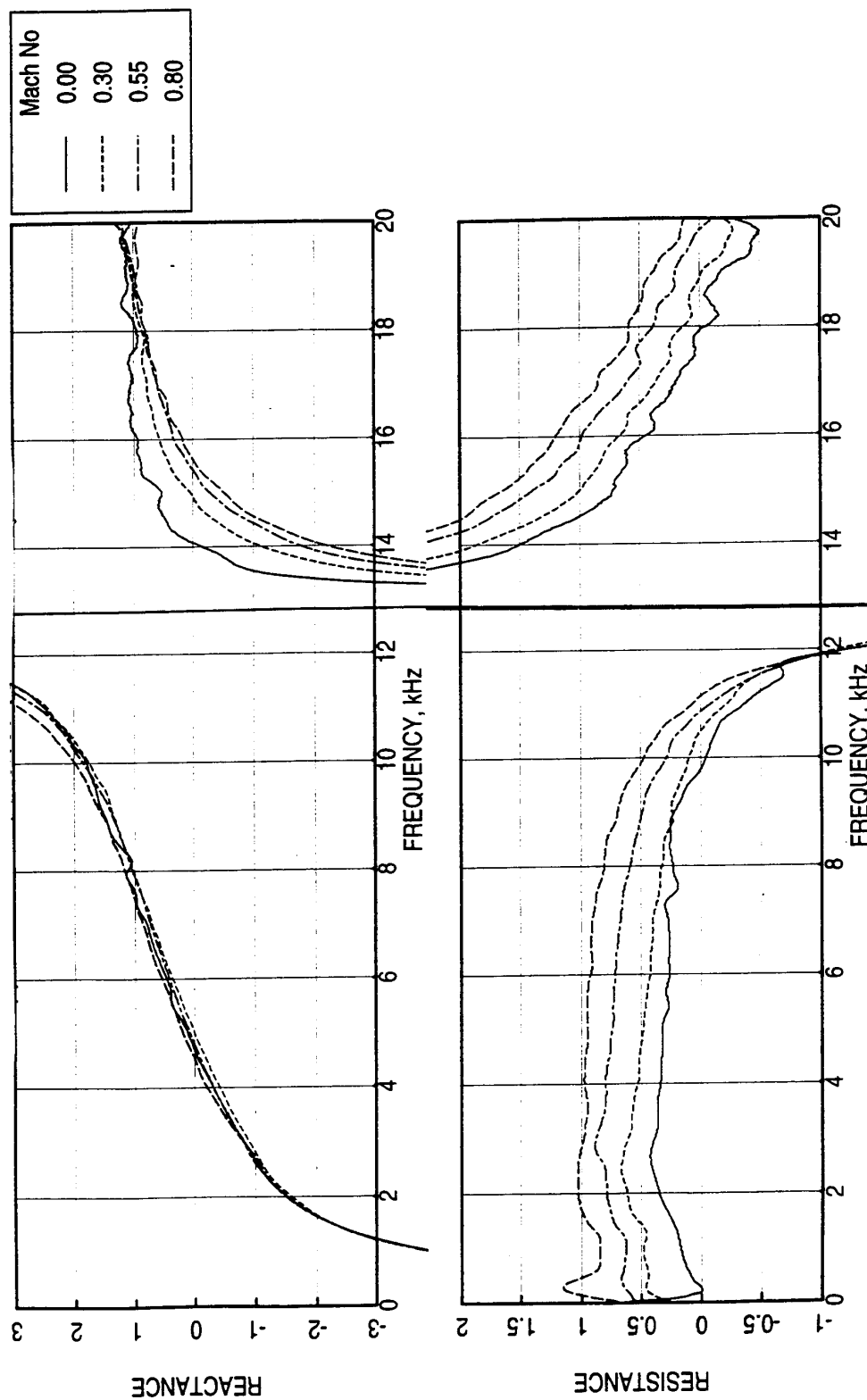


Figure 169. Effect of grazing flow Mach number (M) on in situ impedance for a 0.5"-deep 100 ppi Silicon Carbide foam with a 20 % porous facesheet (d=0.04", t=0.025") in cavity #5 of depth 0.504", T=75°F.



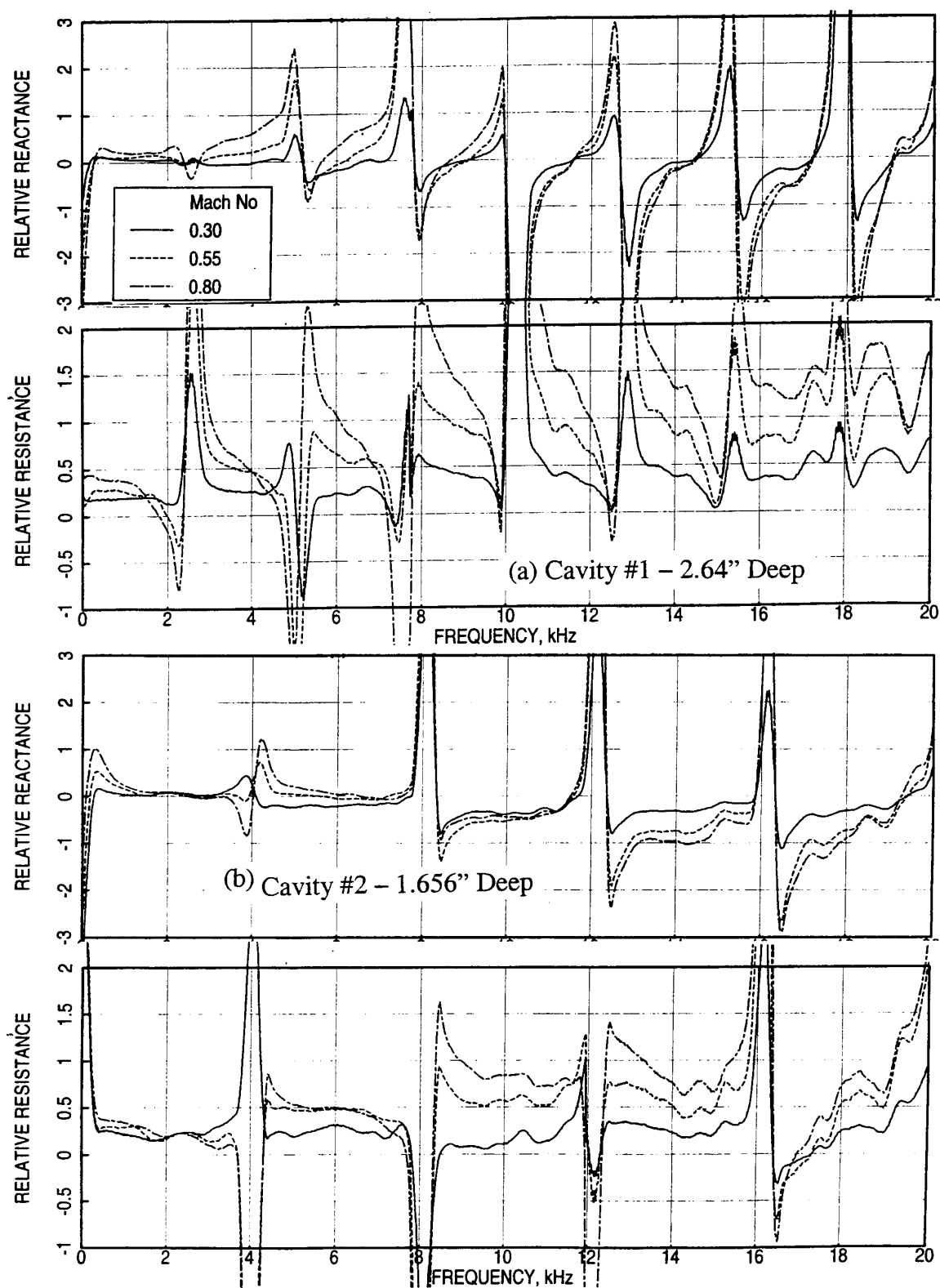


Figure 170. Effect of grazing flow Mach number ( $M$ ) on relative insitu impedance for a 0.5"-deep 100 ppi Silicon Carbide foam with a 20 % porous facesheet ( $d=0.04''$ ,  $t=0.025''$ ) in cavities #1 and #2 of different depths,  $T=75^\circ\text{F}$ .

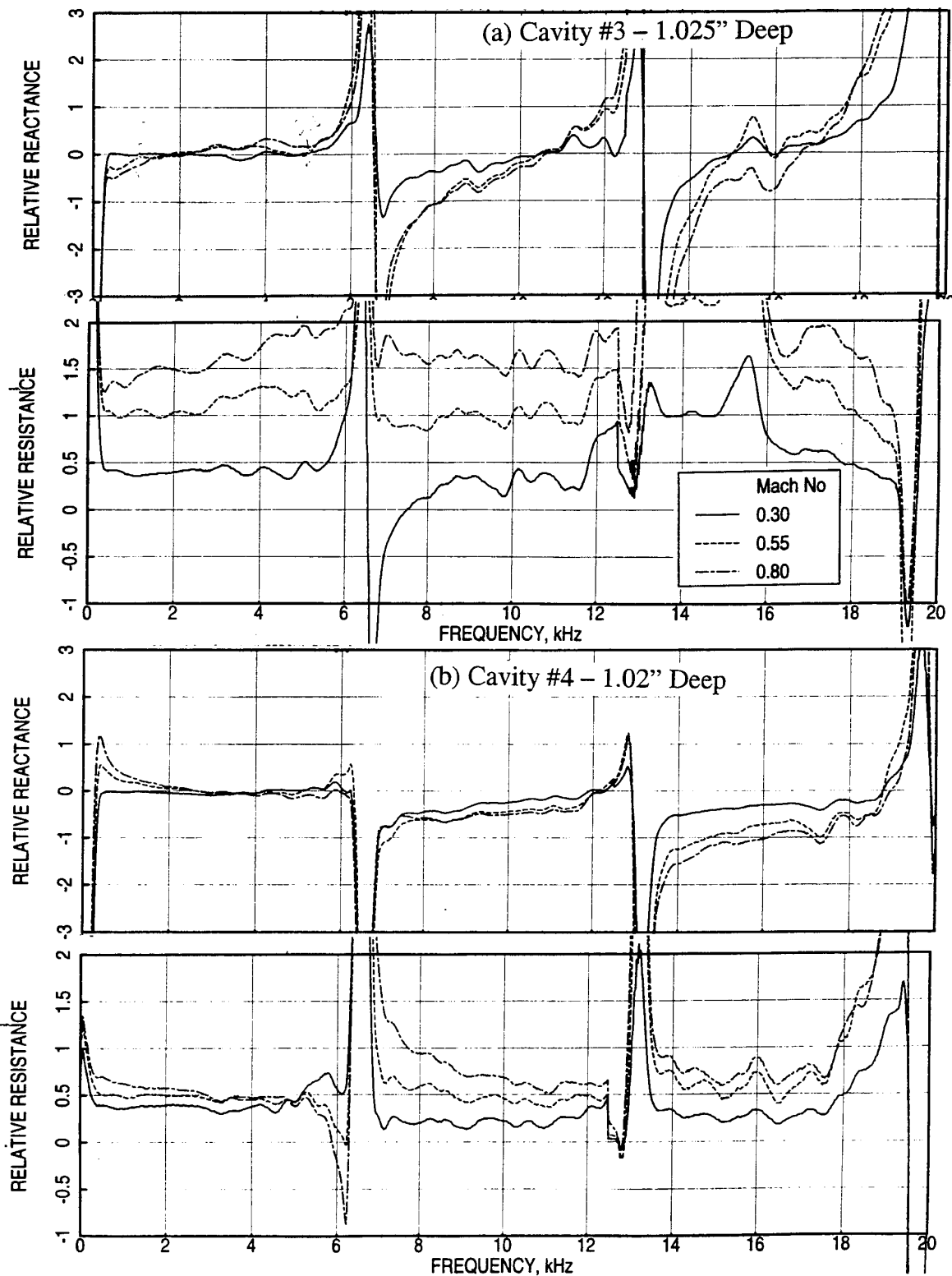


Figure 171. Effect of grazing flow Mach number ( $M$ ) on relative insitu impedance for a 0.5"-deep 100 ppi Silicon Carbide foam with a 20 % porous facesheet ( $d=0.04"$ ,  $t=0.025"$ ) in cavities #3 and #4 of different depths,  $T=75^{\circ}\text{F}$ .

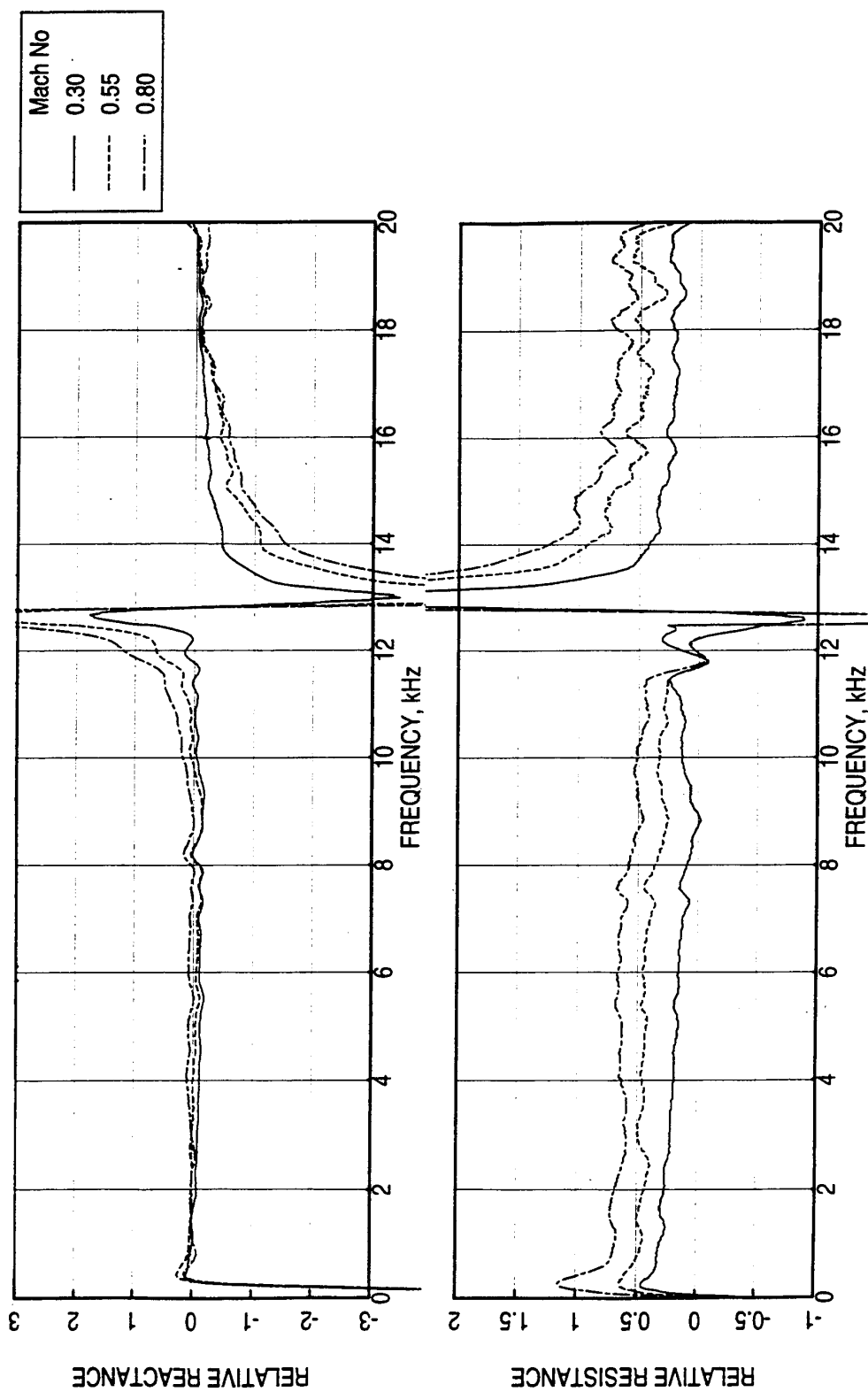


Figure 172. Effect of grazing flow Mach number (M) on relative in situ impedance for a 0.5"-deep 100 ppi Silicon Carbide foam with a 20 % porous facesheet (d=0.04", t=0.025") in cavity #5 of depth 0.504", T=75°F.

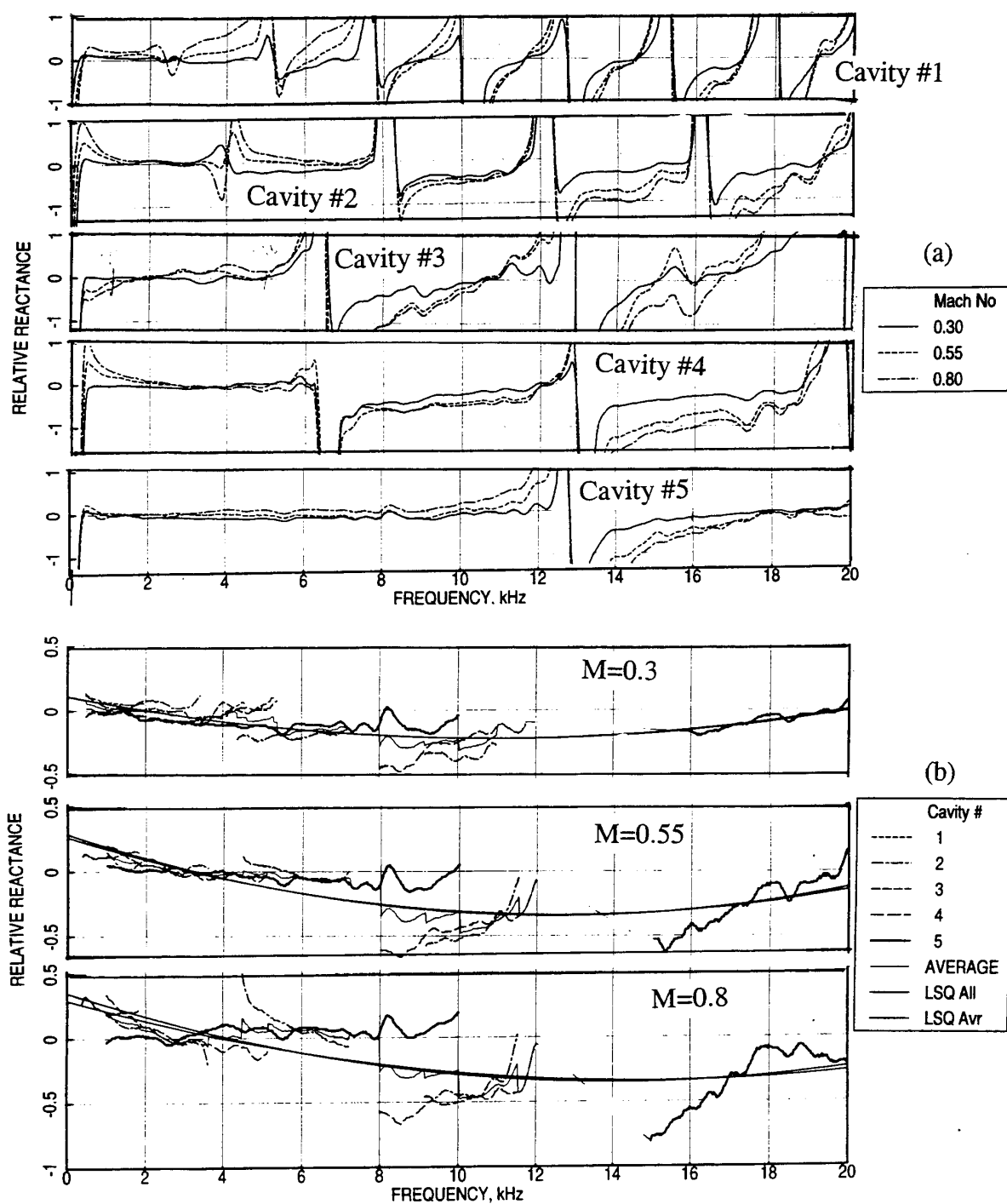


Figure 173. A least square fitting process to evaluate relative reactance using measured data from all 5 tray cavities for a 0.5"-deep 100 ppi Silicon Carbide foam with a 20 % porous facesheet ( $d=0.04''$ ,  $t=0.025''$ ),  $T=75^{\circ}\text{F}$ .

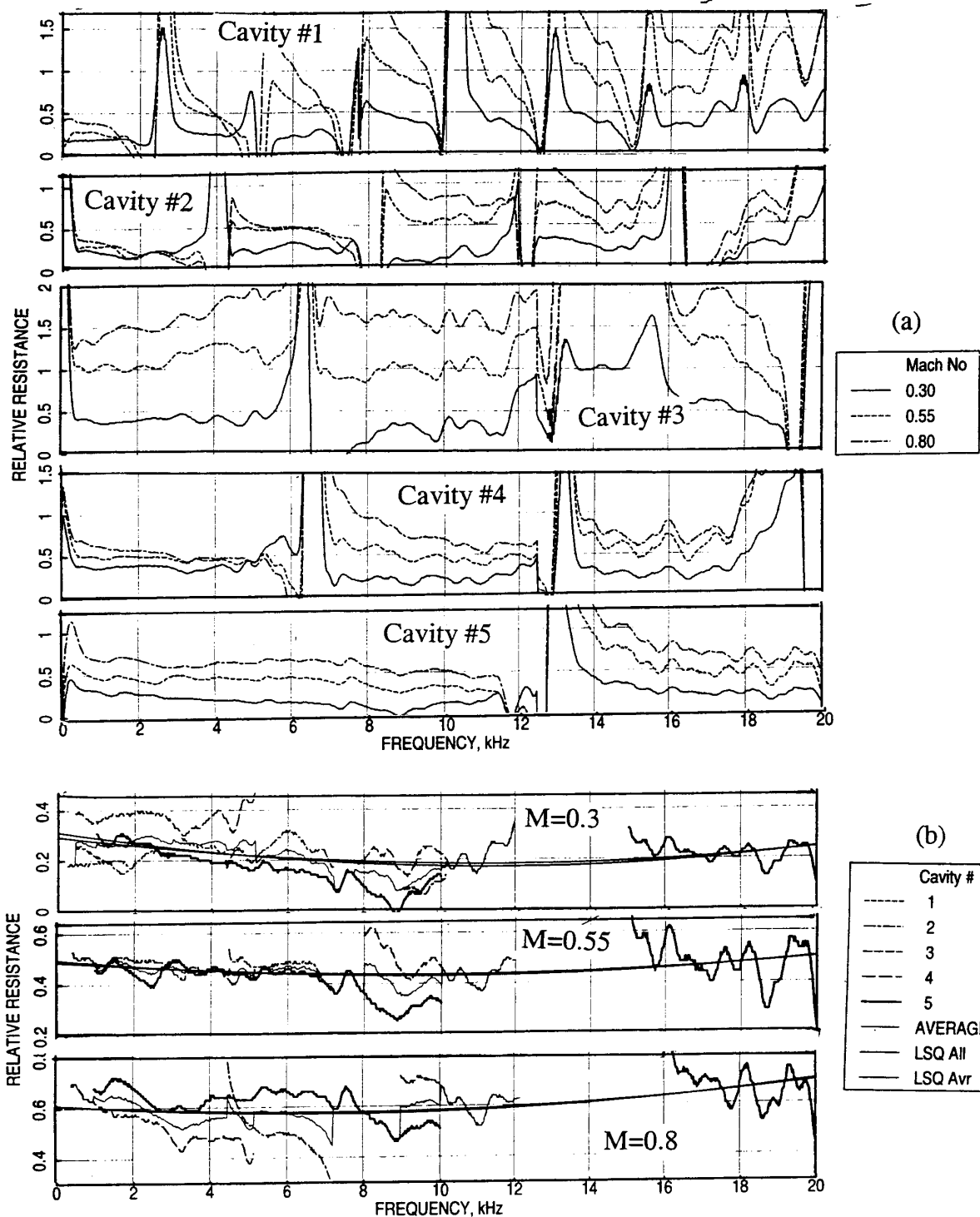


Figure 174. A least square fitting process to evaluate relative resistance using measured data from all 5 tray cavities for a 0.5"-deep 100 ppi Silicon Carbide foam with a 20 % porous facesheet ( $d=0.04''$ ,  $t=0.025''$ ),  $T=75^{\circ}\text{F}$ .

The data used for relative impedance evaluation exhibits some amount of scatter, especially at higher frequencies. There are several reasons for such data scatter. First of all the cavity cross sectional areas covering the facesheet is relatively small. Depending on the position of these cavities the porosity of the portion of the facesheet contained in the individual cavities may be different. The small bulk plugs inserted in the individual cavities may have slight different characteristics and dimensions due to imperfection in manufacturing and installment process. Since, the cavities are located at different axial locations in the flow duct the acoustic and boundary layer characteristics would be different. All these factors are responsible for the scatter observed in the data. However, the use of data from all cavities minimizes the error and gives an average level.

The curve fitted relative impedance results for Config1-1 are shown in Figure 175. The least square data using all data points and using the average of all data are included in this plot. While the trends with respect to grazing flow Mach number are similar for both sets of results, the levels are slightly different. Similar results for config1-2 and Config1-3 are shown in Figures 176 and 177, respectively. Utilizing the least square results (least square fit of all data) of Config1-1, Config1-2, and Config1-3 the effect of facesheet porosity on relative impedance at different grazing flow Mach numbers is evaluated and shown in Figure 178.

The relative impedance can be utilized to construct the absolute normal impedance of liner configurations utilizing the measured normal impedance data without any grazing flow. For example, measured normal impedance for a 0.5"-deep 100 ppi SiC with facesheets of different porosities ( $t=0.025''$  and  $d=0.04''$ ) is shown in Figure 179. Utilizing these results and the evaluated relative impedance at different grazing flow Mach numbers the absolute normal impedance in the presence of grazing flow are calculated and presented in Figures 180 through 185. The effect of grazing flow Mach numbers for 0.5"-deep 100 ppi SiC for different facesheets is shown in Figures 180 through 182. For each configuration the resistance increases and reactance decreases with increasing flow Mach number. The effect of facesheet porosity on normal impedance at different flow Mach numbers is shown in Figures 183 through 185. Again, the resistance and reactance, both, increase with decreasing facesheet porosity.

The facesheet and a small layer of bulk underneath most likely cause the grazing flow effects. By increasing the bulk depth the grazing flow effects on impedance may not alter significantly. Thus, assuming that the grazing flow effects on insitu impedance is independent of bulk depth the same relative impedance results can be utilized for

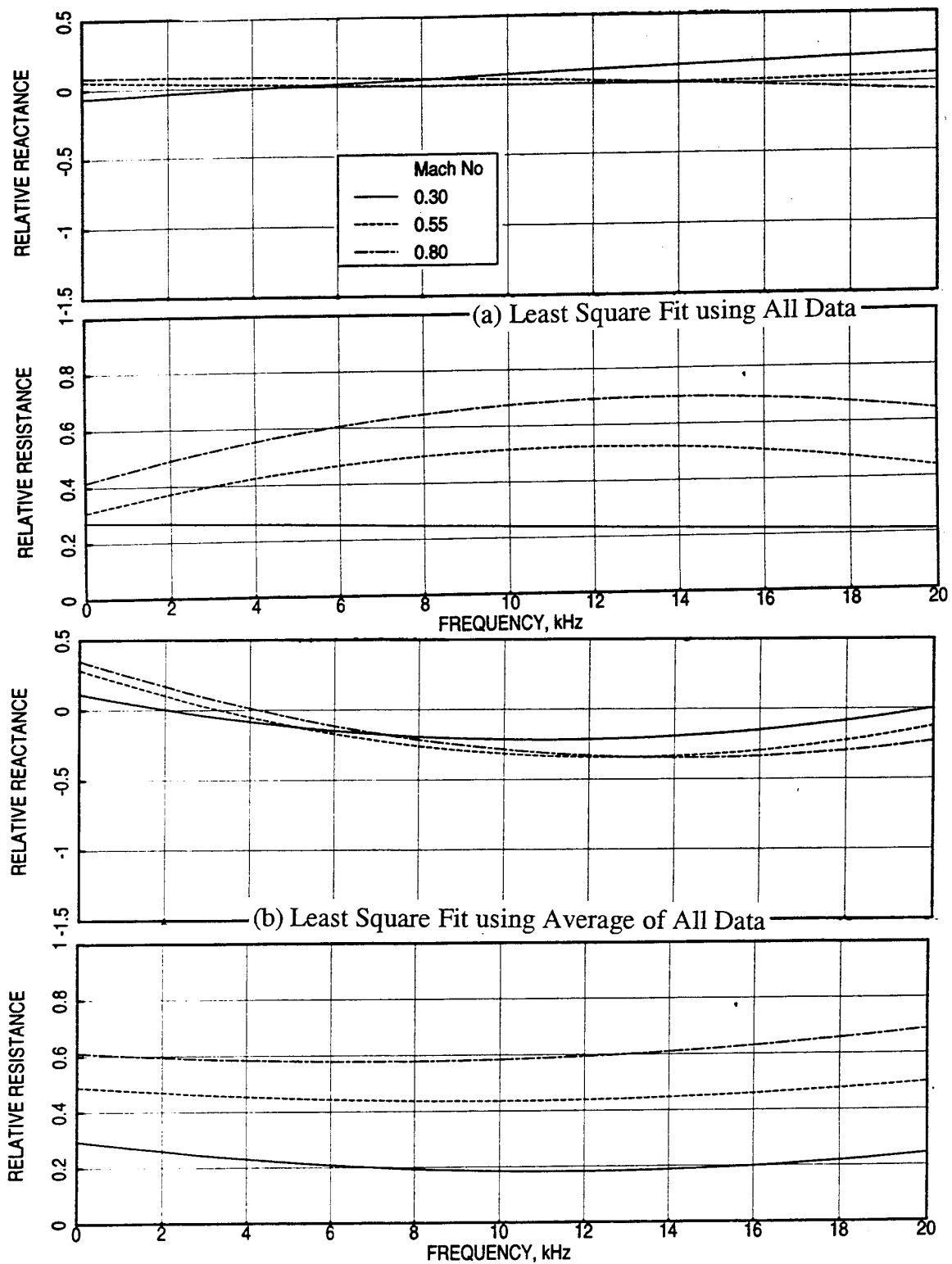


Figure 175. Effect of grazing flow Mach number ( $M$ ) on least square fitted relative in situ impedance for a 0.5"-deep 100 ppi Silicon Carbide foam with a 20 % porous facesheet ( $d=0.04''$ ,  $t=0.025''$ ),  $T=75^{\circ}\text{F}$ .

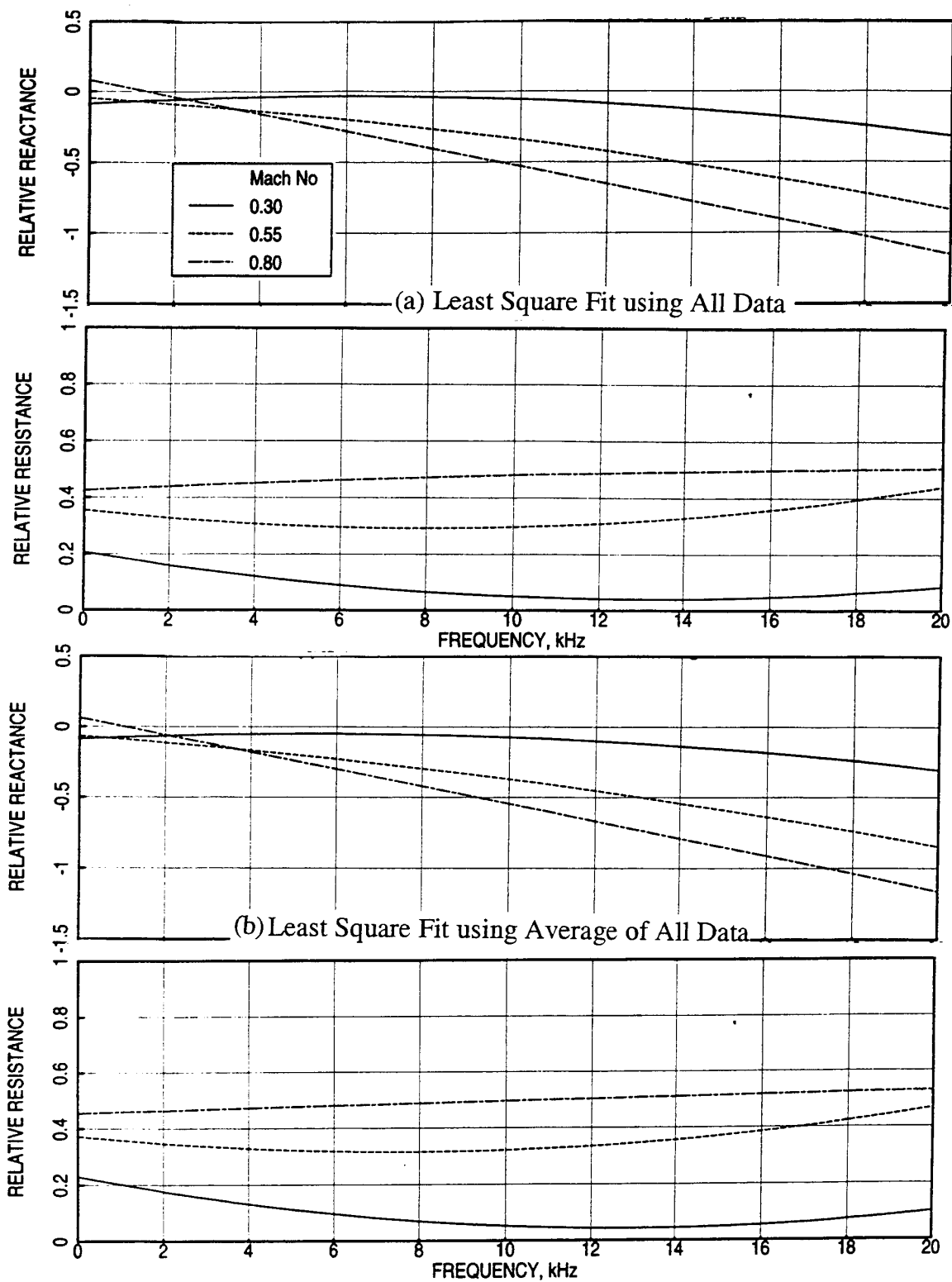


Figure 176. Effect of grazing flow Mach number ( $M$ ) on least square fitted relative insitu impedance for a 0.5"-deep 100 ppi Silicon Carbide foam with a 30 % porous facesheet ( $d=0.04''$ ,  $t=0.025''$ ),  $T=75^{\circ}\text{F}$ .



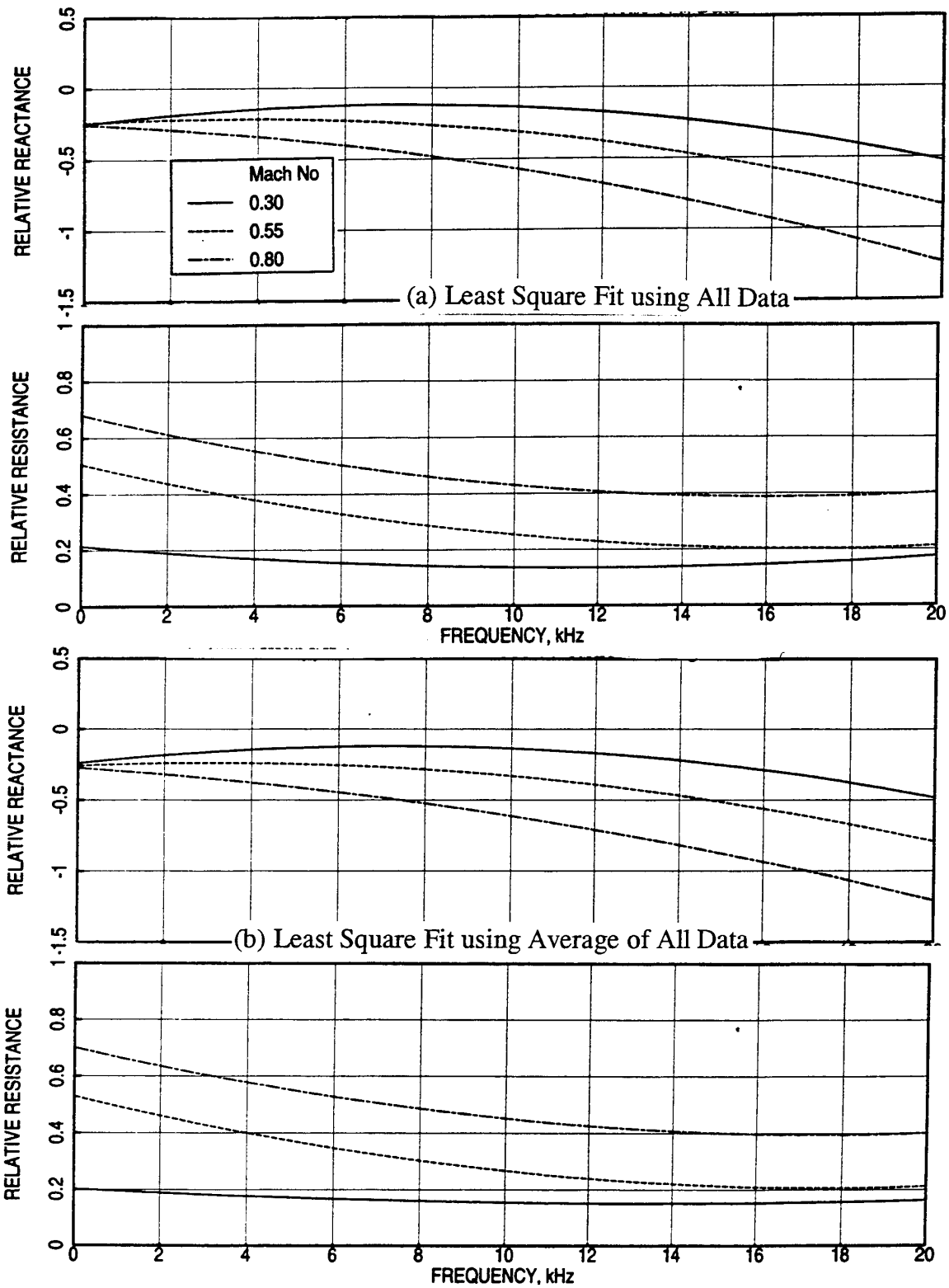


Figure 177. Effect of grazing flow Mach number (M) on least square fitted relative in situ impedance for a 0.5"-deep 100 ppi Silicon Carbide foam with a 40 % porous facesheet (d=0.04", t=0.025", T=75°F).

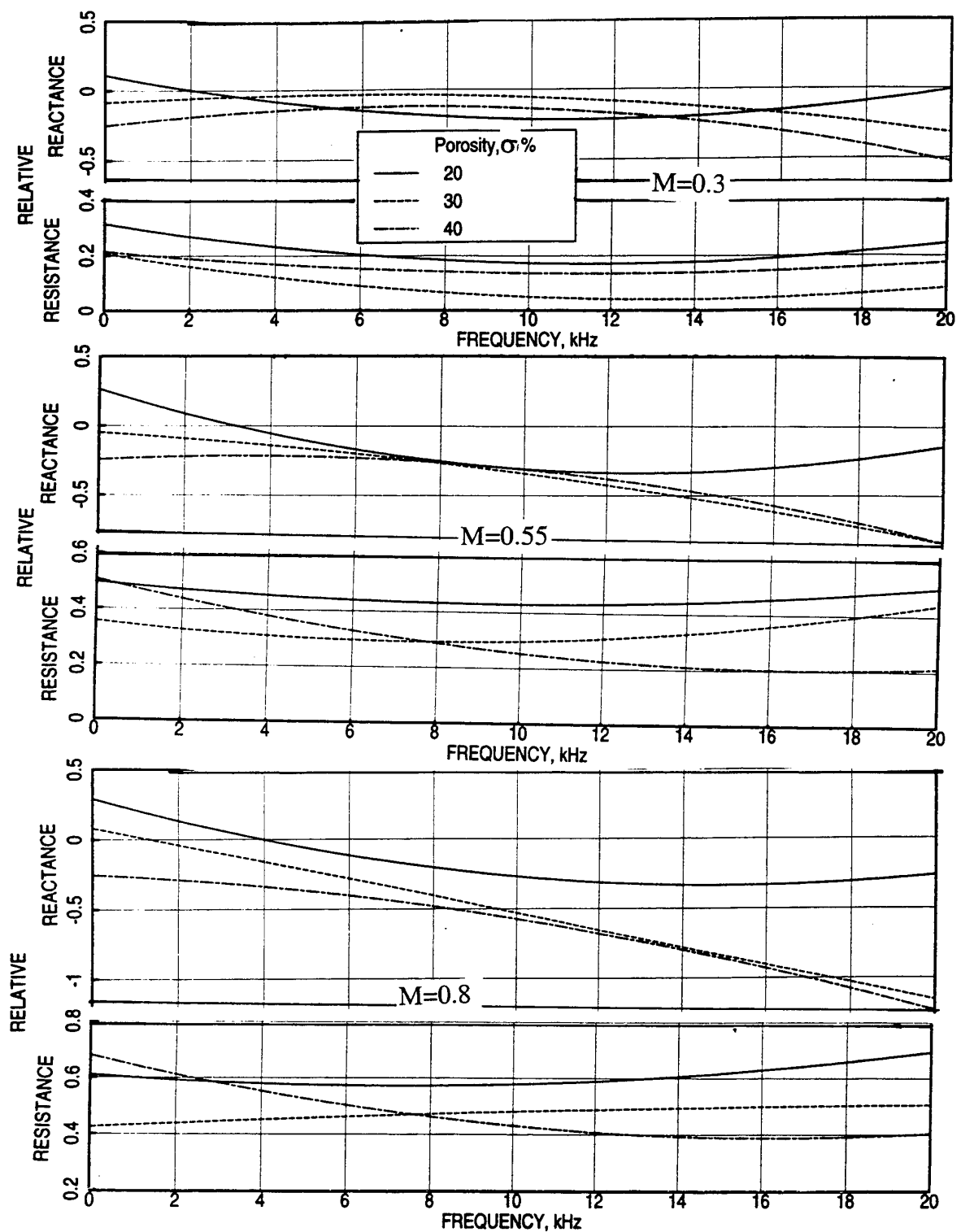


Figure 178. Effect of facesheet porosity ( $\sigma$ ) on least square fitted (using all data) relative insitu impedance for a 0.5"-deep 100 ppi Silicon Carbide foam with perforated facesheets ( $d=0.04"$ ,  $t=0.025"$ ),  $T=75^\circ\text{F}$ .

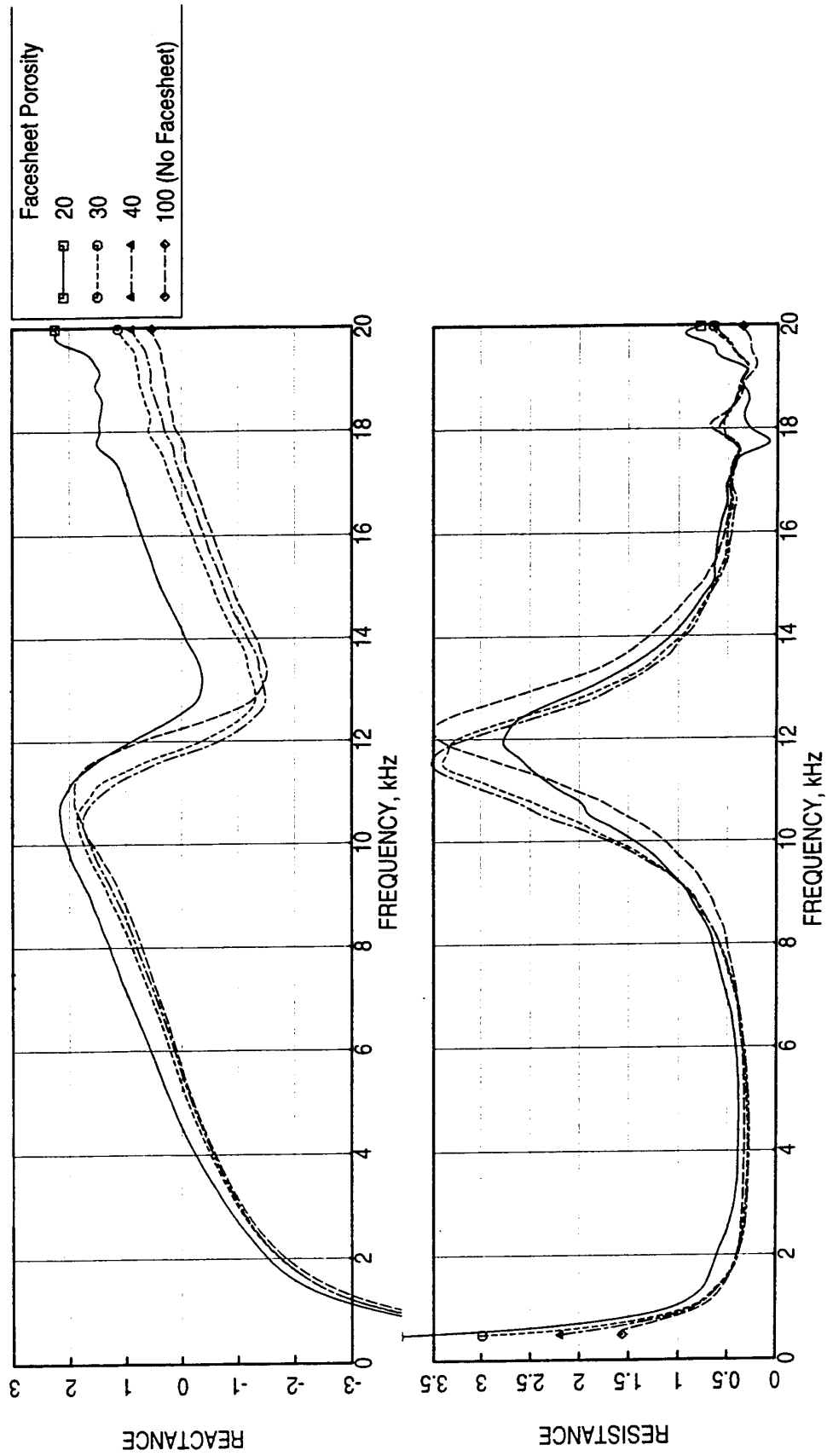


Figure 179. Measured normal impedance for a 0.5"-deep 100 ppi Silicon Carbide foam with perforated facesheets of different porosities ( $d=0.04"$ ,  $t=0.025"$ ), OASPL=150 dB.

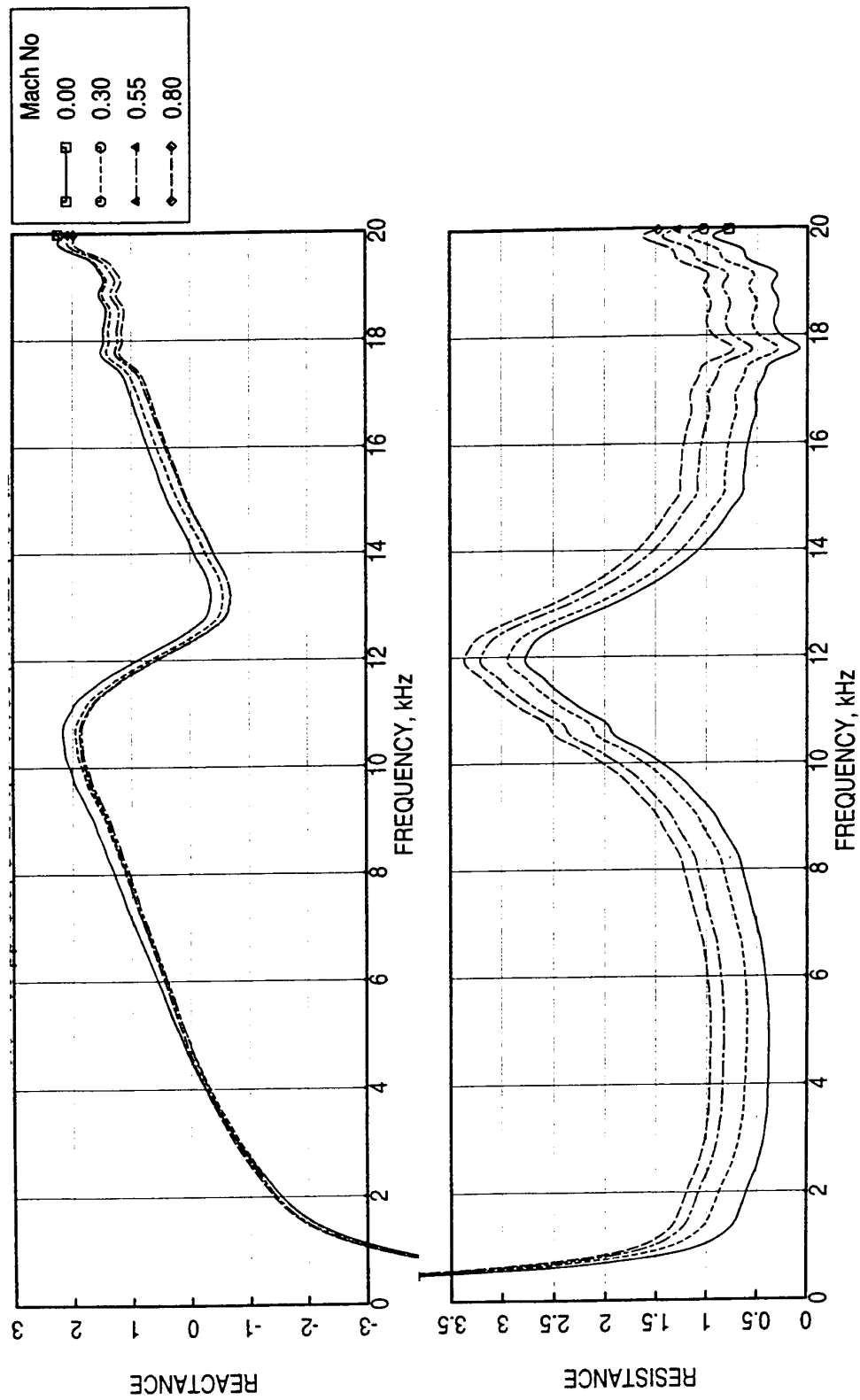


Figure 180. Effect of grazing flow Mach number (M) on normal impedance for a 0.5"-deep 100 ppi Silicon Carbide foam with a 20 % porous facesheet ( $d=0.04"$ ,  $t=0.025"$ ) generated using normal impedance without flow and the curve fitted relative insitu impedance,  $T=75^{\circ}\text{F}$ .

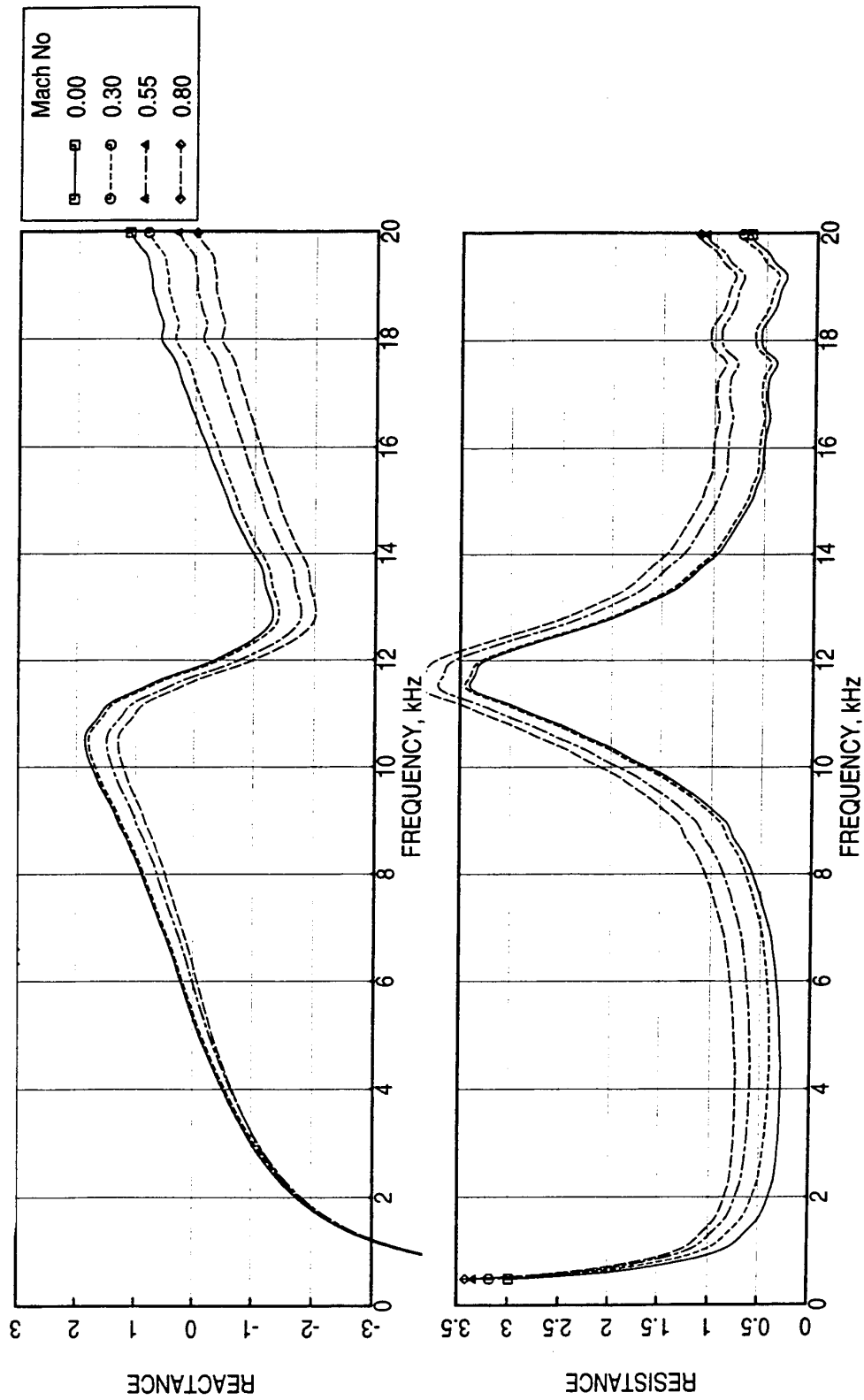


Figure 181. Effect of grazing flow Mach number (M) on normal impedance for a 0.5"-deep 100 ppi Silicon Carbide foam with a 30 % porous facesheet ( $d=0.04"$ ,  $t=0.025"$ ) generated using normal impedance without flow and the curve fitted relative insitu impedance,  $T=75^{\circ}\text{F}$ .

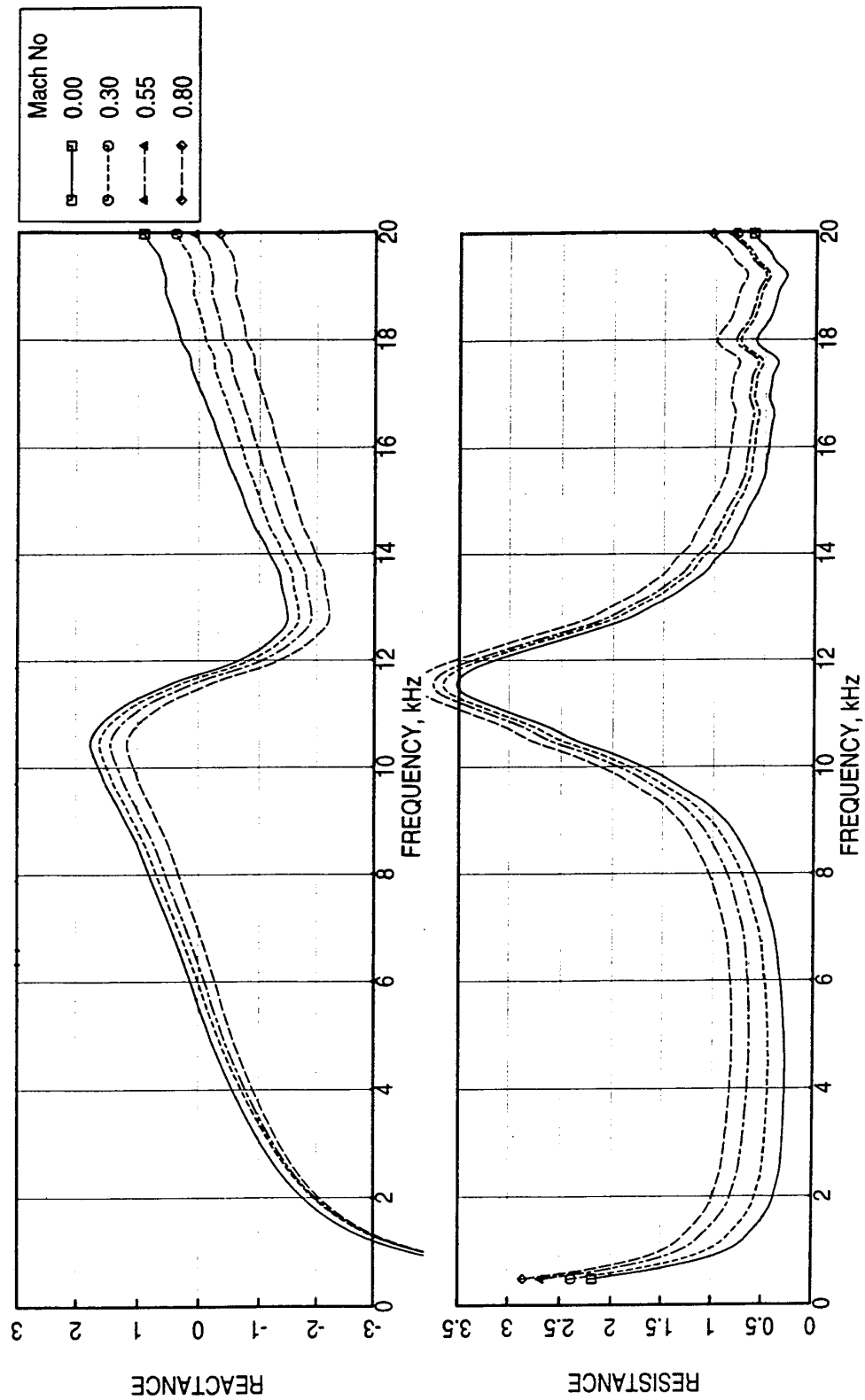


Figure 182. Effect of grazing flow Mach number (M) on normal impedance for a 0.5"-deep 100 ppi Silicon Carbide foam with a 40 % porous facesheet ( $d=0.04"$ ,  $t=0.025"$ ) generated using normal impedance without flow and the curve fitted relative insitu impedance,  $T=75^{\circ}\text{F}$ .

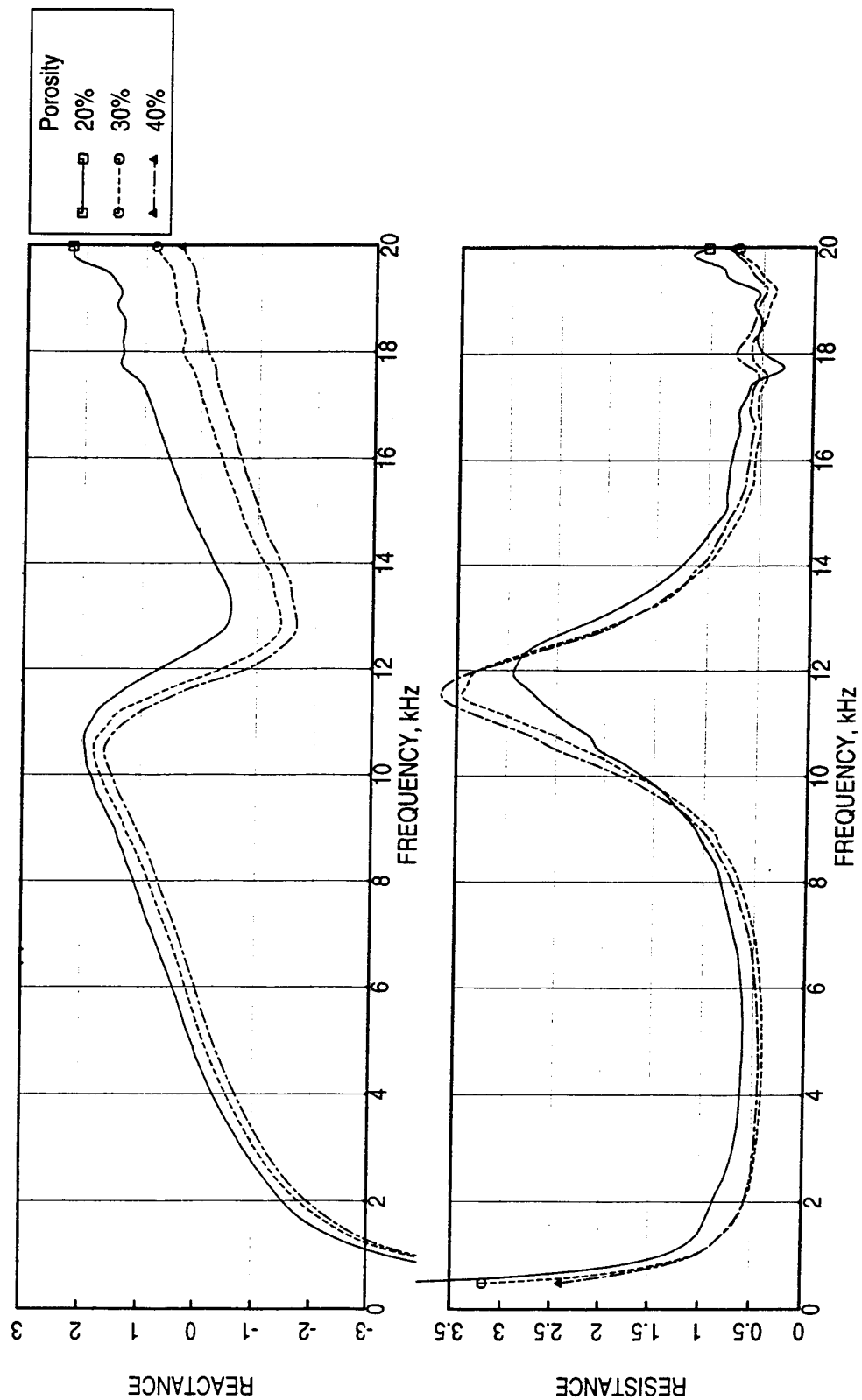


Figure 183. Effect of facesheet porosity ( $\sigma$ ) on normal impedance for a 0.5"-deep 100 ppi Silicon Carbide foam with perforated facesheets ( $d=0.04$ ",  $t=0.025$ ") generated using normal impedance without flow and the curve fitted relative insitu impedance for  $M=0.3$ ,  $T=75^{\circ}\text{F}$ .

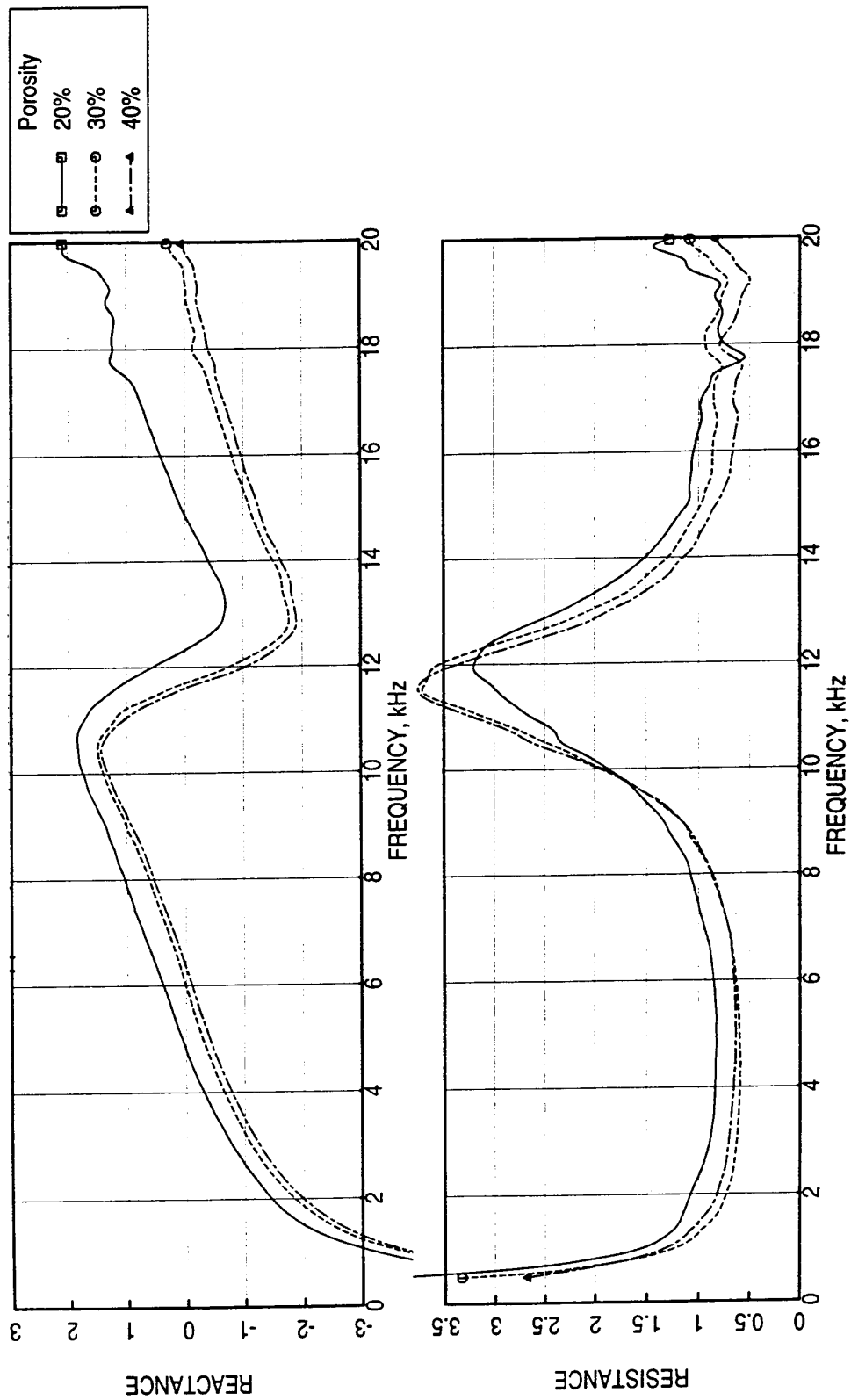


Figure 184. Effect of facesheet porosity ( $\sigma$ ) on normal impedance for a 0.5"-deep 100 ppi Silicon Carbide foam with perforated facesheets ( $d=0.04"$ ,  $t=0.025"$ ) generated using normal impedance without flow and the curve fitted relative insitu impedance for  $M=0.55$ ,  $T=75^{\circ}\text{F}$ .



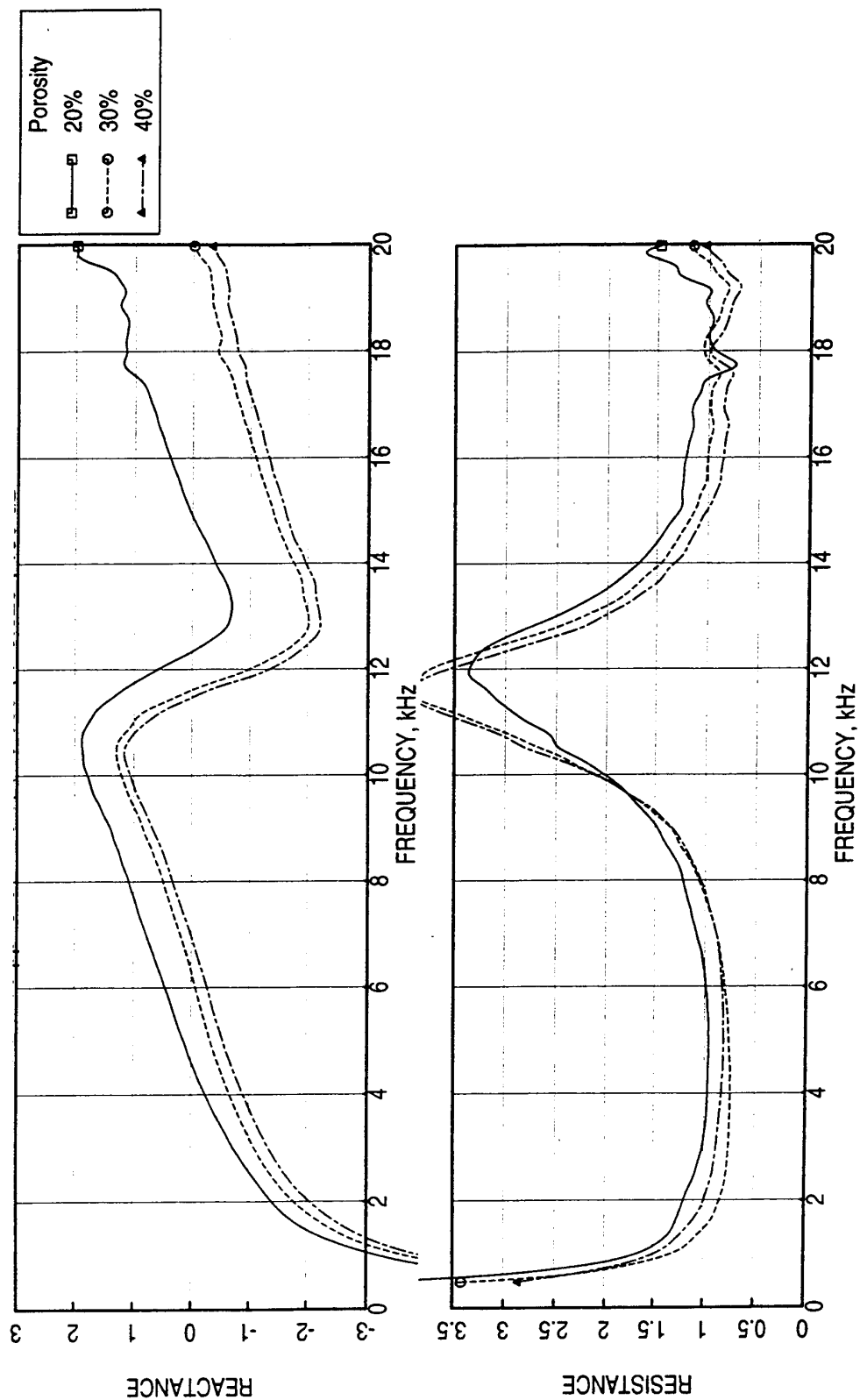


Figure 185. Effect of facesheet porosity ( $\sigma$ ) on normal impedance for a 0.5"-deep 100 ppi Silicon Carbide foam with perforated facesheets ( $d=0.04"$ ,  $t=0.025"$ ) generated using normal impedance without flow and the curve fitted relative insitu impedance for  $M=0.8$ ,  $T=75^\circ\text{F}$ .

configurations with deeper 100 ppi SiC with the same facesheets. Thus, the normal impedance for different scale liners can also be evaluated.

**SDOF Type Liners:** The evaluation process of relative impedance for SDOF type configurations is identical to the process described above for bulk absorbers. Measured insitu impedance at different grazing flow Mach numbers for a 20% porous facesheet ( $t=0.025''$  and  $d=0.04''$ ) over five cavities of different depths is shown in Figures 186 through 188. The resistance and reactance trends with respect to  $M$  are similar to those observed for bulk absorber samples. Utilizing these results the relative impedance is derived and the process is illustrated in Figures 189 and 190. The effect of grazing flow Mach number on the relative impedance for the 20% porous facesheet is thus derived and is shown in Figure 191. Utilizing the all data curve fitted results the effect of grazing flow Mach number on normal impedance is derived and shown in Figure 192. The measured normal impedance without grazing flow, utilized in the derivation, is also shown in this figure. Clearly, the resistance increases and the reactance decreases with increasing Mach number.

#### **6.1.5 Processing & Presentation of Insitu Impedance Data for Heated Flow Conditions:**

Tests are conducted at ambient and heated flow conditions of 200°F and 400°F at grazing flow Mach numbers of 0.3, 0.55, and 0.8 for a number of bulk absorber and SDOF configurations (see Table 8). Measured insitu impedance results for a 0.5''-deep 100 ppi SiC bulk absorber with 30% porous 0.25''-thick facesheet with 0.04'' hole diameter (Config1-2) for a grazing flow Mach number of 0.55 at different temperatures are presented in Figures 193(a) through 197(a) for different cavities. The antiresonance frequencies increase with increasing temperature for each five cases. A relative impedance calculation with respect to ambient temperature would be unrealistic if the procedure described earlier for ambient data is used here. Thus, the frequency is normalized by multiplying a temperature factor, which is the square root of the ratio of reference (or standard) temperature to the test temperature of a cavity in absolute scale (i.e.,  $\sqrt{T_{ref}/T_{test}}$ ). The reference temperature used in the data processing is 75°F (535°R) and the test temperature for each cavity for different Mach number is used as listed in section 4.2. The impedance data is then calculated at the normalized frequency points corresponding to the measured frequency points by the process of interpolation. The interpolated data is plotted with respect to normalized frequency in Figures 193(b) through 197(b) for different cavities. The antiresonance frequencies with respect to normalized frequency coincide for different temperatures.

Thus, the relative impedance for temperatures 200°F and 400°F are computed relative to the impedance at ambient condition for the same Mach number for respective cavities. The

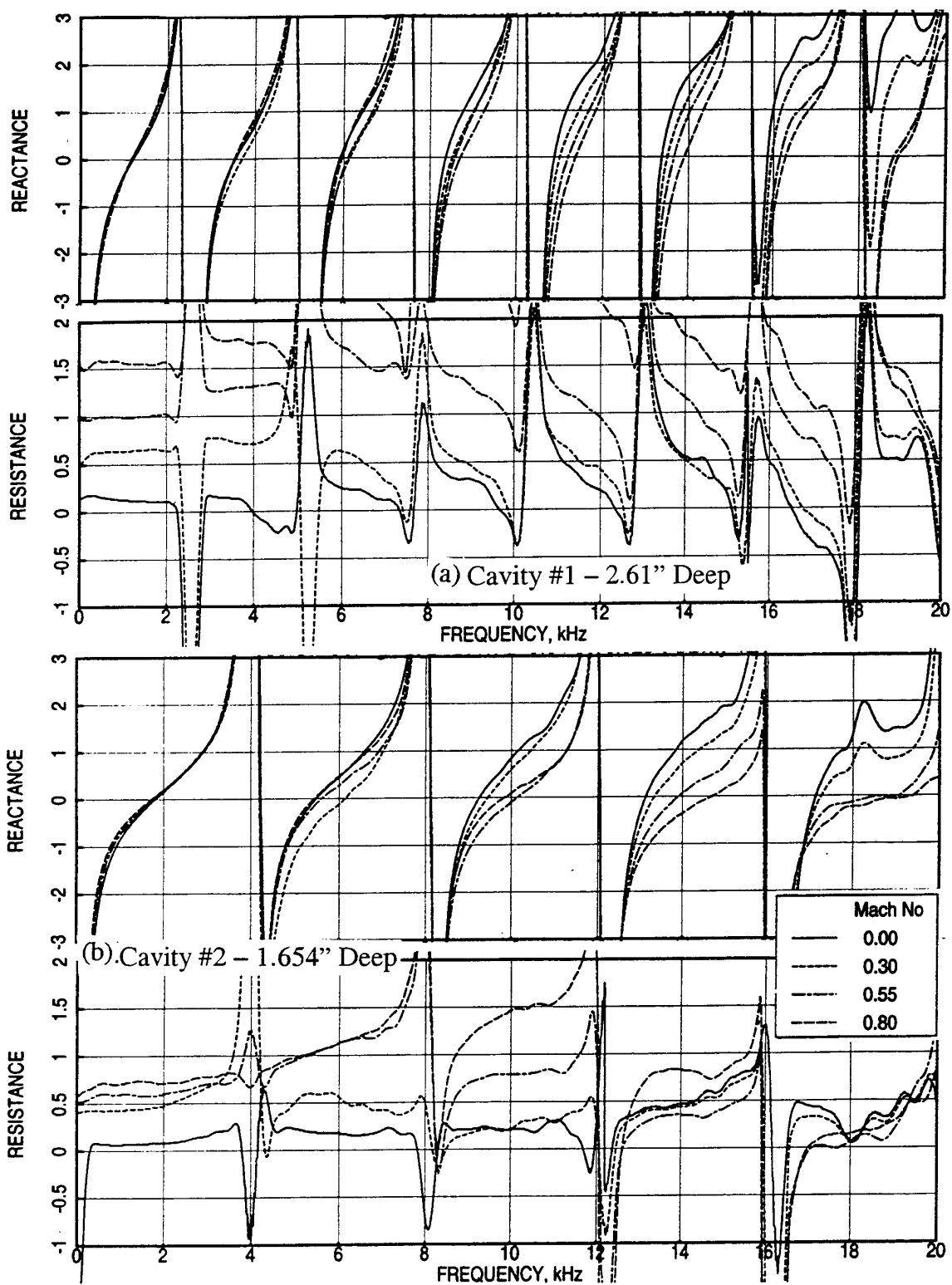


Figure 186. Effect of grazing flow Mach number ( $M$ ) on in situ impedance for a 20 % porous facesheet ( $d=0.04''$ ,  $t=0.025''$ ) over cavities #1 and #2 of different depths,  $T=75^{\circ}\text{F}$ .

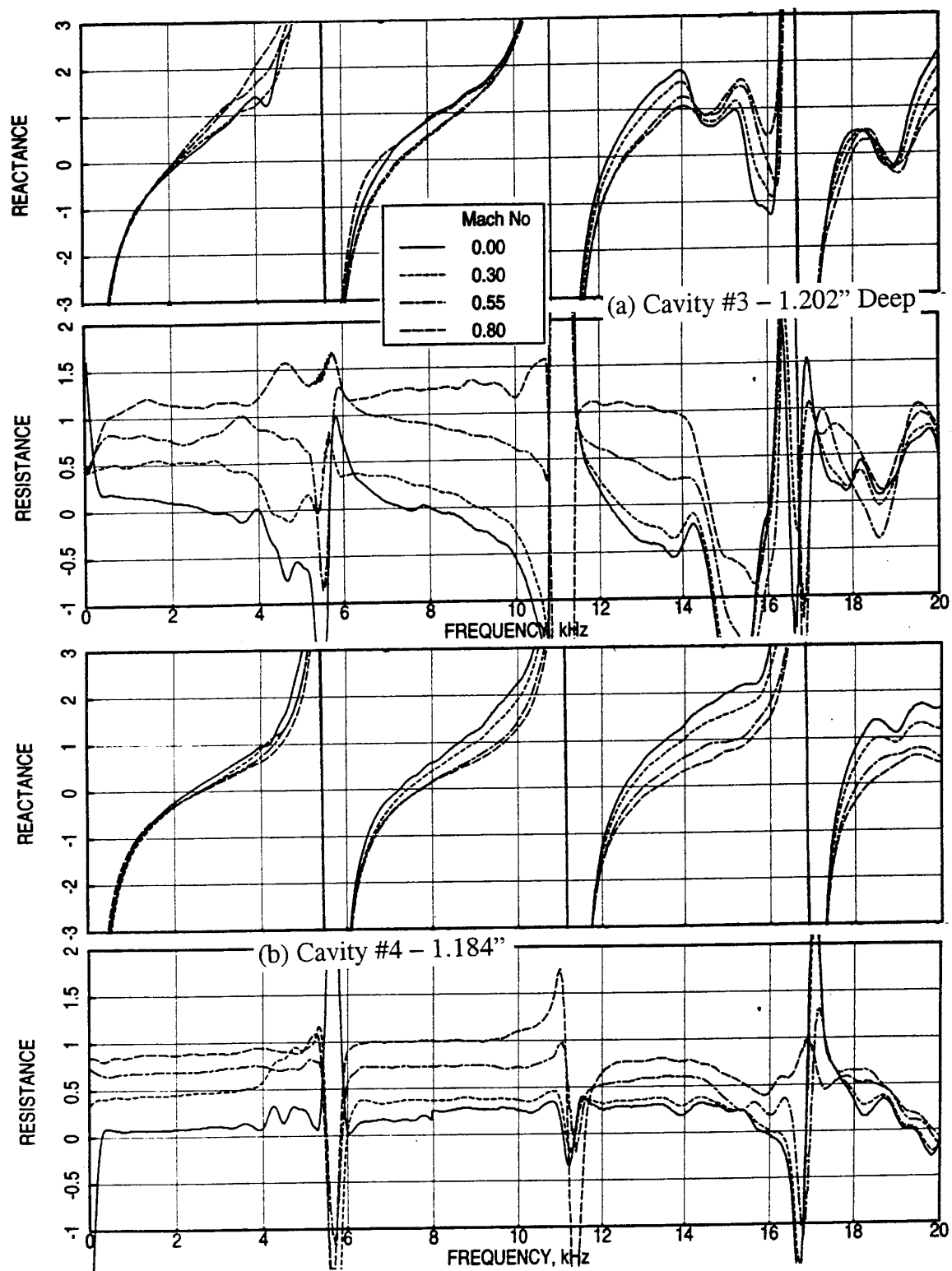


Figure 187. Effect of grazing flow Mach number ( $M$ ) on in situ impedance for a 20 % porous facesheet ( $d=0.04''$ ,  $t=0.025''$ ) over cavities #3 and #4 of different depths,  $T=75^\circ\text{F}$ .

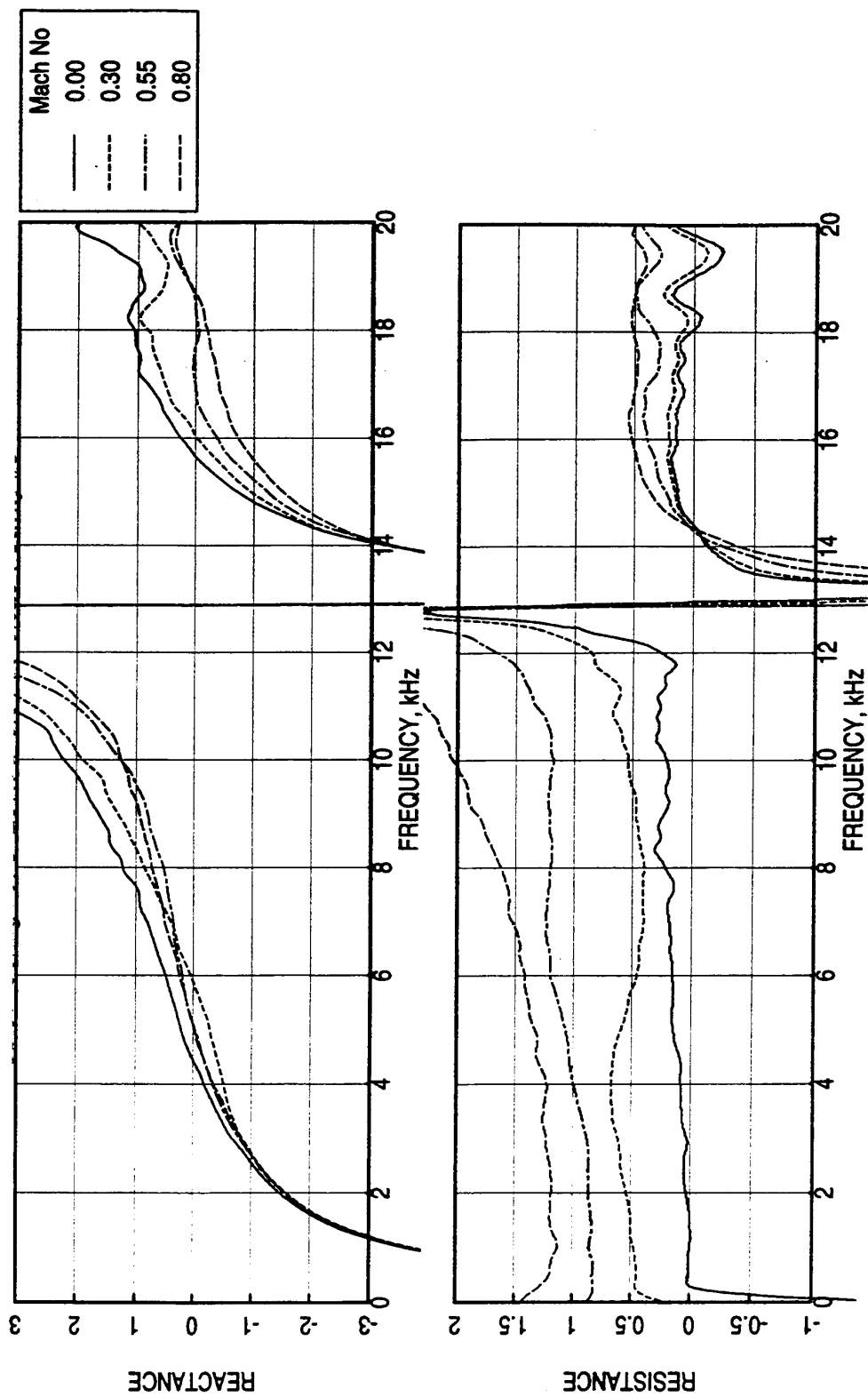


Figure 188. Effect of grazing flow Mach number (M) on in situ impedance for a 20 % porous facesheet ( $d=0.04''$ ,  $t=0.025''$ ) over cavity #5 of depth 0.5'',  $T=75^{\circ}\text{F}$ .

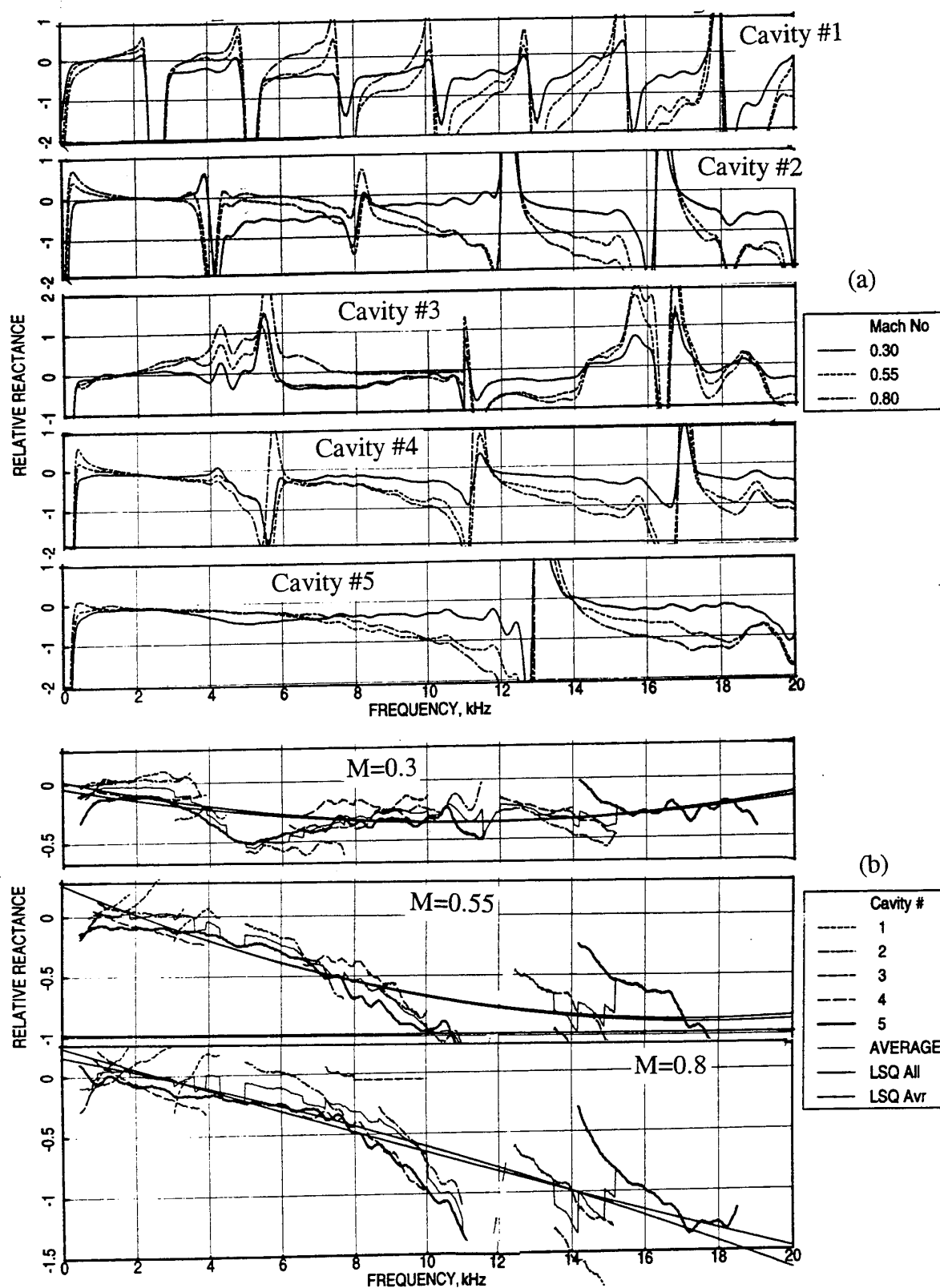


Figure 189. A least square fitting process to evaluate relative reactance using measured data from all 5 tray cavities for a 20 % porous facesheet ( $d=0.04''$ ,  $t=0.025''$ ),  $T=75^{\circ}\text{F}$ .

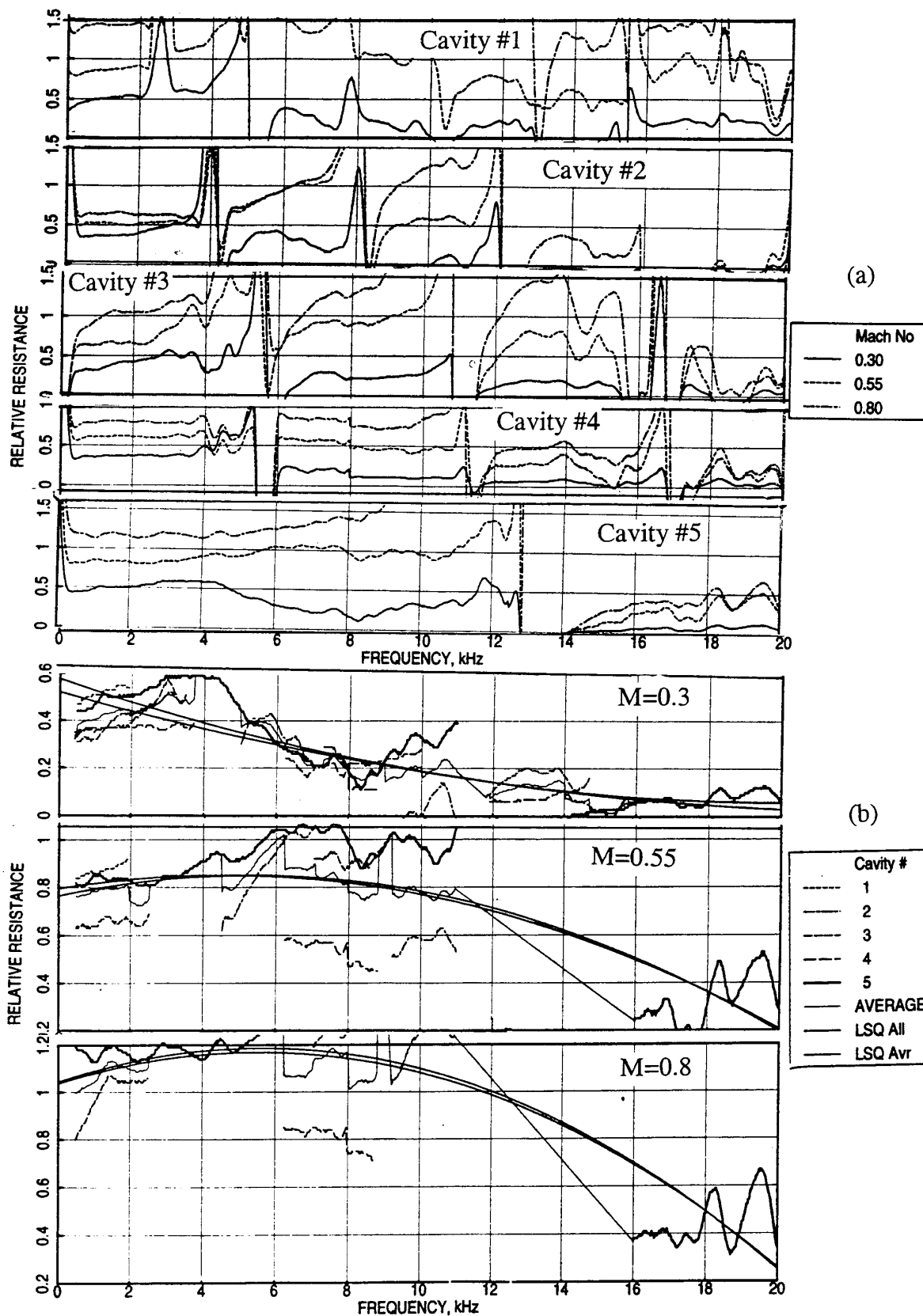


Figure 190. A least square fitting process to evaluate relative resistance using measured data from all 5 tray cavities for a 20 % porous facesheet ( $d=0.04''$ ,  $t=0.025''$ ),  $T=75^{\circ}\text{F}$ .

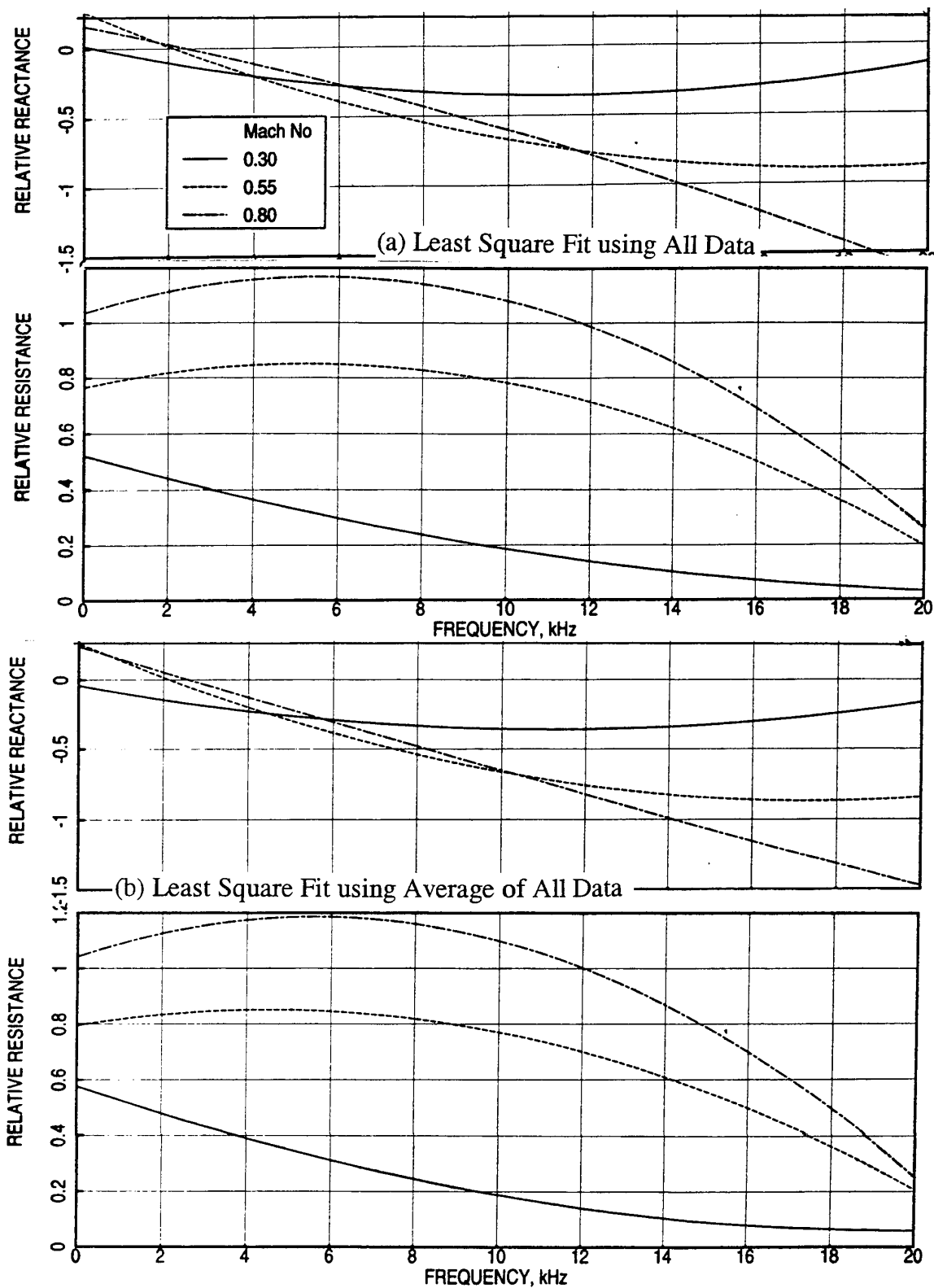


Figure 191. Effect of grazing flow Mach number ( $M$ ) on least square fitted relative insitu impedance for a 20 % porous facesheet ( $d=0.04''$ ,  $t=0.025''$ ),  $T=75^{\circ}\text{F}$ .



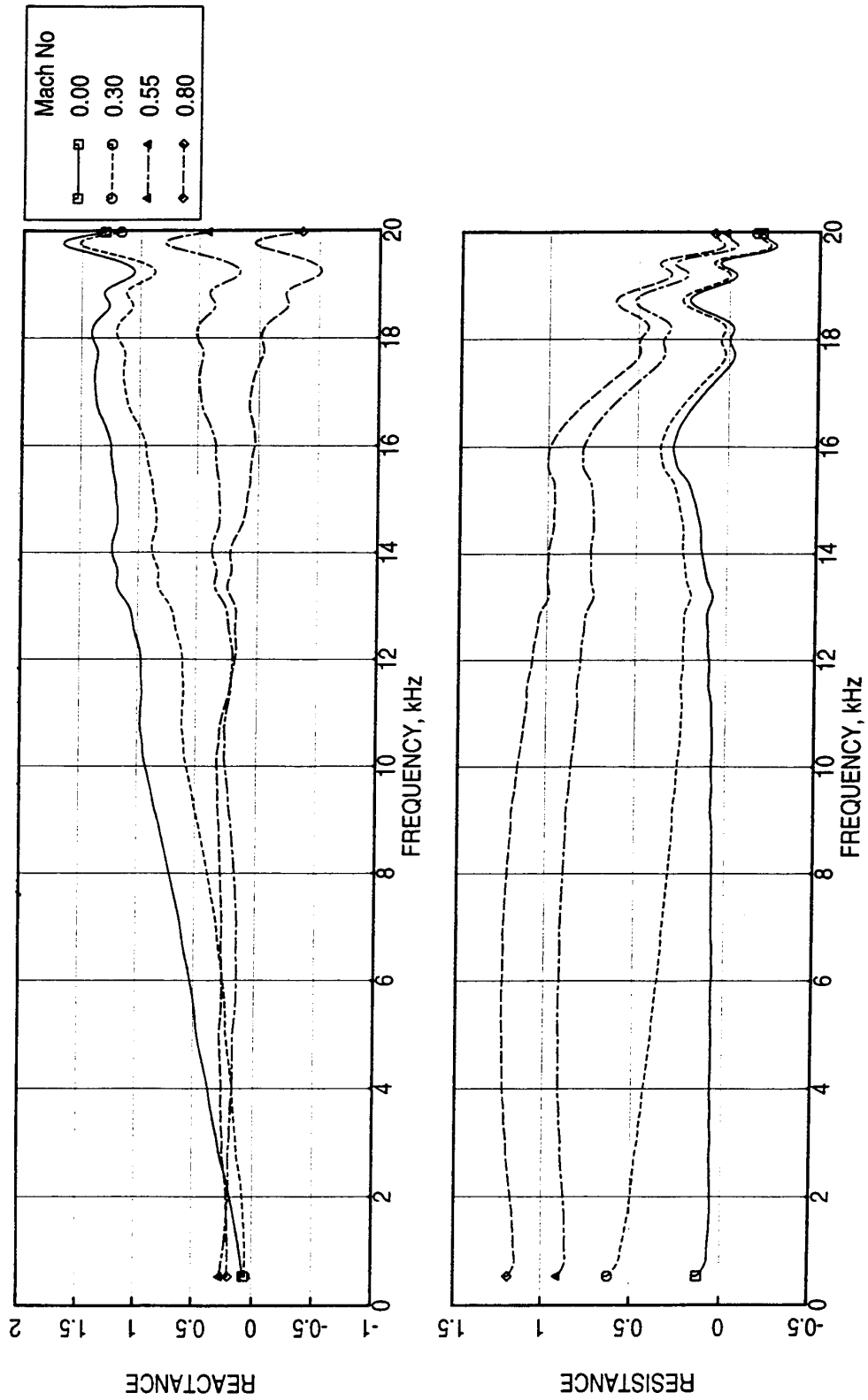


Figure 192. Effect of grazing flow Mach number (M) on normal impedance for a 20 % porous facesheet ( $d=0.04''$ ,  $t=0.025''$ ) generated using normal impedance without flow and the curve fitted relative insitu impedance,  $T=75^{\circ}\text{F}$ .

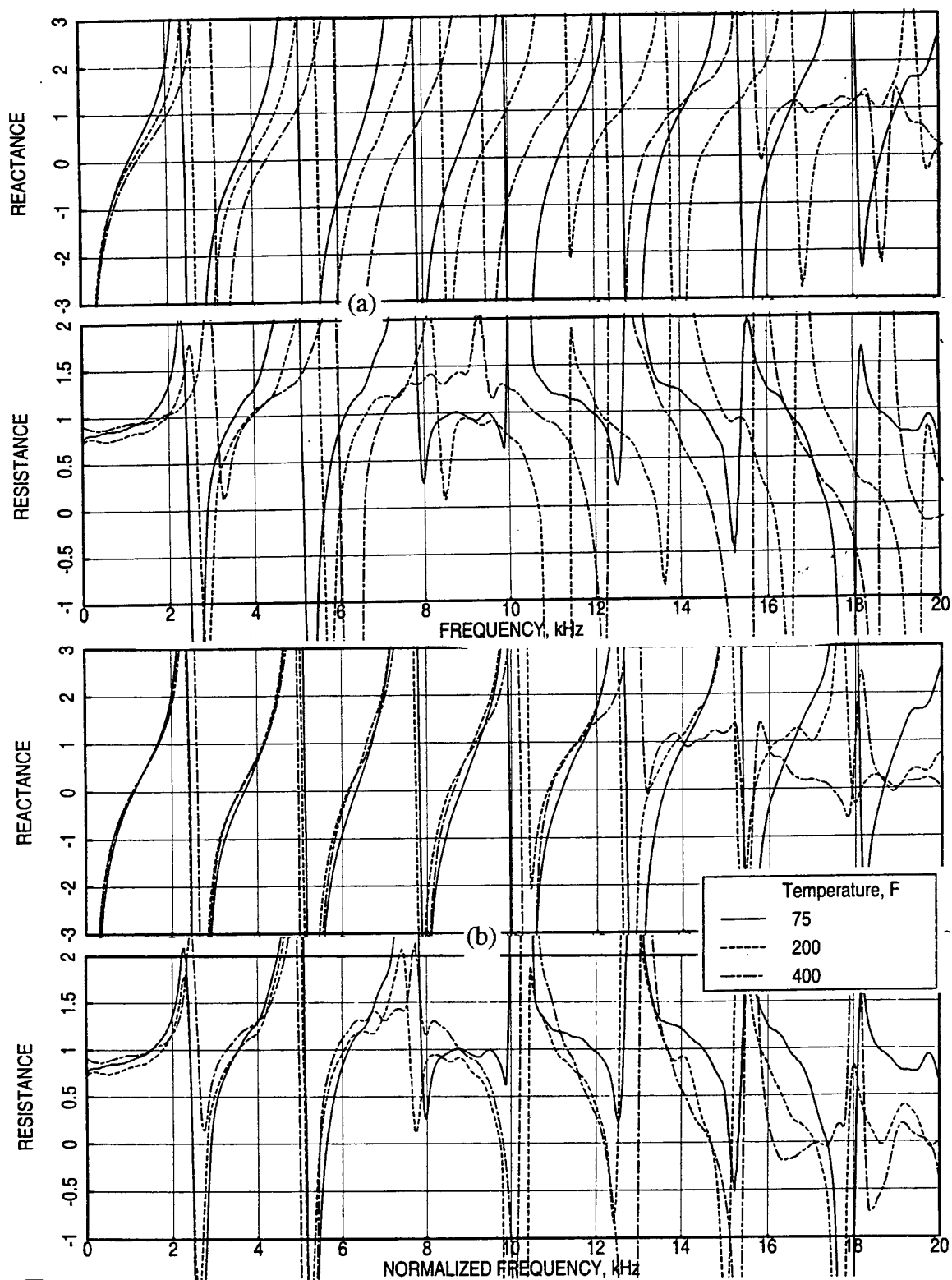


Figure 193. Effect of temperature (T) on insitu impedance for a 0.5"-deep 100 ppi Silicon Carbide foam with a 30 % porous facesheet ( $d=0.04''$ ,  $t=0.025''$ ) over cavity #1 of depth 2.64",  $M=0.55$ .

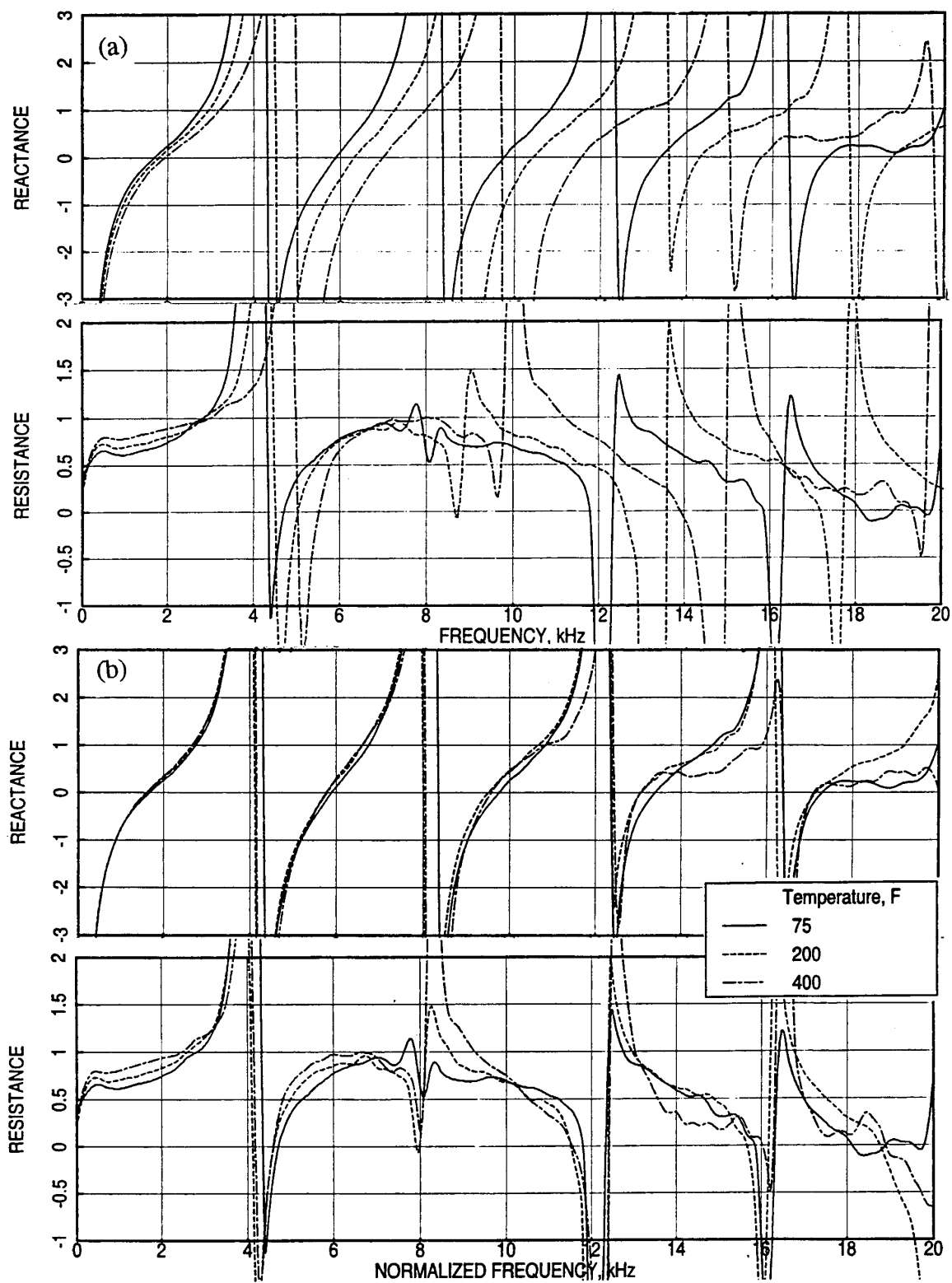


Figure 194. Effect of temperature (T) on in situ impedance for a 0.5''-deep 100 ppi Silicon Carbide foam with a 30 % porous facesheet ( $d=0.04''$ ,  $t=0.025''$ ) over cavity #2 of depth 1.656'',  $M=0.55$ .

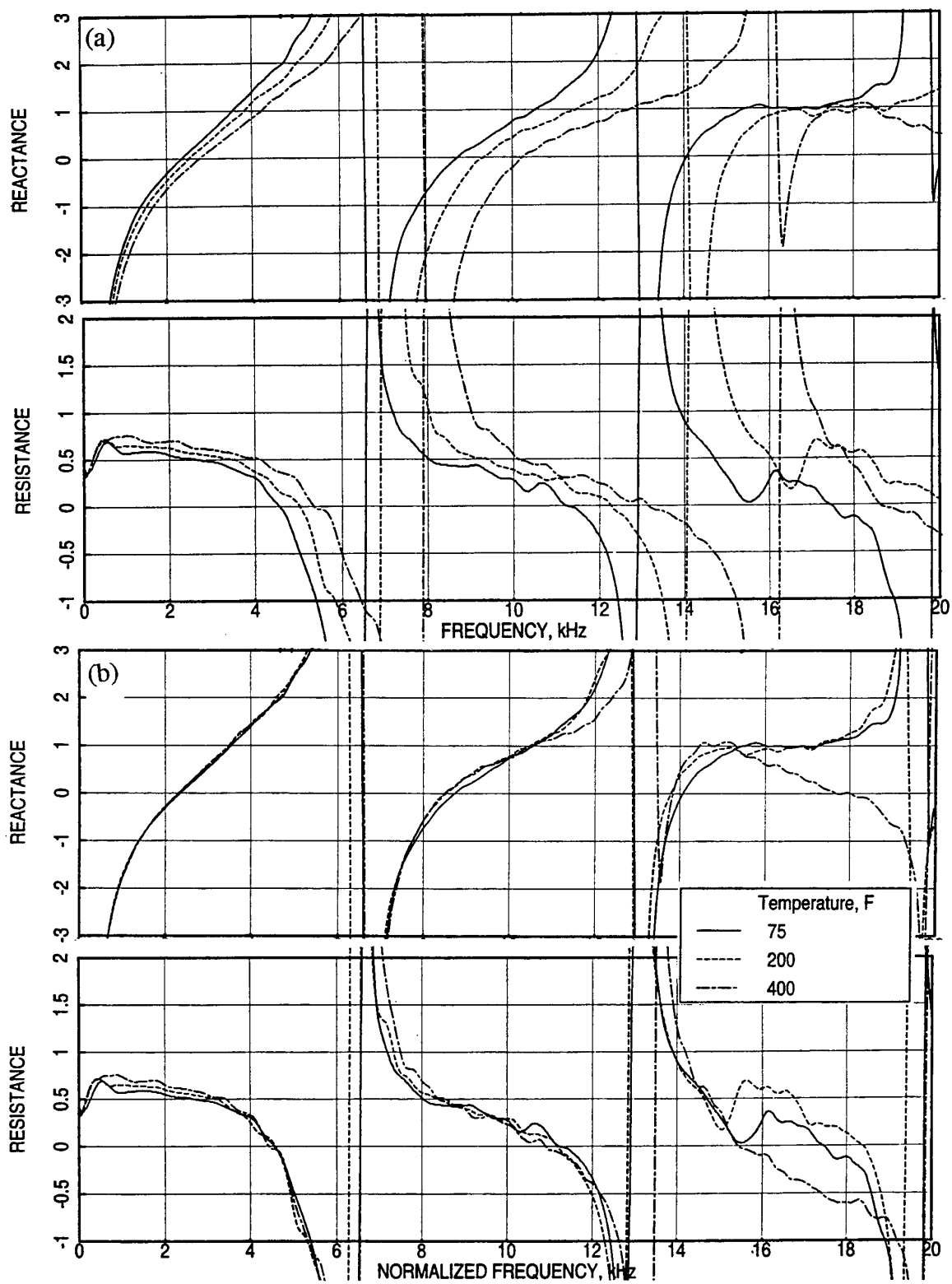


Figure 195. Effect of temperature ( $T$ ) on insitu impedance for a 0.5''-deep 100 ppi Silicon Carbide foam with a 30 % porous facesheet ( $d=0.04''$ ,  $t=0.025''$ ) over cavity #3 of depth 1.025'',  $M=0.55$ .

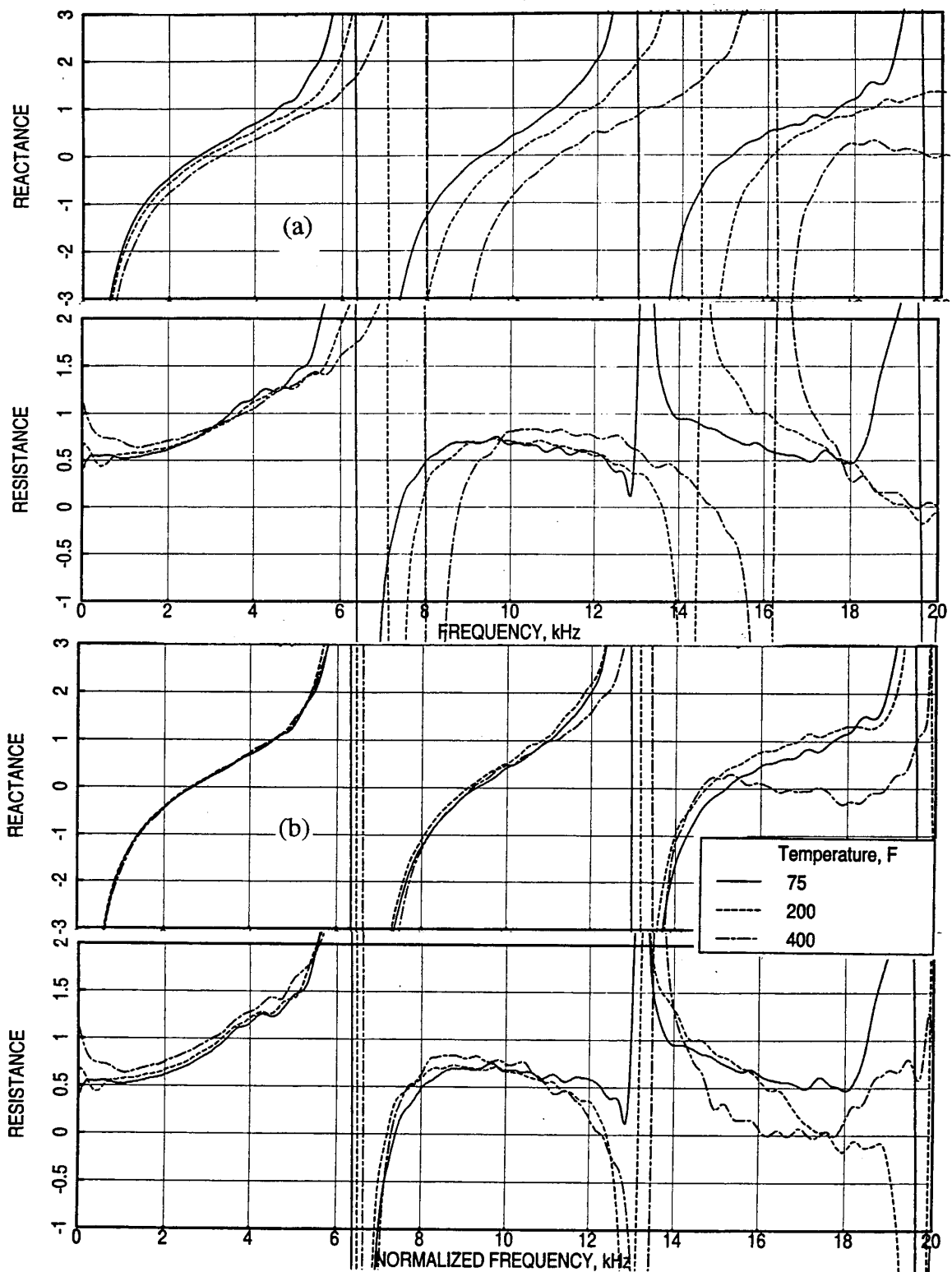


Figure 196. Effect of temperature (T) on insitu impedance for a 0.5''-deep 100 ppi Silicon Carbide foam with a 30 % porous facesheet (d=0.04'', t=0.025'') over cavity #4 of depth 1.02'', M=0.55.

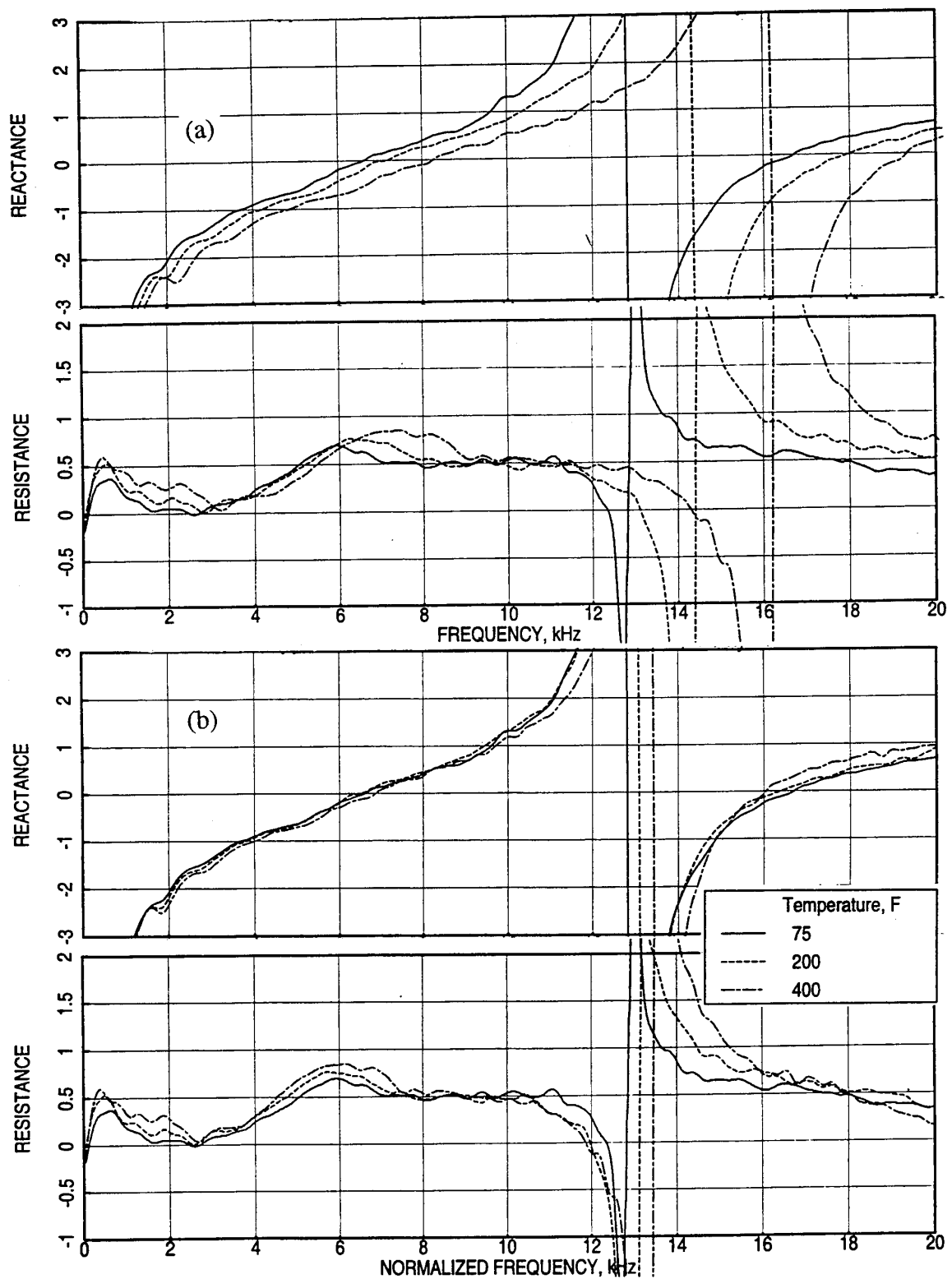


Figure 197. Effect of temperature (T) on insitu impedance for a 0.5"-deep 100 ppi Silicon Carbide foam with a 30 % porous facesheet ( $d=0.04''$ ,  $t=0.025''$ ) over cavity #5 of depth 0.504",  $M=0.55$ .

relative reactance and resistance at frequencies not effected by antiresonances are taken from each cavity for fixed temperatures. Unreasonable data points are also excluded from these data sets. A straight line passing through zero at zero frequency is used to least square fit all the reactance data for fixed temperatures. For resistance, a similar curve fitting is performed, except that the zero frequency data is not forced to zero. Also, an average of each data set at individual frequencies is calculated and used for least square curve fit. The process and the results for Config1-2 for 0.55 Mach number are shown in Figures 198 and 199 for relative reactance and resistance, respectively.

**6.1.6 Prelude for Relative Impedance Presentation:** The high frequency data seems to be inadequate due to the influence of antiresonance frequencies, which are based on the tray cavity depths. For 0.5"-deep cavity, the recovery of data after the antiresonance at about 13 kHz seems to be incomplete up to 16 or 17 kHz. At the same time the deeper cavities, especially the 2.64"-deep cavity is useful only for very low frequencies, which are of lesser importance for the current program. To achieve more reliable data at frequencies above 12 kHz the first cavity for bulk absorber tray is reduced from 2.64" to 0.7". Thus, the data in the range of 12 to 16 kHz become more reliable for this cavity, since the antiresonance occurs at about 9.5 kHz for this depth (see Figure 200). For the same reason two cavities of depth 2.61" (cavity #1) and 1.184" (cavity #4) of SDOF tray are reduced to 0.7" and 0.25" respectively. With this modification the anti resonance moves to about 9.5 kHz and 20 kHz for cavities #1 and #4, respectively (see Figure 201). Several tests are conducted using the modified trays for bulk absorber and SDOF configurations.

Relative impedance characteristics on the basis of current data, especially at frequencies up to 12 kHz, and the existing prediction methods indicate that the relative reactance varies linearly with frequency, with a zero value at zero frequency, and the relative resistance is more or less independent of frequency. Therefore, all the relative impedance data are also curve fitted using a straight line passing through zero at zero frequency for relative reactance and a fixed level for relative resistance. In the following section only the straight-line results for relative impedance are presented.

For parametric study, while the effect of grazing flow on relative impedance for ambient temperature exhibits the similar trend as the absolute impedance, the same is not true for less sensitive parameters, especially for heated cases. This is basically due to the process utilized to evaluate relative impedance. For ambient data the relative impedance is derived with respect to the no flow impedance. However, for heated case, the relative impedance is derived with respect to the unheated data for the same grazing flow Mach number in terms of

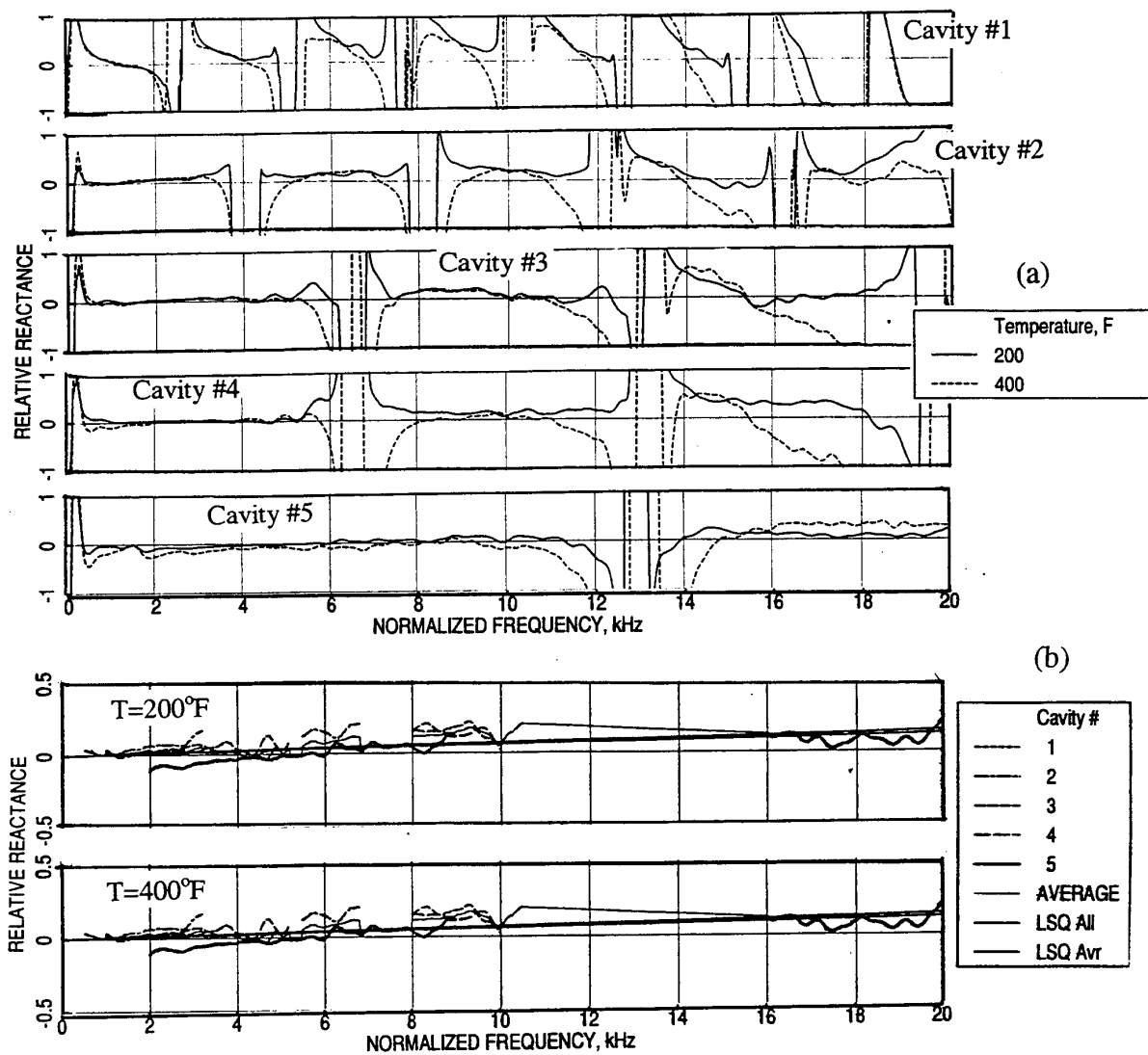


Figure 198. A least square fitting process to evaluate relative reactance for different temperatures using measured data from all 5 tray cavities for a 0.5''-deep 100 ppi Silicon Carbide foam with a 30 % porous facesheet ( $d=0.04''$ ,  $t=0.025''$ ),  $M=0.55$ .



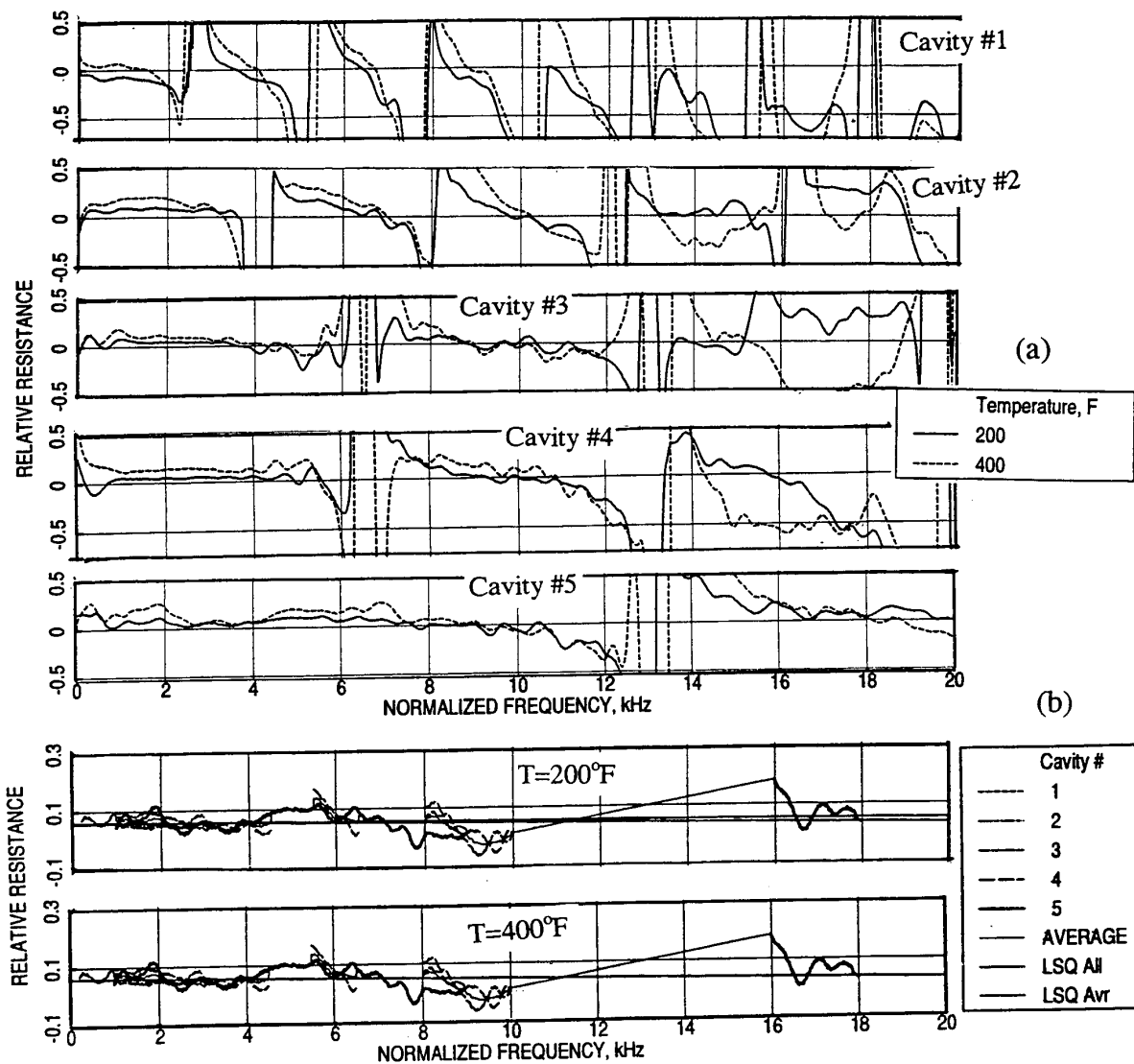


Figure 199. A least square fitting process to evaluate relative resistance for different temperatures using measured data from all 5 tray cavities for a 0.5''-deep 100 ppi Silicon Carbide foam with a 30 % porous facesheet ( $d=0.04''$ ,  $t=0.025''$ ),  $M=0.55$ .

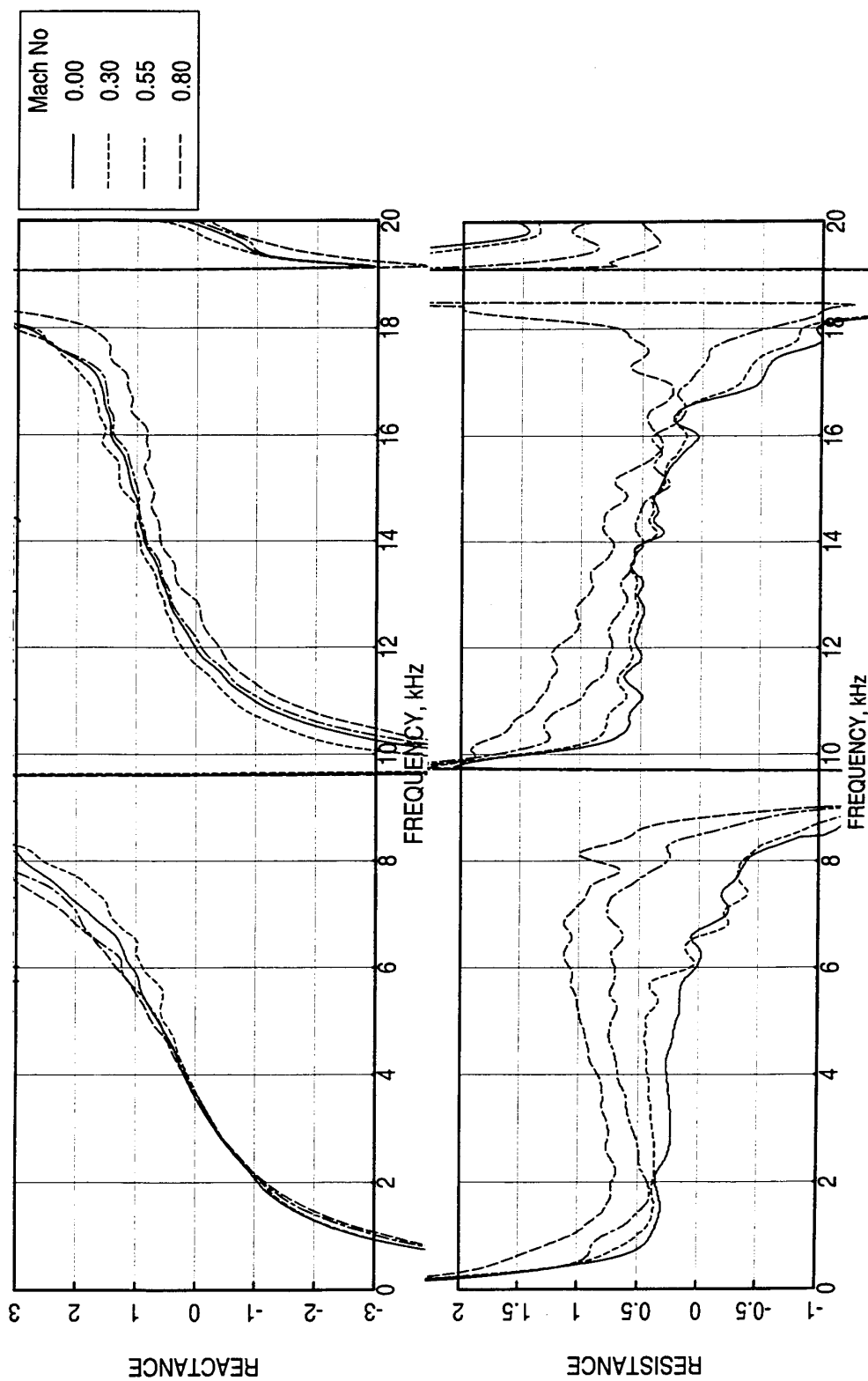


Figure 200. Effect of grazing flow Mach number (M) on in situ impedance for a 0.5"-deep 100 ppi Silicon Carbide foam with a 40 % porous facesheet ( $d=0.10''$ ,  $t=0.025''$ ) in the modified cavity #1 of depth 0.7",  $T=75^{\circ}\text{F}$ .

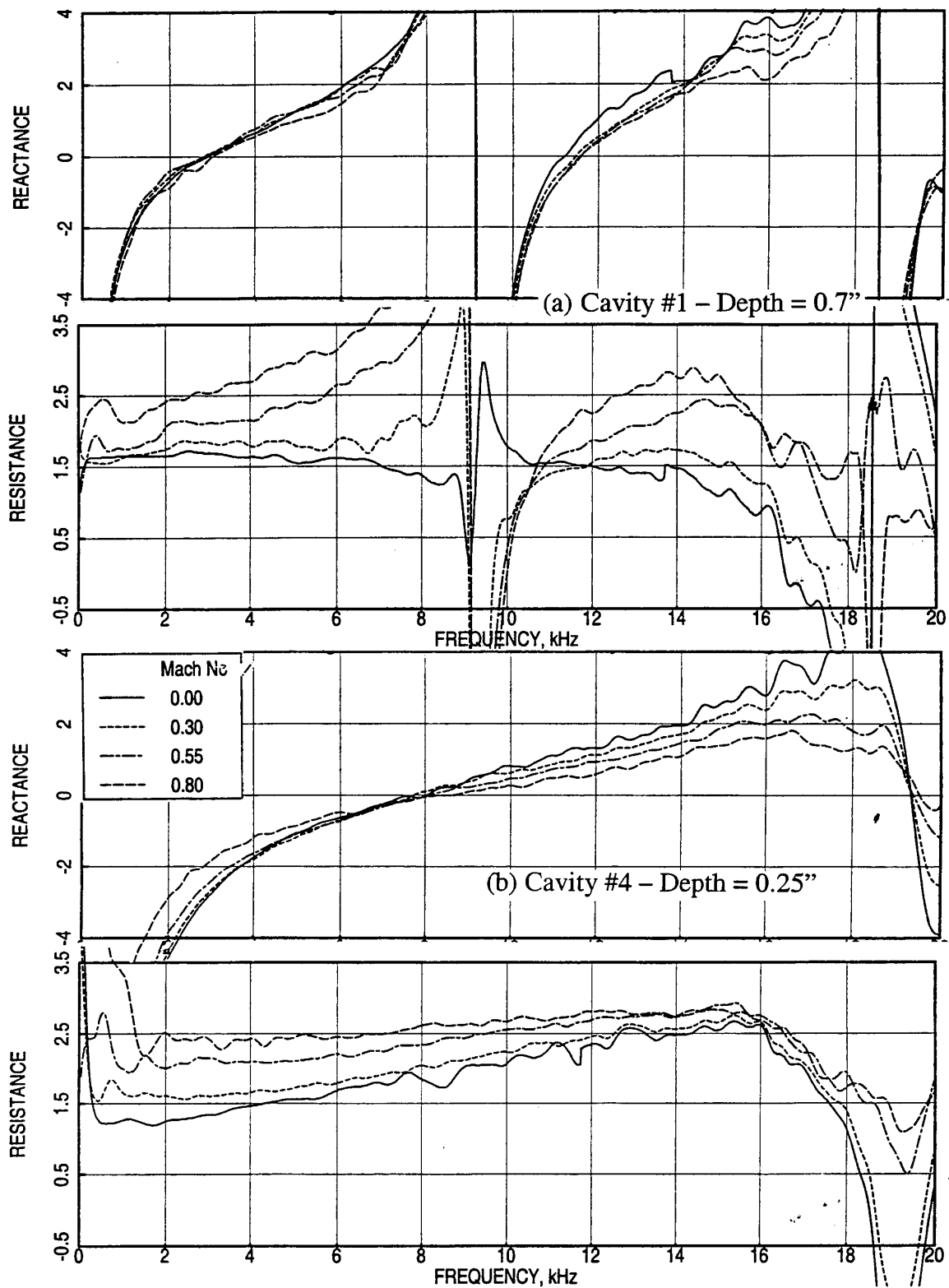


Figure 201. Effect of grazing flow Mach number ( $M$ ) on insitu impedance for a 85 Rayls linear facesheet ( $t=0.01''$ ) over modified cavities #1 and #4 of different depths,  $T=75^{\circ}\text{F}$ .

normalized frequency. Therefore, it is appropriate to show the parametric effects for absolute impedance derived using the normal impedance and the corresponding relative impedance. All the absolute impedance results present in the next section are for a 0.5"-deep liner configuration. Similar results can be derived for liners of different depths.

**6.2 Data Processing and Presentation for Boundary Layer Data:** Boundary layer velocity and temperature profiles are measured at a fixed liner tray location of all configurations utilizing a computer controlled traverse mechanism. Typical velocity profiles showing the effect of flow Mach number and showing the effect of flow temperature for a 100 ppi 0.5"-deep SiC bulk absorber with a 20% porous 0.025"-thick facesheet ( $d=0.04''$ ) are presented in Figures 202 and 203, respectively. The velocity profiles seem to be fully developed. The impact of temperature on velocity profiles is relatively small. Temperature profiles for the same bulk absorber is shown in Figure 204. While the temperature profile trends are reasonable the actual temperature variation with respect to test section height show some amount of scatter. This is possibly due to the variation of steady temperature during the survey. The temperature profiles are currently not used for any liner design development effort.

The boundary layer velocity profiles are utilized to compute local skin friction coefficients ( $C_F$ ), displacement thickness ( $\delta^*$ ), and momentum thickness ( $\theta$ ) as described in reference 1. While the skin friction coefficient is used to select a panel configuration with minimum friction loss, the momentum thickness is used in the correlation process for normal impedance. Typical  $C_F$  and  $\delta^*$  results for a panel compared to hardwall are shown in Figure 205. Unlike the hardwall surface, the panel data for different flow and temperature do not collapse with respect to Reynolds number per unit length. The local skin friction coefficients are lower for the treatment panel compared to the hardwall. The friction coefficient decreases with Reynolds number as well as with decreasing temperature. Displacement thickness for the panel is higher compared to the hardwall. Friction coefficient as well as displacement thickness approach to those of hardwall with decreasing facesheet porosity.

**6.3 Data Processing and Presentation for DC Flow Resistance:** DC flow resistance for various bulk absorber and SDOF panels are measured at a number of flow Mach numbers with varying heated conditions. Typical results of grazing flow Mach number effects on DC flow resistance at ambient temperature are shown in Figure 206 for two facesheets of different porosity. The DC flow resistance increases significantly with increasing grazing flow Mach number keeping its increasing trend with approach velocity. The effect of grazing flow temperature on DC flow resistance for a 9% porous facesheet at fixed grazing flow

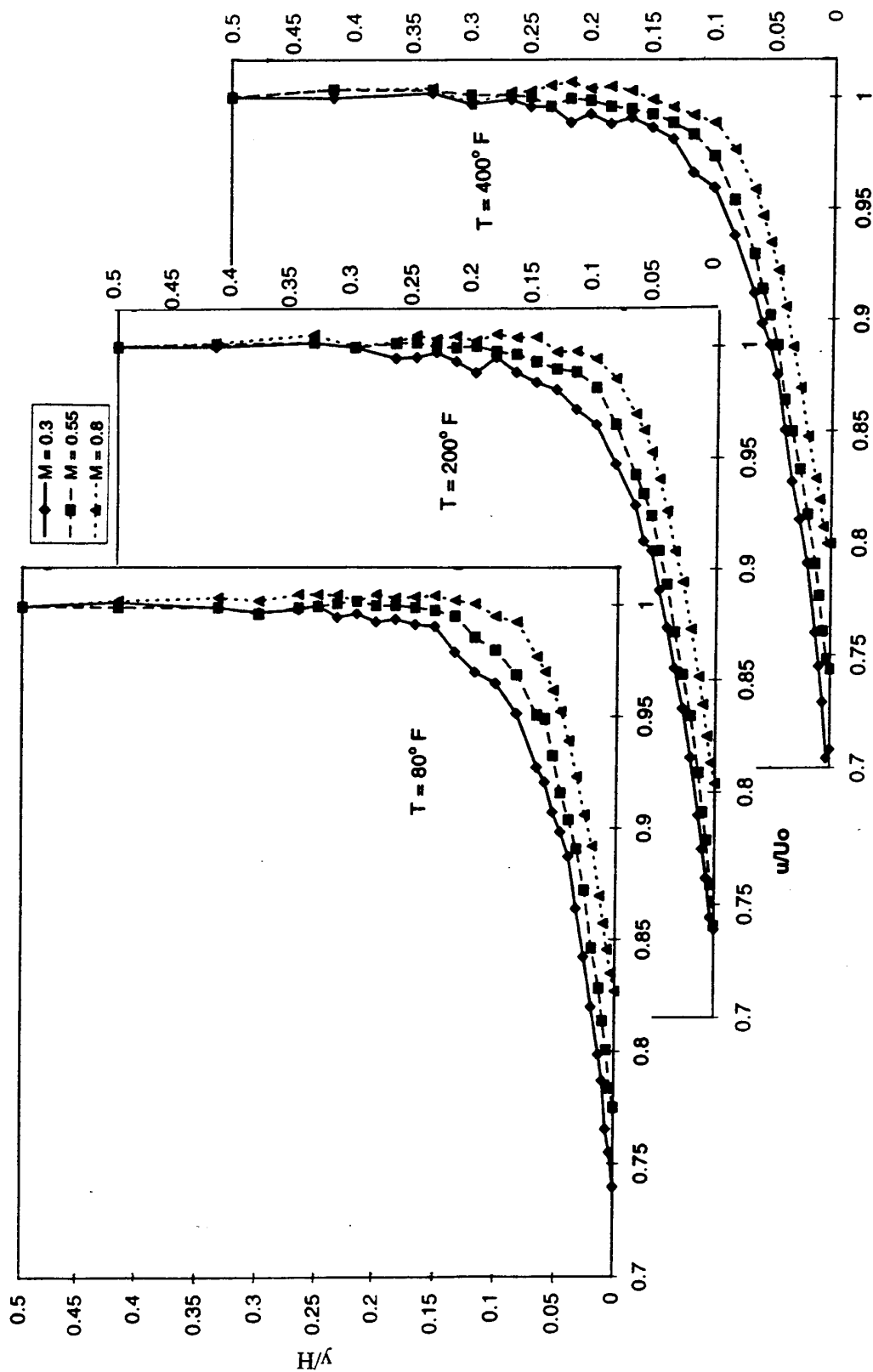


Figure 202. Effect of grazing flow Mach number (M) on boundary layer velocity profile for a 0.5"-deep 100 ppi Silicon Carbide panel with 20% porous 0.025"-thick facesheet with 0.04" diameter holes in a 3" high (H) flow duct.

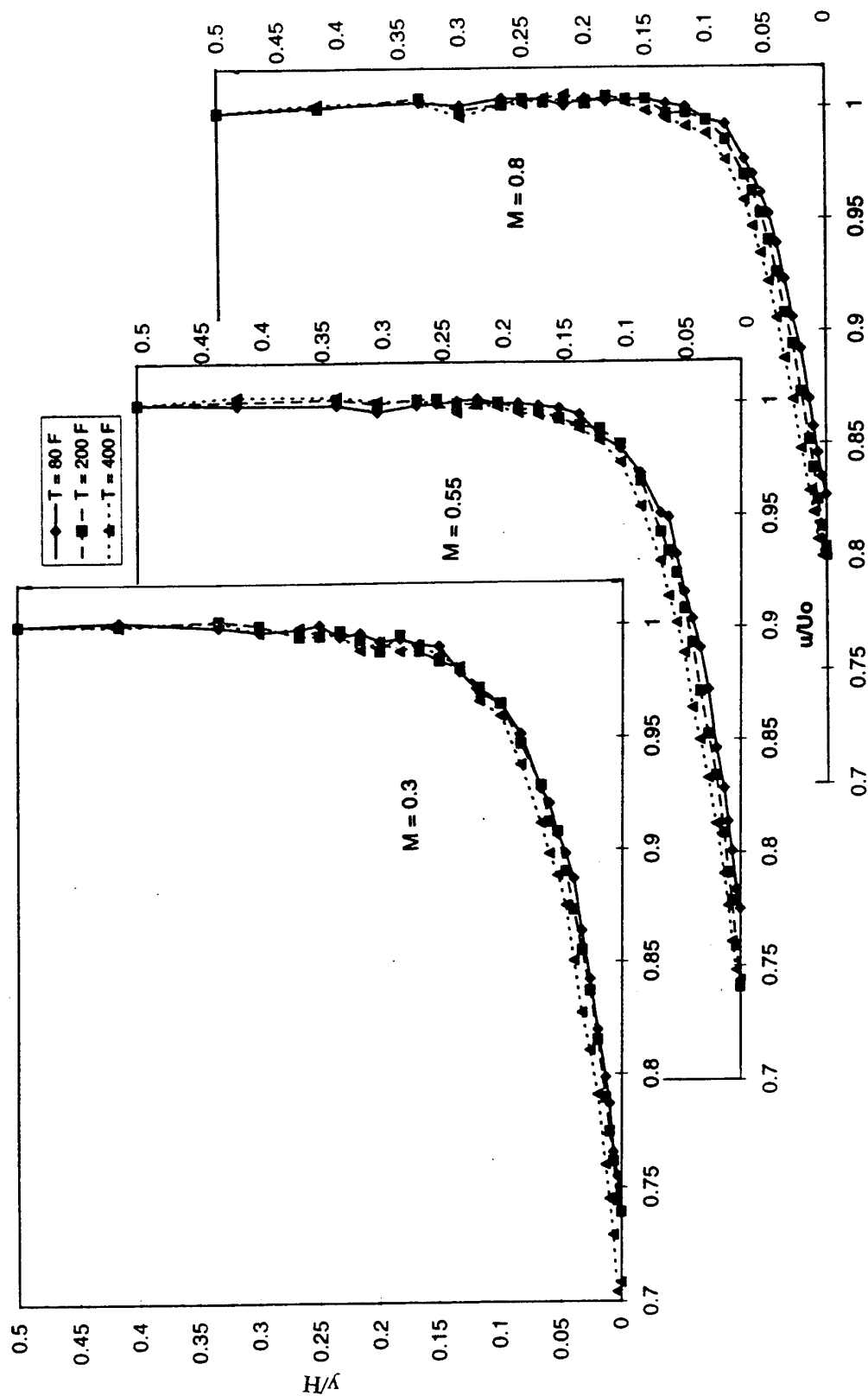


Figure 203. Effect of grazing flow temperature (T) on boundary layer velocity profile for a 0.5"-deep 100 ppi Silicon Carbide panel with 20% porous 0.025"-thick facesheet with 0.04" diameter holes in a 3" high (H) flow duct.

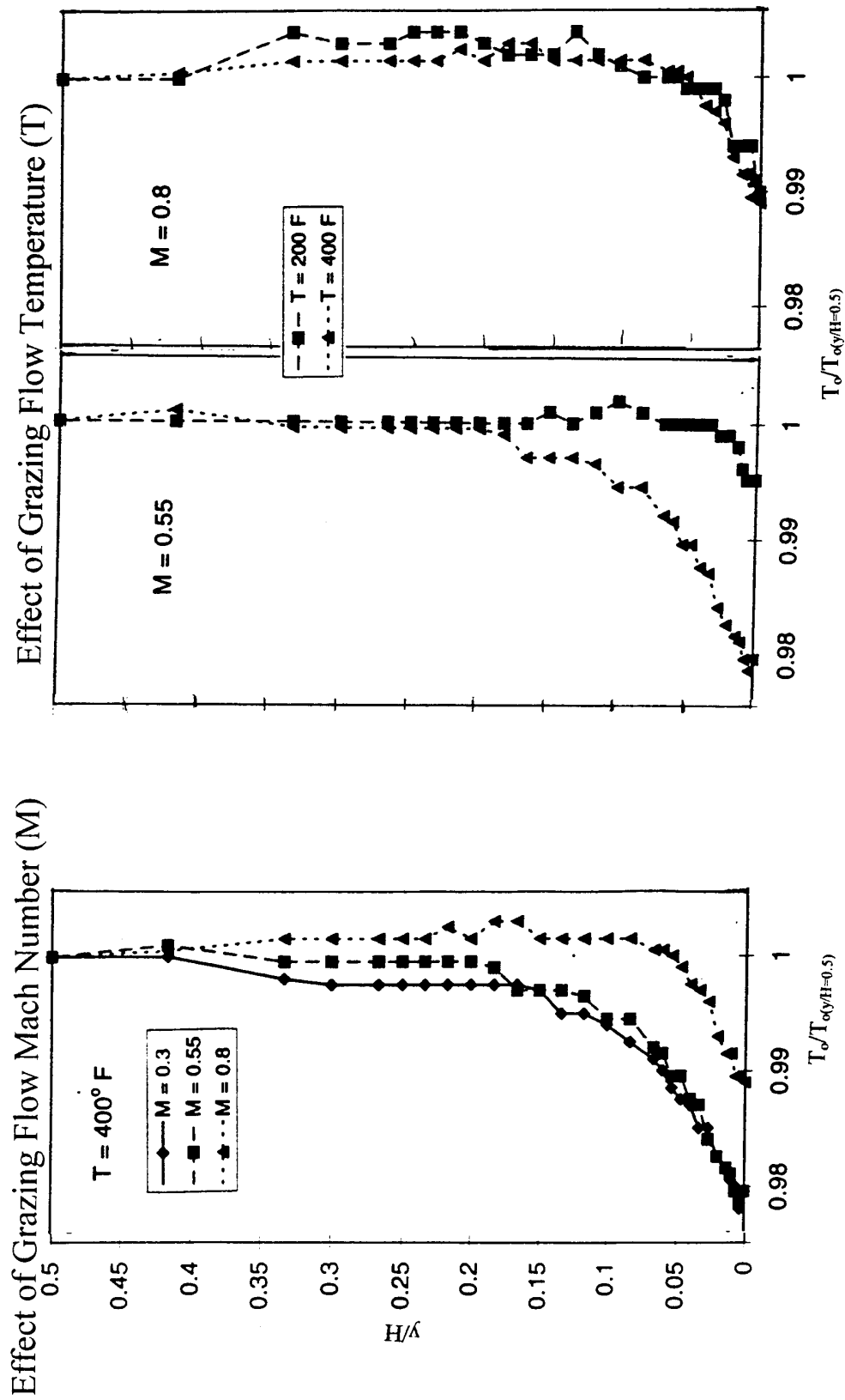


Figure 204. Effect of grazing flow Mach number (M) and grazing flow temperature (T) on boundary layer temperature profile for a 0.5"-deep 100 ppi Silicon Carbide panel with 20% porous 0.025"-thick facesheet with 0.04" diameter holes in a 3" high (H) flow duct.

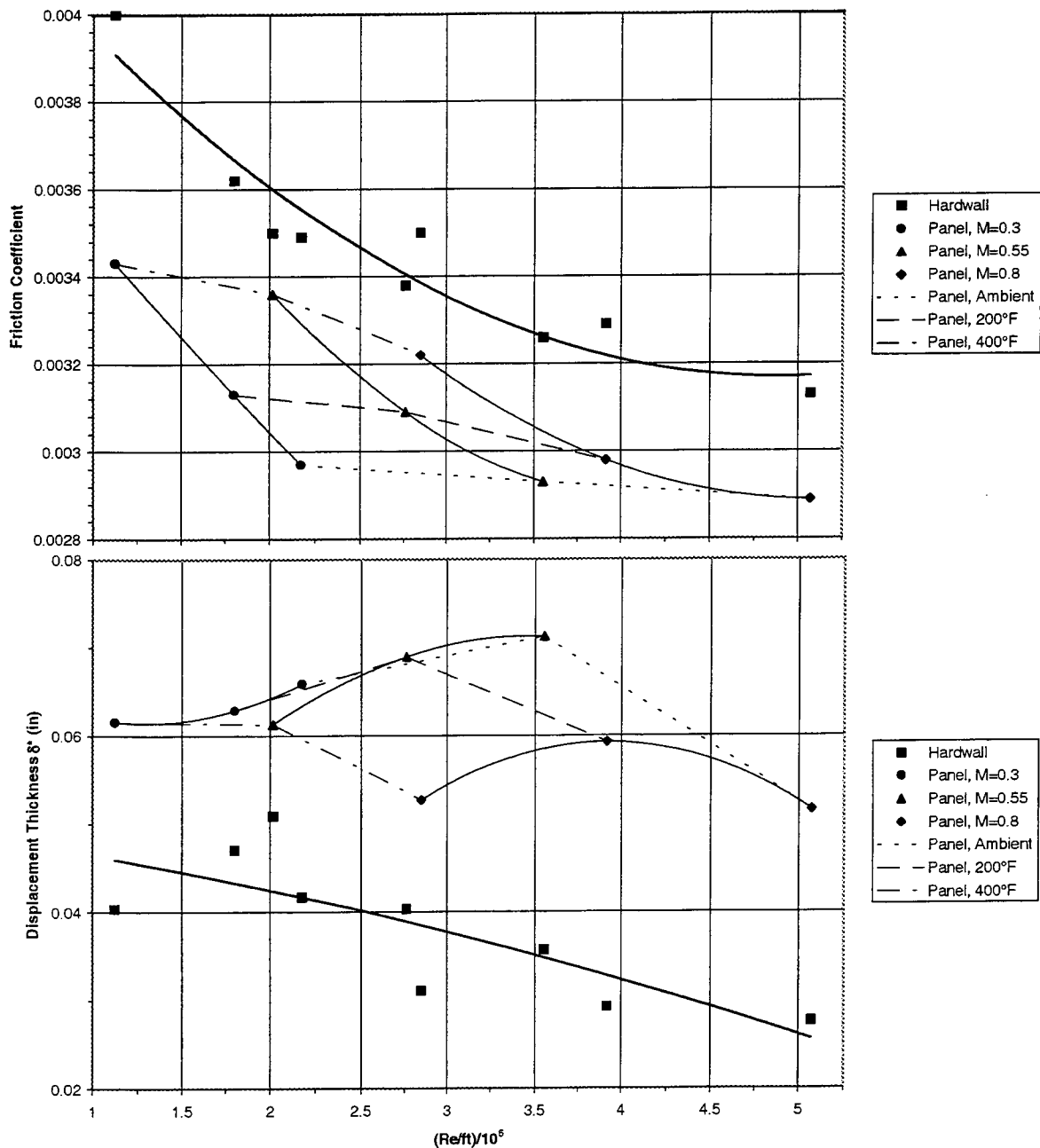


Figure 205. Local skin friction coefficient and displacement thickness for a 0.5"-deep 100 ppi Silicon Carbide panel with 30% porous 0.025"-thick facesheet with 0.04" diameter holes.

Mach numbers is shown in Figures 207 through 209. DC flow resistance decreases with increasing temperature. However, unlike the behavior in the absence of flow, where the corrected DC flow resistance collapses when plotted against corrected approach velocity for different temperatures, the corrected data in the presence of grazing flow does not collapse. The similarity principle for such correction needs to be modified by including a grazing flow Mach number function to achieve desired collapse of the data.



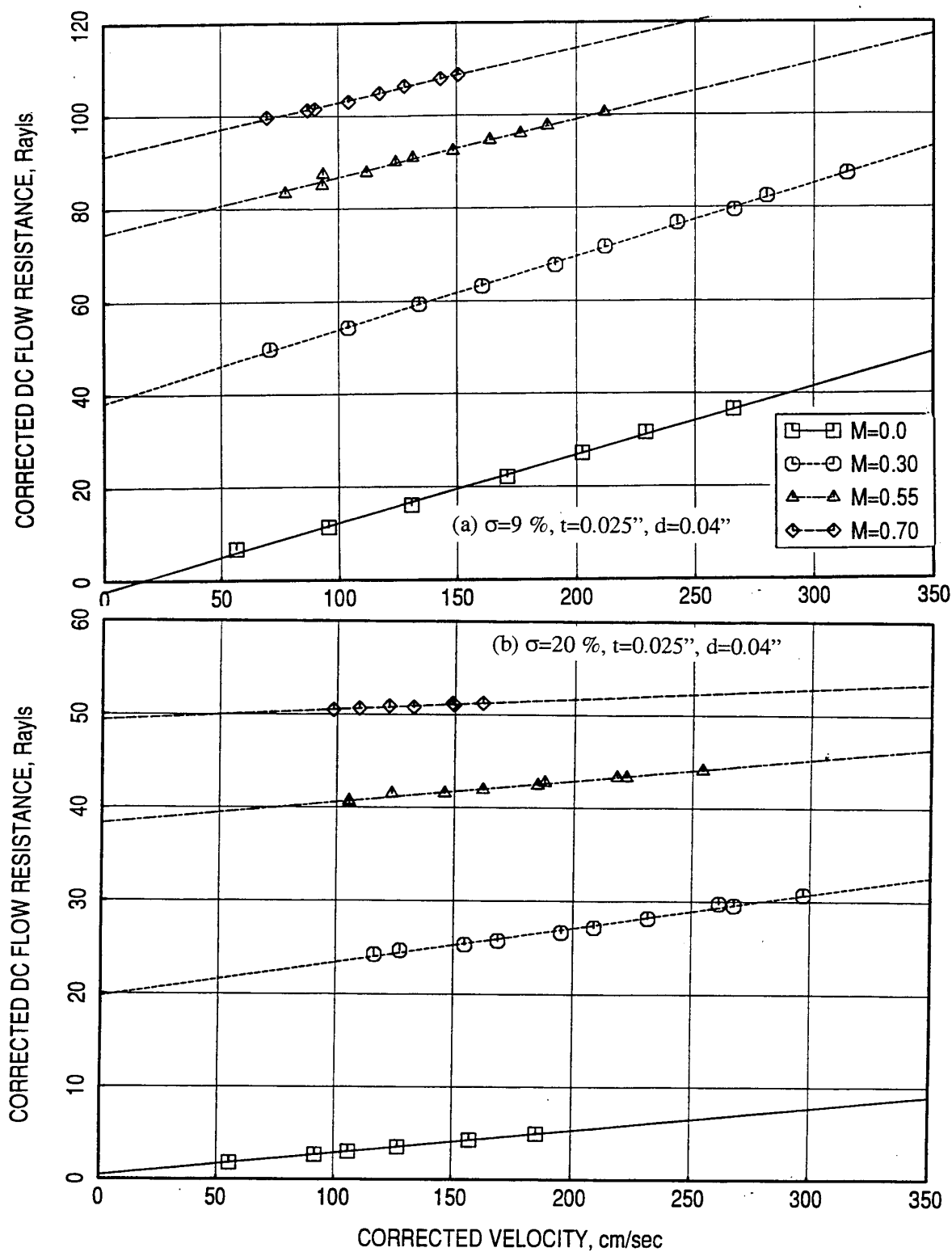


Figure 206. Effect of grazing flow Mach number (M) on DC flow resistance for (a) 9 % and (b) 20 % porous 0.025"-thick facesheets with 0.04" diameter holes at ambient temperature.

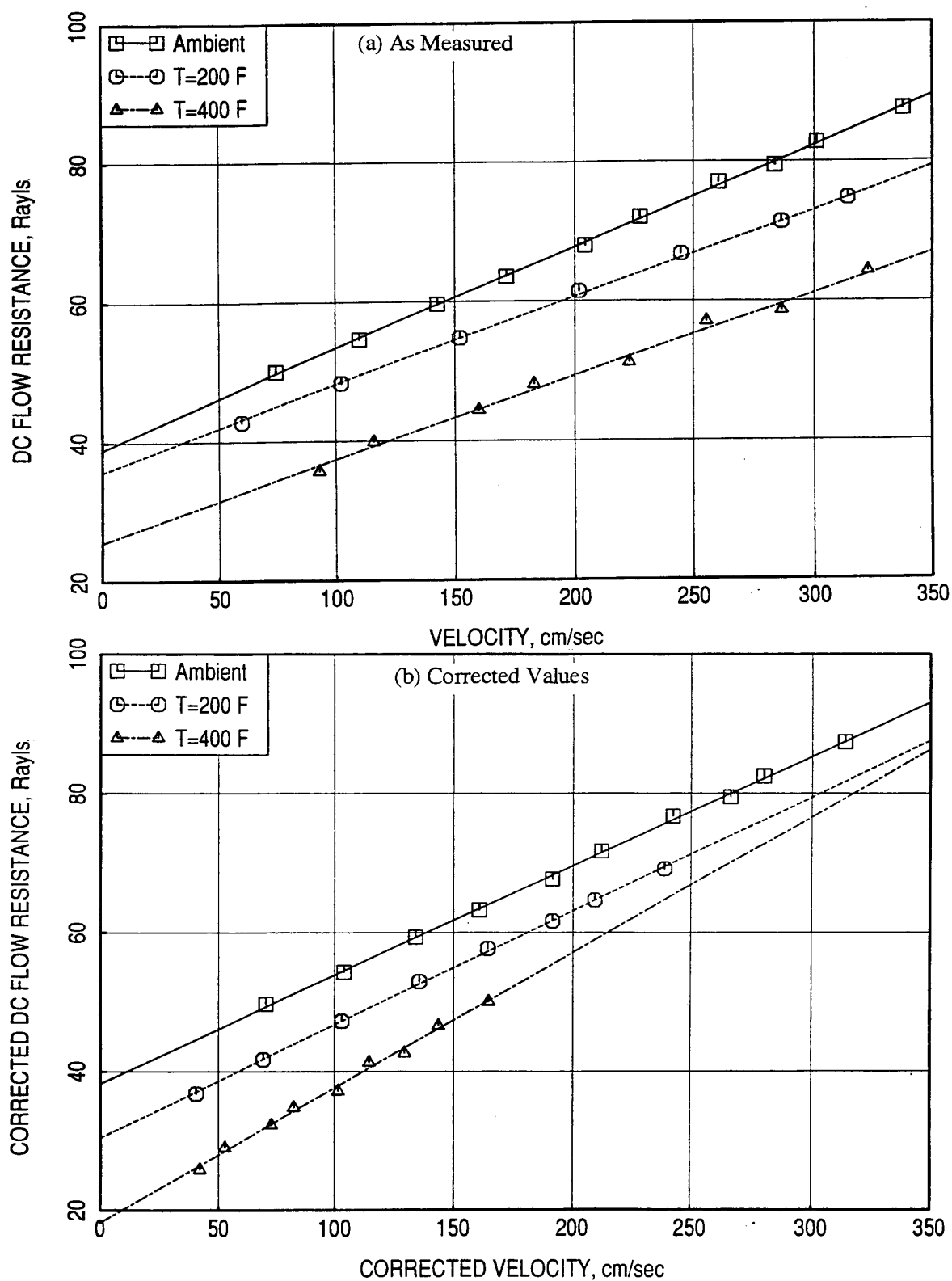


Figure 207. Effect of grazing flow temperature (T) on DC flow resistance for a 9 % porous 0.025"-thick facesheet (d=0.04") plotted (a) as measured against approach velocity and (b) corrected values against corrected approach velocity,  $M=0.3$ .

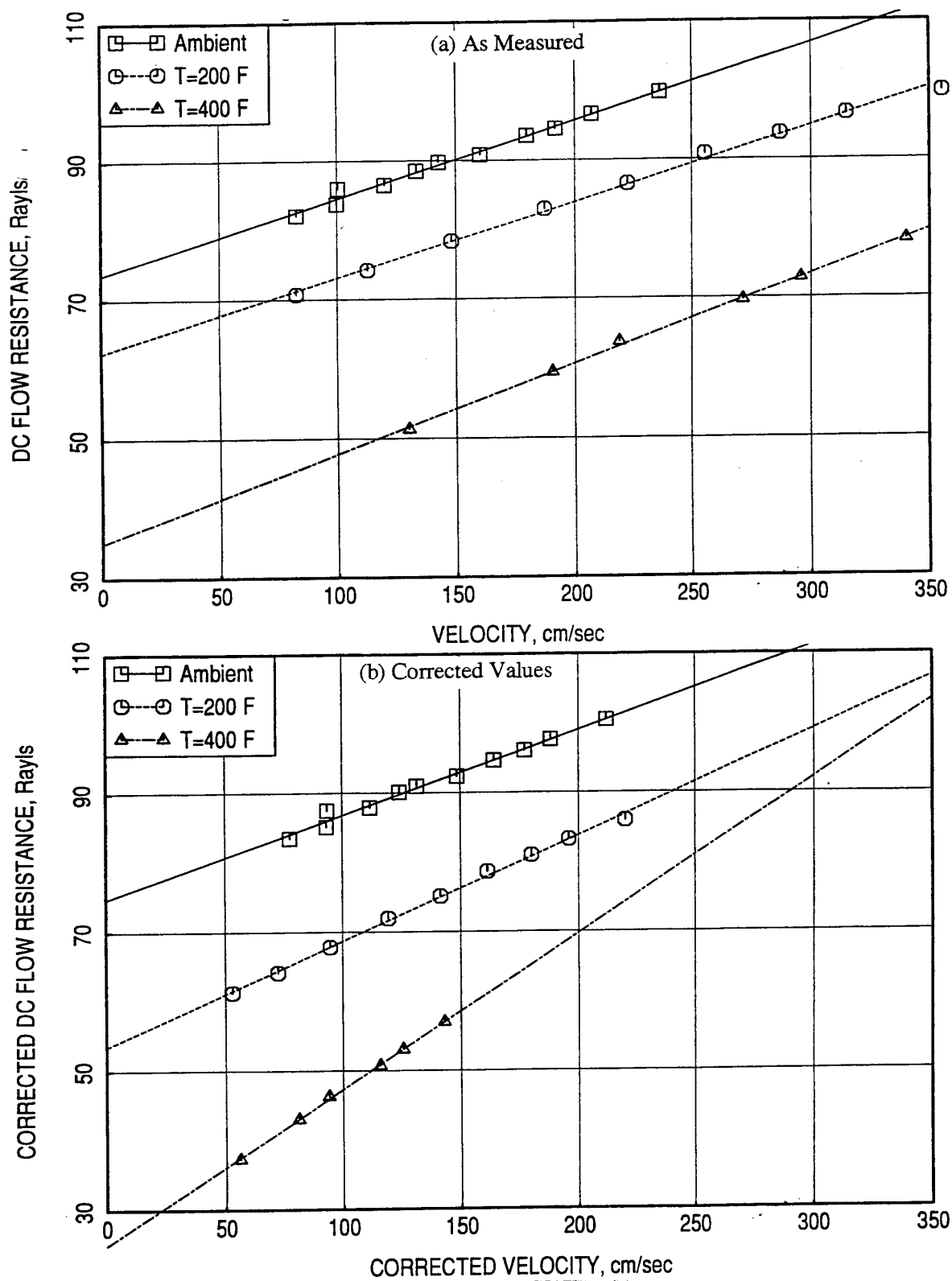


Figure 208. Effect of grazing flow temperature (T) on DC flow resistance for a 9 % porous 0.025"-thick facesheet (d=0.04") plotted (a) as measured against approach velocity and (b) corrected values against corrected approach velocity,  $M=0.55$ .

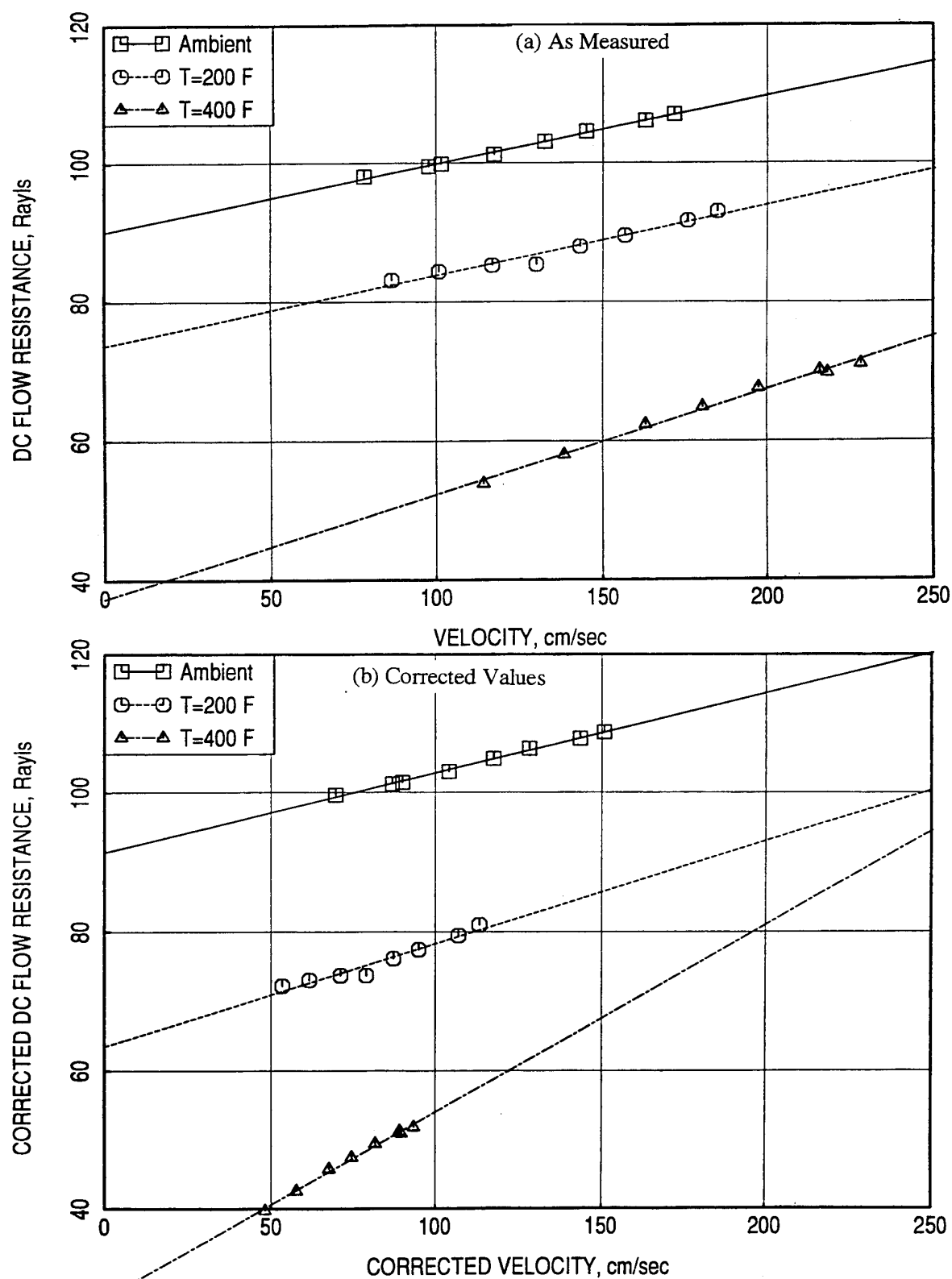


Figure 209. Effect of grazing flow temperature (T) on DC flow resistance for a 9 % porous 0.025"-thick facesheet (d=0.04") plotted (a) as measured against approach velocity and (b) corrected values against corrected approach velocity,  $M=0.7$ .

Typical results for grazing flow effects on DC flow resistance at ambient temperature are shown in Figure 210 for two bulk absorber type panels with different bulk materials. Again, the DC flow resistance increases significantly with increasing grazing flow Mach number maintaining its increasing trend with approach velocity. The effect of grazing flow temperature on DC flow resistance for a 100 ppi 0.5"-deep SiC panel with a 30% porous facesheet at fixed grazing flow Mach numbers is shown in Figures 211 and 212. DC flow resistance decreases with increasing temperature. Again, the corrected data in the presence of grazing flow does not collapse for different temperature conditions.

At higher grazing flow Mach number conditions, especially at higher temperatures, the DC flow resistance trend at lower approach velocities is drastically opposite to the generally expected behavior. In this velocity domain the DC flow resistance is very high and decreases with increasing approach velocity up to a certain level. DC flow resistance begins to increase by further increase of approach velocity. This is further illustrated in Figure 213 for a 100 ppi 0.5"-deep SiC panel with a 40% porous facesheet ( $t=0.025''$  and  $d=0.04''$ ). The data at lower approach velocities, behaving opposite to the expected trend is excluded from the curve fitting process.

#### **6.4 Parametric Study of Flow Duct Data**

Parametric study of various flow duct data, namely, insitu impedance, boundary layer profile and related parameters, and DC flow resistance, are presented in this section. The parameters include the grazing flow, temperature, facesheet properties (i.e., porosity  $\sigma$ , thickness  $t$ , and hole diameter  $d$  for perforates and resistivity for linear facesheets), and bulk type. Two different bulk absorbers, 100 ppi Silicon Carbide (SiC) and standard 12 lbf T-Foam, are used in the flow duct tests. In addition, SDOF type configurations (i.e., facesheet over cavities) are also tested. In these configurations the facesheets used for bulk absorbers are also included. Variation of different parameters for the three configurations are listed in Tables 9 through 11. A hardwall configuration, listed in the tables, are used for boundary layer data only.

The insitu impedance data files for all the configurations tested are listed in Tables A5 through A8 in Appendix A. The corresponding relative impedance data files are listed in Tables A9 through A12. The boundary layer profile data files and the related boundary layer parameters computed from the profiles are listed in Tables A13 through A15 in Appendix A. The DC flow resistance data files for all flow duct configurations are listed in Tables A16 through A18.

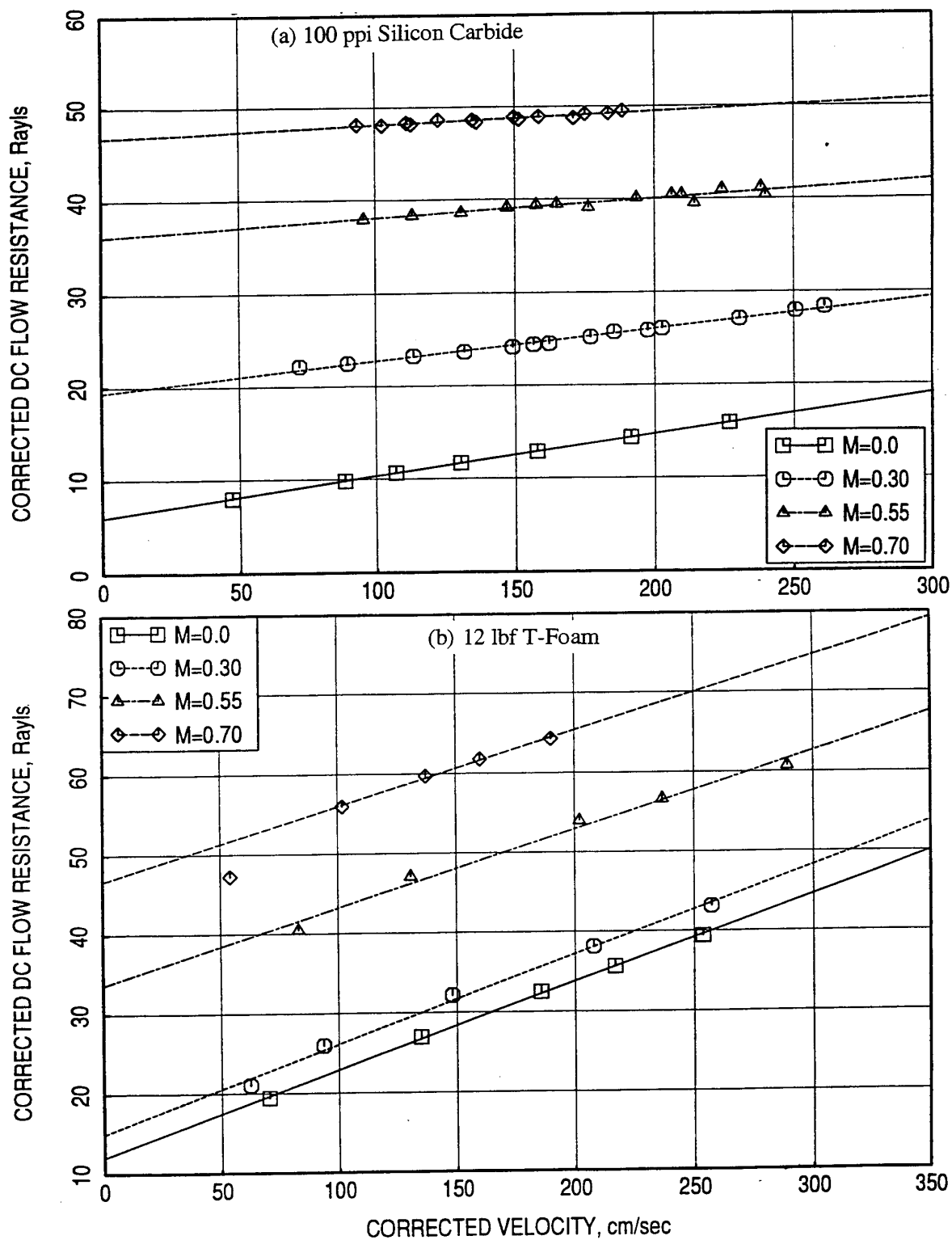


Figure 210. Effect of grazing flow Mach number (M) on DC flow resistance for 0.5"-deep (a) 100 ppi Silicon Carbide and (b) 12 lbf T-Foam panels with 30% porous 0.025"-thick facesheet with 0.04" diameter holes.

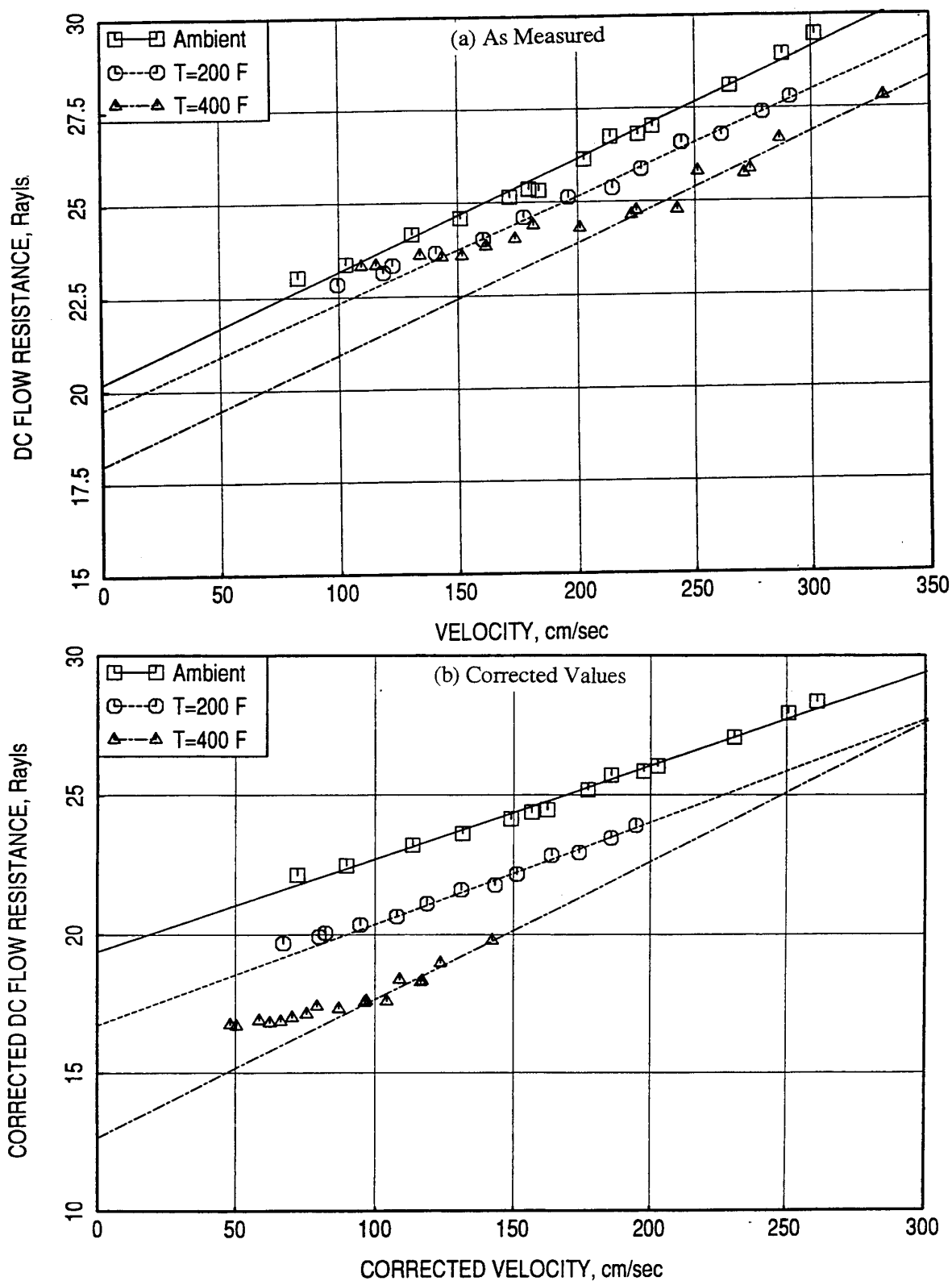


Figure 211. Effect of grazing flow temperature (T) on DC flow resistance for a 0.5"-deep 100 ppi SiC panel with a 30% porous facesheet (t=0.025", d=0.04") plotted (a) as measured against approach velocity and (b) corrected values against corrected approach velocity, M=0.3.

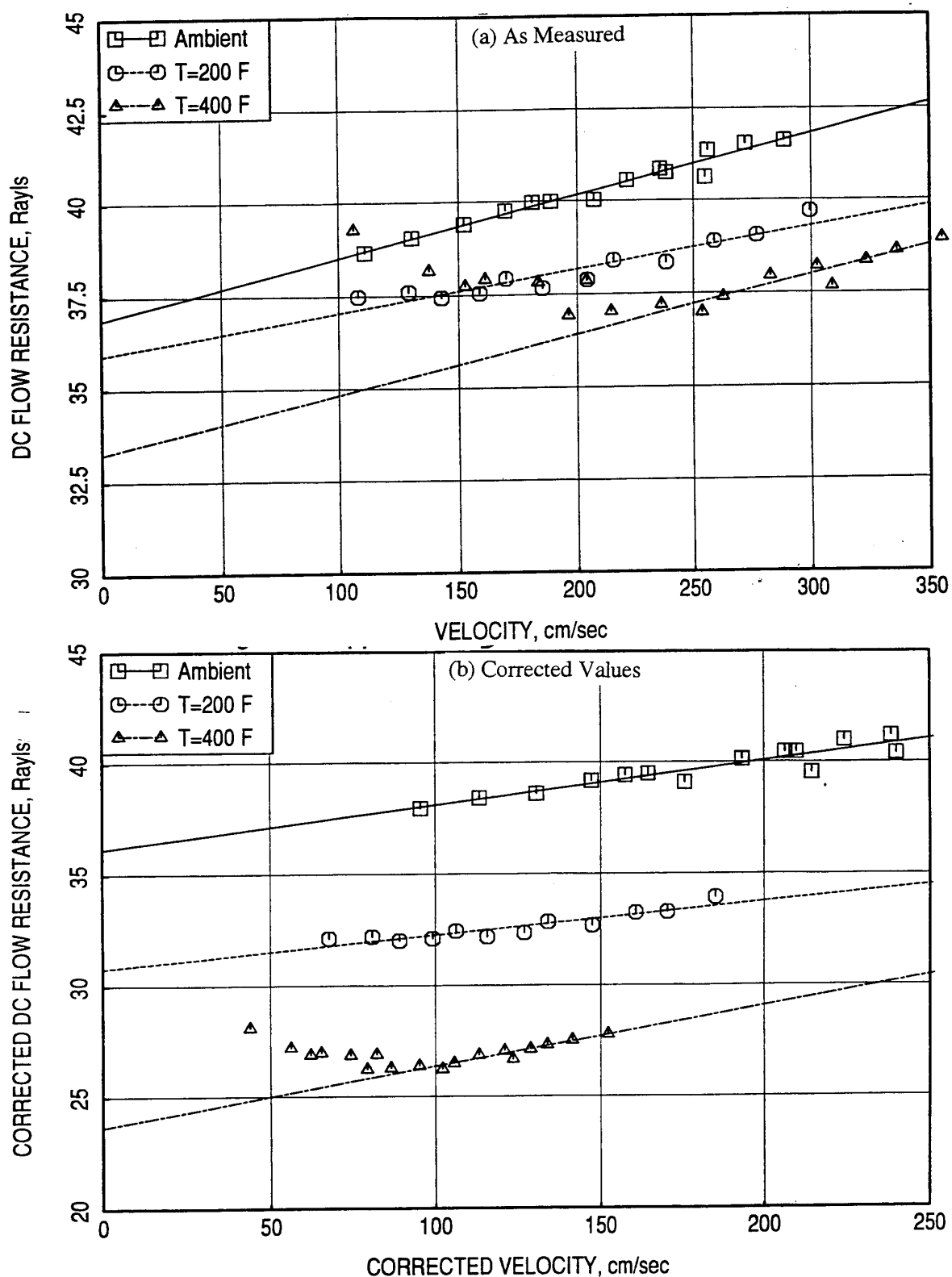


Figure 212. Effect of grazing flow temperature ( $T$ ) on DC flow resistance for a 0.5"-deep 100 ppi SiC panel with a 30% porous facesheet ( $t=0.025"$ ,  $d=0.04"$ ) plotted (a) as measured against approach velocity and (b) corrected values against corrected approach velocity,  $M=0.55$ .



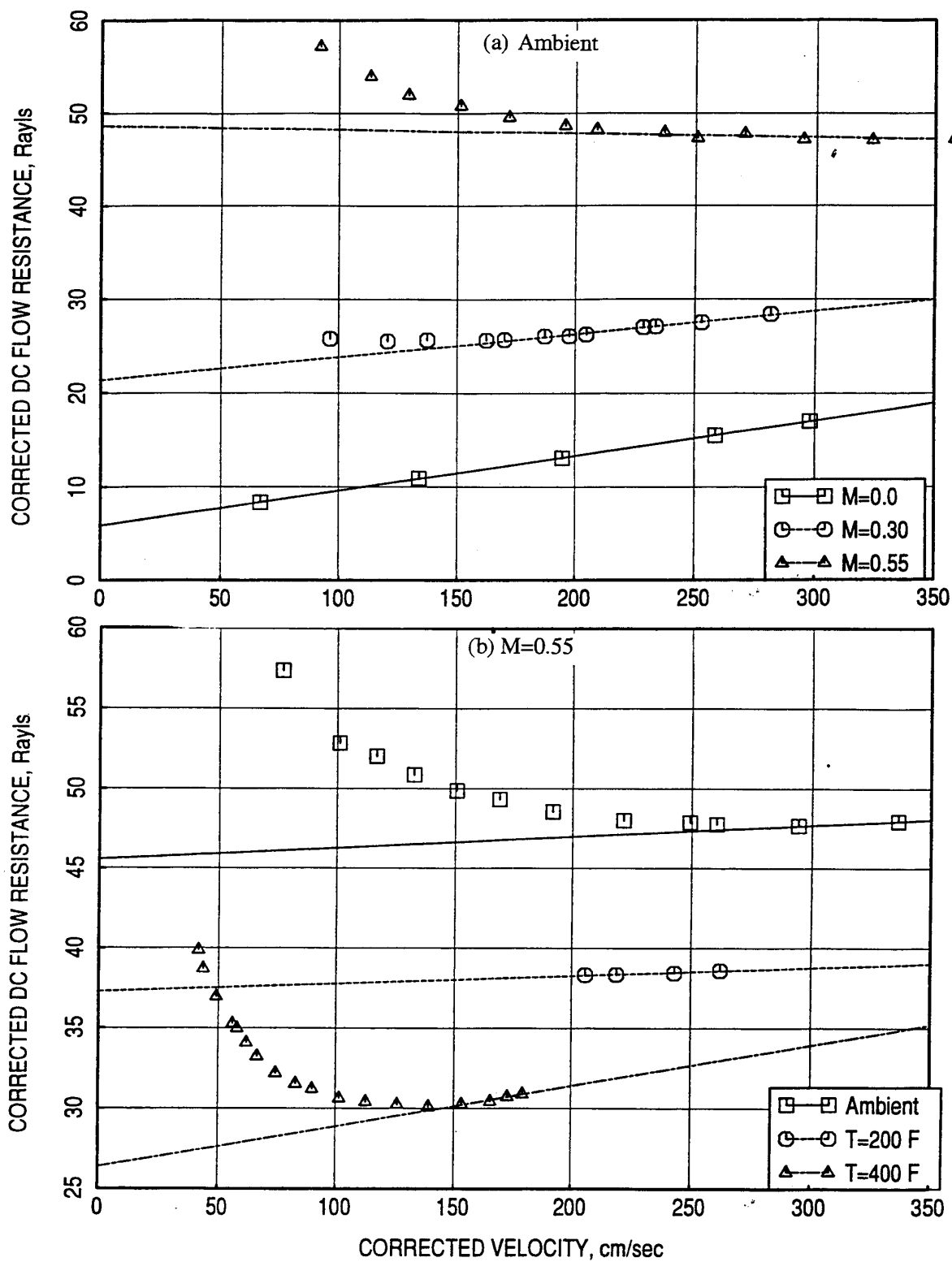


Figure 213. Effect of grazing flow (a) Mach number (M) at ambient temperature and (b) temperature (T) at M=0.55 on DC flow resistance for a 0.5"-deep 100 ppi SiC panel with a 40% porous 0.025"-thick facesheet with 0.04" diameter holes.

Table 9. Parametric variations for 100 ppi 0.5"-deep Silicon Carbide bulk absorber configurations.

1. Effect of Porosity (Thin Facesheet)  
t=0.025", d=0.04"

S=20%	1-1
30%	1-2
40%	1-3
HW	0

2. Effect of Porosity (Thick Facesheet)  
t=0.10", d=0.07"

S =30%	1-4031
35%	1-4075
40%	1-4143
HW	0

3. Effect of Thickness (Smaller Hole diameter) S=40%, d=0.04"

T=0.015"	1-7
0.025"	1-3
0.04"	1-8
0.06"	1-9
0.10"	1-4121

4. Effect of Thickness (Larger Hole Diameter) d=0.07", S=35%

T=0.04"	1-4072
0.10"	1-4075

5. Effect of Hole diameter (Thin Facesheet) S=40%, t=0.025"

D=0.04"	1-3
0.06"	1-5
0.08"	1-6
0.10"	1-4161

6. Effect of Hole Diameter (Thick Facesheet) t=0.10", S=40%

D=0.04"	1-4052
0.07"	1-4075

7. Effect of Linear Facesheet Resistivity

10 Rayls	1-11
15 Rayls	1-12

#### 6.4.1 Effect of Grazing Flow Mach Number at Ambient Temperature

**Insitu Impedance:** Effect of grazing flow Mach number on relative impedance for a few panel configurations is shown in Figures 175 through 177. Those results are obtained using a second order polynomial curve fit. However, the following results in this section are derived using a straight-line passing through zero at zero frequency for relative reactance and an average value, independent of frequency, for relative resistance. Effect of grazing flow on relative impedance for a few typical panels is shown in Figures 214 and 215. Relative resistance increases and relative reactance decreases with increasing grazing flow Mach number. Effect of flow on relative impedance for T-Foam bulk absorbers are insignificant compared to SiC panels. The absolute impedance for several bulk absorbers is computed using the measured normal impedance and the relative impedance. Effect of grazing flow Mach number on these panels is shown in Figures 216 through 218. Similar results using

Table 10. Parametric variations for 12-lbf 0.5"-deep T-Foam bulk absorber configurations.

1. Effect of Porosity (Thin Facesheet)  
t=0.025", d=0.04"

S=20%	6-1
30%	6-2
40%	6-3
HW	0

2. Effect of Porosity (Thick Facesheet)  
t=0.10", d=0.07"

40%	6-4143
HW	0

3. Effect of Thickness (Smaller Hole diameter) S=40%, d=0.04"

0.025"	6-3
0.04"	6-8
0.06"	6-9

4. Effect of Hole diameter (Thin Facesheet) S=40%, t=0.025"

d=0.04"	6-3
0.08"	6-6

Table 11. Parametric variations for SDOF type liner configurations.

1. Effect of Porosity (Thin Facesheet)  
t=0.025", d=0.04"

S=9%	2
15%	4
S=20%	T1-1
30%	T1-2
40%	T1-3
HW	0

2. Effect of Porosity (Thick Facesheet)  
t=0.10", d=0.07"

40%	T1-4143
HW	0

3. Effect of Thickness (Smaller Hole diameter) S=40%, d=0.04"

T=0.025"	T1-3
0.04"	T1-8
0.06"	T1-9
0.10"	T1-4121

4. Effect of Thickness for SDOF Type Panels, S=9%, d=0.04"

T=0.01"	12
0.025"	2
0.06"	15
0.10"	17

5. Effect of Hole diameter (Thin Facesheet) S=40%, t=0.025"

D=0.04"	T1-3
0.06"	T1-5
0.08"	T1-6

6. Effect of Hole diameter for SDOF Type Panels S=9%, t=0.025"

D=0.04"	2
0.08"	11

second order polynomial relative impedance are shown earlier in Figures 180 through 182. On each of Figures 215 through 218 the same facesheet is used for both the bulk materials. Resistance increases and reactance decreases with increasing Mach number. Effect of grazing flow Mach number is very small on the reactance for T-Foam bulk absorbers. Increase of resistance due to increasing Mach number is higher for facesheets of lower porosity. However, the effect on reactance is higher for facesheets of higher porosity.

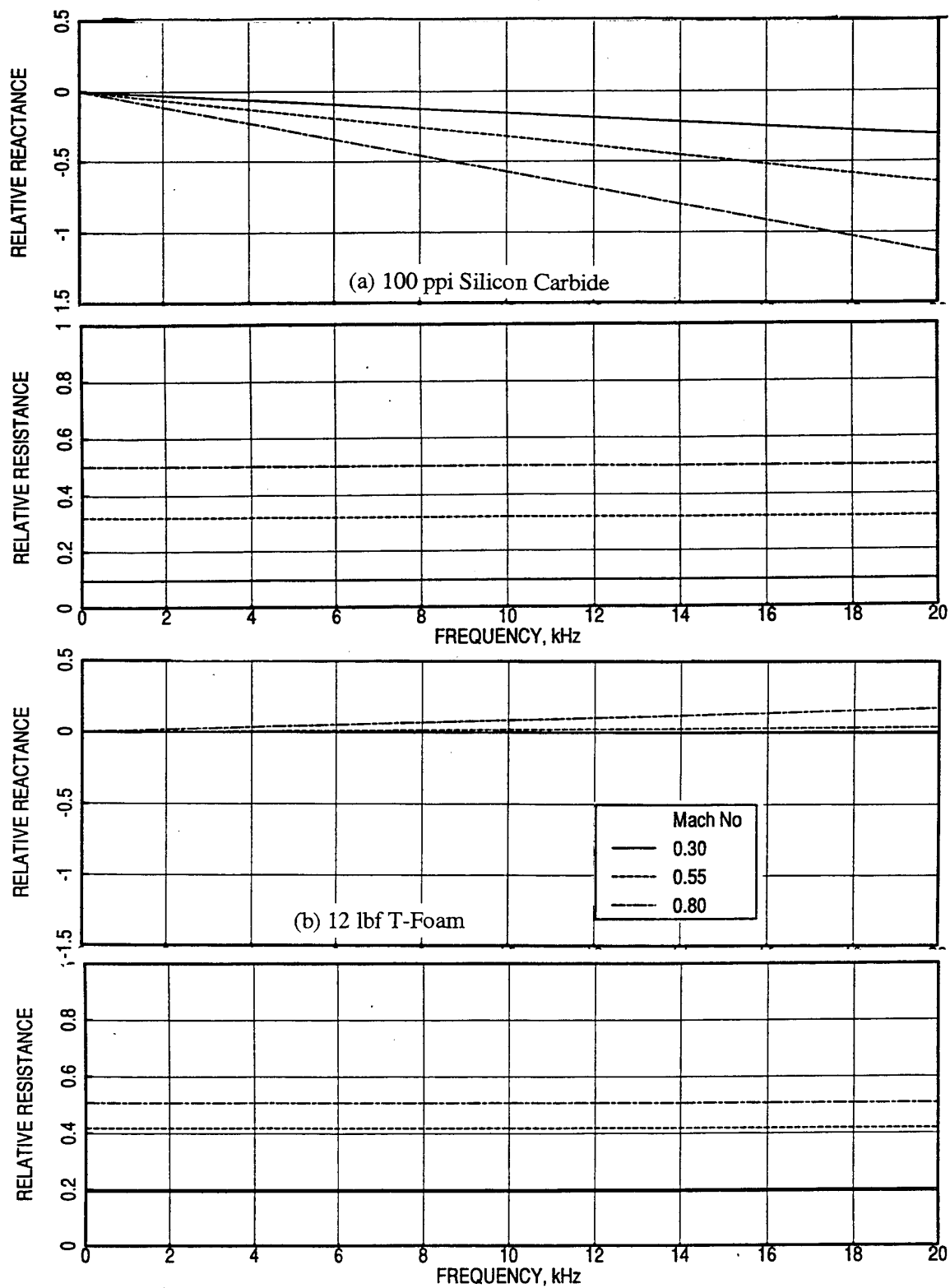


Figure 214. Effect of grazing flow Mach number (M) on relative impedance for 0.5"-deep (a) 100 ppi Silicon Carbide and (b) 12 lbf T-Foam panels with 40% porous 0.025"-thick facesheet with 0.04" diameter holes.

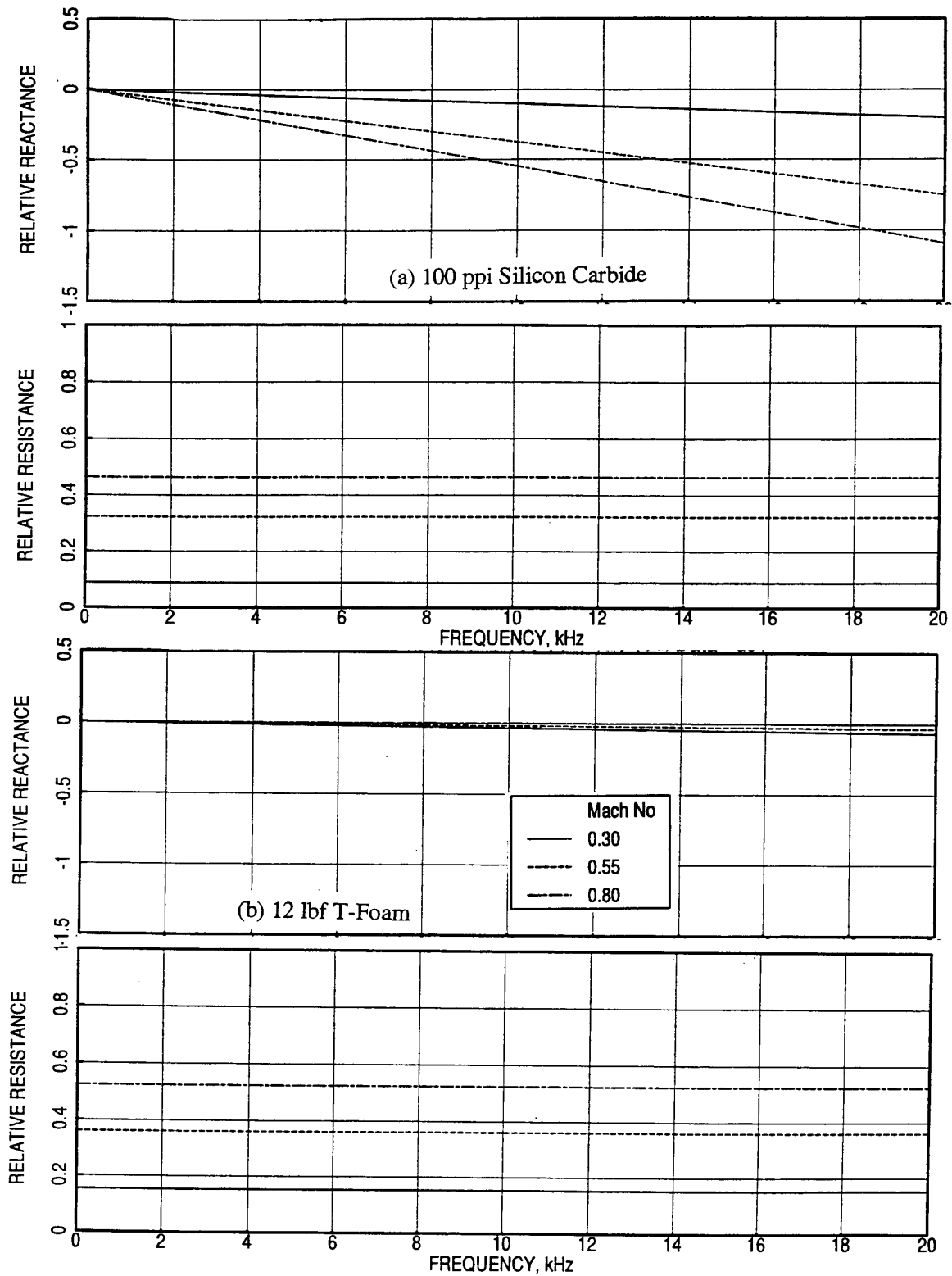


Figure 215. Effect of grazing flow Mach number ( $M$ ) on relative impedance for 0.5''-deep (a) 100 ppi Silicon Carbide and (b) 12 lbf T-Foam panels with 30% porous 0.025''-thick facesheet with 0.04'' diameter holes.

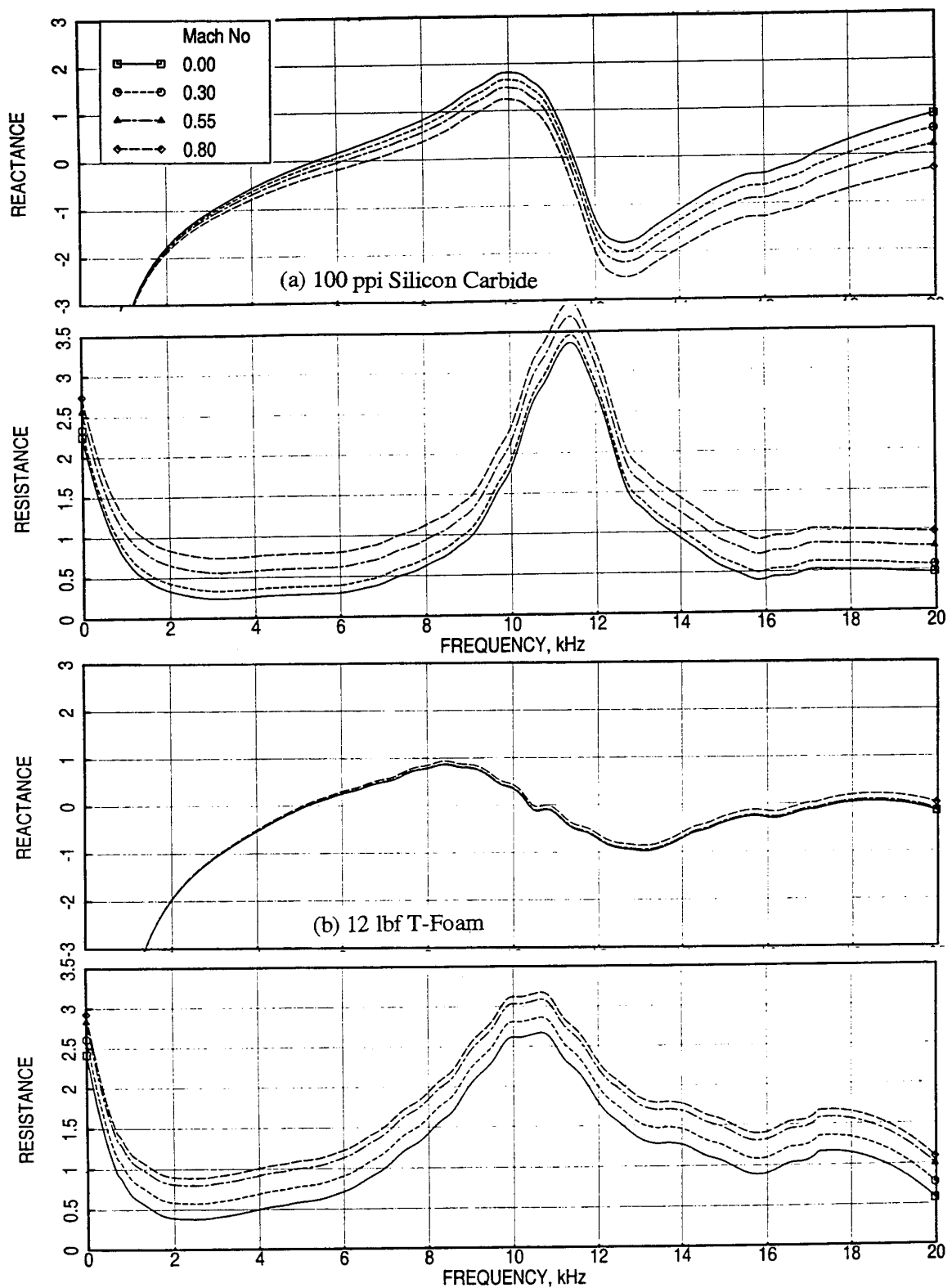


Figure 216. Effect of grazing flow Mach number ( $M$ ) on normal impedance for 0.5"-deep (a) 100 ppi Silicon Carbide and (b) 12 lbf T-Foam panels with 40% porous 0.025"-thick facesheet with 0.04" diameter holes.

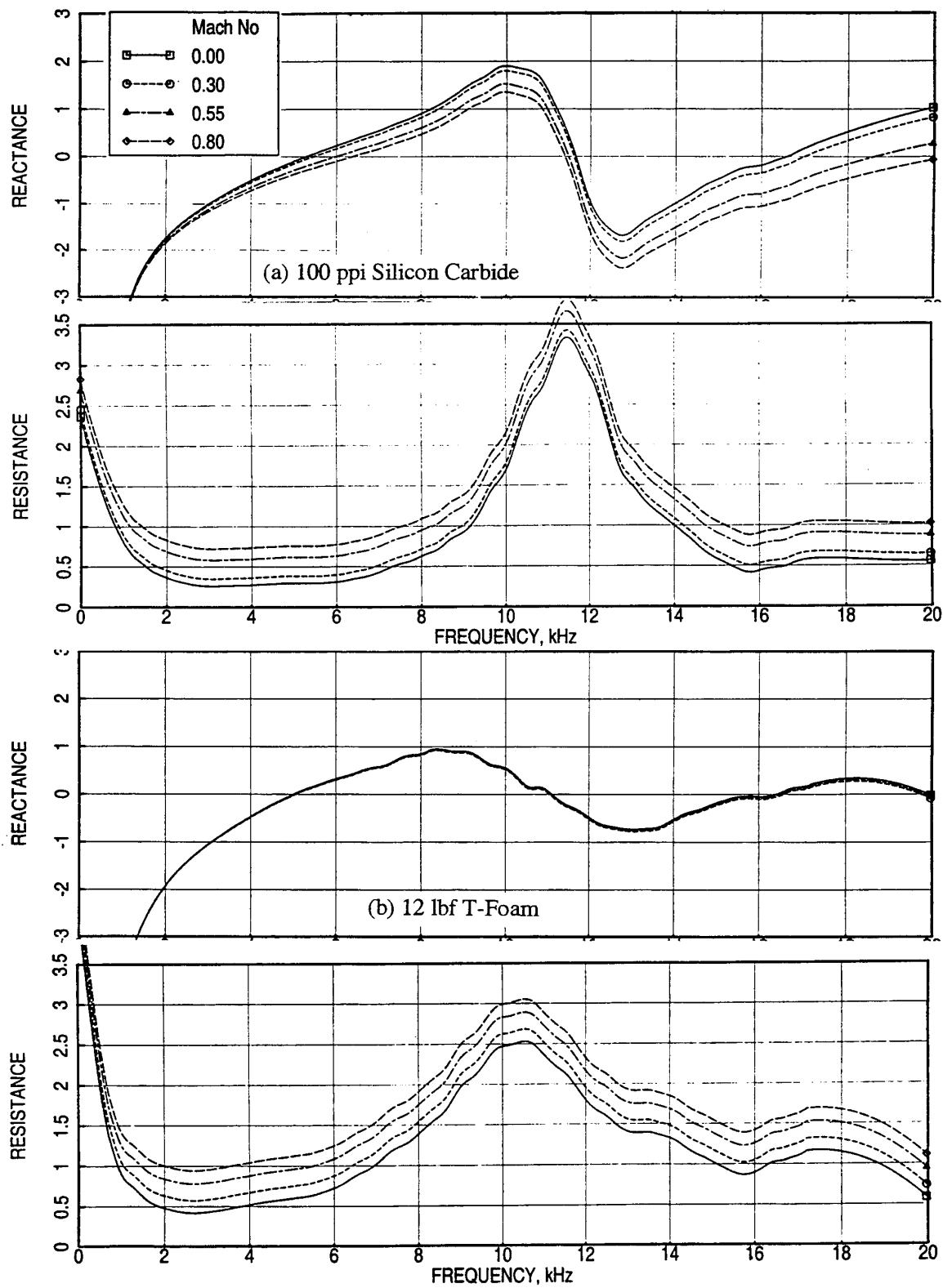


Figure 217. Effect of grazing flow Mach number ( $M$ ) on normal impedance for 0.5''-deep (a) 100 ppi Silicon Carbide and (b) 12 lbf T-Foam panels with 30% porous 0.025''-thick facesheet with 0.04'' diameter holes.

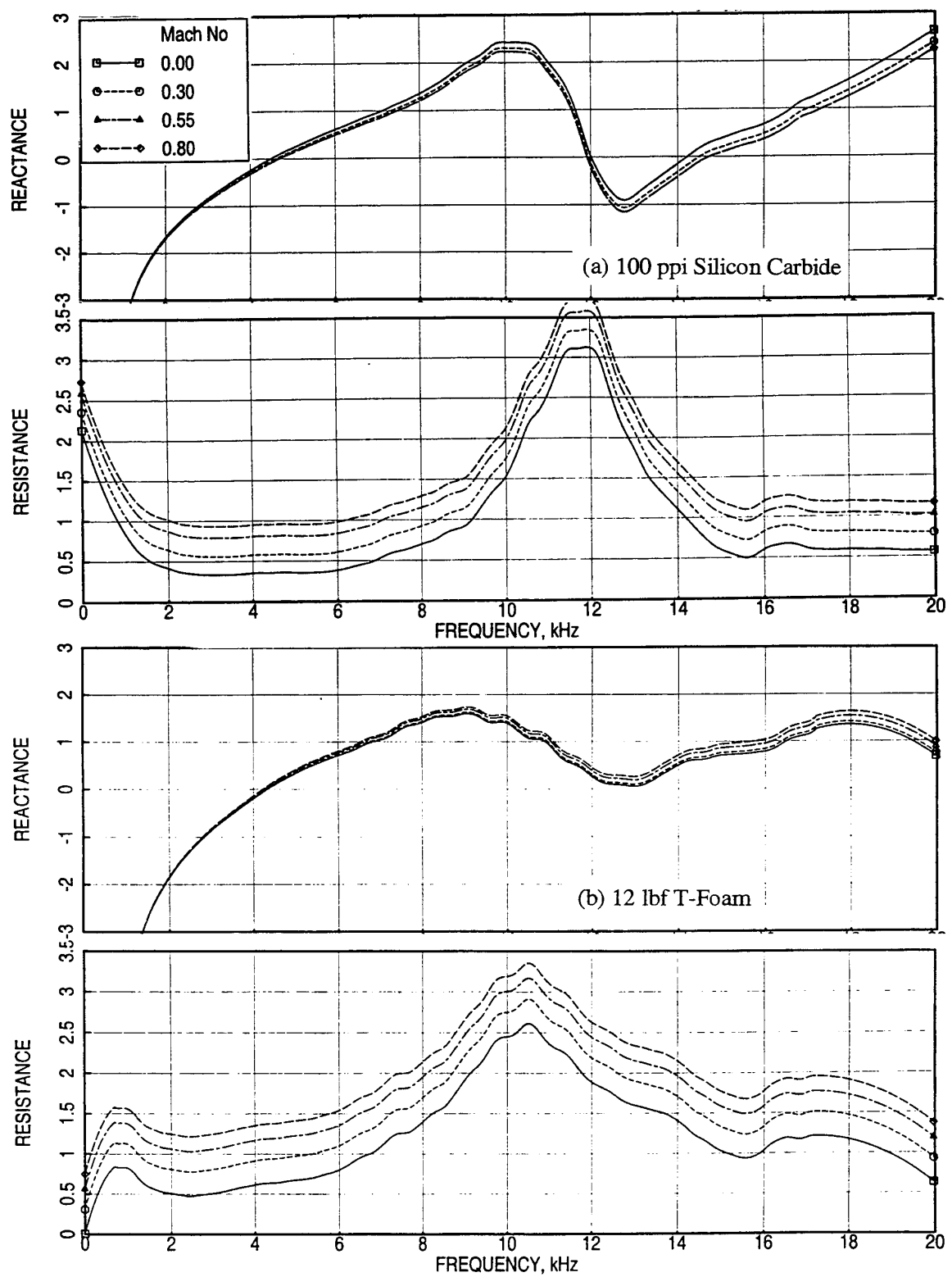


Figure 218. Effect of grazing flow Mach number ( $M$ ) on normal impedance for 0.5"-deep (a) 100 ppi Silicon Carbide and (b) 12 lbf T-Foam panels with 20% porous 0.025"-thick facesheet with 0.04" diameter holes.



Figure 219 shows the effect of Mach number on normal impedance for T-Foam bulk absorbers with two different facesheets. In Figure 219 (a) and (b) the facesheet thickness and facesheet hole diameter are increased, respectively, compared to Figure 216 (b). Grazing flow influence seems to be less effected due to facesheet thickness for T-Foam absorber. However, the increase in hole diameter influences grazing flow effect on normal reactance.

For SDOF type panels the influence of grazing flow on relative impedance is shown in Figures 220 through 222. In general, the relative resistance increases and relative reactance decreases with increasing Mach number. The effect reduces with increasing facesheet porosity. Effect of grazing flow for facesheets of 9% porosity is shown in Figure 222. As expected, the effect is significantly higher compared to highly porous panels. Similar conclusions can be drawn from the absolute impedance results shown in Figures 223 through 226.

**Boundary Layer Profiles and Related Parameters:** Effect of grazing flow Mach number on boundary layer velocity profiles is shown in Figure 202. The velocity profiles seem to be fully developed. Based on the shape and variation of the velocity profiles with respect to Mach number, it can be concluded that the flow becomes more turbulent with increasing Mach number, which is consistent with increasing Reynolds number. Effect of Mach number on the related parameters, namely, displacement thickness and local skin friction coefficient, are presented later in this section.

**DC Flow Resistance:** Effect of grazing flow on DC flow resistance is shown for a few typical configurations in Figures 206, 210, and 213. DC flow resistance increases significantly with grazing flow Mach number for bulk absorbers and SDOF type panels.

#### 6.4.2 Effect of Grazing Flow Temperature

**Insitu Impedance:** Effect of grazing flow temperature on relative impedance for a typical panel is shown in Figure 227 at different grazing flow Mach numbers. Effect of temperature on relative impedance is small. Relative resistance and reactance increase with increasing grazing flow temperature. The absolute impedance for several bulk absorbers are computed using the measured normal impedance, the relative impedance due to Mach number at ambient temperature, and relative impedance due to temperature at a given Mach number. This procedure is illustrated as follows;

$$Z(M,T) = Z(0,amb) + \Delta Z_F(M,amb) + \Delta Z_T(M,T), \quad (6)$$

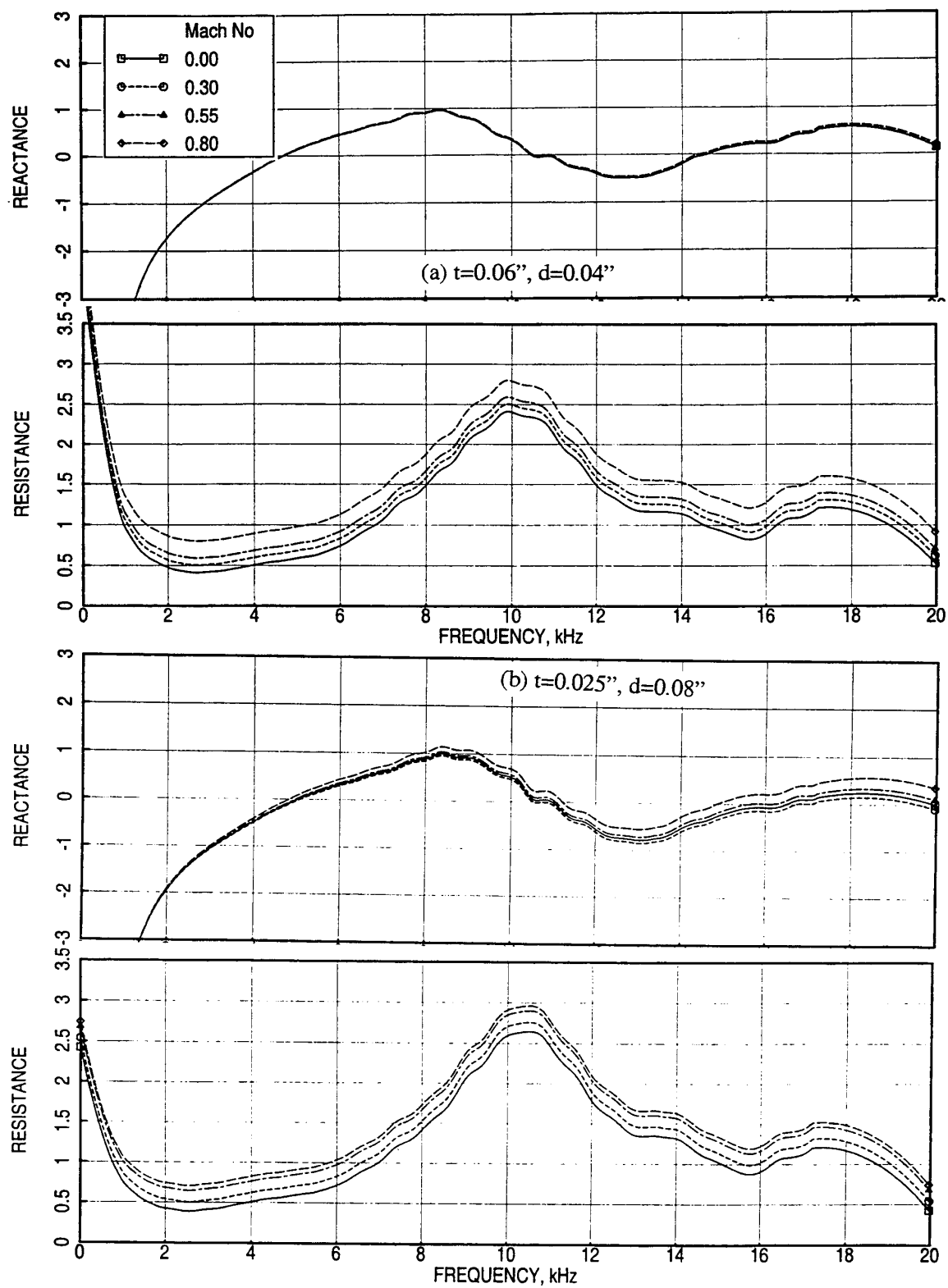


Figure 219. Effect of grazing flow Mach number (M) on normal impedance for a 0.5"-deep 12 lbf T-Foam panel with 40% porous facesheet, (a)  $t=0.06''$ ,  $d=0.04''$  and (b)  $t=0.025''$ ,  $d=0.08''$ .

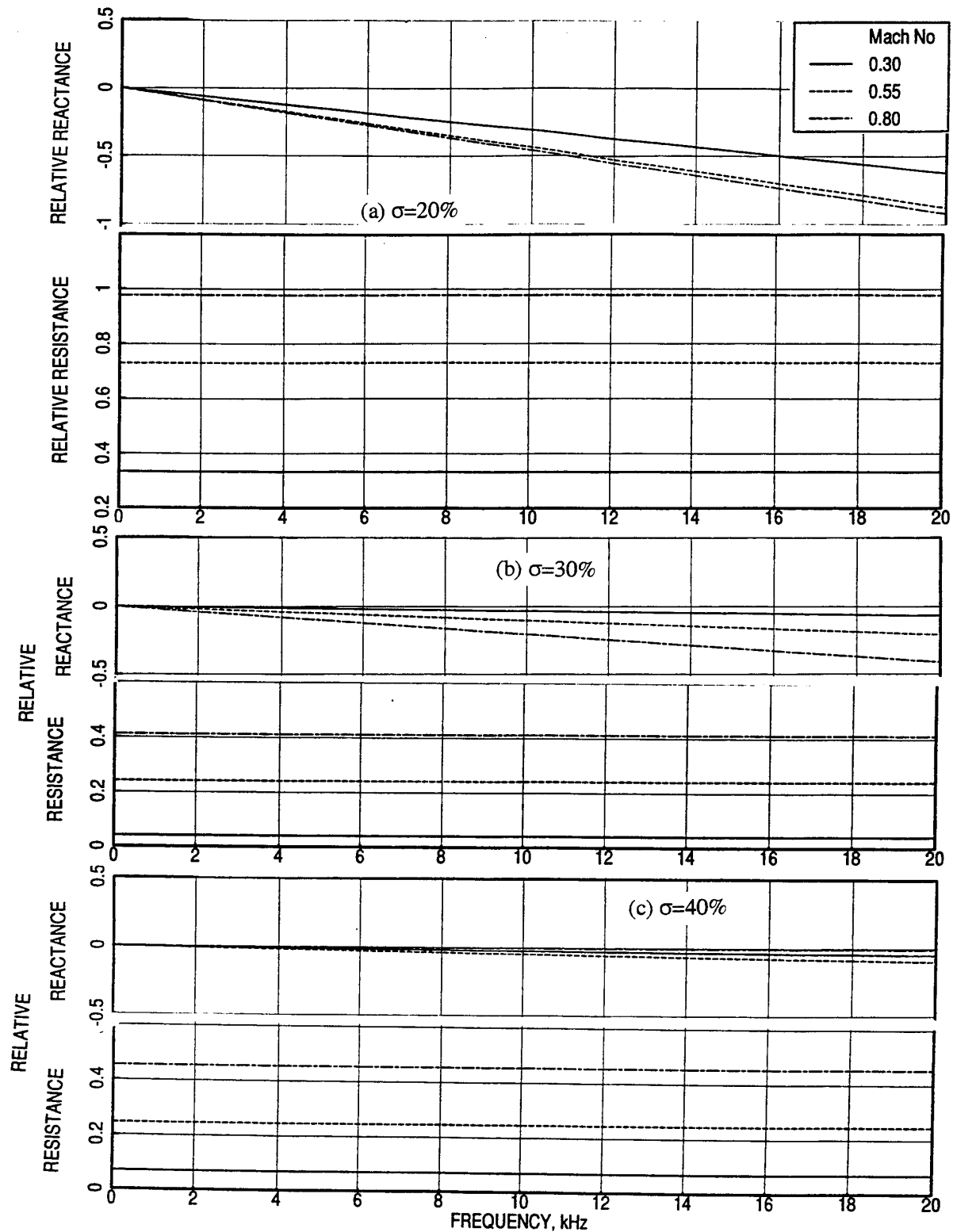


Figure 220. Effect of grazing flow Mach number (M) on relative impedance for 0.025''-thick facesheets with 0.04'' diameter holes, (a)  $\sigma=20\%$ , (b)  $\sigma=30\%$ , and (c)  $\sigma=40\%$ .

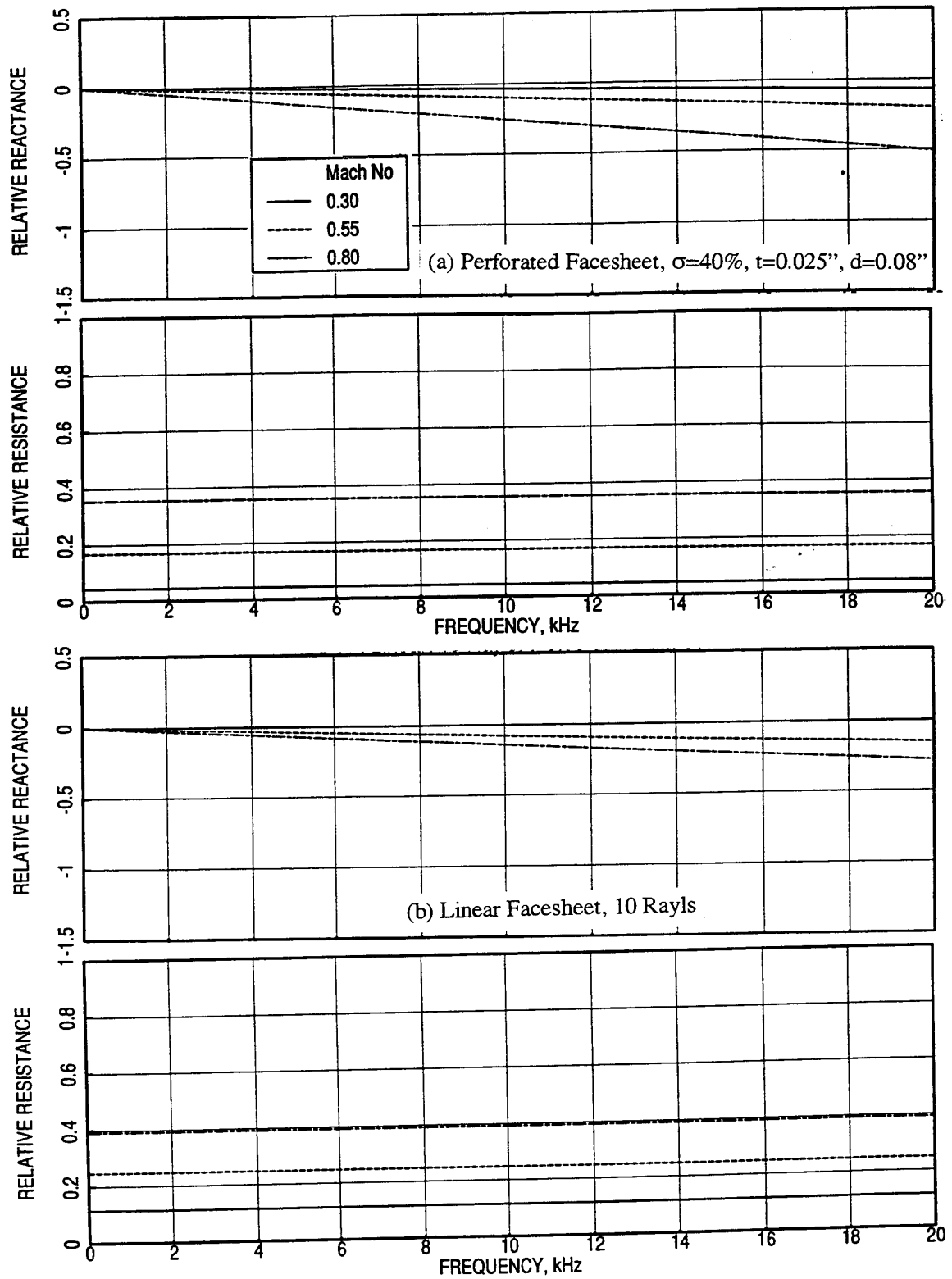


Figure 221. Effect of grazing flow Mach number ( $M$ ) on relative impedance for (a) a 40% porous 0.025"-thick facesheet with 0.04" diameter holes and (b) a linear facesheet of resistivity 10 rayls.

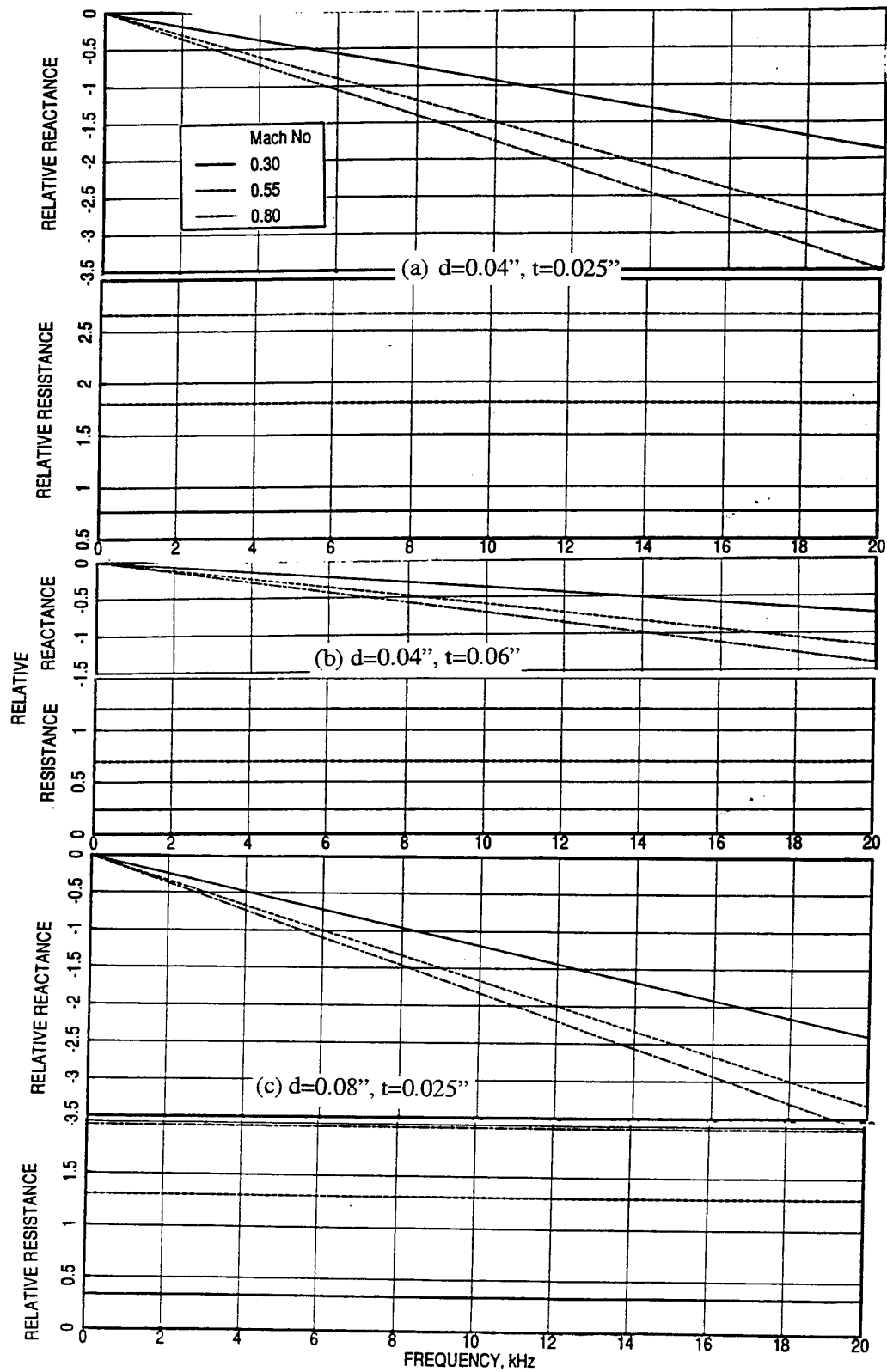


Figure 222. Effect of grazing flow Mach number ( $M$ ) on relative impedance for 9% porous facesheets, (a)  $d=0.04''$ ,  $t=0.025''$ , (b)  $d=0.04''$ ,  $t=0.06''$ , and (c)  $d=0.08''$ ,  $t=0.025''$ .

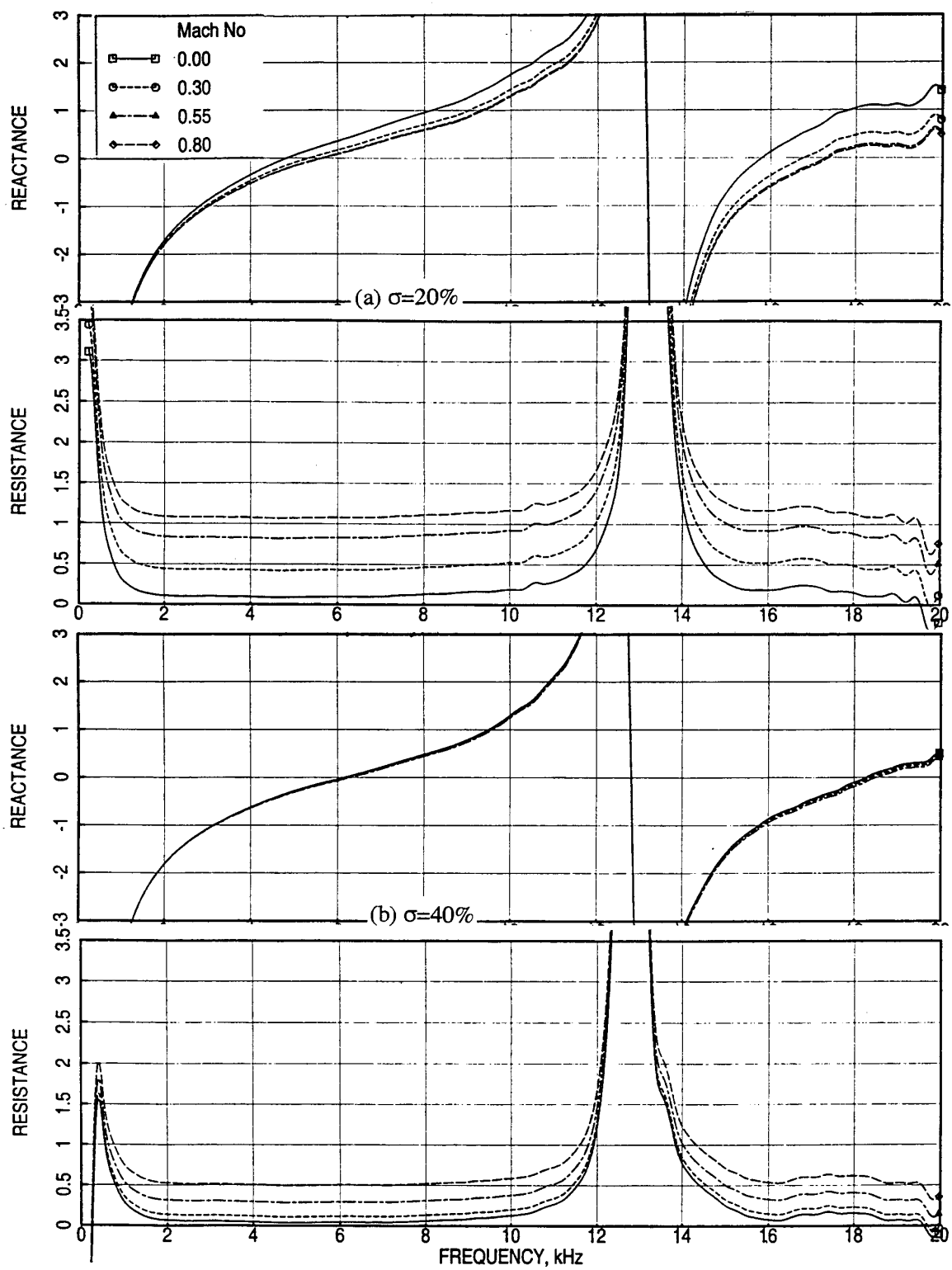


Figure 223. Effect of grazing flow Mach number (M) on normal impedance for 0.025''-thick facesheets with 0.04'' diameter holes over a 0.5''-deep cavity, (a)  $\sigma=20\%$  and (b)  $\sigma=40\%$ .

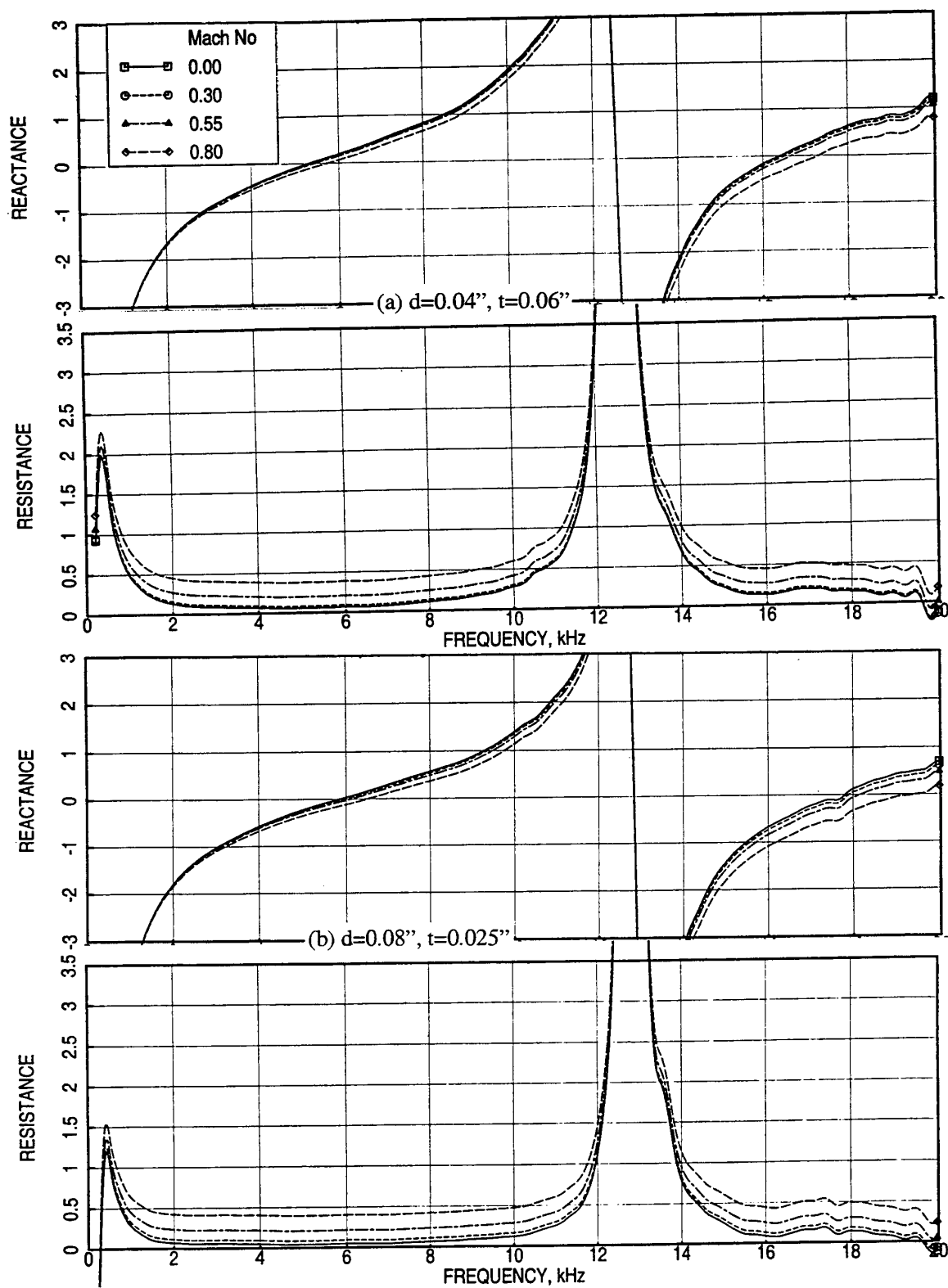


Figure 224. Effect of grazing flow Mach number ( $M$ ) on normal impedance for 40% porous facesheets over a 0.5"-deep cavity, (a)  $d=0.04''$ ,  $t=0.06''$  and (b)  $d=0.08''$ ,  $t=0.025''$ .

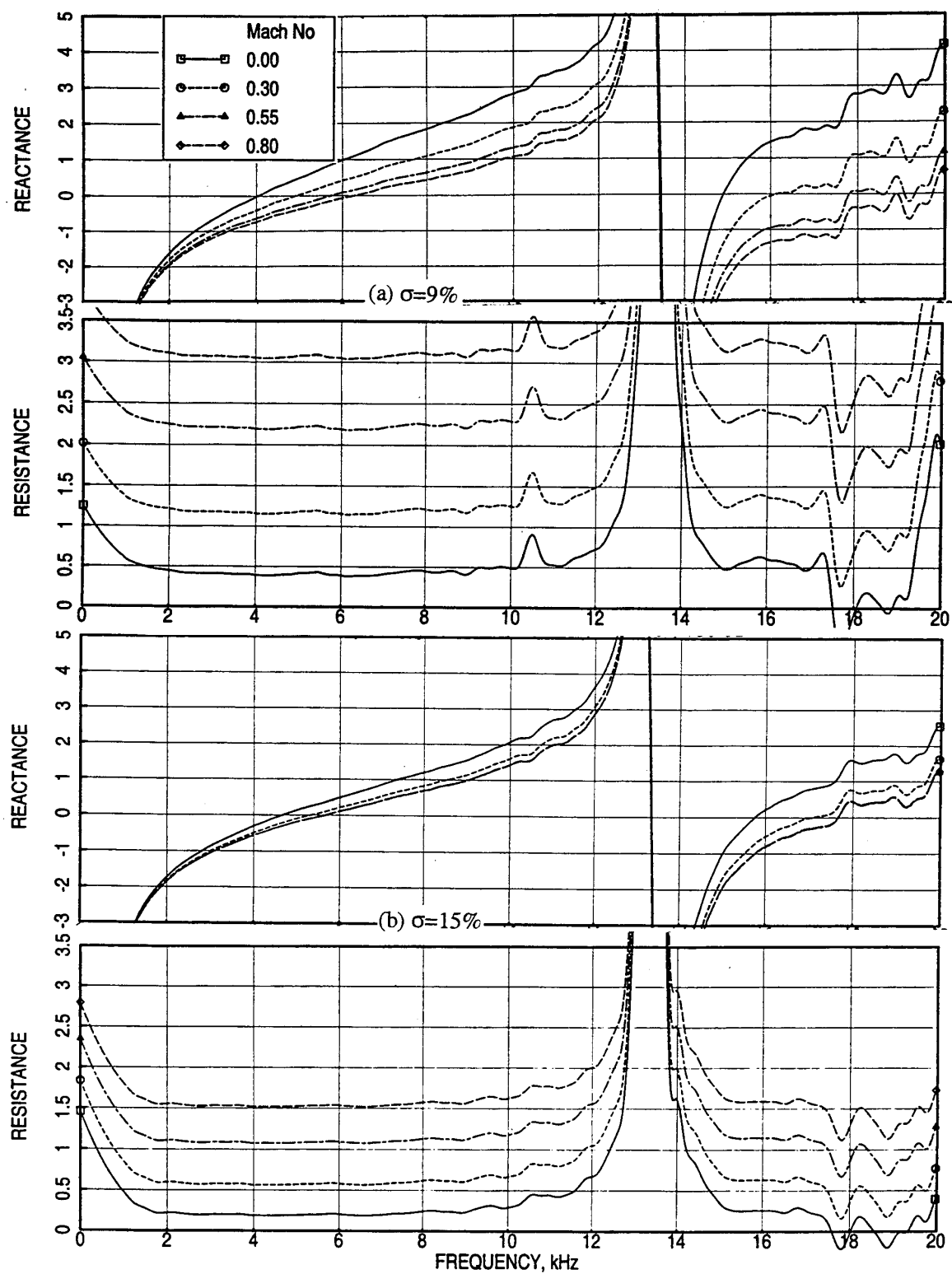


Figure 225. Effect of grazing flow Mach number ( $M$ ) on normal impedance for 0.025''-thick facesheets with 0.04'' diameter holes over a 0.5''-deep cavity, (a)  $\sigma=9\%$  and (b)  $\sigma=15\%$ .



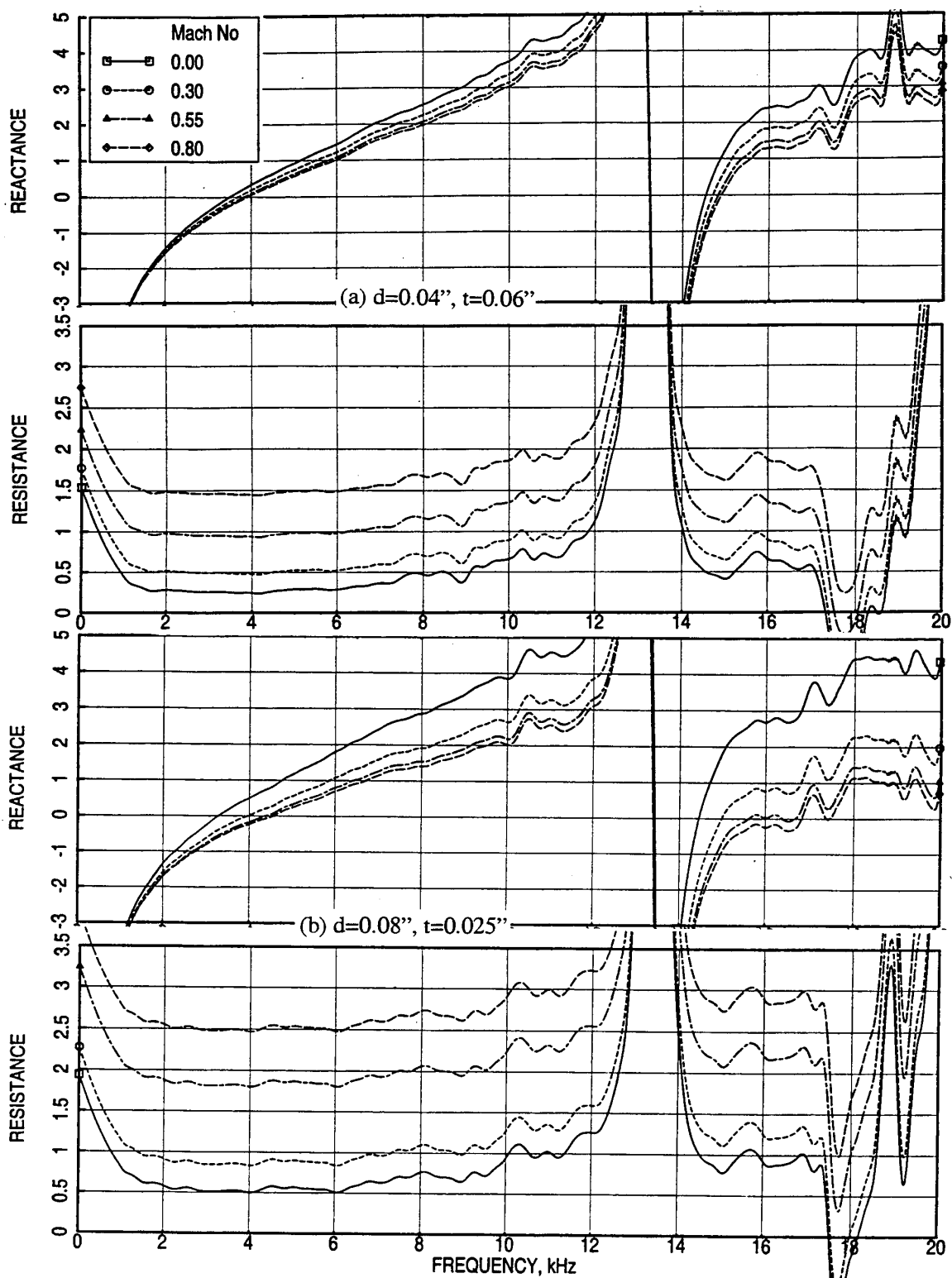


Figure 226. Effect of grazing flow Mach number ( $M$ ) on normal impedance for 9% porous facesheets over a 0.5"-deep cavity, (a)  $d=0.04''$ ,  $t=0.06''$  and (b)  $d=0.08''$ ,  $t=0.025''$ .

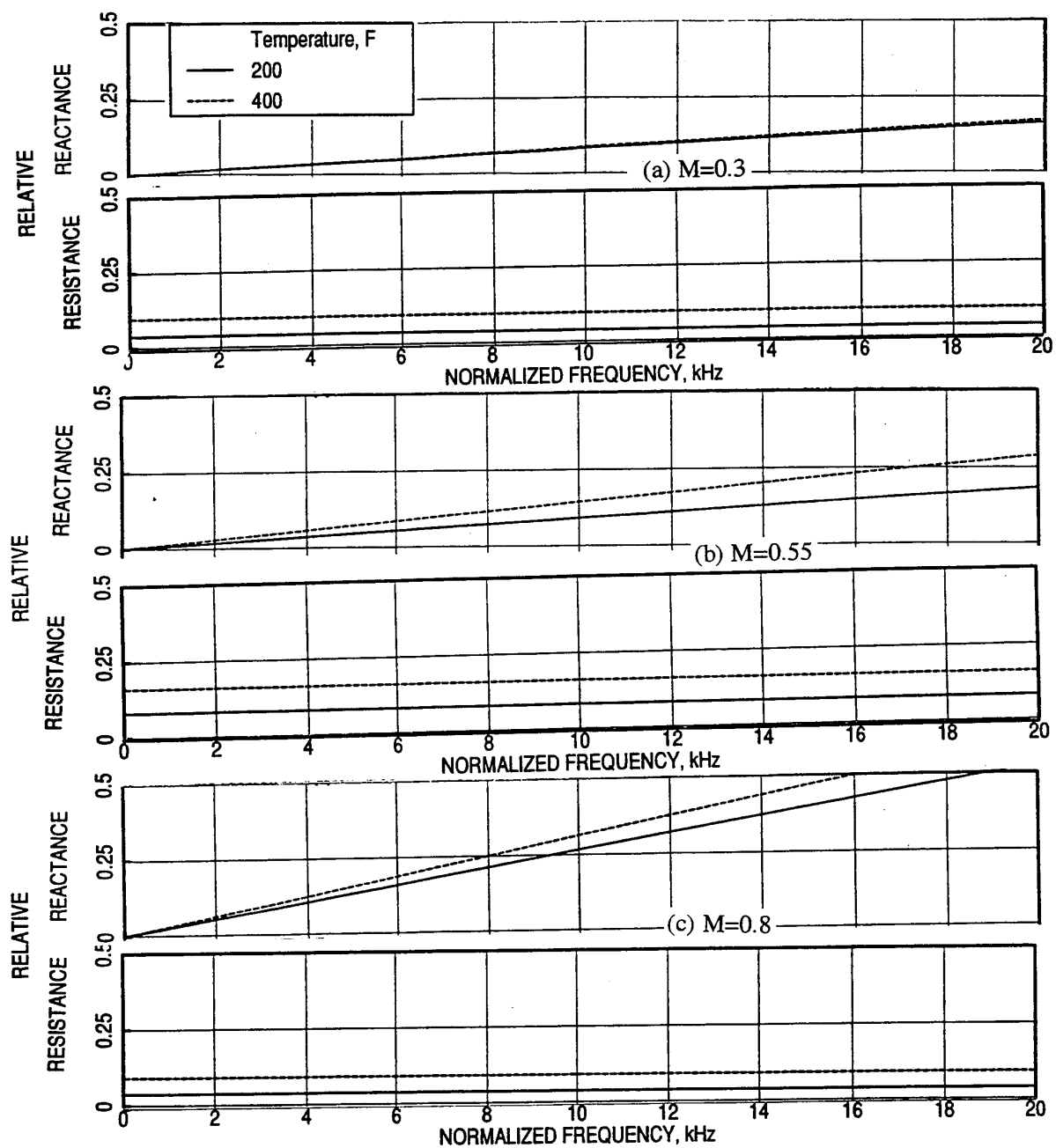


Figure 227. Effect of grazing flow temperature (T) on relative impedance for 0.5"-deep 100 ppi Silicon Carbide panel with 40% porous 0.025"-thick facesheet with 0.04" diameter holes at different grazing flow Mach number.

Where  $Z(M,T)$  = Normal impedance to be evaluated at temperature  $T$  and Mach number  $M$   
 $Z(0,amb)$  = Measured normal impedance at ambient temperature  
 $\Delta Z_F(M,amb)$  = Evaluated relative impedance due to grazing flow Mach number  $M$  at ambient temperature  
 $\Delta Z_T(M,T)$  = Evaluated relative impedance due to grazing flow temperature  $T$  at grazing flow Mach number of  $M$ .

Effect of grazing flow temperature on absolute impedance for a 0.5"-deep 100 ppi SiC panel with a 20% porous facesheet ( $t=0.025''$  and  $d=0.04''$ ) is shown in Figures 228 through 230 at different Mach numbers. In each of these plots the impedance spectra are plotted against the normalized frequency as well as the actual frequency. With respect to normalized frequency the spectral peaks due to antiresonance frequency of the panel coincide at the same frequency. The effect of temperature is clearly observed in these plots. The effect seems to be small. However, the resistance and reactance, both increase with increasing temperature at all Mach numbers. When plotted against actual frequency the antiresonance peaks move to a higher frequency with increasing temperature. Similar results for a 0.5"-deep 12 lbf T-Foam absorber are shown in Figure 231 at  $M=0.55$ . The temperature effect for T-Foam panels seems to be insignificant compared to SiC panels.

For SDOF type panels the influence of grazing flow temperature on normal impedance is shown in Figure 232 for a 20% porous facesheet ( $t=0.025''$  and  $d=0.04''$ ) with a 0.5"-deep cavity at  $M=0.55$ . Temperature effect on normal impedance is small and the resistance and reactance both increase slightly with increasing temperature.

**Boundary Layer Profiles and Related Parameters:** Effect of grazing flow temperature on boundary layer profiles is shown in Figure 203. Based on the shape and variation of the velocity profiles with respect to temperature, it can be concluded that the flow becomes less turbulent with increasing temperature, which is consistent with decreasing Reynolds number. However, the effect of temperature seems to be small. Effect of temperature on the related parameters, namely, displacement thickness and local skin friction coefficient are presented later in this section.

**DC Flow Resistance:** Effect of grazing flow temperature on DC flow resistance is shown for a few typical configurations in Figures 207 through 209 for an SDOF type panel with 9% porous facesheet ( $t=0.025''$  and  $d=0.04''$ ) at different Mach numbers. Similar results for a 0.5"-deep 100 ppi SiC panel with a 30% porous facesheet ( $t=0.025''$  and  $d=0.04''$ ) are shown

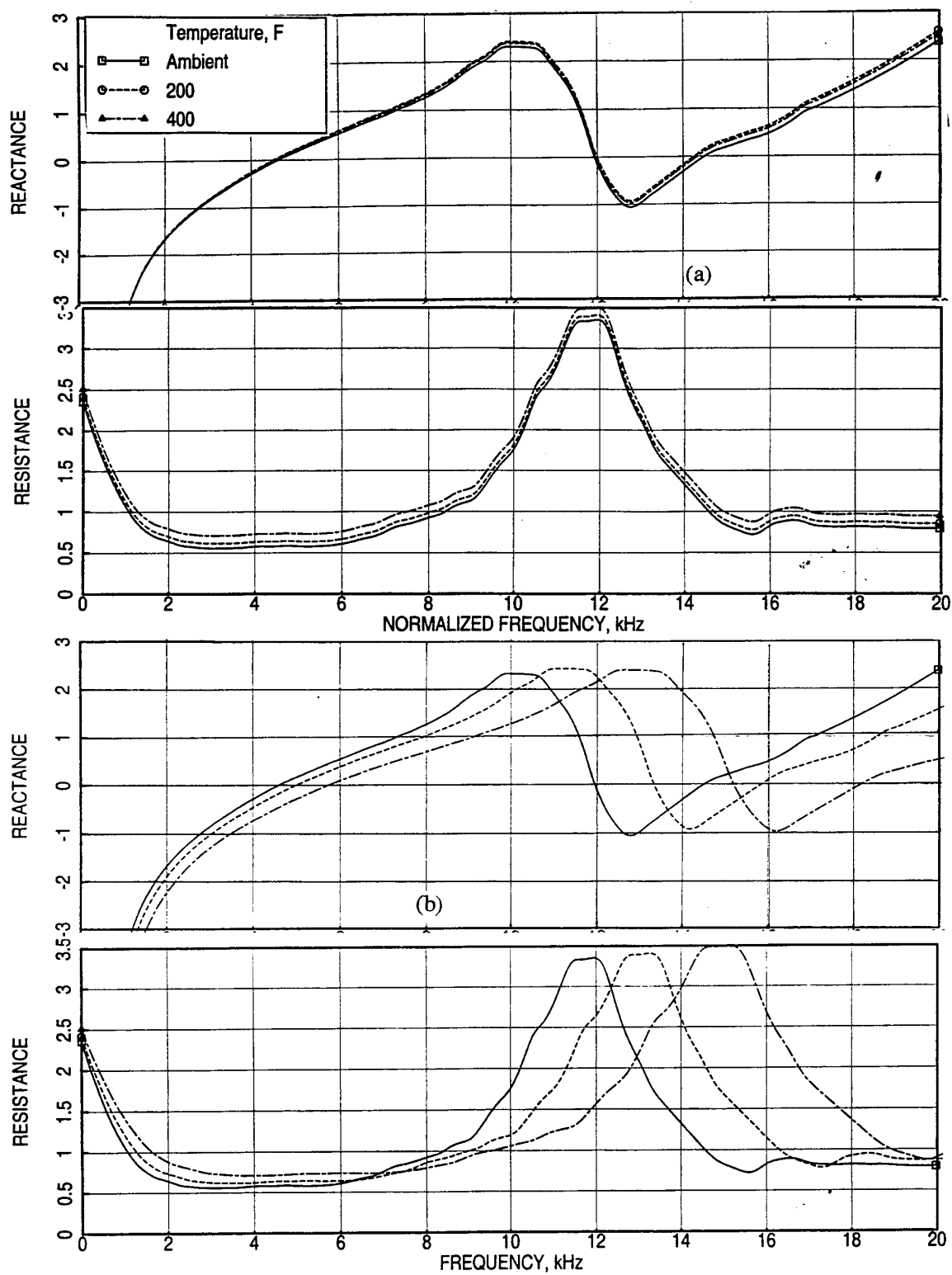


Figure 228. Effect of grazing flow temperature (T) on normal impedance for 0.5"-deep 100 ppi Silicon Carbide panel with 20% porous 0.025"-thick facesheet with 0.04" diameter holes at M=0.3.

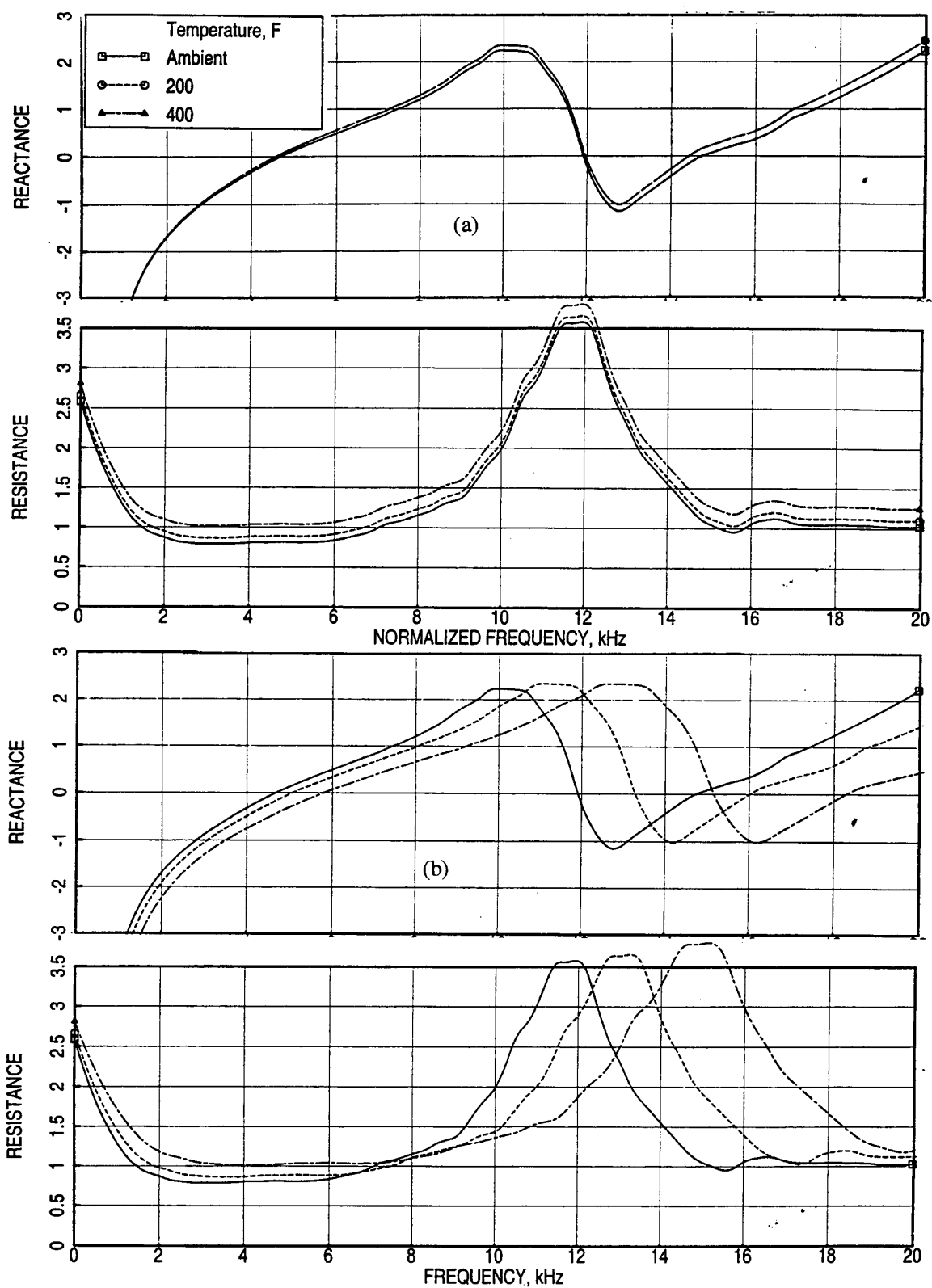


Figure 229. Effect of grazing flow temperature (T) on normal impedance for 0.5"-deep 100 ppi Silicon Carbide panel with 20% porous 0.025"-thick facesheet with 0.04" diameter holes at M=0.55.

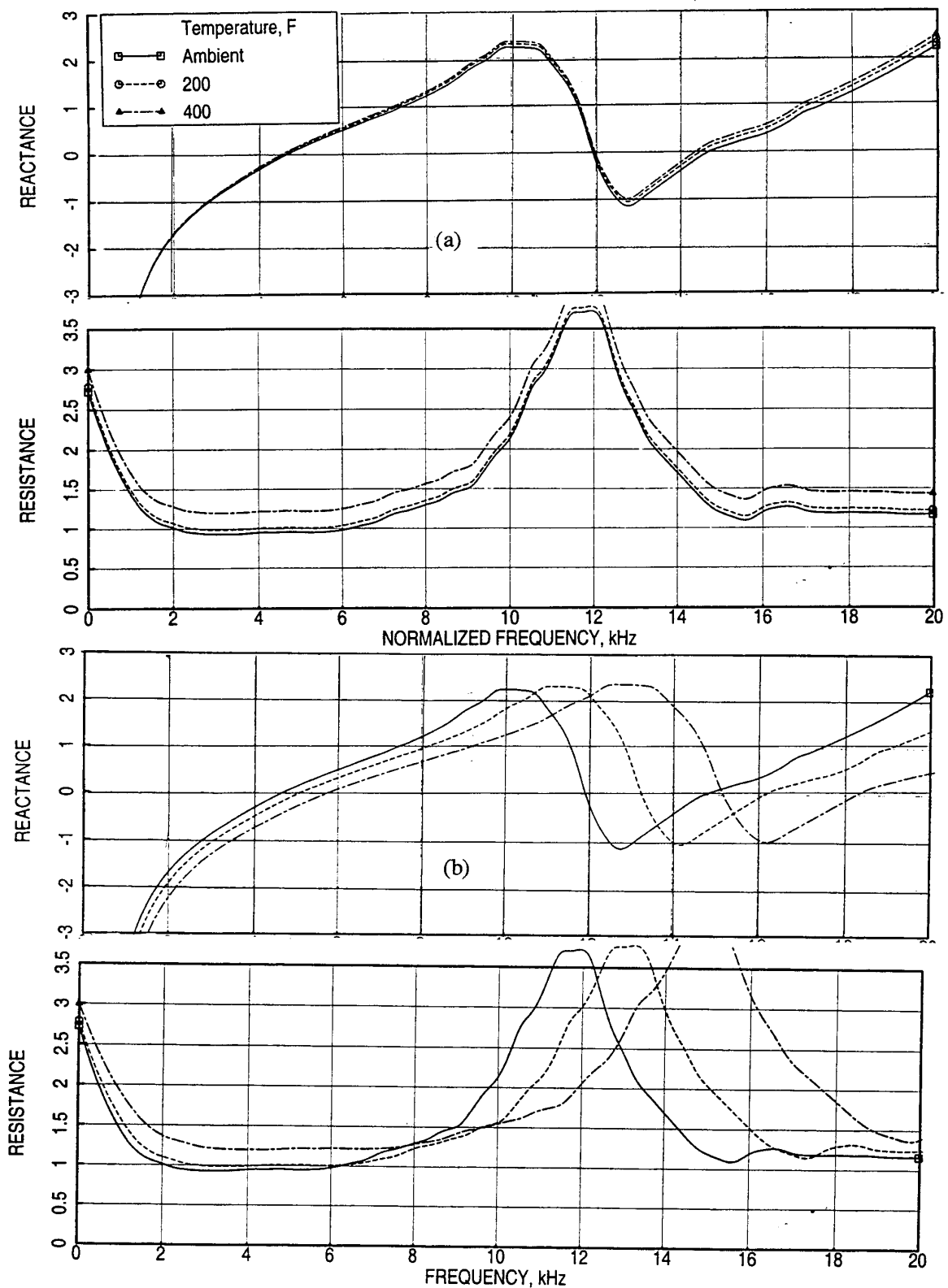


Figure 230. Effect of grazing flow temperature ( $T$ ) on normal impedance for 0.5"-deep 100 ppi Silicon Carbide panel with 20% porous 0.025"-thick facesheet with 0.04" diameter holes at  $M=0.8$ .

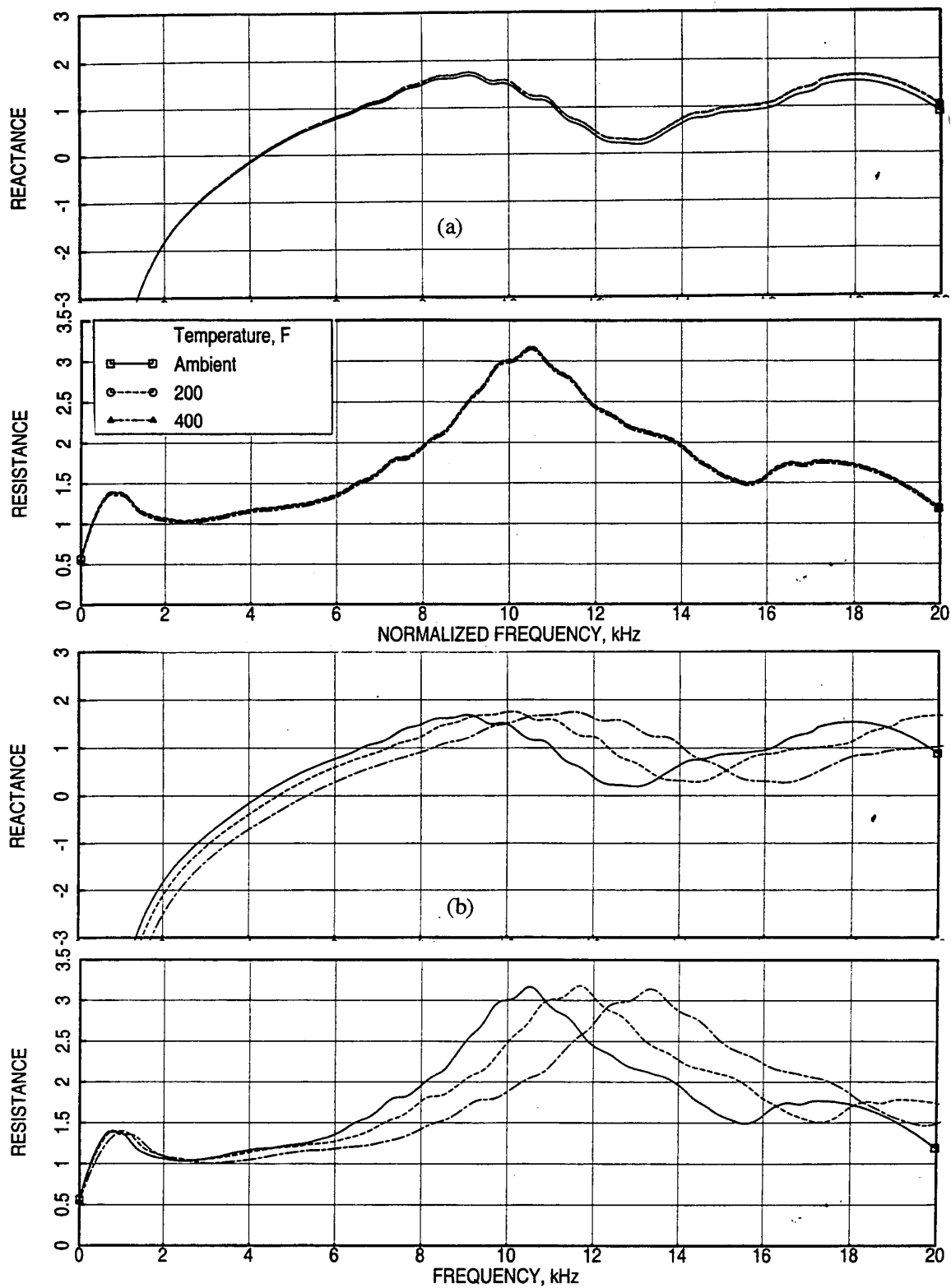


Figure 231. Effect of grazing flow temperature (T) on normal impedance for 0.5"-deep 12 lbf T-Foam panel with 20% porous 0.025"-thick facesheet with 0.04" diameter holes at M=0.55.

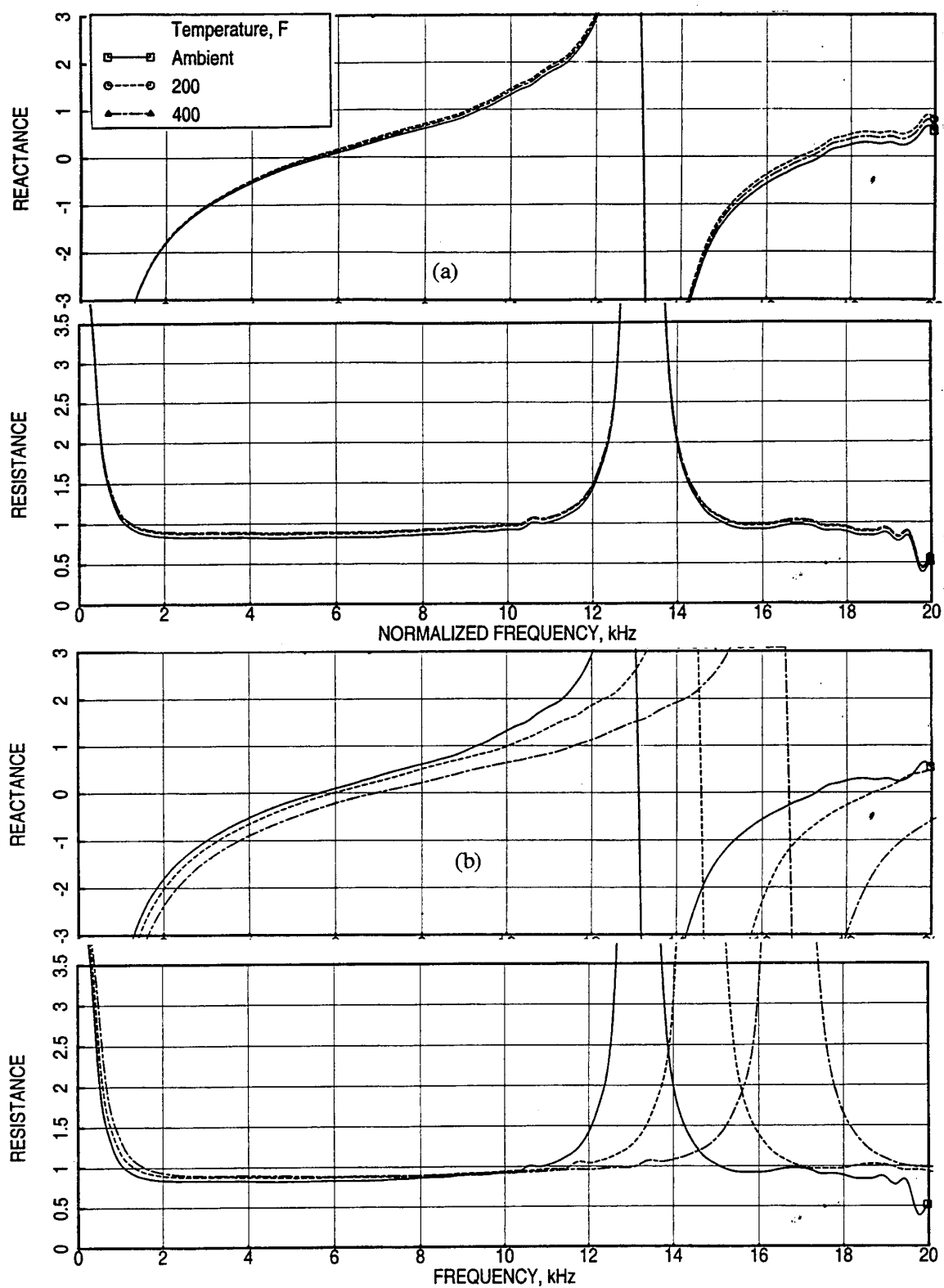


Figure 232. Effect of grazing flow temperature ( $T$ ) on normal impedance for a 20% porous 0.025"-thick facesheet with 0.04" diameter holes over a 0.5"-deep cavity at  $M=0.55$ .



in Figures 211 through 213. DC flow resistance decreases significantly with temperature for bulk absorbers and SDOF type panels.

#### 6.4.3 Effect of Facesheet Porosity

**Insitu Impedance:** Effect of facesheet porosity on absolute impedance for 0.5"-deep bulk absorbers of 100 ppi SiC and 12 lbf T-Foam with 0.025"-thick facesheets ( $d=0.04''$ ) is shown in Figures 233 through 235 at different Mach numbers. Resistance and reactance, both decreases with increasing facesheet porosity. Similar results for a 0.5"-deep SDOF type panel with 0.025"-thick facesheets ( $d=0.04''$ ) is shown in Figure 236. Similar effect of decreasing resistance and reactance with increasing facesheet porosity is observed.

**Boundary Layer Profiles and Related Parameters:** Effect of facesheet porosity on boundary layer parameters for SDOF type panels is shown in Figures 237 through 240. Local friction coefficients ( $C_F$ ) computed using boundary layer velocity profiles (Ref. 1) for various SDOF panels are plotted with respect to grazing flow Mach number at different temperatures (T). Friction coefficients slightly decrease with increasing flow Mach number (i.e., increasing Reynolds number). The hardwall friction coefficient levels are always greater than those for the perforated panels. Friction coefficients decrease with increasing facesheet porosity. The same data is plotted with respect to temperature at different Mach numbers (M) in Figure 238. Friction coefficients slightly decrease with increasing temperature (i.e., decreasing Reynolds number). As observed in Figure 237,  $C_F$  values decrease with increasing facesheet porosity.

The displacement thickness ( $\delta^*$ ) computed from velocity profiles is plotted with respect to flow Mach number and temperature in Figures 239 and 240, respectively. Effect of Mach number and temperature seems to be small on  $\delta^*$ . However,  $\delta^*$  values are the lowest for hardwall configuration and increase with increasing facesheet porosity.

Similar results at a temperature of 200°F are plotted with respect to flow Mach number for bulk absorbers of 0.5"-deep 100 ppi SiC and 12 lbf T-Foam with 0.025"-thick facesheets ( $d=0.04''$ ) in Figure 241. Figure 242 shows the plot of  $C_F$  and  $\delta^*$  with respect to temperature at  $M=0.55$  for the same bulk absorber panels. Qualitatively the effect of flow Mach number, temperature, and facesheet porosity on  $C_F$  and  $\delta^*$  are similar to the SDOF type panels. The  $\delta^*$  levels are lower compared to those for SDOF panels of same facesheet porosity. Figure 243 exhibits the effect of porosity on  $C_F$  and  $\delta^*$  for 0.5"-deep 100 ppi SiC bulk absorbers

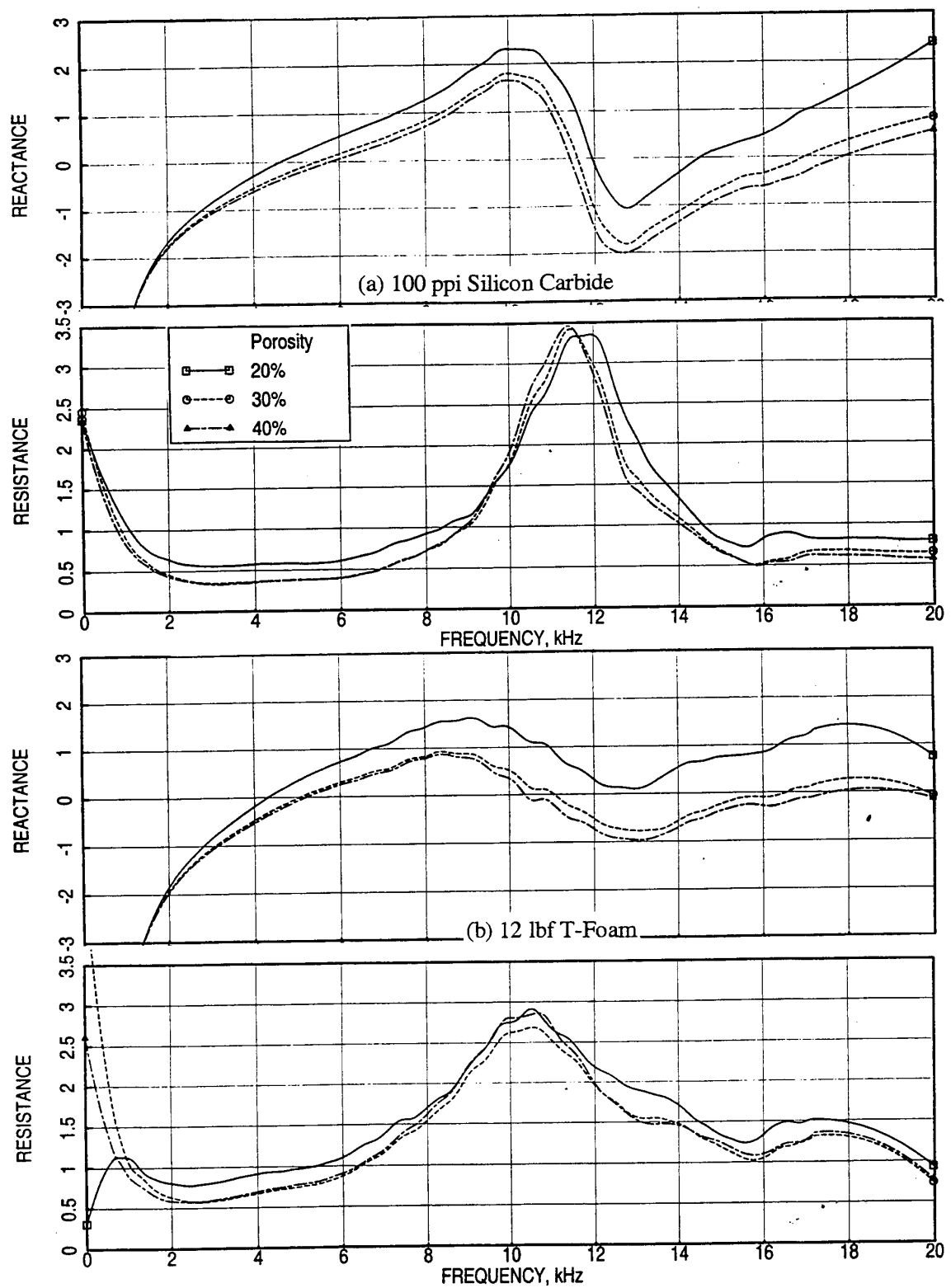


Figure 233. Effect of facesheet porosity ( $\sigma$ ) on normal impedance for 0.5"-deep (a) 100 ppi Silicon Carbide and (b) 12 lbf T-Foam panels for 0.025"-thick facesheet with 0.04" diameter holes,  $M=0.3$ .

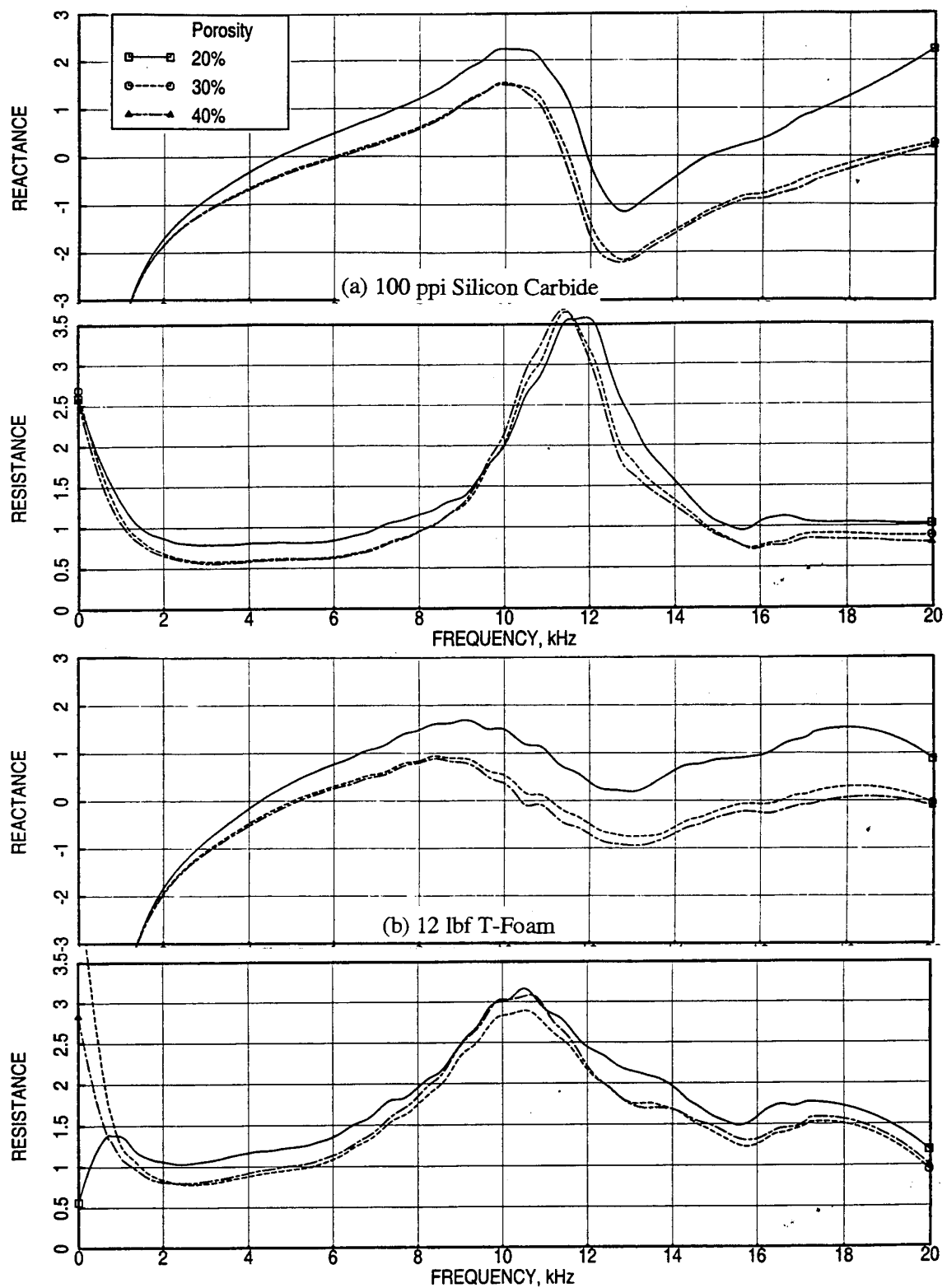


Figure 234. Effect of facesheet porosity ( $\sigma$ ) on normal impedance for 0.5"-deep (a) 100 ppi Silicon Carbide and (b) 12 lbf T-Foam panels for 0.025"-thick facesheet with 0.04" diameter holes,  $M=0.55$ .

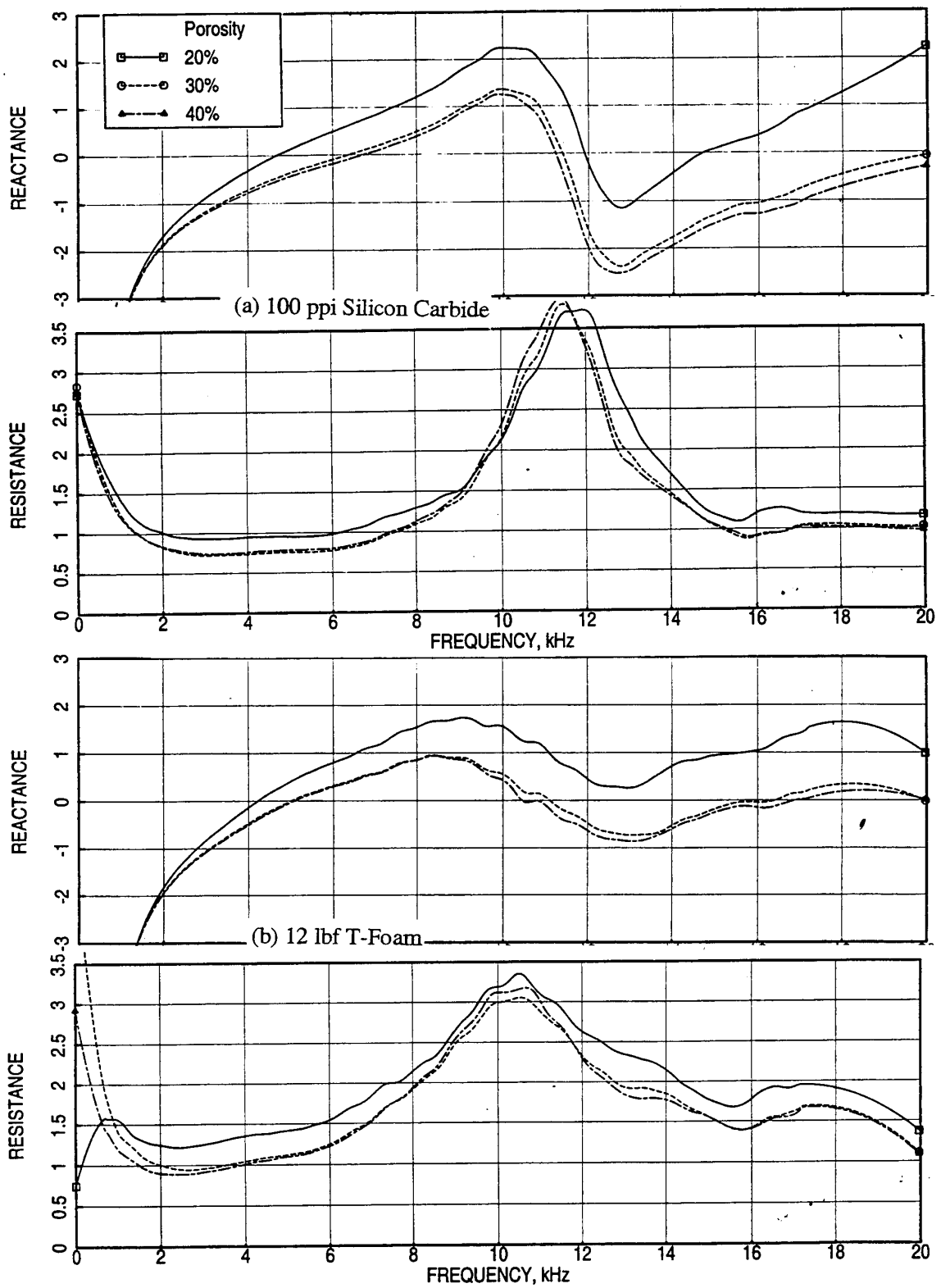


Figure 235. Effect of facesheet porosity ( $\sigma$ ) on normal impedance for 0.5"-deep (a) 100 ppi Silicon Carbide and (b) 12 lbf T-Foam panels for 0.025"-thick facesheet with 0.04" diameter holes,  $M=0.8$ .

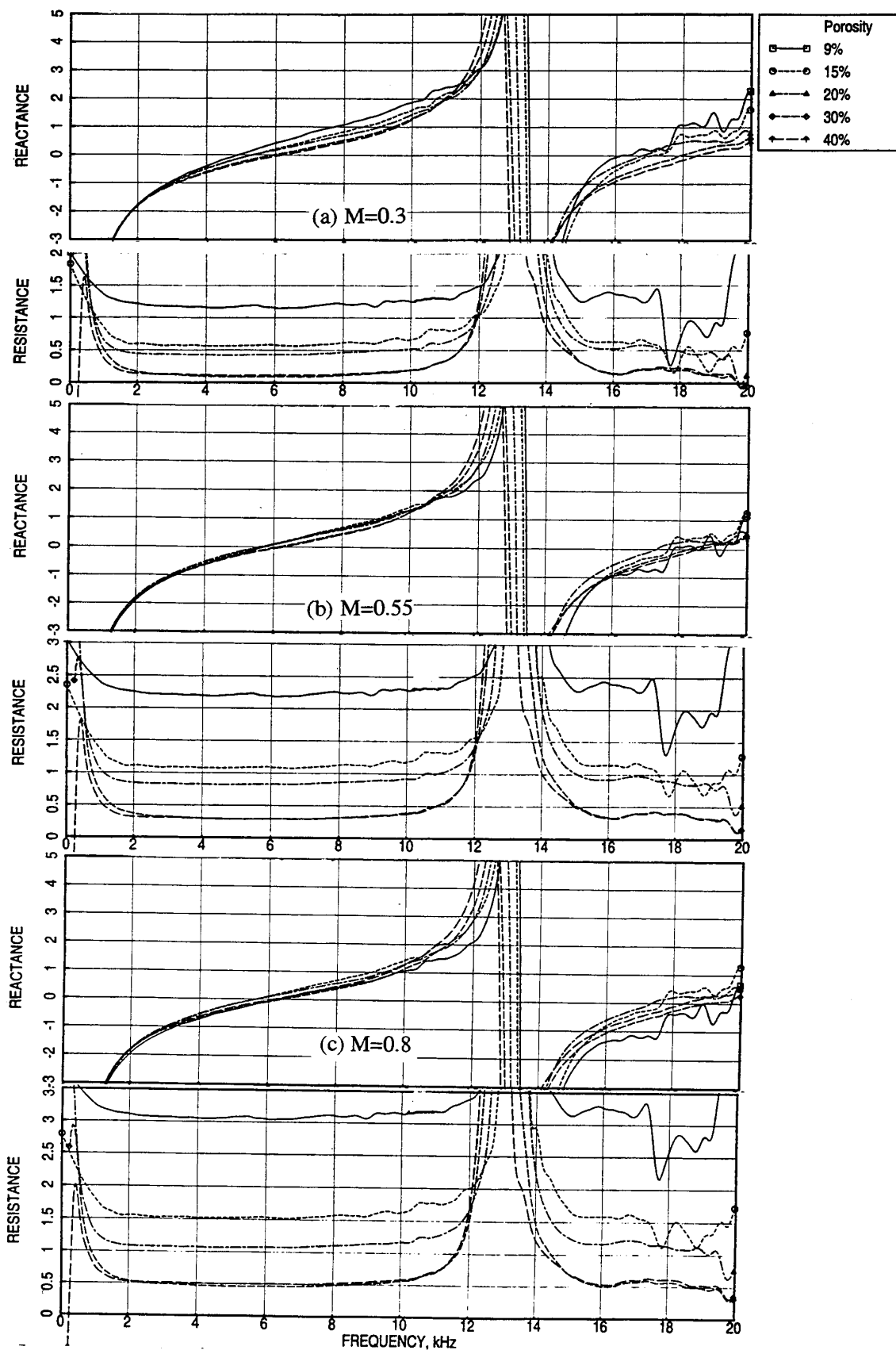


Figure 236. Effect of facesheet porosity ( $\sigma$ ) on normal impedance for 0.5"-deep SDOF type panels with 0.025"-thick facesheet  $d=0.04$ ", (a)  $M=0.3$ , (b)  $M=0.55$ , (c)  $M=0.8$ .

with much thicker facesheets ( $t=0.1''$ ) and with bigger hole diameter ( $d=0.07''$ ). However, the  $C_F$  and  $\delta^*$  trends remain the same as those shown in Figures 241 and 242.

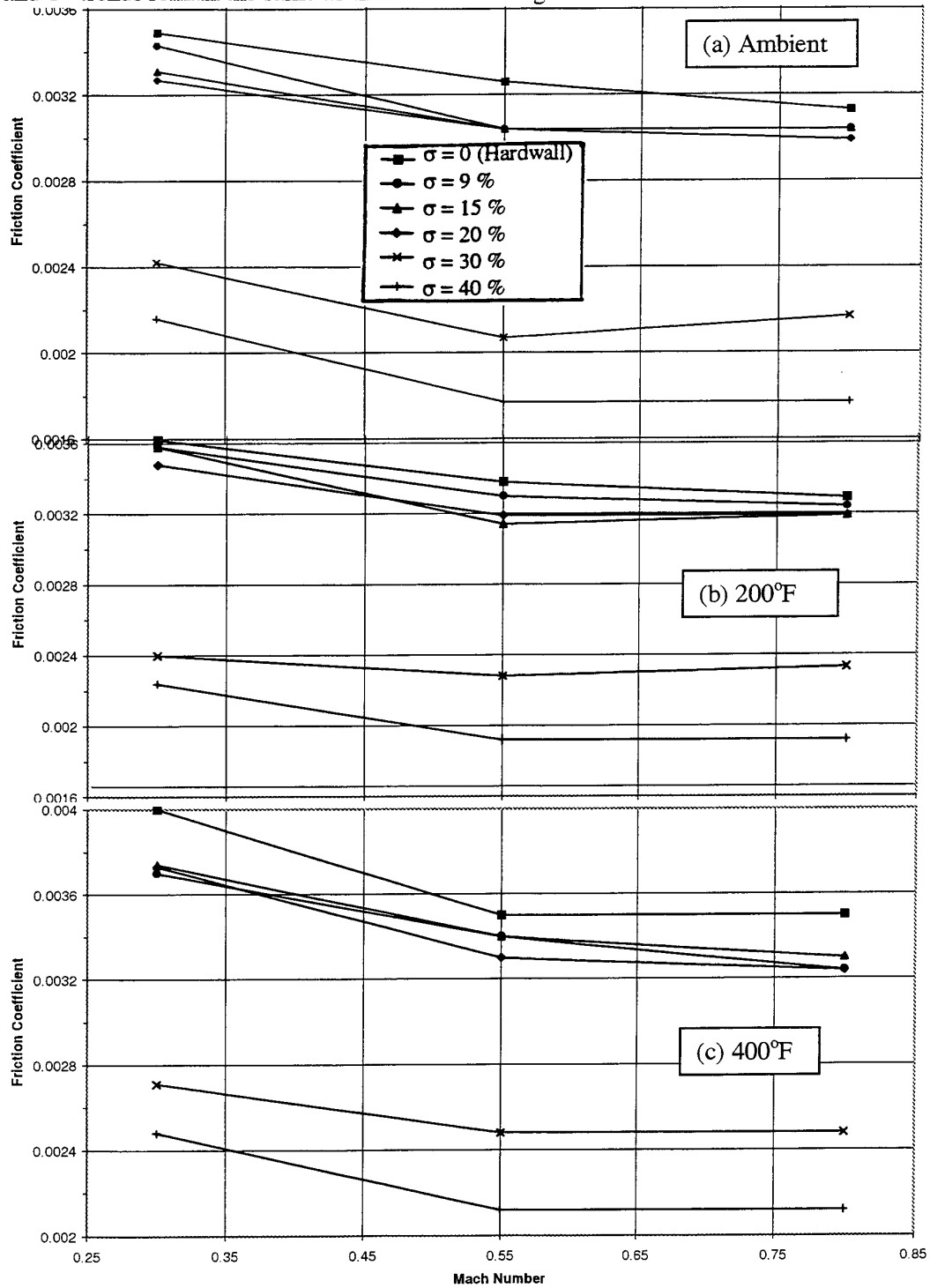


Figure 237. Effect of facesheet porosity on local friction coefficient for SDOF type panels At different temperatures,  $t=0.025''$  and  $d=0.04''$ .

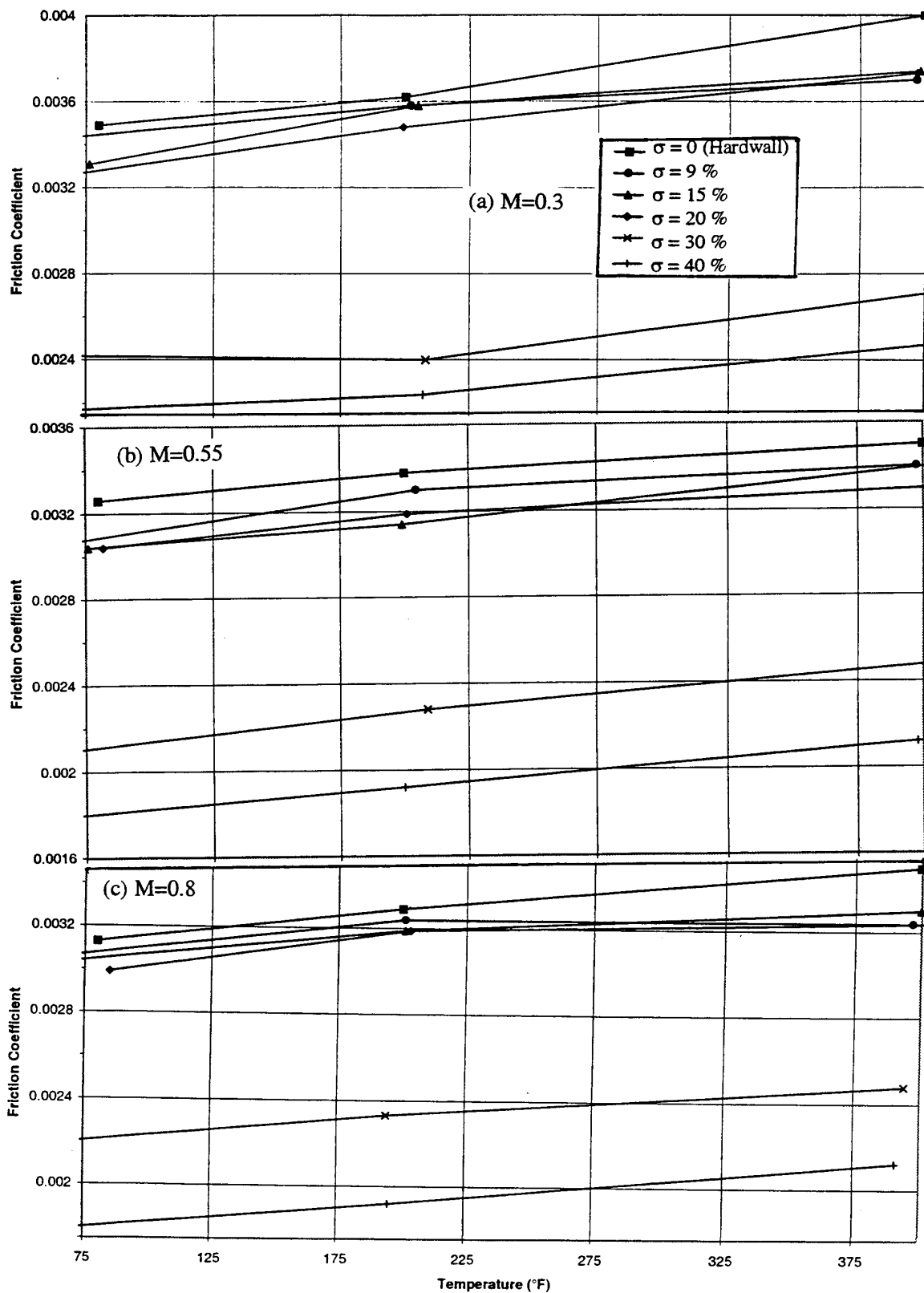


Figure 238. Effect of facesheet porosity on local friction coefficient for SDOF type panels at different Mach numbers,  $t=0.025''$ ,  $d=0.04''$ .

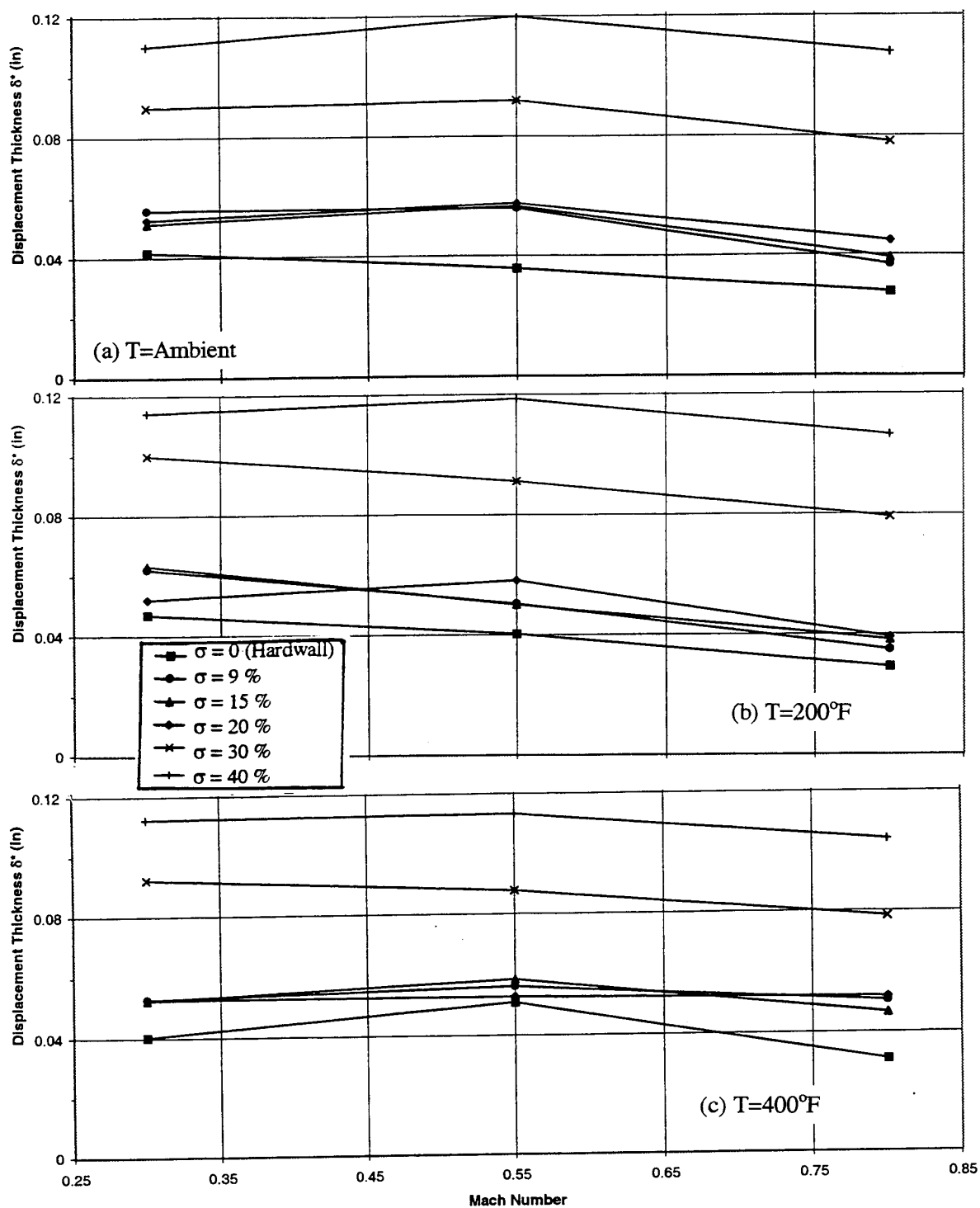


Figure 239. Effect of facesheet porosity on displacement thickness for SDOF type panels at different temperatures,  $t=0.025''$ ,  $d=0.04''$ .



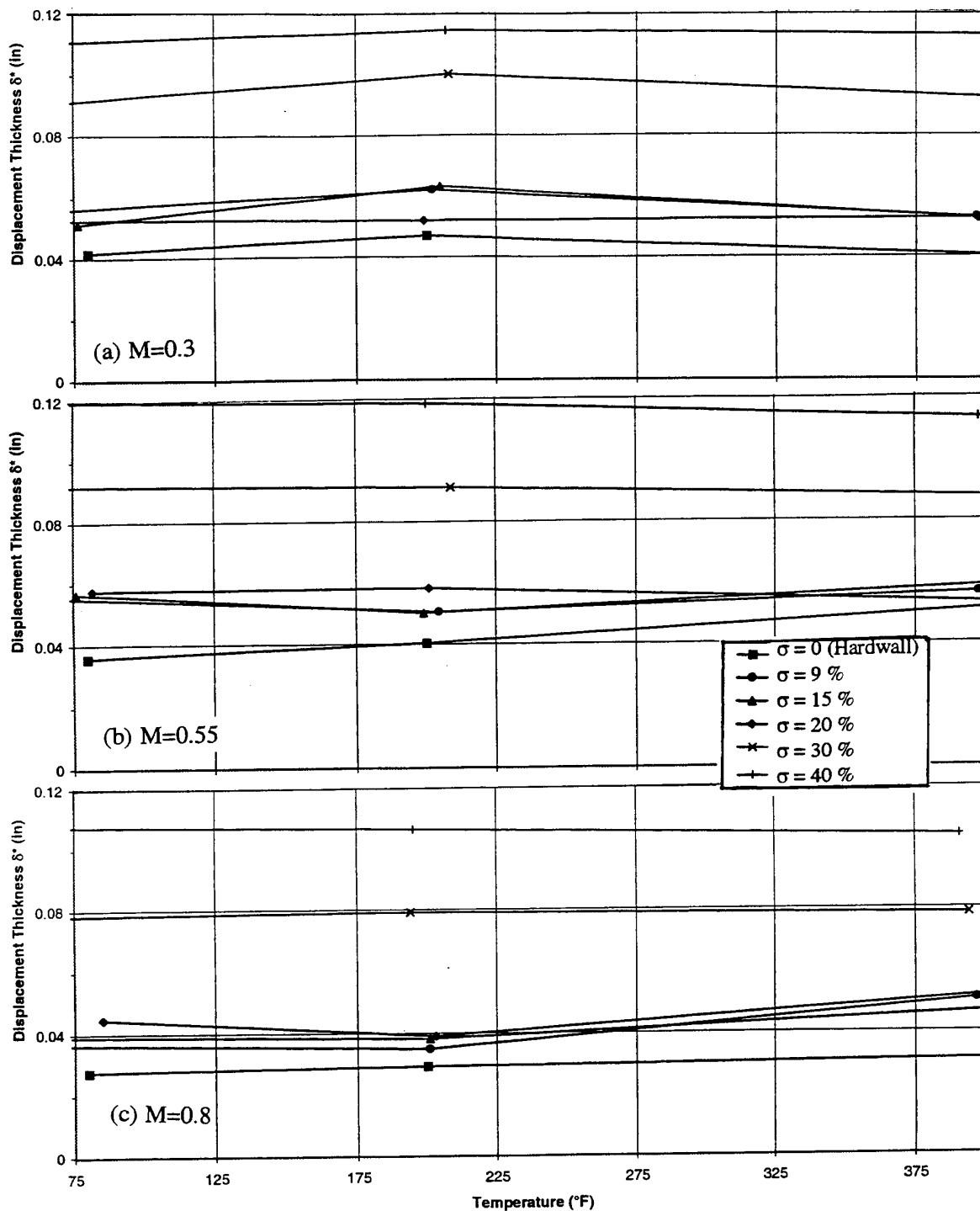


Figure 240. Effect of facesheet porosity on displacement thickness for SDOF type panels at different Mach numbers,  $t=0.025''$ ,  $d=0.04''$ .

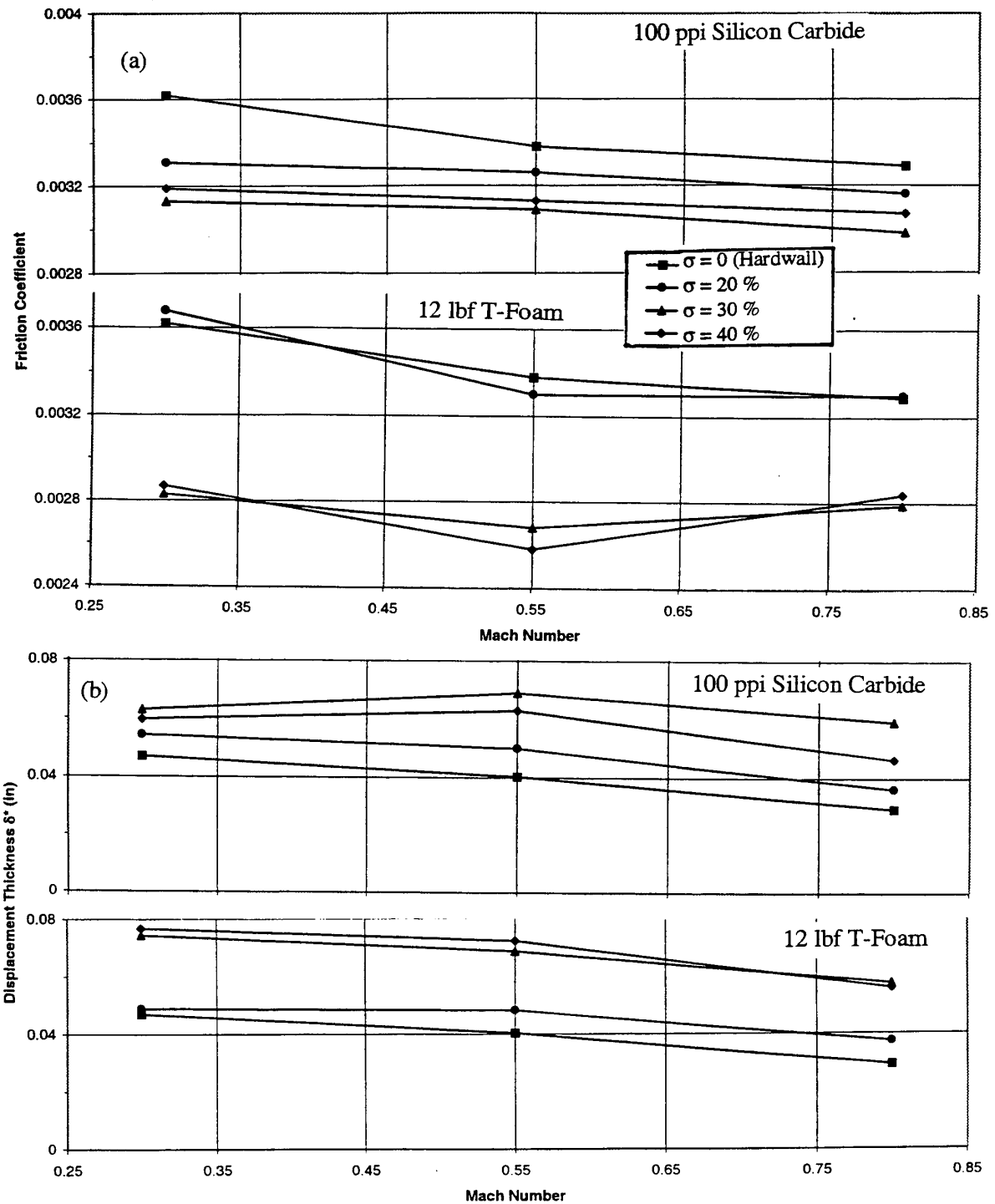


Figure 241. Effect of facesheet porosity on (a) local friction coefficient and (b) displacement thickness for 0.5"-deep 100 ppi Silicon Carbide and 12 lbf T-Foam panels with 0.025"-thick facesheet,  $d=0.04"$ ,  $T=200^\circ\text{F}$ .

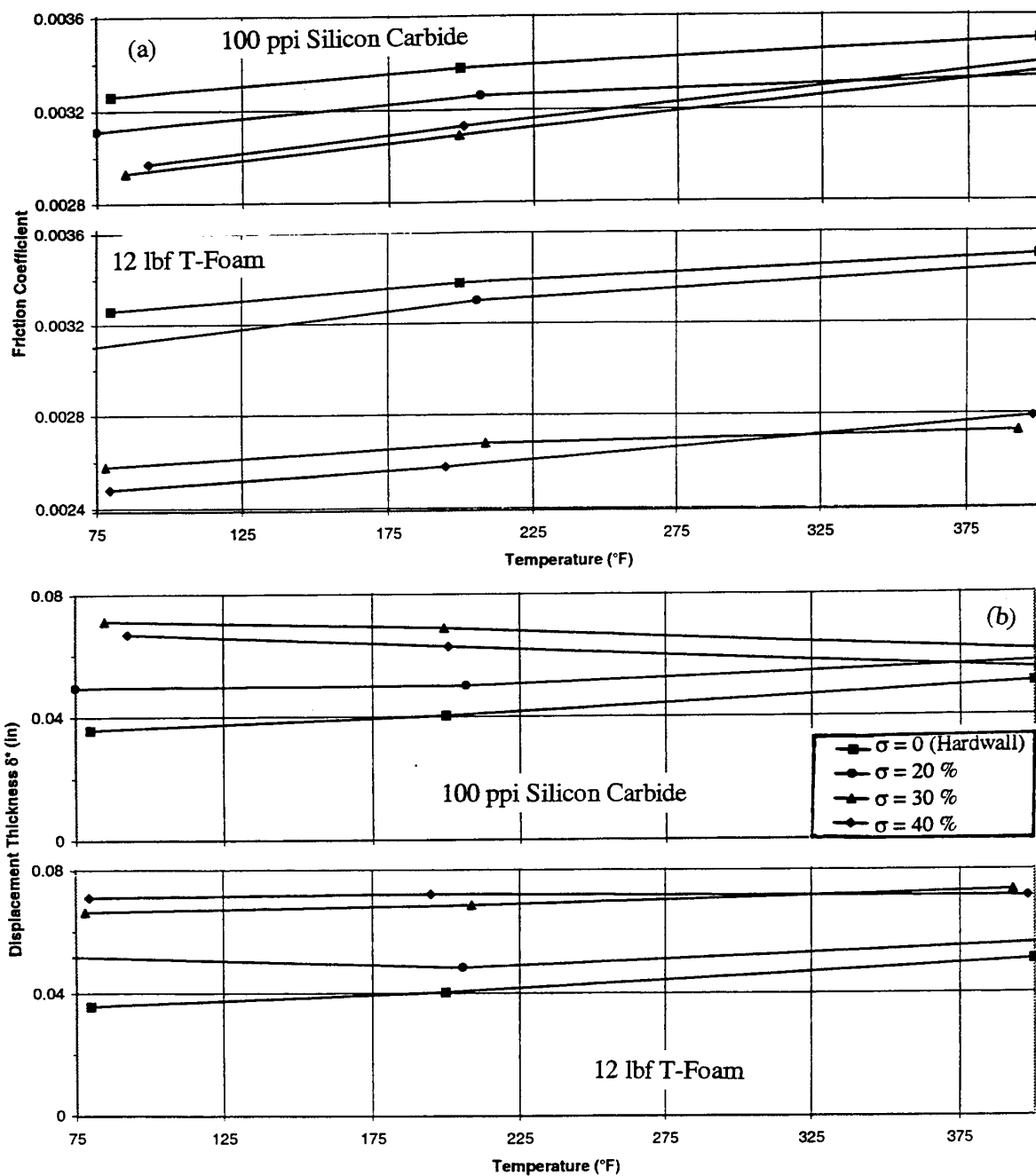


Figure 242. Effect of facesheet porosity on (a) local friction coefficient and (b) displacement thickness for 0.5"-deep 100 ppi Silicon Carbide and 12 lbf T-Foam panels with 0.025"-thick facesheet,  $d=0.04$ ",  $M=0.55$ .

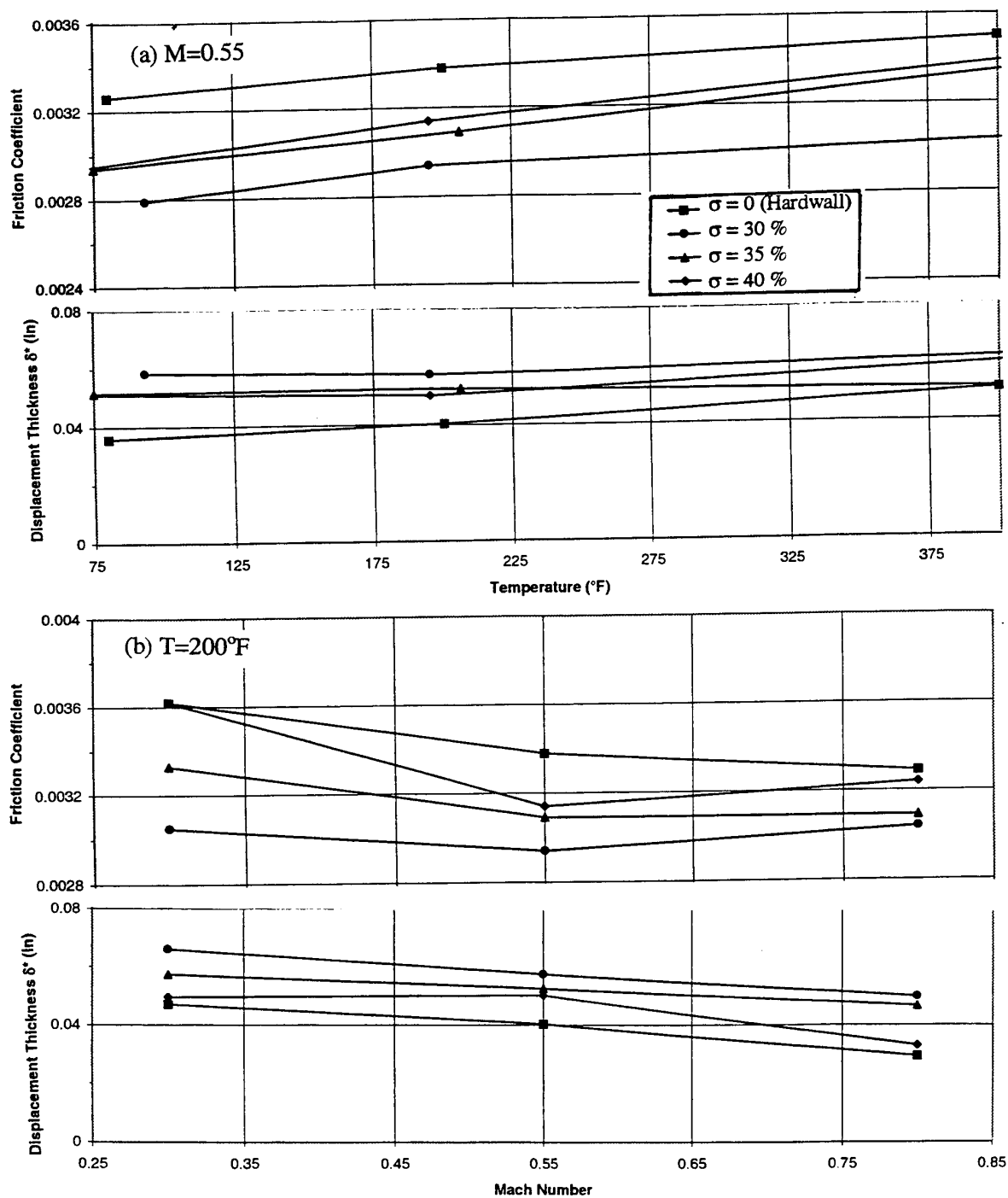


Figure 243. Effect of facesheet porosity on local friction coefficient and displacement thickness for a 0.5"-deep 100 ppi Silicon Carbide bulk panel with 0.10"-thick facesheet,  $d=0.07''$ , (a)  $M=0.55$  and (b)  $T=200^{\circ}\text{F}$ .

**DC Flow Resistance:** Effect of facesheet porosity on DC flow resistance is shown for bulk absorbers of 0.5"-deep 100 ppi SiC and 12 lbf T-Foam with 0.025"-thick facesheets ( $d=0.04''$ ) in Figure 244 for  $M=0$ . Clearly the resistance increases with decreasing porosity. Figures 245 and 246 show the effect of facesheet porosity on DC flow resistance for the same bulk absorber panels in the presence of grazing flow Mach numbers of 0.3 and 0.55, respectively, at ambient temperature. While the 20% and 30% porous facesheets behave in an expected manner that the DC flow resistance increases with decreasing porosity, the 40% porous facesheet results are not predictable. In most cases the levels are higher compared to 30% porous facesheet. This is possibly due to the imperfect manufacturing process, which might not have resulted into proper cylindrical holes on the facesheet.

Effect of facesheet porosity on SDOF type panels is shown in Figure 247. DC flow resistance increases with decreasing facesheet porosity. The effect of increasing DC flow resistance with approach velocity becomes less prominent in the presence of grazing flow, especially for higher porous facesheets.

#### 6.4.4 Effect of Facesheet Thickness

**Insitu Impedance:** Effect of facesheet thickness on absolute impedance for a 0.5"-deep bulk absorbers of 100 ppi SiC and 12 lbf T-Foam with 40% porous facesheets ( $d=0.04''$ ) is shown in Figures 248 through 250 at different Mach numbers. Resistance and reactance, both increases with increasing facesheet thickness. The effect is relatively small for T-Foam bulk absorbers. Similar results for a 0.5"-deep SDOF type panel with facesheets of two different porosities ( $d=0.04''$ ) is shown in Figures 251 through 253 for different grazing flow Mach numbers. Similar effect of increasing resistance and reactance with increasing facesheet thickness is observed. The effect is much higher for 9% porous facesheet compared to 40%.

**Boundary Layer Profiles and Related Parameters:** Effect of facesheet thickness on boundary layer parameters,  $C_F$  and  $\delta^*$ , at a typical temperature of 200°F are plotted with respect to flow Mach number for bulk absorbers of 0.5"-deep 100 ppi SiC and 12 lbf T-Foam with 40% porous facesheets ( $d=0.04''$ ) in Figure 254. For SiC absorbers the effect of increasing facesheet thickness on  $C_F$  and  $\delta^*$  does not follow any specific trend. However, for T-Foam absorbers  $C_F$  decreases and  $\delta^*$  increases with increasing facesheet thickness.

Effect of facesheet thickness on boundary layer parameters for SDOF type panels is shown in Figure 255. In general, local friction coefficients ( $C_F$ ) decreases and displacement thickness

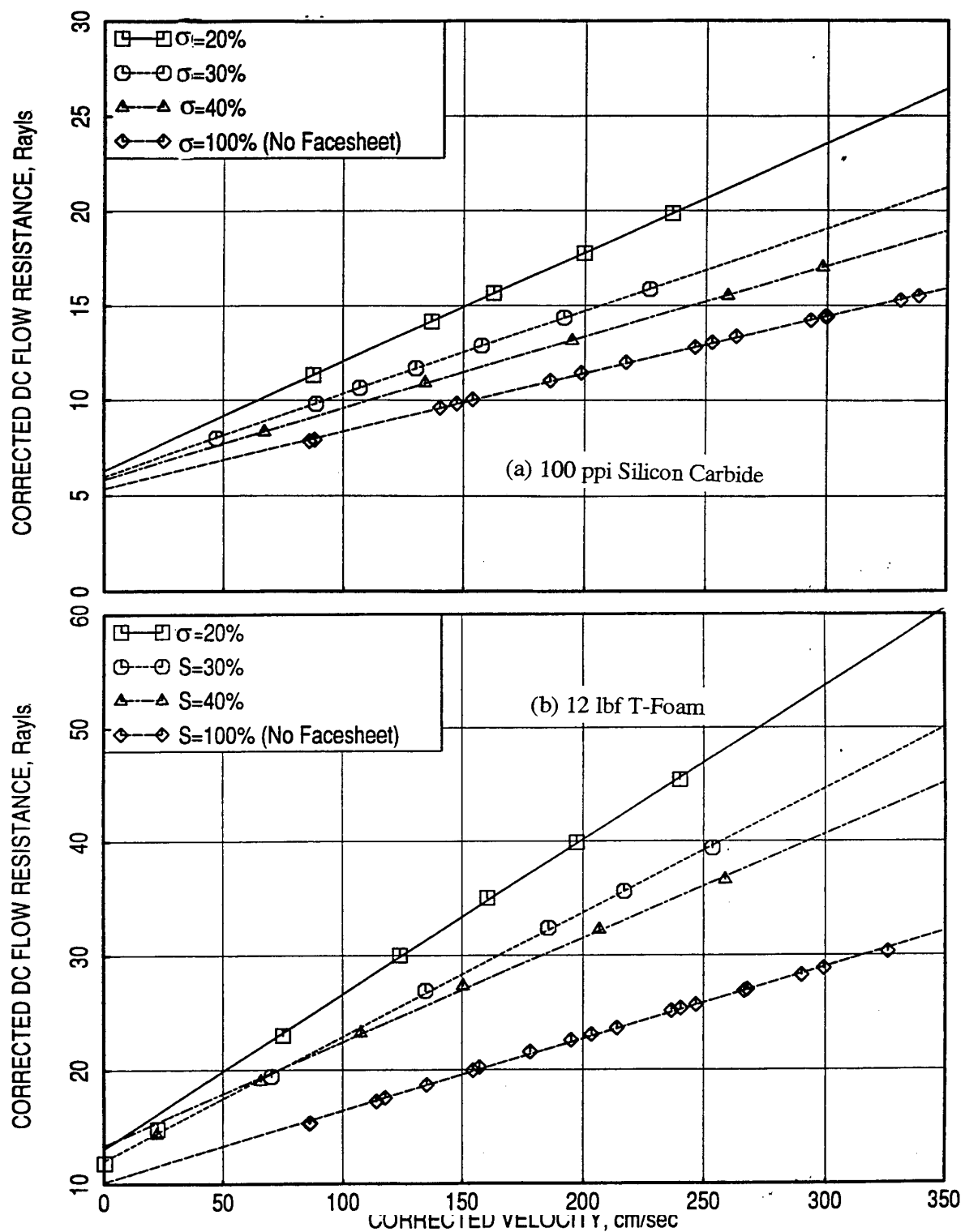


Figure 244. Effect of facesheet porosity ( $\sigma$ ) on DC flow resistance for 0.5"-deep (a) 100 ppi Silicon Carbide and (b) 12 lbf T-Foam panels for 0.025"-thick facesheet with 0.04" diameter holes,  $M=0.0$ .

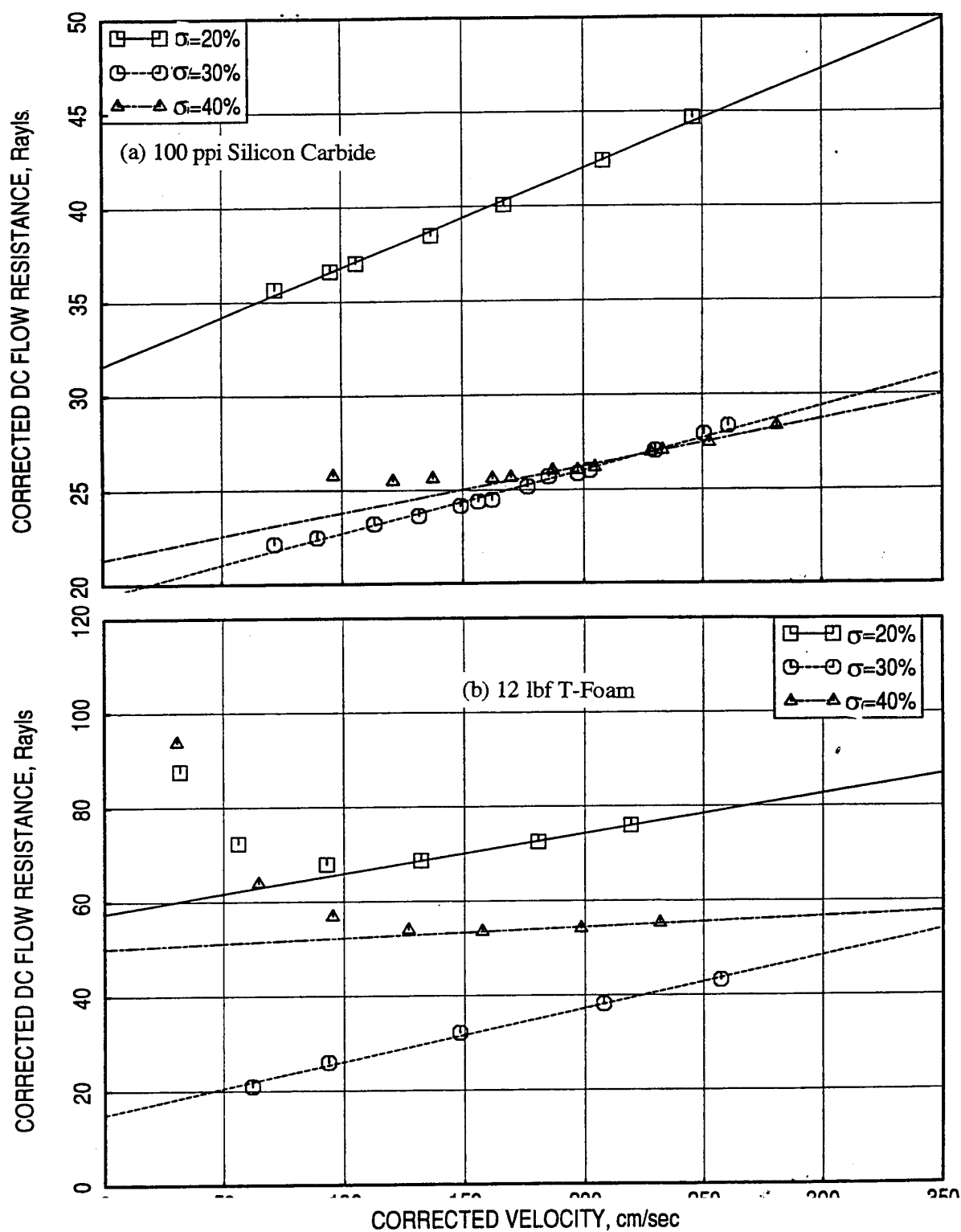


Figure 245. Effect of facesheet porosity ( $\sigma$ ) on DC flow resistance for 0.5"-deep (a) 100 ppi Silicon Carbide and (b) 12 lbf T-Foam panels for 0.025"-thick facesheet with 0.04" diameter holes,  $M=0.3$ .

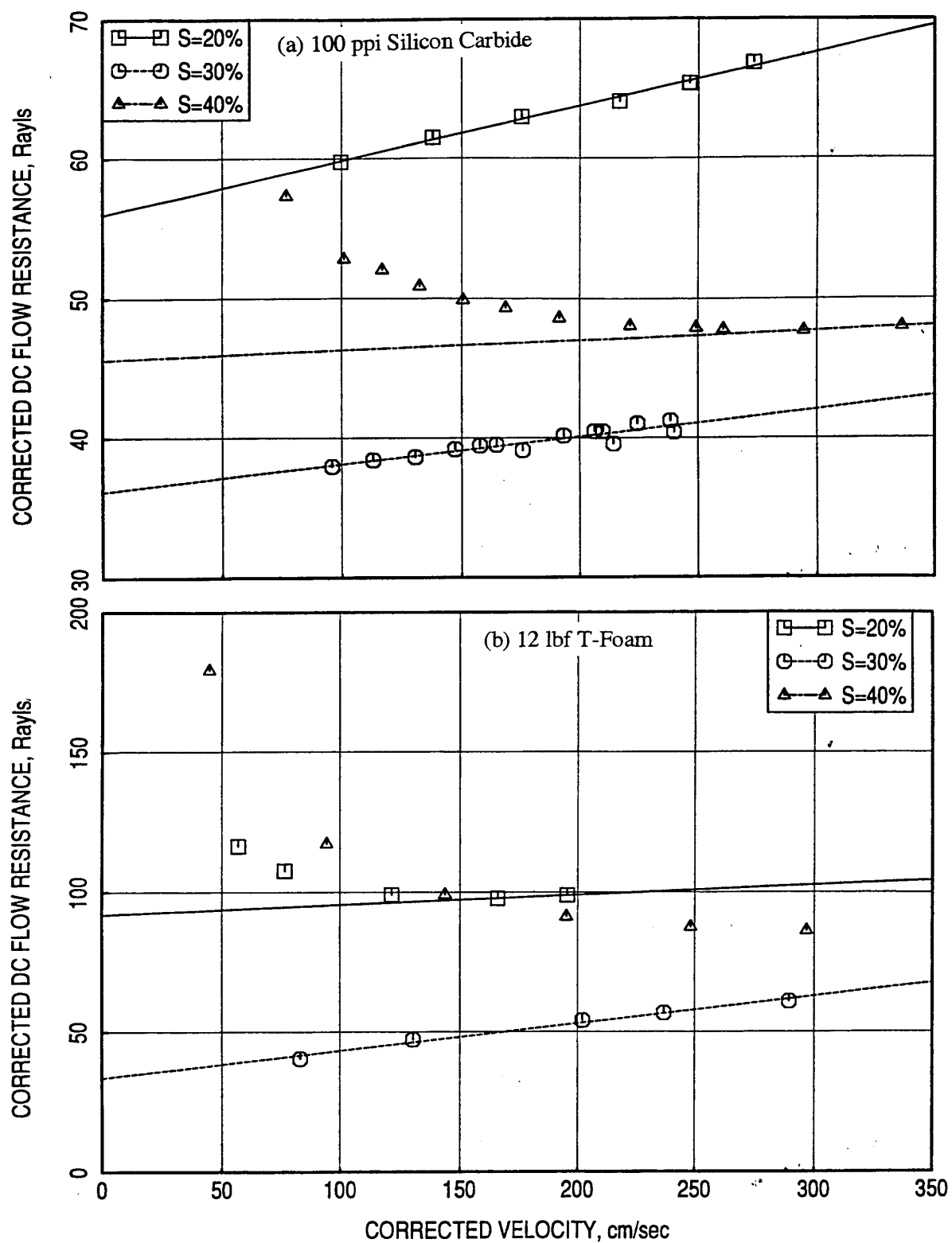


Figure 246. Effect of facesheet porosity ( $\sigma$ ) on DC flow resistance for 0.5"-deep (a) 100 ppi Silicon Carbide and (b) 12 lbf T-Foam panels for 0.025"-thick facesheet with 0.04" diameter holes,  $M=0.55$ .



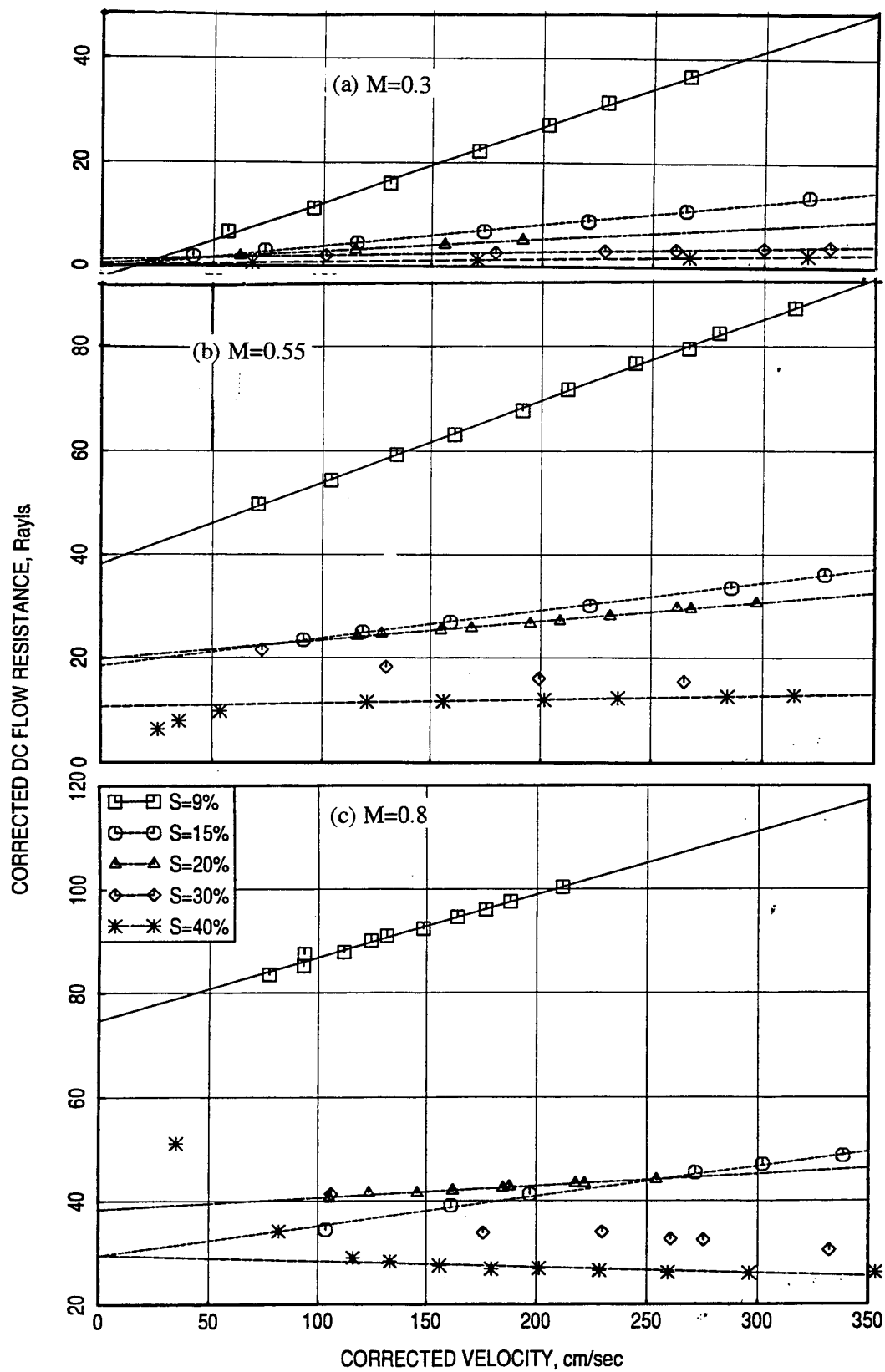


Figure 247. Effect of facesheet porosity ( $\sigma$ ) on DC flow resistance for 0.5"-deep SDOF type panels with 0.025"-thick facesheet  $d=0.04$ ", (a)  $M=0.3$ , (b)  $M=0.55$ , (c)  $M=0.8$ .

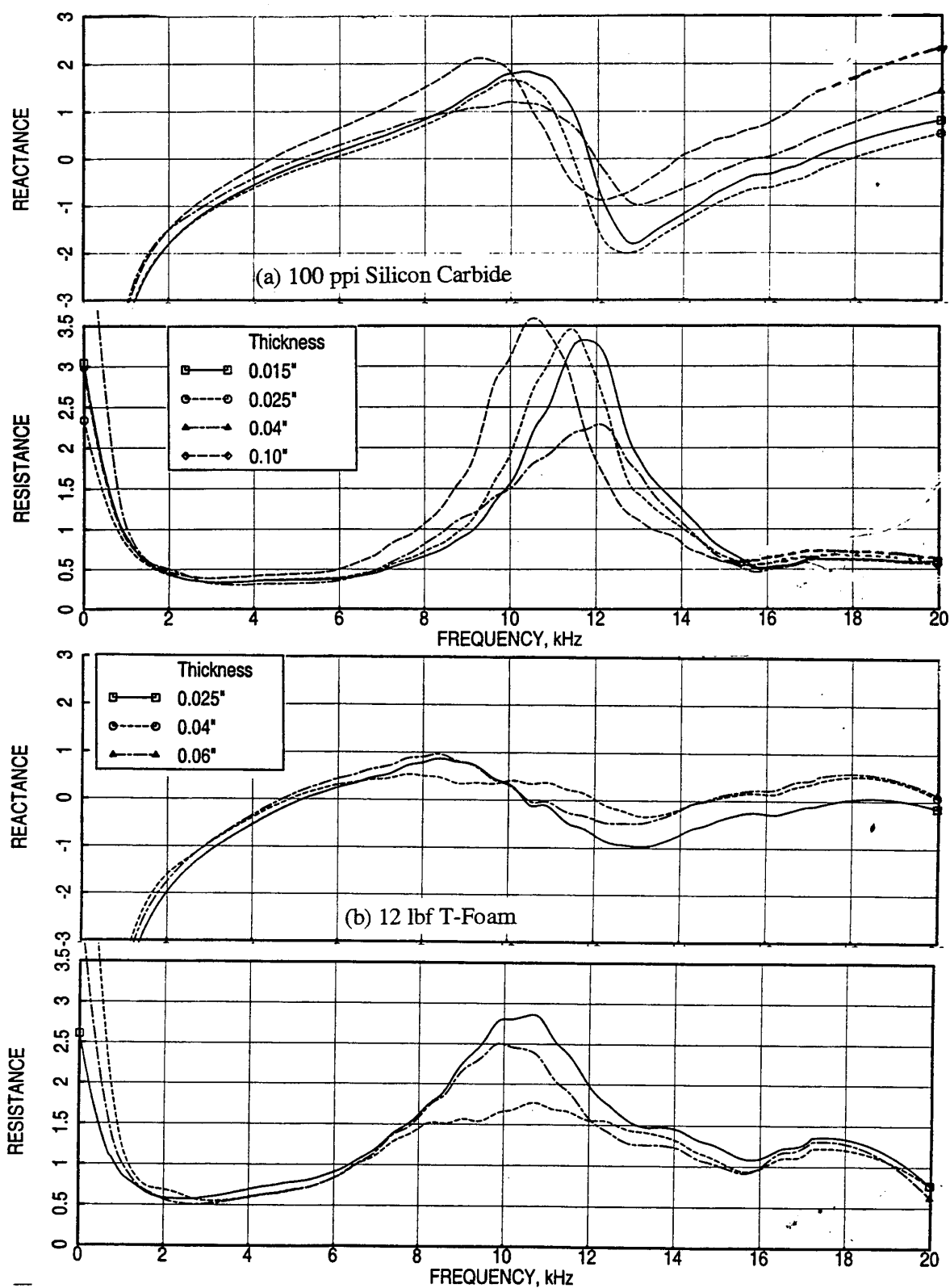


Figure 248. Effect of facesheet thickness ( $t$ ) on normal impedance for 0.5''-deep (a) 100 ppi Silicon Carbide and (b) 12 lbf T-Foam panels for 40% porous facesheet with 0.04'' diameter holes,  $M=0.3$ .

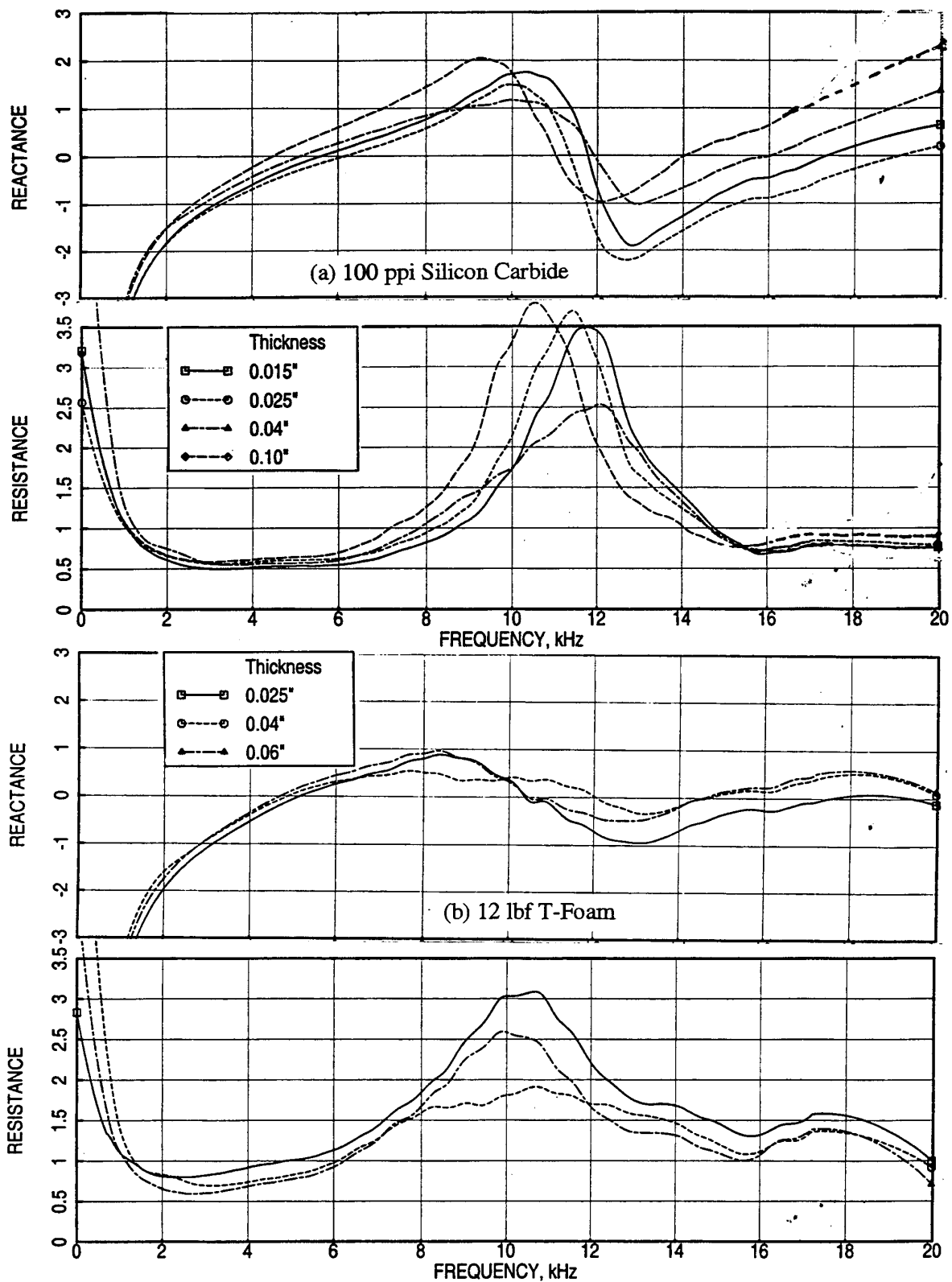


Figure 249. Effect of facesheet thickness ( $t$ ) on normal impedance for 0.5''-deep (a) 100 ppi Silicon Carbide and (b) 12 lbf T-Foam panels for 40% porous facesheet with 0.04'' diameter holes,  $M=0.55$ .

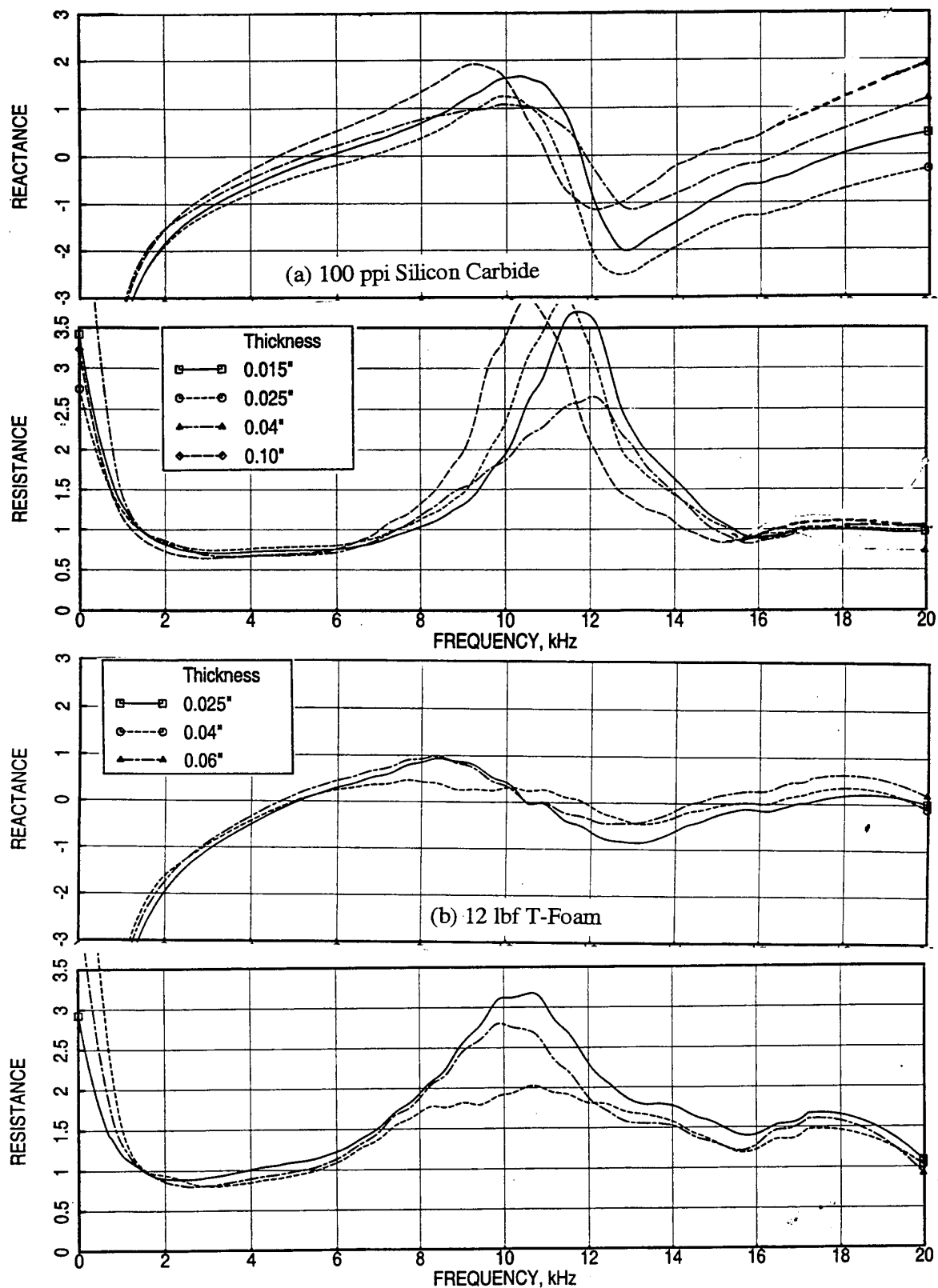


Figure 250. Effect of facesheet thickness ( $t$ ) on normal impedance for 0.5"-deep (a) 100 ppi Silicon Carbide and (b) 12 lbf T-Foam panels for 40% porous facesheet with 0.04" diameter holes,  $M=0.8$ .

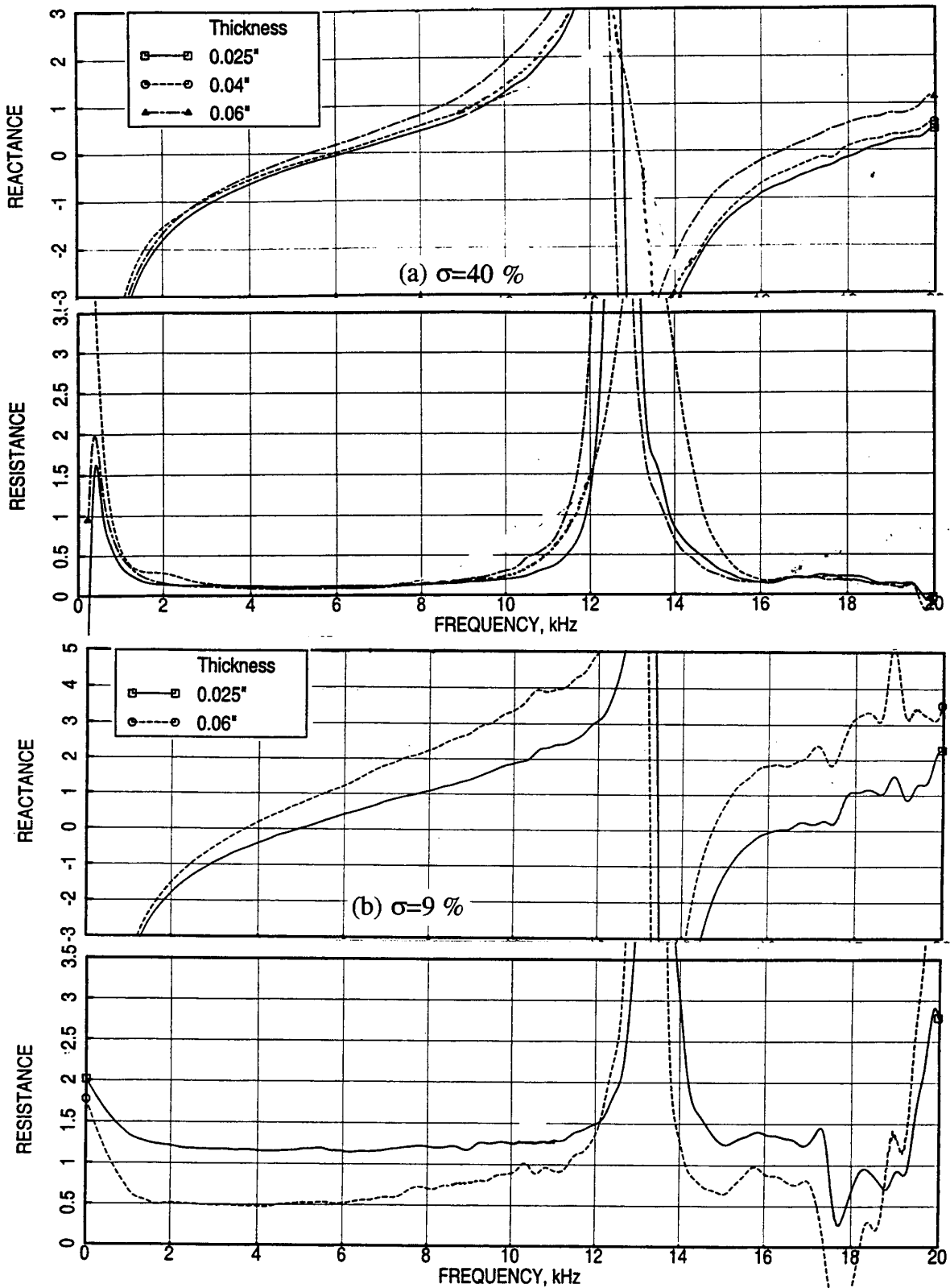


Figure 251. Effect of facesheet thickness (t) on normal impedance for 0.5''-deep SDOF type panels with facesheet hole diameter of 0.04'', M=0.3, (a)  $\sigma=40\%$ , (b)  $\sigma=9\%$ .

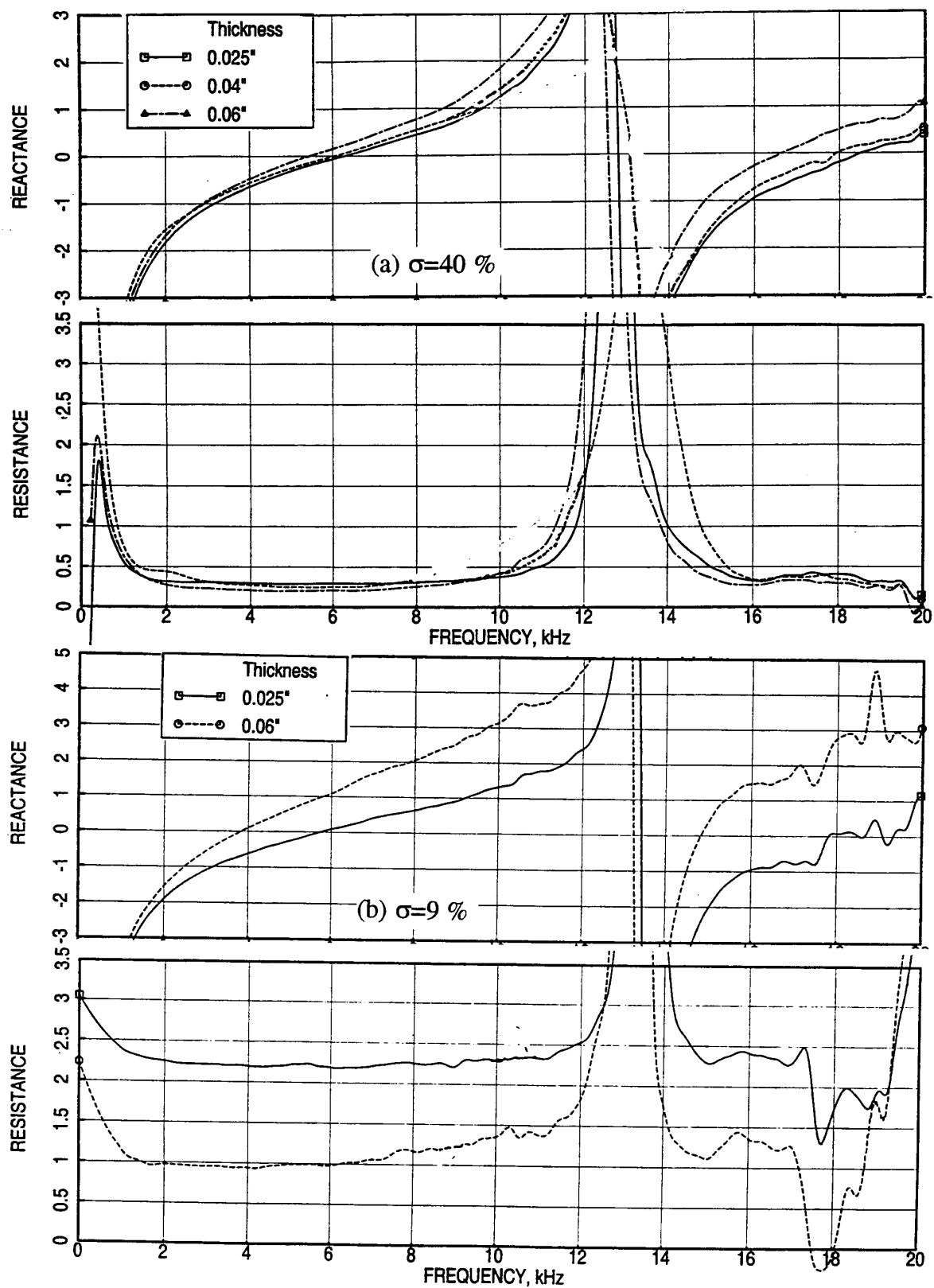


Figure 252. Effect of facesheet thickness ( $t$ ) on normal impedance for 0.5''-deep SDOF type panels with facesheet hole diameter of 0.04'',  $M=0.55$ , (a)  $\sigma=40\%$ , (b)  $\sigma=9\%$ .

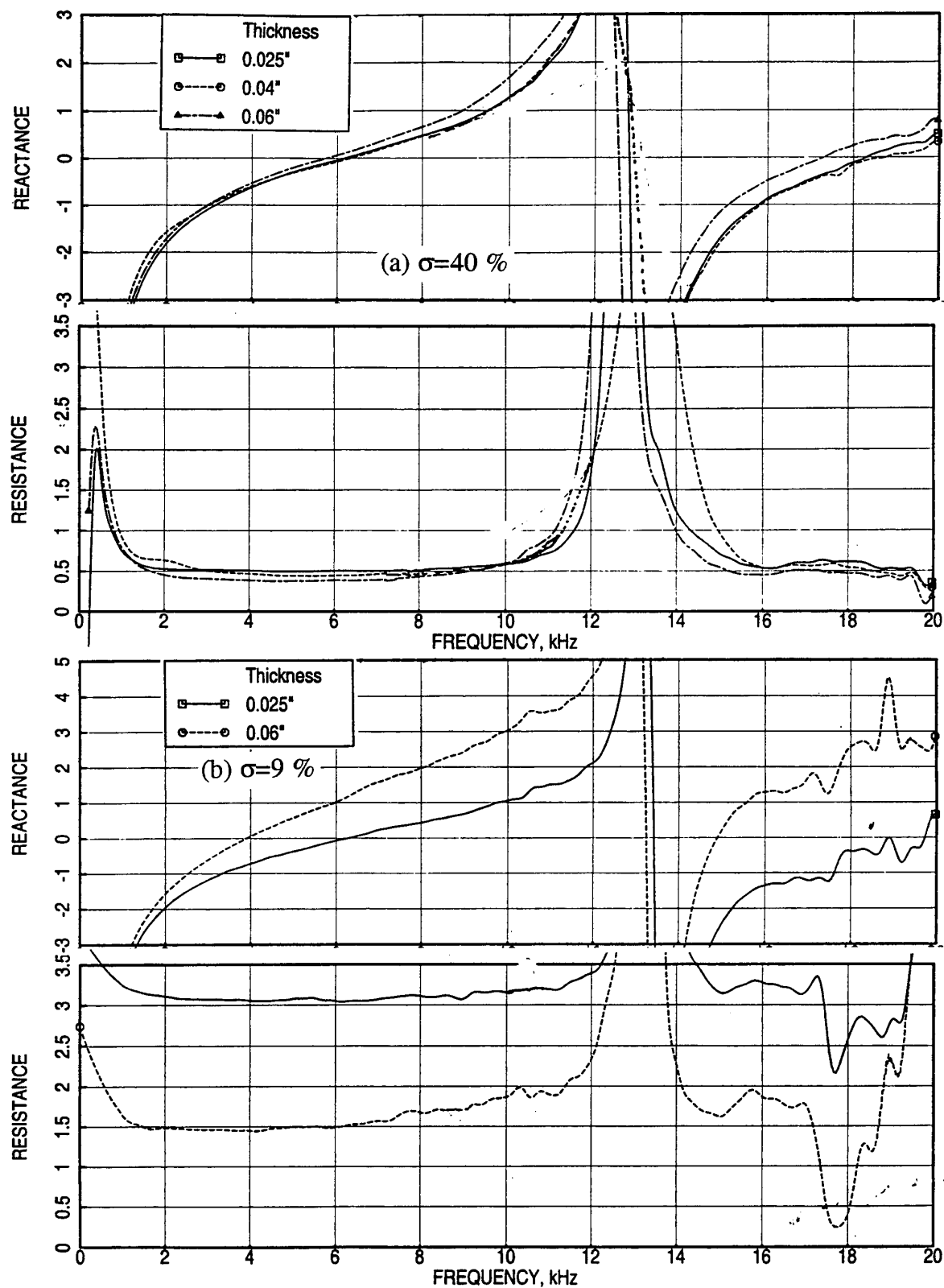


Figure 253. Effect of facesheet thickness (t) on normal impedance for 0.5''-deep SDOF type panels with facesheet hole diameter of 0.04'', M=0.8, (a)  $\sigma=40\%$ , (b)  $\sigma=9\%$ .

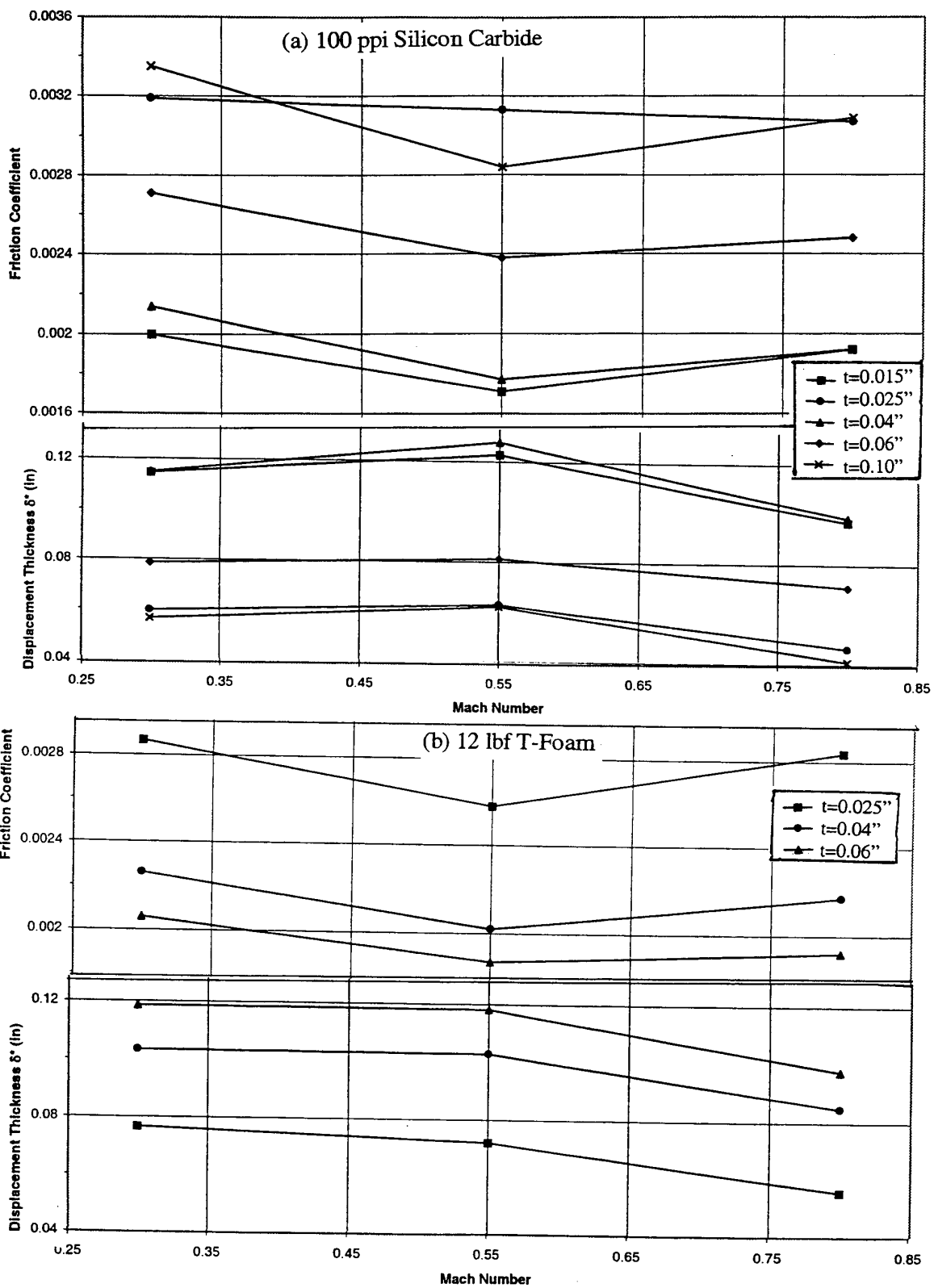


Figure 254. Effect of facesheet thickness ( $t$ ) on local friction coefficient and displacement thickness for 0.5''-deep (a) 100 ppi Silicon Carbide and (b) 12 lbf T-Foam panels with 40% porous facesheet,  $d=0.04''$ ,  $T=200^\circ\text{F}$ .



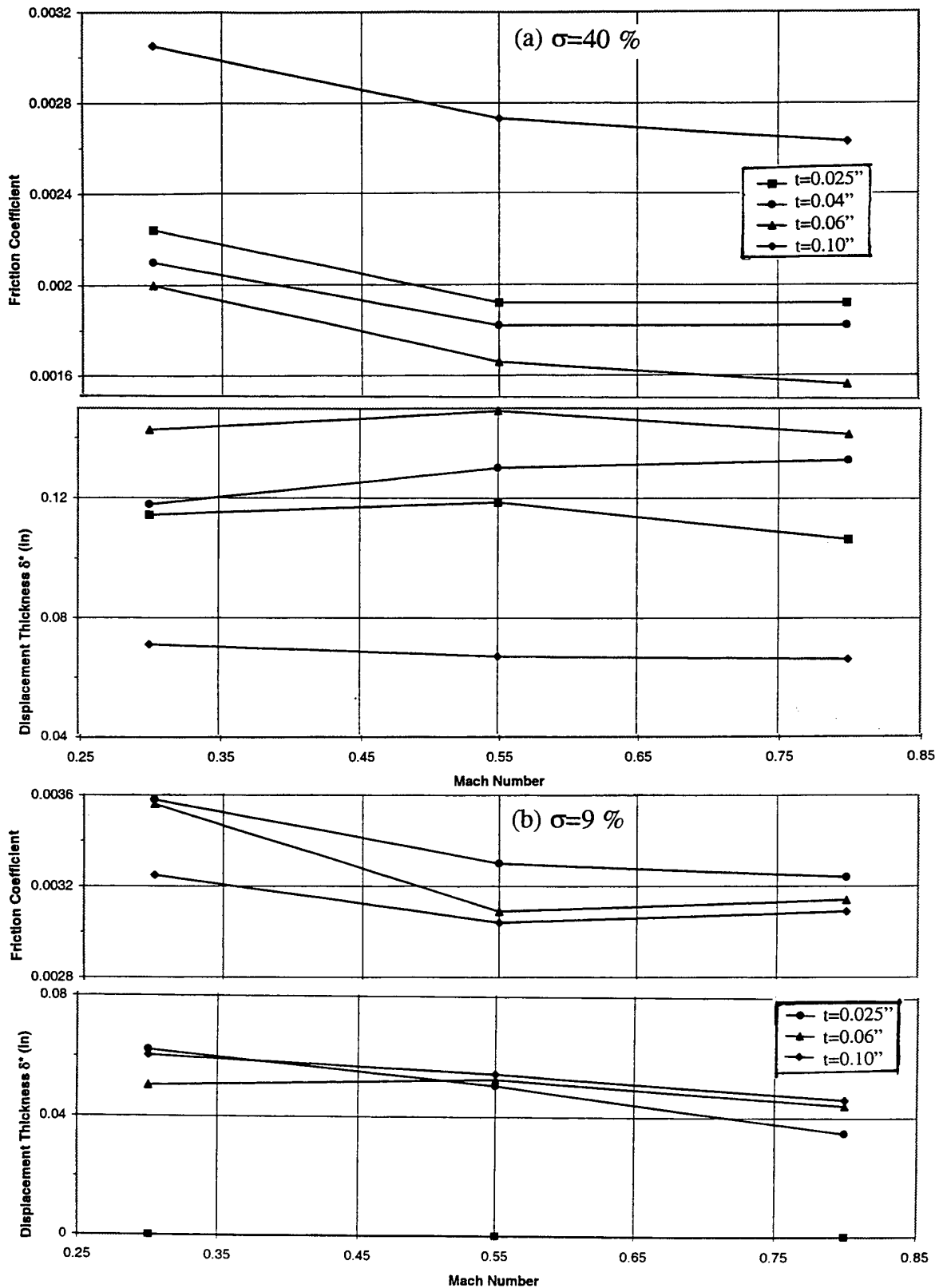


Figure 255. Effect of facesheet thickness ( $t$ ) on local friction coefficient and displacement thickness for 0.5''-deep SDOF type panels with facesheet hole diameter of 0.04'',  $T=200^{\circ}\text{F}$ , (a)  $\sigma=40\%$ , (b)  $\sigma=9\%$ .

( $\delta^*$ ) increases with increasing facesheet thickness. For 40% porous 0.1"-thick facesheet the trend is reversed.

**DC Flow Resistance:** Effect of facesheet thickness on DC flow resistance is shown for bulk absorbers of 0.5"-deep 100 ppi SiC and 12 lbf T-Foam with 40% porous facesheets ( $d=0.04''$ ) in Figures 256 and 257. While, the DC flow resistance is higher due to the inclusion of facesheet over the bulk the effect of its thickness on DC flow resistance does not follow any specific trend. Similar results for a 9% porous facesheet for SDOF type panels are shown in Figure 258.

#### 6.4.5 Effect of Facesheet Hole Diameter

**Insitu Impedance:** Effect of facesheet hole diameter on normal impedance for a 0.5"-deep bulk absorbers of 100 ppi SiC and 12 lbf T-Foam with 40% porous 0.025"-thick facesheets is shown in Figures 259 through 261 at different Mach numbers. In general resistance decreases and reactance increases with increasing facesheet hole diameter. The effect is relatively less for T-Foam bulk absorbers. Similar results for a 0.5"-deep SDOF type panel with 0.025"-thick facesheets of two different porosities is shown in Figures 262 through 264 for different grazing flow Mach numbers. Similar effect of decreasing resistance and increasing reactance with increasing facesheet hole diameter is observed. The effect is much higher for 9% porous facesheet compared to 40%.

**Boundary Layer Profiles and Related Parameters:** Effect of facesheet hole diameter on boundary layer parameters,  $C_F$  and  $\delta^*$ , at a typical temperature of 200°F are plotted with respect to flow Mach number for bulk absorbers of 0.5"-deep 100 ppi SiC and 12 lbf T-Foam, and SDOF type panels with 40% porous 0.025"-thick facesheets in Figures 265 and 266. For bulk absorbers  $C_F$  decreases with increasing facesheet hole diameter and the trend is opposite for SDOF type panels. Similarly,  $\delta^*$  increases for bulk absorbers and decreases for SDOF type panels with increasing facesheet hole diameter.

**DC Flow Resistance:** Effect of facesheet hole diameter on DC flow resistance is shown for bulk absorbers of 0.5"-deep 100 ppi SiC and 12 lbf T-Foam with 40% porous 0.025"-thick facesheets in Figure 267. DC flow resistance increases first and then decreases with increasing facesheet hole diameter. Similar results for a 9% porous facesheet for SDOF type panels are shown in Figure 268. At no flow condition the DC flow resistance increases with increasing facesheet hole diameter and the amount of increase is higher at higher approach

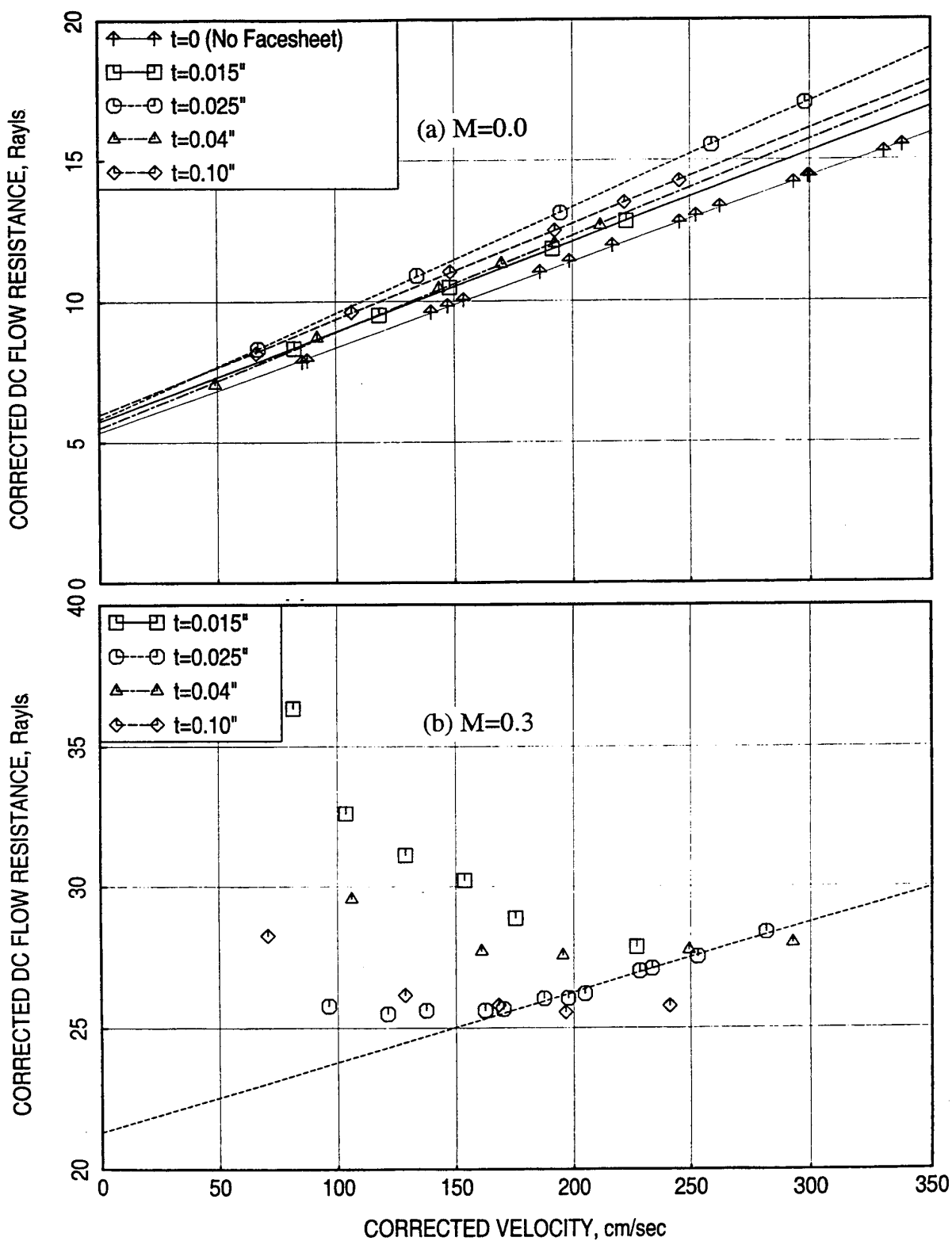


Figure 256. Effect of facesheet thickness ( $t$ ) on DC flow resistance for a 0.5"-deep 100 ppi Silicon Carbide panel with 40% porous facesheet with 0.04" diameter holes, (a)  $M=0$ , (b)  $M=0.3$ .

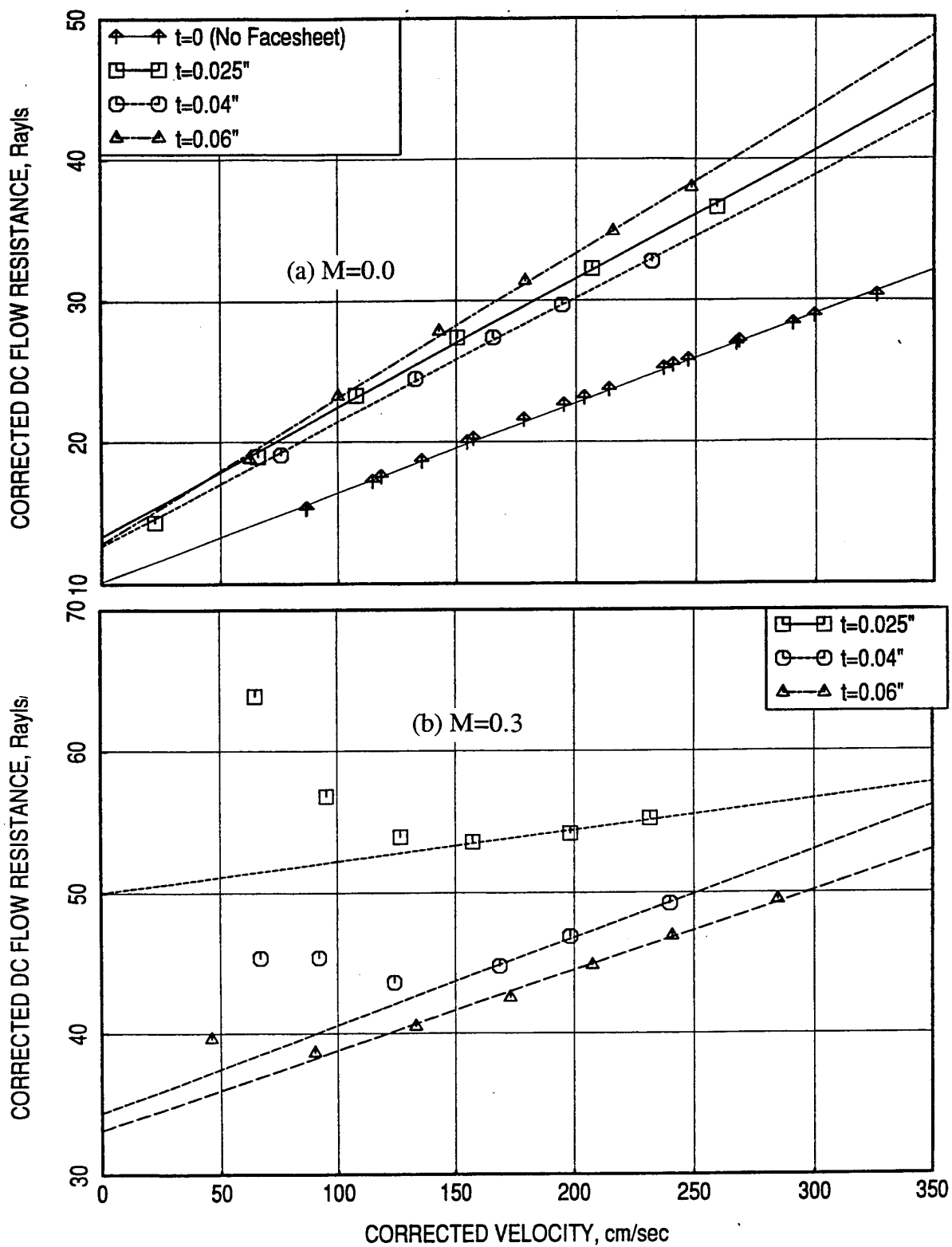


Figure 257. Effect of facesheet thickness ( $t$ ) on DC flow resistance for a 0.5''-deep 12 lbf T-Foam panel with 40% porous facesheet with 0.04'' diameter holes, (a)  $M=0$ , (b)  $M=0.3$ .

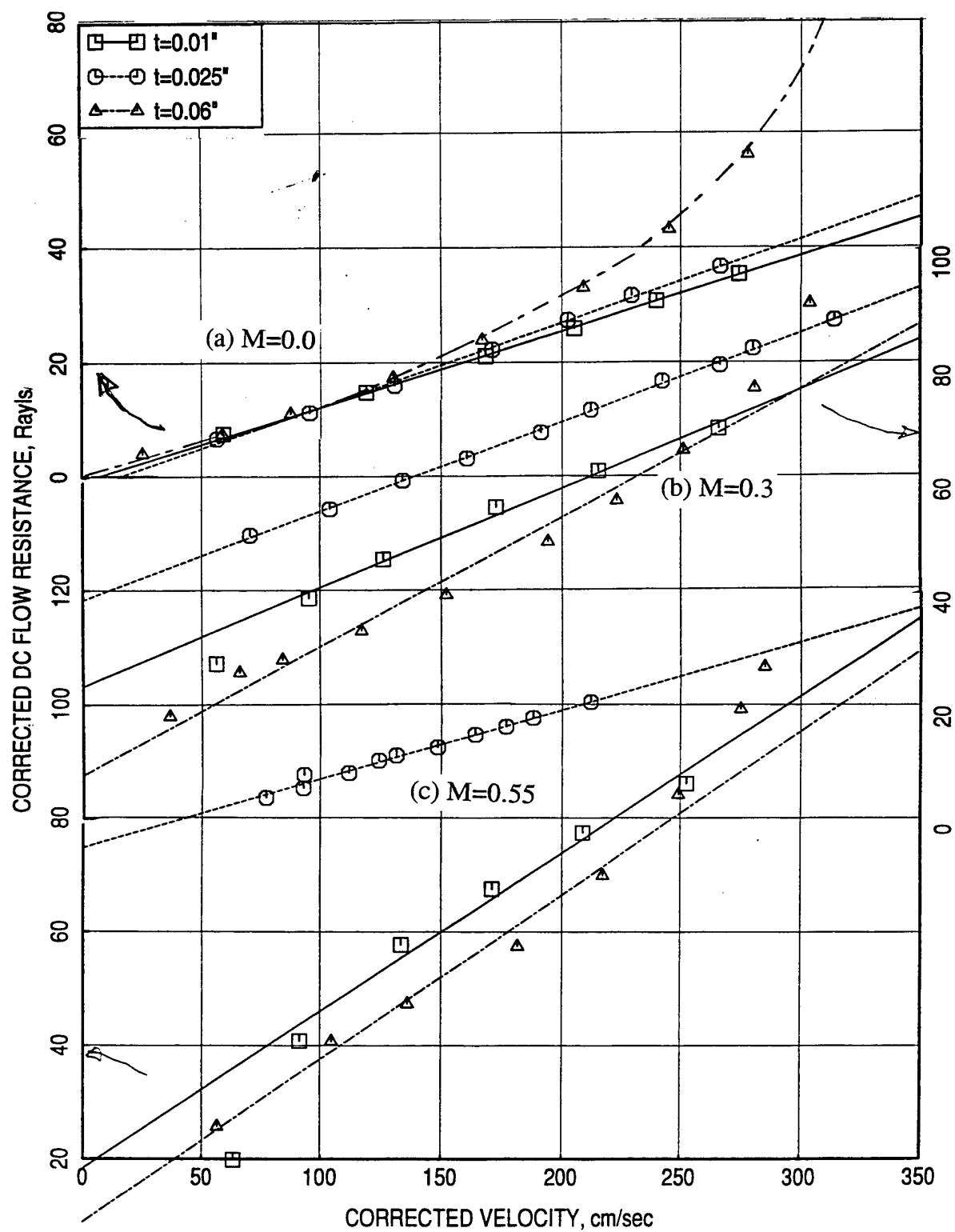


Figure 258. Effect of facesheet thickness ( $t$ ) on DC flow resistance for a 0.5"-deep SDOF type panel with 9% porous facesheet with 0.04" diameter holes, (a)  $M=0$ , (b)  $M=0.3$ , and (c)  $M=0.55$ .

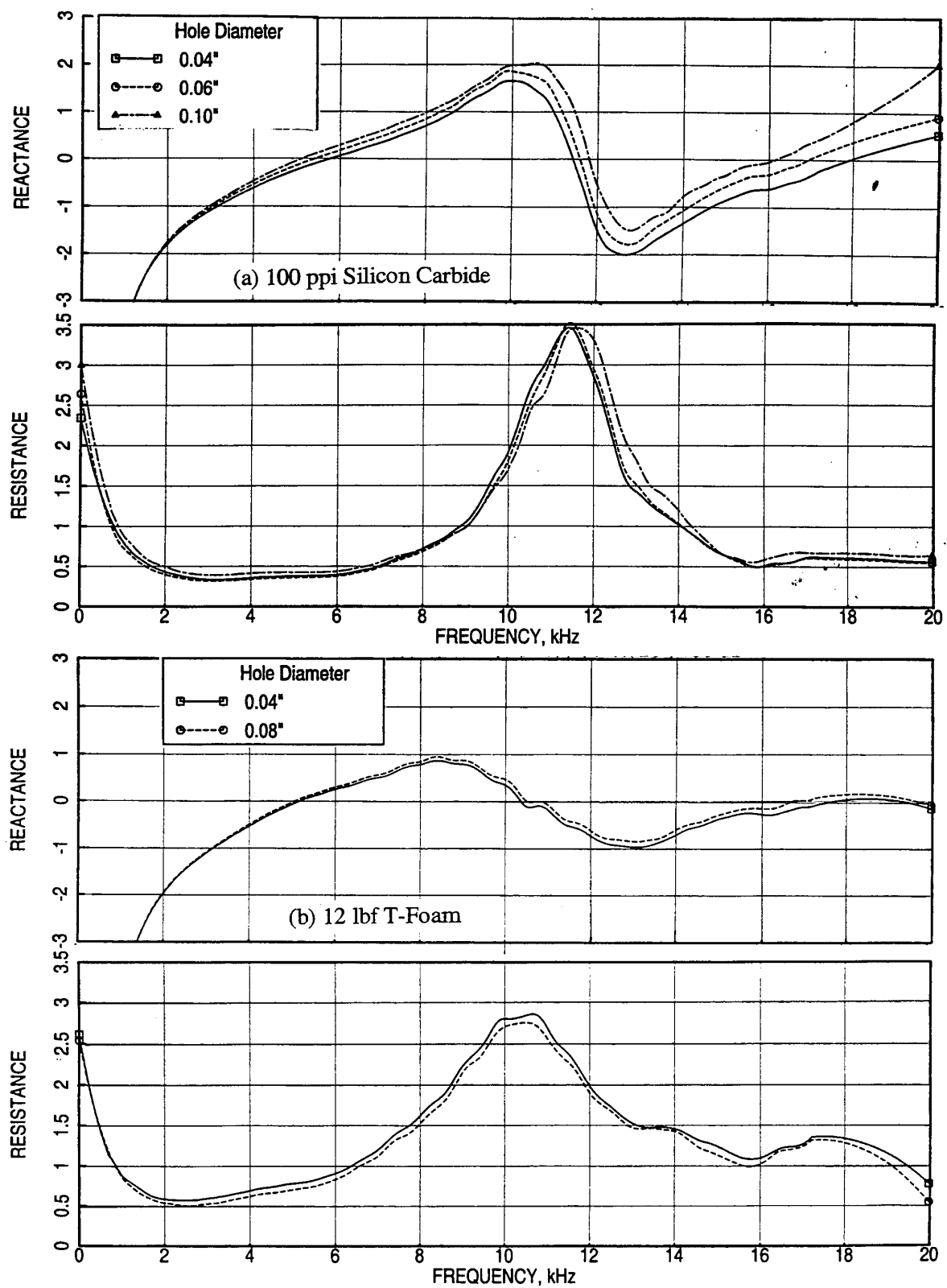


Figure 259. Effect of facesheet hole diameter (d) on normal impedance for 0.5"-deep (a) 100 ppi Silicon Carbide and (b) 12 lbf T-Foam panels for 40% porous 0.025"-thick facesheet,  $M=0.3$ .

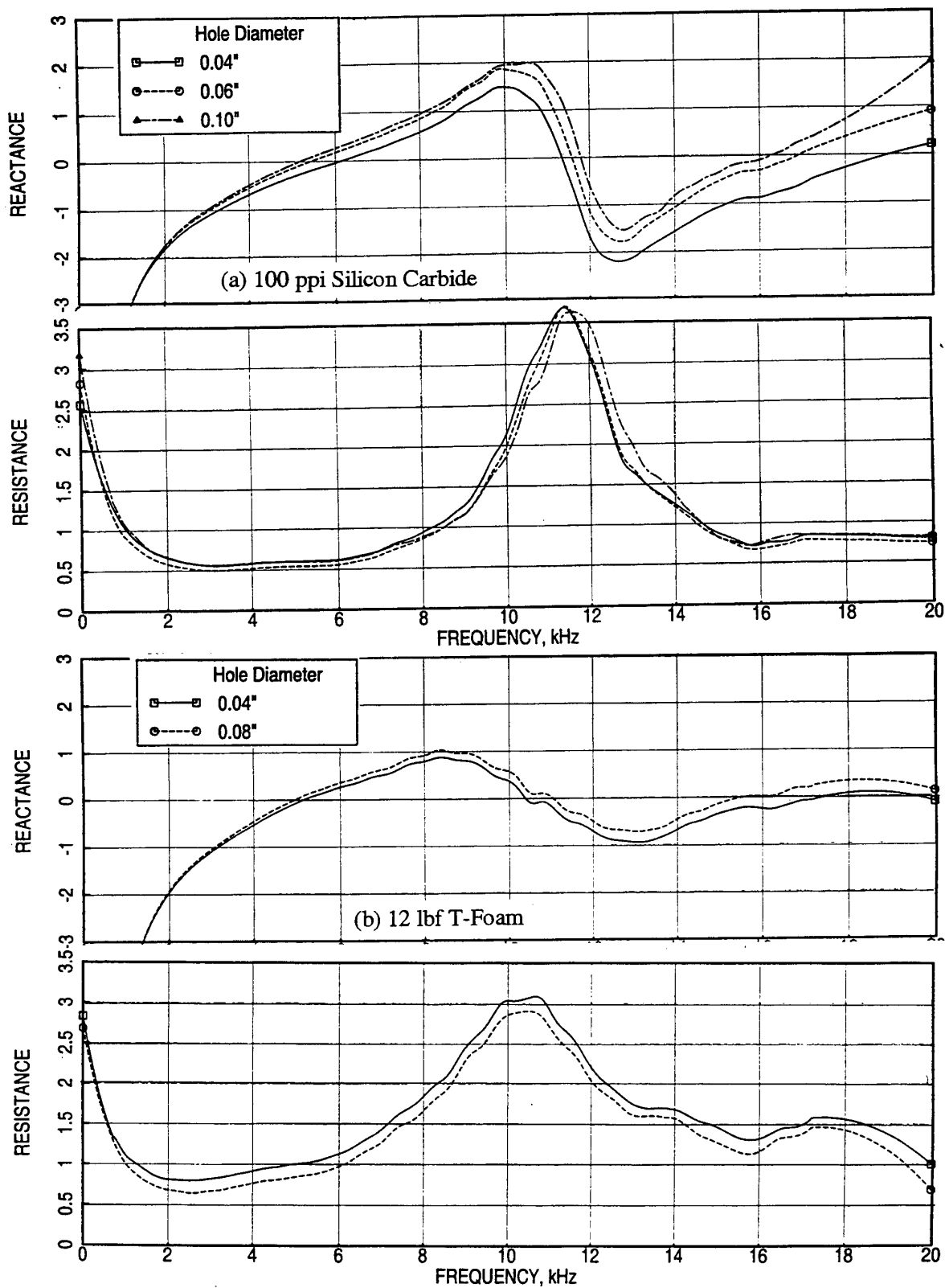


Figure 260. Effect of facesheet hole diameter ( $d$ ) on normal impedance for 0.5"-deep (a) 100 ppi Silicon Carbide and (b) 12 lbf T-Foam panels for 40% porous 0.025"-thick facesheet,  $M=0.55$ .

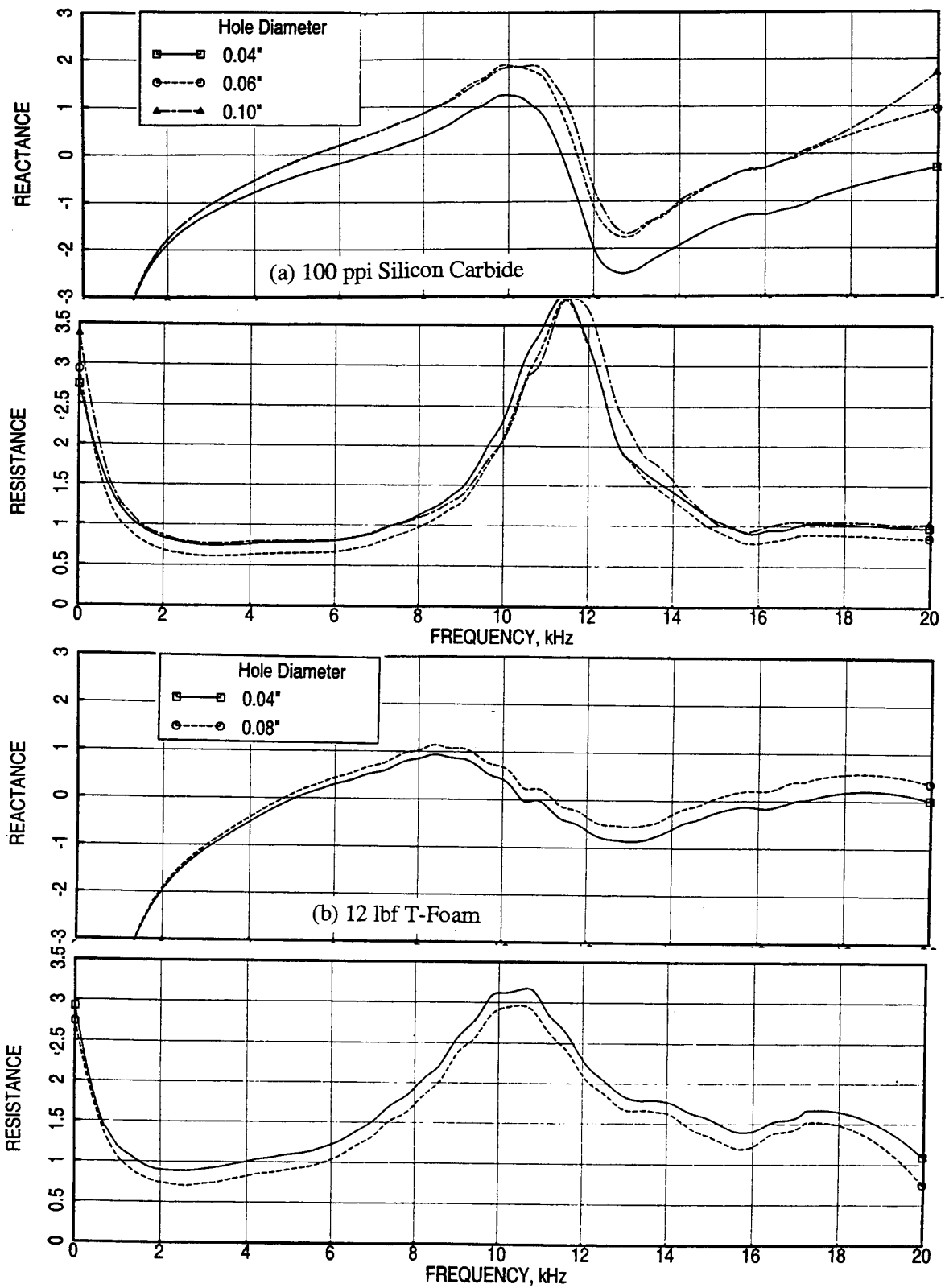


Figure 261. Effect of facesheet hole diameter ( $d$ ) on normal impedance for 0.5"-deep (a) 100 ppi Silicon Carbide and (b) 12 lbf T-Foam panels for 40% porous 0.025"-thick facesheet,  $M=0.8$ .



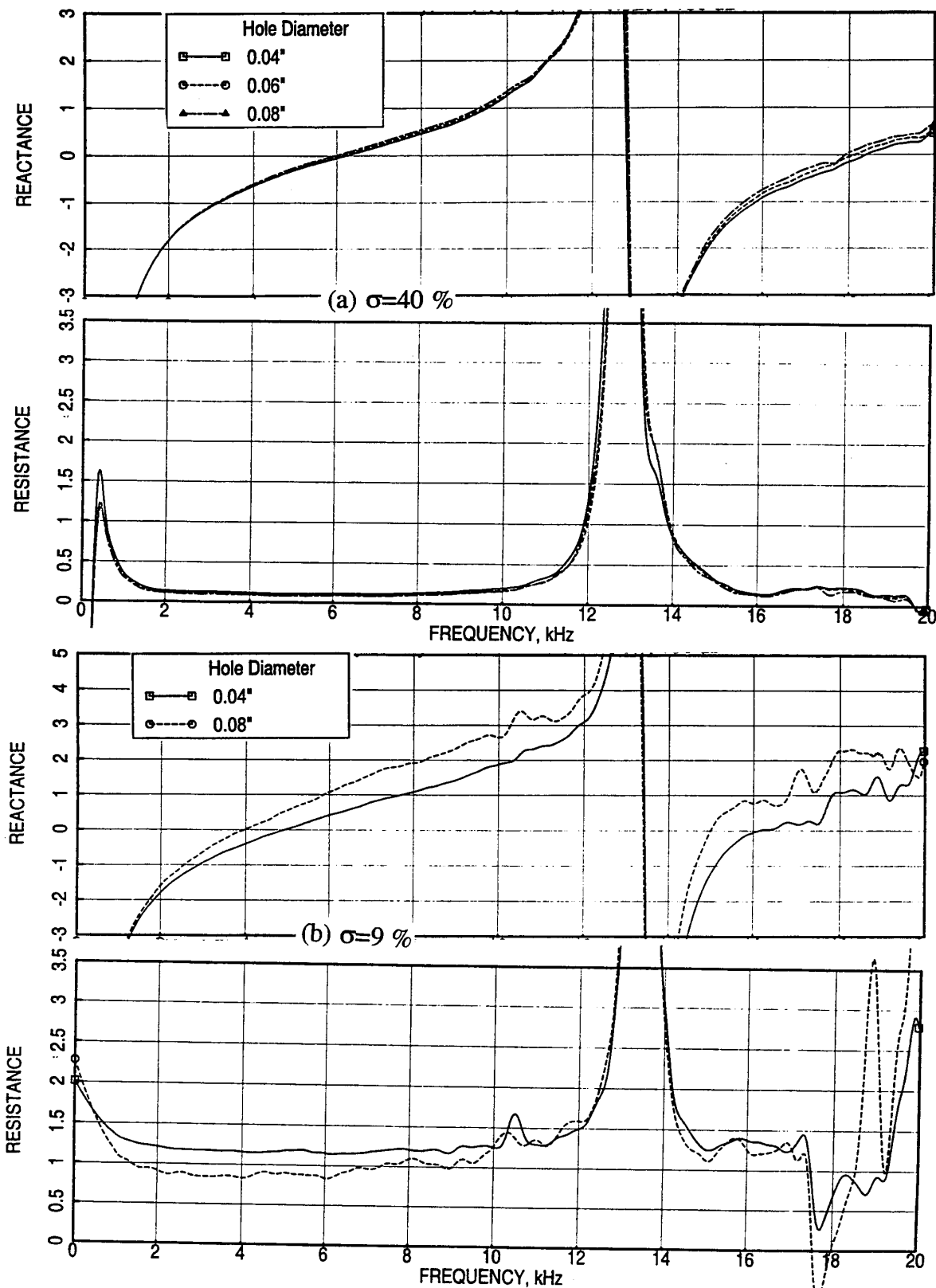


Figure 262. Effect of facesheet hole diameter ( $d$ ) on normal impedance for 0.5''-deep SDOF type panels with 0.025''-thick facesheet,  $M=0.3$ , (a)  $\sigma=40\%$ , (b)  $\sigma=9\%$ .

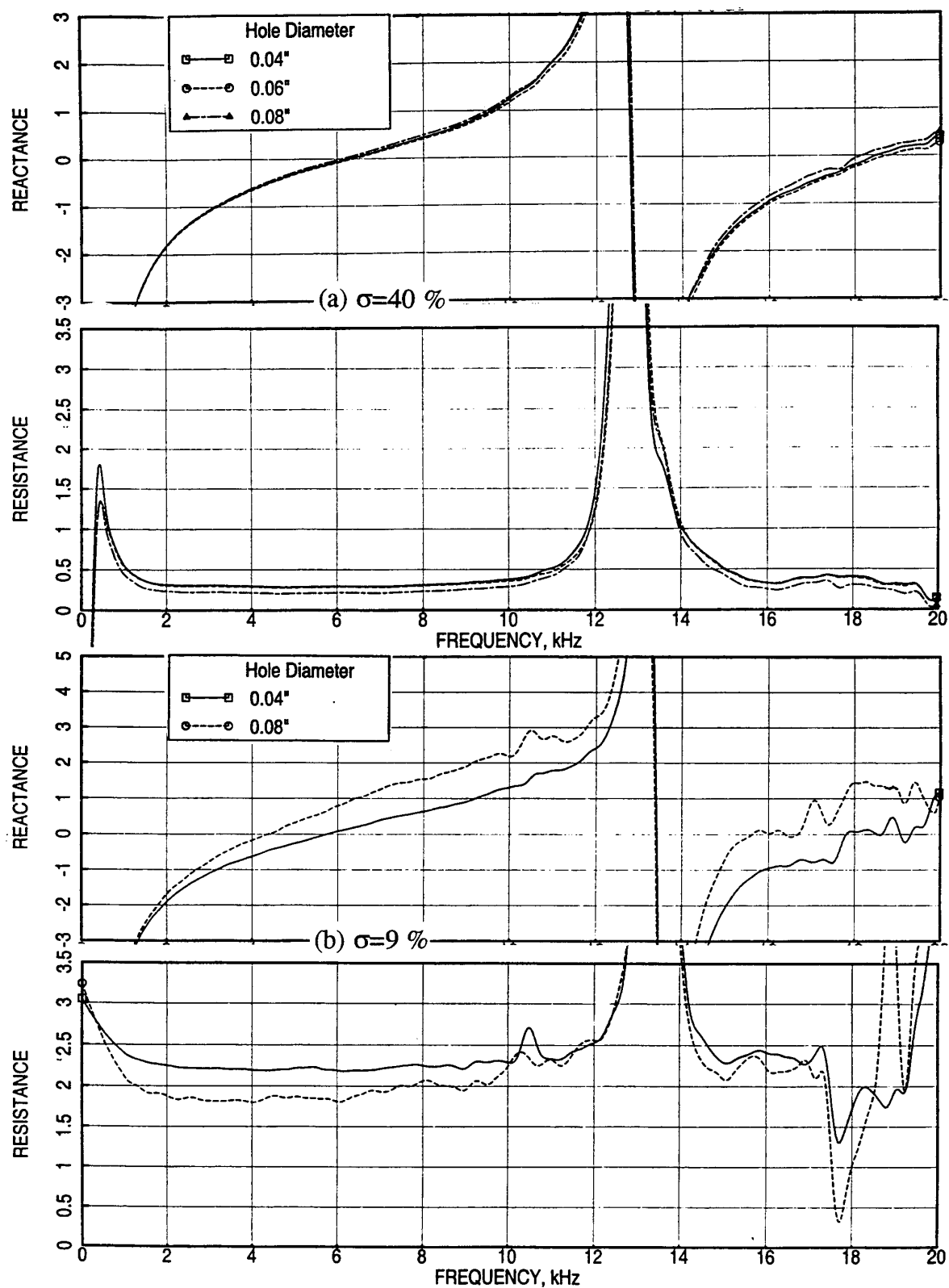


Figure 263. Effect of facesheet hole diameter (d) on normal impedance for 0.5"-deep SDOF type panels with 0.025"-thick facesheet,  $M=0.55$ , (a)  $\sigma=40\%$ , (b)  $\sigma=9\%$ .

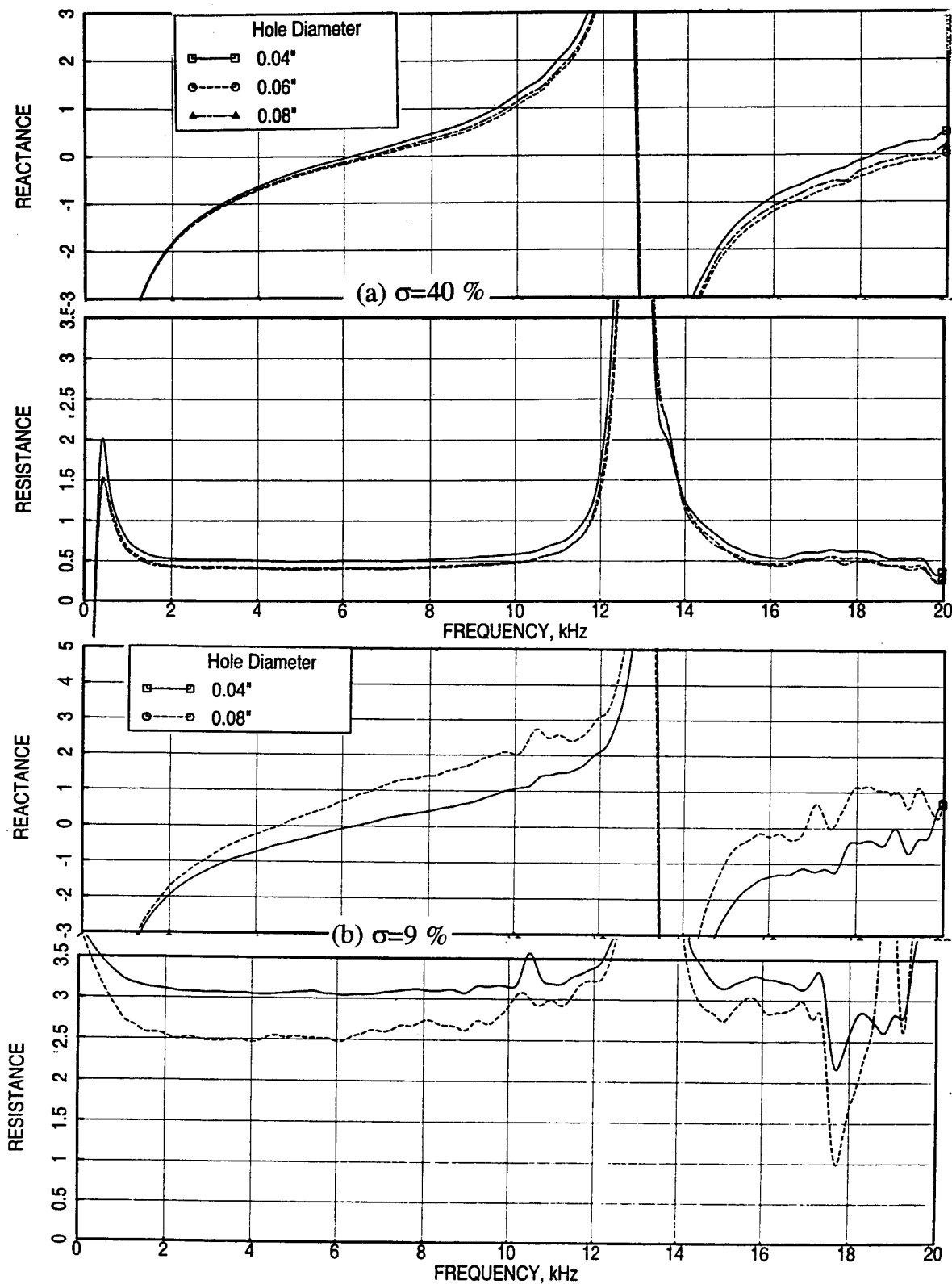


Figure 264. Effect of facesheet hole diameter (d) on normal impedance for 0.5"-deep SDOF type panels with 0.025"-thick facesheet, M=0.8, (a)  $\sigma=40\%$ , (b)  $\sigma=9\%$ .

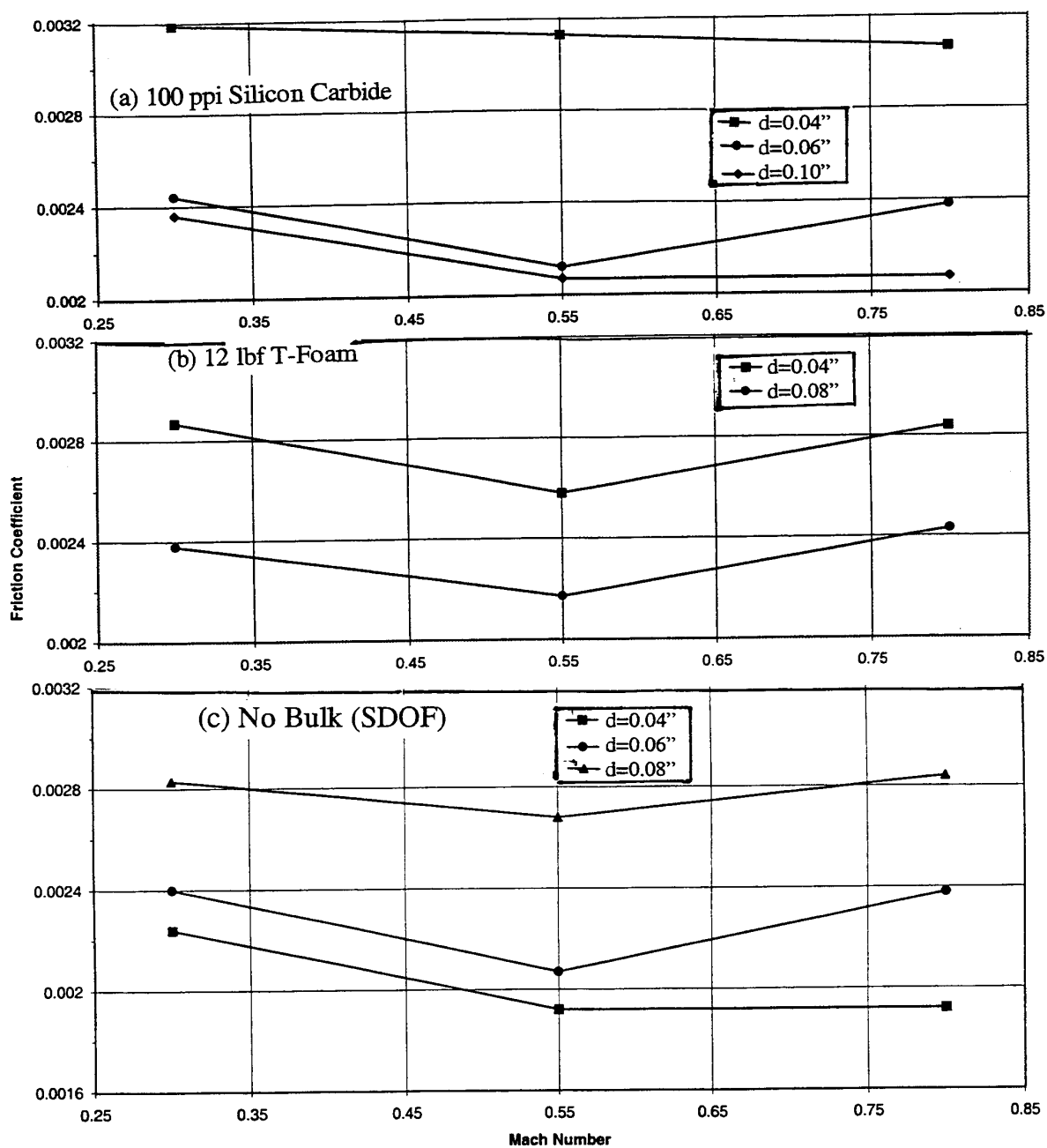


Figure 265. Effect of facesheet hole diameter ( $d$ ) on local friction coefficient for 0.5"-deep (a) 100 ppi Silicon Carbide, (b) 12 lbf T-Foam, and (c) SDOF type panels with 0.025"-thick 40% porous facesheet,  $T=200^{\circ}\text{F}$ .

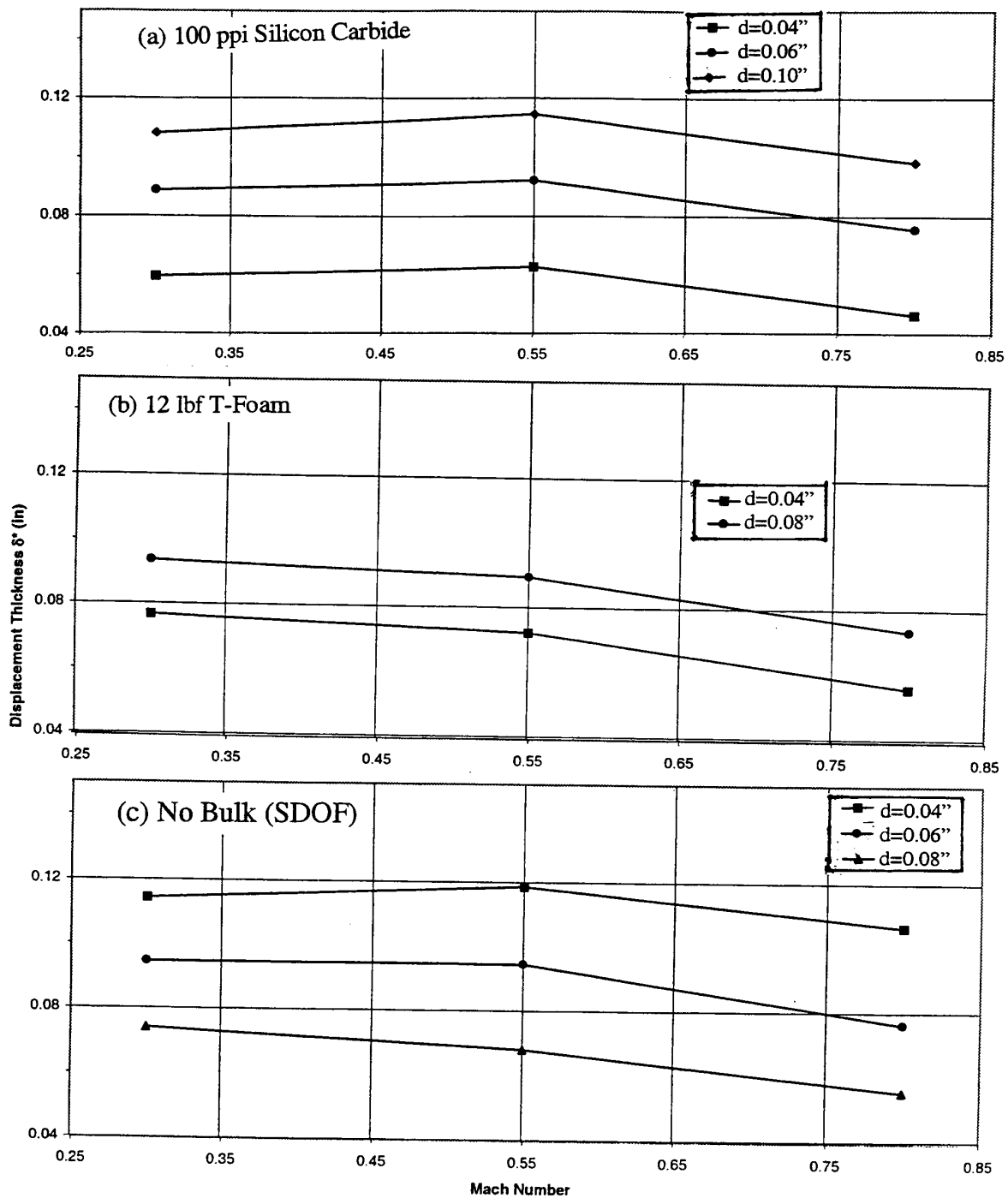


Figure 266. Effect of facesheet hole diameter ( $d$ ) on boundary layer displacement thickness for 0.5"-deep (a) 100 ppi Silicon Carbide, (b) 12 lbf T-Foam, and (c) SDOF type panels with 0.025"-thick 40% porous facesheet,  $T=200^{\circ}\text{F}$ .

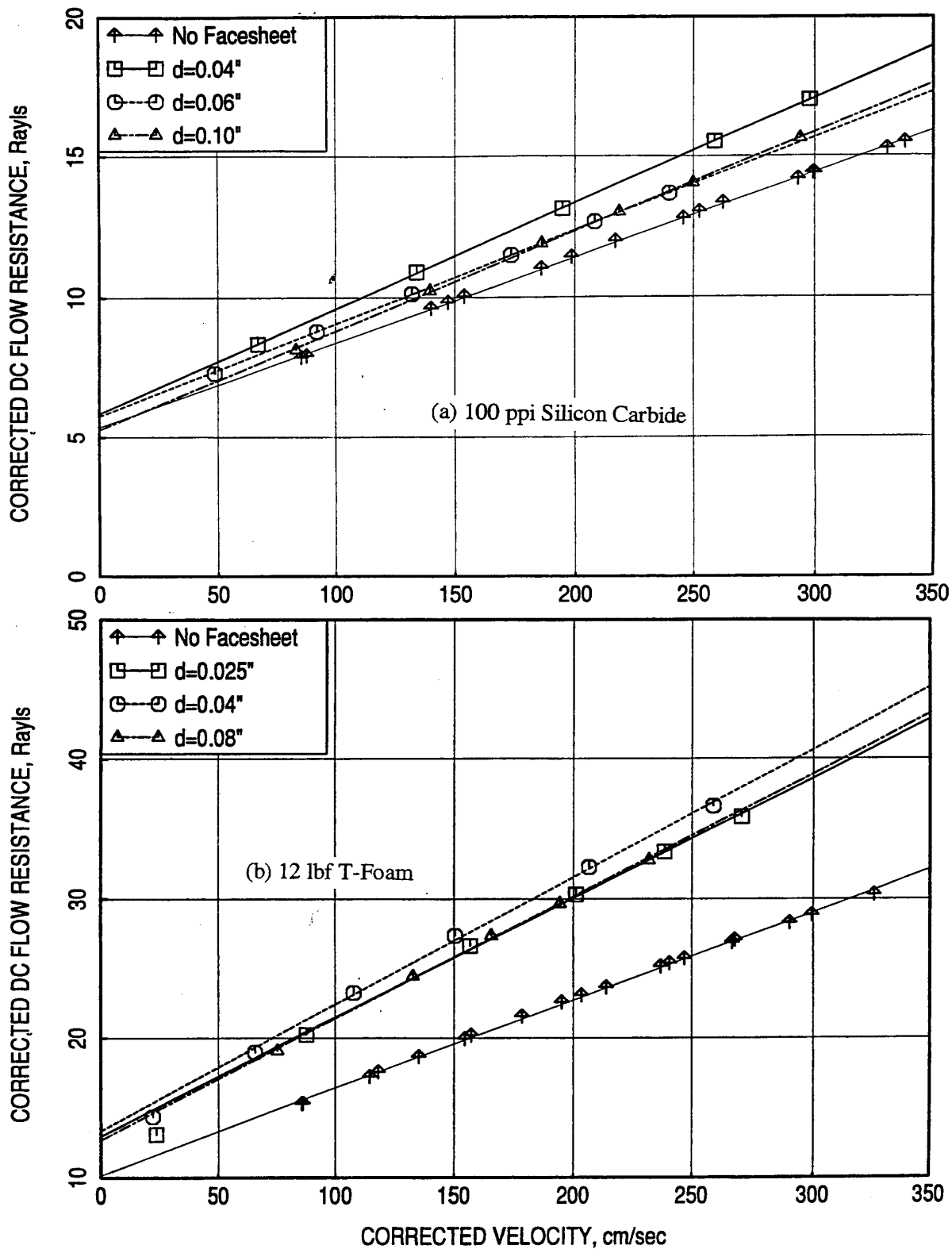


Figure 267. Effect of facesheet hole diameter ( $d$ ) on DC flow resistance for a 0.5"-deep (a) 100 ppi Silicon Carbide and (b) 12 lbf T-Foam panels with 40% porous 0.025"-thick facesheet,  $M=0$ .

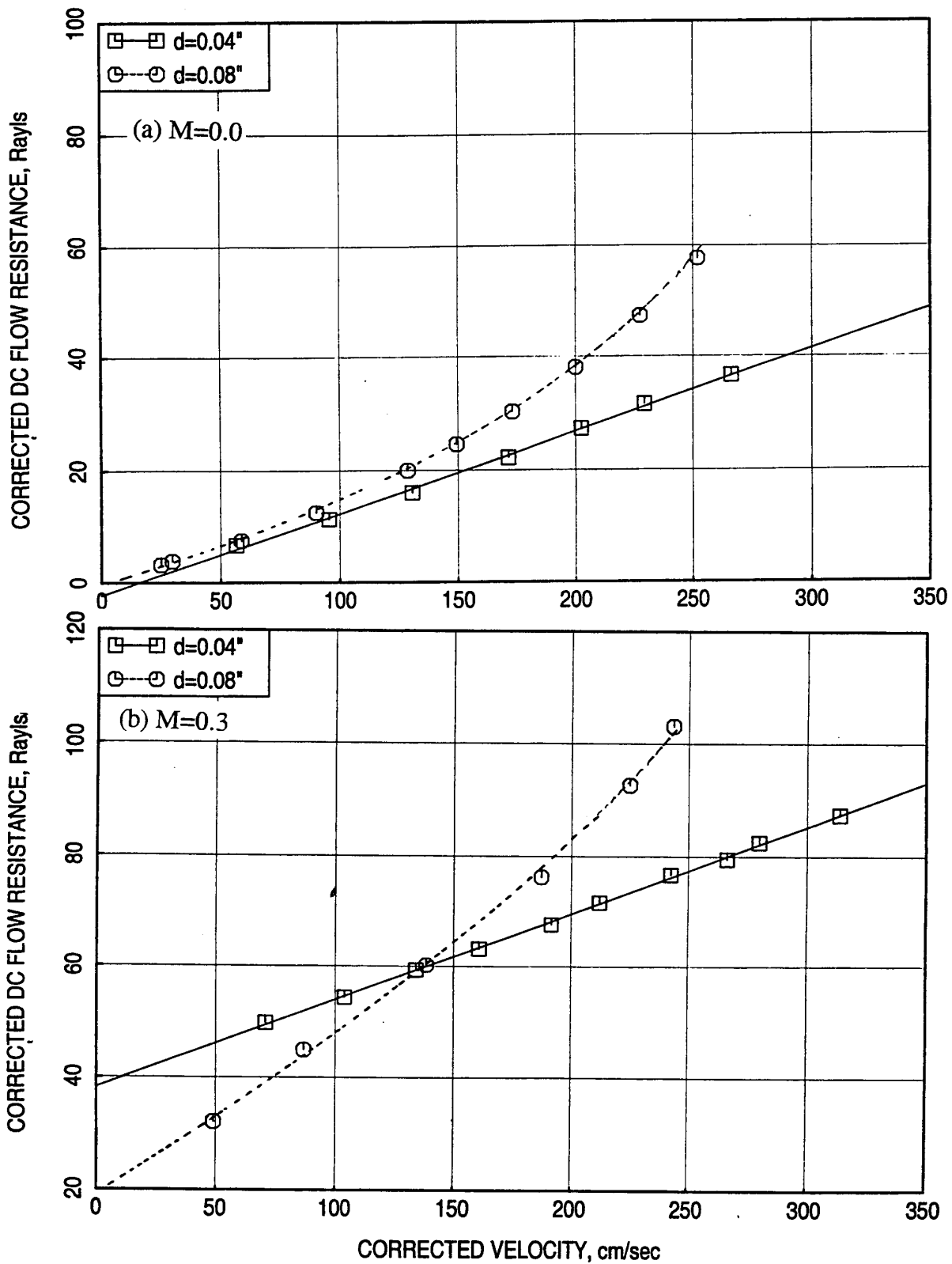


Figure 268. Effect of facesheet hole diameter ( $d$ ) on DC flow resistance for a 0.5"-deep SDOF type panel with 9% porous 0.025"-thick facesheet, (a)  $M=0$ , (b)  $M=0.3$ .

velocity. In the presence of grazing flow the DC flow resistance decreases with facesheet hole diameter. However, at higher approach velocity the trend gets reversed.

#### 6.4.6 Different Bulk Materials

**Insitu Impedance:** Effect of type of bulk material on normal impedance for 0.5"-deep samples with 40% porous 0.025"-thick facesheets ( $d=0.04''$ ) is shown in Figure 269 at different Mach numbers. The resistance and reactance for 12 lbf bulk absorber are higher compared to 100 ppi SiC. The antiresonance occurs at a lower frequency for bulk absorbers compared to the air-filled cavity, indicating a higher effective cavity depth. T-Foam seems to have a higher effective depth compared to SiC.

**DC Flow Resistance:** Effect of bulk property on DC flow resistance for 0.5"-deep samples of SiC, T-Foam, and Feltmetal is shown in Figures 270 and 271. Relevant DC flow resistance values for these materials are listed below. For each type of bulk the resistivity increases with increasing density or ppi for SiC. DC flow resistance is compared for medium and low resistive bulks of different type in Figure 272. While 200 ppi SiC is comparable to 12 lbf T-Foam, the 5% dense Feltmetal is much higher resistive. The 8lbf T-Foam is also comparable to 100 ppi SiC with respect to their DC flow resistance.

#### DC Flow Resistance using 0.5"-Deep Bulk Samples

Bulk ID	Description of the Bulk	A Rayls/cm	B Rayls.sec/cm <sup>2</sup>	R100 Rayls/cm	NLF
B-1	100 ppi SiC	4.214	0.02377	6.591	1.659
B-2	200 ppi SiC	16.41	0.0522	21.63	1.389
B-3	400 ppi SiC	40.02	0.18716	58.736	1.556
B-4	600 ppi SiC	117.93	0.417322	159.683	1.43
B-5	5% Feltmetal (L) (Actual 7.2%)	34.83	0.07464	42.294	1.267
B-6	10% Feltmetal (M) (Actual 10.6%)	68.57	0.1425197	82.802	1.259
B-7	15% Feltmetal (H) (Actual 15.5%)	157.11	0.362205	193.31	1.286
B-8	8 lbf T-Foam (L)	3.5803	0.023213	5.902	1.746
B-9	12 lbf T-Foam (M)	7.979	0.049493	12.9283	1.717
B-10	16 lbf T-Foam (H)	19.47	0.1441	33.876	1.838



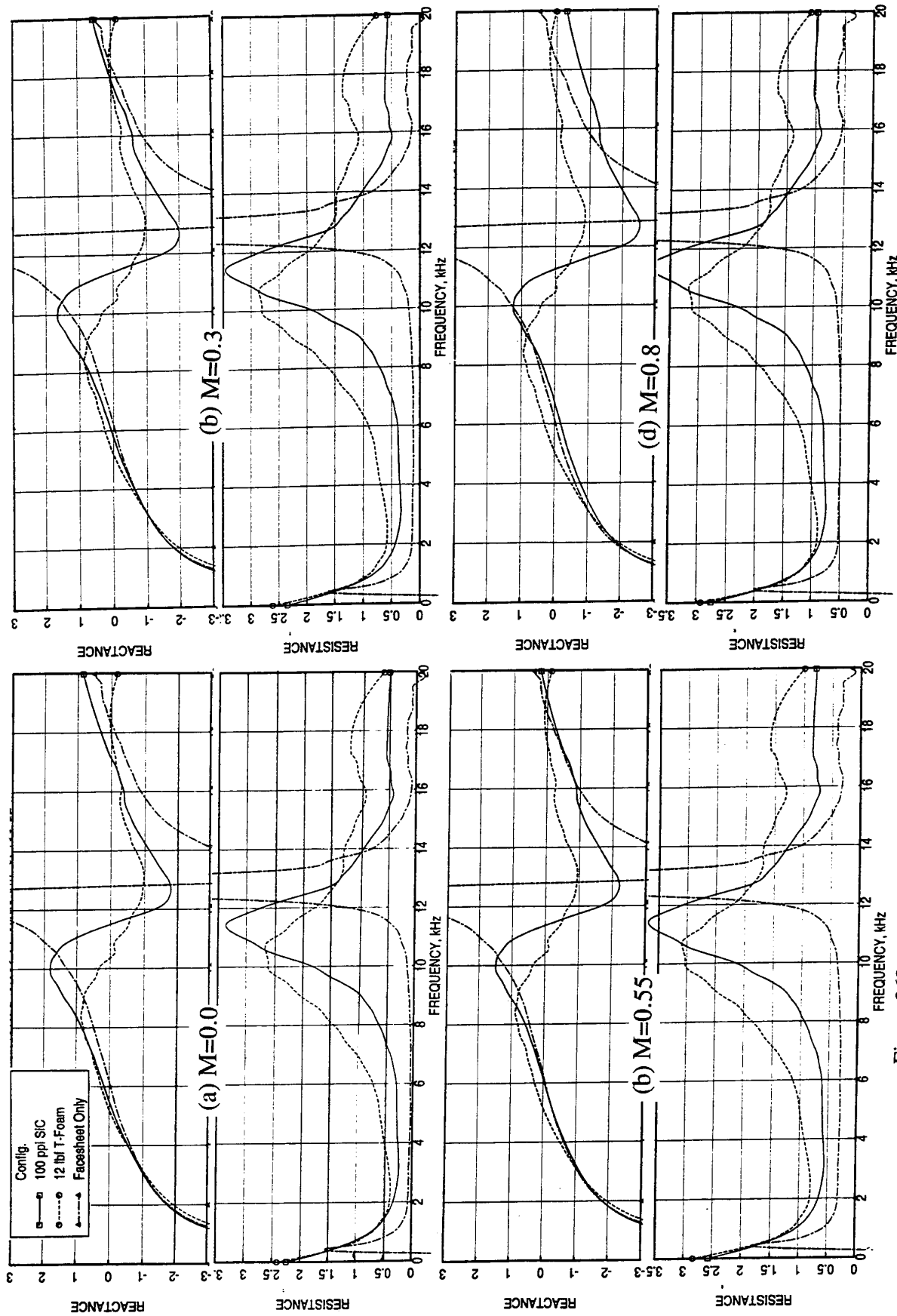


Figure 269. Effect of type of bulk on normal impedance for 0.5"-deep panels for 40% porous 0.025"-thick facesheet ( $d=0.04$ ") at different grazing flow Mach numbers.

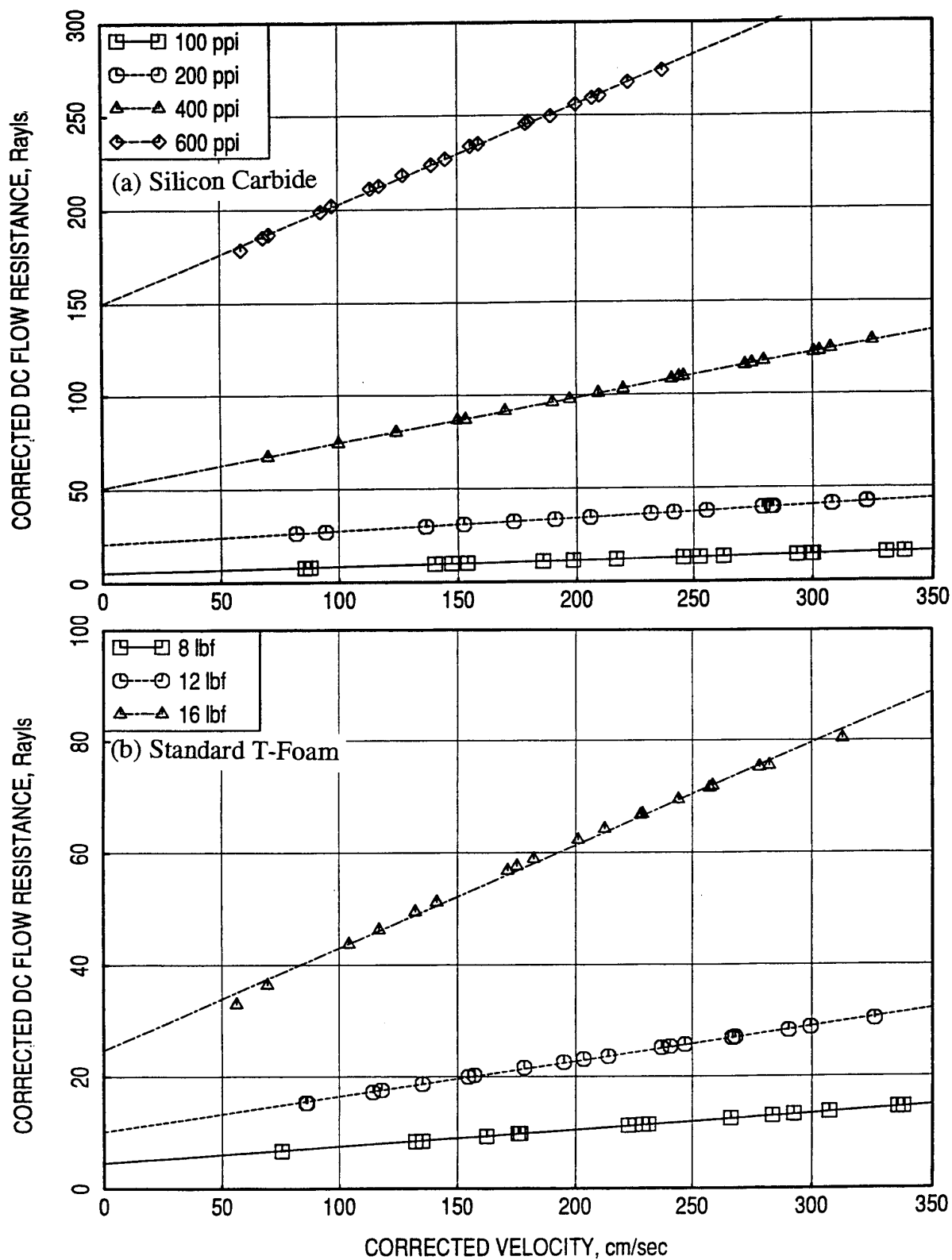


Figure 270. Effect of bulk property on DC flow resistance for 0.5''-deep bulk samples without any facesheet,  $M=0$ , (a) Silicon Carbide and (b) Standard T-Foam.

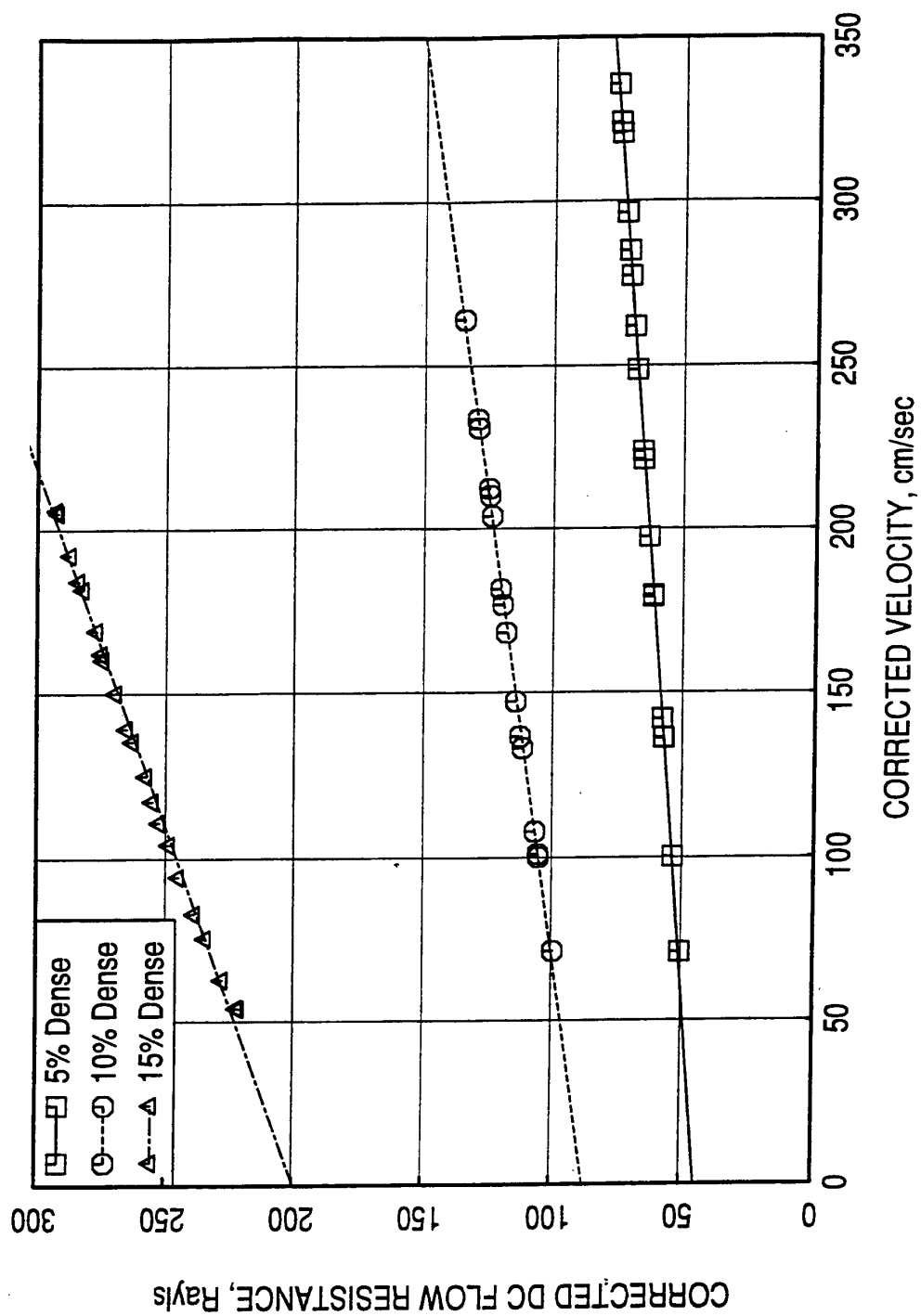


Figure 271. Effect of Feltmetal density on DC flow resistance for 0.5"-deep samples without any facesheet,  $M=0$ .

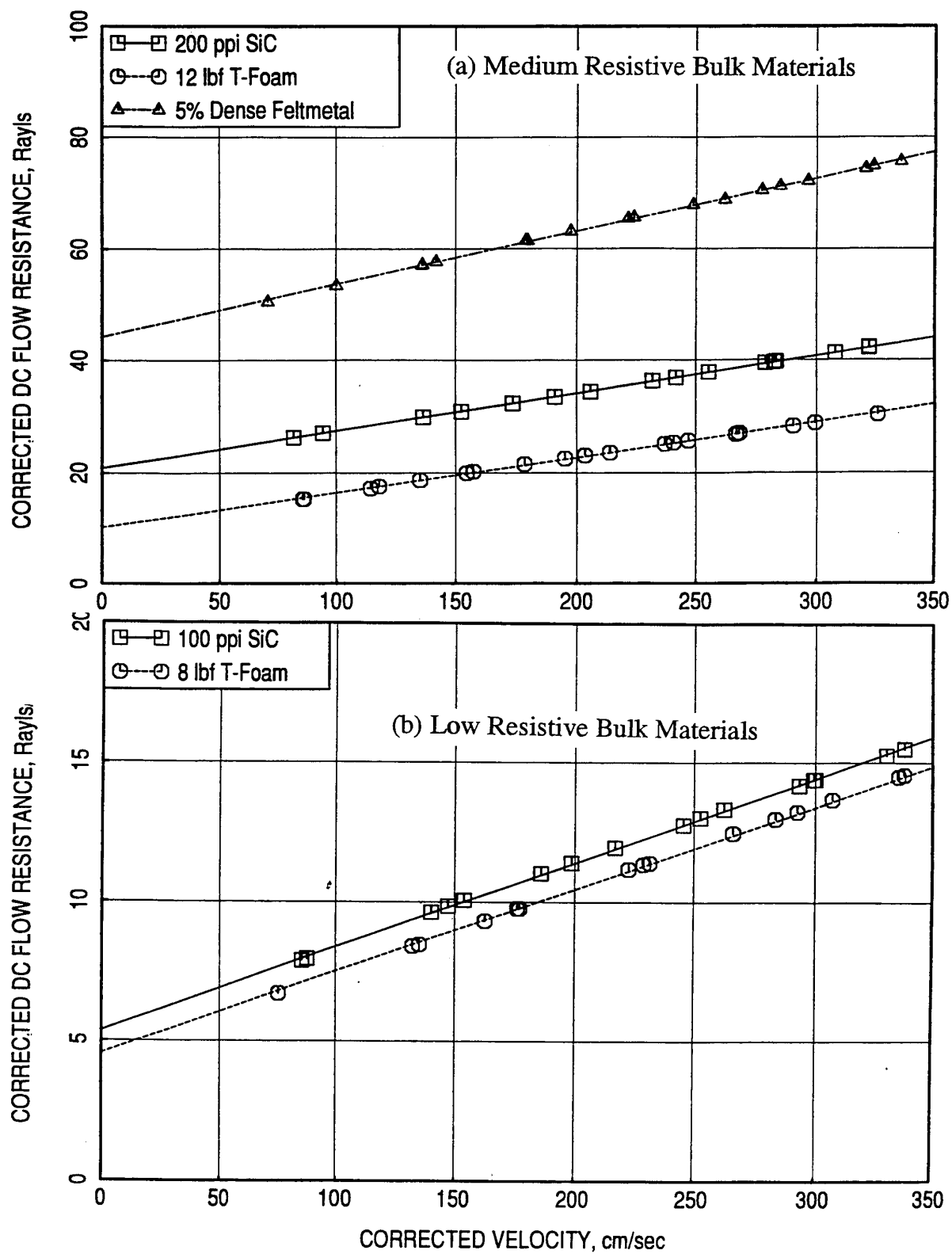


Figure 272. Comparison of DC flow resistance for 0.5"-deep bulk samples of different type without facesheet,  $M=0$ .



## **7.0 INSERTION LOSS MEASUREMENT AT BF GOODRICH'S (PREVIOUSLY ROHR) FLOW DUCT FACILITY**

All insertion loss measurement tests at BF Goodrich's flow duct facility are conducted at five flow conditions including four grazing flow Mach numbers, 0.0, 0.3, 0.55, 0.6, and 0.7, for frequencies up to 15 kHz at ambient temperature. A few panels are also tested at a grazing flow Mach number of 0.8. All the panels are of 14"x7" size with 12"x5" treatment area at the middle. The measurements are made in the flow duct with two reverberant chambers, one upstream and the other downstream of the duct. The acoustic excitation is generated in the upstream chamber (Ref 1). The panels tested include 0.5" and 2.0" deep bulk absorbers of different materials (i.e., Silicon Carbide, T-Foam, and Feltmetal) with facesheets of varying properties. Table 12 lists all the configurations tested under the current phase of HSCT program and the name of the data files containing the test results.

A concern was raised whether the signal to noise ratio in the presence of grazing flow is high enough to give realistic results. To verify this a panel is tested with and without broadband excitation. The measured insertion loss spectra with and without excitation are compared at different grazing flow Mach numbers (see Figure 273). Clearly, the insertion loss with excitation is sufficiently higher compared to those without excitation. This is an indication of the accuracy of measurement technique. While, the insertion loss data is available both in 1/3-octave band and in narrowband forms, the subsequent presentations are made only for narrowband data.

### **7.1 Half Inch Deep Panels:**

**Influence of Grazing Flow Mach Number:** Figure 274 shows the effect of grazing flow Mach number on insertion loss levels for 0.5" bulk absorbers with 100 and 200 ppi SiC materials. In general, the insertion loss decreases with increasing grazing flow Mach number. While the spectral shape for 100 ppi SiC is broader compared to 200 ppi SiC panel the insertion loss peaks are higher for 200 ppi SiC panel. Similar results for T-Foam with two different densities are shown in Figure 275. The bulk density at lower grazing flow Mach numbers effects the peak insertion loss frequency. Influence of grazing flow Mach number on Feltmetal absorbers is shown in Figure 276. Insertion loss peaks are higher for Feltmetal absorbers compared to T-Foam and SiC absorbers.

Table 12. Bulk absorber type liner configurations for insertion loss measurements at BF Goodrich (previously Rohr Inc).

Config.#	Bulk Absorber			Facesheet				Data File Name	
	Bulk ID	Bulk Type	Depth H, in	ID	Porosity $\sigma$ , %	Thickness t, in	Hole Diameter d, in	Narrowband Ends with .smt	1/3-Octave Ends with .tat
1	B-1	100 ppi SiC	0.5	T1-1	20	0.025	0.04	CFG001N	CFG001T
2	B-1	100 ppi SiC	0.5	T1-2	30	0.025	0.04	CFG002N	CFG002T
3	B-1	100 ppi SiC	0.5	T1-3	40	0.025	0.04	CFG003N	CFG003T
4	B-1	100 ppi SiC	0.5	T1-8	40	0.04	0.04	CFG004N	CFG004T
5	B-1	100 ppi SiC	0.5	412-1	40	0.10	0.04	CFG005N	CFG005T
6	B-1	100 ppi SiC	0.5	414-1	40	0.025	0.07	CFG006N	CFG006T
7	B-1	100 ppi SiC	0.5	414-2	40	0.04	0.07	CFG007N	CFG007T
8	B-1	100 ppi SiC	0.5	414-3	40	0.10	0.07	CFG008N	CFG008T
10	B-1	100 ppi SiC	0.5	403	30	0.10	0.07	CFG010N	CFG010T
12	B-1	100 ppi SiC	0.5	401	20	0.10	0.07	CFG012N	CFG012T
13	B-1	100 ppi SiC	0.5	416-1	40	0.025	0.10	CFG013N	CFG013T
14	B-1	100 ppi SiC	0.5	416-2	40	0.10	0.10	CFG014N	CFG014T
17	B-6	T-Foam 10/2	0.5	T1-3	40	0.025	0.04	CFG017N	CFG017T
25	B-21	T-Foam 10/2	2.0	401-1	20	0.10	0.07	CFG025N	CFG025T
27	B-21	T-Foam 10/2	2.0	403-1	30	0.10	0.07	CFG027N	CFG027T
29	B-21	T-Foam 10/2	2.0	414-3	40	0.10	0.07	CFG029N	CFG029T
31	B-20	T-Foam 7	2.0	T1-8	40	0.04	0.04	CFG031N	CFG031T
32	B-20	T-Foam 7	2.0	412-1	40	0.10	0.04	CFG032N	CFG032T
34	B-20	T-Foam 7	2.0	414-2	40	0.04	0.07	CFG034N	CFG034T
35	B-20	T-Foam 7	2.0	414-3	40	0.10	0.07	CFG035N	CFG035T
37	B-20	T-Foam 7	2.0	416-2	40	0.10	0.10	CFG037N	CFG037T
39	B-20	T-Foam 7	2.0	417-2	40	0.10	0.125	CFG039N	CFG039T
40	B-23	T-Foam 10/2	1.2	414-3	40	0.10	0.07	CFG040N	CFG040T
41	B-22	T-Foam 9	2.0	414-3	40	0.10	0.07	CFG041N	CFG041T
42	B-19	T-Foam 7/3	2.0	414-3	40	0.10	0.07	CFG042N	CFG042T
49	B-2	200 ppi SiC	0.5	T1-3	40	0.025	0.04	CFG049N	CFG049T
51	B-5	T-Foam 7	0.5	T1-3	40	0.025	0.04	CFG051N	CFG051T
53	B-8	Feltmetal 5%	0.5	T1-3	40	0.025	0.04	CFG053N	CFG053T
54	B-9	Feltmetal 10%	0.5	T1-3	40	0.025	0.04	CFG054N	CFG054T
55	B-1	100 ppi SiC	0.5	Slotted T1-15	30	0.025	0.04	CFG055N	CFG055T
56	B-1	100 ppi SiC	0.5	T1-10	Linear Facesheet, R100=5 Rayls			CFG056N	CFG056T
R1	B-24	8lbf T-Foam 3 Paper Const	2.0	414-3	40	0.10	0.07	R001N	R001T
R2	B-24	8lbf T-Foam 3 Paper Const	2.0	T1-8	40	0.04	0.04	R002N	R002T
R3	B-24	8lbf T-Foam 3 Paper Const	2.0	414-2	40	0.04	0.07	R003N	R003T
R4	B-25	100 ppi SiC	2.0	414-3	40	0.10	0.07	R004N	R004T
R5	B-25	100 ppi SiC	2.0	T1-8	40	0.04	0.04	R005N	R005T

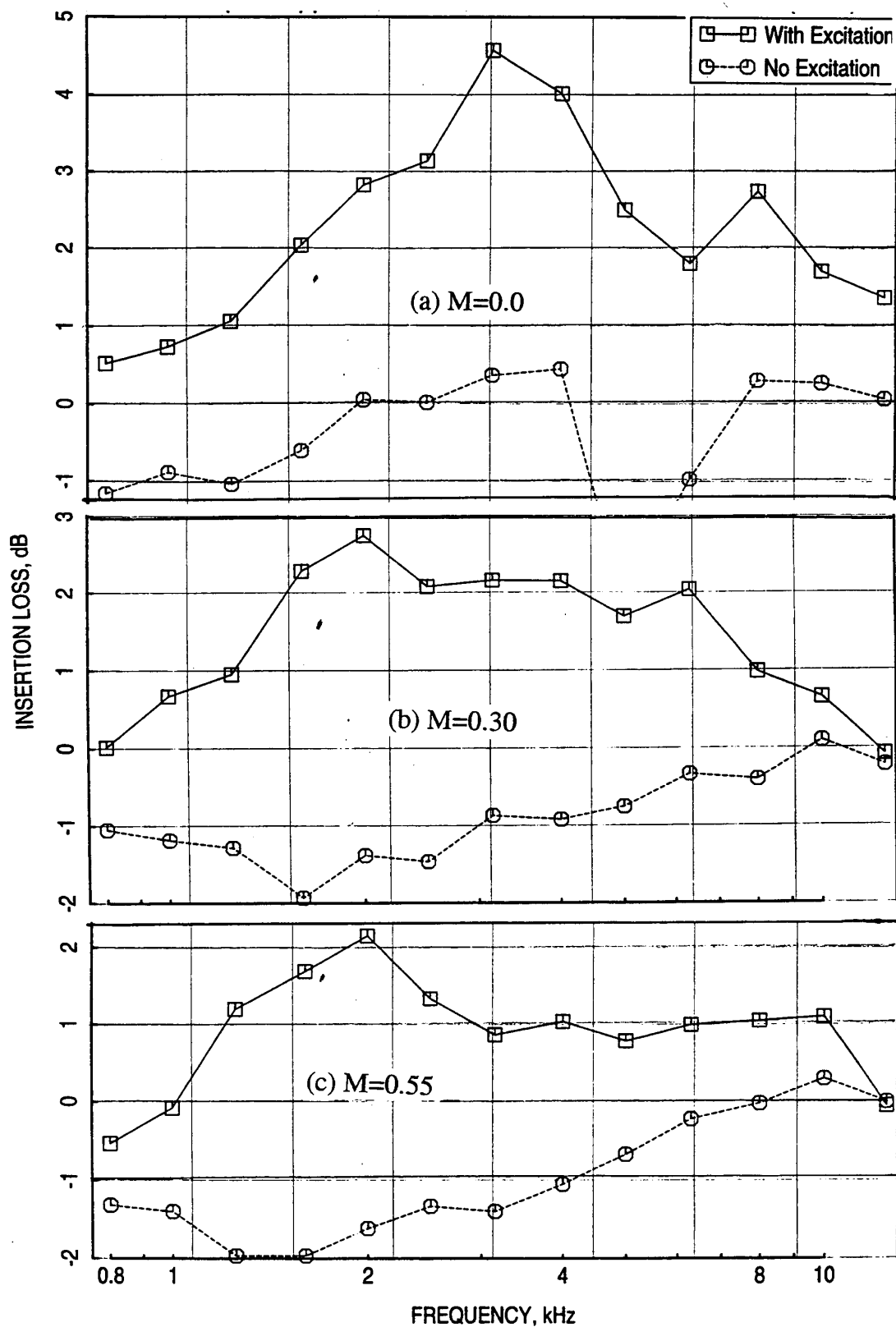


Figure 273. Influence of broadband excitation on insertion loss spectrum for a 0.5"-deep 100 ppi Silicon Carbide panel with 30% porous 0.025"-thick facesheet ( $d=0.04''$ ), measured in a 4"-high (H) flow duct, mounted on one side, at different  $M$ .



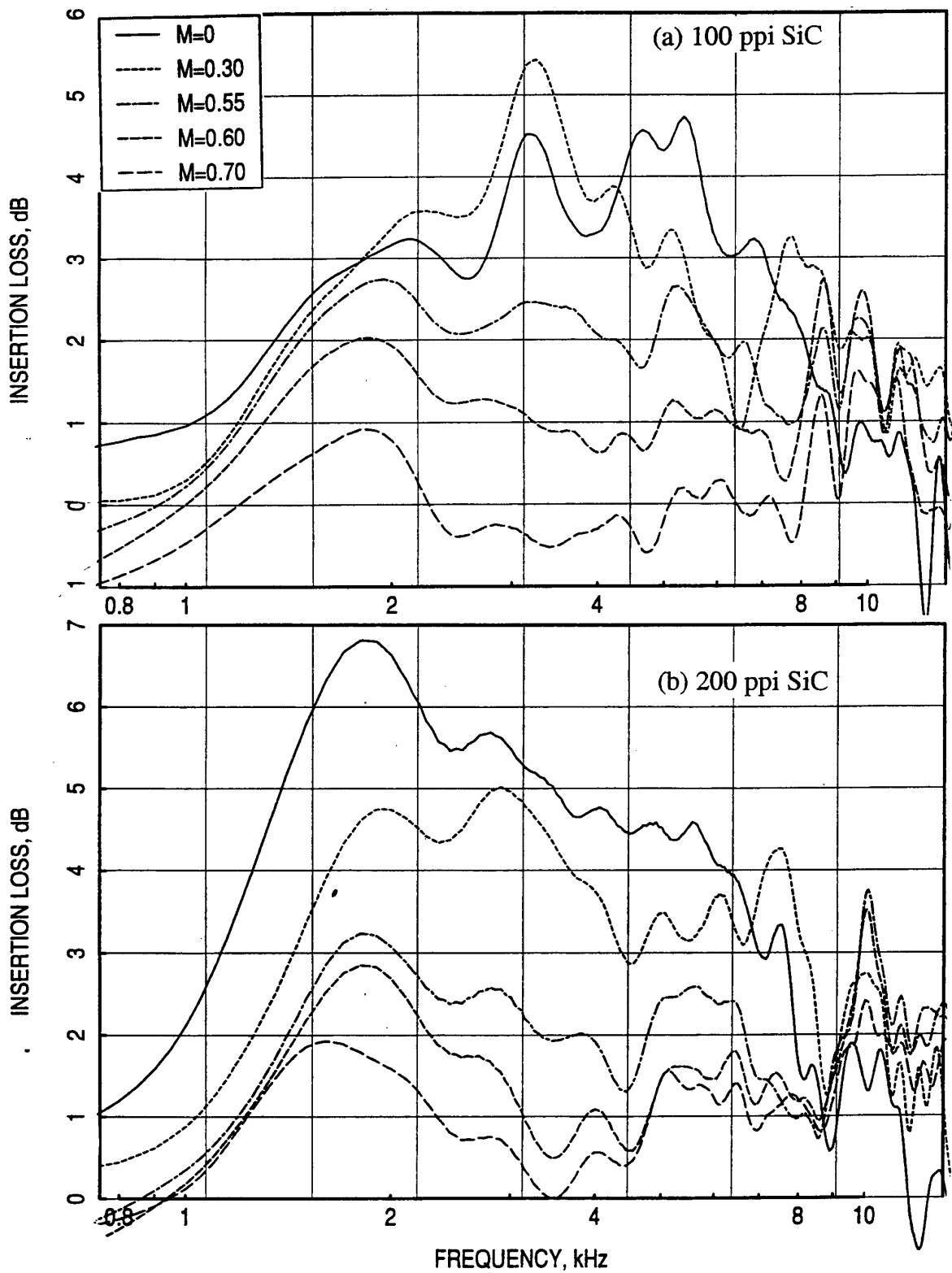


Figure 274. Influence of grazing flow Mach number ( $M$ ) on insertion loss spectrum for 0.5''-deep (a) 100 ppi and (b) 200 ppi Silicon Carbide panels with 40% porous 0.025''-thick facesheet ( $d=0.04''$ ), measured in a 4''-high ( $H$ ) flow duct, mounted on one side.

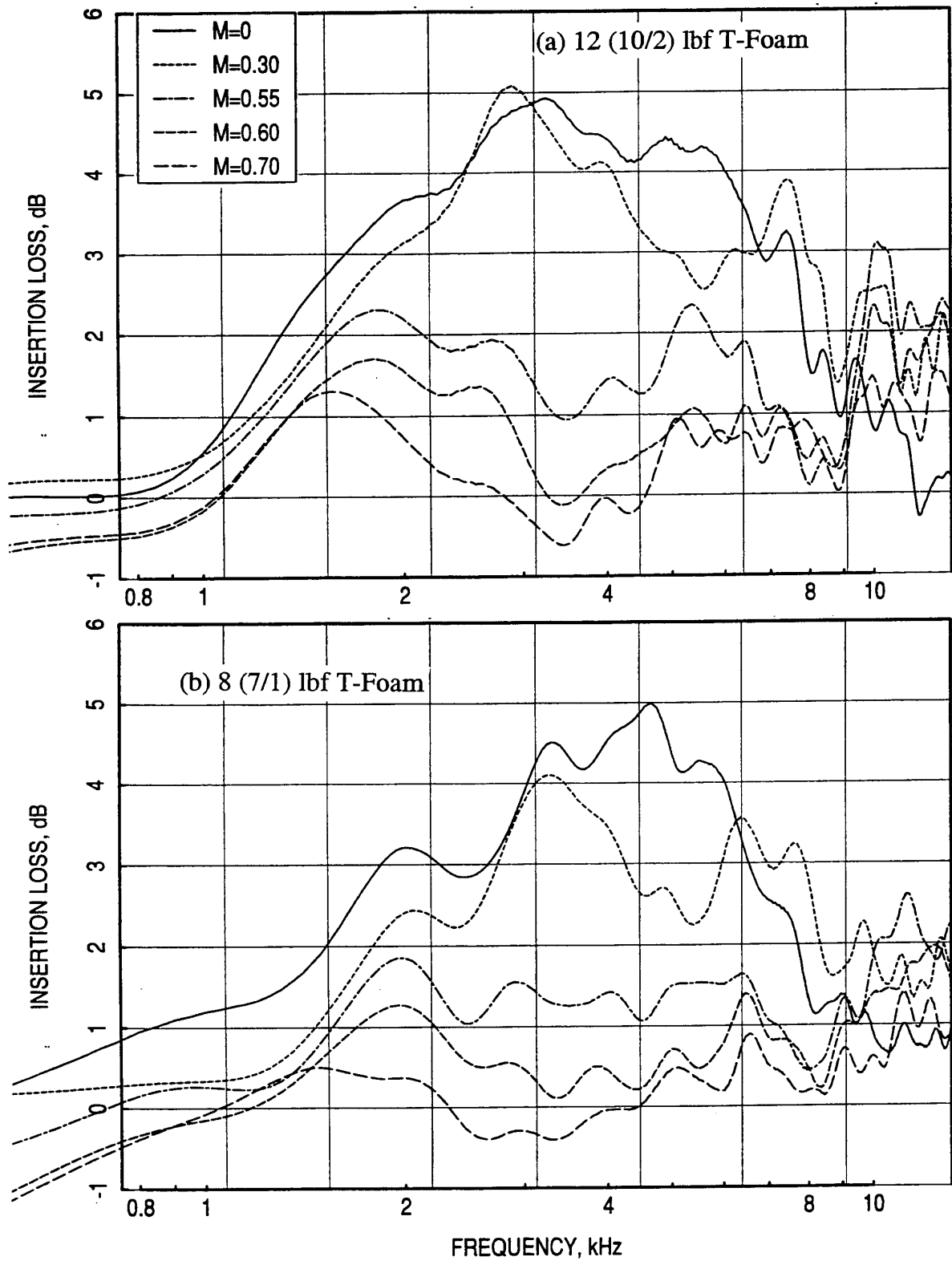


Figure 275. Influence of grazing flow Mach number ( $M$ ) on insertion loss spectrum for 0.5"-deep (a) 12 (10/2) lbf and (b) 8 (7/1) lbf T-Foam panels with 40% porous 0.025"-thick facesheet ( $d=0.04''$ ), measured in a 4"-high ( $H$ ) flow duct, mounted on one side.

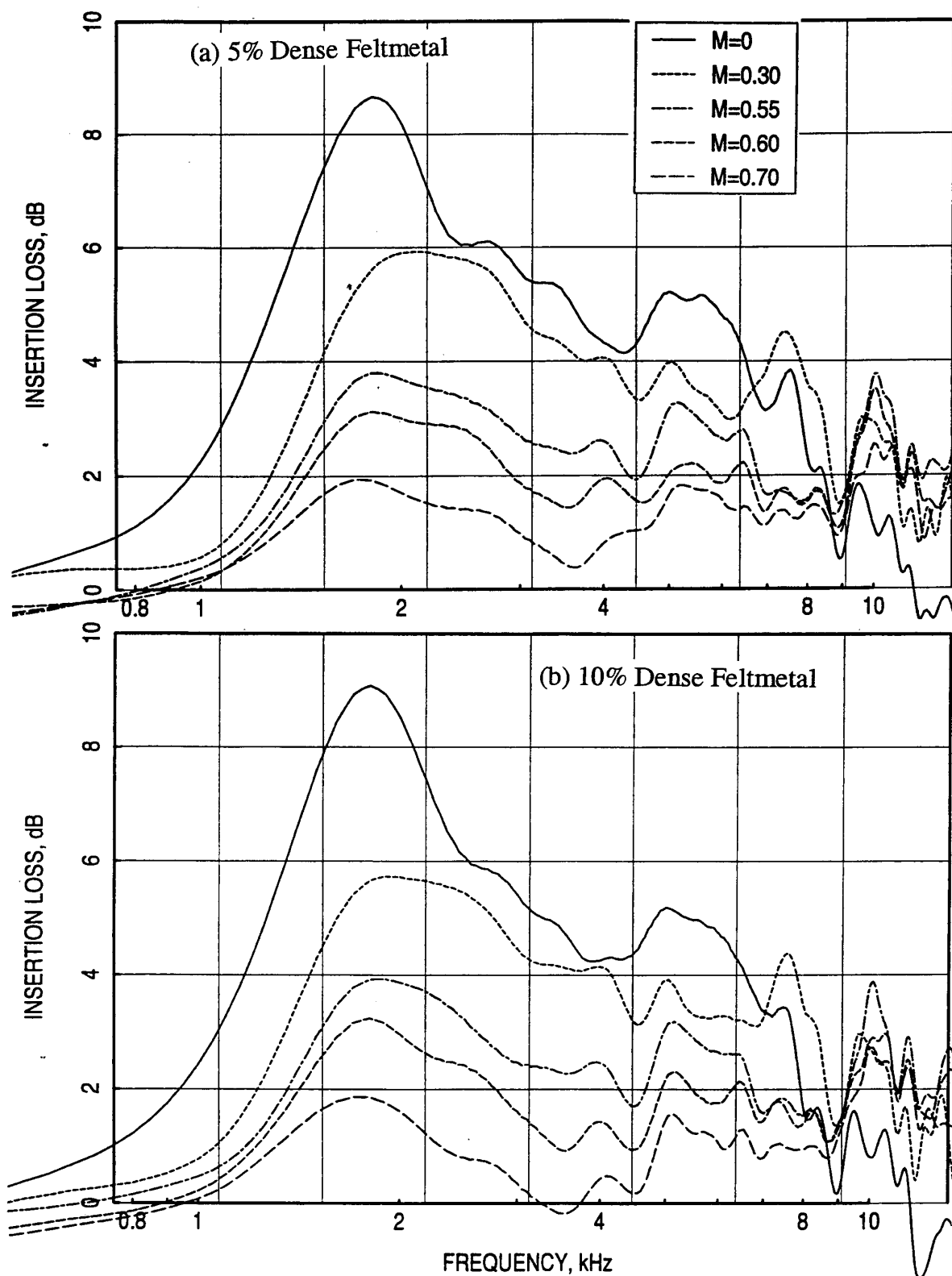


Figure 276. Influence of grazing flow Mach number ( $M$ ) on insertion loss spectrum for 0.5"-deep (a) 5% dense and (b) 10% dense Feltmetal panels with 40% porous 0.025"-thick facesheet ( $d=0.04$ "), measured in a 4"-high ( $H$ ) flow duct, mounted on one side.

**Effect of Facesheet Porosity:** Figure 277 shows the effect of facesheet porosity for 100 ppi SiC panels with 0.025"-thick facesheets and hole diameter of 0.04". At higher grazing flow Mach numbers the 20% porous facesheet suppresses more acoustic energy compared to the other facesheets of higher porosity. However, the situation would be different for heated conditions, since the bulk resistivity would increase and thereby the resistance and reactance for the bulk would be higher. At this situation the facesheet with lower porosity will elevate the impedance levels beyond the optimum values at most frequencies and thereby the acoustic suppression will be lower. Similar results for thicker facesheets with bigger hole diameter are shown in Figure 278. The observed advantage of 20% porous facesheet in Figure 277 has been diminished in the present case due to the increased facesheet thickness, which contributes a much higher reactance for the absorber.

**Effect of Facesheet Thickness:** Effect of facesheet thickness on insertion loss for 100 ppi SiC absorbers with 40% porous facesheets is shown in Figure 279. At no flow condition and at higher grazing flow Mach numbers the 0.04"-thick facesheet results in higher insertion loss. Similar results for facesheets of higher hole diameter ( $d=0.07''$ ) are shown in Figure 280. In this case the facesheet of higher thickness suppresses more acoustic energy. Again, the suppression characteristics are likely to be different at higher temperature conditions.

**Effect of Facesheet Hole Diameter:** Effect of facesheet hole diameter on insertion loss for 100 ppi SiC absorbers is shown in Figure 281. At higher frequencies the 0.10"-thick facesheet suppresses more acoustic energy compared to the other configurations.

**Effect of Bulk Type:** Insertion loss spectra due to bulk absorbers of different materials are compared in Figure 282. Bulk absorbers with 100 ppi Silicon Carbide and 5% dense Feltmetal suppress most acoustic energy compared to the other bulk absorbers.

**Effect of Facesheet Hole Pattern:** Tests are conducted with facesheets of two different hole patterns for 100 ppi SiC absorbers. One facesheet being the conventional perforate with circular holes of 0.04" diameter and the other one is a slotted pattern (see Figure 25) with 3/64"x3/16" oblong holes with side staggered and 1/8" centers. Both facesheets are of the same porosity (30%) and thickness (0.025"). The bulk absorber with slotted facesheet resulted in higher insertion loss (see Figure 283) compared to the bulk absorber with conventional facesheet.

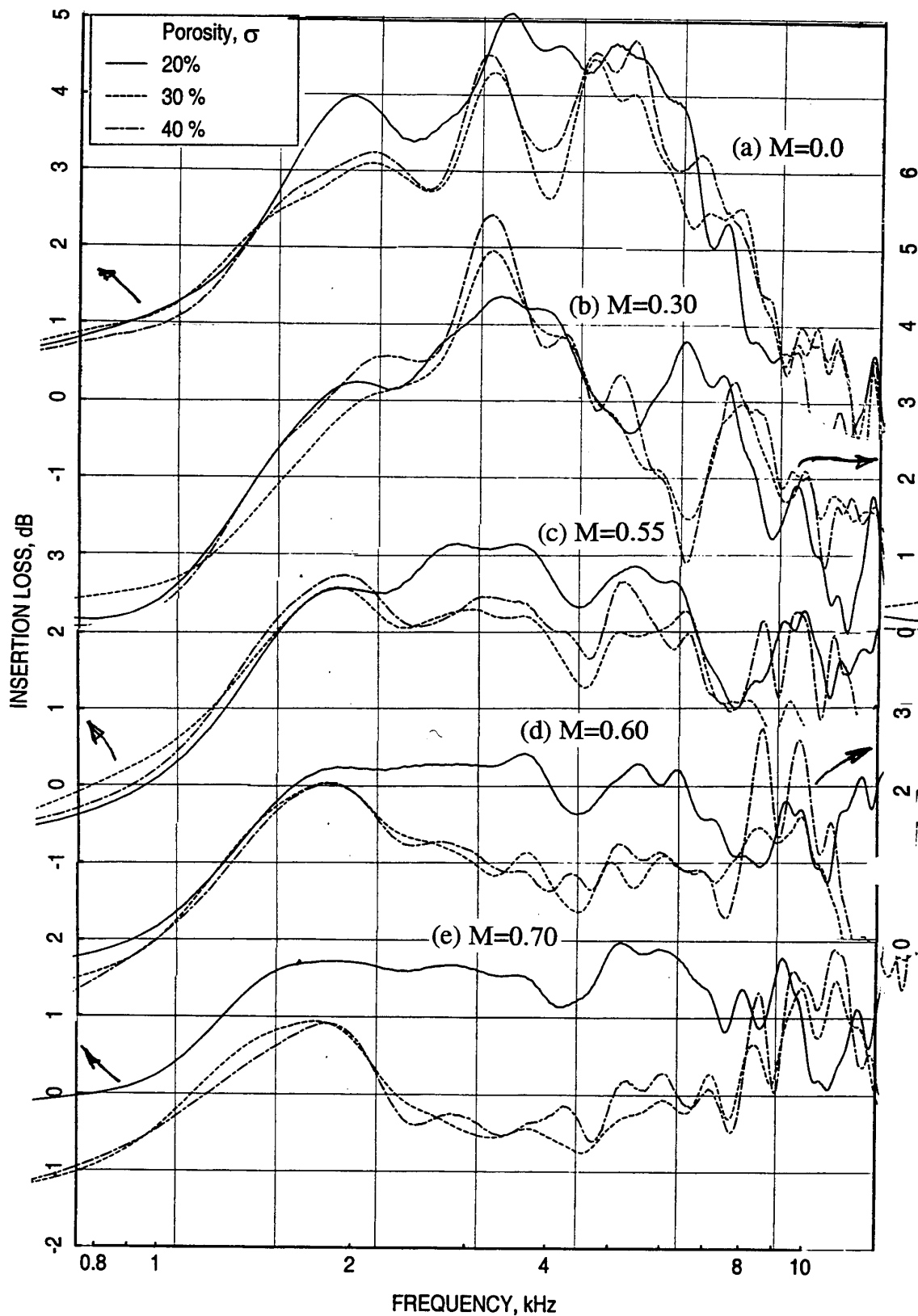


Figure 277. Effect of facesheet porosity ( $\sigma$ ) on insertion loss spectrum for 0.5"-deep 100 ppi SiC panels with 0.025"-thick facesheets ( $d=0.04''$ ), measured in a 4"-high (H) flow duct, mounted on one side for different grazing flow Mach numbers (M).

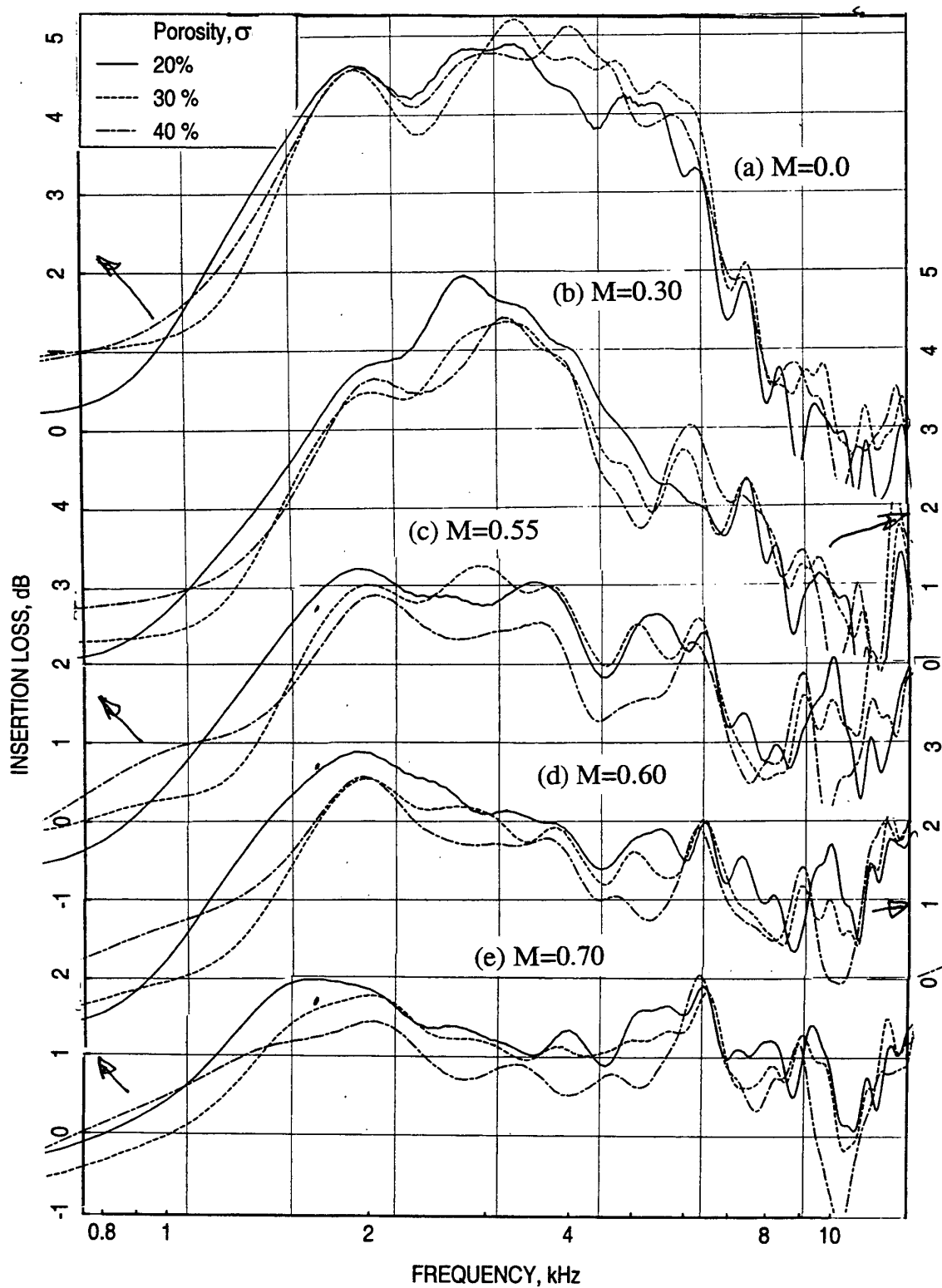


Figure 278. Effect of facesheet porosity ( $\sigma$ ) on insertion loss spectrum for 0.5"-deep 100 ppi SiC panels with 0.10"-thick facesheets ( $d=0.07''$ ), measured in a 4"-high ( $H$ ) flow duct, mounted on one side for different grazing flow Mach numbers ( $M$ ).

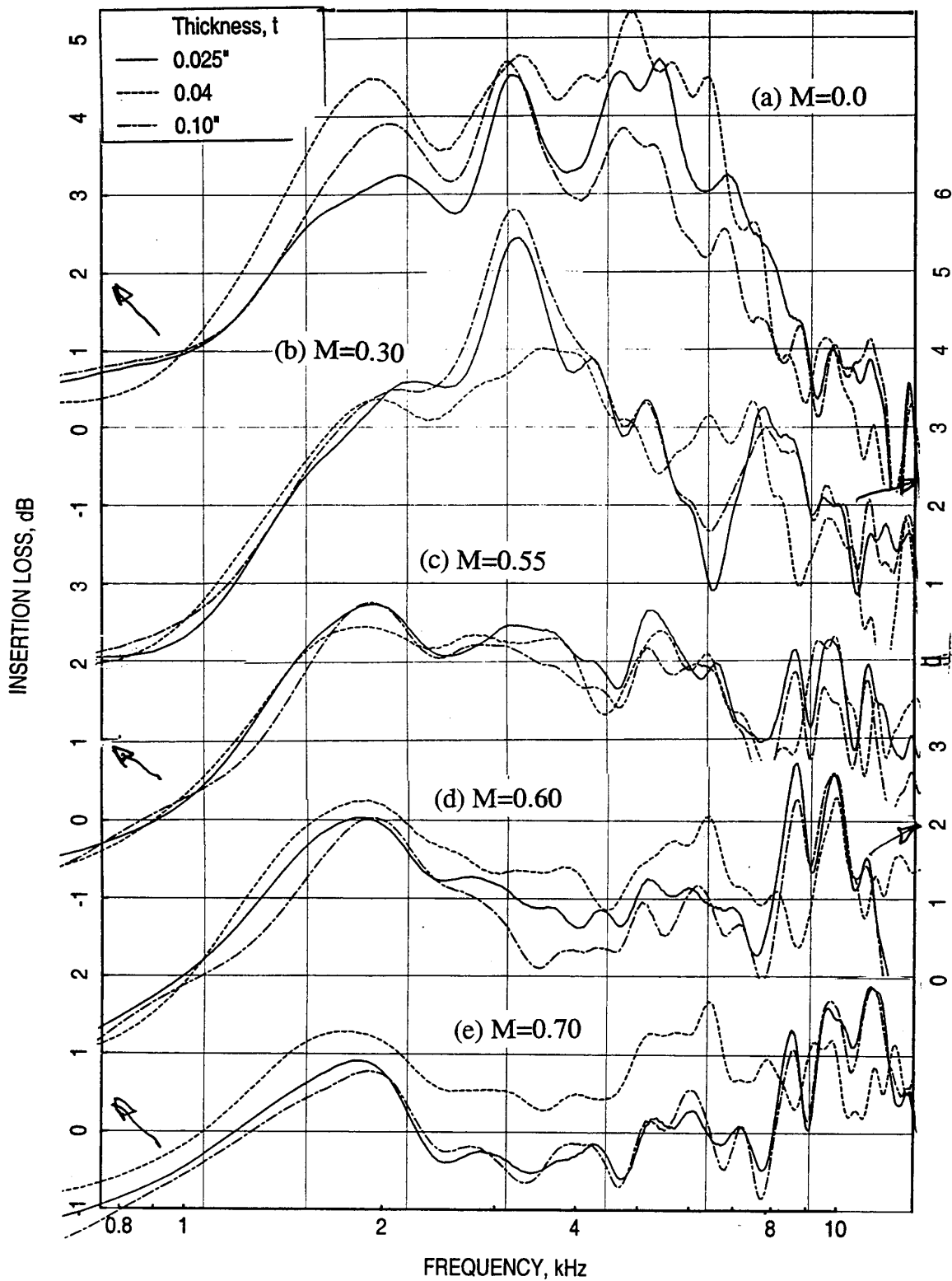


Figure 279. Effect of facesheet thickness ( $t$ ) on insertion loss spectrum for 0.5''-deep 100 ppi SiC panels with 40% porous facesheets ( $d=0.04''$ ), measured in a 4''-high ( $H$ ) flow duct, mounted on one side for different grazing flow Mach numbers ( $M$ ).

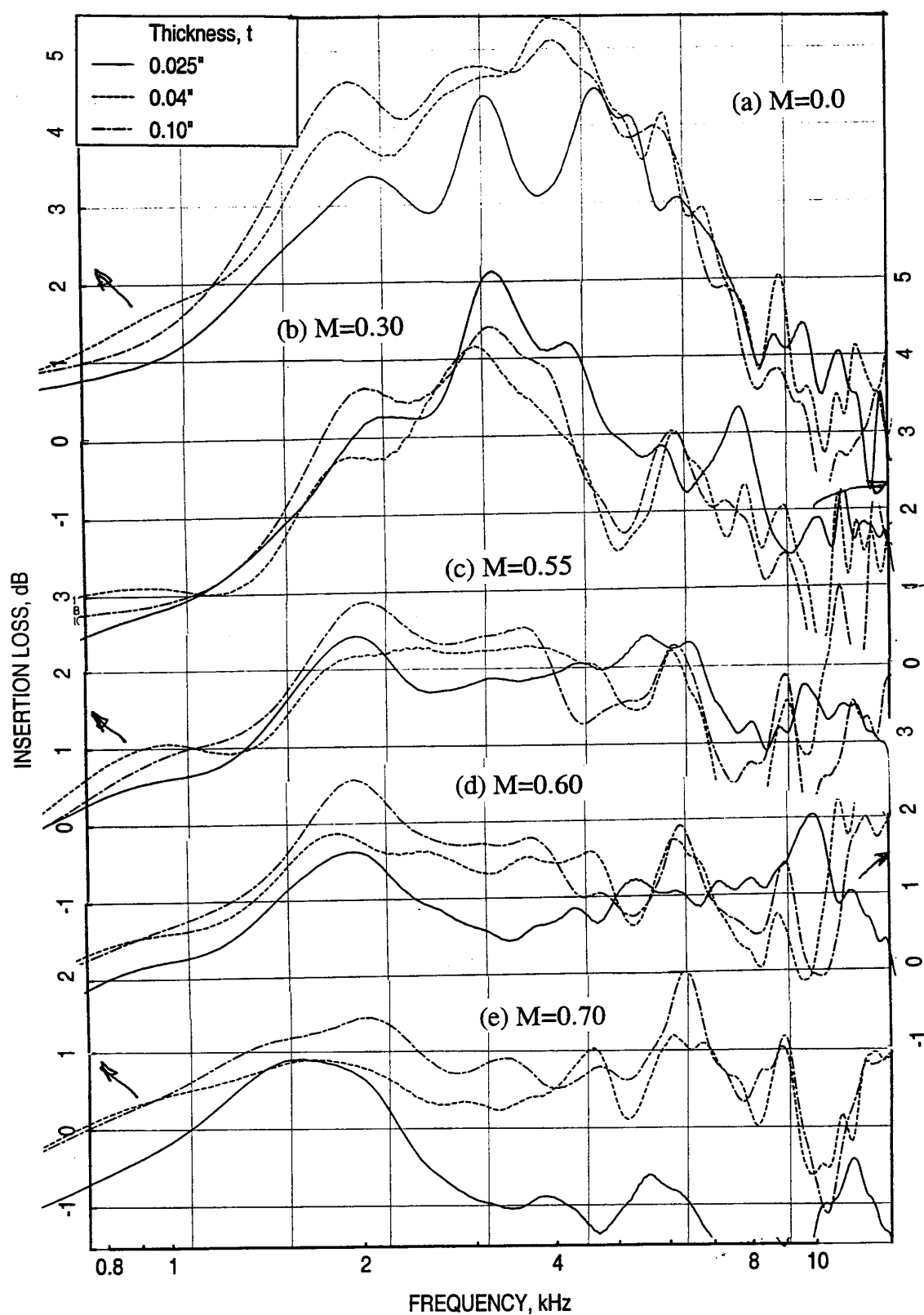


Figure 280. Effect of facesheet thickness ( $t$ ) on insertion loss spectrum for 0.5''-deep 100 ppi SiC panels with 40% porous facesheets ( $d=0.07''$ ), measured in a 4''-high (H) flow duct, mounted on one side for different grazing flow Mach numbers ( $M$ ).



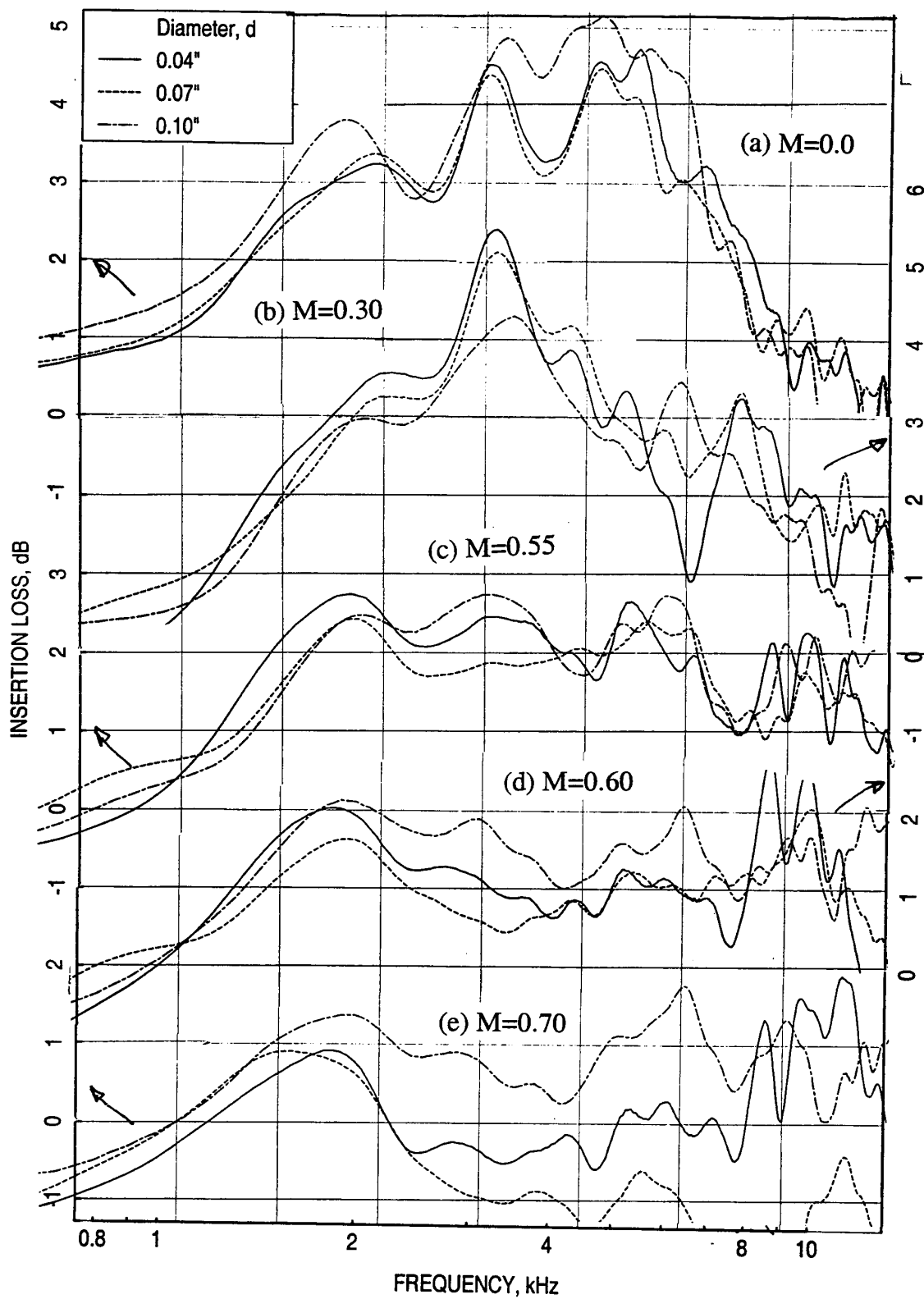


Figure 281. Effect of facesheet hole diameter ( $d$ ) on insertion loss spectrum for 0.5"-deep 100 ppi SiC panels with 40% porous facesheets ( $t=0.025"$ ), measured in a 4"-high ( $H$ ) flow duct, mounted on one side for different grazing flow Mach numbers ( $M$ ).

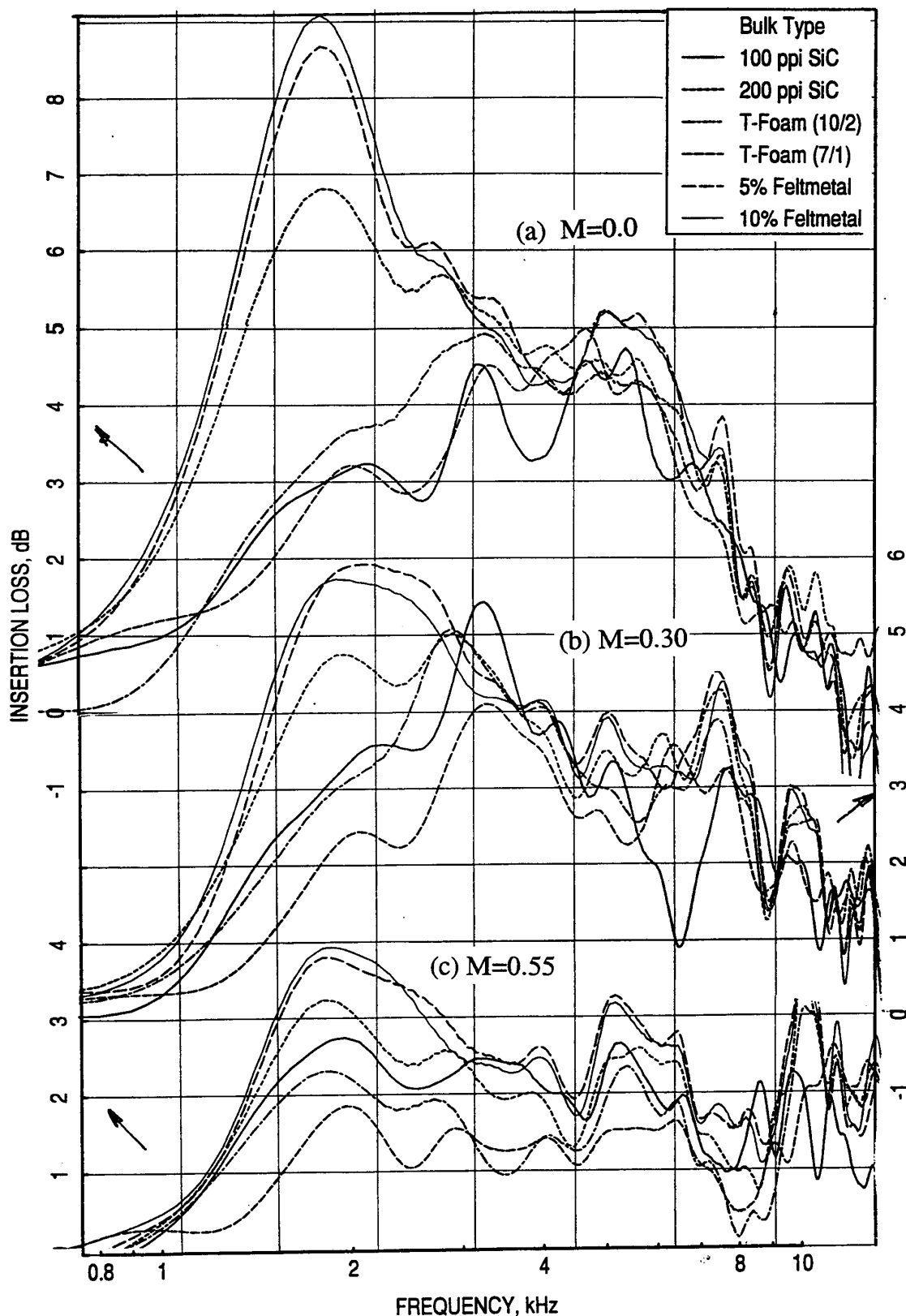


Figure 282. Effect of bulk type on insertion loss spectrum for 0.5"-deep panels with 40% porous 0.025"-thick facesheet ( $d=0.04"$ ), measured in a 4"-high (H) flow duct, mounted on one side for different grazing flow Mach numbers ( $M$ ).

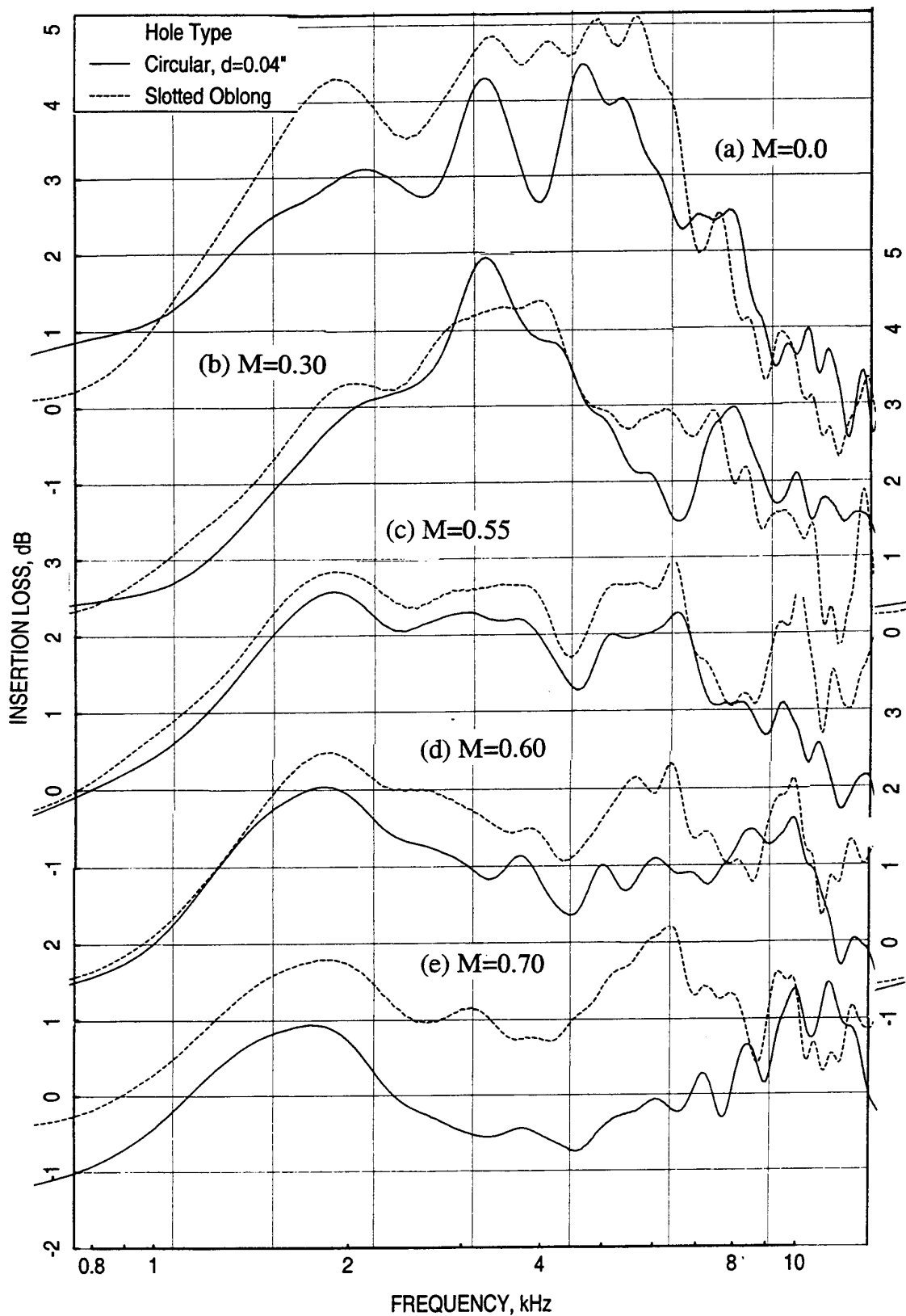


Figure 283. Effect of facesheet hole pattern on insertion loss spectrum for 0.5''-deep 100 ppi SiC panels with 30% porous 0.025''-thick facesheets, measured in a 4''-high (H) flow duct, mounted on one side for different grazing flow Mach numbers (M).

## 7.2 Two Inch Deep Panels:

A limited number of 2"-deep bulk absorber panels are tested to develop scaling correlation for full-scale liners. T-Foams of varying density and construction process is mostly used in these tests. A single panel of 100 ppi SiC is tested for comparison purpose.

**Influence of Grazing Flow Mach Number:** Figure 284 shows the effect of grazing flow Mach number on insertion loss spectrum for 2.0"-deep bulk absorbers with 12 (10/2) lbf and 10 (9/1) lbf T-Foam materials. In general, the insertion loss decreases with increasing grazing flow Mach number. While the spectral shape for 12 lbf T-Foam is broader compared to 10 lbf T-Foam panel the insertion loss peaks are higher for 10 lbf T-Foam panel. Similar results for 10 (7/3) lbf and 8 (7/1) lbf T-Foams are shown in Figure 285. The fiber density of T-Foam is the same for both the panels. The difference in the insertion loss is due to the matrix density. At no flow condition and at  $M=0.3$  the matrix with higher density gives higher insertion loss. However, the effect is insignificant at higher grazing flow Mach numbers. Similar results for 100 ppi SiC and the especially constructed 8 lbf T-Foam with woven 3 paper layers (see Figure 129 for detail) are shown in Figure 286. At lower grazing flow Mach numbers the performance of 100-ppi SiC absorber is better compared to the T-Foam absorber. However, both the absorbers perform similar at mid grazing flow Mach numbers.

**Effect of Facesheet Porosity:** Figure 287 shows the effect of facesheet porosity for 12 (10/2) lbf T-Foam panels with 0.10"-thick facesheets and hole diameter of 0.07". At higher frequencies the 40% porous facesheet suppresses more acoustic energy compared to the other facesheets of lower porosity.

**Effect of Facesheet Thickness:** Effect of facesheet thickness on insertion loss for 8 (7/1) lbf T-Foam absorbers with 40% porous facesheets of 0.04" hole diameter is shown in Figure 288. Impact of facesheet thickness seems to be small for all flow conditions. Similar results for the same bulk with 40% porous facesheets of 0.07" hole diameter are shown in Figure 289. At higher grazing flow Mach numbers the 0.10"-thick facesheet yields more insertion loss compared to 0.04"-thick facesheet.

**Effect of Facesheet Hole Diameter:** Effect of facesheet hole diameter on insertion loss for 8 (7/1) lbf T-Foam absorbers with 40% porous 0.10"-thick facesheets is shown in Figure 290. At higher grazing flow Mach numbers the facesheet with bigger holes yields more insertion loss. At no flow condition and at lower grazing flow Mach numbers the effect of facesheet hole diameter on insertion loss is insignificant.

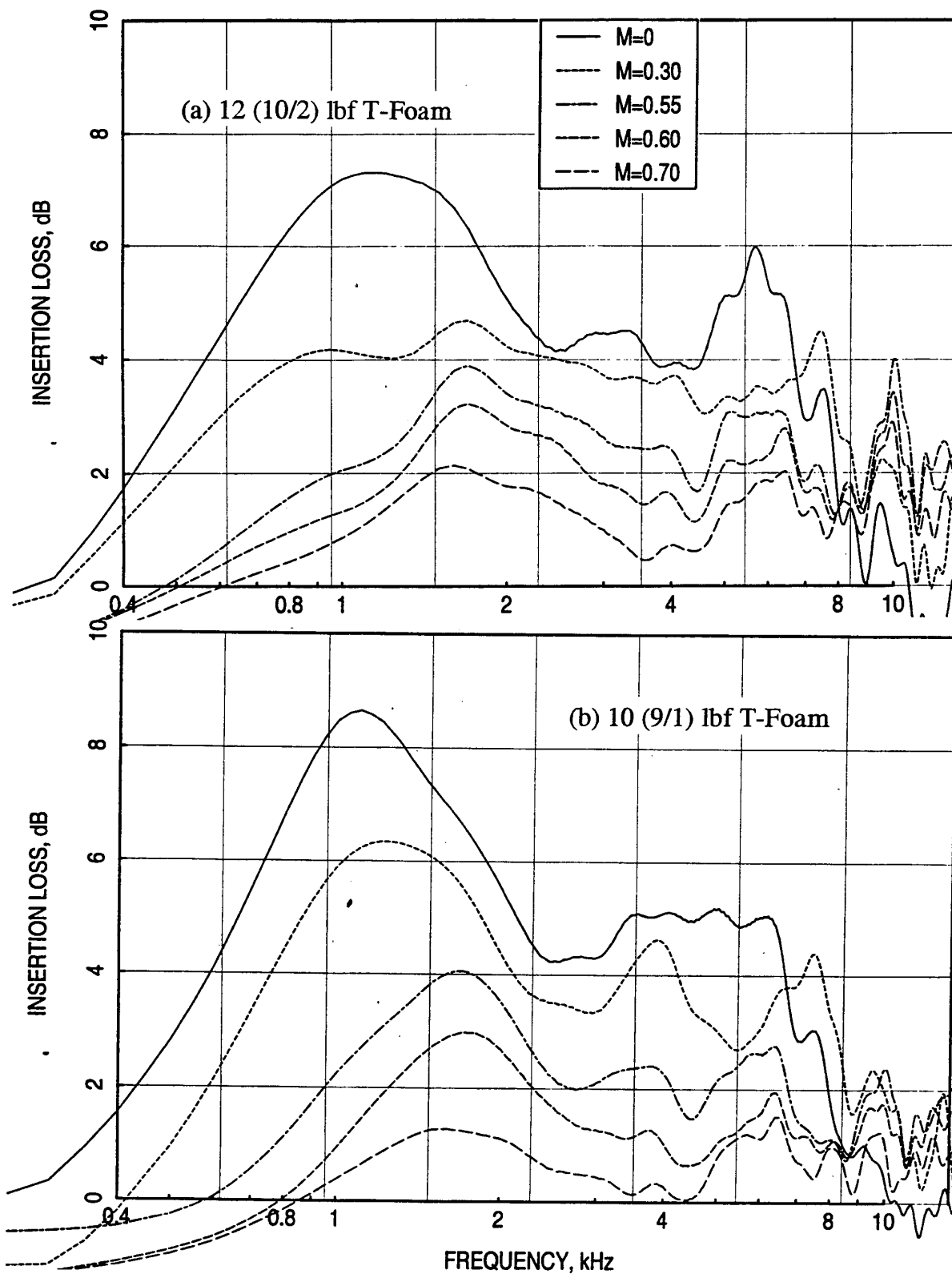


Figure 284. Influence of grazing flow Mach number ( $M$ ) on insertion loss spectrum for 2"-deep (a) 12 (10/2) lbf and (b) 10 (9/1) lbf T-Foam panels with 40% porous 0.10"-thick facesheet ( $d=0.07''$ ), measured in a 4"-high ( $H$ ) flow duct, mounted on one side.

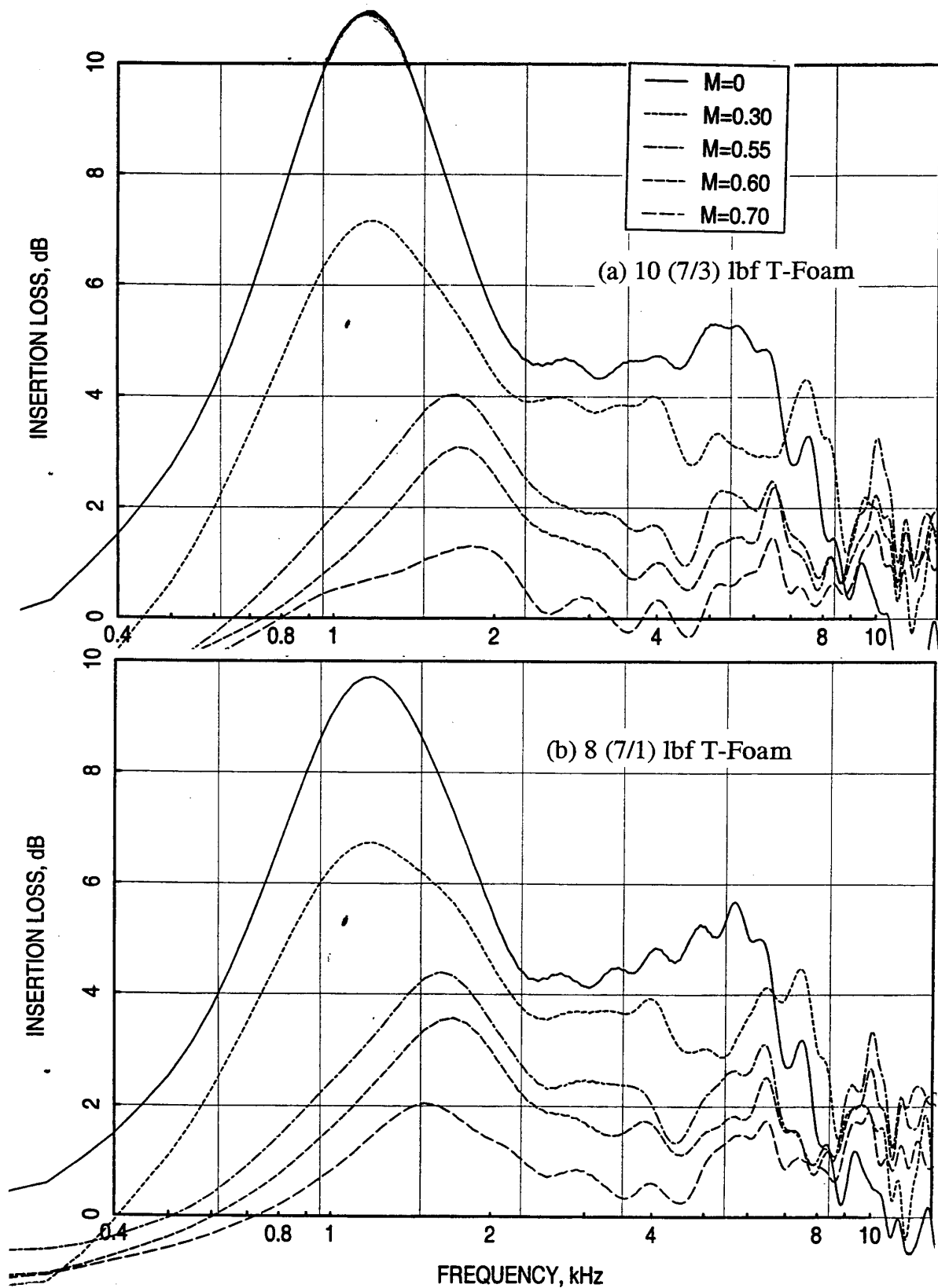


Figure 285. Influence of grazing flow Mach number ( $M$ ) on insertion loss spectrum for 2''-deep (a) 10 (7/3) lbf and (b) 8 (7/1) lbf T-Foam panels with 40% porous 0.10''-thick facesheet ( $d=0.07''$ ), measured in a 4''-high ( $H$ ) flow duct, mounted on one side.

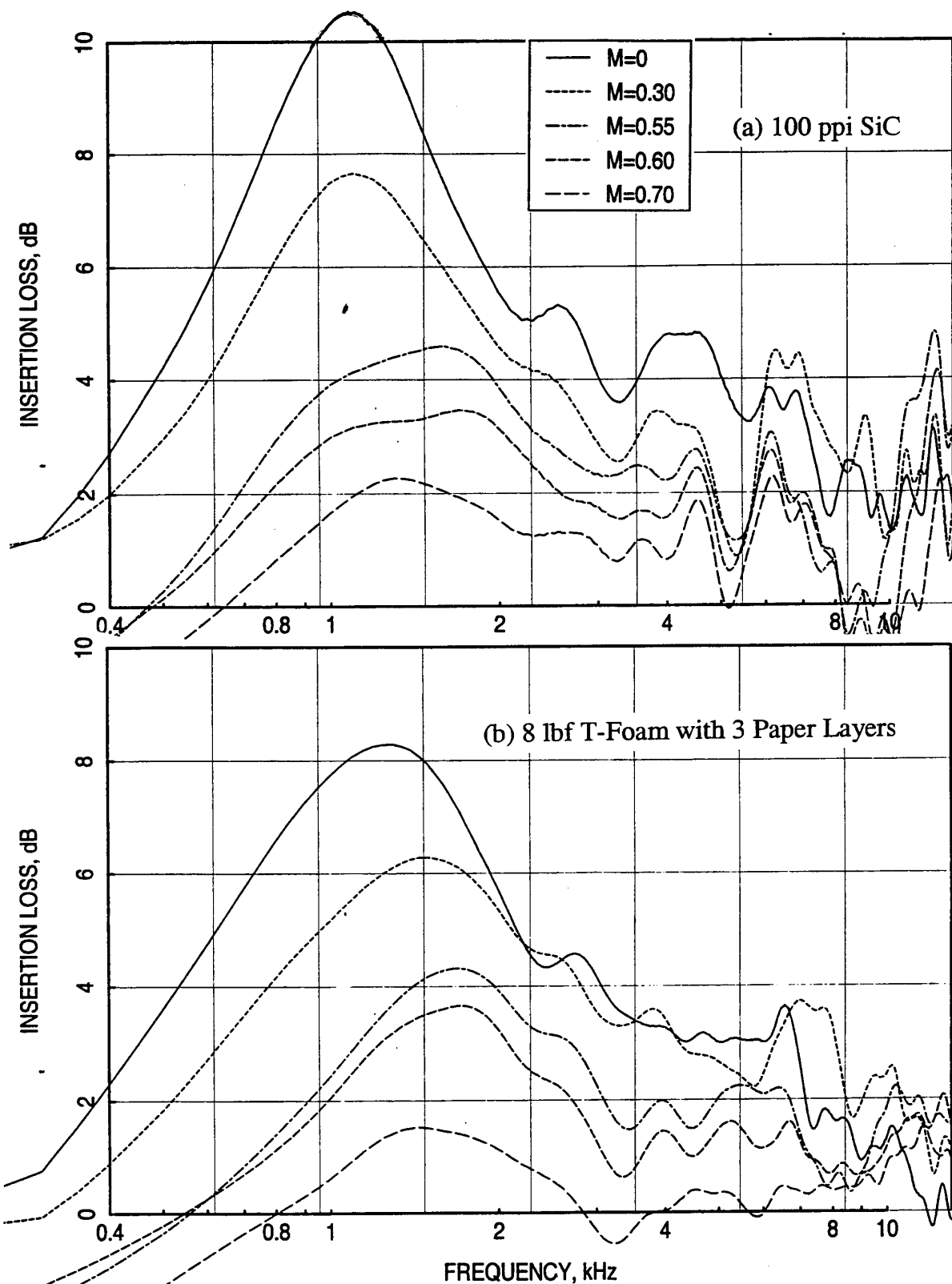


Figure 286. Influence of grazing flow Mach number ( $M$ ) on insertion loss spectrum for 2"-deep (a) 100 ppi SiC and (b) 8 lbf T-Foam with 3 paper layers panels with 40% porous 0.10"-thick facesheet ( $d=0.07''$ ), measured in a 4"-high ( $H$ ) flow duct, mounted on one side.

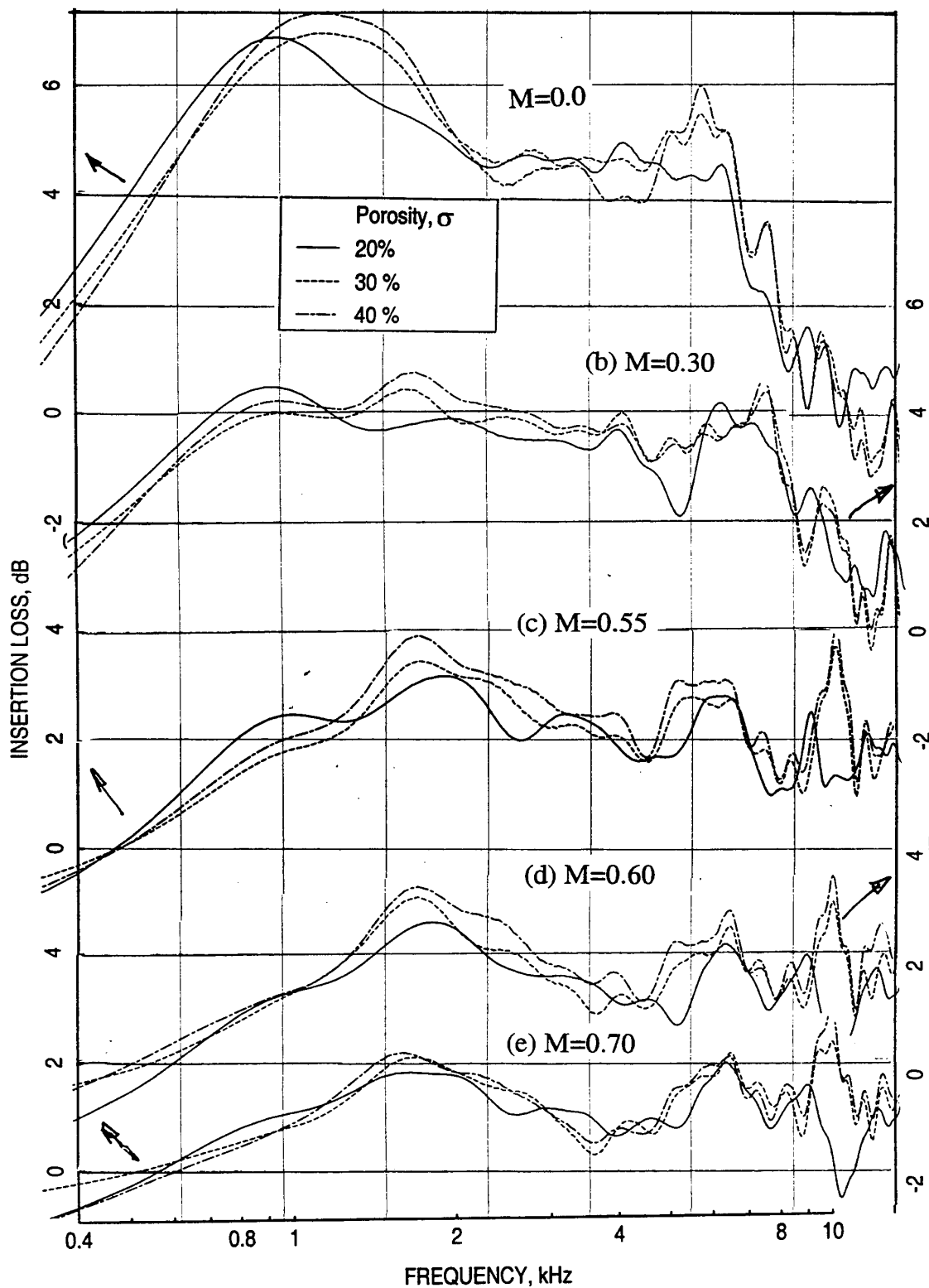


Figure 287. Effect of facesheet porosity ( $\sigma$ ) on insertion loss spectrum for 2"-deep 12 (10/2) lbf T-Foam panels with 0.10"-thick facesheets ( $d=0.07''$ ), measured in a 4"-high (H) flow duct, mounted on one side for different grazing flow Mach numbers ( $M$ ).



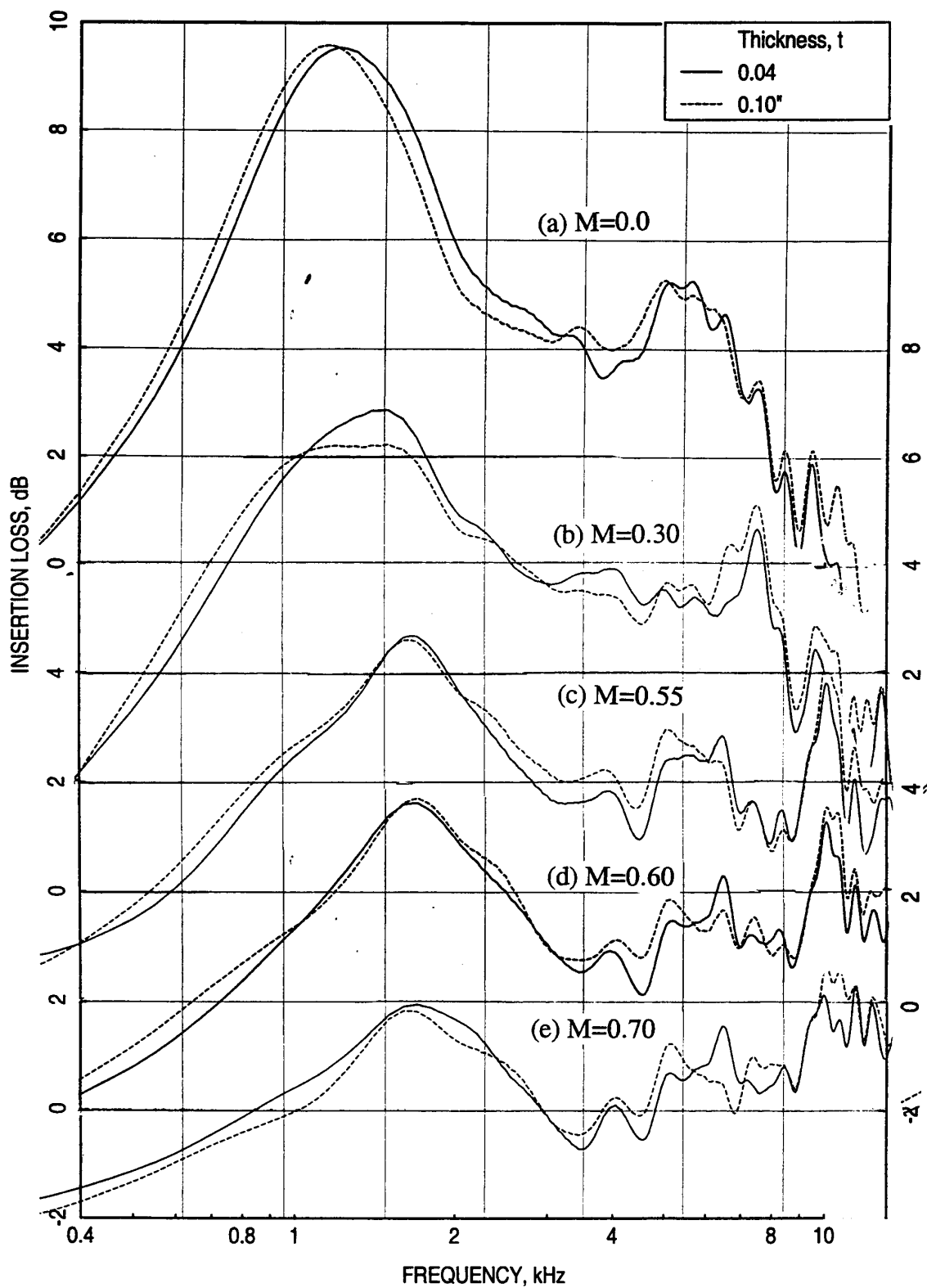


Figure 288. Effect of facesheet thickness ( $t$ ) on insertion loss spectrum for 2"-deep 8 (7/1) lbf T-Foam panels with 40% porous facesheets ( $d=0.04$ "), measured in a 4"-high ( $H$ ) flow duct, mounted on one side for different grazing flow Mach numbers ( $M$ ).

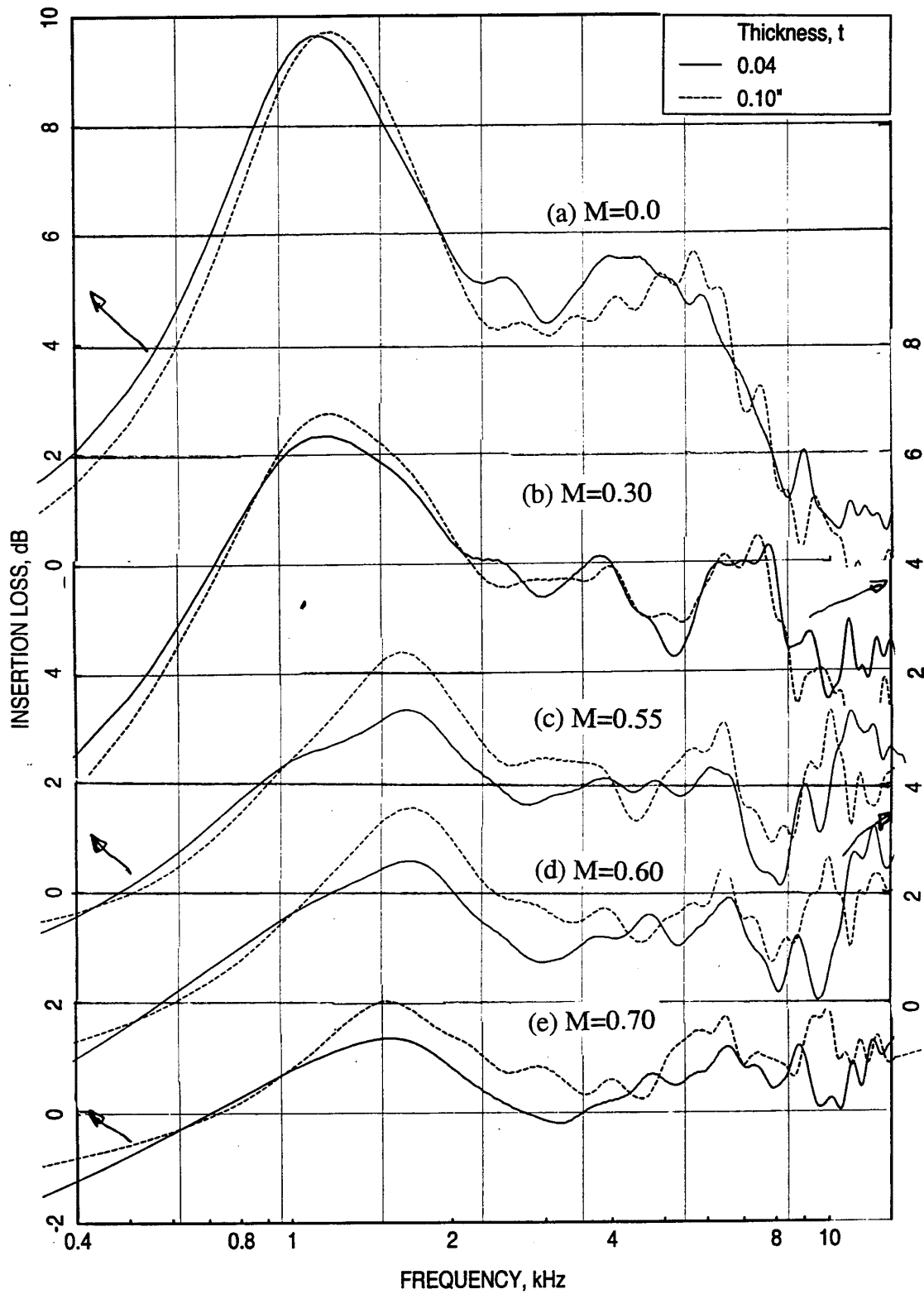


Figure 289. Effect of facesheet thickness ( $t$ ) on insertion loss spectrum for 2"-deep 8 (7/1) lbf T-Foam panels with 40% porous facesheets ( $d=0.07$ "), measured in a 4"-high ( $H$ ) flow duct, mounted on one side for different grazing flow Mach numbers ( $M$ ).

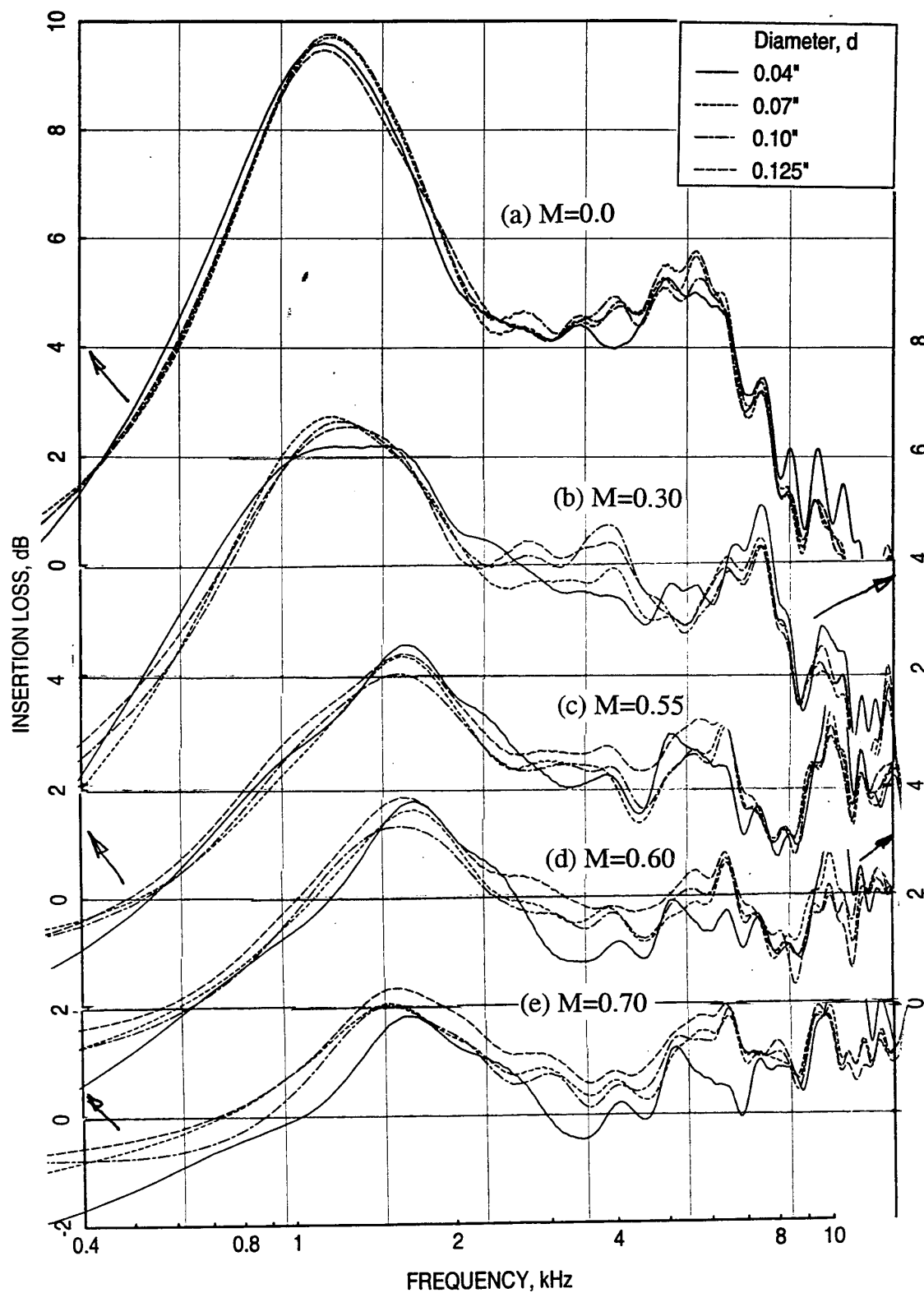


Figure 290. Effect of facesheet hole diameter ( $d$ ) on insertion loss spectrum for 2"-deep 8 (7/1) lbf T-Foam panels with 40% porous 0.10"-thick facesheets, measured in a 4"-high (H) flow duct, mounted on one side for different grazing flow Mach numbers ( $M$ ).

**Effect of T-Foam Density:** Insertion loss spectra due to T-Foam density variation are compared in Figure 291. T-Foam with 7-lbf fiber and 3-lbf matrix seems to be an effective acoustic suppressor at no flow condition and at  $M=0.3$  compared to T-Foam with higher fiber density. However, at higher grazing flow Mach numbers the bulk absorber with 7 lbf fiber and 1 lbf matrix suppresses more acoustic energy compared to the other T-Foam configurations.

**T-Foam with Three Layers of Woven Paper:** Based on the normal impedance the T-Foam with three woven paper construction comes closer to the optimum impedance levels compared to other T-Foam configurations. Effect of facesheet thickness and facesheet hole diameter on insertion loss using a 8 lbf T-Foam with three woven paper layers is shown in Figures 292 and 293. Effect of facesheet thickness seems to be insignificant on insertion loss. The same is the situation with hole diameter for no flow condition and lower grazing flow Mach numbers. At higher grazing flow Mach numbers the facesheet with lower hole diameter contributes more to the insertion loss.

Finally the insertion loss spectra due 2"-deep bulk absorbers, two with 8 lbf T-Foam (one standard and the other with 3 paper layer construction) and a third with 100 ppi Sic, are compared in Figure 294. The 100-ppi Silicon Carbide bulk absorber suppresses most acoustic energy compared to the best of the T-Foam configurations at all grazing flow Mach numbers. The three paper T-Foam configuration performs better compared to the standard one at higher grazing flow Mach numbers.

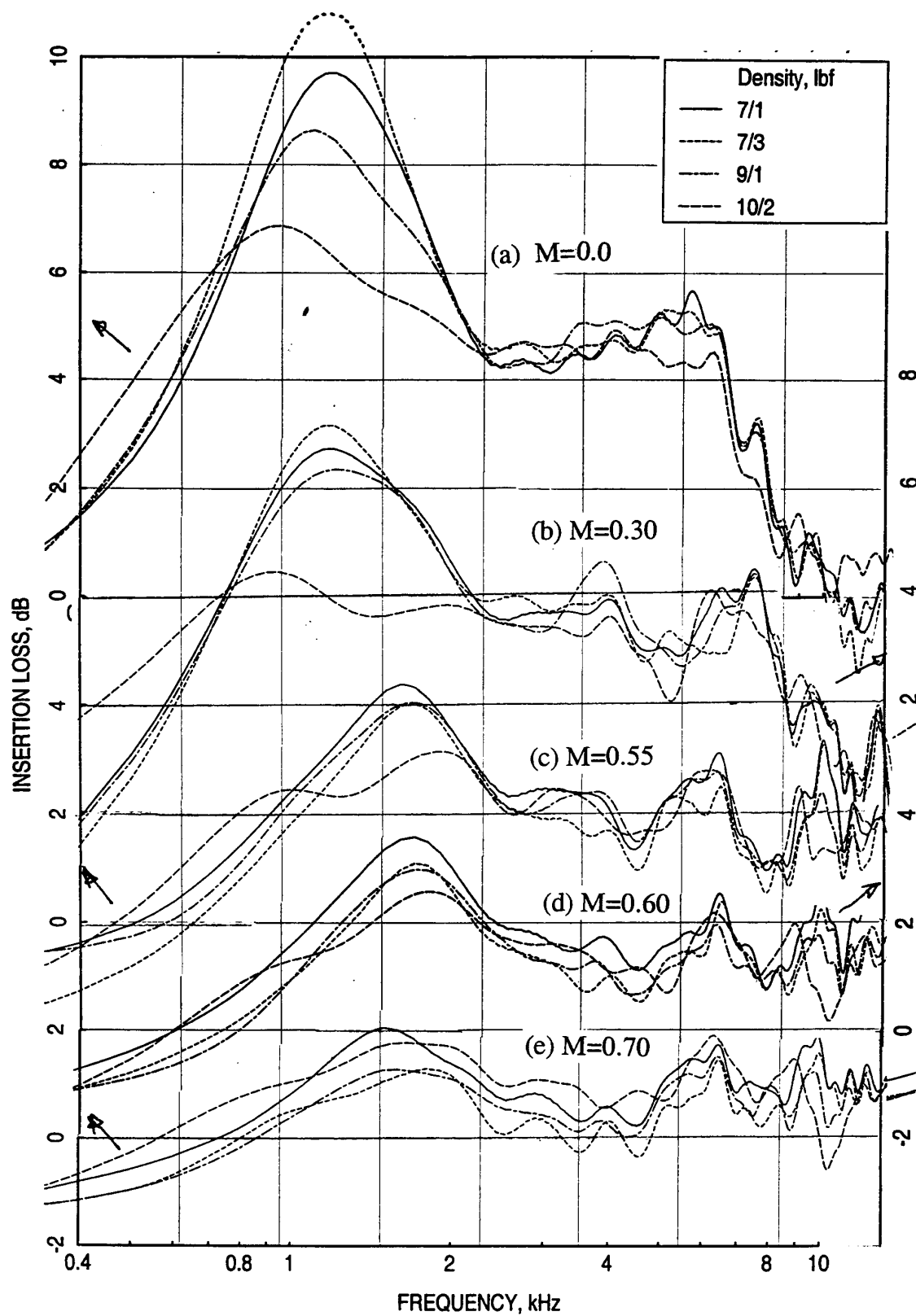


Figure 291. Effect of T-Foam density on insertion loss spectrum for 2''-deep panels with 40% porous 0.10''-thick facesheet ( $d=0.07''$ ), measured in a 4''-high (H) flow duct, mounted on one side for different grazing flow Mach numbers (M).

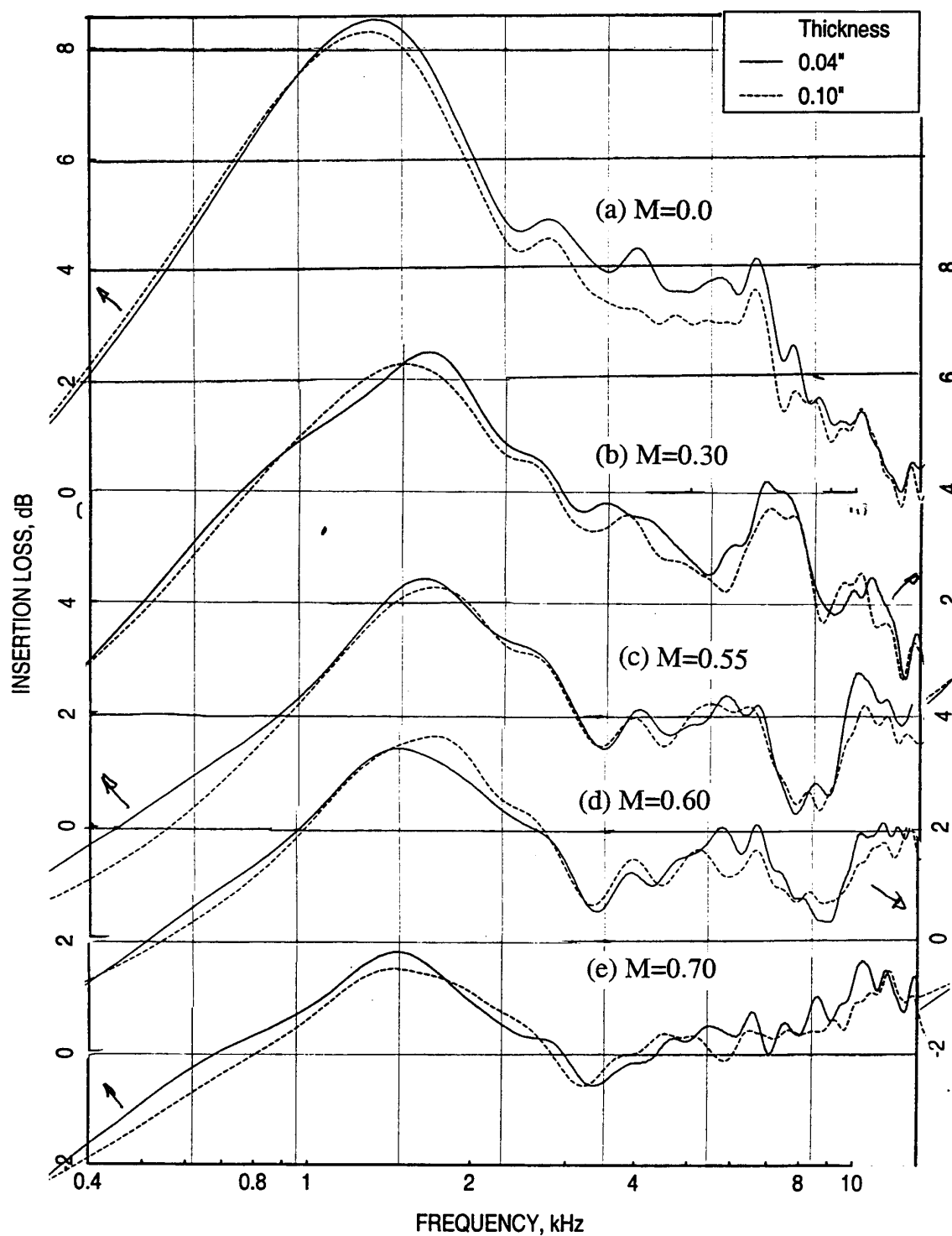


Figure 292. Effect of facesheet thickness ( $t$ ) on insertion loss spectrum for 2"-deep 8 lbf T-Foam with 3 layers paper panels with 40% porous facesheets ( $d=0.07''$ ), measured in a 4"-high ( $H$ ) flow duct, mounted on one side for different grazing flow Mach numbers ( $M$ ).

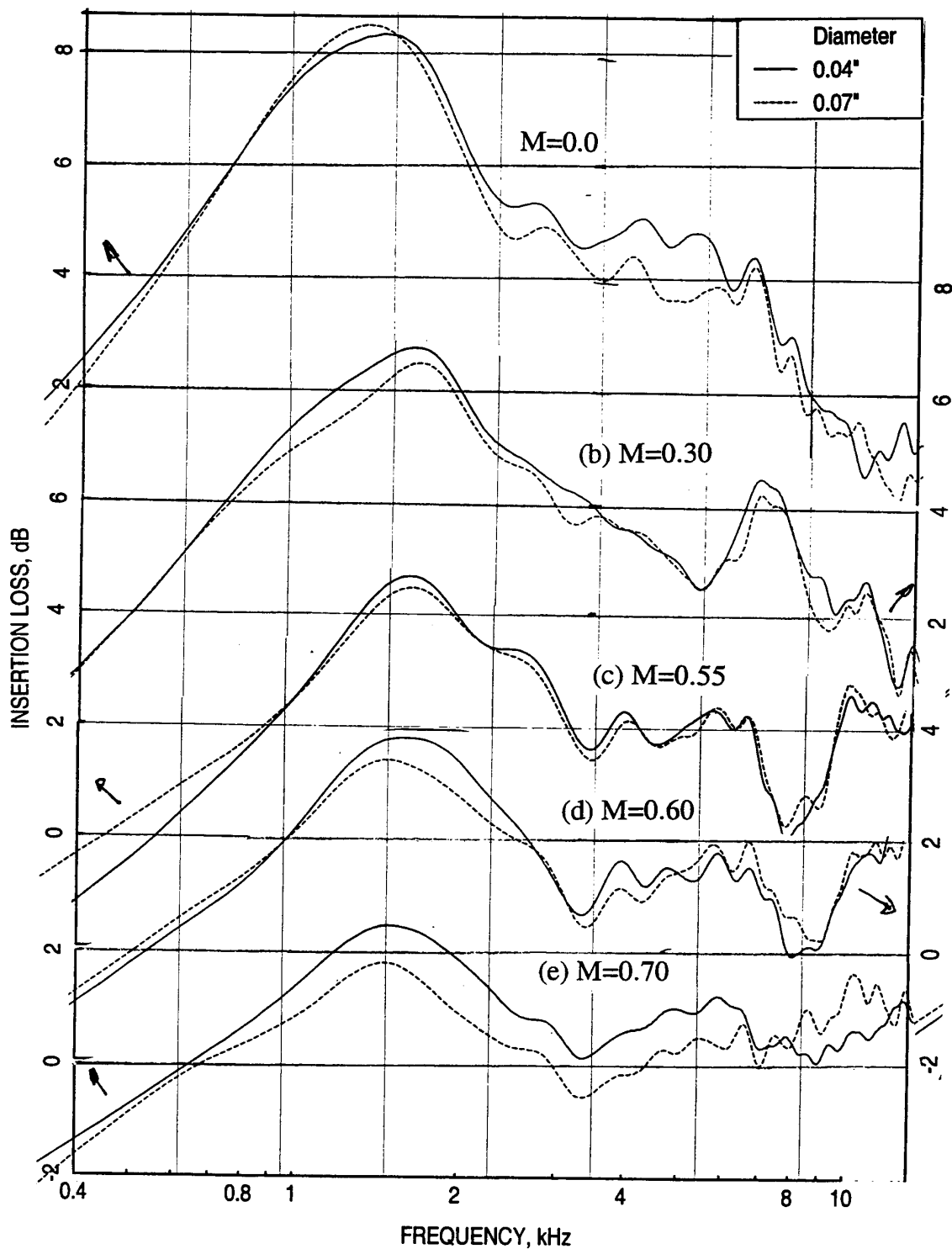


Figure 293. Effect of facesheet hole diameter (d) on insertion loss spectrum for 2"-deep 8 lbf T-Foam with 3 layers paper panels with 40% porous 0.04"-thick facesheets, measured in a 4"-high (H) flow duct, mounted on one side for different grazing flow Mach numbers (M).

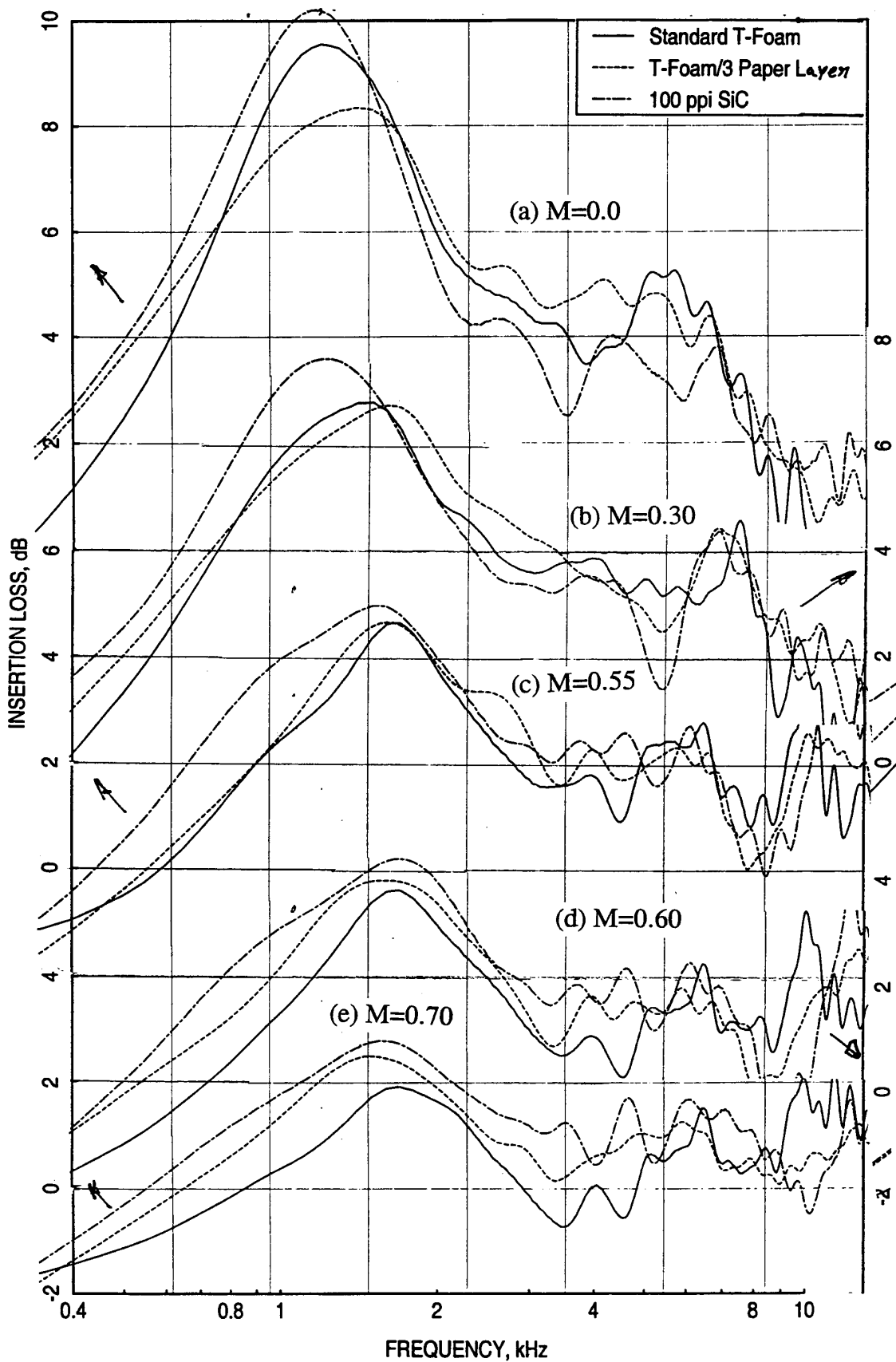


Figure 294. Effect of bulk type and construction on insertion loss spectrum for 2"-deep panels with 40% porous 0.04"-thick facesheet ( $d=0.04''$ ), measured in a 4"-high ( $H$ ) flow duct, mounted on one side for different grazing flow Mach numbers ( $M$ ).





## 8.0 ACOUSTIC SUPPRESSION IN THE FARFIELD DUE TO ACOUSTIC TREATMENT OF MIXER-EJECTOR NOZZLES

Development of correlation to predict normal impedance for any desired acoustic treatment and acoustic suppression due to the treatment applied to an ejector utilizing the laboratory test results are important output of the liner technology program. The normal impedance and acoustic suppression predictions involve correlation of the DC flow resistance and physical properties of a liner at room temperature with its normal impedance at a desired temperature and flow condition and a correlation between the normal impedance and the insertion loss of the liner accounting for liner scaling utilizing the laboratory test results presented in this report.

While the laboratory tests are pursued to achieve this goal utilizing acoustic excitation from drivers at room temperature and moderately heated conditions, it is necessary to improve and validate the correlation for realistic acoustic and aerothermodynamic conditions. Therefore, farfield acoustic data, obtained from several mixer-ejector tests, is utilized to develop and validate the impedance/suppression correlation. For this purpose the internal noise component, which is the noise internal to the ejector radiated to the farfield, is extracted from the measured total farfield noise. The extracted internal noise component in the farfield is utilized in the correlation process.

Measured farfield acoustic data for several mixer-ejector configurations are utilized for internal noise extraction. Typical results for Gen 2.5 mixer-ejector with mixer 8c and with turning vanes are described in this section. The flap length for this 1/7-scale model is 21.7" (160" full-scale). The MAR (mixing area ratio) and penetration for these configurations are 0.95 and 92.5%, respectively (see Figures 295 and 296). All the data presented in this section are with a simulated flight Mach number of 0.32. Tables 13 through 16 list the test conditions for different configurations used for internal noise extraction process. The ejector surface area (area of flaps & sidewalls ) is approximately 686 in<sup>2</sup>. The treatment area is considerably lower due to the untreated spaces between the liner trays and untreated support areas within the trays. The following table lists the treated areas for different configurations.

Configuration Definition	Ejector Area (in <sup>2</sup> )	Flap Area (in <sup>2</sup> )	Sidewall Area (in <sup>2</sup> )	Treatment Area (in <sup>2</sup> )	% wrt Ejector Area	% wrt Full Treatment
Hard Wall	685.9	408.4	277.5	0	0	0
Treated Sidewalls	685.9	408.4	277.5	195.6	28.5	40.4
Treated Flaps	685.9	408.4	277.5	288.5	42.1	59.6
Fully Treated	685.9	408.4	277.5	484.1	70.1	100

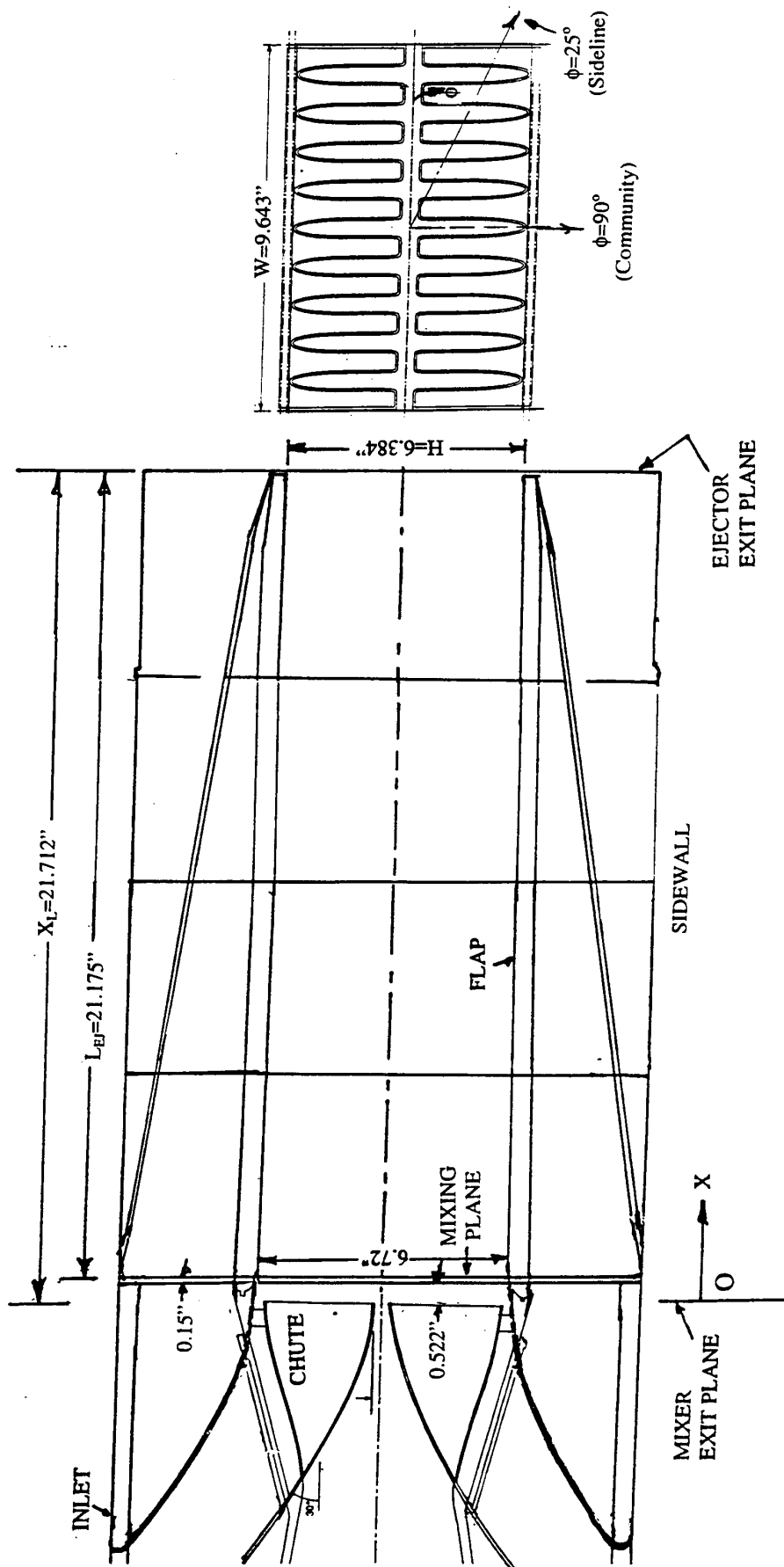


Figure 295. . Side and end views of an aero type 20-cold & 18-hot chute Gen 2.5 mixer ejector nozzle (8cMixer); SAR=2.9, Penetration=92.5%, CER=1.05, MAR=0.95.

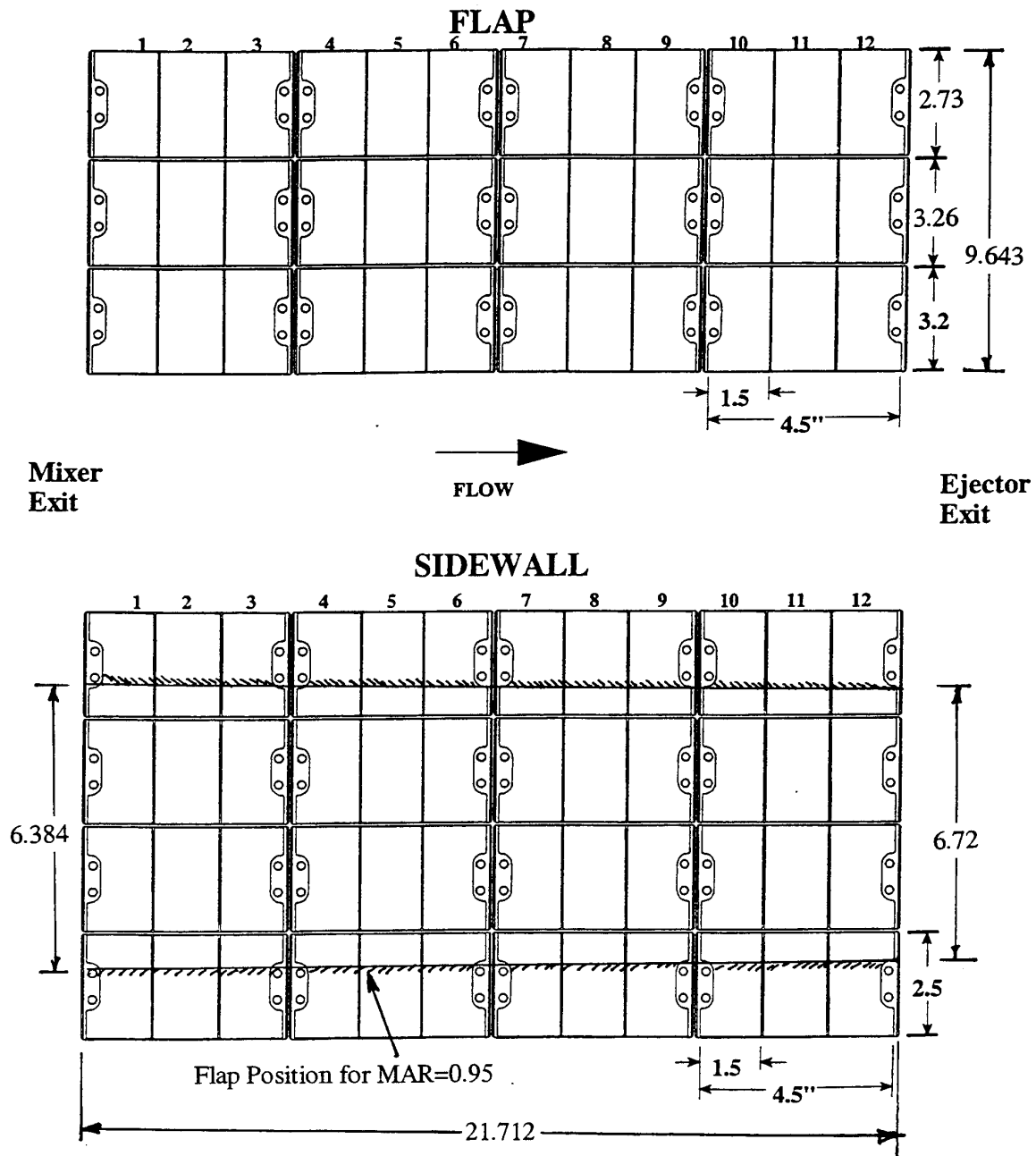


Figure 296. Schematic of acoustic treatment trays for the 21.7" (160" full-scale) flaps and sidewalls for Gen 2.5 mixer-ejector nozzles (all dimensions are in inches).

Table 13. Test conditions for hardwall Gen2.5 Mixer-Ejector with Mixer 8c and with Turning Vanes; 21.7" flaps (160" full-scale); MAR=0.95, MF=0.32; Test No=2820, Configuration =842.13.

Run Number		NPR	T8, °R	V <sub>j,p</sub> , f/s	Pumping	V <sub>mix</sub> , f/s	T <sub>mix</sub> , °R	Degree of Mixing	Mean Flow Conditions		Conditions at Wall Surface	
φ=25°	φ=90°								Mach No	Temp. °F	Mach No	Temp. °F
335	334	2.374	1239	1808	0.822	1031	950	0.92	0.75	375	0.72	350
336	337	2.479	1290	1886	0.812	1079	983	0.91	0.76	390	0.73	365
339	338	2.959	1414	2135	0.738	1261	1079	0.89	0.80	460	0.765	430
340	341	3.256	1479	2263	0.691	1365	1134	0.88	0.83	490	0.78	465
343	342	3.430	1549	2360	0.668	1438	1187	0.87	0.85	530	0.80	500
344	345	4.002	1694	2593	0.553	1624	1328	0.85	0.88	590	0.82	560

Table 14. Test conditions for Fully Treated Gen2.5 Mixer-Ejector with Mixer 8c and with Turning Vanes; 21.7" flaps (160" full-scale); MAR=0.95, MF=0.32; Test No=2820, Configuration =832.13.

Run Number		NPR	T8, °R	V <sub>j,p</sub> , f/s	Pumping	V <sub>mix</sub> , f/s	T <sub>mix</sub> , °R	Degree of Mixing	Mean Flow Conditions		Conditions at Wall Surface	
φ=25°	φ=90°								Mach No	Temp. °F	Mach No	Temp. °F
271	270	2.370	1237	1813	0.767	1018	967	0.92	0.75	375	0.72	350
260	261	2.480	1293	1883	0.759	1069	1002	0.91	0.76	390	0.73	365
268	269	2.960	1418	2133	0.687	1252	1100	0.89	0.80	460	0.765	430
267	266	3.250	1478	2274	0.642	1354	1153	0.88	0.83	490	0.78	465
263	262	3.430	1558	2359	0.622	1429	1213	0.87	0.85	530	0.80	500
264	265	4.000	1692	2598	0.536	1630	1337	0.85	0.88	590	0.82	560

Table 15. Test conditions for Treated Flaps (Hardwall Sidewalls) Gen2.5 Mixer-Ejector with Mixer 8c and with Turning Vanes; 21.7" flaps (160" full-scale); MAR=0.95, MF=0.32; Test No=2820, Configuration =852.13.

Run Number		NPR	T8, °R	V <sub>j,p</sub> , f/s	Pumping	V <sub>mix</sub> , f/s	T <sub>mix</sub> , °R	Degree of Mixing	Mean Flow Conditions		Conditions at Wall Surface	
φ=25°	φ=90°								Mach No	Temp. °F	Mach No	Temp. °F
381	380	2.368	1239	1806	0.797	1025	958	0.92	0.75	375	0.72	350
378	379	2.472	1293	1886	0.787	1073	993	0.91	0.76	390	0.73	365
377	376	2.964	1416	2137	0.713	1258	1089	0.89	0.80	460	0.765	430
374	375	3.257	1485	2268	0.669	1363	1145	0.88	0.83	490	0.78	465
373	372	3.436	1549	2361	0.646	1434	1195	0.87	0.85	530	0.80	500
370	371	4.003	1696	2595	0.554	1624	1328	0.85	0.88	590	0.82	560

Table 16. Test conditions for Treated Sidewalls (Hardwall Flaps) Gen2.5 Mixer-Ejector with Mixer 8c and with Turning Vanes; 21.7" flaps (160" full-scale); MAR=0.95, MF=0.32; Test No=2820, Configuration =862.13.

Run Number		NPR	T8, °R	V <sub>j,p</sub> , f/s	Pumping	V <sub>mix</sub> , f/s	T <sub>mix</sub> , °R	Degree of Mixing	Mean Flow Conditions		Conditions at Wall Surface	
φ=25°	φ=90°								Mach No	Temp. °F	Mach No	Temp. °F
407	406	2.370	1240	1808	0.806	1026	954	0.92	0.75	375	0.72	350
404	405	2.487	1292	1890	0.793	1077	988	0.91	0.76	390	0.73	365
403	402	2.951	1417	2135	0.723	1254	1084	0.89	0.80	460	0.765	430
400	401	3.240	1484	2263	0.678	1357	1140	0.88	0.83	490	0.78	465
399	398	3.434	1555	2365	0.651	1435	1195	0.87	0.85	530	0.80	500
396	397	4.003	1696	2595	0.553	1624	1327	0.85	0.88	590	0.82	560

### 8.1 Internal Noise Extraction Process:

A procedure is developed to extract the internal noise component from the total measured data utilizing SMEM (i.e., Stone Mixer Ejector Model), which is developed to predict mixer-ejector noise components (i.e., internal mixing, internal shock, premerged, merged, and external shock) in the farfield. These predictions are based on geometric and flow parameters associated with test conditions. For the current analysis, premerged, merged, and external shock noise components are combined together and termed as external noise component. The remaining components (internal mixing and internal shock noise) together are termed as internal noise component. In the current procedure the portions of the SMEM, which predict the external noise components only, is taken out. These portions are included in the current internal noise extraction process to get the external noise components in terms of SPL spectra as the initial input.

The predicted external SPL spectra at each polar angle are shifted up or down to match the measured total noise at lower frequencies (up to about 200 Hz.). Removing the low frequency matched external SPL spectrum from the measured total SPL derives the internal noise component. The derived internal SPL spectrum often does not exhibit proper trend at lower frequencies due to the empiricism of the prediction method. The internal noise component is dominant at higher frequencies, as opposed to the external noise, which is dominant in the lower and mid frequency ranges. Thus, the internal SPL is extrapolated by gradually decreasing the level with frequency in the lower frequency range from a frequency, termed as low frequency limit, up to which the derived data looks reasonable. The low frequency limit varies with the test condition. The data is interpolated at any other frequency above the low frequency limit; if the predicted external SPL exceeds the total measured

value. The measured total data at certain frequencies is modified by interpolation if it is identified to be erroneous at those frequencies. Usually such modifications are limited and are made at very low nozzle pressure ratio conditions due to the dominant background noise contamination. The internal noise components in terms of SPL spectra are subtracted from the corrected total SPL spectra and thus the modified external SPL spectra are derived.

The total, the external, and the internal SPL spectra are then utilized to compute PWL, OASPL, PNL, and EPNL. PWL in this process is based on the data at a single azimuthal location. The actual PWL should account for the azimuthal variation of noise field. All the steps described above, including the corrections to total and internal SPL data interpolations, are automated in the extraction code. The difference of PWL between a hardwall and a treated configurations is the acoustic suppression ( $\Delta$ PWL) due to the acoustic treatment. This parameter is used in the development of acoustic suppression/normal impedance correlation. As an example, the internal noise extraction process for a takeoff condition (NPR=3.43, T8=1551°R, V<sub>j</sub>=2359 ft/sec) is described here. The low frequency extrapolation is performed from 800 Hz. (low frequency limit) for the takeoff condition.

**Hardwall Configuration:** The measured farfield and the initially predicted external component of sound pressure level spectra for the hardwall configuration at takeoff condition are shown in Figures 297 through 299. The derived internal SPL does not exhibit proper trend at lower frequencies (up to about 800 Hz). For the hardwall configuration the internal component of SPL in linear scale is decreased to zero at zero frequency from the level at 800 Hz as follows:

$$p^2(f) = p^2(f_o) (f/f_o)^m \quad (7)$$

where;  $p^2(f)$  = Internal component of rms pressure at a frequency  $f$

$p^2(f_o)$  = Internal Component of rms pressure at low frequency limit  $f_o$  (800 Hz for the current case)

=  $10^{\{SPL(f_o)/10\}}$ , SPL( $f_o$ ) being the rms pressure at  $f_o$  in dB

$m$  = Integer exponent

Thus, the internal component of SPL at frequency  $f$  below the low frequency limit in dB is given by;

$$SPL(f) = SPL(f_o) + 10 m \log(f/f_o) \quad (8)$$

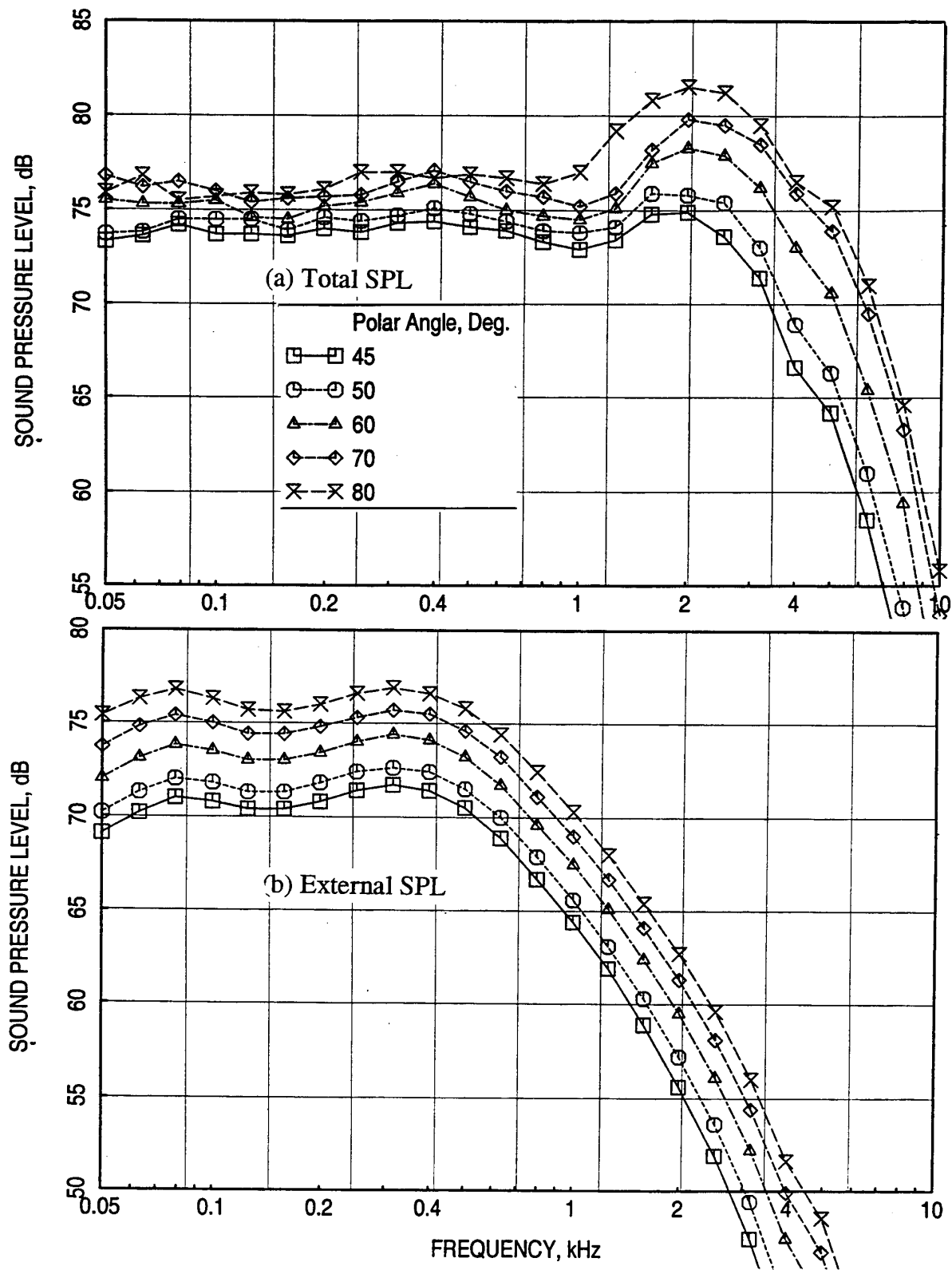


Figure 297. (a) Measured farfield SPL and (b) predicted external component of SPL spectra at various polar angles  $\theta$  for Gen 2.5 model with mixer 8c and 21.7'' long hardwall ejector; NPR=3.43, T8=1549°R,  $V_j$ =2359 ft/sec,  $V_{mix}$ =1438 ft/sec, M=0.32,  $\phi$ =25° {takeoff}.



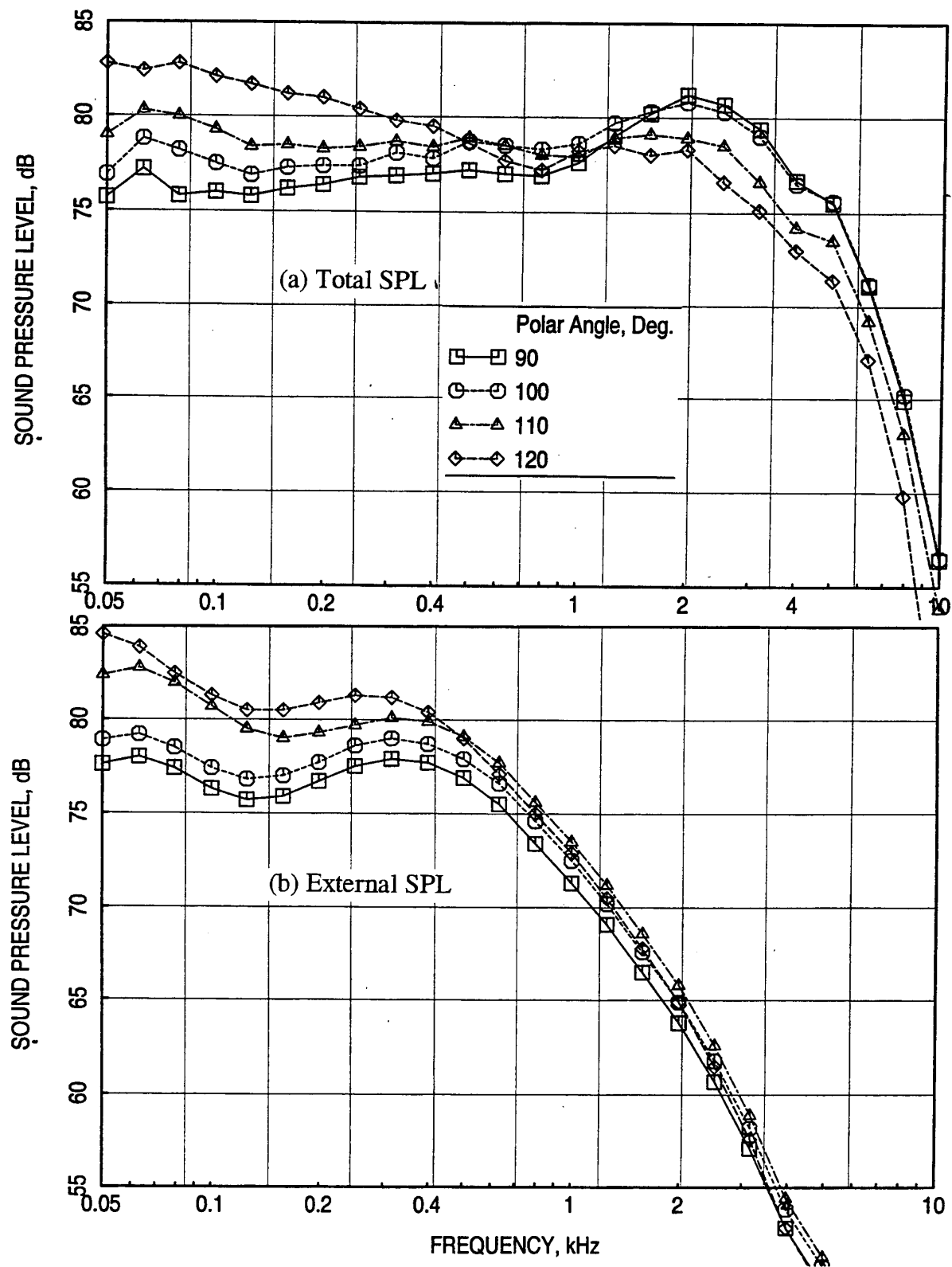


Figure 298. (a) Measured farfield SPL and (b) predicted external component of SPL spectra at various polar angles  $\theta$  for Gen 2.5 model with mixer 8c and 21.7'' long hardwall ejector; NPR=3.43,  $T_8=1549^\circ\text{R}$ ,  $V_j=2359$  ft/sec,  $V_{\text{mix}}=1438$  ft/sec,  $M=0.32$ ,  $\phi=25^\circ$  {takeoff}.

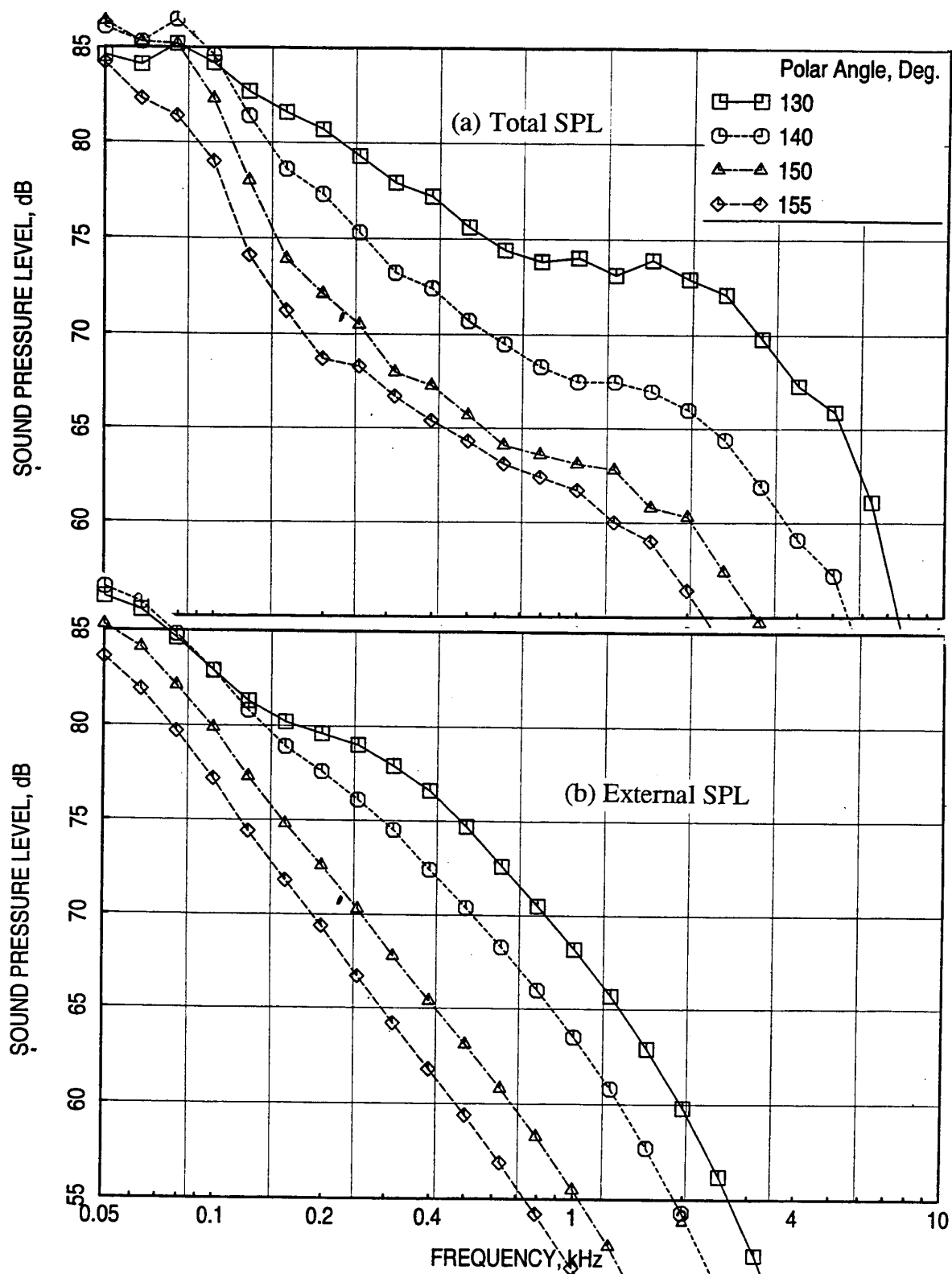


Figure 299. (a) Measured farfield SPL and (b) predicted external component of SPL spectra at various polar angles  $\theta$  for Gen 2.5 model with mixer 8c and 21.7'' long hardwall ejector; NPR=3.43,  $T_8=1549^\circ\text{R}$ ,  $V_j=2359$  ft/sec,  $V_{\text{mix}}=1438$  ft/sec,  $M=0.32$ ,  $\phi=25^\circ$  {takeoff}.

The extraction process is carried out with three different values of  $m$  as 1, 2 and 3. However, there is no impact of  $m$  is seen on total SPL, PWL, PNL, and EPNL. Thus, the results for  $m=2$  are presented in this report. The noise spectra, thus created, are used to compute internal component of OASPL, PNL, PWL, and EPNL. The internal noise spectrum is subtracted from the measured total SPL to create the modified external component of noise spectrum and is used to compute the external component of OASPL, PNL, PWL, and EPNL. The modified internal and external components of SPL spectra are shown in Figures 300 through 302.

**Treated Configuration:** For the corresponding treated configuration (i.e., for takeoff condition in this example) removing the external component from the measured total SPL derives the internal noise component. The internal SPL is extrapolated for the lower frequency range from the low frequency limit (800 Hz for the current case) for the reason described above. The data is interpolated at any other frequency above 800 Hz, if the predicted external SPL exceeds the total measured value or any unrealistic level is observed. Unlike the hardwall configuration, the extrapolation process in the lower frequency range is different for treated case. The SPL difference in dB scale between hardwall and treated configurations for each polar angle at the low frequency limit (i.e., at 800 Hz. for current case) is linearly applied to the lower frequencies, as shown below;

$$SPL_{Treated}(f) = SPL_{Hard}(f) - \{SPL_{Hard}(f_0) - SPL_{Treated}(f_0)\} \{f/f_0\} \quad (9)$$

Where;  $SPL_{Treated}(f)$  = Extrapolated internal component of SPL for treated configuration at frequency  $f$

$SPL_{Hard}(f)$  = Extrapolated internal component of SPL for hardwall configuration at frequency  $f$  based on equation (8).

$SPL_{Hard}(f_0)$  = Internal component of SPL at  $f_0$  for hardwall configuration

$SPL_{Treated}(f_0)$  = Internal component of SPL at  $f_0$  for treated configuration

The internal component of SPL spectra, thus created, is used to compute internal component of OASPL, PNL, PWL, and EPNL. The internal noise spectrum is subtracted from the measured total SPL to create the modified external component of noise spectrum and is used to compute the external component of OASPL, PNL, PWL, and EPNL for the treated configuration. To summarize the results derived from the extraction process the internal and the external components, and the total SPL and PWL spectra and OASPL and PNL directivities for hardwall and treated configurations are compared in Figures 303 through 306. Based on the results shown in Figure 305 the acoustic suppression ( $\Delta PWL$ ) is calculated by subtracting the internal PWL of treated configuration from hardwall configuration.

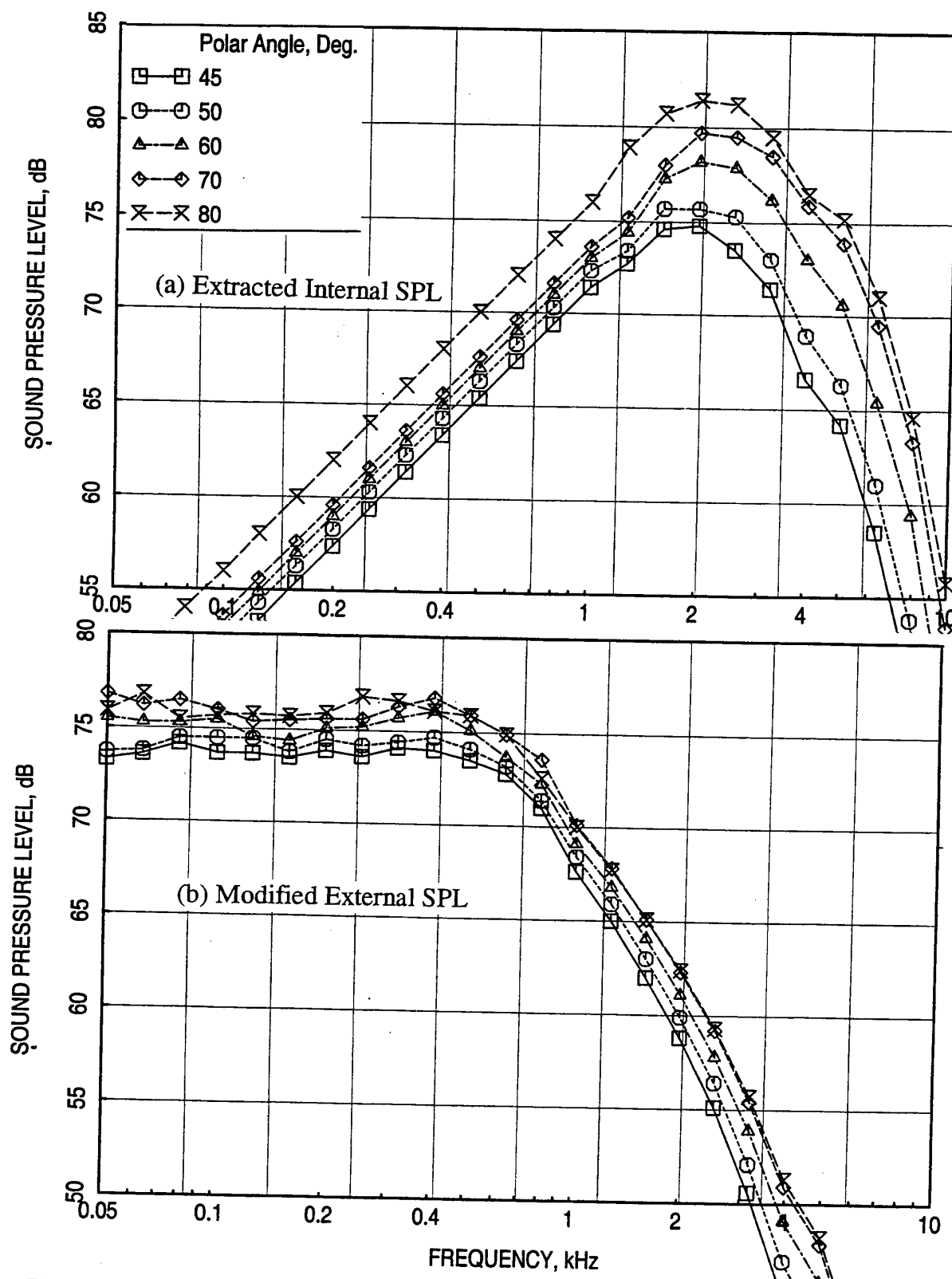


Figure 300. (a) Extracted internal and (b) modified external components of SPL spectra at various polar angles  $\theta$  for Gen 2.5 model with mixer 8c and 21.7" long hardwall ejector; NPR=3.43,  $T_8=1549^\circ\text{R}$ ,  $V_j=2359$  ft/sec,  $V_{\text{mix}}=1438$  ft/sec,  $M=0.32$ ,  $\phi=25^\circ$  {takeoff}.

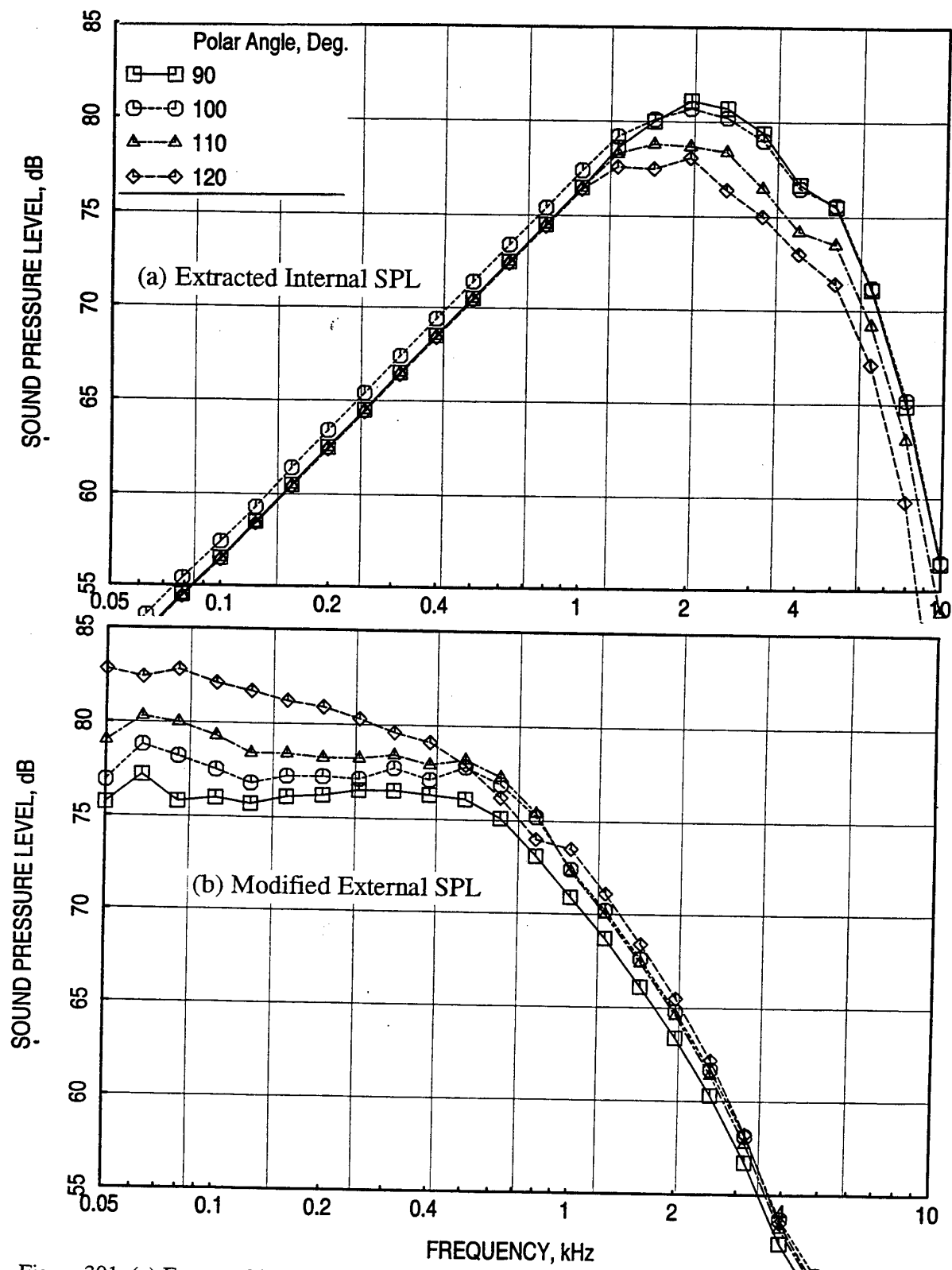


Figure 301. (a) Extracted internal and (b) modified external components of SPL spectra at various polar angles  $\theta$  for Gen 2.5 model with mixer 8c and 21.7" long hardwall ejector; NPR=3.43, T8=1549°R,  $V_j$ =2359 ft/sec,  $V_{mix}$ =1438 ft/sec, M=0.32,  $\phi$ =25° {takeoff}.

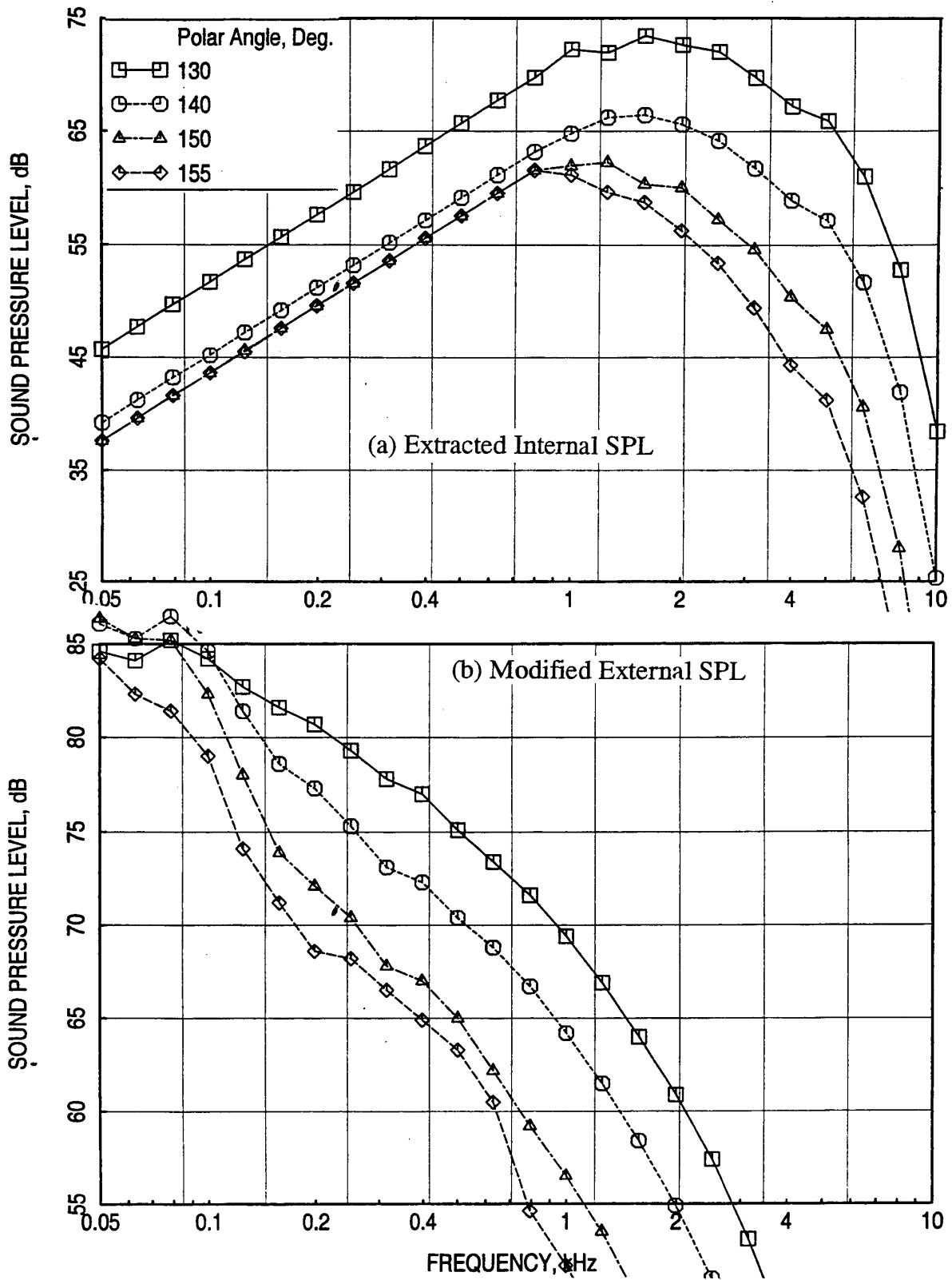


Figure 302. (a) Extracted internal and (b) modified external components of SPL spectra at various polar angles  $\theta$  for Gen 2.5 model with mixer 8c and 21.7" long hardwall ejector; NPR=3.43,  $T_8=1549^\circ\text{R}$ ,  $V_j=2359$  ft/sec,  $V_{\text{mix}}=1438$  ft/sec,  $M=0.32$ ,  $\phi=25^\circ$  {takeoff}.

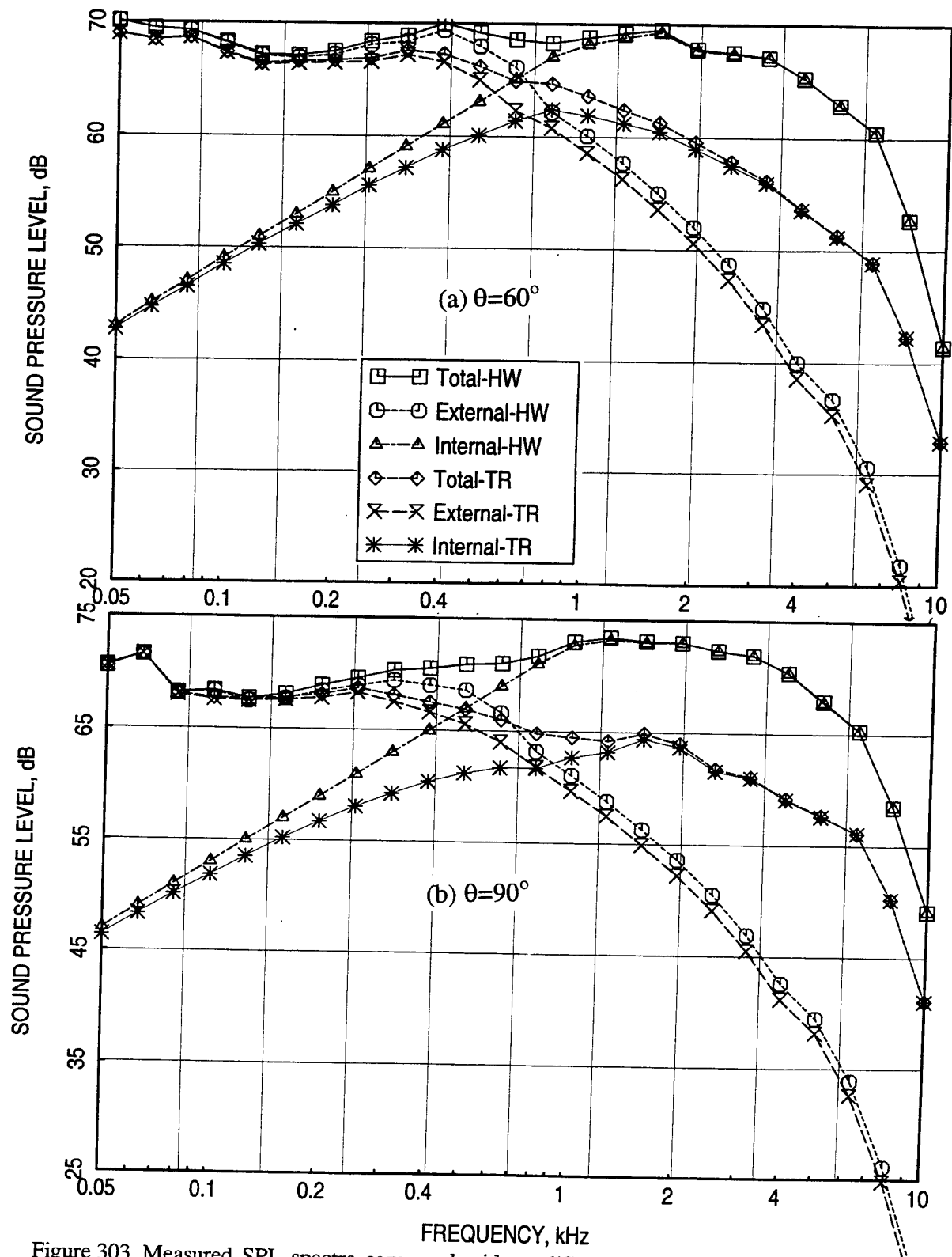


Figure 303. Measured SPL spectra compared with modified predicted external components and extracted internal components for hardwall and fully treated 22.7'' long ejector for Gen 2.5 model with mixer 8c; NPR=3.43, T8=1549°R,  $V_j=2359$  ft/sec,  $V_{mix}=1438$  ft/sec,  $M=0.32$ ,  $\phi=25^\circ$  {takeoff}.

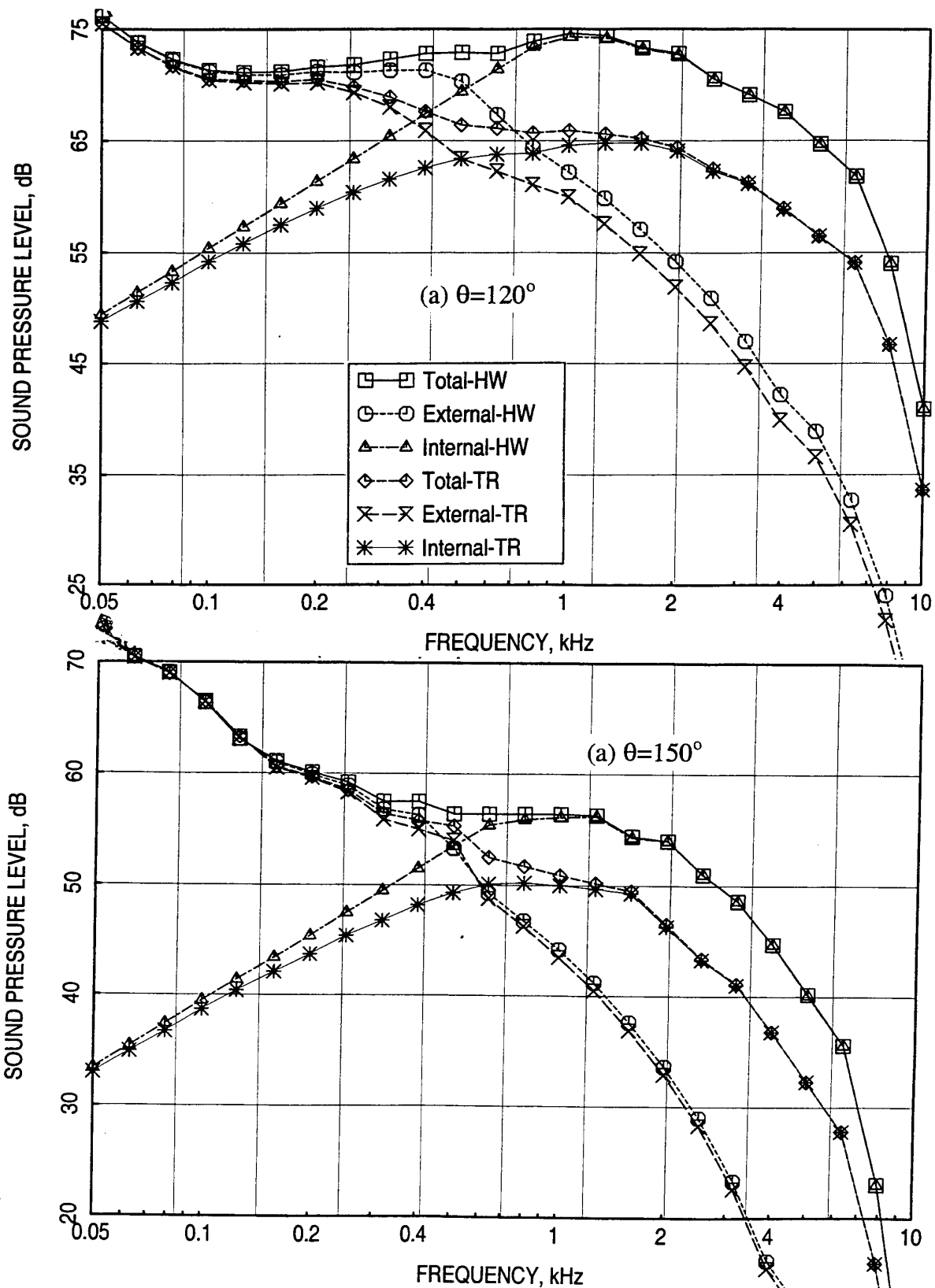


Figure 304. Measured SPL spectra compared with modified predicted external components and extracted internal components for hardwall and fully treated 22.7" long ejector for Gen 2.5 model with mixer 8c; NPR=3.43,  $T_8=1549^\circ\text{R}$ ,  $V_j=2359$  ft/sec,  $V_{\text{mix}}=1438$  ft/sec,  $M=0.32$ ,  $\phi=25^\circ$  {takeoff}.



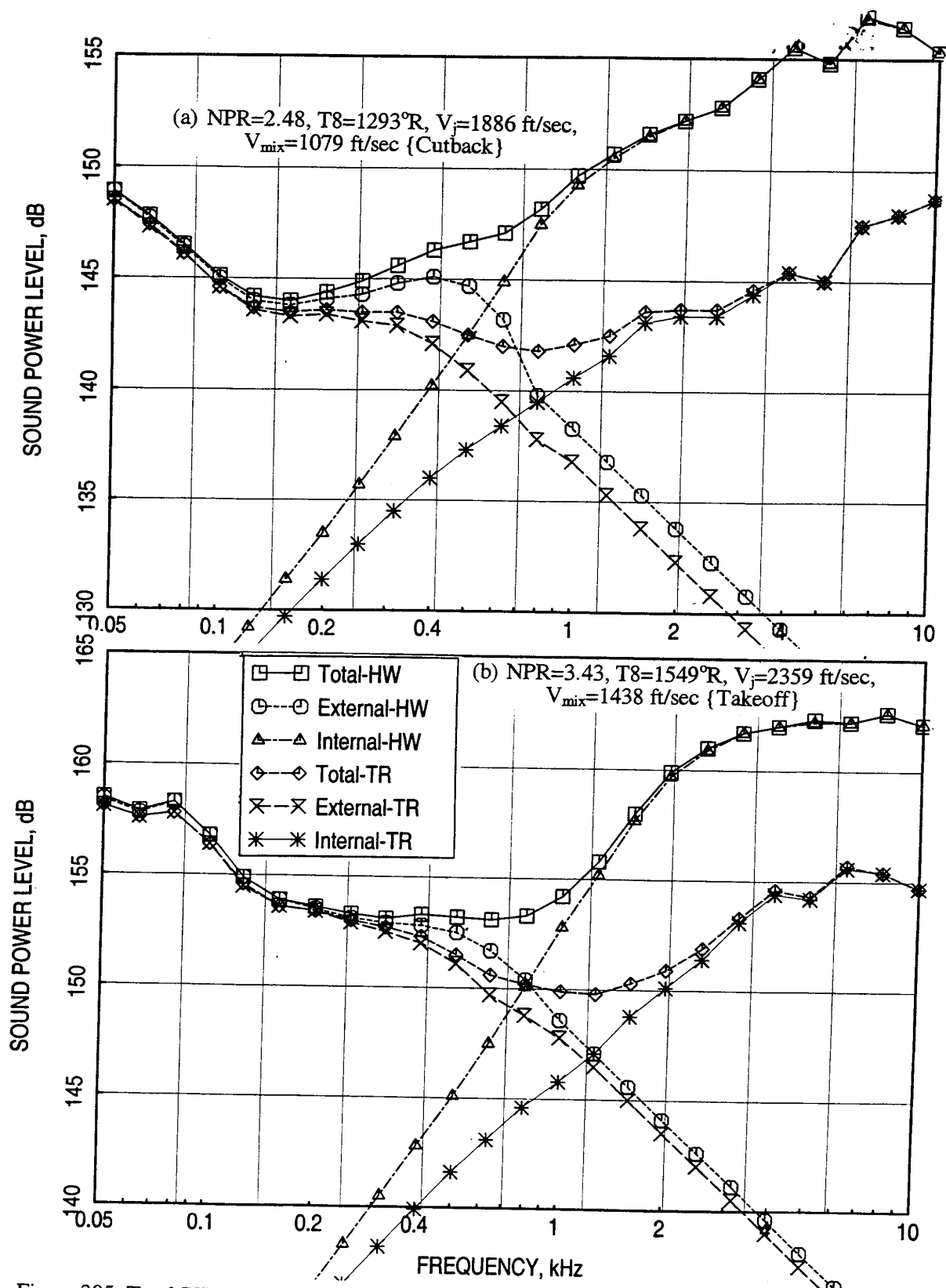


Figure 305. Total PWL spectra compared with modified predicted external components and extracted internal components for hardwall and fully treated 22.7" long ejector for Gen 2.5 model with mixer 8c;  $M=0.32$ ,  $\phi=25^\circ$ .

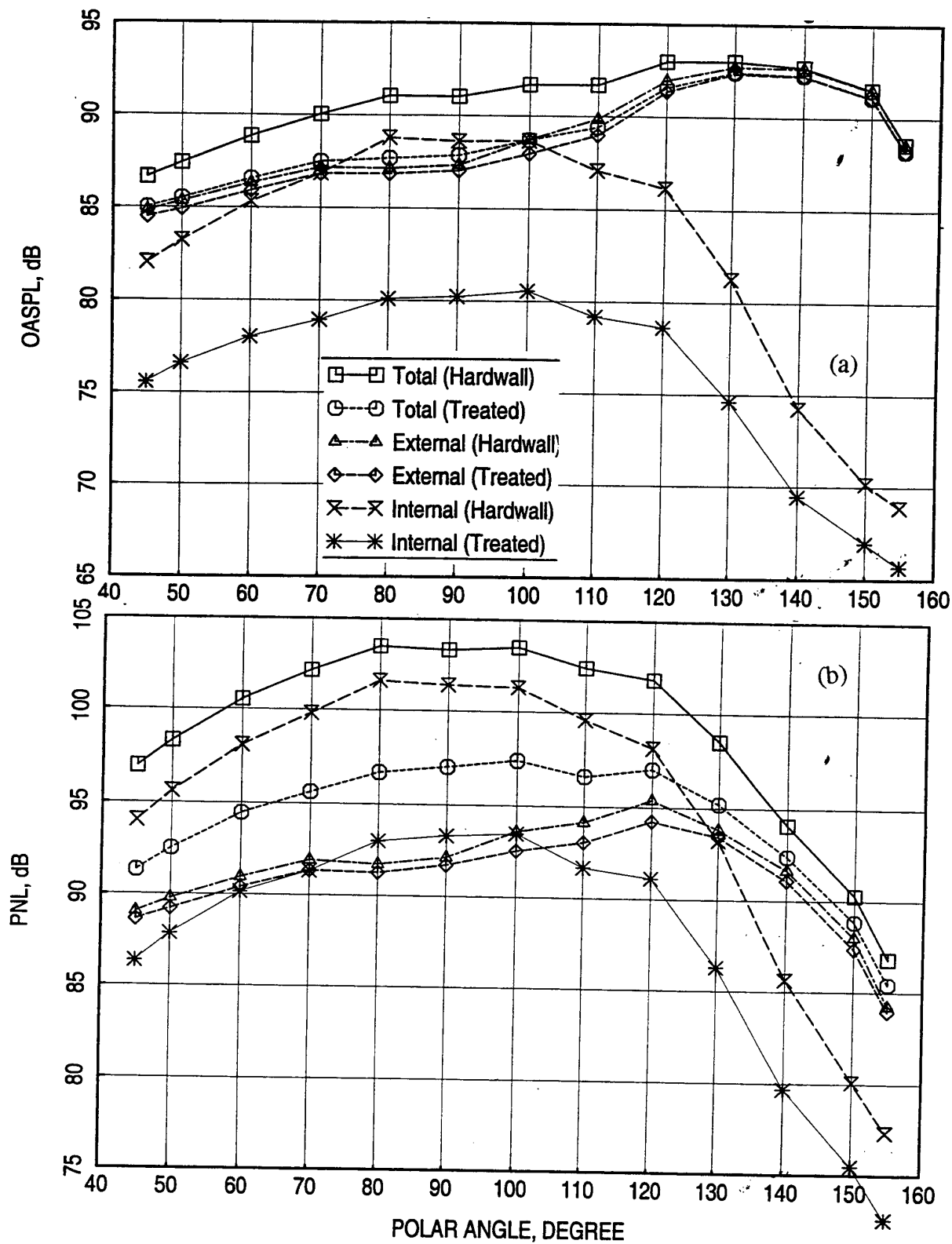


Figure 306. Total OASPL and PNL directivities compared with the modified predicted external components and extracted internal components for hardwall and fully treated 22.7" long ejector for Gen 2.5 model with mixer 8c; NPR=3.43,  $T_8=1549^\circ\text{R}$ ,  $V_j=2359$  ft/sec,  $V_{\text{mix}}=1438$  ft/sec,  $M=0.32$ ,  $\phi=25^\circ$  {takeoff}.

Similar exercise is performed for all different test conditions for hardwall, fully treated, flaps only treated, and sidewalls only treated configurations (see Tables 13 through 16). Acoustic suppression for all three treated configurations is evaluated for all the test conditions at two azimuthal locations  $\phi$ ,  $25^\circ$  and  $90^\circ$ . As an example, acoustic suppression for fully treated and flaps only treated configurations at  $25^\circ$  azimuthal location is shown in Figure 307. Acoustic suppression increases with increasing frequency and peaks up between 1 to 4 kHz. Acoustic suppression remains the same at lower test conditions and then decreases with increasing pressure ratio (or mixed velocity). Acoustic suppression due to flap only treated case is nearly half compared to the fully treated configuration, indicating the impact of sidewall treatment.

## 8.2 Typical Results:

**Effect of Aerothermodynamic Conditions:** Effect of aerothermodynamic conditions on measured SPL spectrum at polar angle  $\theta=90^\circ$  for hardwall and fully treated configurations is shown in Figure 308. In general, the SPL increases with increasing nozzle pressure ratio (NPR) or mixed flow velocity ( $V_{\text{mix}}$ ). For treated configuration the high frequency SPL is significantly lower due to the acoustic suppression caused by ejector treatment. Corresponding PWL results are shown in Figure 309, indicating the high frequency acoustic energy is significantly reduced due to treatment. PNL directivities for hardwall and treated configurations are shown in Figure 310.

Modified external component of SPL at  $\theta=90^\circ$  and PWL spectra for hardwall configuration at different test conditions are shown in Figure 311. While the noise level increases with increasing NPR or  $V_{\text{mix}}$ , clearly the external noise dominates the low frequency region. The external noise components are very little influenced due to ejector treatment. Therefore, for external noise components either hardwall or treated configuration results are shown here. OASPL and PNL directivities of external noise component for treated configuration are shown in Figure 312.

Extracted internal noise SPL spectra for hardwall and treated configurations at different  $\theta$  are shown in Figures 313 through 315. In general, the internal noise dominates the high frequency region. Internal noise levels increase with increasing NPR or  $V_{\text{mix}}$ . Significant noise reduction is observed at high frequency domain due to treatment, which is clearly indicated in Figure 316 in terms of PWL spectra. The acoustic suppression in terms of  $\Delta\text{PWL}$ , as shown in Figure 307, is basically derived from the results shown in Figure 316 as

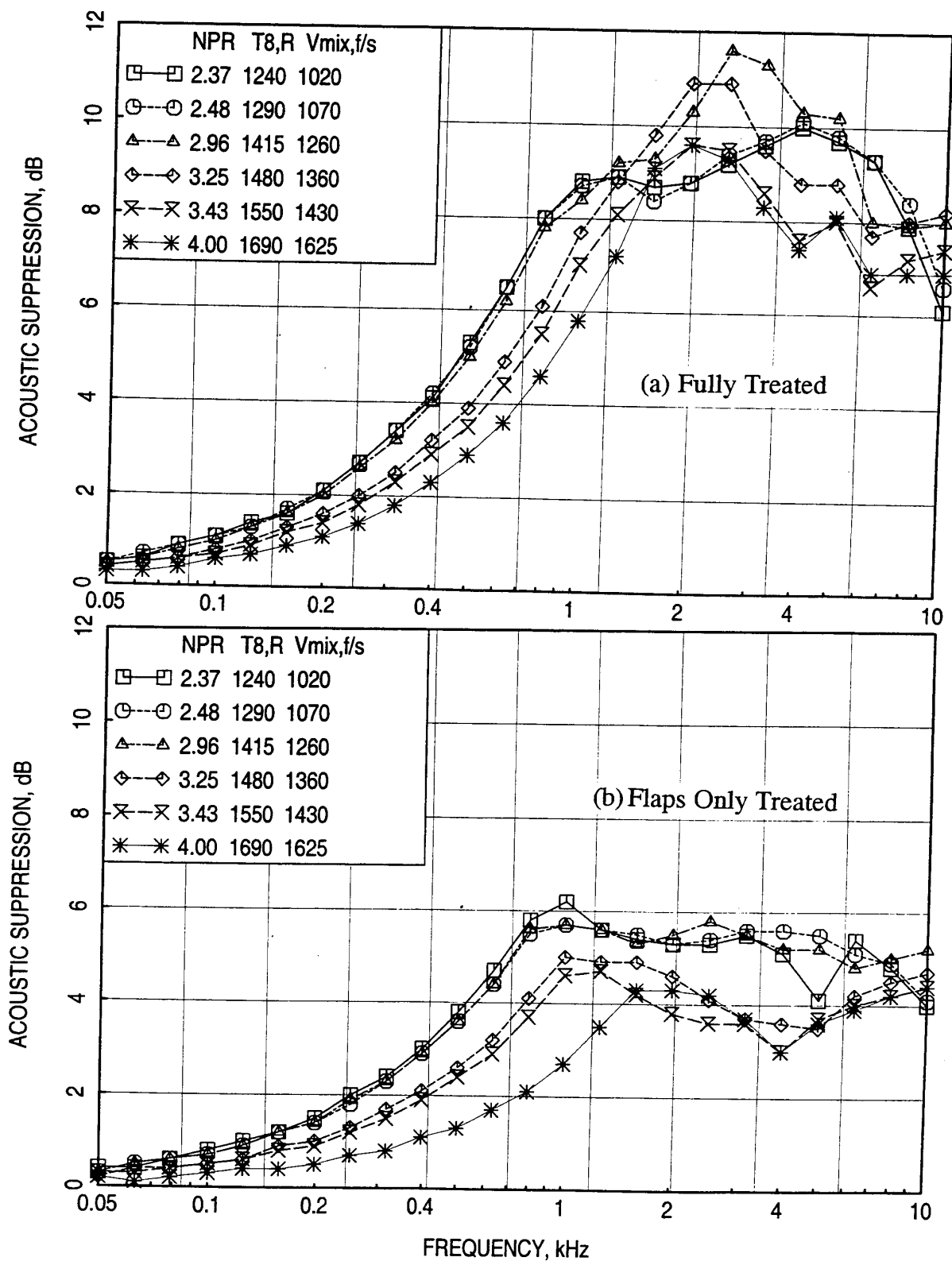


Figure 307. Acoustic suppression at various aerothermodynamic conditions for (a) fully treated and (b) flaps only treated 22.7" long ejector configurations for Gen 2.5 model with mixer 8c,  $M=0.32$ ,  $\phi=25^\circ$ .

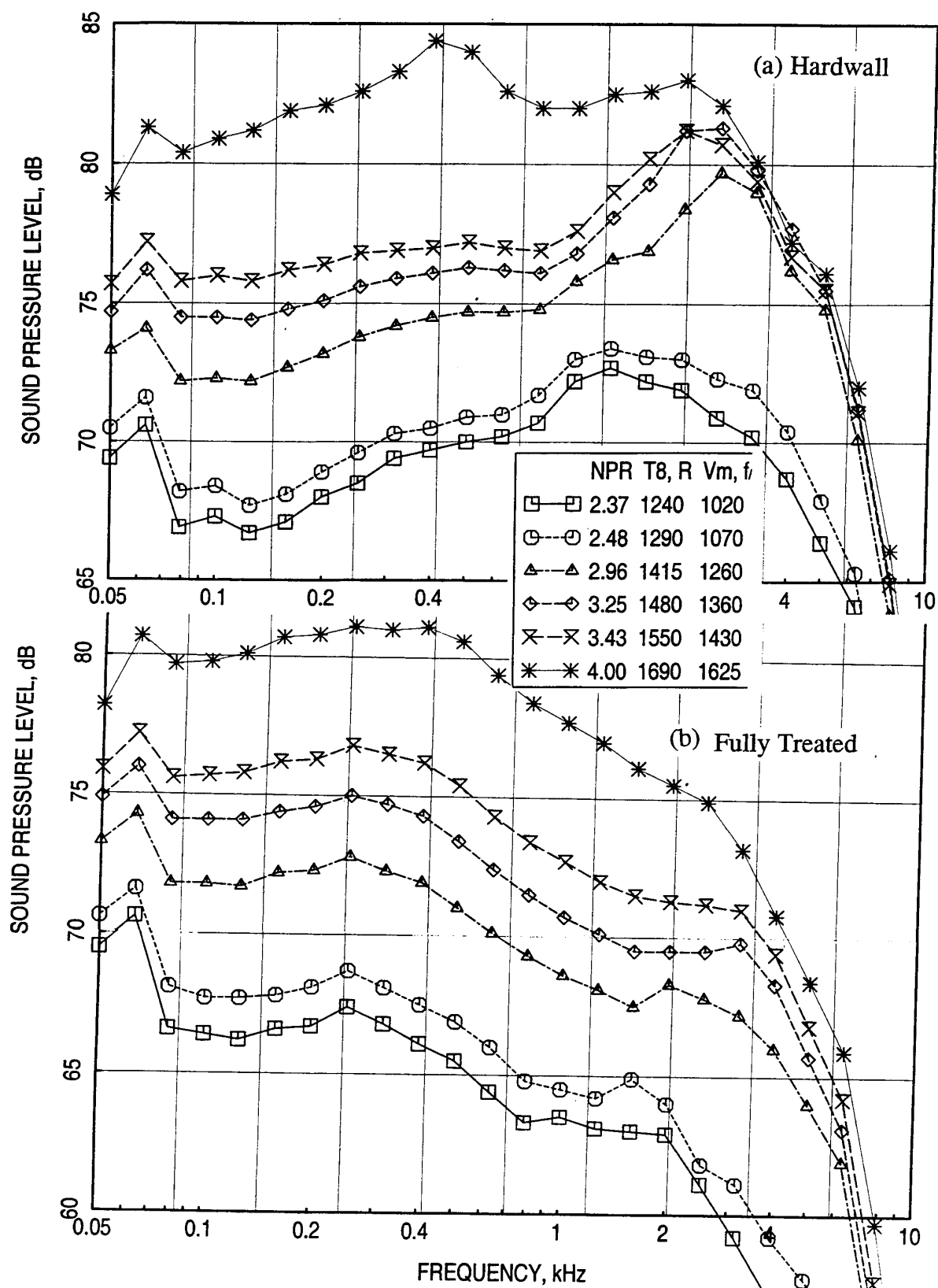


Figure 308. Measured SPL spectra at  $\theta=90^\circ$  for various aerothermodynamic conditions for (a) hardwall and (b) fully treated 22.7" long ejector configurations for Gen 2.5 model with mixer 8c,  $M=0.32$ ,  $\phi=25^\circ$ .

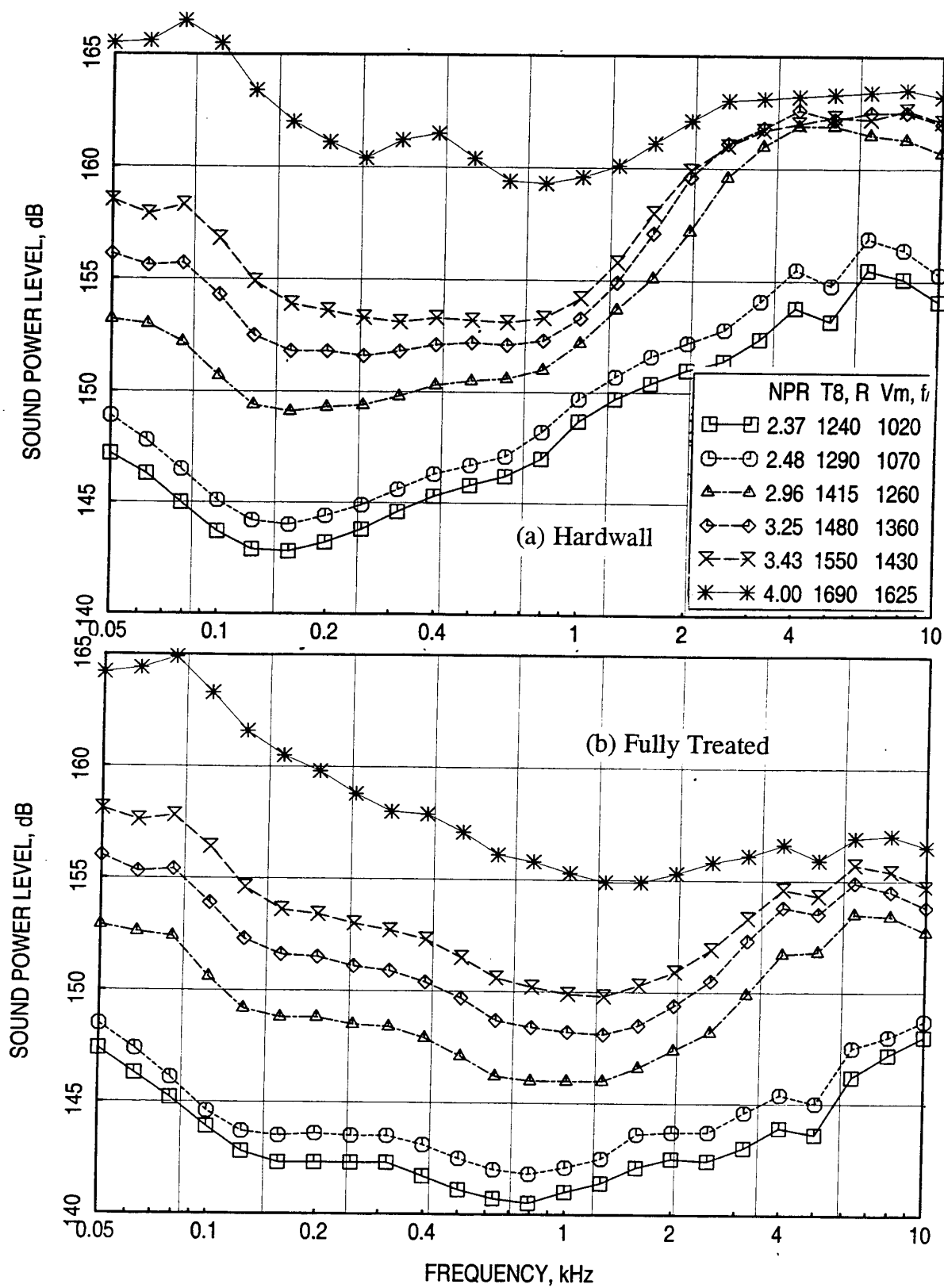


Figure 309. Total PWL spectra for various aerothermodynamic conditions for (a) hardwall and (b) fully treated 22.7" long ejector configurations for Gen 2.5 model with mixer 8c,  $M=0.32$ ,  $\phi=25^\circ$ .

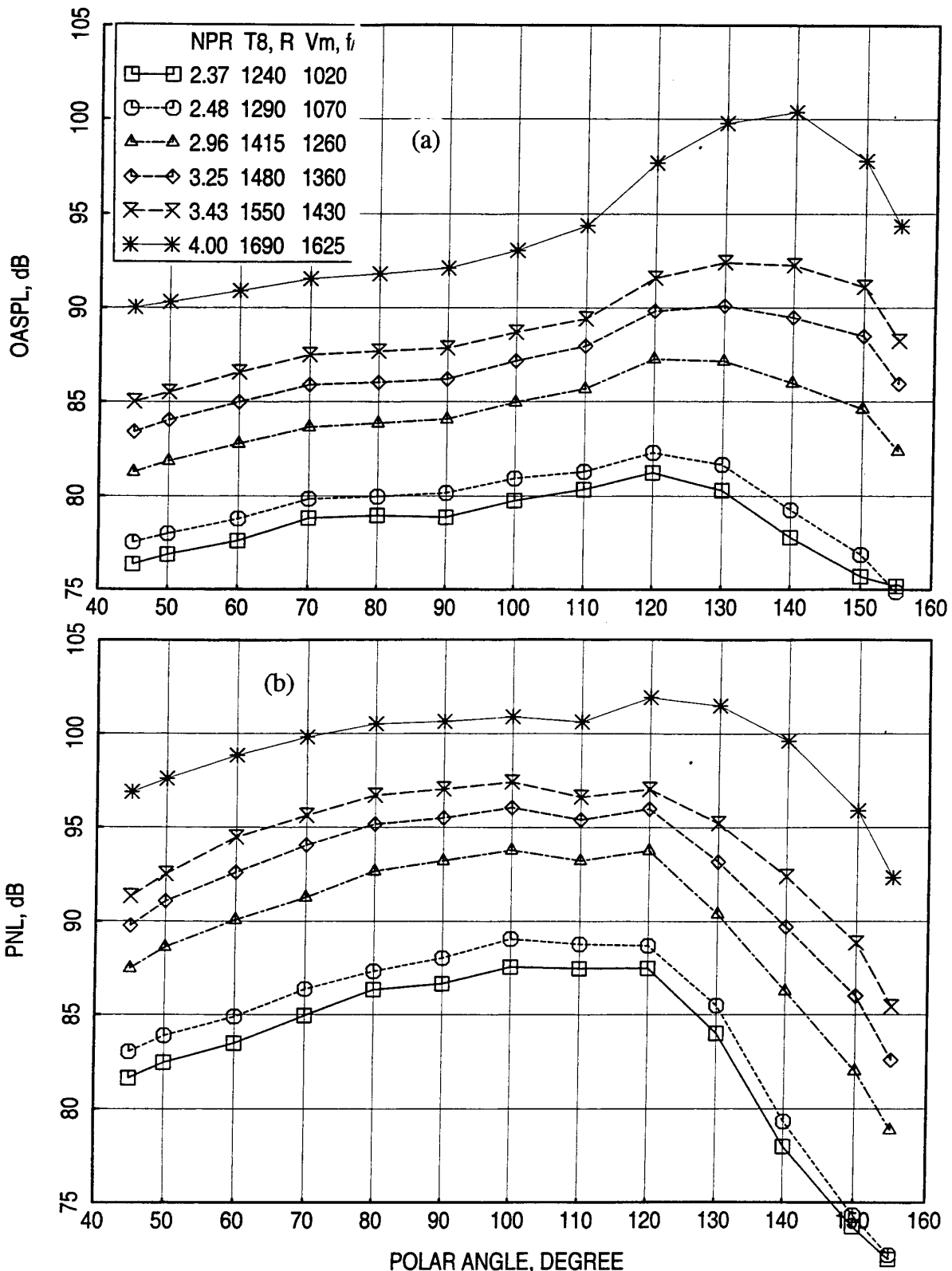


Figure 310. Total OASPL and PNL directivities for various aerothermodynamic conditions for fully treated 22.7" long ejector configuration for Gen 2.5 model with mixer 8c,  $M=0.32$ ,  $\phi=25^\circ$ .

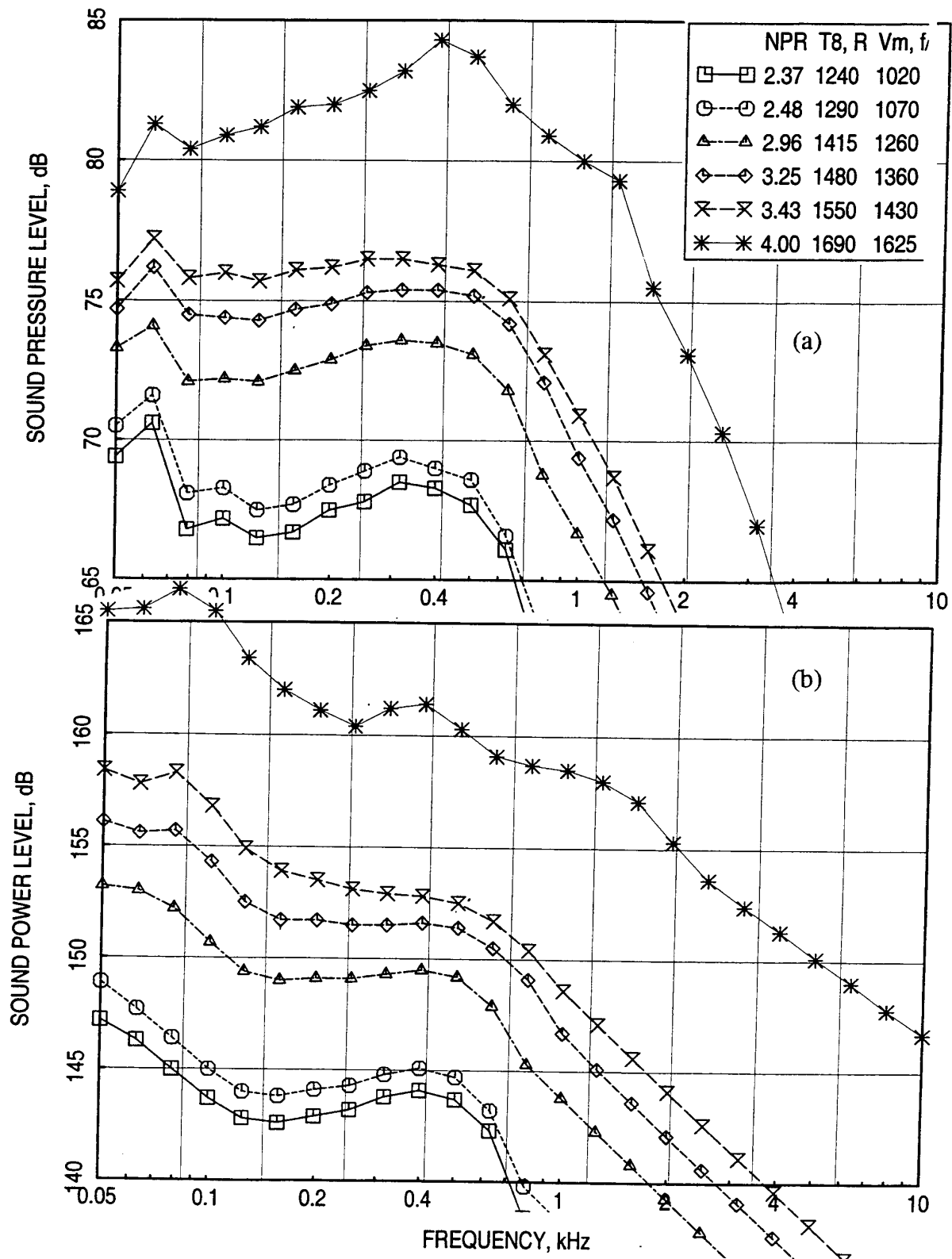


Figure 311. External SPL spectra at  $\theta=90^\circ$  and PWL spectra for various aerothermodynamic conditions for hardwall 22.7" long ejector configuration for Gen 2.5 model with mixer 8c,  $M=0.32$ ,  $\phi=25^\circ$ .



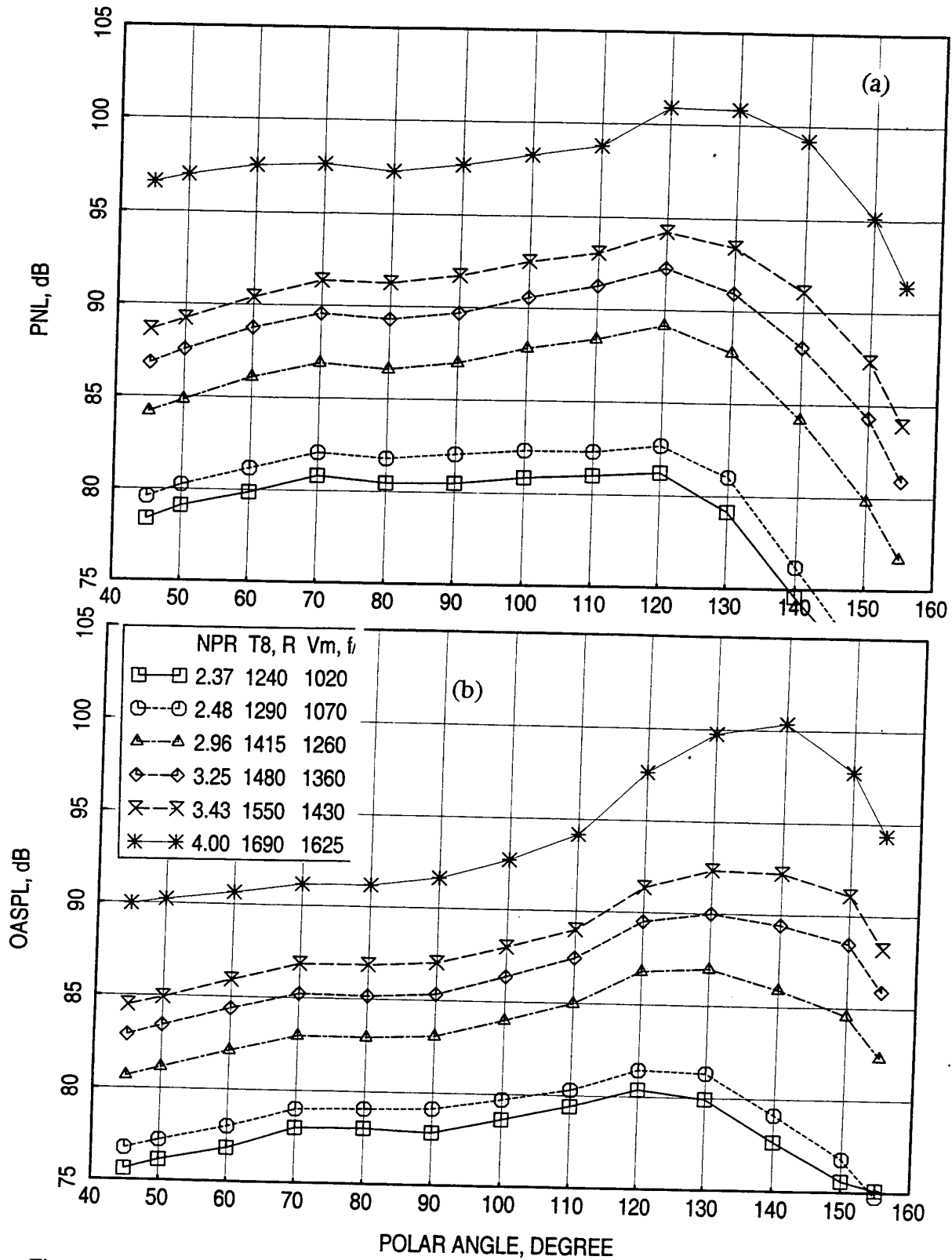


Figure 312. External OASPL and PNL directivities for various aerothermodynamic conditions for fully treated 22.7" long ejector configuration for Gen 2.5 model with mixer 8c,  $M=0.32$ ,  $\phi=25^\circ$ .

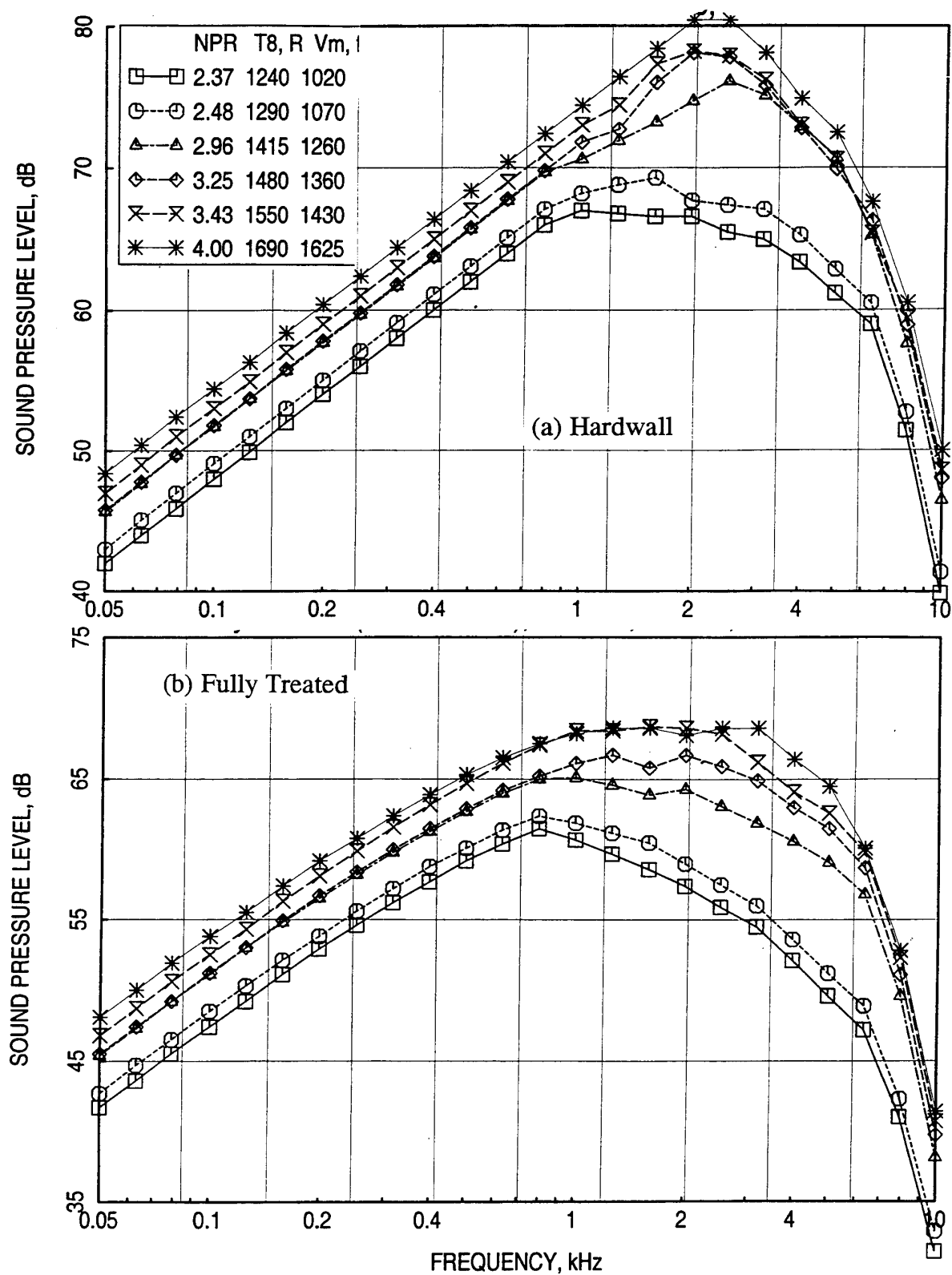


Figure 313. Internal SPL spectra at  $\theta=60^\circ$  for various aerothermodynamic conditions for (a) hardwall and (b) fully treated 22.7" long ejector configurations for Gen 2.5 model with mixer 8c,  $M=0.32$ ,  $\phi=25^\circ$ .

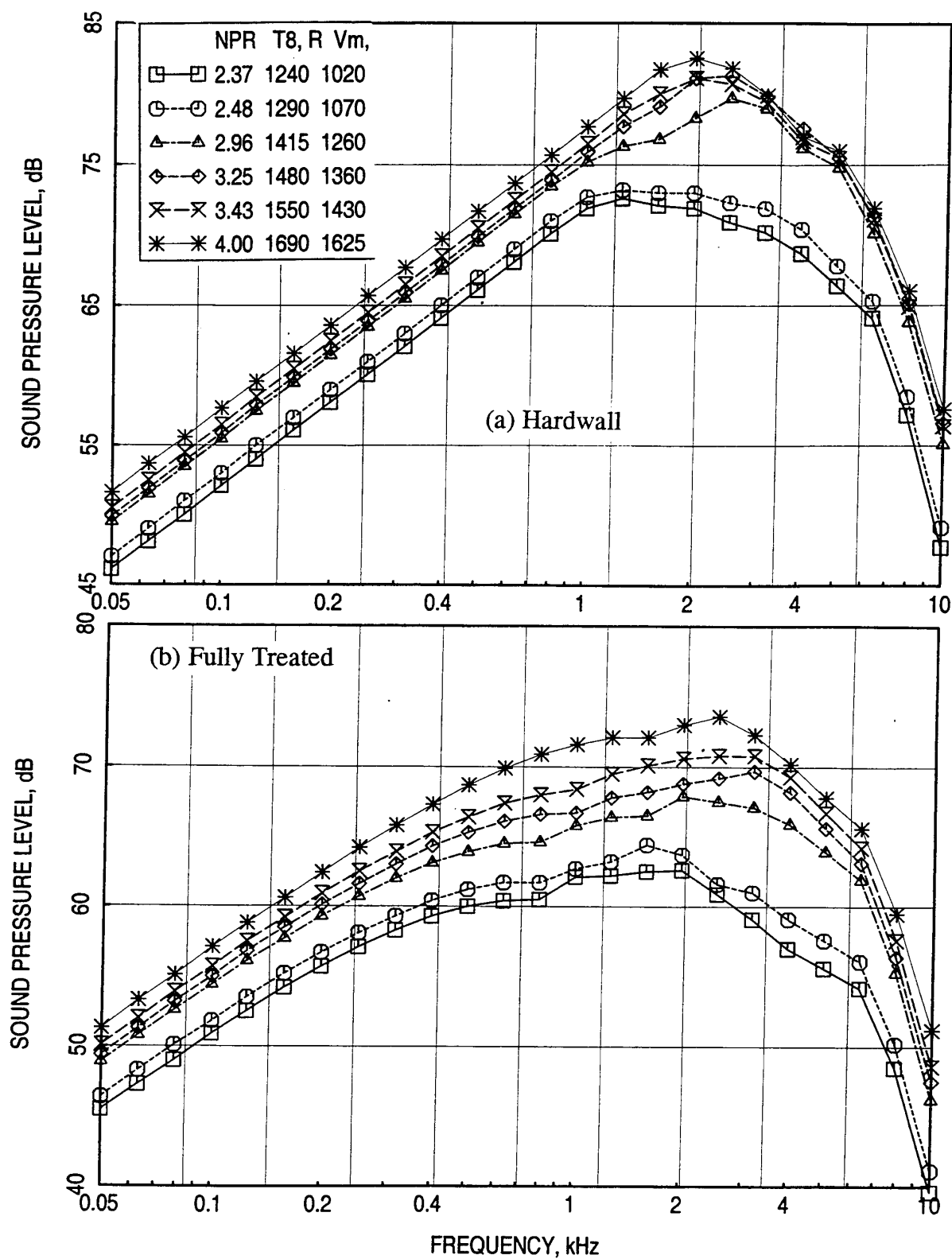


Figure 314. Internal SPL spectra at  $\theta=90^\circ$  for various aerothermodynamic conditions for (a) hardwall and (b) fully treated 22.7" long ejector configurations for Gen 2.5 model with mixer 8c,  $M=0.32$ ,  $\phi=25^\circ$ .

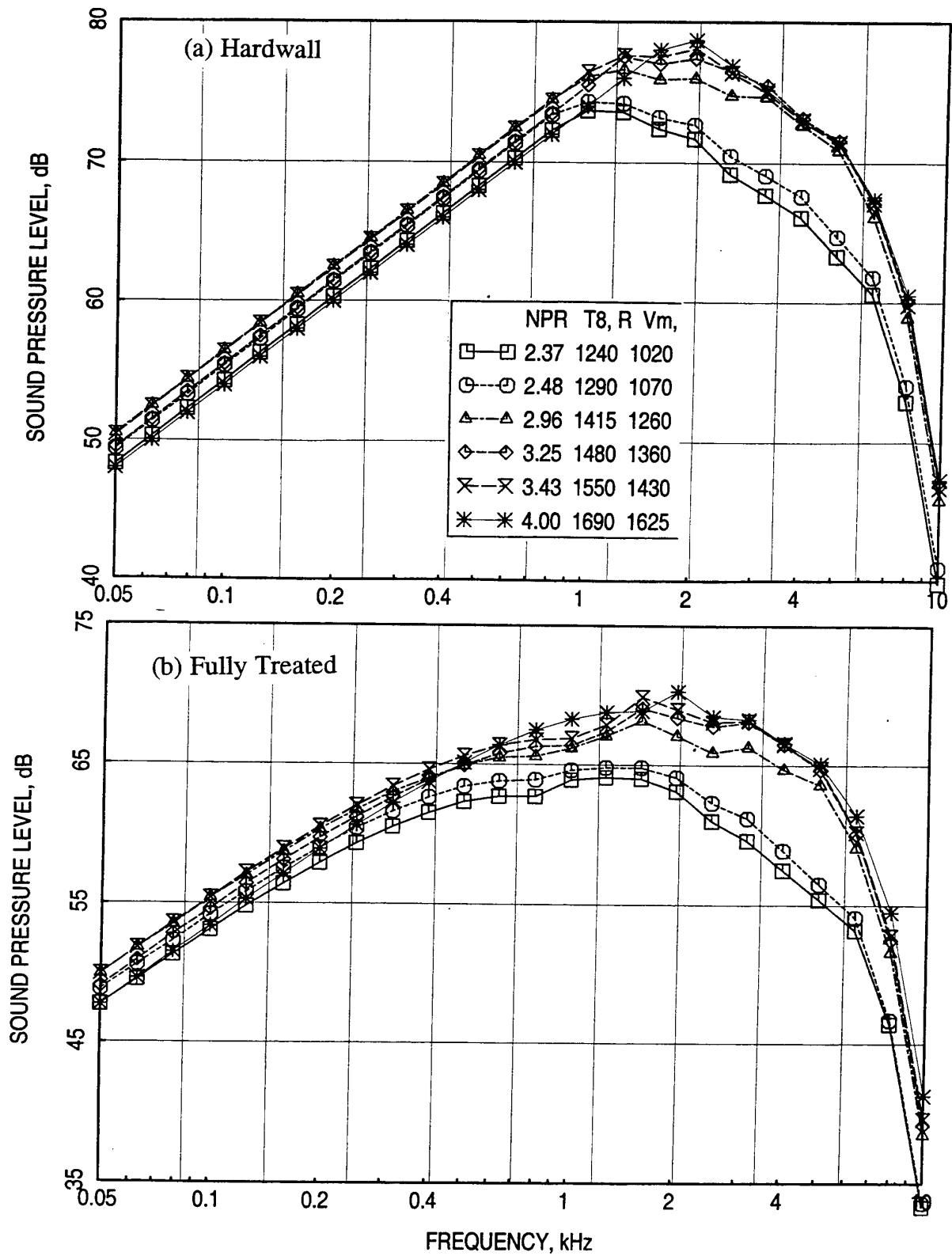


Figure 315. Internal SPL spectra at  $\theta=120^\circ$  for various aerothermodynamic conditions for (a) hardwall and (b) fully treated 22.7" long ejector configurations for Gen 2.5 model with mixer 8c,  $M=0.32$ ,  $\phi=25^\circ$ .

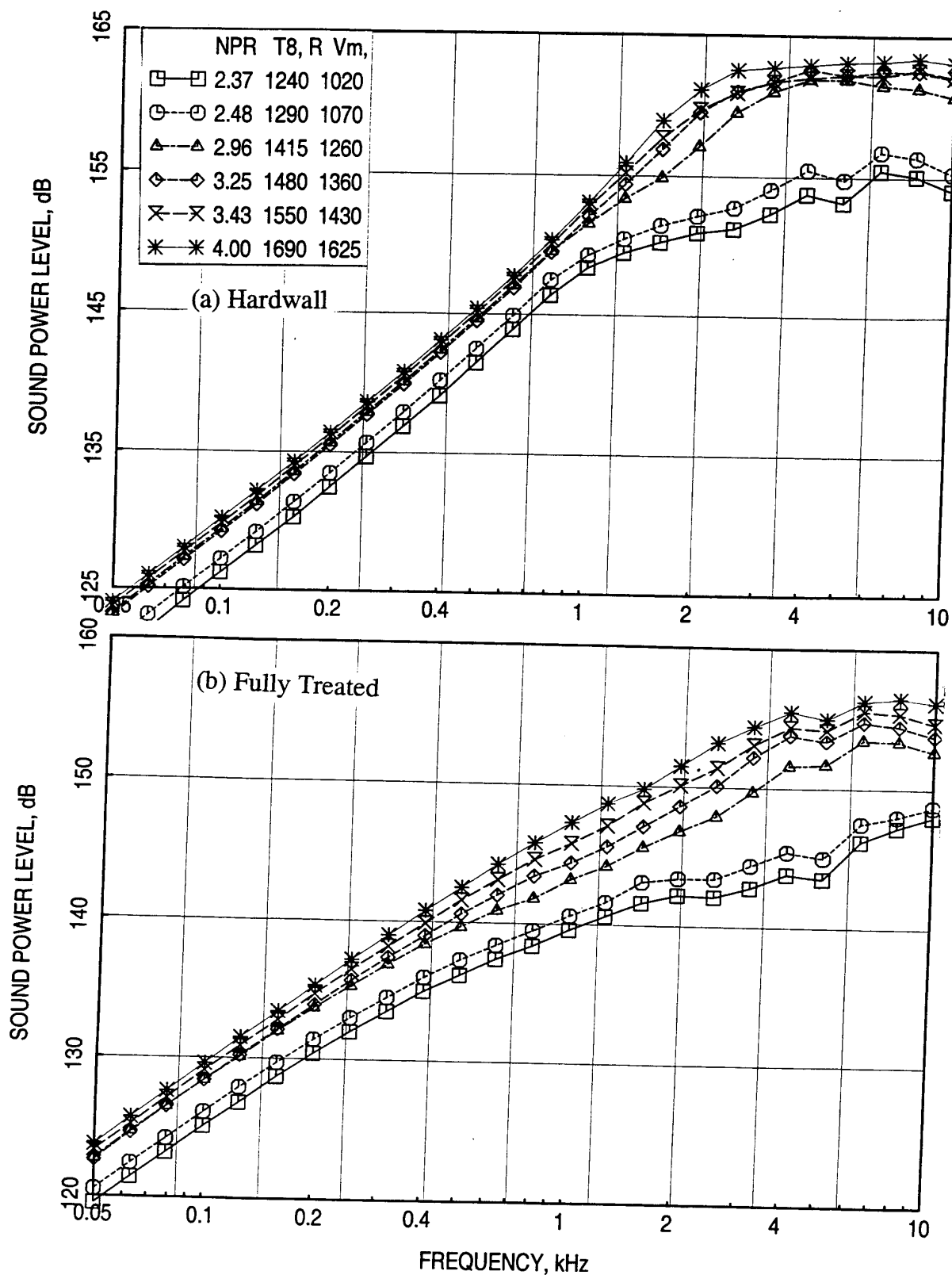


Figure 316. Internal PWL spectra for various aerothermodynamic conditions for (a) hardwall and (b) fully treated 22.7" long ejector configurations for Gen 2.5 model with mixer 8c,  $M=0.32$ ,  $\phi=25^\circ$ .

the difference of PWL between hardwall and treated configurations. OASPL and PNL directivities of internal noise component for treated configuration are shown in Figure 317.

**Effect of Azimuthal Location ( $\phi$ ):** Two dimensional mixer-ejector configurations are tested under HSCT program. The acoustic field for such exhaust systems is unlikely to be axisymmetric in the farfield. Thus, measurements are made at various azimuthal locations  $\phi$ , especially at two locations,  $25^\circ$  and  $90^\circ$ , representing takeoff and cutback flight orientations of the airplane. Measured total and extracted internal SPL at  $\theta=90^\circ$  and PWL spectra for hardwall configuration at different test conditions are shown in Figures 318 and 319, indicating the impact of azimuthal location. Clearly, the noise levels at  $\phi=90^\circ$  are higher at all frequencies for total as well as internal noise components. The dominant noise levels at  $\phi=90^\circ$  are further illustrated in Figure 320 in terms of PNL directivities. External noise component is more axisymmetric in nature, especially in the forward arc. At rear arc the external noise levels are higher at  $\phi=90^\circ$ , especially at higher frequencies. Similar results for fully treated configurations are shown in Figures 321 through 323. Again, the noise levels are higher at  $\phi=90^\circ$  even with fully treated configuration. The effect of azimuthal location on farfield noise level is summarized in Figure 324 in terms of EPNL with respect to NPR for total, external, and internal noise components. Clearly, for each case the EPNL is higher at  $\phi=90^\circ$  compared to  $\phi=25^\circ$ .

**Effect of Treatment Area:** Mixer-ejector configurations with flaps only and sidewalls only treatment are tested to evaluate the impact of treatment area and the relative importance of flap treatment over sidewall treatment on acoustic suppression. Figures 325 and 326 show the SPL spectra comparing various treatment configurations at two polar angles for a cutback condition. The impact of treatment seems to be equally important for flaps and sidewalls. A slightly higher acoustic suppression is observed due to flap treatment. However, the treated flap area is also higher compared to sidewall treatment. This is further illustrated in Figures 327 and 328 in terms of PWL spectra and PNL directivities. Finally, the effect of treatment in terms of EPNL is shown in Figure 329. Clearly, the effect of treatment seems to be equally important for flaps and sidewalls for all test conditions.

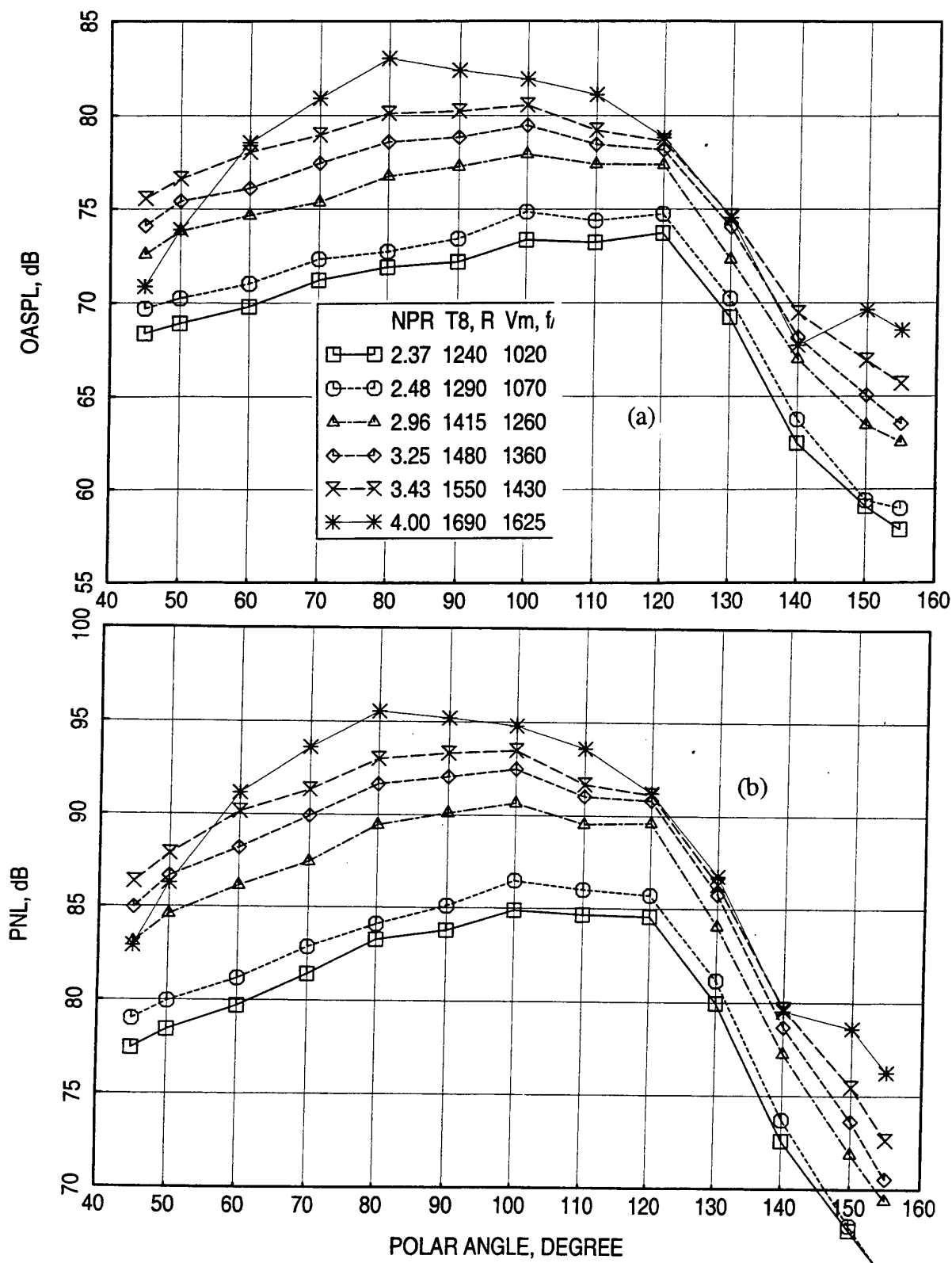


Figure 317. Internal OASPL and PNL directivities for various aerothermodynamic conditions for fully treated 22.7" long ejector configuration for Gen 2.5 model with mixer 8c,  $M=0.32$ ,  $\phi=25^\circ$ .

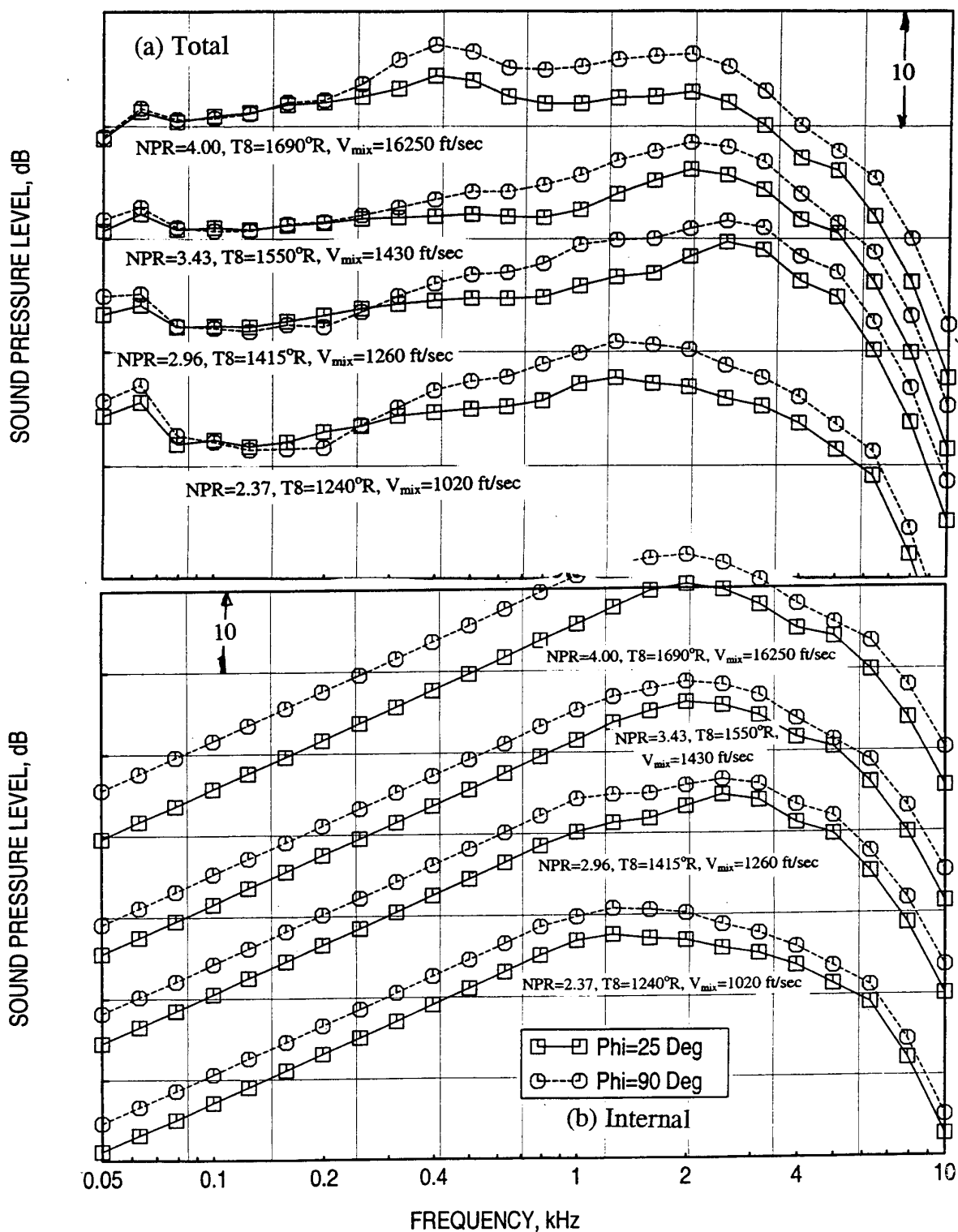


Figure 318. Effect of azimuthal location ( $\phi$ ) on measured and internal SPL spectra at  $\theta=90^\circ$  for various aerothermodynamic conditions for hardwall 22.7" long ejector configuration for Gen 2.5 model with mixer 8c,  $M=0.32$ .



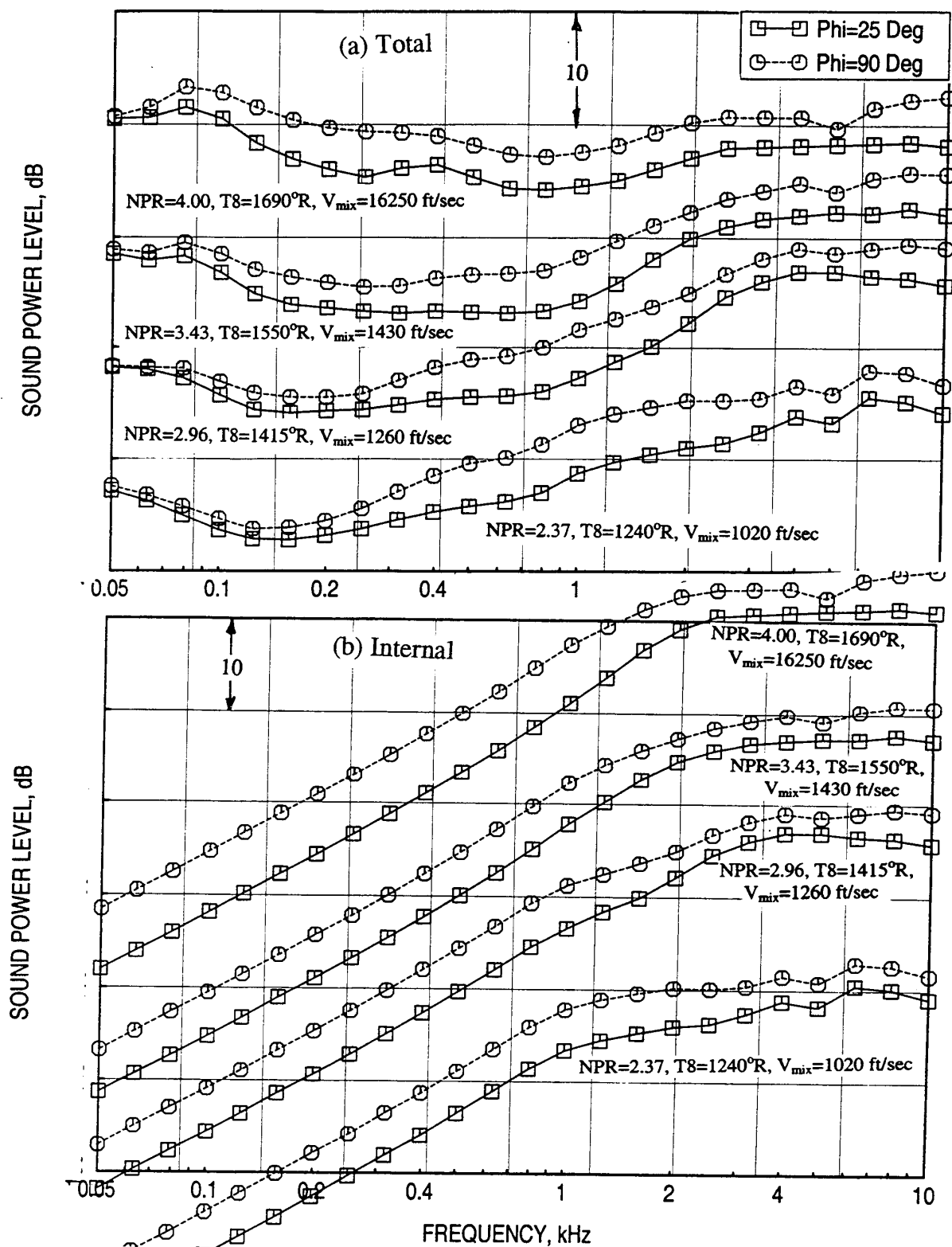


Figure 319. Effect of azimuthal location ( $\phi$ ) on total and internal PWL spectra for various aerothermodynamic conditions for hardwall 22.7" long ejector configuration for Gen 2.5 model with mixer 8c,  $M=0.32$ .



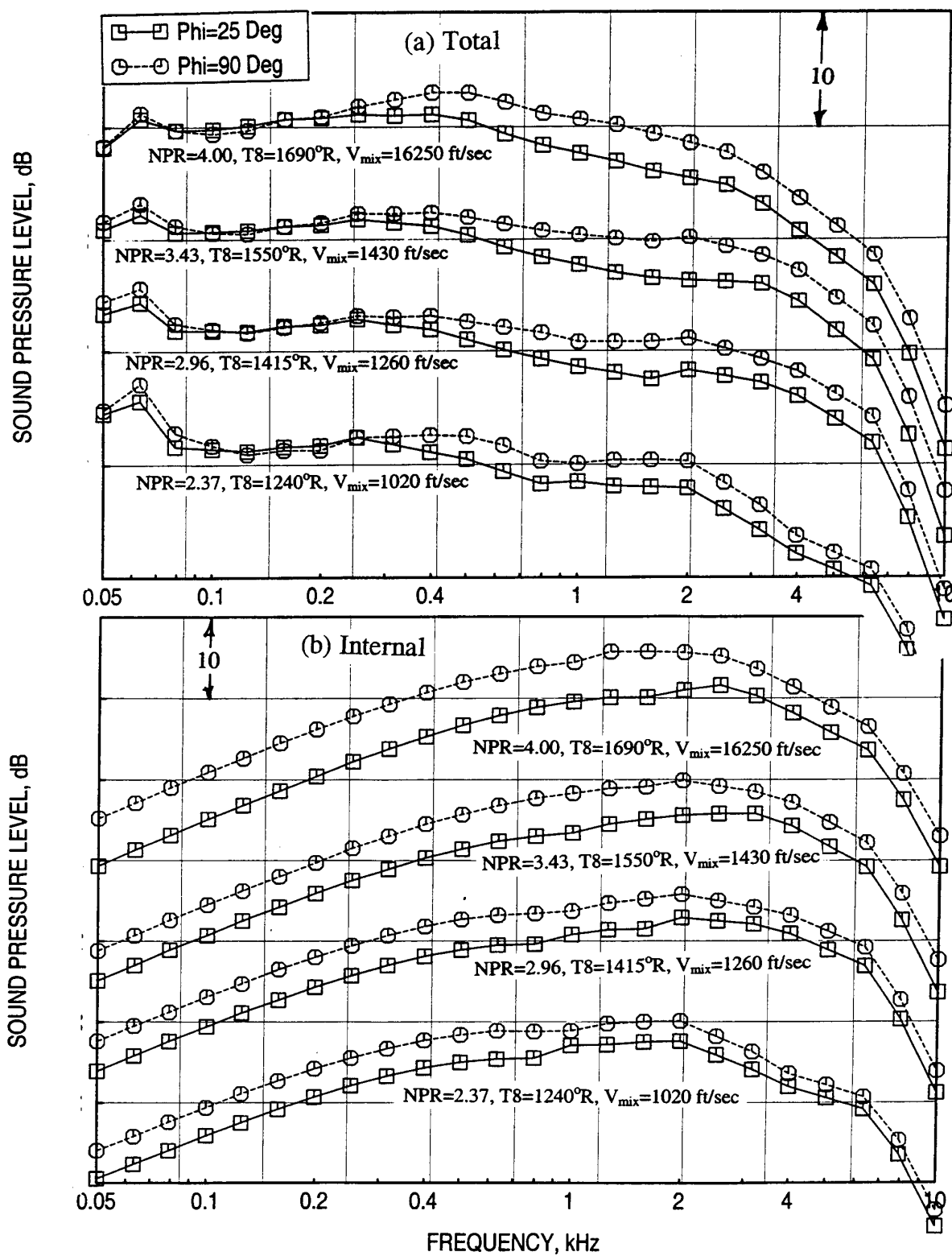


Figure 321. Effect of azimuthal location ( $\phi$ ) on measured and internal SPL spectra at  $\theta=90^\circ$  for various aerothermodynamic conditions for fully treated 22.7" long ejector configuration for Gen 2.5 model with mixer 8c,  $M=0.32$ .

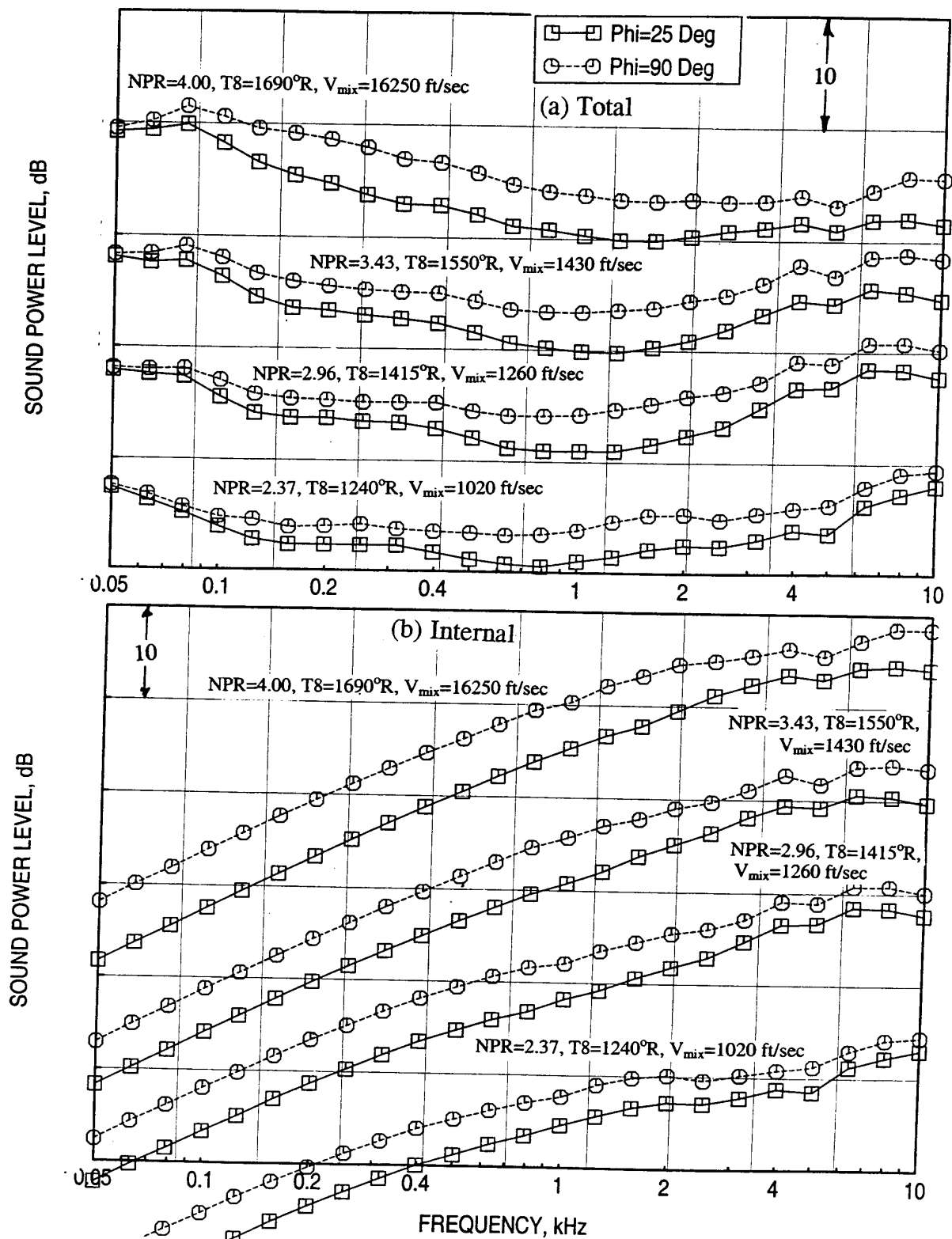


Figure 322. Effect of azimuthal location ( $\phi$ ) on total and internal PWL spectra for various aerothermodynamic conditions for fully treated 22.7" long ejector configuration for Gen 2.5 model with mixer 8c,  $M=0.32$ .



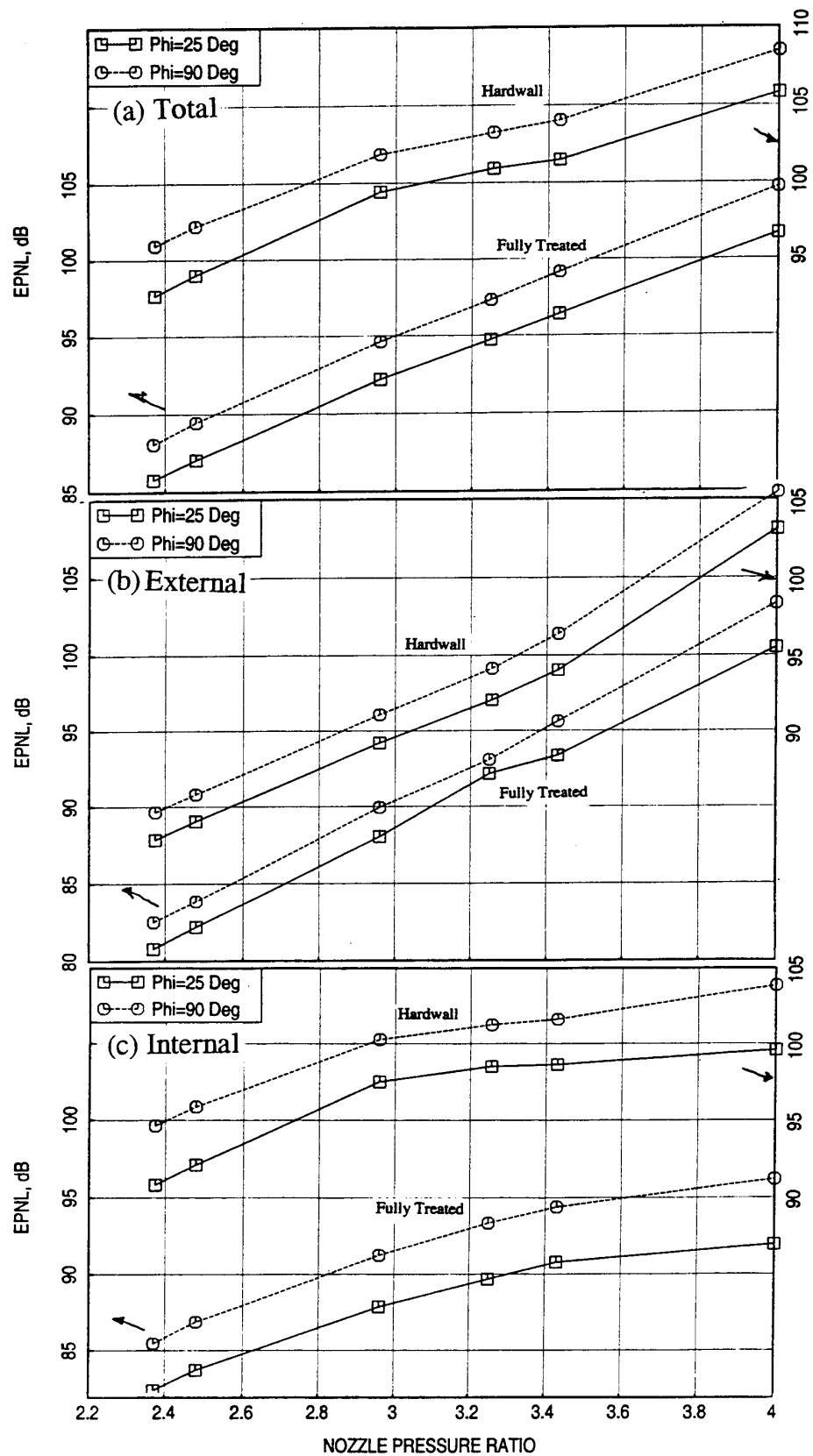


Figure 324. Effect of azimuthal location ( $\phi$ ) on EPNL variation with respect to NPR for hardwall and fully treated 22.7" long ejector configurations for Gen 2.5 model with mixer 8c,  $M=0.32$ .

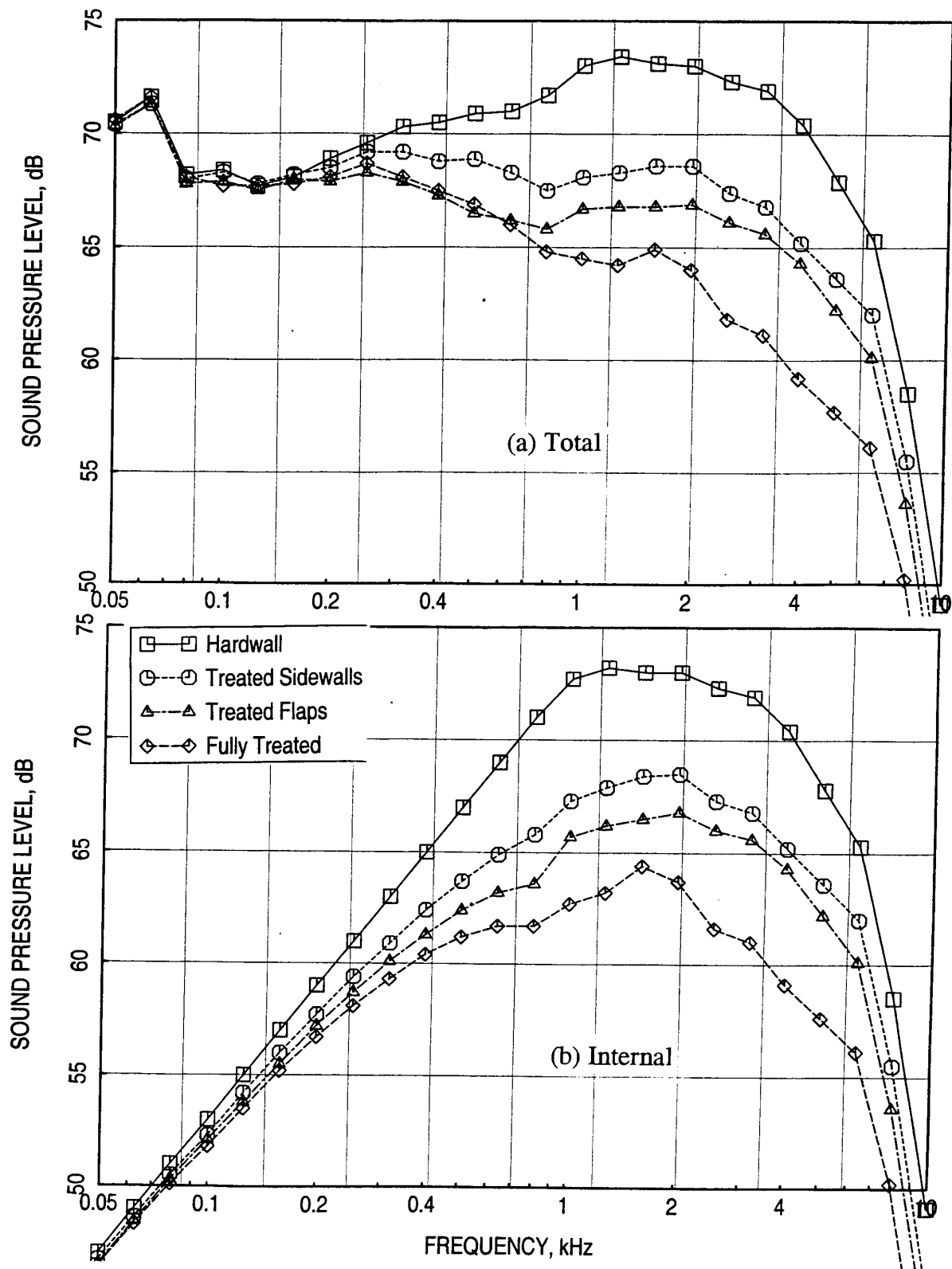


Figure 325. Effect of treatment area on (a) total and (b) internal components of SPL spectra at  $\theta=90^\circ$  for Gen 2.5 model with mixer 8c and 21.7" long ejector; NPR=2.48,  $T_8=1293^\circ\text{R}$ ,  $V_j=1886\text{ ft/sec}$ ,  $V_{\text{mix}}=1079\text{ ft/sec}$ ,  $M=0.32$ ,  $\phi=25^\circ$  {cutback}.

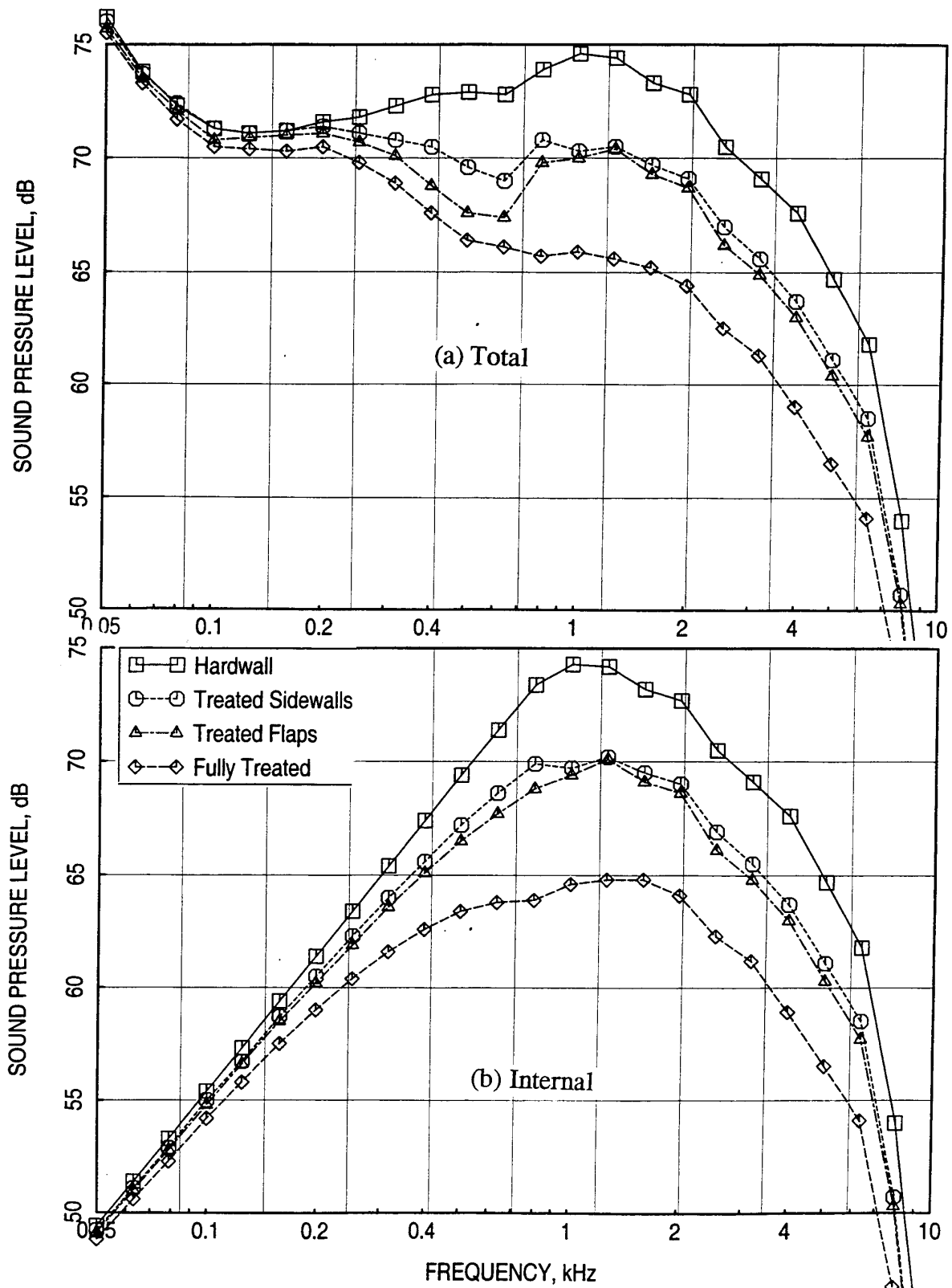


Figure 326. Effect of treatment area on (a) total and (b) internal components of SPL spectra at  $\theta=120^\circ$  for Gen 2.5 model with mixer 8c and 21.7" long ejector; NPR=2.48,  $T_8=1293^\circ\text{R}$ ,  $V_j=1886\text{ ft/sec}$ ,  $V_{\text{mix}}=1079\text{ ft/sec}$ ,  $M=0.32$ ,  $\phi=25^\circ$  {cutback}.



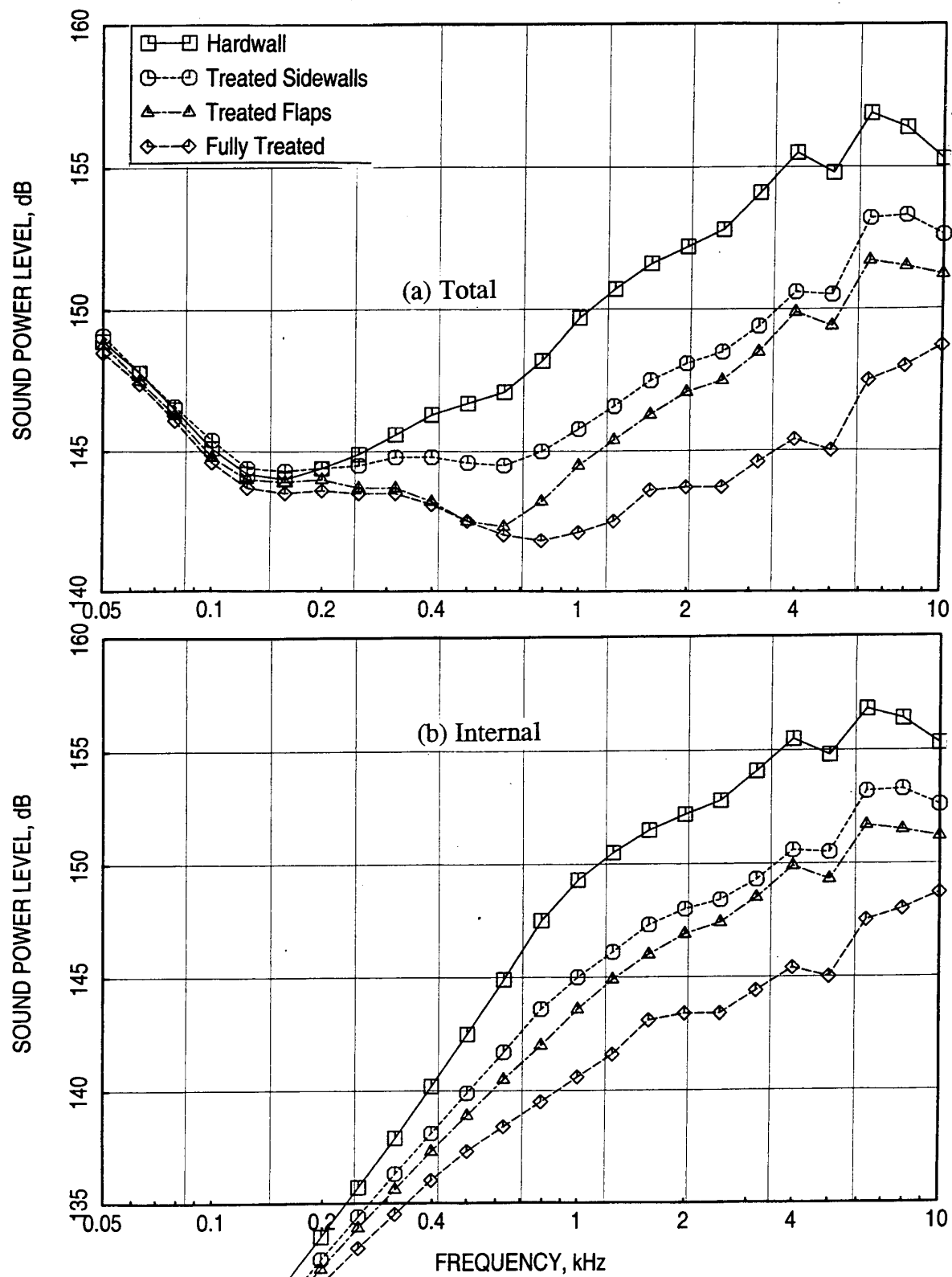


Figure 327. Effect of treatment area on (a) total and (b) internal components of PWL spectra for Gen 2.5 model with mixer 8c and 21.7" long ejector; NPR=2.48, T8=1293°R,  $V_j=1886$  ft/sec,  $V_{mix}=1079$  ft/sec,  $M=0.32$ ,  $\phi=25^\circ$  {cutback}.

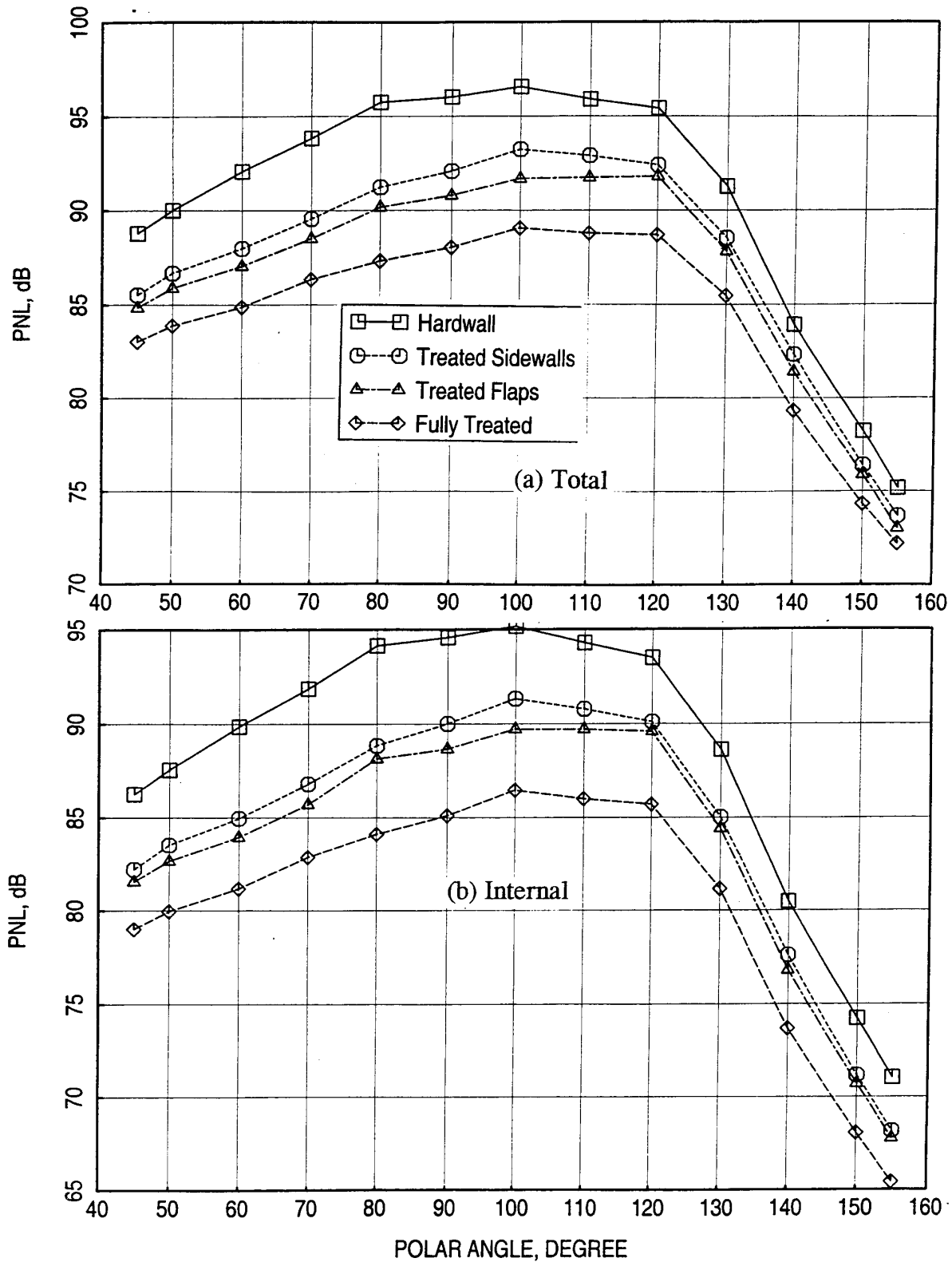


Figure 328. Effect of treatment area on (a) total and (b) internal components of PNL directivities for Gen 2.5 model with mixer 8c and 21.7" long ejector; NPR=2.48, T8=1293°R,  $V_j=1886$  ft/sec,  $V_{mix}=1079$  ft/sec,  $M=0.32$ ,  $\phi=25^\circ$  {cutback}.

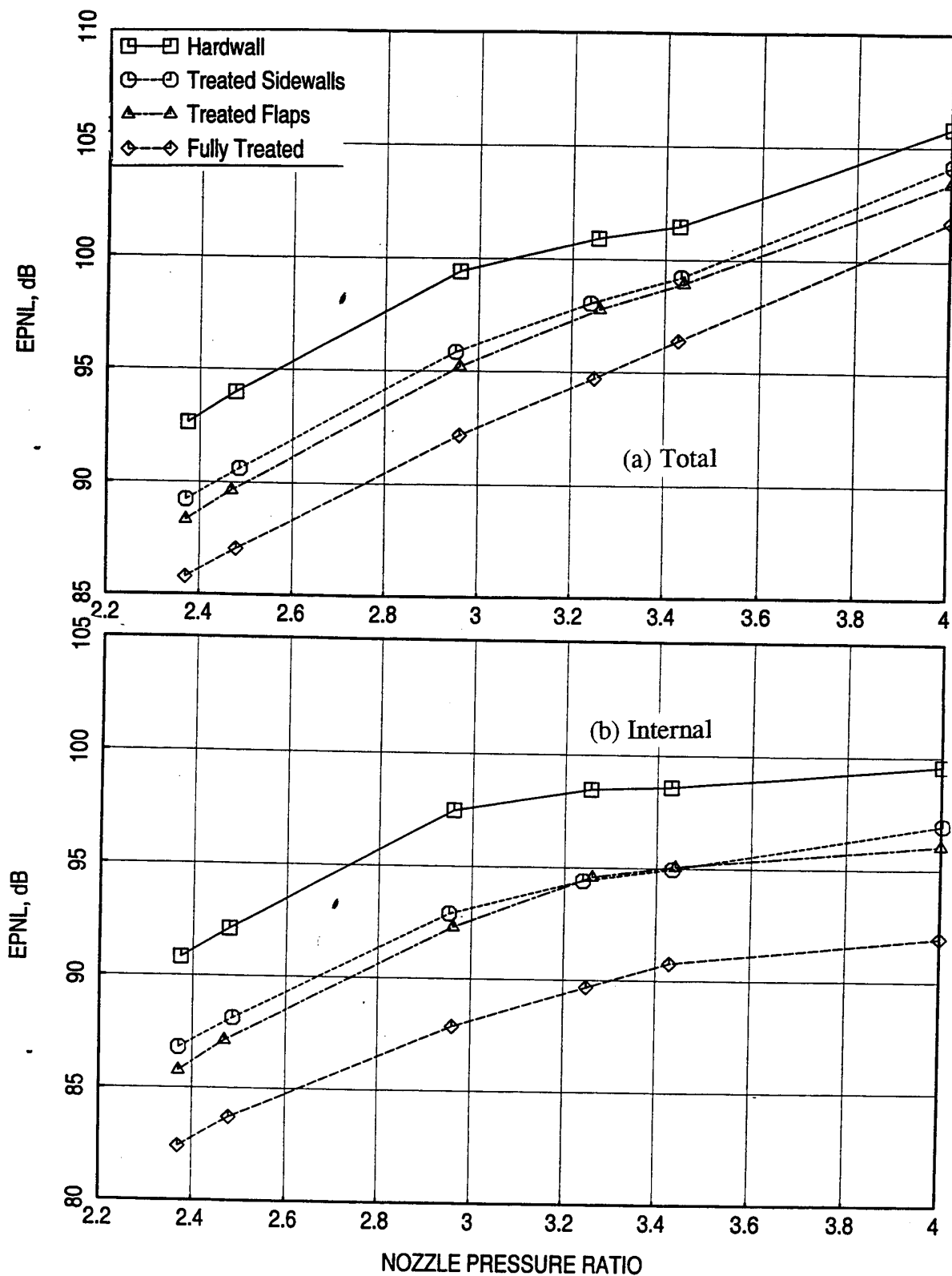


Figure 329. Effect of treatment area on (a) total and (b) internal components of EPNL plotted with respect to NPR for Gen 2.5 model with mixer 8c and 21.7" long ejector,  $M=0.32$ ,  $\phi=25^\circ$  {cutback}.

## 9.0 CONCLUSIONS AND RECOMMENDATIONS

Significant amount of experiments and data analysis planned under the second phase of the Liner Technology Program is performed. The experimental results are presented in this report to illustrate various acoustic characteristics of liner configurations. Limited interpretation of data is included. However, a number of experiments and data analyses crucial to the program are not conducted due to the HSCT Program closeout. Most of the experimental data is successfully utilized in the correlation development to predict normal impedance and acoustic suppression. The correlation development process for normal impedance and acoustic suppression is described in a separate report (Ref. 3). Salient trends and observations of the experimental results are described in different sections of this report. While, the objective of the Liner Technology Program to develop a **liner design methodology** is successfully achieved, a few crucial results are not acquired. In future, when the HSCT Program will be activated, the following aspects are highly recommended to be performed for the improvement of the liner design methodology;

- A few diagnostic tests, using the modified high frequency impedance tube to evaluate complex propagation speed of sound in the bulk medium, are essential.
- Flow duct tests at ambient temperature condition are to be performed for a few bulk absorber panels of Silicon Carbide of different pores/inch (other than 100 ppi), T-Foam of different densities (other than 12 lbf) and constructions, and at least the 5% dense Feltmetal. In total six to seven bulk materials with one or two different facesheets are recommended for flow duct test. The results of these tests will improve the grazing flow effect prediction for normal impedance.
- All the insitu data, already acquired and will be acquired, should be analyzed using the actual propagation speed of sound in the respective bulk medium.
- T-Foam development process needs to be continued to obtain an optimum T-Foam bulk for mixer-ejector application.
- More mixer-ejector acoustic data for different model scale tests are to be utilized in the acoustic suppression prediction correlation to account the aspect of liner scaling.
- The correlations, currently developed, utilized limited amount of data due to the time constraint imposed due to HSCT closeout. It is highly recommended that the correlatons

currently developed are to be improved utilizing more data including the additional data to be acquired in the future.

## **APPENDIX A**

A number of tables are included in this appendix listing the file names containing various test data. Boundary layer parameters calculated from the boundary layer profiles are listed in the tables containing the file names for boundary layer data.



Table A1 (a). Configurations to Study the Effect of Excitation Intensity, Bulk Type, Bulk Depth, & Facesheet Parameters (Porosity, Thickness, & hole Diameter) on High Frequency Normal Impedance

Bulk Material	Depth Nominal/ Actual (in)	Facesheet For Porosites: Porosity, S in %; Thickness, t in inch; Hole Diameter, d in inch																	Intensity OASPL dB										
		All file names end with '.smt'																											
		No	T1-1			T1-2			T1-3			T1-4			T1-6			T1-8			T1-9			T1-10	T1-11	T-12			
		Facesheet	S	t	d	S	t	d	S	t	d	S	t	d	S	t	d	S	t	d	S	t	d	S	t	d	Linear	Linear	Linear
			20,.025,.04		30,.025,.04		40,.025,.04		40,.025,.04		40,.025,.04		40,.025,.08		40,.04,.04		40,.06,.04		5 Rayls		10 Rayls		15 Rayls		15 Rayls				
Facesheet Only			fs250l-t1		fs250l-t2		fs250l-t3		fs250l-t4		fs250l-t6		fs250l-t8		fs250l-t9		fs250l-t10		fs250l-t11		fs250l-t12		fs250l-t12		140				
			fs250-t1		fs250-t2		fs250-t3		fs250-t4		fs250-t6		fs250-t8		fs250-t9		fs250-t10		fs250-t11		fs250-t12		fs250-t12		150				
			fs250h-t1		fs250h-t2		fs250h-t3		fs250h-t4		fs250h-t6		fs250h-t8		fs250h-t9		fs250h-t10		fs250h-t11		fs250h-t12		fs250h-t12		155				
100ppi SiC	0.25	250sic1	250sic1-t1		250sic1-t2		250sic1-t3		250sic1-t4		250sic1-t6		250sic1-t8		250sic1-t9		250sic1-t10		250sic1-t11		250sic1-t12		250sic1-t12		140				
		250sic1	250sic1-t1		250sic1-t2		250sic1-t3		250sic1-t4		250sic1-t6		250sic1-t8		250sic1-t9		250sic1-t10		250sic1-t11		250sic1-t12		250sic1-t12		150				
		250hsic1	250hsic1-t1		250hsic1-t2		250hsic1-t3		250hsic1-t4		250hsic1-t6		250hsic1-t8		250hsic1-t9		250hsic1-t10		250hsic1-t11		250hsic1-t12		250hsic1-t12		155				
100ppi SiC	0.5	500sic1	500sic1-t1		500sic1-t2		500sic1-t3		500sic1-t4		500sic1-t6		500sic1-t8		500sic1-t9		500sic1-t10		500sic1-t11		500sic1-t12		500sic1-t12		140				
		500sic1	500sic1-t1		500sic1-t2		500sic1-t3		500sic1-t4		500sic1-t6		500sic1-t8		500sic1-t9		500sic1-t10		500sic1-t11		500sic1-t12		500sic1-t12		150				
		500hsic1	500hsic1-t1		500hsic1-t2		500hsic1-t3		500hsic1-t4		500hsic1-t6		500hsic1-t8		500hsic1-t9		500hsic1-t10		500hsic1-t11		500hsic1-t12		500hsic1-t12		155				
100ppi SiC	1.0	1000sic1	1000sic1-t1		1000sic1-t2		1000sic1-t3		1000sic1-t4		1000sic1-t6		1000sic1-t8		1000sic1-t9		1000sic1-t10		1000sic1-t11		1000sic1-t12		1000sic1-t12		140				
		1000sic1	1000sic1-t1		1000sic1-t2		1000sic1-t3		1000sic1-t4		1000sic1-t6		1000sic1-t8		1000sic1-t9		1000sic1-t10		1000sic1-t11		1000sic1-t12		1000sic1-t12		150				
		1000hsic1	1000hsic1-t1		1000hsic1-t2		1000hsic1-t3		1000hsic1-t4		1000hsic1-t6		1000hsic1-t8		1000hsic1-t9		1000hsic1-t10		1000hsic1-t11		1000hsic1-t12		1000hsic1-t12		155				
100ppi SiC	2.0	2000sic1	2000sic1-t1		2000sic1-t2		2000sic1-t3		2000sic1-t4		2000sic1-t6		2000sic1-t8		2000sic1-t9		2000sic1-t10		2000sic1-t11		2000sic1-t12		2000sic1-t12		140				
		2000sic1	2000sic1-t1		2000sic1-t2		2000sic1-t3		2000sic1-t4		2000sic1-t6		2000sic1-t8		2000sic1-t9		2000sic1-t10		2000sic1-t11		2000sic1-t12		2000sic1-t12		150				
		2000hsic1	2000hsic1-t1		2000hsic1-t2		2000hsic1-t3		2000hsic1-t4		2000hsic1-t6		2000hsic1-t8		2000hsic1-t9		2000hsic1-t10		2000hsic1-t11		2000hsic1-t12		2000hsic1-t12		155				
200ppi SiC	0.25/0.259	250sic2	250sic2-t1		250sic2-t2		250sic2-t3		250sic2-t4		250sic2-t6		250sic2-t8		250sic2-t9		250sic2-t10		250sic2-t11		250sic2-t12		250sic2-t12		150				
		250hsic2					250hsic2-t3					250hsic2-t8					250hsic2-t11							140					
200ppi SiC	0.5/0.509	500sic2					500sic2-t3					500sic2-t8					500sic2-t11							155					
		500hsic2					500hsic2-t3					500hsic2-t8					500hsic2-t11							140					
200ppi SiC	1.0	1000sic2					1000sic2-t3					1000sic2-t8					1000sic2-t11							150					
		1000hsic2					1000hsic2-t3					1000hsic2-t8					1000hsic2-t11							155					
200ppi SiC	2.0	2000sic2					2000sic2-t3					2000sic2-t8					2000sic2-t11							140					
		2000hsic2					2000hsic2-t3					2000hsic2-t8					2000hsic2-t11							150					
400ppi SiC	0.25	250sic4					250sic4-t3					250sic4-t8					250sic4-t11							155					
		250hsic4					250hsic4-t3					250hsic4-t8					250hsic4-t11							140					
400ppi SiC	0.5	500sic4					500sic4-t3					500sic4-t8					500sic4-t11							155					
		500hsic4					500hsic4-t3					500hsic4-t8					500hsic4-t11							140					
		500hsic4					500hsic4-t3					500hsic4-t8					500hsic4-t11							150					
		500hsic4					500hsic4-t3					500hsic4-t8					500hsic4-t11							155					



Table A1 (b). Configurations to Study the Effect of Excitation Intensity, Bulk Type, Bulk Depth, & Facesheet Parameters (Porosity, Thickness, & hole Diameter) on High Frequency Normal Impedance

Bulk Material		Depth Nominal/ Actual (in)	Facesheet For Perforates: Porosity, S in %; Thickness, t in inch; Hole Diameter, d in inch All file names end with '.smt'																						Intensity OASPL dB
		No	T1-1		T1-2		T1-3		T1-4		T1-6		T1-8		T1-9		T1-10		T1-11		T1-12				
		Facesheet	S	t	d	S	t	d	S	t	d	S	t	d	S	t	d	S	t	d	S	t	d		
			20,.025,.04			30,.025,.04			40,.025,.04			40,.025,.08			40,.04,.04			40,.06,.04			Linear			Linear	
400ppi SiC	1.0	1000lsic4							1000lsic4-t3						1000lsic4-t8						10 Rayls			15 Rayls	
		1000sic4							1000sic4-t3						1000sic4-t8						1000sic4-t10			1000sic4-t11	
		1000hsic4							1000hsic4-t3						1000hsic4-t8						1000hsic4-t10			1000hsic4-t11	
400ppi SiC	2.0	2000lsic4							2000lsic4-t3						2000lsic4-t8						2000lsic4-t10			2000lsic4-t11	
		2000sic4							2000sic4-t3						2000sic4-t8						2000sic4-t10			2000sic4-t11	
		2000hsic4							2000hsic4-t3						2000hsic4-t8						2000hsic4-t10			2000hsic4-t11	
600ppi SiC	0.25/0.257	250lsic6							250lsic6-t3						250lsic6-t8						250lsic6-t10			250lsic6-t11	
		250sic6							250sic6-t3						250sic6-t8						250sic6-t10			250sic6-t11	
		250hsic6							250hsic6-t3						250hsic6-t8						250hsic6-t10			250hsic6-t11	
600ppi SiC	0.5/0.508	500lsic6							500lsic6-t3						500lsic6-t8						500lsic6-t10			500lsic6-t11	
		500sic6							500sic6-t3						500sic6-t8						500sic6-t10			500sic6-t11	
		500hsic6							500hsic6-t3						500hsic6-t8						500hsic6-t10			500hsic6-t11	
T-Foam12(M)	0.25/0.235	250lmftr							250lmftr-t3						250lmftr-t8						250lmftr-t10			250lmftr-t11	
		250mftr							250mftr-t3						250mftr-t8						250mftr-t10			250mftr-t11	
		250hmftr							250hmftr-t3						250hmftr-t8						250hmftr-t10			250hmftr-t11	
T-Foam12(M)	0.5/0.44	500lmftr							500lmftr-t3						500lmftr-t8						500lmftr-t10			500lmftr-t11	
		500mftr							500mftr-t3						500mftr-t8						500mftr-t10			500mftr-t11	
		500hmftr							500hmftr-t3						500hmftr-t8						500hmftr-t10			500hmftr-t11	
T-Foam12(M)	1.0	1000lmftr							1000lmftr-t3						1000lmftr-t8						1000lmftr-t10			1000lmftr-t11	
		1000mftr							1000mftr-t3						1000mftr-t8						1000mftr-t10			1000mftr-t11	
		1000hmftr							1000hmftr-t3						1000hmftr-t8						1000hmftr-t10			1000hmftr-t11	
T-Foam12(M)	2.0/1.95	2000lmftr							2000lmftr-t3						2000lmftr-t8						2000lmftr-t10			2000lmftr-t11	
		2000mftr							2000mftr-t3						2000mftr-t8						2000mftr-t10			2000mftr-t11	
		2000hmftr							2000hmftr-t3						2000hmftr-t8						2000hmftr-t10			2000hmftr-t11	
T-Foam8(L)	0.25/0.24	250lhf							250lhf-t3						250lhf-t8						250lhf-t10			250lhf-t11	
		250lhf / 8tf245							250lhf-t3 / t1-3-8tf245						250lhf-t8 / t1-8-8tf245						250lhf-t10 / t1-10-8tf245			250lhf-t11 / t1-11-8tf245	
		250hlf							250hlf-t3						250hlf-t8						250hlf-t10			250hlf-t11	
T-Foam8(L)	0.5/0.46	500lhf							500lhf-t3						500lhf-t8						500lhf-t10			500lhf-t11	
		500lhf							500lhf-t3						500lhf-t8						500lhf-t10			500lhf-t11	
		500hlf							500hlf-t3						500hlf-t8						500hlf-t10			500hlf-t11	
T-Foam8(L)	1.0	1000lhf							1000lhf-t3						1000lhf-t8						1000lhf-t10			1000lhf-t11	
		1000lhf							1000lhf-t3						1000lhf-t8						1000lhf-t10			1000lhf-t11	
		1000hlf							1000hlf-t3						1000hlf-t8						1000hlf-t10			1000hlf-t11	
		1000lhf							1000lhf-t3						1000lhf-t8						1000lhf-t10			1000lhf-t11	
		1000hlf							1000hlf-t3						1000hlf-t8						1000hlf-t10			1000hlf-t11	
		1000lhf							1000lhf-t3						1000lhf-t8						1000lhf-t10			1000lhf-t11	
		1000hlf							1000hlf-t3						1000hlf-t8						1000hlf-t10			1000hlf-t11	
		1000lhf							1000lhf-t3						1000lhf-t8						1000lhf-t10			1000lhf-t11	
		1000hlf							1000hlf-t3						1000hlf-t8						1000hlf-t10			1000hlf-t11	
		1000lhf							1000lhf-t3						1000lhf-t8						1000lhf-t10			1000lhf-t11	
		1000hlf							1000hlf-t3						1000hlf-t8						1000hlf-t10			1000hlf-t11	
		1000lhf							1000lhf-t3						1000lhf-t8						1000lhf-t10			1000lhf-t11	
		1000hlf							1000hlf-t3						1000hlf-t8						1000hlf-t10			1000hlf-t11	
		1000lhf							1000lhf-t3						1000lhf-t8						1000lhf-t10			1000lhf-t11	
		1000hlf							1000hlf-t3						1000hlf-t8						1000hlf-t10			1000hlf-t11	
		1000lhf							1000lhf-t3						1000lhf-t8						1000lhf-t10			1000lhf-t11	
		1000hlf							1000hlf-t3						1000hlf-t8						1000hlf-t10			1000hlf-t11	
		1000lhf							1000lhf-t3						1000lhf-t8						1000lhf-t10			1000lhf-t11	
		1000hlf							1000hlf-t3						1000hlf-t8						1000hlf-t10			1000hlf-t11	
		1000lhf							1000lhf-t3						1000lhf-t8						1000lhf-t10			1000lhf-t11	
		1000hlf							1000hlf-t3						1000hlf-t8						1000hlf-t10			1000hlf-t11	
		1000lhf							1000lhf-t3						1000lhf-t8						1000lhf-t10			1000lhf-t11	
		1000hlf							1000hlf-t3						1000hlf-t8						1000hlf-t10			1000hlf-t11	
		1000lhf							1000lhf-t3						1000lhf-t8						1000lhf-t10			1000lhf-t11	
		1000hlf							1000hlf-t3						1000hlf-t8						1000hlf-t10			1000hlf-t11	
		1000lhf							1000lhf-t3						1000lhf-t8						1000lhf-t10			1000lhf-t11	
		1000hlf							1000hlf-t3						1000hlf-t8						1000hlf-t10			1000hlf-t11	
		1000lhf							1000lhf-t3						1000lhf-t8						1000lhf-t10			1000lhf-t11	
		1000hlf							1000hlf-t3						1000hlf-t8						1000hlf-t10			1000hlf-t11	
		1000lhf							1000lhf-t3						1000lhf-t8						1000lhf-t10			1000lhf-t11	
		1000hlf							1000hlf-t3						1000hlf-t8						1000hlf-t10			1000hlf-t11	
		1000lhf							1000lhf-t3						1000lhf-t8						1000lhf-t10			1000lhf-t11	
		1000hlf							1000hlf-t3						1000hlf-t8						1000hlf-t10			1000hlf-t11	
		1000lhf							1000lhf-t3						1000lhf-t8						1000lhf-t10			1000lhf-t11	
		1000hlf							1000hlf-t3						1000hlf-t8						1000hlf-t10			1000hlf-t11	
		1000lhf							1000lhf-t3						1000lhf-t8						1000lhf-t10			1000lhf-t11	
		1000hlf							1000hlf-t3						1000hlf-t8						1000hlf-t10			1000hlf-t11	
		1000lhf							1000lhf-t3						1000lhf-t8						1000lhf-t10			1000lhf-t11	
		1000hlf							1000hlf-t3						1000hlf-t8						1000hlf-t10			1000hlf-t11	
		1000lhf							1000lhf-t3						1000lhf-t8						1000lhf-t10			1000lhf-t11	
		1000hlf							1000hlf-t3						1000hlf-t8						1000hlf-t10			1000hlf-t11	
		1000lhf							1000lhf-t3						1000lhf-t8						1000lhf-t10			1000lhf-t11	
		1000hlf							1000hlf-t3						1000hlf-t8						1000hlf-t10			1000hlf-t11	
		1000lhf							1000lhf-t3						1000lhf-t8						1000lhf-t10			1000lhf-t11	
		1000hlf							1000hlf-t3						1000hlf-t8						1000hlf-t10			1000hlf-t11	
		1000lhf							1000lhf-t3						1000lhf-t8						1000lhf-t10			1000lhf-t11	
		1000hlf																							

Table A1 (c). Configurations to Study the Effect of Excitation Intensity, Bulk Type, Bulk Depth, & Facesheet Parameters (Porosity, Thickness, & hole Diameter) on High Frequency Normal Impedance

Bulk Material	Depth Nominal/Actual (in)	Facesheet For Perforates: Porosity, S in %; Thickness, t in inch; Hole Diameter, d in inch All file names end with *.smt																Intensity OASPL dB
		No	T1-1	T1-2	T1-3	T1-4	T1-6	T1-8	T1-9	T1-10	T1-11	T1-12						
		Facesheet	S t d 20,025,04	S t d 30,025,04	S t d 40,025,04	S t d 40,025,04	S t d 40,025,08	S t d 40,04,04	S t d 40,06,04	Linear	Linear	Linear						
T-Foam8(L)	2.0	1117t20	1117t20t1-1	1117t20t1-2	1117t20t1-3	1117t20t1-4	1117t20t1-6	1117t20t1-8	1117t20t1-9	1117t20t1-10	1117t20t1-11	1117t20t1-12						
T-Foam16(H)	0.25/0.245	250htf			250htf-t3			250htf-t8			250htf-t11							
		250htf / 16t245	t1-1-16t245	t1-2-16t245	t1-3-16t245	t1-4-16t245	t1-6-16t245	t1-8-16t245	t1-9-16t245	t1-10-16t245	250htf-t11 / t1-11-t1-12-16t245							
		250htf			250htf-t3			250htf-t8			250htf-t11							
T-Foam16(H)	0.5/0.505	500htf			500htf-t3			500htf-t8			500htf-t11							
		500htf	500htf-t1	500htf-t2	500htf-t3	500htf-t4	500htf-t6	500htf-t8	500htf-t9	500htf-t10	500htf-t11	500htf-t12						
		500htf			500htf-t3			500htf-t8			500htf-t11							
T-Foam16(H)	1.0	1000htf			1000htf-t3			1000htf-t8			1000htf-t11							
		1000htf	1000htf-t1	1000htf-t2	1000htf-t3	1000htf-t4	1000htf-t6	1000htf-t8	1000htf-t9	1000htf-t10	1000htf-t11	1000htf-t12						
		1000htf			1000htf-t3			1000htf-t8			1000htf-t11							
T-Foam16(H)	2.0	2000htf			2000htf-t3			2000htf-t8			2000htf-t11							
		2000htf	2000htf-t1	2000htf-t2	2000htf-t3	2000htf-t4	2000htf-t6	2000htf-t8	2000htf-t9	2000htf-t10	2000htf-t11	2000htf-t12						
		2000htf			2000htf-t3			2000htf-t8			2000htf-t11							
Peltmetal (L) 5%	0.25/0.248	250lfrm	250lfrm-t1	250lfrm-t2	250lfrm-t3	250lfrm-t4	250lfrm-t6	250lfrm-t8	250lfrm-t9	250lfrm-t10	250lfrm-t11	250lfrm-t12						
	6.8%	250lfrm	250lfrm-t1	250lfrm-t2	250lfrm-t3	250lfrm-t4	250lfrm-t6	250lfrm-t8	250lfrm-t9	250lfrm-t10	250lfrm-t11	250lfrm-t12						
		250lfrm	250lfrm-t1	250lfrm-t2	250lfrm-t3	250lfrm-t4	250lfrm-t6	250lfrm-t8	250lfrm-t9	250lfrm-t10	250lfrm-t11	250lfrm-t12						
Peltmetal (L) 5%	0.5/0.512	500lfrm	500lfrm-t1	500lfrm-t2	500lfrm-t3	500lfrm-t4	500lfrm-t6	500lfrm-t8	500lfrm-t9	500lfrm-t10	500lfrm-t11	500lfrm-t12						
	7.2%	500lfrm	500lfrm-t1	500lfrm-t2	500lfrm-t3	500lfrm-t4	500lfrm-t6	500lfrm-t8	500lfrm-t9	500lfrm-t10	500lfrm-t11	500lfrm-t12						
		500lfrm	500lfrm-t1	500lfrm-t2	500lfrm-t3	500lfrm-t4	500lfrm-t6	500lfrm-t8	500lfrm-t9	500lfrm-t10	500lfrm-t11	500lfrm-t12						
Peltmetal (L) 5%	1.0/1.022	1000lfrm	1000lfrm-t1	1000lfrm-t2	1000lfrm-t3	1000lfrm-t4	1000lfrm-t6	1000lfrm-t8	1000lfrm-t9	1000lfrm-t10	1000lfrm-t11	1000lfrm-t12						
	6.2%	1000lfrm	1000lfrm-t1	1000lfrm-t2	1000lfrm-t3	1000lfrm-t4	1000lfrm-t6	1000lfrm-t8	1000lfrm-t9	1000lfrm-t10	1000lfrm-t11	1000lfrm-t12						
		1000lfrm	1000lfrm-t1	1000lfrm-t2	1000lfrm-t3	1000lfrm-t4	1000lfrm-t6	1000lfrm-t8	1000lfrm-t9	1000lfrm-t10	1000lfrm-t11	1000lfrm-t12						
Peltmetal (L) 5%	2.0/2.04	2000lfrm	2000lfrm-t1	2000lfrm-t2	2000lfrm-t3	2000lfrm-t4	2000lfrm-t6	2000lfrm-t8	2000lfrm-t9	2000lfrm-t10	2000lfrm-t11	2000lfrm-t12						
	6.2%	2000lfrm	2000lfrm-t1	2000lfrm-t2	2000lfrm-t3	2000lfrm-t4	2000lfrm-t6	2000lfrm-t8	2000lfrm-t9	2000lfrm-t10	2000lfrm-t11	2000lfrm-t12						
		2000lfrm	2000lfrm-t1	2000lfrm-t2	2000lfrm-t3	2000lfrm-t4	2000lfrm-t6	2000lfrm-t8	2000lfrm-t9	2000lfrm-t10	2000lfrm-t11	2000lfrm-t12						
Peltmetal(M)10%	0.25/0.254	250lfrm			250lfrm-t3			250lfrm-t8			250lfrm-t11							
	8.9%	250lfrm	250lfrm-t1	250lfrm-t2	250lfrm-t3	250lfrm-t4	250lfrm-t6	250lfrm-t8	250lfrm-t9	250lfrm-t10	250lfrm-t11	250lfrm-t12						
		250lfrm			250lfrm-t3			250lfrm-t8			250lfrm-t11							
Peltmetal(M)10%	0.5/0.505	500lfrm			500lfrm-t3			500lfrm-t8			500lfrm-t11							
	10.6%	500lfrm	500lfrm-t1	500lfrm-t2	500lfrm-t3	500lfrm-t4	500lfrm-t6	500lfrm-t8	500lfrm-t9	500lfrm-t10	500lfrm-t11	500lfrm-t12						
		500lfrm			500lfrm-t3			500lfrm-t8			500lfrm-t11							

Table A1 (d). Configurations to Study the Effect of Excitation Intensity, Bulk Type, Bulk Depth, & Facesheet Parameters (Porosity, Thickness, & hole Diameter) on High Frequency Normal Impedance

Bulk Material	Depth Nominal/ Actual (in)	Facesheet For Perforates: Porosity, S in %; Thickness, t in inch; Hole Diameter, d in inch																				Intensity OASPL dB		
		All file names end with 'smt'																						
		No	T1-1		T1-2		T1-3		T1-4		T1-6		T1-8		T1-9		T1-10		T1-11		T-12			
		S	t	d	S	t	d	S	t	d	S	t	d	S	t	d	S	t	d	S	t	d		
		Facesheet	20,025,04		30,025,04	40,025,04		40,025,04		40,025,04	40,025,08		40,04,04	40,04,04	40,06,04		1000lmfm-t10		Linear	5 Rayls	10 Rayls	15 Rayls	Linear	
Feltmetal(M)10%	1.0/1.017	1000lmfm	1000mfm-t1			1000mfm-t2	1000mfm-t3	1000mfm-t3	1000mfm-t4	1000mfm-t4	1000mfm-t6	1000mfm-t8	1000mfm-t8	1000mfm-t9	1000mfm-t10	1000mfm-t11	1000mfm-t12	1000mfm-t13	1000mfm-t14	1000mfm-t15	1000mfm-t16	1000mfm-t17	1000mfm-t18	140
10%		1000hmfm					1000hmfm-t3	1000hmfm-t3				1000hmfm-t8	1000hmfm-t8				1000hmfm-t10							150
Feltmetal(M)10%	2.0/2.03	2000lmfm					2000lmfm-t3	2000lmfm-t3				2000lmfm-t8	2000lmfm-t8				2000lmfm-t10							155
10%		2000hmfm	2000mfm-t1			2000mfm-t2	2000mfm-t3	2000mfm-t3	2000mfm-t4	2000mfm-t4	2000mfm-t6	2000mfm-t8	2000mfm-t8	2000mfm-t9	2000mfm-t10	2000mfm-t11	2000mfm-t12	2000mfm-t13	2000mfm-t14	2000mfm-t15	2000mfm-t16	2000mfm-t17	2000mfm-t18	140
Feltmetal (H) 15%	0.25/0.262	250lhfm					250lhfm-t3	250lhfm-t3				250lhfm-t8	250lhfm-t8				250lhfm-t10							155
17%		250hhfm	250hfm-t1			250hfm-t2	250hfm-t3	250hfm-t3	250hfm-t4	250hfm-t4	250hfm-t6	250hfm-t8	250hfm-t8	250hfm-t9	250hfm-t10	250hfm-t11	250hfm-t12	250hfm-t13	250hfm-t14	250hfm-t15	250hfm-t16	250hfm-t17	250hfm-t18	140
Feltmetal (H) 15%	0.5/0.508	500lhfm					500lhfm-t3	500lhfm-t3				500lhfm-t8	500lhfm-t8				500lhfm-t10							155
15.5%		500hhfm	500hfm-t1			500hfm-t2	500hfm-t3	500hfm-t3	500hfm-t4	500hfm-t4	500hfm-t6	500hfm-t8	500hfm-t8	500hfm-t9	500hfm-t10	500hfm-t11	500hfm-t12	500hfm-t13	500hfm-t14	500hfm-t15	500hfm-t16	500hfm-t17	500hfm-t18	140
Feltmetal (H)15%	1.0/1.02	1000lhfm					1000lhfm-t3	1000lhfm-t3				1000lhfm-t8	1000lhfm-t8				1000lhfm-t10							155
14.9%		1000hhfm	1000hfm-t1			1000hfm-t2	1000hfm-t3	1000hfm-t3	1000hfm-t4	1000hfm-t4	1000hfm-t6	1000hfm-t8	1000hfm-t8	1000hfm-t9	1000hfm-t10	1000hfm-t11	1000hfm-t12	1000hfm-t13	1000hfm-t14	1000hfm-t15	1000hfm-t16	1000hfm-t17	1000hfm-t18	140
Feltmetal (H)15%	2.0/2.035	2000lhfm					2000lhfm-t3	2000lhfm-t3				2000lhfm-t8	2000lhfm-t8				2000lhfm-t10							155
14.9%		2000hhfm	2000hfm-t1			2000hfm-t2	2000hfm-t3	2000hfm-t3	2000hfm-t4	2000hfm-t4	2000hfm-t6	2000hfm-t8	2000hfm-t8	2000hfm-t9	2000hfm-t10	2000hfm-t11	2000hfm-t12	2000hfm-t13	2000hfm-t14	2000hfm-t15	2000hfm-t16	2000hfm-t17	2000hfm-t18	140
							2000hhfm-t3	2000hhfm-t3				2000hhfm-t8	2000hhfm-t8				2000hhfm-t10							150
																								155

Table A2 (a). Additional Configurations to Study the Effect of Excitation Intensity, Bulk Type, Bulk Depth, & Facesheet Parameters (Porosity, Thickness, & hole Diameter) on High Frequency Normal Impedance

Bulk Material	Depth Nominal/ Actual (in)	Facesheet For Perforates: Porosity, S in %; Thickness, t in inch; Hole Diameter, d in inch																Intensity OASPL dB
		All file names end with '.smt'																
		T1-5	T1-7	14	28	29	32	34	36	38	40	42						
		S t d	S t d	S t d	S t d	S t d	S t d	S t d	S t d	S t d	S t d	S t d	S t d	S t d	S t d	S t d	S t d	
		40,025,06	40,015,04	35,10,07	40,10,04	40,125,04	40,025,07	40,10,07	40,025,10	40,025,125	40,025,14	40,14,04						
Facesheet Only					fs250l-28	fs250l-29			fs250l-36	fs250l-38								
		fs250-l5	fs250-l7	fs250-14	fs250-28	fs250-29	fs250-32	fs250-34	fs250h-36	fs250h-38	fs250-40	fs250-42						
					fs250h-28	fs250h-29			fs250l-36	fs250h-38								
100ppi SiC	0.25	250sic1-t5	250sic1-t7	250sic1-14	250sic1-28	250sic1-29	250sic1-32	250sic1-34	250sic1-36	250sic1-38	250sic1-40	250sic1-42						
					250hsic1-28	250hsic1-29			250hsic1-36	250hsic1-38								
100ppi SiC	0.5				500lsic1-28	250lsic1-29			500lsic1-36	500lsic1-38								
		500sic1-t5	500sic1-t7	500sic1-14	500sic1-28	500sic1-29	500sic1-32	500sic1-34	500sic1-36	500sic1-38	200sic1-40	500sic1-42						
					500hsic1-28	500hsic1-29			500hsic1-36	500hsic1-38								
100ppi SiC	1.0				1000lsic1-14	1000lsic1-29			1000lsic1-34	1000lsic1-38								
		1000sic1-t5	1000sic1-t7	1000sic1-14	1000sic1-28	1000sic1-29	1000sic1-32	1000sic1-34	1000sic1-36	1000sic1-38	1000sic1-40	1000sic1-42						
					1000hsic1-14	1000hsic1-29			1000hsic1-34	1000hsic1-38								
100ppi SiC	2.0				2000lsic1-14	2000lsic1-29			2000lsic1-34	2000lsic1-38								
		2000sic1-t5	2000sic1-t7	2000sic1-14	2000sic1-28	2000sic1-29	2000sic1-32	2000sic1-34	2000sic1-36	2000sic1-38	2000sic1-40	2000sic1-42						
					2000hsic1-14	2000hsic1-29			2000hsic1-34	2000hsic1-38								
200ppi SiC	0.25/0.259	250sic2-t5	250sic2-t7	250sic2-14				250sic2-34										
200ppi SiC	0.5/0.509	500sic2-t5	500sic2-t7	500sic2-14				500sic2-34										
200ppi SiC	1.0	1000sic2-t5	1000sic2-t7	1000sic2-14				1000sic2-34										
200ppi SiC	2.0	2000sic2-t5	2000sic2-t7	2000sic2-14				2000sic2-34										
400ppi SiC	0.25	250sic4-t5	250sic4-t7	250sic4-14				250sic4-34										
400ppi SiC	0.5	500sic4-t5	500sic4-t7	500sic4-14				500sic4-34										
400ppi SiC	1.0	1000sic4-t5	1000sic4-t7	1000sic4-14				1000sic4-34										
400ppi SiC	2.0	2000sic4-t5	2000sic4-t7	2000sic4-14				2000sic4-34										
600ppi SiC	0.25/0.257	250sic6-t5	250sic6-t7	250sic6-14				250sic6-34										
600ppi SiC	0.5/0.508	500sic6-t5	500sic6-t7	500sic6-14				500sic6-34										
T-Foam12(M)	0.25/0.235																	
		250mtf-t5	250 mtf -t7	250 mtf -14	250mtf-28	250mtf-29	250mtf-32	250mtf-34	250mtf-36	250mtf-38	250mtf-40	250mtf-42						
					250hmtf-28	250hmtf-29			250hmtf-36	250hmtf-38								
T-Foam12(M)	0.5/0.44				500lmtf-28	500lmtf-29			500lmtf-36	500lmtf-38								
		500mtf-t5	500 mtf -t7	500 mtf -14	500mtf-28	500mtf-29	500mtf-32	500mtf-34	500mtf-36	500mtf-38	500mtf-40	500mtf-42						
					500hmtf-28	500hmtf-29			500hmtf-36	500hmtf-38								
T-Foam12(M)	1.0				1000lmtf-28	1000lmtf-29			1000lmtf-36	1000lmtf-38								
		1000mtf-t5	1000 mtf -t7	1000 mtf -14	1000mtf-28	1000mtf-29	1000mtf-32	1000mtf-34	1000mtf-36	1000mtf-38	1000mtf-40	1000mtf-42						
					1000hmtf-28	1000hmtf-29			1000hmtf-36	1000hmtf-38								

Table A2 (b). Additional Configurations to Study the Effect of Excitation Intensity, Bulk Type, Bulk Depth, & Facesheet Parameters (Porosity, Thickness, & hole Diameter) on High Frequency Normal Impedance

Bulk Material	Depth Nominal/ Actual (in)	Facesheet For Perforates: Porosity, S in %; Thickness, t in inch; Hole Diameter, d in inch All file names end with '.smt'																								Intensity OASPL dB
		T1-5		T1-7		14		28		29		32		34		36		38		40		42				
		S	t	d	S	t	d	S	t	d	S	t	d	S	t	d	S	t	d	S	t	d	S	t	d	
		40,.025,.06		40,.015,.04		35,.10,.07		40,.10,.04		40,.125,.04		40,.025,.07		40,.10,.07		40,.025,.10		40,.025,.125		40,.025,.14		40,.14,.04				
T-Foam12(M)	2.0/1.95																									
		2000mtf-15		2000 mtf -17		2000 mtf -14		2000mtf-28		2000mtf-29		2000mtf-32		2000mtf-34		2000mtf-36		2000mtf-38		2000mtf-40		2000mtf-42				
								2000hmf-28		2000hmf-29																
T-Foam8(L)	0.5/0.46	500lrf-15		500lrf-17																						
T-Foam8(L)	1.0	1000lrf-15		1000lrf-17																						
T-Foam8(L)	2.0	1117uf20t1-5		1117uf20t1-7																						
T-Foam16(H)	0.5/0.505	500htf-15		500htf-17																						
T-Foam16(H)	1.0	1000htf-15		1000htf-17																						
T-Foam16(H)	2.0	2000htf-15		2000htf-17																						
Feltmetal (L) 5%	0.25/0.248																									
	6.8%	250lrf-15		250 lrf -17		250 lrf -14		250lrf-28		250lrf-29		250lrf-32		250lrf-34		250lrf-36		250lrf-38		250lrf-40		250lrf-42				
								250hlfm-28		250hlfm-29																
Feltmetal (L) 5%	0.5/0.512							500lrf-28		500lrf-29																
	7.2%	500lrf-15		500 lrf -17		500 mtf -14		500lrf-28		500lrf-29		500lrf-32		500lrf-34		500lrf-36		500lrf-38		500lrf-40		500lrf-42				
								1000lrf-28		1000lrf-29																
Feltmetal (L) 5%	1.0/1.022							1000lrf-28		1000lrf-29		1000lrf-32		1000lrf-34		1000lrf-36		1000lrf-38		1000lrf-40		1000lrf-42				
	6.2%	1000lrf-15		1000 lrf -17		1000 mtf -14		1000hlfm-28		1000hlfm-29																
								2000lrf-28		2000lrf-29																
Feltmetal (L) 5%	2.0/2.04							2000lrf-28		2000lrf-29		2000lrf-32		2000lrf-34		2000lrf-36		2000lrf-38		2000lrf-40		2000lrf-42				
	6.2%	2000lrf-15		2000 lrf -17		2000 mtf -14		2000hlfm-28		2000hlfm-29		2000hlfm-32		2000hlfm-34		2000hlfm-36		2000hlfm-38		2000hlfm-40		2000hlfm-42				
								2000hlfm-28		2000hlfm-29																

Table A3 (a) . Normal Impedance for T-Foam Bulk- All files end with 'smt'

Facesheet Parameters	File Name for 2" -Deep T-Foam Samples										
	TF19	TF20	TF21	TF22	TF33	TF39	TF40	TF46	TF47		
Bulk Only	1117tf19r	1117tf20	1117tf21	1117tf22	90298t33	90898tf39	90898tf40	90898tf46	90898tf47		
S=20%, t=0.025", d=0.04"	1117tf19t1-1	1117tf20t1-1	1117tf21t1-1	1117tf22t1-1	90298t33-t1	90898tf39-t1	90898tf40-t1	90898tf46-t1	90898tf47-t1		
S=30%, t=0.025", d=0.04"	1117tf19t1-2	1117tf20t1-2	1117tf21t1-2	1117tf22t1-2	90298t33-t2	90898tf39-t2	90898tf40-t2	90898tf46-t2	90898tf47-t2		
S=40%, t=0.025", d=0.04"	1117tf19t1-3	1117tf20t1-3	1117tf21t1-3	1117tf22t1-3	90298t33-t3	90898tf39-t3	90898tf40-t3	90898tf46-t3	90898tf47-t3		
S=40%, t=0.025", d=0.025"	1117tf19t1-4	1117tf20t1-4	1117tf21t1-4	1117tf22t1-4	90298t33-t4						
S=40%, t=0.025", d=0.06"	1117tf19t1-5	1117tf20t1-5	1117tf21t1-5	1117tf22t1-5	90298t33-t5						
S=40%, t=0.025", d=0.08"	1117tf19t1-6	1117tf20t1-6	1117tf21t1-6	1117tf22t1-6	90298t33-t6						
S=40%, t=0.015", d=0.04"	1117tf19t1-7	1117tf20t1-7	1117tf21t1-7	1117tf22t1-7	90298t33-t7						
S=40%, t=0.04", d=0.04"	1117tf19t1-8	1117tf20t1-8	1117tf21t1-8	1117tf22t1-8	90298t33-t8						
S=40%, t=0.06", d=0.04"	1117tf19t1-9	1117tf20t1-9	1117tf21t1-9	1117tf22t1-9	90298t33-t9						
Linear – 5 cgs Rayls	1117tf19t1-10	1117tf20t1-10	1117tf21t1-10	1117tf22t1-10	90298t33-t10						
Linear – 10 cgs Rayls	1117tf19t1-11	1117tf20t1-11	1117tf21t1-11	1117tf22t1-11	90298t33-t11						
Linear – 15 cgs Rayls	1117tf19t1-12	1117tf20t1-12	1117tf21t1-12	1117tf22t1-12	90298t33-t12						
S=20%, t=0.10", d=0.07"					90398t33-1	90898tf39-1	90898tf40-1	90898tf46-1	90898tf47-1		
S=25%, t=0.10", d=0.07"					90398t33-2	90898tf39-2	90898tf40-2	90898tf46-2	90898tf47-2		
S=30%, t=0.10", d=0.07"					90398t33-3	90898tf39-3	90898tf40-3	90898tf46-3	90898tf47-3		
S=35%, t=0.06", d=0.025"					90398t33-4						
S=35%, t=0.10", d=0.025"					90398t33-5						
S=35%, t=0.06", d=0.04"					90398t33-6						
S=35%, t=0.10", d=0.04"					90398t33-7						
S=35%, t=0.06", d=0.06"					90398t33-8						
S=35%, t=0.10", d=0.06"					90398t33-9						
S=35%, t=0.025", d=0.07"					90398t33-10						
S=35%, t=0.04", d=0.07"					90398t33-11						
S=35%, t=0.06", d=0.07"					90398t33-12						
S=35%, t=0.08", d=0.07"					90398t33-13						
S=35%, t=0.10", d=0.07"					90398t33-14	90898tf39-14	90898tf40-14	90898tf46-14	90898tf47-14		
S=35%, t=0.125", d=0.07"					90398t33-15						
S=35%, t=0.06", d=0.08"					90398t33-16						
S=35%, t=0.10", d=0.08"					90398t33-17						
S=35%, t=0.025", d=0.10"					90398t33-18						

Table A3 (b) . Normal Impedance for T-Foam Bulk- All files end with '.smt'

File Name for 2"-Deep T-Foam Samples									
Facesheet Parameters	TF19	TF20	TF21	TF22	TF33	TF39	TF40	TF46	TF47
S=35%, t=0.04", d=0.10"					90398t33-19				
S=35%, t=0.06", d=0.10"					90398t33-20				
S=35%, t=0.08", d=0.10"					90398t33-21				
S=35%, t=0.10", d=0.10"					90398t33-22				
S=35%, t=0.125", d=0.10"					90398t33-23				
S=35%, t=0.06", d=0.125"					90398t33-24				
S=35%, t=0.10", d=0.125"					90398t33-25				
S=40%, t=0.04", d=0.025"									
S=40%, t=0.10", d=0.025"					90398t33-27				
S=40%, t=0.10", d=0.04"					90398t33-28				
S=40%, t=0.125", d=0.04"									
S=40%, t=0.04", d=0.06"									
S=40%, t=0.10", d=0.06"									
S=40%, t=0.025", d=0.07"					90398t33-31				
S=40%, t=0.04", d=0.07"					90398t33-32				
S=40%, t=0.10", d=0.07"					90398t33-33				
S=40%, t=0.10", d=0.08"					90398t33-34	90898t39-14	90898t40-14	90898t46-14	90898t47-14
S=40%, t=0.025", d=0.10"					90398t33-35				
S=40%, t=0.10", d=0.10"					90398t33-36				
S=40%, t=0.025", d=0.125"					90398t33-37				
S=40%, t=0.10", d=0.125"									
S=40%, t=0.025", d=0.14"					90398t33-39				
S=40%, t=0.10", d=0.14"									
S=40%, t=0.14", d=0.04"					90398t33-41				
S=40%, t=0.025", d=0.056"									
S=40%, t=0.025", d=0.075"									
S=35%, t=0.06", d=0.14"									
S=35%, t=0.10", d=0.14"									
S=35%, t=0.14", d=0.07"					90398t33-46				
S=35%, t=0.14", d=0.10"					90398t33-47				
S=37%, t=0.04", d=0.054"					90398t33-48				
S=37%, t=0.025", d=0.045"									

Table A4. Low Frequency (up to 6 kHz) Normal Impedance Data Files for T-Foam Samples (1.25" Dia)

File Name	Description
TF37-1C.SMT;1	Bulk Only (TF37c), 150 dB
TF37-1CF.SMT;3	Bulk (TF37c) with Facesheet, S=37%, t=0.025", d=0.045", 150 dB
TF37-2C.SMT;1	Bulk Only (TF37c), 150 dB
TF37-2CF.SMT;1	Bulk (TF37c) with Facesheet, S=37%, t=0.025", d=0.045", 150 dB
TF39.SMT;1	Bulk Only (TF39), 150 dB
TF39C.SMT;1	Bulk Only (TF39c), 150 dB
TF39CF.SMT;1	Bulk (TF39c) with Facesheet, S=37%, t=0.025", d=0.045", 150 dB
TF39F.SMT;1	Bulk (TF39) with Facesheet, S=37%, t=0.025", d=0.045", 150 dB
TF40.SMT;1	Bulk Only (TF40), 150 dB
TF40C.SMT;1	Bulk Only (TF40c), 150 dB
TF40CF.SMT;1	Bulk (TF40c) with Facesheet, S=37%, t=0.025", d=0.045", 150 dB
TF40F.SMT;1	Bulk (TF40) with Facesheet, S=37%, t=0.025", d=0.045", 150 dB
TF42.SMT;1	Bulk (TF42) Only, 150 dB
TF42FS.SMT;1	Bulk (TF42) with Facesheet, S=37%, t=0.025", d=0.045", 150 dB
TF45.SMT;1	Bulk (TF45) Only, 150 dB
TF45FS.SMT;3	Bulk (TF45) with Facesheet, S=37%, t=0.025", d=0.045", 150 dB
TF46.SMT;1	Bulk (TF46) Only, 150 dB
TF46FS.SMT;1	Bulk (TF46) with Facesheet, S=37%, t=0.025", d=0.045", 150 dB
TF46FSL.SMT;1	Bulk (TF46) with Facesheet, S=37%, t=0.025", d=0.045", 140 dB
TF46FSL2.SMT;2	Bulk (TF46) with Facesheet, S=37%, t=0.025", d=0.045", 120 dB
TF46FSL3.SMT;1	Bulk (TF46) with Facesheet, S=37%, t=0.025", d=0.045", 130 dB
TF47.SMT;1	Bulk (TF47) Only, 150 dB
TF47FS.SMT;1	Bulk (TF47) with Facesheet, S=37%, t=0.025", d=0.045", 150 dB
TF47FSL.SMT;1	Bulk (TF47) with Facesheet, S=37%, t=0.025", d=0.045", 140 dB
TF47FSL2.SMT;1	Bulk (TF47) with Facesheet, S=37%, t=0.025", d=0.045", 120 dB
TF47FSL3.SMT;2	Bulk (TF47) with Facesheet, S=37%, t=0.025", d=0.045", 130 dB
TFL19.SMT;7	Bulk (TF19) Only, 150 dB
TFL19L.SMT;1	Bulk (TF19) Only, 140 dB
TFL19R.SMT;1	Bulk (TF19) Only, 150 dB - Repeat
TFL19T11.SMT;1	Bulk (TF19) with Facesheet, S=20%, t=0.025", d=0.04", 150 dB
TFL20.SMT;1	Bulk (TF20) Only, 150 dB
TFL20T11.SMT;1	Bulk (TF20) with Facesheet, S=20%, t=0.025", d=0.04", 150 dB
TFL21.SMT;1	Bulk (TF21) Only, 150 dB
TFL21T11.SMT;1	Bulk (TF21) with Facesheet, S=20%, t=0.025", d=0.04", 150 dB
TFL22.SMT;1	Bulk (TF22) Only, 150 dB
TFL22T11.SMT;1	Bulk (TF22) with Facesheet, S=20%, t=0.025", d=0.04", 150 dB
TFL23.SMT;1	Bulk (TF23) Only, 150 dB
TFL23T11.SMT;1	Bulk (TF23) with Facesheet, S=20%, t=0.025", d=0.04", 150 dB
TFL24.SMT;1	Bulk (TF24) Only, 150 dB
TFL24T11.SMT;1	Bulk (TF24) with Facesheet, S=20%, t=0.025", d=0.04", 150 dB
TFL32.SMT;1	Bulk (TF32) Only, 150 dB
TFL32T11.SMT;1	Bulk (TF32) with Facesheet, S=20%, t=0.025", d=0.04", 150 dB
TFL33.SMT;1	Bulk (TF33) Only, 150 dB
TFL33T11.SMT;1	Bulk (TF33) with Facesheet, S=20%, t=0.025", d=0.04", 150 dB
TFL34.SMT;1	Bulk (TF34) Only, 150 dB
TFL34C.SMT;1	Bulk (TF34c) Only, 150 dB
TFL34CT11.SMT;1	Bulk (TF34c) with Facesheet, S=20%, t=0.025", d=0.04", 150 dB
TFL34T11.SMT;1	Bulk (TF34) with Facesheet, S=20%, t=0.025", d=0.04", 150 dB
TFL36.SMT;1	Bulk (TF36) Only, 150 dB
TFL36T11.SMT;1	Bulk (TF36) with Facesheet, S=20%, t=0.025", d=0.04", 150 dB



Table A5. In-situ impedance data files for 100 ppi 0.5" deep Silicon Carbide bulk panels (continued).

Configuration	Temp °F	Facesheet Description	File names for Relative Impedance Data at Different Grazing Flow Mach Number M.			
			All files end with ".cor"	All files end with ".smt" (A few files end with ".smc")		
		S, %, t, in, d, in	M = 0.00	M = 0.30	M = 0.55	M = 0.80
1-4161	Amb 200 400	40, 0.025, 0.10	W022699000	W022699001 W022699006 W022699009	W022699002 W022699005 W022699008	W022699003 W022699004 W022699007
1-8	Amb 200 400	40, 0.04, 0.04	W011499000	W011499001 W011499006 W011499009	W011499002 W011499005 W011499008	W011499003 W011499004 W011499007
1-4121	Amb 200 400	40, 0.10, 0.04	W120198000	W120198001 W120198006 W120198009	W120198002 W120198005 W120198008	W120198003 W120198004 W120198007
1-5	Amb 200 400	40, 0.025, 0.06	W010699000	W010699001 W010699006 W010699009	W010699002 W010699005 W010699008	W010699003 W010699004 W010699007
1-4052	Amb 200 400	35, 0.10, 0.04	W112498000	W112498001 W112498006 W112498009	W112498002 W112498005 W112498008	W112498003 W112498004 W112498007
1-7	Amb 200 400	40, 0.015, 0.04	W102098000	W101998001 W101998006 W101998009	W101998002 W101998005 W101998008	W101998003 W101998004 W101998007
1-4072	Amb 200 400	35, 0.04, 0.07	W092898000	W092898001 W092898006 W092898009	W092898002 W092898005 W092898008	W092898003 W092898004 W092898007
1-4075	Amb 200 400	35, 0.10, 0.07	W60498000	W60498001 W60498006 W60498009	W60498002 W60498005 W60498008	W60498003 W60498004 W60498007
1-4031	Amb 200 400	30, 0.10, 0.07	W0806002	W0806003 W0806008 W0806011	W0806004 W0806007 W0806010	W0806005 W0806006 W0806009
1-12	Amb 200 400	Linear, 15 Rayls	W519001	W519002 W519007 W519010	W519003 W519006 W519009	W519004 W519005 W519008
1-11	Amb 200 400	Linear, 10 Rayls	W427003	W427004 W427009 W427013	W427005 W427008 W427012	W427006 W427007 W427010
1-4143	Amb 200 400	40, 0.10, 0.07	W41301	W46003 W46009 W46012	W46005 W46008 W46011	W46006 W46007 W46010

Table A5. In-situ impedance data files for 100 ppi 0.5" deep Silicon Carbide bulk panels (Concluded).

Configurat ion	Temp °F	Facesheet Description	File names for Relative Impedance Data at Different Grazing Flow Mach Number M.			
		Porosity, S , Thickness, t, Hole Diameter d	All files end with ".cor"	All files end with ".smt" (A few files end with ".smc")		
		S, %, t, in, d, in	M = 0.00	M = 0.30	M = 0.55	M = 0.80
1-6	Amb 200 400	40, 0.025, 0.08		W21001 W21004 W21008	W21002 W21005 W21007	W21003 W21009 W21006
1-9	Amb 200 400	40, 0.06, 0.04		W111901 W111906 W111909	W111902 W111905 W111908	W111903 W111904 W111907
1-3	Amb 200 400	40, 0.025, 0.04		W10-6-2 W10-6-7 W10-6-10	W10-6-3 W10-6-6 W10-6-9	W10-6-4 W10-6-5 W10-6-8
1-2	Amb 200 400	30, 0.025, 0.04	W9-15-1	W9-15-2 W9-16-1 W9-16-4	W9-15-3 W9-16-2 W9-16-5	W9-15-4 W9-16-3 W9-16-6
1-1	Amb 200 400	20, 0.025, 0.04	Wn021	Wn022 Wn024 Wn027	Wn018 Wn025 Wn028	Wn019 Wn026 Wn029

Table A6. In-situ impedance data files for 12 lbf 0.5" deep T-Foam bulk panels.

Configurat ion	Temp °F	Facesheet Description	File names for Relative Impedance Data at Different Grazing Flow Mach Number M.			
		Porosity, S , Thickness, t, Hole Diameter d	All files end with ".cor"	All files end with ".smt" (A few files end with ".smc")		
		S, %, t, in, d, in	M = 0.00	M = 0.30	M = 0.55	M = 0.80
6-8	Amb 200 400	40, 0.04, 0.04	W020599000	W020599001  W020599006 W020599009	W020599002 W020599005 W020599008	W020599003 W020599004 W020599007
6-4	Amb 200 400	40, 0.025, 0.025	W101298000	W101298001  W101298006 W101298009	W101298002 W101298005 W101298008	W101298003 W101298004 W101298007
6-11	Amb 200 400	Linear, 10 Rayls	W033199000	W033199001 W033199006 W033199009	W033199002 W033199005 W033199008	W033199003 W033199004 W033199007
6-4143	Amb 200 400	40, 0.10, 0.07	W526001	W526002 W526007 W526010	W526003 W526006 W526009	W526004 W526005 W526008
6-6	Amb 200 400	40, 0.025, 0.08	W041299000	W041299001 W041299006 W041299009	W041299002 W041299005 W041299008	W041299003 W041299004 W041299007
6-9	Amb 200 400	40, 0.06, 0.04	W505001	W505002 W505008 W505011	W505004 W505007 W505010	W505005 W505006 W505009
6-3	Amb 200 400	40, 0.025, 0.04	093098000	093098001 093098006 0930980009	0930980002 0930980005 0930980008	0930980003 0930980004 0930980007
6-2	Amb 200 400	30, 0.025, 0.04	W0714000	W717001 W717006 W717009	W717002 W717005 W717008	W717003 W717004 W717007w
6-1	Amb 200 400	20, 0.025, 0.04	W427002	W421002 W421011 W421010	W421003 W421006 W421009	W421004 W421005 W421008

Table A7. In-situ impedance data files for SDOF type panels with facesheets used for bulk absorber panels.

Configuration	Temp °F	Facesheet Description	File names for Relative Impedance Data at Different Grazing Flow Mach Number M.			
			All files end with “.cor”	All files end with “.smt” (A few files end with “.smc”)		
		Porosity, S , Thickness, t, Hole Diameter d				
		S, %, t, in, d, in	M = 0.00	M = 0.30	M = 0.55	M = 0.80
t1-8	Amb 200 400	40, 0.04, 0.04	W031999000	W031999001 W031999006 W031999009	W031999002 W031999005 W031999008	W031999003 W031999004 W031999007
t1-4121	Amb 200 400	40, 0.10, 0.04	W041599000	W041599001 W041599006 W041599009	W041599002 W041599005 W041599008	W041599003 W041599004 W041599007
t1-5	Amb 200 400	40, 0.025, 0.06	W041699000	W041699001 W041699006 W041699009	W041699002 W041699005 W041699008	W041699003 W041699004 W041699007
t1-11	Amb 200 400	Linear, 10 Rayls	W040999000	W040999001 W040999006 W040999009	W040999002 W040999005 W040999008	W040999003 W040999004 W040999007
t1-4143	Amb 200 400	40, 0.10, 0.07	W032999000	W033099001 W033099006 W033099009	W033099002 W033099005 W033099008	W033099003 W033099004 W033099007
t1-6	Amb 200 400	40, 0.025, 0.08	W040799000	W040799001 W040799006 W040799009	W040799002 W040799005 W040799008	W040799003 W040799004 W040799007
t1-9	Amb 200 400	40, 0.06, 0.04	W032499000	W032499001 W032499006 W032499009	W032499002 W032499005 W032499008	W032499003 W032499004 W032499007
t1-3	Amb 200 400	40, 0.025, 0.04	W022499000	W022499001 W022499006 W022499009	W022499002 W022499005 W022499008	W022499003 W022499004 W022499007
t1-2	Amb 200 400	30, 0.025, 0.04	W021999000	W021999001 W021999006 W021999009	W021999002 W021999005 W021999008	W021999003 W021999004 W021999007
t1-1	Amb 200 400	20, 0.025, 0.04	W9-26-1	W9-26-2 W9-26-5 W9-26-8	W9-26-3 W9-26-6 W9-26-9	W9-26-4 W9-26-7 W9-26-10

Table A8. In-situ impedance data files for SDOF type panels with facesheets of lower porosities.

Configurat ion	Temp °F	Facesheet Description	File names for Relative Impedance Data at Different Grazing Flow Mach Number M.			
			All files end with “.cor’	All files end with “.smt’ (A few files end with “.smc”)		
		Porosity, S , Thickness, t, Hole Diameter d  S, %, t, in, d, in	M = 0.00	M = 0.30	M = 0.55	M = 0.80
2	Amb 200 400	9, 0.025, 0.04	W102301	W102302 W102307 W102310	W102303 W102306 W102309	W102304 W102305 W102308
4	Amb 200 400	15, 0.025, 0.04	Wn8-21-1	Wn8-22-1 W9-9-4 W9-10-1	Wn8-22-2 W9-9-5 W9-10-2	Wn8-22-3 W9-9-6 W9-10-3
11	Amb 200 400	9, 0.025, 0.08	W41001	W33001 W33006 W33009	W33002 W33005 W33008	W33003 W33004 W33007
12	Amb	9, 0.01, 0.04	W415001	W415002	W415004	W415005
15	Amb 200 400	9, 0.06, 0.04	W121001	W121002 W121007 W121010	W121003 W121006 W121009	W121004 W121005 W121008
17	Amb 200 400	9, 0.10, 0.04	W011399000	W011299001 W011299006 W011299009	W011299002 W011299005 W011299008	W011299003 W011299004 W011299007
25	Amb 200 400	Linear, 85 Rayls	W091498000	W091498001 W091498006 W091498009	W091498002 W091498005 W091498008	W091498003 W091498004 W091498007

## **Explanation of data contained in \*.d11 files for Relative In-situ Impedance In Tables A9 through A12:**

### **1. For Ambient conditions:**

Example of a file name - **wn1-2-30.d11**

wn - white noise excitation,

1 - bulk #1, which is 100 ppi SiC,

2 - Facesheet 2, which is 0.025"-thick 30% porous with 0.04" hole diameter

30 - Grazing flow Mach number of 0.30

Relative resistance and reactance are evaluated with respect to no grazing flow condition (i.e., Relative level = Level at a Grazing flow Mach - Level at no grazing flow). The measured relative impedance data is tabulated with respect to frequency for each of the five cavities excluding the data at and near the anti resonance frequencies and for frequencies the data looks unreal. The caption R Cavity #11 represents relative resistance data for cavity 1 for the first frequency segment. The relative reactance data follows the relative resistance as X Cavity #11.

All the resistance and reactance data are used to compute average levels at all available frequencies. The data is used for a Least square fit (LSQ) to a 2<sup>nd</sup> order polynomial. This is done using all the data as well as using the averaged data. The polynomial coefficients, thus, derived are listed following the relative reactance data. Finally, the least square data are computed for all frequencies up to 20 kHz and listed in the data file.

### **2. For Heated Conditions :**

Example of File Name - **wn1-1-200-30.d11**

wn - white noise excitation,

1 - bulk #1, which is 100 ppi SiC,

1 - Facesheet 1, which is 0.025"-thick 20% porous with 0.04" hole diameter

200 - Nominal Flow temperature in degree F

30 - Grazing flow Mach number of 0.30

Relative resistance and reactance are evaluated with respect to ambient data for a fixed grazing flow (i.e., Relative level = Level at a heated condition - Level at ambient temperature). Before computing the relative levels the frequency is normalized by square root of the temperature ratio (i.e., Normalized Frequency = Frequency x Square root of  $T_{amb}/T_{hot}$ , Temperatures in absolute scale). The impedance values for heated conditions are interpolated to match the normalized ambient frequencies (i.e., same as actual frequencies). Using the interpolated data the relative impedance is evaluated. The measured relative impedance data is tabulated with respect to normalized frequency for each of five cavities excluding the data at and near the anti resonance frequencies and for frequencies the data looks unreal in the same way as described for ambient data. It should be noted that the frequencies listed for the heated conditions are normalized frequencies.

Table A9. Relative impedance data files for 100 ppi 0.5" deep Silicon Carbide bulk panels  
(Continued).

Configurat ion	Temp °F	Facesheet Description, Porosity, S , Thickness, t, Hole Diameter d	File names for Relative Impedance Data at Different Grazing Flow Mach Number M. All files end with ".d01"		
			M = 0.30	M = 0.55	M = 0.80
1-4161	Amb 200 400	40, 0.025, 0.10	wn1-4161-30 wn1-4161-200-30 wn1-4161-400-30	wn1-4161-55 wn1-4161-200-55 wn1-4161-400-55	wn1-4161-80 wn1-4161-200-80 wn1-4161-400-80
1-8	Amb 200 400	40, 0.04, 0.04	wn1-8-30 wn1-8-200-30 wn1-8-400-30	wn1-8-55 wn1-8-200-55 wn1-8-400-55	wn1-8-80 wn1-8-200-80 wn1-8-400-80
1-4121	Amb 200 400	40, 0.10, 0.04	wn1-4121-30 wn1-4121-200-30 wn1-4121-400-30	wn1-4121-55 wn1-4121-200-55 wn1-4121-400-55	wn1-4121-80 wn1-4121-200-80 wn1-4121-400-80
1-5	Amb 200 400	40, 0.025, 0.06	wn1-5-30 wn1-5-200-30 wn1-5-400-30	wn1-5-55 wn1-5-200-55 wn1-5-400-55	wn1-5-80 wn1-5-200-80 wn1-5-400-80
1-4052	Amb 200 400	35, 0.10, 0.04	wn1-4052-30 wn1-4052-200-30 wn1-4052-400-30	wn1-4052-55 wn1-4052-200-55 wn1-4052-400-55	wn1-4052-80 wn1-4052-200-80 wn1-4052-400-80
1-7	Amb 200 400	40, 0.015, 0.04	wn1-7-30 wn1-7-200-30 wn1-7-400-30	wn1-7-55 wn1-7-200-55 wn1-7-400-55	wn1-7-80 wn1-7-200-80 wn1-7-400-80
1-4072	Amb 200 400	35, 0.04, 0.07	wn1-4072-30 wn1-4072-200-30 wn1-4072-400-30	wn1-4072-55 wn1-4072-200-55 wn1-4072-400-55	wn1-4072-80 wn1-4072-200-80 wn1-4072-400-80
1-4075	Amb 200 400	35, 0.10, 0.07	wn1-4075-30 wn1-4075-200-30 wn1-4075-400-30	wn1-4075-55 wn1-4075-200-55 wn1-4075-400-55	wn1-4075-80 wn1-4075-200-80 wn1-4075-400-80
1-4031	Amb 200 400	30, 0.10, 0.07	wn1-4031-30 wn1-4031-200-30 wn1-4031-400-30	wn1-4031-55 wn1-4031-200-55 wn1-4031-400-55	wn1-4031-80 wn1-4031-200-80 wn1-4031-400-80
1-12	Amb 200 400	Linear, 15 Rayls	wn1-12-30 wn1-12-200-30 wn1-12-400-30	wn1-12-55 wn1-12-200-55 wn1-12-400-55	wn1-12-80 wn1-12-200-80 wn1-12-400-80
1-11	Amb 200 400	Linear, 10 Rayls	wn1-11-30 wn1-11-200-30 wn1-11-400-30	wn1-11-55 wn1-11-200-55 wn1-11-400-55	wn1-11-80 wn1-11-200-80 wn1-11-400-80
1-4143	Amb 200 400	40, 0.10, 0.07	wn1-4143-30 wn1-4143-200-30 wn1-4143-400-30	wn1-4143-55 wn1-4143-200-55 wn1-4143-400-55	wn1-4143-80 wn1-4143-200-80 wn1-4143-400-80

Table A9. Relative impedance data files for 100 ppi 0.5" deep Silicon Carbide bulk panels (Concluded).

Configurat ion	Temp °F	Facesheet Description, Porosity, S , Thickness, t, Hole Diameter d	File names for Relative Impedance Data at Different Grazing Flow Mach Number M. All files end with ".d01"		
		S, %, t, in, d, in	M = 0.30	M = 0.55	M = 0.80
1-6	Amb 200 400	40, 0.025, 0.08	wn1-6-200-30 wn1-6-400-30	wn1-6-200-55 wn1-6-400-55	wn1-6-200-80 wn1-6-400-80
1-9	Amb 200 400	40, 0.06, 0.04	wn1-9-200-30 wn1-9-400-30	wn1-9-200-55 wn1-9-400-55	wn1-9-200-80 wn1-9-400-80
1-3	Amb 200 400	40, 0.025, 0.04	wn1-3-30 wn1-3-200-30 wn1-3-400-30	wn1-3-55 wn1-3-200-55 wn1-3-400-55	wn1-3-80 wn1-3-200-80 wn1-3-400-80
1-2	Amb 200 400	30, 0.025, 0.04	wn1-2-30 wn1-2-200-30 wn1-2-400-30	wn1-2-55 wn1-2-200-55 wn1-2-400-55	wn1-2-80 wn1-2-200-80 wn1-2-400-80
1-1	Amb 200 400	20, 0.025, 0.04	wn1-1-30 wn1-1-200-30 wn1-1-400-30	wn1-1-55 wn1-1-200-55 wn1-1-400-55	wn1-1-80 wn1-1-200-80 wn1-1-400-80

Note : Facesheet 11 of config1-11 has nominal resistivity of 10 Rayls. However, the measurement shows it to be closer to 13 Rayls



Table A10. Relative impedance data files for 12 lbf 0.5" deep T-Foam bulk panels .

Configurat ion	Temp °F	Facesheet Description, Porosity, S , Thickness, t, Hole Diameter d	File names for Relative Impedance Data at Different Grazing Flow Mach Number M. All files end with “.d01’		
		S, %, t, in, d, in	M = 0.30	M = 0.55	M = 0.80
6-8	Amb 200 400	40, 0.04, 0.04	wn6-8-30 wn6-8-200-30 wn6-8-400-30	wn6-8-55 wn6-8-200-55 wn6-8-400-55	wn6-8-80 wn6-8-200-80 wn6-8-400-80
6-4	Amb 200 400	40, 0.025, 0.025	wn6-4-30 wn6-4-200-30 wn6-4-400-30	wn6-4-55 wn6-4-200-55 wn6-4-400-55	wn6-4-80 wn6-4-200-80 wn6-4-400-80
6-11	Amb 200 400	Linear, 10 Rayls	wn6-11-30 wn6-11-200-30 wn6-11-400-30	wn6-11-55 wn6-11-200-55 wn6-11-400-55	wn6-11-80 wn6-11-200-80 wn6-11-400-80
6-4143	Amb 200 400	40, 0.10, 0.07	wn6-4143-30 wn6-4143-200-30 wn6-4143-400-30	wn6-4143-55 wn6-4143-200-55 wn6-4143-400-55	wn6-4143-80 wn6-4143-200-80 wn6-4143-400-80
6-6	Amb 200 400	40, 0.025, 0.08	wn6-6-30 wn6-6-200-30 wn6-6-400-30	wn6-6-55 wn6-6-200-55 wn6-6-400-55	wn6-6-80 wn6-6-200-80 wn6-6-400-80
6-9	Amb 200 400	40, 0.06, 0.04	wn6-9-30 wn6-9-200-30 wn6-9-400-30	wn6-9-55 wn6-9-200-55 wn6-9-400-55	wn6-9-80 wn6-9-200-80 wn6-9-400-80
6-3	Amb 200 400	40, 0.025, 0.04	wn6-3-30 wn6-3-200-30 wn6-3-400-30	wn6-3-55 wn6-3-200-55 wn6-3-400-55	wn6-3-80 wn6-3-200-80 wn6-3-400-80
6-2	Amb 200 400	30, 0.025, 0.04	wn6-2-30 wn6-2-200-30 wn6-2-400-30	wn6-2-55 wn6-2-200-55 wn6-2-400-55	wn6-2-80 wn6-2-200-80 wn6-2-400-80
6-1	Amb 200 400	20, 0.025, 0.04	wn6-1-30 wn6-1-200-30 wn6-1-400-30	wn6-1-55 wn6-1-200-55 wn6-1-400-55	wn6-1-80 wn6-1-200-80 wn6-1-400-80

Table A11. Relative impedance data files for SDOF type panels with facesheets used for bulk absorber panels.

Configuration	Temp °F	Facesheet Description, Porosity, S, Thickness, t, Hole Diameter d	File names for Relative Impedance Data at Different Grazing Flow Mach Number M. All files end with ".d01"		
		S, %, t, in, d, in	M = 0.30	M = 0.55	M = 0.80
t1-8	Amb 200 400	40, 0.04, 0.04	wnt1-8-30 wnt1-8-200-30 wnt1-8-400-30	wnt1-8-55 wnt1-8-200-55 wnt1-8-400-55	wnt1-8-80 wnt1-8-200-80 wnt1-8-400-80
t1-4121	Amb 200 400	40, 0.10, 0.04	wnt1-4121-30 wnt1-4121-200-30 wnt1-4121-400-30	wnt1-4121-55 wnt1-4121-200-55 wnt1-4121-400-55	wnt1-4121-80 wnt1-4121-200-80 wnt1-4121-400-80
t1-5	Amb 200 400	40, 0.025, 0.06	wnt1-5-30 wnt1-5-200-30 wnt1-5-400-30	wnt1-5-55 wnt1-5-200-55 wnt1-5-400-55	wnt1-5-80 wnt1-5-200-80 wnt1-5-400-80
t1-11	Amb 200 400	Linear, 10 Rayls	wnt1-11-30 wnt1-11-200-30 wnt1-11-400-30	wnt1-11-55 wnt1-11-200-55 wnt1-11-400-55	wnt1-11-80 wnt1-11-200-80 wnt1-11-400-80
t1-4143	Amb 200 400	40, 0.10, 0.07	wnt1-4143-30 wnt1-4143-200-30 wnt1-4143-400-30	wnt1-4143-55 wnt1-4143-200-55 wnt1-4143-400-55	wnt1-4143-80 wnt1-4143-200-80 wnt1-4143-400-80
t1-6	Amb 200 400	40, 0.025, 0.08	wnt1-6-30 wnt1-6-200-30 wnt1-6-400-30	wnt1-6-55 wnt1-6-200-55 wnt1-6-400-55	wnt1-6-80 wnt1-6-200-80 wnt1-6-400-80
t1-9	Amb 200 400	40, 0.06, 0.04	wnt1-9-30 wnt1-9-200-30 wnt1-9-400-30	wnt1-9-55 wnt1-9-200-55 wnt1-9-400-55	wnt1-9-80 wnt1-9-200-80 wnt1-9-400-80
t1-3	Amb 200 400	40, 0.025, 0.04	wnt1-3-30 wnt1-3-200-30 wnt1-3-400-30	wnt1-3-55 wnt1-3-200-55 wnt1-3-400-55	wnt1-3-80 wnt1-3-200-80 wnt1-3-400-80
t1-2	Amb 200 400	30, 0.025, 0.04	wnt1-2-30 wnt1-2-200-30 wnt1-2-400-30	wnt1-2-55 wnt1-2-200-55 wnt1-2-400-55	wnt1-2-80 wnt1-2-200-80 wnt1-2-400-80
t1-1	Amb 200 400	20, 0.025, 0.04	wnt1-1-30 wnt1-1-200-30 wnt1-1-400-30	wnt1-1-55 wnt1-1-200-55 wnt1-1-400-55	wnt1-1-80 wnt1-1-200-80 wnt1-1-400-80

Table A12. Relative impedance data files for SDOF type panels with facesheets of lower porosities.

Configurat ion	Temp °F	Facesheet Description, Porosity, S , Thickness, t, Hole Diameter d	File names for Relative Impedance Data at Different Grazing Flow Mach Number M. All files end with “.d01”		
		S, %, t, in, d, in	M = 0.30	M = 0.55	M = 0.80
2	Amb 200 400	9, 0.025, 0.04	wn-2-30 wn-2-200-30 wn-2-400-30	wn-2-55 wn-2-200-55 wn-2-400-55	wn-2-80 wn-2-200-80 wn-2-400-80
4	Amb 200 400	15, 0.025, 0.04	wn-4-30 wn-4-200-30 wn-4-400-30	wn-4-55 wn-4-200-55 wn-4-400-55	wn-4-80 wn-4-200-80 wn-4-400-80
11	Amb 200 400	9, 0.025, 0.08	wn-11-30 wn-11-200-30 wn-11-400-30	wn-11-55 wn-11-200-55 wn-11-400-55	wn-11-80 wn-11-200-80 wn-11-400-80
12	Amb	9, 0.01, 0.04	wn-12-30	wn-12-55	wn-12-80
15	Amb 200 400	9, 0.06, 0.04	wn-15-30 wn-15-200-30 wn-15-400-30	wn-15-55 wn-15-200-55 wn-15-400-55	wn-15-80 wn-15-200-80 wn-15-400-80
17	Amb 200 400	9, 0.10, 0.04	wn-17-30 wn-17-200-30 wn-17-400-30	wn-17-55 wn-17-200-55 wn-17-400-55	wn-17-80 wn-17-200-80 wn-17-400-80
25	Amb 200 400	Linear, 85 Rayls	wn-25-30 wn-25-200-30 wn-25-400-30	wn-25-55 wn-25-200-55 wn-25-400-55	wn-25-80 wn-25-200-80 wn-25-400-80

Table A13. Boundary Layer Parameters Derived by Curve Fitting the Measured Boundary Layer Profile data for SDOF Type Panels (continued)

File Name (* .blt)	Measured Centerline Data		Parameters Derived by Curve fitting					
	Mach No.	Tem p °F	C <sub>F</sub>	Mach No	δ (Inch)	δ' (Inch)	θ (Inch)	PT/PTE
Hardwall Configuration								
Hwt024	0.30	Amb	0.00349	0.28429	0.4	0.04168	0.03022	0.99005
Hwt025	0.55	Amb	0.00326	0.50408	1.39394	0.03573	0.01682	0.99376
Hwt026	0.80	Amb	0.00313	0.6899	1.18687	0.02765	0.01108	0.99057
Hwt027	0.30	200	0.00362	0.28429	0.49091	0.04706	0.03419	0.99083
Hwt028	0.55	200	0.00338	0.50408	1.33839	0.04035	0.02122	0.99237
Hwt032	0.80	200	0.00329	0.67778	1.26263	0.02927	0.01164	0.99093
Hwt033	0.30	400	0.00400	0.28143	0.4	0.04038	0.02919	0.99056
Hwt036	0.55	400	0.00350	0.47347	1.57576	0.05088	0.02802	0.99260
Hwt039	0.80	400	0.00350	0.65758	1.23738	0.03106	0.01331	0.99045
Config2; SDOF, S=9%, t=0.025", d=0.04"								
B102301	0.30	Amb	0.00343	0.28143	1.4899	0.05568	0.03473	0.99670
B102302	0.55	Amb	0.00304	0.51224	1.42222	0.05591	0.03360	0.98920
B102303	0.80	Amb	0.00304	0.70202	1.14646	0.03672	0.01860	0.98543
B102306	0.30	200	0.00358	0.28143	1.5	0.06213	0.04015	0.99629
B102305	0.55	200	0.00330	0.50612	1.34445	0.05047	0.02968	0.99001
B102304	0.80	200	0.00324	0.70202	1.13636	0.03490	0.01714	0.98621
B102309	0.30	400	0.00370	0.29	0.5	0.05275	0.03810	0.98954
B102308	0.55	400	0.00340	0.52449	1.55556	0.05621	0.03222	0.98982
B102307	0.80	400	0.00324	0.71414	1.40909	0.05050	0.02673	0.98292
Config4; SDOF, S=15%, t=0.025", d=0.04"								
B18-22-1	0.30	Amb	0.00331	0.28143	0.5	0.05125	0.03727	0.99039
B18-22-2	0.55	Amb	0.00304	0.53061	1.51111	0.05672	0.03326	0.98910
B18-22-3	0.80	Amb	0.00304	0.70202	1.18687	0.03906	0.02007	0.98495
B19-9-5	0.30	200	0.00358	0.28143	1.5	0.06334	0.04118	0.99621
B19-9-2	0.55	200	0.00314	0.51224	0.5	0.05010	0.03453	0.97102
B19-9-4	0.80	200	0.00319	0.70202	1.25758	0.03815	0.01864	0.98640
B19-10-1	0.30	400	0.00374	0.28143	0.5	0.05248	0.03797	0.99018
B19-10-2	0.55	400	0.00340	0.51224	1.58889	0.05852	0.03397	0.99002
B19-10-3	0.80	400	0.00330	0.70202	1.37879	0.04650	0.02401	0.98456
Config1-1; SDOF, S=20%, t=0.025", d=0.04"								
B9-26-1	0.30	Amb	0.00327	0.28143	0.5	0.05253	0.03816	0.99015
B9-26-2	0.55	Amb	0.00304	0.52449	1.6	0.05763	0.03329	0.98982
B9-26-3	0.80	Amb	0.00299	0.70202	1.29798	0.04470	0.02353	0.98410
B9-26-4	0.30	200	0.00348	0.28143	0.5	0.05204	0.03775	0.99025
B9-26-5	0.55	200	0.00319	0.51224	1.6	0.05820	0.03379	0.99014
B9-26-6	0.80	200	0.00319	0.70202	1.21717	0.03899	0.01965	0.98547
B9-26-7	0.30	400	0.00373	0.28143	0.5	0.05263	0.03807	0.99015
B9-26-8	0.55	400	0.00330	0.51224	0.5	0.05282	0.03628	0.96951
B9-26-9	0.80	400	0.00324	0.71010	1.36869	0.05179	0.02812	0.98196

Table A13. Boundary Layer Parameters Derived by Curve Fitting the Measured Boundary Layer Profile data for SDOF Type Panels (continued).

File Name (*blt)	Measured Centerline Data		Parameters Derived by Curve fitting					
	Mach No.	Tem p °F	C <sub>F</sub>	Mach No	δ (Inch)	δ* (Inch)	θ (Inch)	PT/PTE
Config1-2; SDOF, S=30%, t=0.025", d=0.04"								
B021999001	0.30	Amb	0.00242	0.28143	0.56061	0.08996	0.06198	0.98532
B021999002	0.55	Amb	0.00207	0.50612	0.53333	0.09202	0.05968	0.95275
B021999003	0.80	Amb	0.00217	0.70202	0.5	0.07811	0.04875	0.92383
B021999006	0.30	200	0.00240	0.28143	0.57071	0.10	0.06736	0.98413
B021999005	0.55	200	0.00228	0.50612	0.54444	0.09119	0.05946	0.95400
B021999004	0.80	200	0.00233	0.70202	0.51010	0.07923	0.04944	0.92427
B021999009	0.30	400	0.00271	0.28143	0.55051	0.09224	0.06274	0.98476
B021999008	0.55	400	0.00248	0.50612	0.53333	0.08780	0.05740	0.95474
B021999007	0.80	400	0.00248	0.70202	0.50	0.07840	0.04878	0.92366
Config1-3; SDOF, S=40%, t=0.025", d=0.04"								
BI022499001	0.30	Amb	0.00216	0.28143	0.62121	0.11017	0.07409	0.98395
BI022499002	0.55	Amb	0.00177	0.50612	0.61111	0.11996	0.07514	0.94710
BI022499003	0.80	Amb	0.00177	0.70202	0.56061	0.10789	0.06439	0.90840
BI022499006	0.30	200	0.00224	0.28143	0.62121	0.11432	0.07598	0.98342
BI022499005	0.55	200	0.00192	0.50612	0.61111	0.11861	0.07447	0.94764
BI022499004	0.80	200	0.00192	0.70202	0.56061	0.10648	0.06371	0.90947
BI022499009	0.30	400	0.00248	0.28143	0.63131	0.11233	0.07528	0.98392
BI022499008	0.55	400	0.00212	0.50612	0.60	0.11336	0.07166	0.94887
BI022499007	0.80	400	0.00212	0.70202	0.57071	0.10416	0.06288	0.91260
Config1-8; SDOF, S=40%, t=0.04", d=0.04"								
BI031999001	0.30	Amb	0.00200	0.29143	0.61111	0.11776	0.07715	0.98153
BI031999002	0.55	Amb	0.00171	0.51837	0.64444	0.12933	0.08021	0.94373
BI031999003	0.80	Amb	0.00177	0.71616	0.70202	0.12998	0.07804	0.90845
BI031999006	0.30	200	0.00210	0.28429	0.60101	0.11786	0.07676	0.98214
BI031999005	0.55	200	0.00182	0.51837	0.64444	0.13010	0.08046	0.94346
BI031999004	0.80	200	0.00182	0.71010	0.69192	0.13277	0.07907	0.90691
BI031999009	0.30	400	0.00220	0.28143	0.62121	0.12408	0.08025	0.98221
BI031999008	0.55	400	0.00192	0.51224	0.61111	0.12597	0.07738	0.94369
BI031999007	0.80	400	0.00192	0.70202	0.56061	0.11351	0.06664	0.90441
Config1-4121; SDOF, S=40%, t=0.10", d=0.04"								
BI041599001	0.30	Amb	0.00255	0.28143	0.50000	0.07852	0.05431	0.98561
BI041599002	0.55	Amb	0.00233	0.50612	0.50000	0.07665	0.05093	0.95752
BI041599003	0.80	Amb	0.00248	0.70202	0.50000	0.06400	0.04095	0.93664
BI041599006	0.30	200	0.00305	0.28143	0.54040	0.07108	0.05059	0.98779
BI041599005	0.55	200	0.00273	0.50612	0.50000	0.06720	0.04548	0.96241
BI041599004	0.80	200	0.00263	0.70202	0.52020	0.06637	0.04242	0.93687
BI041599009	0.30	400	0.00327	0.28143	0.50000	0.06757	0.04781	0.98749
BI041599008	0.55	400	0.00279	0.50612	0.50000	0.07194	0.04817	0.95997
BI041599007	0.80	400	0.00284	0.70202	0.50000	0.06379	0.04071	0.93693

Table A13. Boundary Layer Parameters Derived by Curve Fitting the Measured Boundary Layer Profile data for SDOF Type Panels (continued).

File Name (* .blt)	Measured Centerline Data		Parameters Derived by Curve fitting					
	Mach No.	Tem p °F	C <sub>F</sub>	Mach No	δ (Inch)	δ* (Inch)	θ (Inch)	PT/PTE
Config1-5; SDOF, S=40%, t=0.025", d=0.06"								
BI041699001	0.30	Amb	0.00218	0.28143	0.53030	0.09689	0.06457	0.98352
BI041699002	0.55	Amb	0.00187	0.50612	0.50000	0.09730	0.06106	0.94751
BI041699003	0.80	Amb	0.00222	0.72424	0.50000	0.07558	0.04705	0.92221
BI041699006	0.30	200	0.00240	0.28143	0.53030	0.09463	0.06341	0.98387
BI041699005	0.55	200	0.00207	0.50612	0.50000	0.09453	0.05977	0.94883
BI041699004	0.80	200	0.00238	0.71616	0.50000	0.07636	0.04752	0.92296
BI041699009	0.30	400	0.00253	0.28143	0.55051	0.09958	0.06639	0.98369
BI041699008	0.55	400	0.00222	0.50612	0.50000	0.09428	0.05959	0.94897
BI041699007	0.80	400	0.00248	0.70808	0.50000	0.07875	0.04885	0.92227
Config1-11; SDOF, Linear Facesheet, 10 Rayls, t=0.03"								
BI040999001	0.30	Amb	0.00214	0.28143	0.55051	0.10270	0.06802	0.98322
BI040999002	0.55	Amb	0.00182	0.50612	0.53333	0.10611	0.06614	0.94650
BI040999003	0.80	Amb	0.00197	0.70202	0.5	0.08940	0.05432	0.91410
BI040999006	0.30	200	0.00242	0.28143	0.62121	0.10609	0.07195	0.98448
BI040999005	0.55	200	0.00197	0.50612	0.52222	0.10262	0.06415	0.94709
BI040999004	0.80	200	0.00212	0.70202	0.5	0.08795	0.05358	0.91537
BI040999009	0.30	400	0.00267	0.28143	0.58081	0.09815	0.06663	0.98464
BI040999008	0.55	400	0.00212	0.50612	0.54444	0.10539	0.06612	0.94779
BI040999007	0.80	400	0.00228	0.70202	0.5	0.08789	0.05349	0.91546
Config1-4143; SDOF, S=40%, t=0.10", d=0.07"								
BI033099001	0.30	Amb	0.00246	0.28143	0.53030	0.08601	0.05909	0.98518
BI033099002	0.55	Amb	0.00207	0.50612	0.52222	0.09175	0.05923	0.95199
BI033099003	0.80	Amb	0.00217	0.70202	0.5	0.07944	0.04943	0.92267
BI033099006	0.30	200	0.00257	0.28143	0.56061	0.09101	0.06246	0.98516
BI033099005	0.55	200	0.00222	0.506	0.5	0.08719	0.05632	0.95233
BI033099004	0.80	200	0.00233	0.70202	0.5	0.07805	0.04866	0.92393
BI033099009	0.30	400	0.00279	0.28143	0.54040	0.08769	0.06008	0.98519
BI033099008	0.55	400	0.00243	0.50612	0.52222	0.08829	0.05739	0.95365
BI033099007	0.80	400	0.00248	0.70202	0.5	0.07837	0.04876	0.92369
Config1-6; SDOF, S=40%, t=0.025", d=0.08"								
BI040799001	0.30	Amb	0.00263	0.28429	0.5	0.07593	0.05285	0.98577
BI040799002	0.55	Amb	0.00253	0.51837	0.5	0.06824	0.04601	0.98016
BI040799003	0.80	Amb	0.00284	0.78283	1.5	0.05389	0.02793	0.98007
BI040799006	0.30	200	0.00283	0.28571	0.5	0.07410	0.05174	0.98596
BI040799005	0.55	200	0.00268	0.51224	0.5	0.06816	0.04598	0.96107
BI040799004	0.80	200	0.00284	0.72222	0.5	0.05548	0.03547	0.94213
BI040799009	0.30	400	0.00301	0.28143	0.5	0.07560	0.05253	0.98612
BI040799008	0.55	400	0.00273	0.51224	0.5	0.07329	0.04886	0.95839
BI040799007	0.80	400	0.00299	0.71616	0.5	0.05684	0.03633	0.94162

Table A13. Boundary Layer Parameters Derived by Curve Fitting the Measured Boundary Layer Profile data for SDOF Type Panels (continued).

File Name (* .blt)	Measured Centerline Data		Parameters Derived by Curve fitting					
	Mach No.	Temp °F	C <sub>F</sub>	Mach No	$\delta$ (Inch)	$\delta^*$ (Inch)	$\theta$ (Inch)	PT/PTE
Config1-9; SDOF, S=40%, t=0.06", d=0.04"								
bl032499001	0.30	Amb	.00200	.29857	.72727	.13488	.08938	.98128
bl032499002	0.55	Amb	.00151	.53061	.67778	.14970	.08949	.93639
bl032499003	0.80	Amb	.00146	.71616	.62121	.14001	.07911	.89190
bl032499006	0.30	200	.00200	.29286	.72222	.14266	.09264	.98096
bl032499005	0.55	200	.00166	.53061	.70000	.14907	.09028	.93831
bl032499004	0.80	200	.00156	.71414	.63131	.14141	.08007	.89297
bl032499009	0.30	400	.00200	.28286	.67677	.14386	.09096	.98106
bl032499008	0.55	400	.00177	.52449	.65556	.14275	.08576	.93847
bl032499007	0.80	400	.00171	.70808	.63131	.13823	.07899	.89646
Config11; SDOF, S=9%, t=0.025", d=0.08"								
b33001	0.30	Amb	.00358	.28143	.50000	.04299	.03126	.99193
b33002	0.55	Amb	.00309	.51224	1.52222	.05419	.03124	.99038
b33003	0.80	Amb	.00309	.70202	1.14646	.03629	.01823	.98565
b33006	0.30	200	.00360	.28143	.50000	.04908	.03565	.99080
b33005	0.55	200	.00324	.50612	1.50000	.05628	.03313	.99001
b33004	0.80	200	.00319	.70202	1.18687	.04019	.02085	.98446
b33009	0.30	400	.00394	.28143	.50000	.04750	.03441	.99111
b33008	0.55	400	.00350	.50612	1.37778	.05237	.03079	.98988
b33007	0.80	400	.00340	.70202	1.15657	.04081	.02147	.98373
Config12; SDOF, S=9%, t=0.01", d=0.04"								
b415001	0.30	Amb	.00333	.28429	.50000	.04994	.03633	.99045
b415002	0.55	Amb	.00314	.53061	1.32222	.04522	.02538	.99024
b415003	0.80	Amb	.00299	.71010	1.24747	.04100	.02100	.98468
Config15; SDOF, S=9%, t=0.06", d=0.04"								
b121001	0.30	Amb	.00341	.28143	.50000	.04758	.03465	.99107
b121002	0.55	Amb	.00294	.50612	.50000	.05021	.03474	.97155
b121003	0.80	Amb	.00294	.70202	1.34848	.04375	.02238	.98518
b121006	0.30	200	.00356	.28143	.50000	.05030	.03652	.99057
b121005	0.55	200	.00309	.50612	.50000	.05260	.03628	.97026
b121004	0.80	200	.00314	.70202	1.28788	.04414	.02307	.98422
b121009	0.30	400	.00370	.28143	.53535	.05576	.04037	.99025
b121008	0.55	400	.00345	.50612	1.51111	.05482	.03165	.99041
b121007	0.80	400	.00330	.70202	1.33838	.04783	.02539	.98345

Table A13. Boundary Layer Parameters Derived by Curve Fitting the Measured Boundary Layer Profile data for SDOF Type Panels (concluded).

File Name (*blt)	Measured Centerline Data		Parameters Derived by Curve fitting					
	Mach No.	Temp °F	C <sub>F</sub>	Mach No	$\delta$ (Inch)	$\delta^*$ (Inch)	$\theta$ (Inch)	PT/PTE
Config17; SDOF, S=9%, t=0.10", d=0.04"								
b011299001	0.30	Amb	.00307	.29286	.50000	.05754	.04152	.98838
b011299002	0.55	Amb	.00284	.52449	.50000	.05373	.03690	.96760
b011299003	0.80	Amb	.00294	.72828	1.29798	.04307	.02201	.98385
b011299006	0.30	200	.00325	.28286	.50000	.06031	.04331	.98865
b011299005	0.55	200	.00304	.51837	.50000	.05437	.03731	.96794
b011299004	0.80	200	.00309	.73030	1.33838	.04617	.02392	.98304
b011299009	0.30	400	.00362	.28143	.58586	.06135	.04444	.99020
b011299008	0.55	400	.00319	.51224	.50000	.05647	.03868	.96746
b011299007	0.80	400	.00324	.70404	1.46970	.04951	.02556	.98449
Config25; SDOF, Linear Facesheet, 85 Rayls, t=0.035"								
b091498001	0.30	Amb	.00319	.28143	.50000	.05668	.04098	.98940
b091498002	0.55	Amb	.00304	.54286	1.60000	.05740	.03288	.98923
b091498003	0.80	Amb	.00299	.74040	1.26768	.04389	.02274	.98256
b091498006	0.30	200	.00362	.28143	.50000	.04796	.03486	.99101
b091498005	0.55	200	.00309	.52449	.50000	.05158	.03540	.96889
b091498004	0.80	200	.00309	.73434	1.31818	.04627	.02413	.98253
b091498009	0.30	400	.00384	.28143	.50000	.04923	.03567	.99078
b091498008	0.55	400	.00324	.50612	.50000	.05486	.03770	.96904
b091498007	0.80	400	.00324	.72020	1.41919	.04916	.02554	.98337



Table A14. Boundary Layer Parameters Derived by Curve Fitting the Measured Boundary Layer Profile data for 100 ppi 0.5" deep Silicon Carbide bulk panels (continued).

File Name (* .blt)	Measured Centerline Data		Parameters Derived by Curve fitting					
	Mach No.	Temp °F	C <sub>F</sub>	Mach No	δ (Inch)	δ* (Inch)	θ (Inch)	PT/PTE
Config1-1; Bulk Panel/Facesheet, S=20%, t=0.025", d=0.04"								
BI001	0.30	Amb	0.00329	0.28143	0.47273	0.05056	0.03669	0.98998
BI002	0.55	Amb	0.00311	0.5102	1.5	0.04939	0.02744	0.99129
BI003	0.80	Amb	0.00307	0.64546	1.5	0.03116	0.01124	0.99276
BI004	0.30	200	0.00331	0.28143	0.44545	0.05428	0.03893	0.98865
BI005	0.55	200	0.00326	0.52857	1.5	0.05001	0.02766	0.9906
BI006	0.80	200	0.00316	0.67778	1.5	0.03628	0.01514	0.99038
BI007	0.30	400	0.00337	0.28143	0.44545	0.05923	0.04198	0.98768
BI008	0.55	400	0.00334	0.52857	1.9	0.0575	0.03007	0.99165
BI009	0.80	400	0.00329	0.69394	1.5	0.04462	0.02155	0.98699
Config1-2; Bulk Panel/Facesheet, S=30%, t=0.025", d=0.04"								
BI9-15-1	0.30	Amb	0.00297	0.28143	0.52727	0.06581	0.0472	0.98838
BI9-15-2	0.55	Amb	0.00293	0.55306	1.5	0.0712	0.04481	0.98469
BI9-15-3	0.80	Amb	0.00289	0.7303	1.5	0.0516	0.02686	0.98305
BI9-16-1	0.30	200	0.00313	0.28143	0.49091	0.06283	0.04486	0.9881
BI9-16-2	0.55	200	0.00309	0.54082	1.5	0.06891	0.04305	0.98583
BI9-16-3	0.80	200	0.00298	0.71818	1.5	0.05925	0.0328	0.98062
BI9-16-4	0.30	400	0.00343	0.28143	0.5	0.06154	0.04404	0.98855
BI9-16-5	0.55	400	0.00336	0.53469	1.5	0.06129	0.03677	0.98786
BI9-16-6	0.80	400	0.00322	0.70202	1.5	0.05269	0.0278	0.98377
Config1-3; Bulk Panel/Facesheet, S=40%, t=0.025", d=0.04"								
B10-6-1	0.30	Amb	0.00293	0.28143	0.47273	0.06310	0.04486	0.98762
B10-6-2	0.55	Amb	0.00297	0.55306	1.5	0.06677	0.04125	0.98575
B10-6-3	0.80	Amb	0.00292	0.73030	1.5	0.04908	0.02490	0.98404
B10-6-6	0.30	200	0.00319	0.28143	0.47273	0.05961	0.04262	0.98827
B10-6-5	0.55	200	0.00313	0.54694	1.5	0.06286	0.03806	0.98696
B10-6-4	0.80	200	0.00307	0.71414	1.5	0.04636	0.02286	0.98567
B10-6-9	0.30	400	0.00337	0.28143	0.42727	0.05756	0.04071	0.98753
B10-6-8	0.55	400	0.00340	0.54082	1.5	0.05529	0.03177	0.9890
B10-6-7	0.80	400	0.00329	0.70202	1.5	0.04382	0.02084	0.98704
Config1-4161; Bulk Panel/Facesheet, S=40%, t=0.025", d=0.10"								
BI022699001	0.30	Amb	0.00220	0.28143	0.57071	0.10163	0.06824	0.98389
BI022699002	0.55	Amb	0.00177	0.50612	0.54444	0.10956	0.06806	0.94597
BI022699003	0.80	Amb	0.00192	0.70202	0.55051	0.098	0.05963	0.91441
BI022699006	0.30	200	0.00236	0.28143	0.62121	0.10834	0.07310	0.98419
BI022699005	0.55	200	0.00207	0.50612	0.64444	0.11460	0.07374	0.95148
BI022699004	0.80	200	0.00207	0.70202	0.56061	0.09852	0.06006	0.91541
BI022699009	0.30	400	0.00200	0.28143	0.63131	0.13632	0.08566	0.981
BI022699008	0.55	400	0.00177	0.50612	0.61111	0.13489	0.08093	0.94164
BI022699007	0.80	400	0.00187	0.70202	0.5202	0.10971	0.06357	0.90108

Table A14. Boundary Layer Parameters Derived by Curve Fitting the Measured Boundary Layer Profile data for 100 ppi 0.5" deep Silicon Carbide bulk panels (continued).

File Name (* .blt)	Measured Centerline Data		Parameters Derived by Curve fitting					
	Mach No.	Temp °F	C <sub>F</sub>	Mach No	δ (Inch)	δ* (Inch)	θ (Inch)	PT/PTE
Config1-8; Bulk Panel/Facesheet, S=40%, t=0.04", d=0.04"								
B011499001	0.30	Amb	0.002	0.28429	0.58081	0.11182	0.07335	0.98241
B011499002	0.55	Amb	0.00161	0.51837	0.57778	0.12278	0.07466	0.94094
B011499003	0.80	Amb	0.00187	0.70202	0.5	0.09281	0.05590	0.91123
B011499006	0.30	200	0.00214	0.28429	0.59091	0.11491	0.07829	0.98227
B011499005	0.55	200	0.00177	0.50612	0.61111	0.12777	0.05887	0.94421
B011499004	0.80	200	0.00192	0.70202	0.51010	0.09899	0.05590	0.90780
B011499009	0.30	400	0.00240	0.28143	0.59091	0.11029	0.07289	0.98323
B011499008	0.55	400	0.00202	0.50612	0.56667	0.11357	0.07050	0.94620
B011499007	0.80	400	0.00212	0.70202	0.52020	0.09709	0.05827	0.91089
Config1-4121; Bulk Panel/Facesheet, S=40%, t=0.10", d=0.04"								
B120198001	0.30	Amb	0.00285	0.28143	0.5	0.06701	0.04764	0.98757
B120198002	0.55	Amb	0.00248	0.50612	0.53333	0.07299	0.04938	0.96173
B120198003	0.80	Amb	0.00263	0.70202	0.5	0.05696	0.03673	0.94329
B120198006	0.30	200	0.00335	0.28143	0.5	0.05636	0.04073	0.98946
B120198005	0.55	200	0.00284	0.50612	0.5	0.06211	0.04240	0.96509
B120198004	0.80	200	0.00309	0.73030	1.5	0.04109	0.01857	0.98723
B120198009	0.30	400	0.00354	0.28143	0.63131	0.06621	0.04799	0.99018
B120198008	0.55	400	0.00314	0.50612	0.5	0.05811	0.03981	0.96727
B120198007	0.80	400	0.00309	0.70202	0.5	0.05273	0.03397	0.94747
Config1-5; Bulk Panel/Facesheet, S=40%, t=0.025", d=0.06"								
B010799001	0.30	Amb	0.00234	0.29571	0.5	0.08552	0.05789	0.98290
B010799002	0.55	Amb	0.00212	0.52449	0.5	0.08374	0.05442	0.95094
B010799003	0.80	Amb	0.00228	0.72222	0.5	0.07173	0.04502	0.92618
B010799006	0.30	200	0.00244	0.28286	0.5	0.08872	0.05951	0.98380
B010799005	0.55	200	0.00212	0.50612	0.5	0.09219	0.05870	0.94993
B010799004	0.80	200	0.00238	0.71818	0.5	0.07544	0.04702	0.92344
B010799009	0.30	400	0.00267	0.28143	0.5	0.08729	0.05874	0.98419
B010799008	0.55	400	0.00238	0.51837	0.5	0.08711	0.05605	0.95030
B010799007	0.80	400	0.00273	0.73232	0.5	0.06674	0.04194	0.92948
Config1-4052; Bulk Panel/Facesheet, S=35%, t=0.10", d=0.04"								
B112498001	0.30	Amb	0.00319	0.28143	0.5	0.05483	0.03976	0.98973
B112498002	0.55	Amb	0.00279	0.50612	0.5	0.05731	0.03943	0.96765
B112498003	0.80	Amb	0.00279	0.70202	0.5	0.05003	0.03236	0.95002
B112498006	0.30	200	0.00356	0.28143	0.5	0.04938	0.03588	0.99074
B112498005	0.55	200	0.00304	0.50612	0.5	0.05397	0.03719	0.96950
B112498004	0.80	200	0.00304	0.70202	1.45959	0.05105	0.02702	0.98381
B112498009	0.30	400	0.00390	0.28143	0.53030	0.04873	0.03533	0.99139
B112498008	0.55	400	0.00340	0.50612	0.5	0.04899	0.03376	0.97229
B112498007	0.80	400	0.00335	0.70202	1.24747	0.04168	0.02139	0.98474

Table A14. Boundary Layer Parameters Derived by Curve Fitting the Measured Boundary Layer Profile data for 100 ppi 0.5" deep Silicon Carbide bulk panels (continued).

File Name (*blt)	Measured Centerline Data		Parameters Derived by Curve fitting					
	Mach No.	Temp °F	C <sub>F</sub>	Mach No	δ (Inch)	δ* (Inch)	θ (Inch)	PT/PTE
Config1-7; Bulk Panel/Facesheet, S=40%, t=0.015", d=0.04"								
B101998001	0.30	Amb	0.00208	0.28429	0.52020	0.10042	0.06577	0.98238
B101998002	0.55	Amb	0.00197	0.50612	0.51111	0.09484	0.06035	0.94963
B101998003	0.80	Amb	0.00222	0.71212	0.5	0.07650	0.04773	0.92349
B101998006	0.30	200	0.00200	0.28571	0.55051	0.11459	0.07304	0.98102
B101998005	0.55	200	0.00171	0.50612	0.56667	0.12276	0.07424	0.94253
B101998004	0.80	200	0.00192	0.70808	0.5	0.09731	0.05771	0.90625
B101998009	0.30	400	0.00222	0.28143	0.56061	0.11341	0.07300	9.98202
B101998008	0.55	400	0.00187	0.50612	0.53333	0.11539	0.06973	0.94262
B101998007	0.80	400	0.00197	0.70202	0.5	0.10123	0.05940	0.90444
Config1-4072; Bulk Panel/Facesheet, S=35%, t=0.04", d=0.07"								
B092898001	0.30	Amb	0.00311	0.28143	0.5	0.05893	0.04249	0.98900
B092898002	0.55	Amb	0.00304	0.52449	1.6	0.05710	0.03286	0.98993
B092898003	0.80	Amb	0.00304	0.70202	1.20707	0.03948	0.02022	0.98506
B092898006	0.30	200	0.00339	0.28143	0.5	0.05524	0.03996	0.98967
B092898005	0.55	200	0.00309	0.50612	0.5	0.05233	0.03610	0.97041
B092898004	0.80	200	0.00314	0.70202	1.31818	0.04104	0.02039	0.98595
B092898009	0.30	400	0.00349	0.28143	0.58081	0.06493	0.04688	0.98955
B092898008	0.55	400	0.00330	0.50612	0.5	0.05290	0.03640	0.97012
B092898007	0.80	400	0.00335	0.70202	1.23737	0.04284	0.02237	0.98408
Config1-4075; Bulk Panel/Facesheet, S=35%, t=0.10", d=0.07"								
B1604001	0.30	Amb	0.00327	0.28143	0.5	0.05281	0.03836	0.99010
B1604002	0.55	Amb	0.00294	0.50612	0.5	0.05166	0.03572	0.97074
B1604003	0.80	Amb	0.00299	0.70202	1.31818	0.04165	0.02097	0.98566
B1604006	0.30	200	0.00333	0.28143	0.5	0.05732	0.04136	0.98929
B1604005	0.55	200	0.00309	0.50612	0.5	0.05253	0.03623	0.97029
B1604004	0.80	200	0.00309	0.70202	1.39899	0.04668	0.02412	0.98471
B1604009	0.30	400	0.00358	0.28143	0.5	0.05754	0.04141	0.98926
B1604008	0.55	400	0.00335	0.50612	0.5	0.05120	0.03526	0.97106
B1604007	0.80	400	0.00335	0.70202	1.22727	0.04313	0.02269	0.98379
Config1-4031; Bulk Panel/Facesheet, S=30%, t=0.10", d=0.07"								
B0806001	0.30	Amb	0.00293	0.30429	0.5	0.06433	0.04580	0.98609
B0806002	0.55	Amb	0.00279	0.52449	0.5	0.05837	0.03989	0.96490
B0806003	0.80	Amb	0.00294	0.73636	1.40909	0.04782	0.02462	0.98311
B0806008	0.30	200	0.00305	0.28714	0.5	0.06602	0.04692	0.98726
B0806007	0.55	200	0.00294	0.52449	0.5	0.05738	0.03921	0.96550
B0806006	0.80	200	0.00304	0.72626	1.45959	0.04992	0.02585	0.98335
B0806011	0.30	400	0.00315	0.28143	0.5	0.07111	0.04994	0.98686
B0806010	0.55	400	0.00304	0.51224	0.5	0.06228	0.04236	0.96426
B0806009	0.80	400	0.00319	0.73232	1.5	0.05418	0.02857	0.98204

Table A14. Boundary Layer Parameters Derived by Curve Fitting the Measured Boundary Layer Profile data for 100 ppi 0.5" deep Silicon Carbide bulk panels (continued).

File Name (*.blt)	Measured Centerline Data		Parameters Derived by Curve fitting					
	Mach No.	Temp °F	C <sub>F</sub>	Mach No	δ (Inch)	δ* (Inch)	θ (Inch)	PT/PTE
Config1-12; Bulk Panel/Linear Facesheet, 15 Rayls, t=0.04"								
b519001	0.30	Amb	.00297	.30857	.50000	.06239	.04454	.98612
b519002	0.55	Amb	.00268	.53061	.50000	.06279	.04257	.96159
b519003	0.80	Amb	.00273	.72020	.50000	.05433	.03483	.94352
b519006	0.30	200	.00305	.29143	.50000	.06590	.04681	.98692
b519005	0.55	200	.00279	.53061	.50000	.06355	.04299	.96117
b519004	0.80	200	.00284	.71414	.50000	.05531	.03548	.94335
b519009	0.30	400	.00321	.28429	.50000	.06899	.04866	.98699
b519008	0.55	400	.00289	.52449	.50000	.06734	.04527	.95987
b519007	0.80	400	.00294	.72424	.50000	.05877	.03740	.93860
Config1-11; Bulk Panel/Linear Facesheet, 10 Rayls, t=0.03"								
b427001	0.30	Amb	.00281	.29000	.50000	.07032	.04955	.98622
b427002	0.55	Amb	.00268	.53061	.50000	.06217	.04219	.96195
b427003	0.80	Amb	.00284	.76465	1.50000	.05376	.02808	.98084
b427006	0.30	200	.00295	.28143	.50000	.06987	.04930	.98708
b427005	0.55	200	.00273	.51837	.50000	.06543	.04428	.96172
b427004	0.80	200	.00299	.76667	1.50000	.05287	.02727	.98118
b427009	0.30	400	.00289	.51224	.50000	.06768	.04563	.96135
b427007	0.55	400	.00299	.71818	.50000	.05654	.03612	.94165
b427010	0.80	400	.00323	.28143	.54545	.07251	.05145	.98768
Config1-4143; Bulk Panel/Facesheet, S=40%, t=0.10", d=0.07"								
b46001	0.30	Amb	.00321	.28143	.50000	.05504	.03989	.98970
b46002	0.55	Amb	.00294	.50612	.50000	.05122	.03541	.97100
b46003	0.80	Amb	.00294	.70202	1.38889	.04688	.02447	.98446
b46006	0.30	200	.00362	.28143	.52525	.04945	.03595	.99117
b46005	0.55	200	.00314	.50612	.50000	.05013	.03462	.97163
b46004	0.80	200	.00324	.70202	1.19697	.03306	.01515	.98792
b46009	0.30	400	.00360	.28143	.53030	.05890	.04251	.98962
b46008	0.55	400	.00340	.50612	1.60000	.06049	.03558	.98994
b46007	0.80	400	.00330	.70202	1.35858	.04693	.02452	.98411
Config1-6; Bulk Panel/Facesheet, S=40%, t=0.025", d=0.08"								
b21001	0.30	Amb	.00299	.28571	.50000	.06159	.04421	.98818
b21002	0.55	Amb	.00279	.53061	.50000	.05553	.03801	.96584
b21003	0.80	Amb	.00289	.73636	1.46970	.04602	.02275	.98466
b21004	0.30	200	.00313	.28571	.50000	.06344	.04531	.98785
b21005	0.55	200	.00294	.51837	.50000	.05768	.03947	.96605
b21006	0.80	200	.00319	.71616	1.47980	.05522	.02976	.98199
b21007	0.30	400	.00309	.51837	.50000	.05994	.04082	.96480
b21008	0.55	400	.00347	.28143	.50000	.06090	.04362	.98866
b21009	0.80	400	.00299	.73636	1.50000	.05646	.03041	.98093

Table A14. Boundary Layer Parameters Derived by Curve Fitting the Measured Boundary Layer Profile data for 100 ppi 0.5" deep Silicon Carbide bulk panels (concluded).

File Name (* .blt)	Measured Centerline Data		Parameters Derived by Curve fitting					
	Mach No.	Temp °F	$C_F$	Mach No	$\delta$ (Inch)	$\delta^*$ (Inch)	$\theta$ (Inch)	PT/PTE
Config 1-9; Bulk Panel/Facesheet, S=40%, t=0.06", d=0.04"								
b111901	0.30	Amb	.00248	.28429	.50505	.08120	.05587	.98501
b111902	0.55	Amb	.00217	.50612	.53333	.08670	.05698	.95519
b111903	0.80	Amb	.00228	.70202	.50000	.07297	.04602	.92842
b111906	0.30	200	.00271	.28143	.50000	.07853	.05425	.98562
b111905	0.55	200	.00238	.50612	.50000	.08121	.05330	.95526
b111904	0.80	200	.00248	.70404	.50000	.07098	.04483	.92993
b111909	0.30	400	.00297	.28143	.50000	.07700	.05332	.98588
b111908	0.55	400	.00273	.50612	.50000	.07340	.04900	.95922
b111907	0.80	400	.00279	.70404	.50000	.06580	.04184	.93476

Table A15. Boundary Layer Parameters Derived by Curve Fitting the Measured Boundary Layer Profile data for 12 lbf 0.5" deep T-Foam bulk panels (continued).

File Name (*blt)	Measured Centerline Data		Parameters Derived by Curve fitting					
	Mach No.	Temp °F	C <sub>F</sub>	Mach No	δ (Inch)	δ* (Inch)	θ (Inch)	PT/PTE
Config6-1; Bulk Panel/Facesheet, S=20%, t=0.025", d=0.04"								
b421001	0.30	Amb	.00343	.28143	.50000	.04706	.03427	.99117
b421002	0.55	Amb	.00309	.51224	1.40000	.05204	.03057	.98988
b421003	0.80	Amb	.00330	.70202	.50000	.02851	.01748	.97200
b421006	0.30	200	.00368	.28143	.59091	.04907	.03562	.99221
b421005	0.55	200	.00330	.51224	1.42222	.04825	.02705	.99093
b421004	0.80	200	.00330	.70202	.77273	.03734	.02205	.97664
b421009	0.30	400	.00392	.28143	.50000	.04745	.03439	.99111
b421008	0.55	400	.00345	.50612	1.38889	.05617	.03386	.98913
b421007	0.80	400	.00345	.70202	1.06566	.03624	.01871	.98444
Config6-2; Bulk Panel/Facesheet, S=30%, t=0.025", d=0.04"								
bl717001	0.30	Amb	.00285	.28143	.50000	.06780	.04811	.98743
bl717002	0.55	Amb	.00258	.51224	.50000	.06637	.04498	.96200
bl717003	0.80	Amb	.00289	.74848	1.46970	.05153	.02683	.98196
bl717006	0.30	200	.00283	.28143	.50000	.07435	.05191	.98632
bl717005	0.55	200	.00268	.50612	.50000	.06862	.04633	.96166
bl717004	0.80	200	.00279	.70202	.50000	.05726	.03686	.94305
bl717009	0.30	400	.00293	.28143	.51010	.07958	.05496	.98571
bl717008	0.55	400	.00273	.50612	.50000	.07335	.04898	.95925
bl717007	0.80	400	.00299	.70202	.50000	.05747	.03692	.94290
Config6-3; Bulk Panel/Facesheet, S=40%, t=0.025", d=0.04"								
b093098001	0.30	Amb	.00273	.28143	.50000	.07258	.05095	.98661
b093098002	0.55	Amb	.00248	.50612	.50000	.07098	.04775	.96042
b093098003	0.80	Amb	.00268	.70202	.50000	.05623	.03627	.94400
b093098006	0.30	200	.00287	.28143	.53535	.07672	.05393	.98678
b093098005	0.55	200	.00258	.50612	.50000	.07221	.04840	.95981
b093098004	0.80	200	.00284	.70202	.50000	.05567	.03587	.94458
b093098009	0.30	400	.00313	.28143	.50000	.07129	.05005	.98685
b093098008	0.55	400	.00279	.51837	.50000	.07137	.04769	.95852
b093098007	0.80	400	.00314	.75454	1.50000	.05900	.03193	.97918
Config6-8; Bulk Panel/Facesheet, S=40%, t=0.04", d=0.04"								
b020599001	0.30	Amb	.00212	.29286	.59596	.10815	.07214	.98231
b020599002	0.55	Amb	.00192	.53061	.56667	.10408	.06605	.94565
b020599003	0.80	Amb	.00207	.71414	.50000	.08312	.05109	.91716
b020599006	0.30	200	.00226	.29000	.55556	.10349	.06843	.98225
b020599005	0.55	200	.00202	.51837	.54444	.10300	.06494	.94655
b020599004	0.80	200	.00217	.71616	.50000	.08497	.05190	.91517
b020599009	0.30	400	.00248	.28429	.56061	.10221	.06798	.98325
b020599008	0.55	400	.00217	.51224	.52222	.09932	.06254	.94746
b020599007	0.80	400	.00233	.70808	.50000	.08509	.05204	.91668

Table A15. Boundary Layer Parameters Derived by Curve Fitting the Measured Boundary Layer Profile data for 12 lbf 0.5" deep T-Foam bulk panels (continued).

File Name (* .blt)	Measured Centerline Data		Parameters Derived by Curve fitting					
	Mach No.	Temp °F	C <sub>F</sub>	Mach No	δ (Inch)	δ* (Inch)	θ (inch)	PT/PTE
Config6-4; Bulk Panel/Facesheet, S=40%, t=0.025", d=0.025"								
b101298001	0.30	Amb	.00232	.29143	.52020	.08941	.06049	.98330
b101298002	0.55	Amb	.00212	.51224	.54444	.09146	.05959	.95285
b101298003	0.80	Amb	.00228	.70202	.50000	.07413	.04663	.92738
b101298006	0.30	200	.00259	.29429	.53535	.08643	.05927	.98392
b101298005	0.55	200	.00228	.51837	.54444	.09038	.05888	.95237
b101298004	0.80	200	.00238	.70202	.50000	.07592	.04754	.92582
b101298009	0.30	400	.00279	.28143	.50000	.08272	.05641	.98493
b101298008	0.55	400	.00248	.51224	.50000	.08338	.05426	.95322
b101298007	0.80	400	.00258	.70202	.50000	.07417	.04654	.92743
Config6-11; Bulk Panel/Linear Facesheet, 10 Rayls, t=0.03"								
bl033199001	0.30	Amb	.00253	.28571	.50000	.07929	.05470	.98505
bl033199002	0.55	Amb	.00233	.51837	.50000	.07649	.05068	.95574
bl033199003	0.80	Amb	.00284	.82929	1.50000	.04730	.02245	.98139
bl033199006	0.30	200	.00265	.29000	.53030	.08412	.05794	.98462
bl033199005	0.55	200	.00248	.51837	.50000	.07667	.05071	.95567
bl033199004	0.80	200	.00263	.72828	.50000	.06396	.04047	.93280
bl033199009	0.30	400	.00273	.28143	.50000	.08515	.05766	.98454
bl033199008	0.55	400	.00263	.51224	.50000	.07746	.05116	.95622
bl033199007	0.80	400	.00284	.73030	.50000	.06302	.03982	.93349
Config6-4143; Bulk Panel/Facesheet, S=40%, t=0.10", d=0.07"								
bl526001	0.30	Amb	.00291	.30000	.50000	.06459	.04600	.98641
bl526002	0.55	Amb	.00273	.53673	.50000	.05905	.04018	.96302
bl526003	0.80	Amb	.00289	.74242	1.50000	.04955	.02514	.98342
bl526006	0.30	200	.00293	.28143	.50000	.07080	.04985	.98692
bl526005	0.55	200	.00273	.51224	.50000	.06591	.04465	.96227
bl526004	0.80	200	.00304	.74242	1.47980	.04888	.02468	.98346
bl526009	0.30	400	.00313	.28143	.50505	.07217	.05065	.98682
bl526008	0.55	400	.00294	.50612	.50000	.06597	.04468	.96307
bl526007	0.80	400	.00319	.72828	1.50000	.05400	.02849	.98227
Config6-6; Bulk Panel/Facesheet, S=40%, t=0.025", d=0.08"								
bl041299001	0.30	Amb	.00214	.28714	.50505	.09507	.06273	.98242
bl041299002	0.55	Amb	.00202	.53673	.50000	.08999	.05729	.94552
bl041299003	0.80	Amb	.00233	.75050	.50000	.07132	.04430	.92187
bl041299006	0.30	200	.00238	.28143	.52020	.09357	.06256	.98376
bl041299005	0.55	200	.00217	.51837	.50000	.08953	.05728	.94906
bl041299004	0.80	200	.00243	.74242	.50000	.07328	.04545	.92133
bl041299009	0.30	400	.00244	.28286	.50505	.09582	.06296	.98283
bl041299008	0.55	400	.00228	.51224	.50000	.09161	.05828	.94915
bl041299007	0.80	400	.00258	.72020	.50000	.07382	.04605	.92465

Table A15. Boundary Layer Parameters Derived by Curve Fitting the Measured Boundary Layer Profile data for 12 lbf 0.5" deep T-Foam bulk panels (concluded).

File Name (* .blt)	Measured Centerline Data		Parameters Derived by Curve fitting					
	Mach No.	Temp °F	C <sub>F</sub>	Mach No	δ (Inch)	δ* (Inch)	θ (Inch)	PT/PTE
Config6-9; Bulk Panel/Facesheet, S=40%, t=0.06", d=0.04"								
bl505001	0.30	Amb	.00200	.29714	.59596	.11747	.07630	.98045
bl505002	0.55	Amb	.00171	.51837	.60000	.12336	.07587	.94256
bl505003	0.80	Amb	.00182	.70808	.50000	.09776	.05794	.90586
bl505006	0.30	200	.00206	.28429	.59091	.11862	.07663	.98178
bl505005	0.55	200	.00187	.51224	.58889	.11827	.07335	.94490
bl505004	0.80	200	.00192	.70404	.50000	.09778	.05798	.90675
bl505009	0.30	400	.00232	.28143	.58586	.11332	.07406	.98270
bl505008	0.55	400	.00207	.50612	.57778	.11320	.07077	.94724
bl505007	0.80	400	.00212	.70404	.50000	.09448	.05648	.90951



**Definition of the parameters used in DC flow resistance data files  
in Tables A16 through A18:**

Rdc -	DC flow resistance as evaluated from the measured flow rate & pressure drop parameters, Rayls
Vel -	Approach velocity through the liner sample as evaluated from the measured flow rate & pressure drop parameters, cm/sec
CorRdc -	Corrected DC flow resistance at standard conditions, Rayls
CorVel -	Corrected approach velocity at standard conditions, cm/sec
SamTs -	Static temperature of the liner sample, °F
SamPs -	Static pressure of the liner sample, psi
Flmdp -	Pressure drop across the flow meter, psi
FlmTs -	Static temperature at flow meter, °F
FlmPs -	Static pressure at flow meter, psi
Plmdp -	Plenum pressure drop, psi
TstPt -	Total pressure of the test section, psi
TstTt -	Total temperature of the test section, °F
TstPs -	Static pressure of the test section, psi

Table A16. DC flow resistance data files for 100 ppi 0.5" deep Silicon Carbide bulk panels.

Configurat ion	Temp °F	Facesheet Description, Porosity, S, Thickness, t, Hole Diameter d	File names for DC flow resistance Data at Different Grazing Flow Mach Number M. All files end with ".lsq"			
			M = 0.0	M = 0.30	M = 0.55	M = 0.70
Bulk Only	Amb		100sic.smt			
1-4161	Amb	40, 0.025, 0.10	dc022699000	dc022699001	dc022699002	dc022699003
1-8	Amb	40, 0.04, 0.04	d011499000	d011499001	d011499002	d011499003
1-4121	Amb	40, 0.10, 0.04	d120198000	d120198001	d120198002	d120198003
1-5	Amb	40, 0.025, 0.06	d121698000	d121698001	d121698002	d121698003
1-4052	Amb	35, 0.10, 0.04	d112498000	d112498004	d112498002	d112498003
1-7	Amb 200 400	40, 0.015, 0.04	d102098000	d102098001	d102098002	d102098003
				d102098006	d102098005	d102098004
				d102098009	d102098008	d102098007
1-4072	Amb 200 400	35, 0.04, 0.07	d092298000	d092298001	d092298002	d092298003
				d092298006	d092298005	d092298004
				d092298009	d092298008	d092298007
1-4075	Amb 200 400	35, 0.10, 0.07	dc605000	dc605001	dc605002	dc605003
				dc605006	dc605005	dc605004
				dc605009	dc605008	dc605007
1-4031	Amb 200 400	30, 0.10, 0.07	d0807000	d0807003	d0807002	d0807004
				d0807007	d0807006	d0807005
				d0807010	d0807009	d0807008
1-12	Amb 200 400	Linear, 15 Rayls	d522001	d522002	d522003	d522004
				d522007	d522006	d522005
				d522010	d522009	d522008
1-11	Amb 200 400	Linear, 10 Rayls	dc51001	dc51002	dc51003	dc51004
				dc51008	dc51007	dc51006
				dc51011	dc51010	dc51009
1-4143	Amb 200 400	40, 0.10, 0.07	d48001	d48002	d48003	d48004
				d48007	d48006	d48005
				d48010	d48009	d48008
1-6	Amb 200 400	40, 0.025, 0.08	d021601	d021602	d021603	d021604
				d021607	d021606	d021605
				d021610	d021609	d021608
1-9	Amb 200 400	40, 0.06, 0.04	d120201	d120102	d120104	d120105
				d120204	d120203	d120202
				d120207	d120206	d120205
1-3	Amb 200 400	40, 0.025, 0.04	d100901	d100902	d100905	d100906
				d100910	d100909	d100907
				d100913	d100912	d100911
1-2	Amb 200 400	30, 0.025, 0.04	d9-20-1	d9-20-2	d9-20-3	d9-20-4
				d9-20-5	d9-20-6	d9-20-7
				d9-20-8	d9-20-10	d9-20-12
1-1	Amb 200 400	20, 0.025, 0.04	dc054	dc068	dc065	
				dc081	dc082	
				dc083	dc084	

Note : Data for Configs 1-6 & 1-9 may have some problem.

Table A17. DC flow resistance data files for 12 lbf 0.5" deep T-Foam bulk panels.

Configuration	Temp °F	Facesheet Description, Porosity, S, Thickness, t, Hole Diameter d	File names for DC flow resistance Data at Different Grazing Flow Mach Number M. All files end with ".lsq"			
			M = 0.0	M = 0.30	M = 0.55	M = 0.70
Bulk Only	Amb		mtfoam.smt			
6-8	Amb	40, 0.04, 0.04	d020599000	d020599001	d020599002	d020599003
6-4	Amb 200 400	40, 0.025, 0.025	d101598000	d101598001 d101598006 d101598009	d101598002 d101598005 d101598008	d101598003 d101598004 d101598007
6-11		Linear, 10 Rayls	dc033199000	dc033199001	dc033199002	dc033199003
6-4143	Amb 200 400	40, 0.10, 0.07	dc527001	dc527002 dc527007 dc527010	dc527003 dc527006 dc527009	dc527004 dc527005 dc527008
6-6		40, 0.025, 0.08	dc041299000	dc041299001	dc041299002	dc041299003
6-9	Amb 200 400	40, 0.06, 0.04	dc514001	dc514002 dc514007 dc514010	dc514003 dc514006 dc514009	dc514004 dc514005 dc514008
6-3	Amb 200 400	40, 0.025, 0.04	d100198000	d100198001 d100198006 d100198009	d100198002 d100198005 d100198008	d100198003 d100198004 d100198007
6-2	Amb 200 400	30, 0.025, 0.04	dc730001	dc730002 dc730007 dc730010	dc730003 dc730006 dc730009	dc730004 dc730005 dc730008
6-1	Amb 200 400	20, 0.025, 0.04	d424001	d424002 d424007 d424010	d424003 d424006 d424009	d424004 d424005 d424008

Table A18. DC flow resistance data files for SDOF type panels.

Configur- ation	Temp °F	Facesheet Description, Porosity, S, Thickness, t, Hole Diameter d	File names for DC flow resistance Data at Different Grazing Flow Mach Number M. All files end with “.lsq”			
		S, %, t, in, d, in	M = 0.0	M = 0.30	M = 0.55	M = 0.70
t1-8	Amb	40, 0.04, 0.04	dc030899000	dc030899001	dc030899002	dc030899003
t1-4121	Amb	40, 0.10, 0.04	dc041599000	dc041599001	dc041599002	dc041599003
t1-5	Amb	40, 0.025, 0.06	dc041699000	dc041699001	dc041699002	dc041699003
t1-11	Amb	Linear, 10 Rayls	dc040999000	dc040999001	dc040999002	dc040999003
t1-4143	Amb	40, 0.10, 0.07	dc032999000	dc033099001	dc033099002	dc033099003
t1-6	Amb	40, 0.025, 0.08	dc040799000	dc040799001	dc040799002	dc040799003
t1-9	Amb	40, 0.06, 0.04	dc032499000	dc032499001	dc032499002	dc032499003
t1-3	Amb	40, 0.025, 0.04	dc1250	d111302	d111303	d111305
t1-2	Amb	30, 0.025, 0.04	d021999000	d021999001	d021999002	d021999003
t1-1	Amb 200 400	20, 0.025, 0.04	d10-1-1	d10-1-3 d10-1-11 d10-1-12	d10-1-4 d10-1-10 d10-1-13	d10-1-5 d10-1-9 d10-1-14
2	Amb 200 400	9, 0.025, 0.04	d102901	d102903 d102908 d102913	d102904 d102907 d102912	d102905 d102906 d102910
4	Amb 200 400	15, 0.025, 0.04	dc110	dc100 dc103 dc106	dc099 dc104 dc107	dc101 dc105 dc108
11	Amb 200 400	9, 0.025, 0.08	d4101	d4102 d4107 d4110	d4103 d4106 d4109	d4104 d4105 d4108
12	Amb	40, 0.01, 0.04	d415001	d415002	d415003	d415004
15	Amb 200 400	40, 0.06, 0.04	d010801	d121602 d121607 d010804	d121603 d121606 d010803	d121604 d121605 d010802
17*		30, 0.10, 0.04	d011299000	d011299001	d011299002	d011299003
25	Amb 200 400	Linear, 85 Rayls	d091598000	d091598001 d091598006 d091598009	d091598002 d091598005 d091598008	d091598003 d091598004 d091598007

Note: Config17 (SDOF) data may have some problem.



## REFERENCES

1. Salikuddin M., "Acoustic characteristics of various treatment panel designs for HSCT ejector liner acoustic technology development program". 1999, HSR/CPC Coordination Memo No: GE99-025-N.
2. Salikuddin M., "Development of a liner design methodology and relevant results of acoustic suppression in the farfield for mixer-ejector nozzles". 1999, HSR/CPC Coordination Memo No: GE99-032-N.
3. Rice, E. J. and Salikuddin M., "Models for acoustically treated mixer-ejector suppressors and the related acoustic impedance models for bulk absorbers with heated grazing flow". 1999, HSR/CPC Coordination Memo No: GE99-033-N.

REPORT DOCUMENTATION PAGE			Form Approved OMB No. 0704-0188	
Public reporting burden for this collection of information is estimated to average 1 hour per response, including the time for reviewing instructions, searching existing data sources, gathering and maintaining the data needed, and completing and reviewing the collection of information. Send comments regarding this burden estimate or any other aspect of this collection of information, including suggestions for reducing this burden, to Washington Headquarters Services, Directorate for Information Operations and Reports, 1215 Jefferson Davis Highway, Suite 1204, Arlington, VA 22202-4302, and to the Office of Management and Budget, Paperwork Reduction Project (0704-0188), Washington, DC 20503.				
1. AGENCY USE ONLY (Leave blank)		2. REPORT DATE September 2006		3. REPORT TYPE AND DATES COVERED Final Contractor Report
4. TITLE AND SUBTITLE  Acoustic Characteristics of Various Treatment Panel Designs Specific to HSCT Mixer-Ejector Application			5. FUNDING NUMBERS  WBS 984754.02.07.03.04.01 NAS3-26617 NAS3-27235	
6. AUTHOR(S)  M. Salikuddin, K. Kinzie, D.D. Vu, L.E. Langenbrunner, and G.T. Szczepkowski				
7. PERFORMING ORGANIZATION NAME(S) AND ADDRESS(ES)  General Electric Aircraft Engines One Neumann Way Cincinnati, Ohio 45215-1915			8. PERFORMING ORGANIZATION REPORT NUMBER  E-15680	
9. SPONSORING/MONITORING AGENCY NAME(S) AND ADDRESS(ES)  National Aeronautics and Space Administration Washington, DC 20546-0001			10. SPONSORING/MONITORING AGENCY REPORT NUMBER  NASA CR-2006-214401	
11. SUPPLEMENTARY NOTES  Project manager, Clayton L. Meyers, Aeronautics Division, NASA Glenn Research Center, organization code PRV, 216-433-3882.				
12a. DISTRIBUTION/AVAILABILITY STATEMENT  Unclassified - Unlimited Subject Category: 07  Available electronically at <a href="http://gltrs.grc.nasa.gov">http://gltrs.grc.nasa.gov</a> This publication is available from the NASA Center for AeroSpace Information, 301-621-0390.			12b. DISTRIBUTION CODE	
13. ABSTRACT (Maximum 200 words)  The development process of liner design methodology is described in several reports. The results of the initial effort of concept development, screening, laboratory testing of various liner concepts, and preliminary correlation (generic data) are presented in a report Acoustic Characteristics of Various Treatment Panel Designs for HSCT Ejector Liner Acoustic Technology Development Program. The second phase of laboratory test results of more practical concepts and their data correlations are presented in this report (product specific). In particular, this report contains normal incidence impedance measurements of several liner types in both a static rig and in a high temperature flow duct rig. The flow duct rig allows for temperatures up to 400 °F with a grazing flow up to Mach 0.8. Measurements of impedance, DC flow resistance, and in the flow rig cases, impact of the liner on boundary layer profiles are documented. In addition to liner rig tests, a limited number of tests were made on liners installed in a mixer-Ejector nozzle to confirm the performance of the liner prediction in an installed configuration.				
14. SUBJECT TERMS  Propulsion systems (aircraft)			15. NUMBER OF PAGES 451	
			16. PRICE CODE	
17. SECURITY CLASSIFICATION OF REPORT Unclassified	18. SECURITY CLASSIFICATION OF THIS PAGE Unclassified	19. SECURITY CLASSIFICATION OF ABSTRACT Unclassified	20. LIMITATION OF ABSTRACT	





